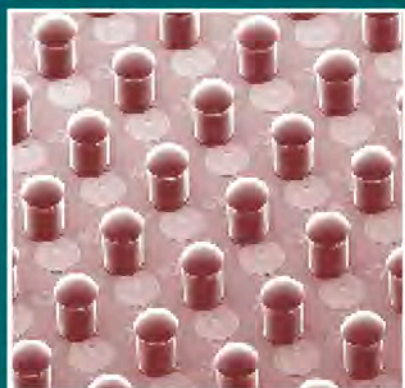


WOODHEAD PUBLISHING IN MATERIALS



# Nanolithography and patterning techniques in microelectronics

Edited by David Bucknall



WP

# Nanolithography and patterning techniques in microelectronics



# Nanolithography and patterning techniques in microelectronics

---

Edited by  
David G. Bucknall

**Woodhead Publishing and Maney Publishing  
on behalf of  
The Institute of Materials, Minerals & Mining**

**CRC Press  
Boca Raton Boston New York Washington, DC**

**WOODHEAD PUBLISHING LIMITED**  
Cambridge England

Woodhead Publishing and Maney Publishing Limited on behalf of the Institute of Materials, Minerals & Mining

Published by Woodhead Publishing Limited, Abington Hall, Abington  
Cambridge CB1 6AH, England  
www.woodheadpublishing.com

Published in North America by CRC Press LLC, 6000 Broken Sound Parkway, NW,  
Suite 300, Boca Raton, FL 33487, USA

First published 2005, Woodhead Publishing Limited and CRC Press LLC  
© 2005, Woodhead Publishing Limited  
The authors have asserted their moral rights.

This book contains information obtained from authentic and highly regarded sources. Reprinted material is quoted with permission, and sources are indicated. Reasonable efforts have been made to publish reliable data and information, but the authors and the publishers cannot assume responsibility for the validity of all materials. Neither the authors nor the publishers, nor anyone else associated with this publication, shall be liable for any loss, damage or liability directly or indirectly caused or alleged to be caused by this book.

Neither this book nor any part may be reproduced or transmitted in any form or by any means, electronic or mechanical, including photocopying, microfilming and recording, or by any information storage or retrieval system, without permission in writing from the publishers.

The consent of Woodhead Publishing Limited and CRC Press LLC does not extend to copying for general distribution, for promotion, for creating new works, or for resale. Specific permission must be obtained in writing from Woodhead Publishing Limited or CRC Press LLC for such copying.

Trademark notice: Product or corporate names may be trademarks or registered trademarks, and are used only for identification and explanation, without intent to infringe.

British Library Cataloguing in Publication Data

A catalogue record for this book is available from the British Library.

Library of Congress Cataloging in Publication Data

A catalog record for this book is available from the Library of Congress.

Woodhead Publishing Limited ISBN-13: 978-1-85573-931-4 (book)

Woodhead Publishing Limited ISBN-10: 1-85573-931-3 (book)

Woodhead Publishing Limited ISBN-13: 978-1-84569-090-8 (e-book)

Woodhead Publishing Limited ISBN-10: 1-84569-090-7 (e-book)

CRC Press ISBN-10: 0-8493-3447-0

CRC Press order number: WP3447

The publishers' policy is to use permanent paper from mills that operate a sustainable forestry policy, and which has been manufactured from pulp which is processed using acid-free and elementary chlorine-free practices. Furthermore, the publishers ensure that the text paper and cover board used have met acceptable environmental accreditation standards.

Project managed by Macfarlane Production Services, Markyate, Hertfordshire  
(macfarl@aol.com)

Typeset by Replika Press Pvt Ltd, India

Printed by T J International Limited, Padstow, Cornwall, England

# Contents

---

<i>Contributor contact details</i>	<i>ix</i>	
<i>Preface</i>	<i>xiii</i>	
1	Block copolymer nanolithography	1
	M TRAWICK, University of Richmond, USA, D ANGELESCU, Schlumberger-Doll Research, USA, P CHAIKIN and R REGISTER, Princeton Institute for the Science and Technology of Materials, USA	
1.1	Introduction	1
1.2	Block copolymer self-assembly	2
1.3	Methods for pattern transfer	10
1.4	Approaches to long-range ordering	23
1.5	Conclusion	32
1.6	Acknowledgments	33
1.7	References	33
2	Surface-induced structure formation of polymer blends	39
	R J COMPOSTO and H-J CHUNG, University of Pennsylvania, USA	
2.1	Introduction	39
2.2	Background	41
2.3	Experimental techniques	44
2.4	Surface-induced patterns of binary polymer blends	48
2.5	Future trends	63
2.6	Conclusion	64
2.7	References	65
3	Rapid prototyping of functional microfabricated devices by soft lithography	76
	D B WOLFE and G M WHITESIDES, Harvard University, USA	
3.1	Introduction	76

3.2	Developments in soft lithographic techniques	77
3.3	Conclusions and outlook	106
3.4	Further information	108
3.5	Acknowledgements	109
3.6	References	109
4	Chemomechanical surface modification of materials for patterning	120
	M LINFORD, R DAVIS, S MAGLEBY, L HOWELL, G JIANG and C THULIN, Brigham Young University, USA	
4.1	Introduction	120
4.2	The chemistry of scribed silicon	123
4.3	Chemomechanical nanopatterning of silicon	128
4.4	Patterning silicon at the micron scale	133
4.5	Applications I: Preparation of surfaces for matrix assisted laser desorption/ionization (MALDI) mass spectrometry	136
4.6	Applications II: Preparation of masters for microcontact printing ( $\mu$ CP) by scribing	144
4.7	Future trends	144
4.8	References	148
5	Patterning of polymer thin films	155
	P J YOO, K Y SUH, Y S KIM, D-Y KHANG and H H LEE, Seoul National University, Korea	
5.1	Introduction	155
5.2	Patterning by capillary lithography	155
5.3	Influence of dispersion forces on patterning	165
5.4	Patterning by polymer dewetting	168
5.5	Patterning by stress for metal/polymer bilayers	175
5.6	References	181
6	Ion beam patterning	184
	G W GRIME, University of Surrey, UK	
6.1	Introduction	184
6.2	Ion-solid interactions	184
6.3	The use of ion beams for microfabrication	197
6.4	Ion beam equipment	202
6.5	Specific techniques and examples	206
6.6	Future trends	210
6.7	Sources of further information and advice	214
6.8	References	215

7	Nanofabrication by shadow deposition through nanostencils	218
	J BRUGGER, Ecole Polytechnique Fédérale de Lausanne, Switzerland and G KIM, Kyungpook National University, Korea	
7.1	Introduction	218
7.2	Surface patterning by deposition through stencils	220
7.3	Ultra-thin solid-state membranes	224
7.4	Nanofabrication using nanostencils	227
7.5	Limitations of stencil technology	232
7.6	Conclusion	233
7.7	Acknowledgements	234
7.8	References	235
8	Photolithography beyond the diffraction limit	238
	G J LEGGETT, University of Sheffield, UK	
8.1	Introduction	238
8.2	Photochemistry of self-assembled monolayers	240
8.3	Near-field optics and lithography	247
8.4	Near-field scanning optical microscopy	249
8.5	Lithography based upon near-field scanning optical microscopy	250
8.6	Towards the future: apertureless NSOM	260
8.7	Acknowledgements	262
8.8	References	262
9	Ink-jet printing as a tool in manufacturing and instrumentation	267
	D WALLACE and D HAYES, MicroFab Technologies, Inc., USA	
9.1	Introduction	267
9.2	Electronics manufacturing applications	271
9.3	Display manufacturing applications	278
9.4	Photonics applications	280
9.5	Integrated electro-optic assemblies	282
9.6	Biomedical manufacturing and instrumentation applications	285
9.7	Implementation considerations	291
9.8	Equipment	293
9.9	Future trends	294
9.10	Conclusion	295
9.11	References	296

viii	Contents	
10	Actuators and patterns for microfluidic control	299
	A AJDARI and P TABELING, Ecole Supérieure de Physique et de Chimie Industrielles, France	
10.1	Introduction	299
10.2	PDMS actuators and microfluidics	300
10.3	Nanopatterning for microfluidics	307
10.4	Conclusion	317
10.5	Acknowledgements	318
10.6	References	318
11	Manipulation of biomolecules and reactions	320
	T THORSEN, Massachusetts Institute of Technology, USA	
11.1	Introduction	320
11.2	Manipulation and sorting of biomolecules	321
11.3	Microfluidic tools for molecular biology	334
11.4	Future trends	339
11.5	Sources of further information and advice	340
11.6	References	341
12	Nonlithographic patterning: application of inkjet printing in organic-based devices	349
	Y YOSHIOKA and G E JABBOUR, Arizona State University, USA	
12.1	Introduction	349
12.2	Inkjet printing technology	352
12.3	Design aspects of inkjet printing	353
12.4	Inkjet anode patterning of OLEDs	357
12.5	Acknowledgements	367
12.6	References	367
13	High-resolution printing techniques for plastic electronics	373
	G BLANCHET, DuPont Central Research and J ROGERS, University of Illinois and Beckman Institute, USA	
13.1	Introduction	373
13.2	Contact printing with high-resolution stamps	374
13.3	Thermal transfer printing	389
13.4	Conclusion	395
13.5	Acknowledgements	396
13.6	References	396
	Index	399

## Contributor contact details

---

(\* = main contact)

### Chapter 1

Dr M. Trawick  
Department of Physics  
University of Richmond  
Richmond  
VA 23173  
USA

Dr D. Angelescu  
Schlumberger-Doll Research  
36 Old Quarry Road  
Ridgefield  
CT 06877  
USA

Professor R. Register\*  
Department of Chemical Engineering  
The Engineering Quadrangle  
Princeton University  
Princeton  
NJ 08544-5263  
USA

E-mail: [register@princeton.edu](mailto:register@princeton.edu)

Dr P. Chaikin  
Department of Physics  
Princeton University  
Princeton  
NJ 08544-5263  
USA

### Chapter 2

Professor R.J. Composto\* and  
Dr H-J. Chung  
Department of Materials Science  
University of Pennsylvania  
Philadelphia  
PA 19104-6272  
USA

E-mail: [composto@lrsn.upenn.edu](mailto:composto@lrsn.upenn.edu)

### Chapter 3

Dr D.B. Wolfe and Professor  
G.M. Whitesides\*  
Department of Chemistry and  
Chemical Biology  
Harvard University  
12 Oxford Street  
Cambridge  
MA 02138  
USA

E-mail: [gwhitesides@gmwgroup.harvard.edu](mailto:gwhitesides@gmwgroup.harvard.edu)

## Chapter 4

Professor M. Linford\*, Dr R. Davis,  
Dr S. Magleby, Dr L. Howell,  
Mr G. Jiang and Dr C. Thulin  
Department of Chemistry and  
Biochemistry  
Brigham Young University  
Provo  
UT 84602  
USA

E-mail: [mrlinford@chem.byu.edu](mailto:mrlinford@chem.byu.edu)

## Chapter 5

Dr P.J. Yoo, Dr K.Y. Suh, Dr Y.S. Kim,  
Dr D-Y Khang and Professor H.H.  
Lee\*  
School of Chemical Engineering  
Seoul National University  
Seoul 151-744  
Korea

E-mail: [honghlee@snu.ac.kr](mailto:honghlee@snu.ac.kr)

## Chapter 6

Dr G.W. Grime  
Department of Physics  
University of Surrey  
Guildford  
Surrey GU2 7XH  
UK

E-mail: [g.grime@surrey.ac.uk](mailto:g.grime@surrey.ac.uk)

## Chapter 7

Professor J. Brugger\*  
Microsystemes Laboratory  
Ecole Polytechnique Federale de  
Lausanne (EPFL)  
Microtechnique (Batiment Station  
17 BM)  
CH - 1015 Lausanne  
Switzerland

E-mail: [juergen.brugger@epfl.ch](mailto:juergen.brugger@epfl.ch)

Professor G. Kim  
School of Mechanical Engineering  
Kyungpook National University  
Daegu 702-701  
Republic of Korea

E-mail: [gyuman.kim@knu.ac.kr](mailto:gyuman.kim@knu.ac.kr)

## Chapter 8

Professor G.J. Leggett  
Department of Chemistry  
University of Sheffield  
Brook Hill  
Sheffield S3 7HF  
UK

E-mail: [graham.leggett@sheffield.ac.uk](mailto:graham.leggett@sheffield.ac.uk)

## Chapter 9

Dr D. Wallace\* and Dr D. Hayes  
MicroFab Technologies, Inc.  
1104 Summit Ave  
Suite 110  
Plano, TX 75074  
USA

E-mail: [dwallace@microfab.com](mailto:dwallace@microfab.com)  
[www.microfab.com](http://www.microfab.com)

## Chapter 10

Dr A. Ajdari and Professor  
P. Tabeling\*  
Laboratoire Théorie et  
Microfluidique  
UMR 7083 CNRS-ESRCI  
Ecole Supérieure de Physique et de  
Chimie Industrielle  
10 rue Vauquelin  
75231 Paris  
France  
E-mail: patrick.tabeling@espci.fr

## Chapter 11

Dr T. Thorsen  
Massachusetts Institute of Technology  
Department of Mechanical  
Engineering  
77 Massachusetts Ave  
Cambridge  
MA 02139  
USA  
E-mail: thorsen@mit.edu

## Chapter 12

Dr Y. Yoshiooka and Dr G.E. Jabbour\*  
Research and Development, Director  
Flexible Display Center  
Department of Chemical and  
Materials Engineering  
Arizona State University  
ASU Research Park  
7700 S. River Parkway  
Tempe  
AZ 85284  
USA  
E-mail: jabbour@asu.edu

## Chapter 13

Dr G Blanchet  
DuPont Central Research  
Wilmington  
DE 19880  
USA  
Professor J. Rogers\*  
3355 Beckman Institute  
University of Illinois  
405 N. Matthews Ave  
Urbana  
IL 61801  
USA  
E-mail: jrogers@uiuc.edu



## Preface

---

The foundation of modern day lithography dates back to the Tang dynasty (618–906 AD). During this period printing using inked blocks cut from wood was first invented. The first printing known was patterning textiles and creation of short religious texts, although it did not take long before the earliest known book was printed in China in 868. The technology advanced with the introduction of moveable type in the 1040s and two colour printing as early as 1340. The next most significant development in transfer technology did not occur until 1798 when Alois Senefelder discovered the principle of ‘lithography’, a term derived from the Greek for ‘writing on stone’. Using porous stone surfaces, Senefelder created a design on the stone surface using grease, and after proper treatment and inking he was able to transfer an exact copy of the patterned (greased) areas onto a sheet of paper. In 1822 Nicéphore Niepce managed to copy an etched print onto a glass plate coated by bitumen dissolved in lavender oil. After several hours exposure to sunlight through a mask, the unshaded bitumen areas became hard. By comparison the shaded areas were unaffected and were easily washed away with a turpentine-lavender oil mixed solvent. A plate developed in this way by Niepce and used by Lemaitre in 1827 to make an etched copy of an engraving, is the earliest known example of photolithography and chemical milling to produce pattern transfer. Those who are familiar with photolithography will note that this approach corresponds to negative resist photolithography. Clearly then Niepce can be considered to be the true father of modern photolithography. The accuracy of feature size achieved in the 1820s was only 0.5–1 mm and the technique did not advance very rapidly until the 1960s when the microelectronics industry adopted it as a route to creating transistor based technologies. In 1961 the feature size of multiple transistors etched into Si was only 5  $\mu$ m, however, demand for ever smaller feature sizes led to continual developments in photolithography. The limitation in feature size achievable through photolithography is largely dominated by the wavelength of the light used. Diffraction effects from the edge of the photomask leads to blurring of the replicated image compared to the sharp features of the original mask. However, as the methods for using shorter and shorter wavelengths

were adopted to overcome the optical diffraction limitations, creation of ever smaller feature size structures has meant that feature sizes of approximately 100 nm are currently possible using X-ray or extreme UV wavelengths. This relentless reduction of feature size was first noted in 1965 by Gordon Moore of IBM who observed that the feature size of a single transistor reduced by approximately 50% every 12 months, although in 1975 he revised this to 24 months (although 18 months is more widely quoted). This reduction in feature size has become known as Moore's law and indeed the size of transistors has indeed followed the same predicted trend for the last 30 years.

Despite all these advances, a majority of these techniques have been developed specifically with the needs of the electronics and MEMs industries in mind. In this respect, the processes used are optimized for planar substrates and utilize many materials which are largely not bio-compatible. In addition, the use of short wavelength sources and multi-step processes to build up the desired architectures has meant that the equipment and resources required to produce these structures are a massive financial investment, only reachable by the largest global industries. The use of these 'mainstream' or 'conventional' lithographic approaches is in many cases prohibitive to creating a wide range of fabricated structures and devices, where the demands imposed by the electronics industry are no longer valid. In such cases, the limiting factors seem to all fall into one or more of three key areas; the immense costs involved, bio-incompatibility, and requirement for non-planar surfaces. To overcome these short-comings whole new areas of lithography, in the broadest sense of its meaning, are being developed that cover a wide range of alternative approaches to create defined patterns and structures. Arguably the most elegant of these approaches that have been explored, not only because of its simplicity but also through minimal human intervention, is the exploitation of molecular self-assembly. The most supreme examples of this approach are those observed in nature, where bio-molecular self-assembly create an infinite variety of elegant and complex structural architectures from the simplest of building blocks. Only now are we beginning to understand how to adapt these methods to our own needs. In recent years the number of widely differing approaches reported in the literature to create both micro- and nano-structured materials has exploded. This book attempts to capture some of the more important and most exciting of these 'non-conventional' lithographic methods and how they can be applied to device fabrication. The variety of methods described in this book, range from molecular self-assembly, through to larger length scale methods such as soft-lithography, which in some ways brings the technological development full circle to the historical wood block printing methods first exploited well over a millennium ago during the Tang dynasty.

David G. Bucknall  
Atlanta, USA

# Block copolymer nanolithography

---

M TRAWICK, University of Richmond, USA,  
D ANGELESCU, Schlumberger-Doll Research, USA,  
P CHAIKIN and R REGISTER, Princeton Institute for the  
Science and Technology of Materials, USA

## 1.1 Introduction

Block copolymer lithography is based on the self-assembly of block copolymer molecules into periodic microdomains, on the 10 to 100 nanometer length scale. In contrast to conventional photolithography, which has the ability to reproduce an arbitrary pattern of light that has been projected through a pre-patterned photomask, block copolymer lithography is limited to reproducing only those periodic patterns generated by the self-assembly of block copolymer molecules. The block copolymers thus function as templates in these processes; the structures they form are lithographically transferred into other materials such as metals or semiconductors to form finished devices, typically arrays of dots or lines of one material on a substrate of different material.

Although the number of different structures that can be generated this way is limited, for those structures that can be made, block copolymer lithography presents an attractive strategy for economically accessing large-area, dense arrays of nanoscale features. Starting from thin-film block copolymer templates it is now possible to use semiconductor-compatible techniques to obtain periodically patterned semiconductors or insulators [1–3], arrays of metallic [4], quantum [5] and magnetic dots [6, 7], or thin metal lines [8, 9]. An indication of existing commercial interest in block copolymer lithography is the recent development of ultra-dense memory devices such as magnetic hard drives [7] and FLASH memory chips [10] based on this technology.

The next section of this chapter (1.2) describes some of the nanoscale patterns that can be generated by block copolymer self-assembly, and how the bulk morphologies are modified by polymer-substrate interactions in thin films. The following section (1.3) describes several strategies for lithographically transferring these patterns into other materials, e.g., so as to produce an array of metal or semiconductor dots. The final section of this chapter (1.4) describes a number of approaches for controlling the orientation

and increasing the long-range order of the periodic patterns generated by block copolymer self-assembly prior to pattern transfer.

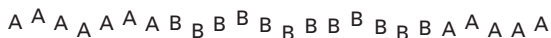
## 1.2 Block copolymer self-assembly

Several excellent books and review articles have recently been devoted to the chemistry and physics of block copolymers [11–14], to which the interested reader is directed; only a brief overview will be presented here. A ‘block’ is a sequence of identical molecular building blocks (monomers) covalently bound together; a linear block copolymer consists of two or more chemically distinct blocks (e.g., polystyrene and polyisoprene) covalently linked end-to-end, forming a single chain-like molecule. Many of the copolymers we will discuss in this chapter are linear diblock copolymers, consisting of two such blocks, generically denoted as species ‘A’ and ‘B’ (Fig. 1.1(a)). More complex molecules are also possible, such as copolymers consisting of two different species joined end-to-end in three separate blocks (ABA triblock copolymers, Fig. 1.1(b)) or three different species joined end-to-end (ABC triblock terpolymers, Fig. 1.1(c)). Just as oil and vinegar tend to separate in a salad dressing, the constituent blocks of a block copolymer may wish to separate from each other; however, the molecular connectivity constraint imposed by linking the blocks together prevents the two blocks from separating macroscopically like the salad dressing does. Instead, the material may self-assemble into ‘microdomains’ (or ‘nanodomains’) formed by the two blocks, with dimensions dictated by the polymer molecule’s size (typically, 10 to 100 nm).

In bulk, diblock copolymers can self-assemble into lamellar, cylindrical, or spherical microdomain morphologies, as shown in Fig. 1.2. To a useful first approximation, the microdomain structure that prevails from among these three is dictated by the relative volume fractions of the two blocks, independent of the polymer species. For example, with a 1:1 A:B ratio by volume, lamellae generally form; at a 3:1 A:B ratio, cylinders of B form and



(a)

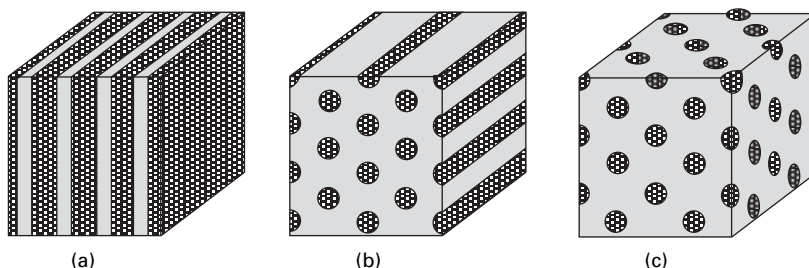


(b)



(c)

1.1 Schematic diagram of (a) an AB diblock copolymer, (b) an ABA triblock copolymer, and (c) an ABC triblock terpolymer.



1.2 Three equilibrium phases of a diblock copolymer: (a) lamellae, (b) cylinders, and (c) spheres. Microdomains rich in the two different blocks are denoted as dark (minority block) and light (majority block).

pack hexagonally in a matrix of A; and at ratios of 6:1 and above, spheres of B form on a body-centered-cubic lattice in an A matrix. A fourth morphology, the gyroid phase, is now established to be the stable phase in bulk over a narrow range of compositions between cylinders and lamellae [15, 16]; however, the gyroid phase apparently reconstructs (to lamellae, in at least one case [17]) in the very thin films desired for nanolithography, and will not be discussed further here. The bulk phase behavior of ABA triblock copolymers is similar to that of diblocks, in that these systems can also form lamellae, cylinders, and spheres [11], while ABC triblock terpolymers can form quite intricate morphologies, such as spheres of species A embedded in cylinders of B embedded in a matrix of C [14].

The precise dividing lines between these phases – where a small alteration in A:B ratio during polymer synthesis causes a different phase to prevail – depends to second order on the ‘stiffness’ (statistical segment length) of the two blocks [18], and on the strength of the repulsive interaction between the blocks [11, 16]. The strength of interblock repulsion is effectively gauged through the product  $\chi N$ , where  $\chi$  is the Flory interaction parameter (representing the strength of the repulsion between individual A and B monomer units), and  $N$  is the degree of polymerization. At sufficiently low  $\chi N$ , the two blocks will mix rather than microphase separate; since  $\chi$  typically decreases with increasing temperature, it is possible in carefully designed cases to induce a transformation from one of the microphase-separated morphologies in Fig. 1.2 to the mixed state, an order-disorder transition (ODT), at a temperature  $T_{\text{ODT}}$ . Although short-range density correlations may persist above  $T_{\text{ODT}}$ , all long-range order is destroyed. Clearly  $T_{\text{ODT}}$  is a sensitive function of  $N$ , and it can thus be adjusted over a wide range for a given chemistry (A, B combination) and A:B ratio simply by changing the polymer’s chain length.

For each of the morphologies shown in Fig. 1.2, the microdomain patterns formed are periodic; the lattice constant  $\lambda$ , typically tens of nanometers, can be controlled by adjusting the length of the polymer chains during synthesis ( $\lambda \sim N^{2/3}$  in the so-called ‘strong segregation limit’ [11, 19]). The period  $\lambda$

also increases with the strength of intersegmental repulsion, ideally as  $\chi^{1/6}$  [19]; the densities and statistical segment lengths of polymers are temperature-dependent as well, though generally less so than  $\chi$ , such that  $\lambda$  generally decreases weakly with increasing temperature [20].

### 1.2.1 Glass transition temperature ( $T_g$ )

For noncrystallizable polymers consisting of a single monomer unit ('homopolymers'), the principal thermal transition of interest is the glass transition, where upon heating, the material changes from a vitreous solid to a viscous or rubbery liquid. This transition is critically important in lithographically patterned thin films as well, for unless the material is crosslinked, heating it above  $T_g$  will permit flow and eradicate the pattern. Table 1.1 lists representative values of  $T_g$  for several of the polymers mentioned in this chapter.

Microphase-separated block copolymers typically show two glass transitions, at temperatures near those of the homopolymers corresponding to their constituent blocks. For the material to flow freely, or for the block copolymer molecules to diffuse appreciably, the material must be heated above both  $T_g$ s. With extended annealing above the upper  $T_g$ , the movement of individual polymer chains can lead to significant reordering of the microdomains they compose, with the rate accelerating with increasing temperature. Generally, the microdomain structure becomes more ordered over time, with grain size increasing and the density of lattice defects decreasing. However, a practical upper temperature limit is set by the thermal stability of the polymer, as all polymers will spontaneously undergo crosslinking or chain scission (or both) at sufficiently high temperatures.

*Table 1.1* Quasistatic glass transition temperatures for several amorphous homopolymers employed as constituents of block copolymers. From reference [21] except as indicated

Abbreviations	Chemical name	$T_g$ ( $^{\circ}\text{C}$ )
PB	high-1,4-polybutadiene	$-90^{\circ}$
PtBA	poly( <i>tert</i> -butylacrylate)	43
PnBMA	poly( <i>n</i> -butylmethacrylate)	20
PDMS	poly(dimethylsiloxane)	$-117$
PEP	poly(ethylene- <i>alt</i> -propylene)	$-59^{\text{a,c}}$
PI	high-1,4-polyisoprene	$-60^{\circ}$
PMMA	poly(methylmethacrylate)	105
PPMDSS	poly(pentamethyldisilylstyrene)	$100^{\text{b}}$
PS	Polystyrene	100
PVP	poly(2-vinylpyridine)	104

<sup>a</sup>From ref. [22].

<sup>b</sup>From ref. [23].

<sup>c</sup>Representative value, dependent on chemical microstructure.

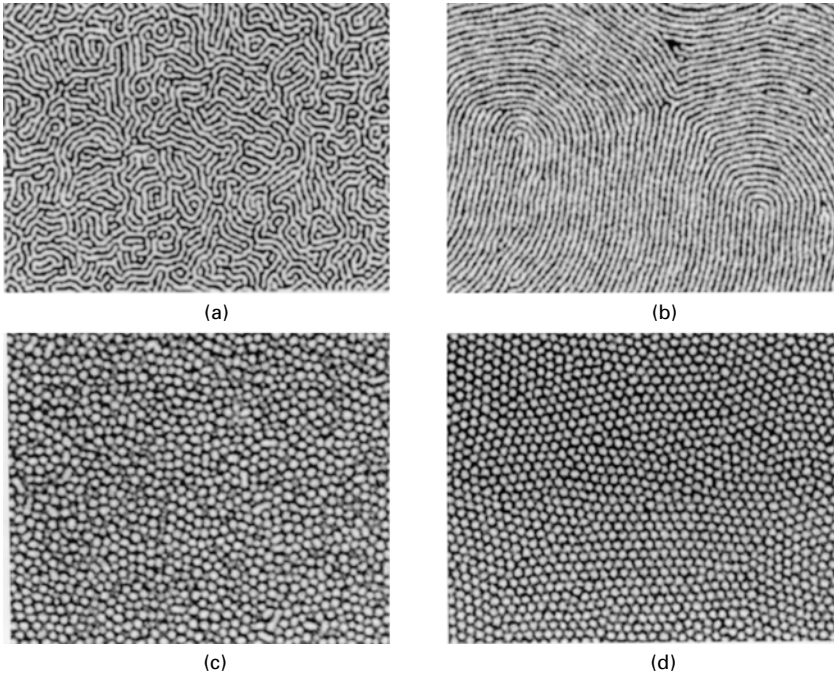
## 1.2.2 Block copolymer morphology in thin films

In lithographic applications, block copolymers are used as thin films [24], generally applied to a substrate by spin-coating from dilute solution. The phase behavior of block copolymers in thin films is actually far richer and more complex than in bulk; the many effects of the interfaces with both the substrate and the air remain active fields of experimental and theoretical investigation [25–27]. In the interest of brevity, we restrict our discussion here to only those interfacial effects that are likely to have a direct bearing on lithographic processing, specifically those effects that may be deliberately exploited and those that must be assiduously avoided.

For lithography, one generally wants only a single layer of periodic microdomains on a surface, as a two-dimensional template for pattern transfer. As a first approximation, the morphology of a particular block copolymer material in a thin film will often be the same as that in bulk. For example, a diblock copolymer which forms cylinders in bulk will generally form cylinders as a thin film as well. The primary effect of the substrate is on the orientation of the cylinders: if a substrate is coated with a layer of the polymer equal in thickness to the lattice spacing in bulk, and if both the substrate and the air interface are preferentially wetted by the majority block (that is, the interfacial energy between the majority block and both surfaces is less than that between the minority block and the surfaces), then the free energy of the system is minimized by forming a layer of cylinders oriented parallel to the surface, completely embedded within a matrix of the majority block. Any other orientation of the cylinders would lead to cylinders terminating at the two surfaces, increasing the free energy. Similar structures containing two, three, etc., layers of cylinders, oriented parallel to the substrate and stacked in a staggered fashion, are obtained for suitable (commensurate) film thicknesses.

Similar to the behavior seen in cylinders, a single-layer film of a sphere-forming diblock copolymer forms a two-dimensional triangular lattice of spheres covering the substrate; in thicker films, spheres stack above the interstices of the previous layer. For lamella-forming diblock copolymers, commensurate film thicknesses typically lead to lamellae oriented parallel to the substrate; such a film shows no in-plane features, and is thus uninteresting as a lithographic template.

As in bulk, annealing block copolymer thin films above  $T_g$  allows reordering of the microdomains they compose, with the film becoming more ordered over time. Figure 1.3(a) and (b) show scanning electron microscope images of a cylinder-forming polystyrene-polybutadiene (PS-PB) diblock copolymer both before (a) and after annealing above  $T_g$  [17]. In the annealed sample, the orientation of the cylinders is correlated over perhaps ten or twenty lattice constants, compared to at most two or three in the unannealed film. Figure 1.3(c) and (d) are of a polystyrene-polyisoprene (PS-PI) diblock that

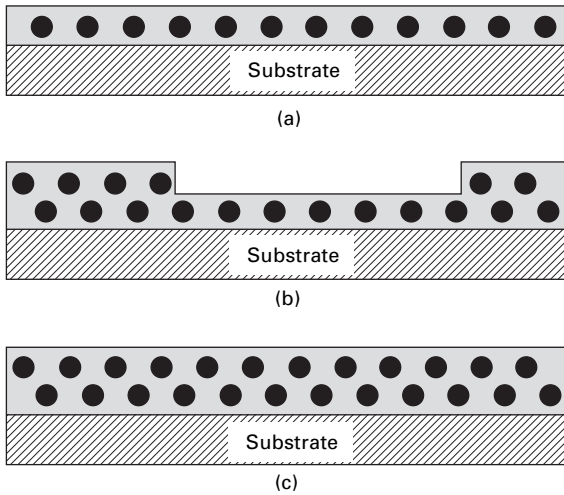


1.3 Scanning electron microscope images of polystyrene-polydiene diblock copolymer thin films; the polydiene domains are stained with  $\text{OsO}_4$  and thus appear bright in the images. Top: a cylinder-forming PS-PB diblock before (a) and after (b) thermal annealing above  $T_g$ . Bottom: a sphere-forming PS-PI diblock before (c) and after (d) thermal annealing [17].

forms spheres [17]. Again, after annealing the film forms a polygrain triangular lattice of spheres (d), with a grain size of about ten lattice constants, whereas the unannealed film in (c) is much more disordered. These correlation lengths would be expected to increase with additional annealing, leading to larger grains.

### 1.2.3 Islands, holes, and terraces

For film thicknesses incommensurate with an integral number of microdomain layers, the system does not form a laterally uniform fractional layer of cylinders (or spheres or lamellae); this would present a huge cost in free energy to the system, since as noted above, a given polymer (of given  $N$ ) has a very strongly preferred microdomain size at a given temperature. Instead, the film minimizes its free energy by spontaneously forming a series of terraces [26], so that the thickness of the film varies between the two nearest commensurate thicknesses, as shown in Fig. 1.4. If the average thickness of the film is just



**1.4** A schematic diagram of the cross-section of a block copolymer thin film, showing the effects of increasing average film thickness. The microdomains of the minority block, in black, are either spheres or cylinders shown in cross-section. (a) A commensurate film thickness with one complete layer of spheres or cylinders. (b) An incommensurate film thickness, depicting a single-layer 'hole' in an otherwise two-layer thick film. (c) A commensurate film thickness with two layers of spheres or cylinders.

above that needed to form a uniform single layer of microdomains, the film will be mostly a single layer of cylinders (or spheres or lamellae), but with some areas as 'islands' of two layers. If the thickness of the film is just under two layers, the film will be mostly two layers of spheres, with some areas as 'holes' that are one layer thick.

These islands and holes have an energy cost, since every terrace step increases the area of contact between the polymer film and the air. (The surface tension of the polymer tends to minimize this contact, and in the absence of microdomain structure would flatten the film to a uniform thickness.) Because of the energy cost of a terrace step due to surface tension, height differences across terraces are actually more gradual than the depictions in Fig. 1.4, with the film thickness changing over several lattice constants laterally. At these terrace steps, where the local film thickness lies between whole number multiples of the lattice constant, the size of the microdomains may differ slightly from their equilibrium size in bulk. In cases where one or two wetting layers are also present (see next section), the microdomain structure may even reconstruct at the borders of these terraces; cylinder-forming diblocks have been found to form spheres [28–30], short cylinders perpendicular to the substrate [30], and perforated lamellae [30] in regions where the local film thickness is incommensurate with the lattice constant.

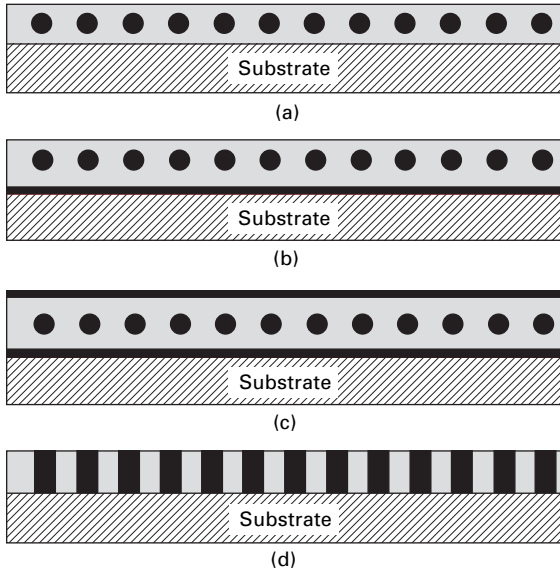
With annealing above  $T_g$ , the energy cost of the terraces is gradually reduced by a progressive coarsening of the islands or holes into larger and larger structures. (Diffusion of individual molecules can lead to mass transfer from one area of a film to another, allowing small islands to shrink and larger islands to grow.) In fact, when a film is first cast, its surface may initially be completely flat, with islands or holes developing only after long anneal times. Sometimes apparently random variations in film thickness of a few percent over micron length scales can be a precursor to island or hole formation, and may signal an incommensurate film thickness. Additionally, because of the temperature dependence of the lattice constant ( $\lambda \sim \chi^{1/6}$ ), films which are of a commensurate thickness at one temperature may spontaneously form islands or holes at another temperature.

For block copolymer lithography, islands and holes are a nuisance, and care must be taken to control the copolymer layer thickness so as to avoid them. Even if identifiable islands and holes do not form, the variations in film thickness that are their precursors can wreak havoc on later processing, for instance by leading to an unacceptable spread in the amount of time required to etch through a layer. In our experience, controlling film thickness is particularly challenging if there are any topographical features on the substrate with vertical dimensions on the same scale as the lattice constant. In such cases, surface tension can cause the copolymer film to be wicked up at the edges of tall features, increasing the film thickness right next to the feature while depleting the copolymer film in the local vicinity; these local nonuniformities can lead to island and hole formation locally even when the film thickness is optimal over most of the surface area.

#### 1.2.4 Other substrate interactions: wetting layers and neutral substrates

In thin films of sphere- and cylinder-forming diblocks, if either the substrate or the air has a strong preferential interaction with the minority rather than the majority block, the copolymer film forms a ‘wetting layer’ (or ‘brush layer’) at the interface [28, 31], as shown in Fig. 1.5. The minimum free energy is obtained for film thicknesses that allow for a whole number of domains (spheres or cylinders) plus a wetting layer at one or both interfaces. For other film thicknesses, the film again forms a series of terraces bounding either islands or holes, with the number of sphere or cylinder layers alternating between the two nearest whole numbers, and the wetting layers always preserved.

For lithography, wetting layers in block copolymer films are nuisances, though generally manageable. Wetting layers at the air interface make imaging somewhat more difficult [28], and can act as a diffusional resistance in wet chemical processing by hindering diffusion of reactants in and products out.



1.5 The effects of preferential substrate-polymer interactions. (a) The majority block preferentially wets both the substrate and air interfaces. (b) The minority block wets the substrate. (c) The minority block wets both interfaces. (d) The substrate is neutral, causing cylinders or lamellae to orient perpendicular to the substrate.

Wetting layers at either interface add more material to be etched through or removed during pattern transfer, but only in the case of polymers which leave a solid inorganic residue after etching (such as polydimethylsiloxane, PDMS, or polyferrocenyldimethylsilane, PFS) would such wetting layers constitute a serious complication, though usually still one which can be circumvented via a change in etching gases or conditions. However, the presence of a uniform layer of the block meant to be an 'etch stop' certainly has the potential to affect the fidelity of the pattern transfer.

Yet another behavior of diblock copolymer thin films can be observed in the cylindrical and lamellar phases if the substrate does not have any preferential interaction with either block, a so-called 'neutral substrate.' Naively, one might suspect that a cylindrical or lamellar film would have no preferred orientation on such a substrate, since the energetic cost of either interaction is the same. Russell and coworkers, however, have shown [32] that in such cases, the entropy of such a system is maximized (and thus the free energy minimized) when the cylinders or lamellae in the film are oriented perpendicular to the substrate, as shown in Fig. 1.5(d). They were able to realize a neutral surface by grafting to the substrate a thin layer of a random copolymer of styrene and methylmethacrylate (that is, with randomly alternating units of both species) with the same overall composition as the cylinder-forming PS-PMMA diblock copolymer which constituted the overlying film [33]. The

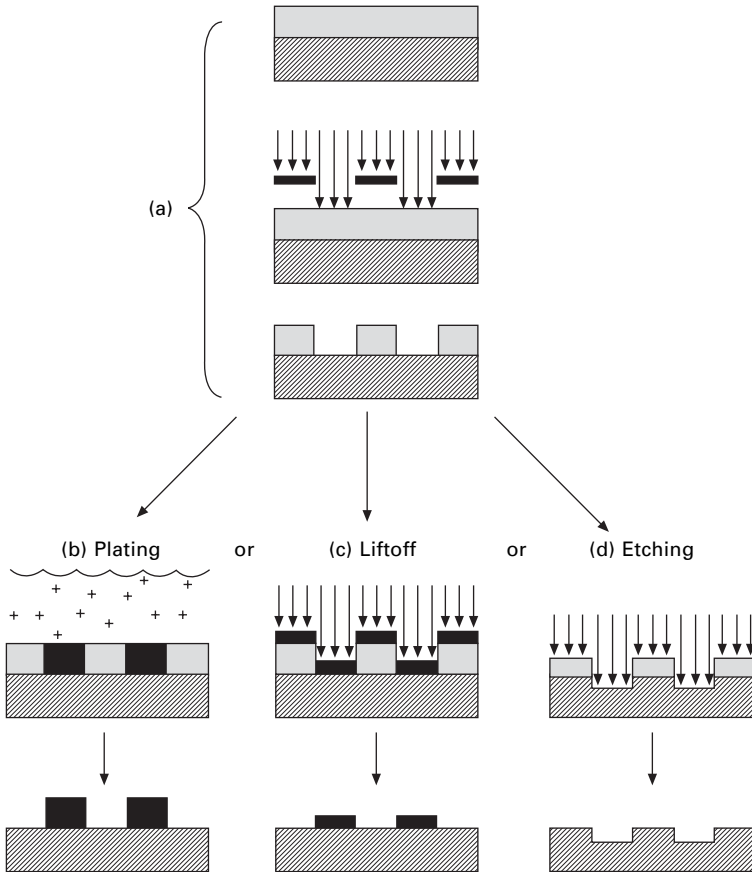
random copolymer remained at the substrate, presenting the block copolymer with a neutral surface.

For lithographic applications, since the microdomains formed by block copolymers are used as two-dimensional templates for pattern transfer, a triangular array of upright cylinders is topologically similar to a triangular array of spheres: both look like circles (or dots) from above. Similarly, an array of upright lamellae (perpendicular to the substrate) is similar to an array of cylinders oriented parallel to the surface: from above, both look like stripes. Each of these configurations has been successfully used for pattern transfer. However, there are several reasons why the perpendicularly oriented cylinders and lamellae are more desirable for lithographic processing than their counterparts. First, these films do not form islands or holes, because the perpendicular lamellae and cylinders may be of any height (and thus there is no preferred film thickness). They also do not form wetting layers at the neutral substrate surface. In fact, because these perpendicularly oriented structures ideally extend all the way to the substrate, any etching process that removes them exposes bare substrate, without the need for any additional etching of the majority component. Additionally, the microdomain walls are perpendicular to the surface, allowing for sharp contrast in pattern transfer. Most importantly, the high-aspect ratio of these microdomains makes additional processing (e.g., liftoff) easier, and facilitates high-aspect ratios in the final product, a goal which can be particularly challenging for pattern transfer at the nanoscale. The disadvantage, of course, is that a neutral surface must be prepared; the random copolymer approach used successfully for PS-PMMA is not readily extended to all interesting combinations of monomers.

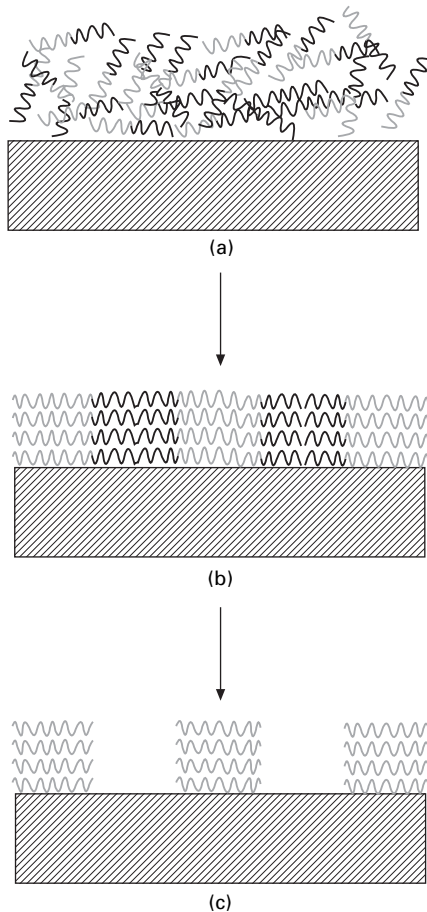
### 1.3 Methods for pattern transfer

In a standard photolithography process, illustrated in Fig. 1.6, a thin layer of a photosensitive polymer, or photoresist, is applied to a surface, for example by spin coating. One then selectively exposes some areas of the photoresist by shining light through a previously fabricated photomask. When washed in a developing solution, either the exposed areas (for a positive photoresist) or unexposed areas (for a negative photoresist) are preferentially dissolved away. The result is a patterned photoresist layer in which some areas of the original surface remain covered with photoresist, while other areas are left bare. At this stage, the pattern now in the photoresist layer can be transferred to other materials by such means as plating, liftoff, or etching, after which the remaining photoresist can be removed.

In block copolymer lithography, illustrated in Fig. 1.7, a surface is coated with a thin layer of a copolymer, which functions analogously to the photoresist. But rather than reproducing the pattern from a photomask, the block copolymer produces its own pattern through self-assembly into one of its equilibrium



**1.6 Standard photolithography and pattern transfer for a positive photoresist system.** (a) Exposure and developing. (b) Plating: the surface is exposed to a liquid containing metal ions, which are preferentially reduced and deposited on the bare areas. The preferential deposition is either due to chemical specificity (in which case the photoresist acts as a simple physical barrier), or, in the case of electroplating, a DC voltage is applied to the surface, in which case the photoresist acts as an electrical insulator. After plating, the photoresist is removed, typically by washing with a solvent. (c) Liftoff: a thin layer of another material is deposited over the entire surface, for instance by thermal evaporation or sputtering. When the photoresist is removed by washing with a solvent, material is left only where it was deposited on bare areas. (d) Etching: the photoresist is applied on top of a thin layer of another material. After patterning, the photoresist acts as a protective barrier to either wet chemical etching, or dry etching by a plasma (reactive ion etching, or RIE). After etching, the photoresist can be removed by a solvent.



**1.7 Block copolymer lithography.** (a) Disordered copolymer film as cast on a substrate. (b) After annealing, self-assembly into ordered microdomains. (c) After selective domain removal.

phases (i.e., periodic spheres, cylinders, or lamellae). One type of domain (e.g., either the cylinders or the matrix in a cylinder-forming block copolymer) is then selectively removed, analogous to the developing step in standard photolithography. This selective removal of one of the copolymer domains is the real crux of pattern transfer in block copolymer lithography, and can be accomplished in a variety of ways for different copolymer systems. It is this particular aspect of pattern transfer that will be the focus of this section.

Once one type of microdomain within the copolymer film has been selectively removed, pattern transfer can continue using either plating, liftoff, or etching techniques. In principle, these techniques are the same for both photolithography and block copolymer lithography, though in practice the smaller feature size of the latter can present some additional challenges. We

assume that the reader is familiar with these techniques, and therefore we will mention them only in passing, to concentrate better on issues unique to block copolymer lithography.

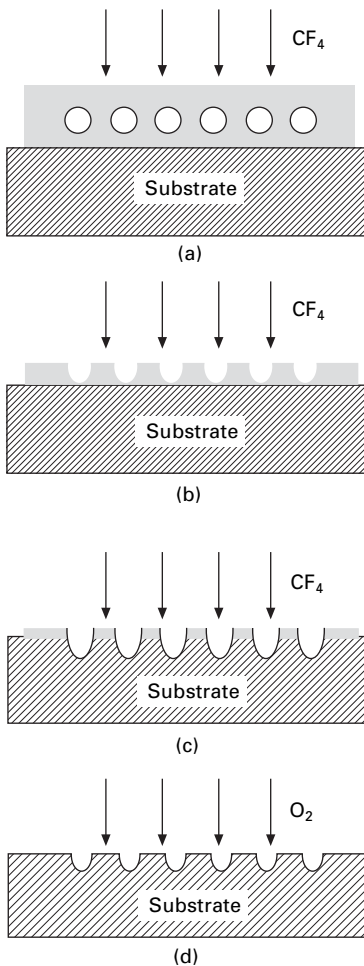
We will further focus our discussion in this section by noting that, for single-layer block copolymer films, domain removal techniques are often equally effective for all morphologies. One might be concerned that, for example, diffusion of reactants through a glassy polystyrene matrix to reach polyisoprene spheres (or diffusion of reaction products out) could be severely hindered. But the extreme thinness of these diffusional ‘barriers’ (of order 10 nm) often presents only a modest resistance in practice. In the converse case, where the matrix is removed, there is no diffusional resistance (save the possibility of a wetting layer at the film-solution interface), but complete removal of the matrix will leave the internal microdomains (cylinders or spheres) unattached to the substrate. Since the three morphologies shown in Fig. 1.2 (spheres, cylinders, lamellae) are available to flexible-chain block copolymers of all chemistries (e.g., PS-PMMA, PFS-PI...), the algorithm for designing a lithography process using block copolymers is thus straightforward: (i) select whichever polymer components allow for convenient pattern transfer techniques with available process equipment, (ii) choose their relative volume fractions in the block copolymer to produce the desired morphology, and (iii) adjust the total block copolymer molecular weight (or chain length  $N$ ) to produce the desired periodicity, where the lower limit on  $N$  (hence  $\lambda$ ) is set by the ODT (i.e., a useful polymer must have  $T_{\text{ODT}}$  above the process temperature).

A variety of effective pattern transfer techniques has been developed, which we divide below according to whether the selective domain removal requires contact with an organic or aqueous solution – ‘wet’ techniques – and those where no liquid is present – ‘dry’ techniques, especially reactive ion etching (RIE). We then discuss some strategies for improving aspect ratios in these processes.

### 1.3.1 ‘Wet’ techniques for selective domain removal

There are several different techniques that use wet chemical processing to remove selectively one of the domains from a copolymer film. As a first case study, we consider ozonolysis of polyisoprene (PI) or polybutadiene (PB) blocks. Both of these elastomers contain carbon-carbon double bonds along their backbones, which makes them susceptible to chain scission by ozonolysis. By choosing a second block such as polystyrene (PS), which is largely resistant to ozone, this process can be used selectively to remove one of the domains from a block copolymer [34–36]. (In fact, ozonation has the opposite effect on polystyrene, causing it to crosslink and rendering it insoluble [37].)

Figure 1.8 shows the ozonolysis process used by Harrison *et al.* [37] on both PS-PI sphere-forming and PS-PB cylinder-forming copolymer thin films. They used an ozone generator to produce 4% ozone in oxygen, which they bubbled through a reactor filled with deionized water at room temperature, in which their sample was held on a Teflon stage. Treatment in the reactor for four minutes was sufficient to produce either spherical or cylindrical voids within the PS matrix, indicating an adequate permeability of the majority PS matrix both to ozone – allowing it to diffuse to the minority PI or PB domains – and to the resulting small PI and PB fragments, allowing them to



1.8 Pattern transfer process of Harrison *et al.*, following treatment of a polystyrene-polydiene film with ozone to selectively remove the discrete polydiene domains. Reproduced with permission from reference [37].

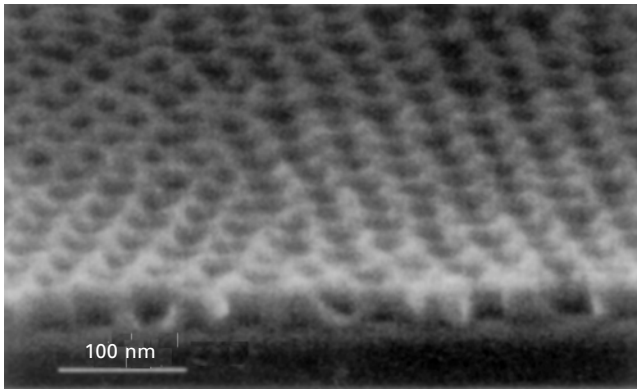
diffuse out of the film and into the surrounding water. By subsequent reactive ion etching with  $\text{CF}_4$  (a 'dry' process) the pattern was transferred into the underlying substrate. In principle, they could have stopped etching upon reaching the substrate, and performed either liftoff or plating.

Ozonolysis can also be performed in a dry process, using an ozone-laden gas stream. In later work by Hashimoto *et al.* [38], ozonolysis was performed on much thicker (100–300 micron) PS-PI films in the gyroid phase by holding the films in an ozone atmosphere for 24 hours to degrade the minority PI. However, to remove the PI fragments, the film had to be soaked in ethanol for an additional 24 hours. True 'dry' processing with ozone would require the cleavage of the polydiene block into fragments so small that they become volatile, which has not yet been achieved.

Like the work by Hashimoto *et al.* [38], many of the other chemical schemes that selectively remove domains in different diblock systems have been developed with an eye to producing bulk nanoporous materials, but these could also be applied to thin films on substrates, so we briefly review several here. Zalusky *et al.* [39] removed the minority polylactide (PLA) block from a cylinder-forming PS-PLA copolymer through hydrolysis by soaking a bulk polymer in a 0.5 M solution of sodium hydroxide in a 40/60 methanol/water solution, typically for about one week at 65 °C. The samples were then washed with methanol and dried under vacuum for 14 hours. Presumably, the times for degradation and drying would be much less for thin film samples suitable for lithography. Liu *et al.* [40] hydrolyzed cylindrical poly(*tert*-butyl acrylate) (*Pt*BA) domains from a poly(2-cinnamoyl ethyl methacrylate) (PCEMA) matrix in a *Pt*BA-PCEMA block copolymer. They treated free-standing films 50 nm thick, obtained by microtoming bulk specimens, by first exposing them to ultraviolet (UV) light to crosslink the PCEMA, then by soaking them in a 0.050 M  $(\text{CH}_3)_3\text{SiI}$  solution in  $\text{CH}_2\text{Cl}_2$  for 2–3 days to convert the *tert*-butyl groups into trimethylsilyl groups, and then in a 5%/95% water/methanol solution to hydrolyze the trimethylsilyl groups. This process does not remove the entire *Pt*BA block, but only the *tert*-butyl side groups (44% of the monomer mass), thus producing cylindrical voids narrower than the cylindrical microdomains in the original structure. Ndoni *et al.* [41] used immersion in liquid anhydrous hydrogen fluoride (HF) to remove the minority PDMS domains (both spherical and gyroid) from PDMS-PS copolymers. Despite the glassy PS matrix, facile diffusion of HF into the film, and the byproduct  $\text{Si}(\text{CH}_3)_2\text{F}_2$  out, allowed them to completely remove spherical PDMS microdomains even in films 500  $\mu\text{m}$  thick.

Another extremely successful strategy has been the use of deep UV light to degrade minority PMMA domains in PS-PMMA, as demonstrated by Russell *et al.* [42, 43] using PS-PMMA diblock copolymers forming PMMA cylinders and induced to stand perpendicular to the substrate (via methods

discussed further below). As with ozonation, the most significant effect of UV radiation on the polystyrene matrix is crosslinking, as evidenced by its decreased solubility. By contrast, the PMMA acts as a positive resist upon UV exposure, its solubility increased by chain scission. After exposing a microphase-separated thin film to a 254 nm UV dose of 25 J/cm<sup>2</sup>, the PMMA blocks can be preferentially removed by washing with acetic acid. To completely remove the PMMA block from the copolymer, it is necessary for UV to break the polymer chain between the PMMA block and the PS block, so a high dose of UV is required. Although the UV exposure is a ‘dry’ process, the subsequent acetic acid wash is ‘wet’. Note that by using vertical cylinders rather than spheres, there is no PS layer to etch through. Figure 1.9 shows the results of their process, after the PMMA block has been removed.



1.9 Cross-sectional scanning electron microscope image obtained from a thin film of a PS-PMMA diblock after removal of the cylinder-forming PMMA block. Reproduced with permission from reference [42].

These different wet routes to selective removal of microdomains for lithography can all produce fine results; each is sufficiently selective to produce excellent contrast for features of any size. The two major factors that should influence the choice between these different routes are: (i) availability of polymers, and (ii) chemical compatibility with the remaining materials and processes (for instance, ozone could damage underlayers; HF requires special handling equipment regardless of substrate).

### 1.3.2 Selective removal of domains by reactive ion etching

Another route to selective domain removal in block copolymer lithography is reactive ion etching, or RIE [44], which offers several advantages over

wet processes. RIE plasmas are typically active only at sample surfaces and do not diffuse through a copolymer coating to degrade underlying materials, which largely eliminates compatibility problems. Another inherent advantage to RIE is that where domain degradation and subsequent removal of a domain are often two separate steps for wet processing, they are combined in a single step for RIE. The elimination of additional processing steps can be even greater in the case of removing minority domains such as spheres that are totally enclosed in a matrix of the majority block. After removing spherical domains to produce spherical voids, an additional step is required to remove the matrix and expose the underlying surface: a step that is often performed by RIE anyway. In such a case where subsequent RIE is required after wet chemical processing anyway, it is only natural to look for ways to use RIE for selective domain removal.

Most of the polymer blocks that have been used as nanolithography templates are composed of C, H, O, and N, and show very little contrast in the etch rates between their blocks in either  $\text{CF}_4$  or  $\text{O}_2$  etching. However, a study by Asakawa and Hiraoka [45] did demonstrate etch contrast ratios of about 1:2 for PS-PMMA in  $\text{CF}_4$ ,  $\text{O}_2$ ,  $\text{H}_2$ , and Ar plasmas, presumably reflecting the same tendency towards depolymerization which PMMA shows upon UV exposure. After coating silicon substrates with PS-PMMA copolymers that formed PMMA spheres in a PS matrix, they first used  $\text{O}_2$  RIE to remove the minority PMMA block from the matrix, and to etch the underlying PS down to the bare silicon substrate. They then used  $\text{CF}_4$  RIE to etch holes into the silicon, with the remaining PS acting as a mask. The etch rate contrast between the Si and PS was approximately 5:1, but the small thickness of the remaining PS mask only allowed them to produce holes with an aspect ratio (depth:diameter) of 1:2. After etching pits into the Si, the remaining PS was removed by  $\text{O}_2$  etching.

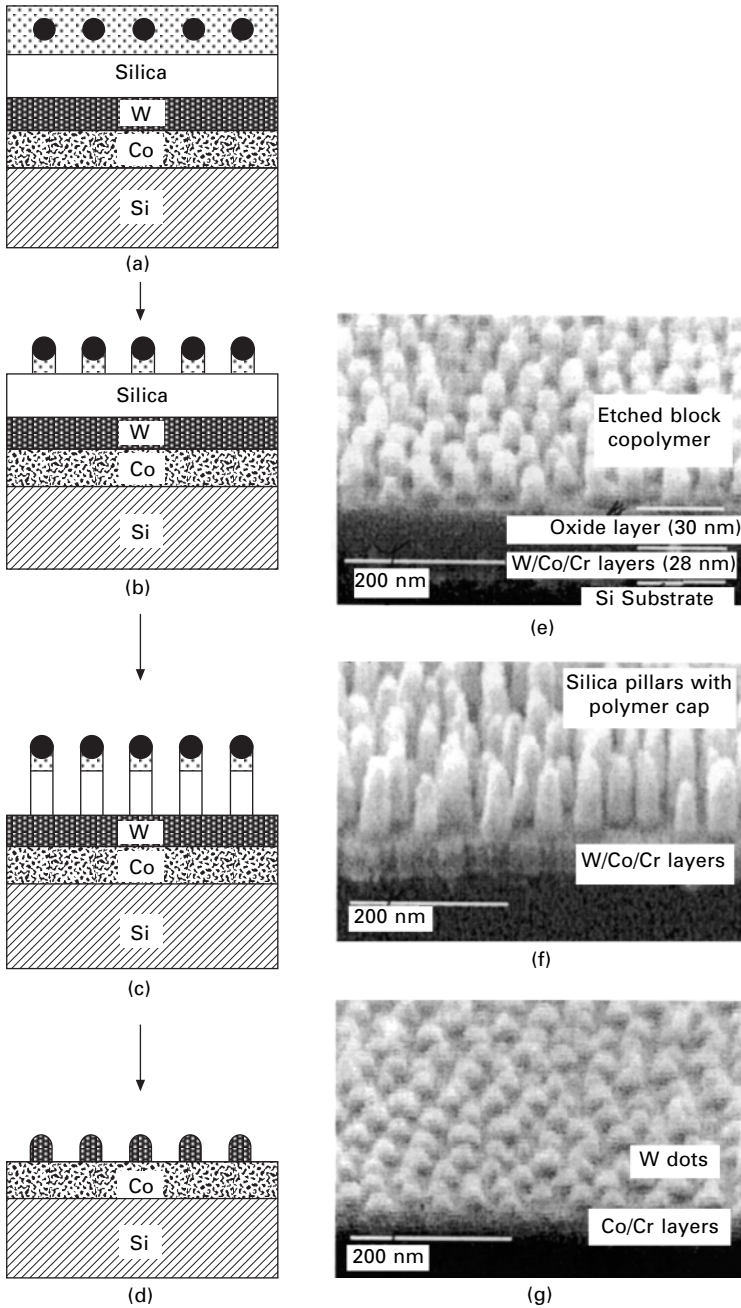
In general, etch rates in  $\text{O}_2$  plasma are dramatically slowed in polymers containing over 10% silicon by weight, which forms a silicon-oxide barrier [46]. This selectivity has been exploited as the basis of multilevel resist schemes in standard photolithography for high-aspect-ratio features. While the extremely low  $T_g$  values of siloxane polymers can make their films unstable once the other copolymer block has been removed, there have been efforts to develop block copolymer lithography using other silicon-based polymers for  $\text{O}_2$  RIE contrast. Chan, Thomas and coworkers employed polymers containing poly(pentamethyldisilylstyrene) (PPMDSS) blocks; exposure of PPMDSS to an oxygen plasma generates the desired silicon oxide surface layer, but this process is also accompanied by significant roughening of the surface, sufficient to limit its applications in nanolithography [47]. However, treatment of PI-PPMDSS-PI triblocks with ozone and simultaneous UV irradiation, followed by a soak in deionized water (making this a 'wet' process), was successful both in degrading the PI and converting

the PPMDS to a silicon oxycarbide ceramic stable to 400 °C [48]. A successful 'all-dry' process capitalizing on the etch resistance of silicon-based polymers has yet to be developed for block copolymer nanolithography.

The most successful system for intrinsic RIE contrast in block copolymer lithography has been through the organometallic polymer polyferrocenyl-dimethylsilane (PFS) [49], which is highly resistant to both O<sub>2</sub> and CHF<sub>3</sub> plasma etching. Vancso, Thomas, and coworkers [6, 50] took advantage of this, using PI-PFS and PS-PFS diblock copolymers, with the minority PFS forming spheres. Upon O<sub>2</sub> etching, an oxide layer forms on the PFS domains, leading to an etch ratio selectivity of approximately 40:1 [50]. This etch mask could then be used in a multilayer process, illustrated in Fig. 1.10, to transfer the pattern into a thin film of tungsten, and eventually forming an array of magnetic cobalt dots following the original positions of the PFS spheres [6].

As an alternative to using organometallic polymers, there are several methods for incorporating metal into copolymer domains after polymer synthesis, to increase their etch resistance. One such method, demonstrated by Park *et al.*, involves the incorporation of osmium into minority PB or PI domains in a PS matrix [1]. A thin PS-PB film was spin coated onto a silicon nitride surface, where it microphase separated to form PB cylinders within a PS matrix. The film was then exposed to OsO<sub>4</sub> vapor, which diffused into the polymer film and attacked the carbon-carbon double bonds in the PB block. When etched in a CF<sub>4</sub>-O<sub>2</sub> RIE, the osmium acted as an etch barrier, providing an etch contrast of approximately 2:1 between the stained and unstained blocks. Etching continued until the original microdomain pattern was transferred into the underlying silicon nitride.

Metal nanoparticles have also been incorporated into copolymer microdomains, both by direct adsorption of preformed nanoparticles from solution and by evaporation of metal onto the surface. Aside from increasing etch resistance, these methods offer the possibility of directly forming arrays of nanoscopic metal dots, or conductive metal wires. As examples of the nanoparticle route, Zehner *et al.* dipped PS-PMMA films into solutions containing passivated 1–2 nm gold [51] and palladium [52] nanoparticles, which were preferentially adsorbed onto the PS domains. The Pd particles may in turn be used as seeds for electroless copper deposition [52], but it is difficult to make continuous metal wires this way. If only discrete metal dots are desired, it is possible to coassemble the metal nanoparticles and the block copolymer in solution, and deposit these micelles directly on a substrate, as shown by Spatz *et al.* [53]. As an example of the evaporation route, Morkved *et al.* were the first to show that gold evaporated onto a PS-PMMA film formed nanometer scale islands preferentially on the PS domains [54].



1.10 RIE pattern transfer process of Cheng *et al.* (a) PS-PFS diblock copolymer on silica-tungsten-cobalt multilayer. (b) After selective etching of PS matrix with  $O_2$  RIE. (c) After etching silica with  $CHF_3$  RIE. (d) After  $CF_4 + O_2$  RIE and ashing. (e), (f), and (g) are scanning electron micrographs of the surfaces corresponding to (b), (c), and (d), respectively. Reproduced with permission from reference [6].

### 1.3.3 Strategies for improving aspect ratios

One of the greatest challenges in block copolymer lithography is achieving high-aspect-ratio features. High-aspect ratios may be required in the features of a finished device, as in arrays of magnetic pillars for information storage, which must be significantly taller than their diameter in order for the magnetic director to lie exclusively along the long axis of the particle, as would be desired for a quantized magnetic disk [55]. High-aspect ratios may also be required in intermediate stages of a lithography process, for instance in a metal liftoff procedure, which requires both that features in the copolymer mask be significantly taller than the thickness of the subsequent metal coating, and that edges of features in the mask be very close to vertical so as to avoid step-coverage.

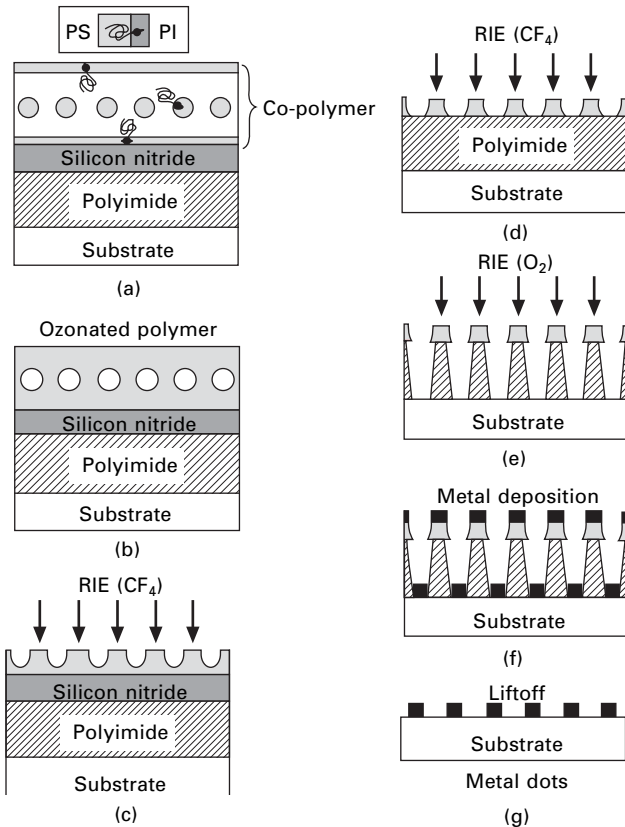
In crafting features with high-aspect ratios, a good strategy is to use vertically oriented microdomains where possible. For example, to obtain a hexagonal pattern of high-aspect ratio dots, a thicker copolymer film of hexagonally packed cylinders standing on end has better potential to produce high-aspect ratio features than a thinner copolymer film of hexagonally packed spheres. Similarly, to produce striped patterns, a thicker film of vertically oriented lamellae would be preferable to a thinner film of horizontally oriented cylinders.

Russell and coworkers have successfully employed this strategy, using thick films of PS-PMMA block copolymers to produce arrays of hexagonally packed PMMA cylindrical microdomains oriented perpendicular to the surface. In one study, after removing the PMMA, they filled the cylindrical cavities with cobalt through electrodeposition, producing an array of vertically oriented magnetic pillars 500 nm in length and 14 nm in diameter [43]. In another study [56], a 30 nm PS-PMMA film was employed, such that PMMA removal produced vertically oriented cylindrical cavities 16 nm in diameter by 30 nm deep. They then sequentially evaporated 3 nm Cr and 9 nm gold over the entire film and removed the polymer layer by sonication in toluene to yield an array of hexagonally packed metal dots with an aspect ratio of approximately 1:1; complete filling of the cavities should produce a ratio of 2:1.

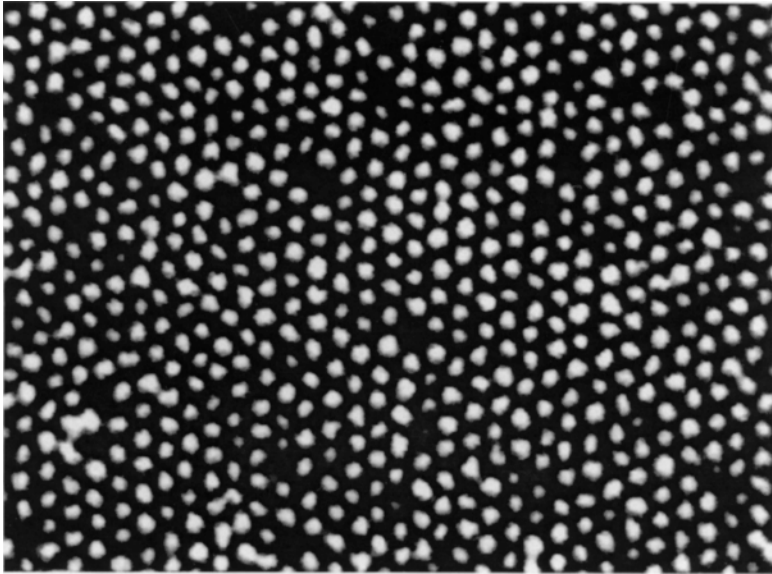
Orienting cylinders perpendicular to a substrate is no small task, as discussed in the preceding section. The approach of ‘neutralizing’ the interaction of the two blocks with the substrate by the grafting of random copolymers to it [33] has already been discussed. However, Russell and coworkers have also found that if preferential interactions with the substrate are not too strong, an electric field can be applied to generate alignment of cylinders perpendicular to the substrate, capitalizing on the significant difference in dielectric constant between PS and PMMA. By biasing electrodes above and below the copolymer film, and heating to temperatures above the upper  $T_g$  of the copolymer, cylindrical domains reorient themselves parallel to the external field [43],

provided the field strength exceeds a critical threshold value [57]. The two methods – partial or total surface ‘neutralization’ and electric field poling – can also be applied together [32, 42], to lower the threshold field strength.

Park *et al.* [4] used a different strategy to achieve high-aspect ratio features, putting a sphere-forming PS-PI diblock over sacrificial silicon nitride and polyimide undercoatings, as shown in Fig. 1.11. The PI block was degraded by ozonation, and the resulting pattern was etched into the underlying silicon nitride by  $\text{CF}_4$  RIE. The resulting pattern in the nitride layer acted as a mask with a very high etch contrast for  $\text{O}_2$  RIE, which etched the polyimide layer down to the silicon substrate, generating pits with a 3:1 aspect ratio. Subsequently, 20 nm of metal (Ti/Au 5/15 nm) were deposited and the remaining polyimide lifted off, leaving metal features with an aspect ratio of approximately 1:1, though complete filling of the pits would produce higher aspect ratios. A scanning electron micrograph of the resulting array of Ti/Au dots is shown in Fig. 1.12.



1.11 Trilevel pattern transfer process of Park *et al.* Reproduced with permission from reference [4].



1.12 Plan-view scanning electron microscope image of Ti/Au dots fabricated by Park *et al.* using the process illustrated in Fig. 1.11. Average center-to-center spacing of dots is 39 nm. Reproduced and modified with permission from reference [4].

For even higher aspect ratios, one desires cylinders of smaller diameter. Although it is possible to control the size and spacing of cylindrical microdomains in a pure diblock copolymer by choosing the lengths of the blocks appropriately, one can only do so within certain narrow ranges. For example, although one can make cylinders smaller at a fixed intercylinder spacing by shrinking the minority block volume fraction, it must remain greater than about 0.17 to avoid a transition to the spherical phase. Uniform partial removal of the cylinder-forming block, as employed by Liu *et al.* [40] through the cleavage of the *Pt*BA sidegroup, can potentially generate cylindrical voids with diameters much smaller than their center-to-center spacings. Jeong, Russell and coworkers [58, 59] extended this approach considerably by introducing a small amount of a PMMA homopolymer into a cylinder-forming PS-PMMA diblock; the homopolymer preferentially segregated into the PMMA microdomains, swelling the cylinders slightly from 22 nm in diameter to 24 nm. After casting a film with this copolymer-homopolymer blend, they could remove the homopolymer from the film via an acetic acid wash, without disturbing the PS matrix, leaving 6 nm pores in the center of each cylindrical PMMA domain. These narrow pores could, in principle, be used as lithographic masks to make extremely high-aspect-ratio cylinders.

## 1.4 Approaches to long-range ordering

Short range microdomain order in block copolymer films is usually excellent. However, many of the potential applications of block copolymer lithography are strongly dependent upon (and often limited by) the degree of long-range order existing in the polymer film. For example, to take advantage of the full storage potential of memory devices fabricated by block copolymer nanolithography, requirements of addressability imply a regular lattice arrangement of the dots; similarly, continuous straight metal lines across a large substrate area are desired in many applications. The requirement for long-range order has been widely recognized by the research community, with several recent research efforts aimed in this direction.

This final section of the chapter will be devoted to an up-to-date review of techniques available for inducing long-range order in thin block copolymer films. These approaches will be divided into categories based on the mechanisms involved in the ordering process. Some of these techniques are extensions of earlier work on aligning bulk block copolymers, in which case the closest bulk correspondent will be described; other techniques are specific to thin films. Earlier reviews dedicated to or touching upon block copolymer lithography [24, 26, 60–62] have also discussed some long-range ordering techniques; we will not duplicate these reviews here, but will rather give an overview of earlier processes with an emphasis on those developed very recently, some of which have been presented only in conference abstracts or Ph.D. theses as of this writing (and may have appeared in specialized journals since).

### 1.4.1 Thermal methods

Annealing a block copolymer thin film above its upper  $T_g$  (while remaining below  $T_{ODT}$ ) increases the mobility of the block copolymer molecules, allowing them to hop diffusively from one microdomain to the next. Although the lowest energy state theoretically consists of a completely ordered microdomain structure, in reality the times required to approach it are unreasonably long, and in practice thermal annealing alone will yield a thin film with a multigrain structure, where the individual micron-size grains are far below their limiting size. Careful dynamical studies by Harrison *et al.* employing time-lapse atomic force microscopy (AFM) have revealed that the size of the grains increases as the  $1/4$  power of time for cylinder-forming block copolymer films, as a result of topological defect annihilation [63, 64]; they also found a similar exponent for grain growth in films of sphere-forming block copolymers [65]. The low value ( $1/4$ ) of the exponent renders this method inefficient in creating a specimen with macroscopic grains; in the best cases, grains extending over tens of microdomains after several hours of thermal

annealing were obtained, as shown in Figs 1.3 (b) and (d). Furthermore, no control of the grain orientation is achieved by annealing, since the thermal field is isotropic.

Sweeping thermal gradients, on the other hand, were successfully employed by Hashimoto *et al.* to yield highly oriented lamellar microdomains in bulk PS-PI block copolymers [66]. Their experimental setup effectively created a ‘melting-solidification front’ – a 30 °C/mm temperature gradient, spanning  $T_{\text{ODT}}$  – which was swept through the sample at 400 nm/sec. The resulting specimen showed excellent alignment of the lamellar normals in the direction of the moving gradient. Recently, we [67] have applied a similar approach to dynamically anneal a monolayer film of a cylinder-forming PS-PEP diblock copolymer, where PEP is poly(ethylene-*alt*-propylene). By employing a substrate with a built-in microfabricated resistive point-heater, a large amount of heat was dissipated in a microscopic volume, creating a strong radial temperature gradient. By controlling the power to the heater, a radial melting-solidification front was swept through the film surrounding the heater, again employing a temperature range spanning  $T_{\text{ODT}}$ . When the power to the point heater was reduced in an oscillatory fashion (such that the melting-solidification front swept several times through the same region of the sample), the grain size obtained was increased approximately 50-fold (to many tens of  $\mu\text{m}$ ) when compared to samples annealed at a uniform constant temperature for the same duration; however, as in the case of annealing in an isotropic field, no macroscopic orientation of the grains was obtained.

#### 1.4.2 Solvent-mediated methods

A significant increase in grain size has also been achieved by annealing samples in a suitable solvent vapor atmosphere; the ‘annealing’ may even be conducted at ambient temperature. Solvent present in the block copolymer film has a similar effect to an increase in temperature: it enhances the mobility of the block copolymer molecules, allowing for faster grain growth. But unlike raising the temperature to increase mobility, solvent annealing does not run up against the limitation of thermal degradation of the polymer. Kim *et al.* easily achieved grain diameters of several  $\mu\text{m}$  (hundreds of lattice spacing units) this way [68], in a PS-PEO diblock forming PEO cylinders, where PEO is poly(ethylene oxide). In addition, solvent evaporation can act as a directional field when a concentration gradient can be created through the film, normal to the substrate; such gradients are possible for thicker films, or for very rapid evaporations. Thus, by controlling the evaporation rate, cylindrical and lamellar block copolymers can orient their microdomains either in the plane of the film or perpendicular to it [68]. It would be interesting to see whether a strong in-plane concentration gradient could direct the in-plane orientation of the microdomain grains; this effect has not yet been demonstrated.

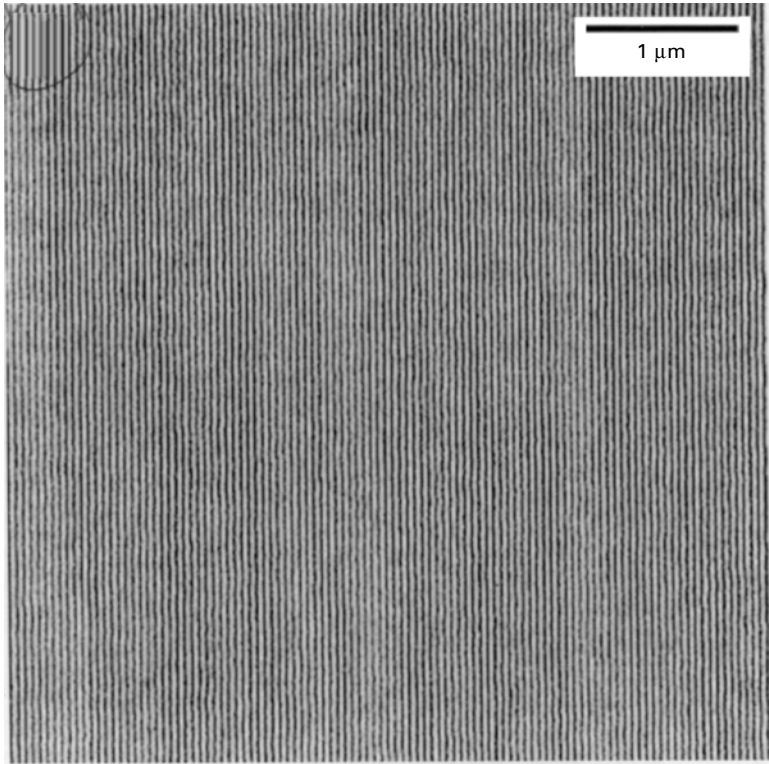
### 1.4.3 Epitaxial patterning methods

An effective way to produce a block copolymer thin film with long-range order is to create a periodic pattern on the substrate, which is then replicated by the block copolymer microdomain structure. The substrate pattern can be topographical, chemical, or both. This method essentially induces epitaxial self-assembly of the block copolymer; in such techniques, the block copolymer does not generate the pattern, but rather replicates a pre-existing pattern that must be produced by other methods.

In the first use of a patterned substrate to template a block copolymer film, Fasolka *et al.* employed the faceting transformation of a miscut Si (113) wafer to generate a substrate with a periodic height modulation [69]. A lamellar PS-*Pn*BMA block copolymer film, where *Pn*BMA is poly(*n*-butylmethacrylate), of thickness  $\lambda/2$  ( $\lambda$  being the lamellar spacing) was applied to the corrugated substrate; the substrate height modulations resulted in a periodic modulation of film thickness. In the thicker regions, uniform half-lamellae formed parallel to the substrate, but in the thinner regions the PS sheets broke up into disk-like domains, thus generating a periodic alternation in microdomain structure which replicates the underlying topography. It is interesting to note that, provided the amplitude of the substrate pattern is close to  $\lambda/2$ , any substrate pattern – even one bearing no relationship to the block copolymer morphology – should be mirrored by the block copolymer film.

A subsequent study by Rockford *et al.* [70] modified similar substrates by grazing-angle evaporation of gold, which deposited on only one side of the Si (113) facets to create a periodic, topographically and chemically patterned substrate. Sub-monolayer PS-PMMA block copolymer films of lamellar spacing  $\lambda$  faithfully reproduced surface patterns which were commensurate with  $\lambda$ , by orienting normal to the surface. A subsequent study showed that for precisely commensurate substrates, the perpendicular orientation of the lamellae, and in-plane registration with the substrate pattern, could even be replicated in block copolymer films a few  $\lambda$  thick [71].

A different approach was employed in a recent study by Nealey, de Pablo, and coworkers, where a purely chemical periodic surface pattern was generated by using extreme UV interference lithography [72]. The openings in line patterns lithographically generated on a photoresist layer permitted modification of an underlying self-assembled monolayer (SAM), which resulted in a chemically heterogeneous but flat surface. A lamellar PS-PMMA block copolymer was subsequently applied; the lamellae self-assembled normal to the substrate, perfectly reproducing the original, defect-free, pattern, as shown in Fig. 1.13, even for block copolymer films slightly thicker than  $\lambda$ .



1.13 Chemically pre-patterned substrates exhibiting straight lines, generated by deep-UV interference lithography, are perfectly reproduced in the microdomains of a PS-PMMA diblock of commensurate period. Plan-view scanning electron microscope image; the lamellar microdomains are oriented perpendicular to the substrate, and the PS lamellae appear bright. Reproduced with permission from reference [72].

#### 1.4.4 Graphoepitaxy

Several studies have used micron-scale substrate features to template the orientation of the nanoscale block copolymer microdomains; the ability of sharp features much larger than a crystal's lattice spacing to induce orientation of the lattice in thin films is termed 'graphoepitaxy'. For example, we have found [73] that the atomically straight step edges on cleaved mica substrates induce the alignment of a sphere-forming PS-PEP block copolymer; initially, a row of spheres aligns in the 'foot' of the step, along the step's entire macroscopic length. By annealing, this orientation could be extended for as much as  $2\ \mu\text{m}$  perpendicular to the step – a distance comparable to the grain size in films of this same PS-PEP annealed similarly on unpatterned substrates. Thus, while graphoepitaxy can be very effective in orienting the microdomains,

a single step edge produces only ‘needle-like’ grains: large in one dimension, but micron-scale in the other.

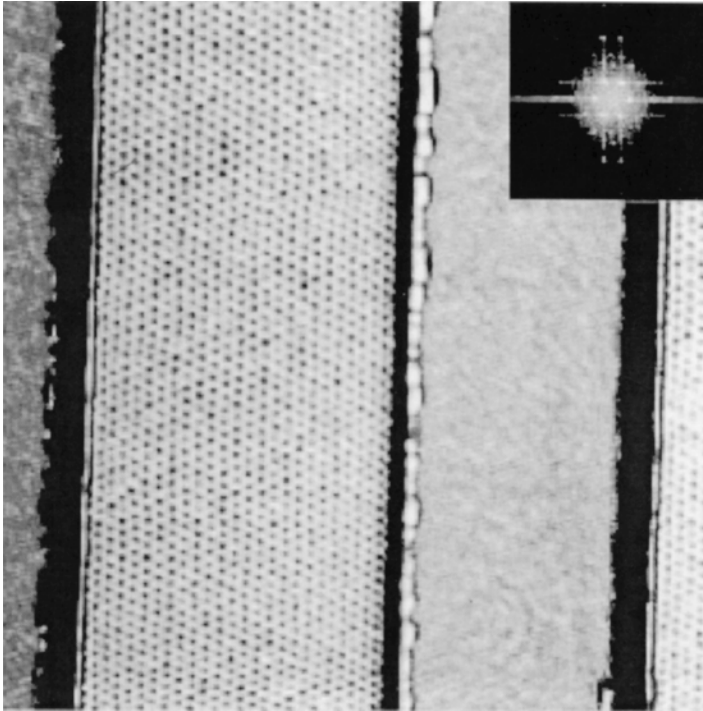
The most extensive studies of graphoepitaxy in block copolymer thin films are those of Segalman, Kramer, and coworkers, who used monolayer sphere-forming PS-PVP films, where PVP is poly(2-vinylpyridine), cast on rectangular microfabricated mesas: millimeters long, with a range of micron-scale widths [74]. After annealing, the resulting microdomain pattern was ordered over the whole surface of the mesa (very few topological defects still remaining), thus proving that neither the atomic smoothness of the edge nor its up (or down) direction are essential for alignment. In addition, such microfabricated substrates can be easily mass produced. However, the authors found a qualitative difference between alignment in the ‘troughs’ and ‘mesas’ of the micropatterned substrates; in the troughs, the (10) planes of the 2D hexagonal lattice of spheres were aligned with the step edge, as with mica cleavage steps, but on the mesas, the (10) planes made a small angle to the step edge, an angle controlled by the polymer film’s curvature as it passes over the step edge [75]. Thus, for best registration and addressability, troughs are preferred.

Cheng *et al.* have also demonstrated alignment of microdomains of a thermally annealed sphere-forming PS-PFS block copolymer inside microfabricated troughs [76]. The micron-scale substrate pattern was produced by interference lithography; the ordered block copolymer template was subsequently used in order to fabricate silica posts, thus taking the technology one step closer to integration and industrial applications. Finally, such microfabricated troughs can be coupled with solvent annealing to produce arrays of block copolymer cylinders standing end-on, having both high aspect ratio and exceptionally good in-plane alignment directed by the walls of the trough, as demonstrated by Kim *et al.* [68] and reproduced in Fig. 1.14.

#### 1.4.5 Electric field alignment

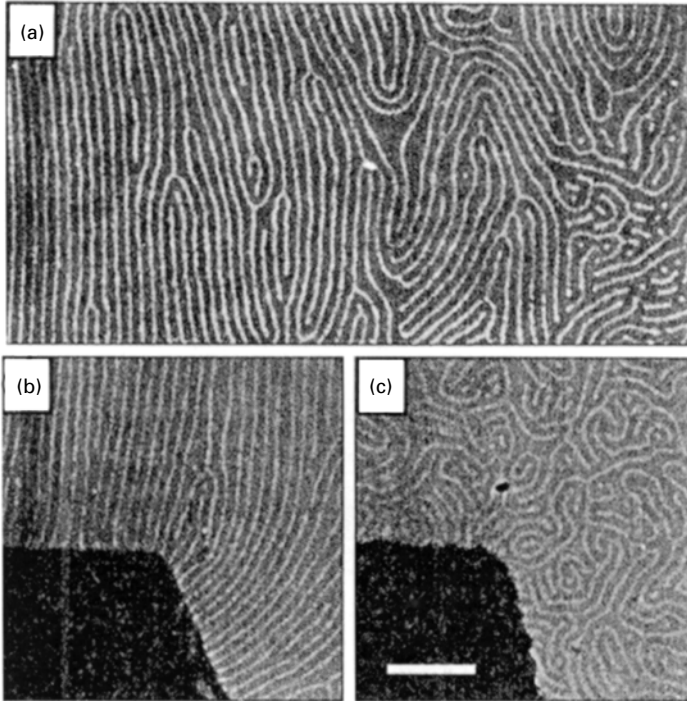
As first shown by Amundson *et al.* [77], strong electric fields can align bulk block copolymers, provided there is a sufficient dielectric constant difference between the homopolymers of the two blocks, as in PS-PMMA; lamellae orient their normals perpendicular to the direction of the applied field (the minimal electrostatic energy configuration), with the azimuthal orientation being random. The same experiment could be attempted with bulk samples of polymers forming cylindrical microdomains; in that case the cylinders should orient parallel to the direction of the field. The electric fields required are much stronger, however, making this method inefficient for aligning bulk cylinder-forming block copolymers.

An elegant pioneering study by Morkved *et al.* demonstrated in-plane electric field alignment of a cylinder-forming PS-PMMA block copolymer



*1.14* Atomic force microscope image of a solvent-annealed film of PS-PEO diblock copolymer, confined inside microfabricated troughs, showing a high degree of order of cylinders oriented perpendicular to the substrate. The alignment direction is templated by the walls, and persists along the full length of the trough. Reproduced with permission from [68].

[78]. Pairs of electrodes were microfabricated on a flat substrate, with gaps on the order of a few  $\mu\text{m}$ . In-plane fields as high as  $35 \text{ kV/cm}$  could thus be generated by applying only moderate voltages across the electrodes. The diblock copolymer film was cast on top of the microfabricated structures, and annealed under high electric fields. Good alignment of the cylinders parallel to the direction of the field was observed for fields higher than  $\approx 25 \text{ kV/cm}$ , as shown in Fig. 1.15. One drawback of the technique is that the lateral extent of the region that could be aligned – the region between the electrodes – was of the order of only a few  $\mu\text{m}$ . As discussed in the section on pattern transfer, out-of-plane electric fields have been successfully used to create standing cylindrical microdomains in block copolymer thin films [57]; the electric field, however, had no effect on the lateral ordering of the pattern in that case.



1.15 Films of PS-PMMA diblock copolymer annealed in a strong electric field. (a) The transition between good and poor alignment is seen as the magnitude of the electric field decreases from left to right. (b) When annealed in a strong electric field, the cylinders align parallel to the direction of the applied field (fringe region at the end of electrode shown). (c) with no electric field applied, the cylinders assume the characteristic disordered 'fingerprint' pattern. Reproduced with permission from reference [78].

#### 1.4.6 Solvent directional crystallization

Thomas and coworkers have employed the directional crystallization of a solvent (such as benzoic acid) in order to generate an anisotropic substrate. In the initial study [79], the PE-PEP-PE triblock copolymer used contained crystallizable polyethylene (PE) endblocks, which epitaxially crystallized onto the benzoic acid template, thus creating lamellae with an orientation perpendicular to the substrate and parallel to one of the benzoic acid crystalline directions. Later work showed that a variation of this technique can align non-crystalline lamellar PS-PMMA and cylindrical PS-PI block copolymers in thin films [80]. The alignment directions of the lamellae and cylinders coincide with the fast crystallization direction of the solvent used (benzoic acid or anthracene). Very importantly, this technique resulted in an oriented array of standing cylinders when the film thickness was smaller than the

intercylinder separation. The oriented, hexagonally packed, arrangement of the cylinders in this case was apparent from the six peaks present in the Fourier transform of the pattern. However, the breadths of these six peaks indicate that while the rows of 'dots' are uniformly spaced and well-aligned with the crystallization direction, the registration between these rows is not as good, which would pose problems for addressable media applications.

#### 1.4.7 Flow-induced alignment

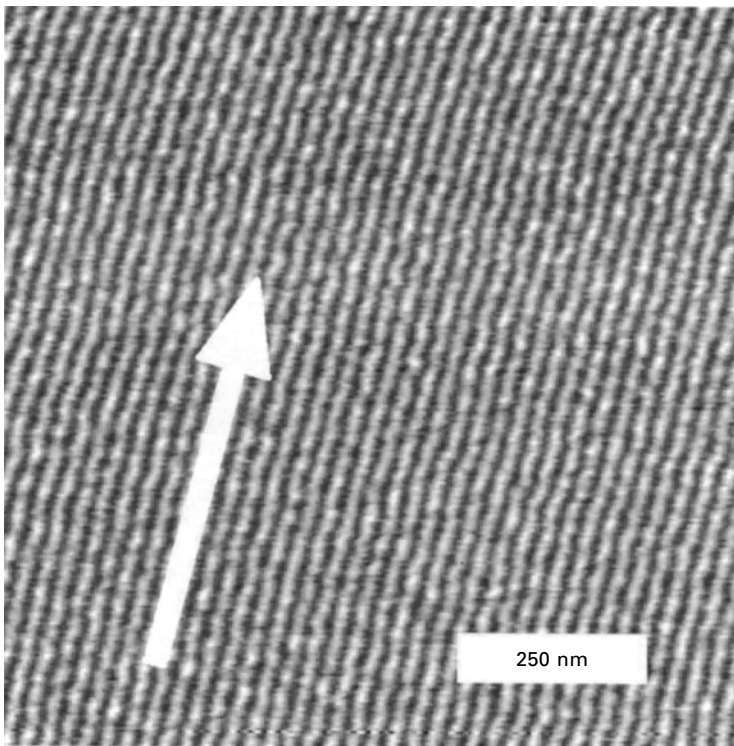
Flow-induced alignment is now a well-known phenomenon in bulk block copolymers, with the first report [81] demonstrating that cylindrical microdomains in a PS-PB-PS triblock copolymer could be aligned into a near-single-crystal texture by extrusion. Though a direct translation of this process to thin films (extruding specimens on the order of 50 nm thick) would seem daunting, other approaches to generating flow in thin films have recently been used to induce alignment in cylinder-forming block copolymers. Sundrani and Sibener induced flow in a monolayer film of a PS-PMMA diblock copolymer inside microfabricated silicon nitride troughs [82] via capillary flow into the corners of the trough, resulting in alignment perpendicular to the trough edges. The alignment persisted along the whole length of the troughs, and improved with prolonged annealing above the upper  $T_g$ .

Kimura *et al.* have demonstrated alignment in a thin film of cylinder-forming diblock copolymer via flow induced by solvent evaporation [83]. The technique consists of allowing the solvent to slowly evaporate from a polymer solution droplet pinned on an inclined substrate. The upward flow induced in the droplet causes the alignment of cylindrical microdomains. The technique provides a high quality of alignment over millimeter scales, but has only been demonstrated in rather thick films (tens of lattice spacings thick) and does not seem to be easily extendable to single-layer films.

While these two approaches operate on films with the free surface exposed, alignment of bulk block copolymers typically confines the specimen between bounding surfaces. The most common means for flow-aligning bulk specimens in the laboratory is through either steady [84] or reciprocating [85–88] shear, which have been repeatedly demonstrated to effectively align lamellar [86, 88] and cylindrical [84, 85] microdomains. Partial alignment has been demonstrated via reciprocating shear for sphere-forming block copolymers in bulk [87]; while some orientations of the lattice are strongly suppressed, the final specimen contains a substantial density of twin grain boundaries which are not removed by shearing.

Only very recently have results emerged from shearing thin block copolymer films, presumably because of the difficulty in applying well-controlled shear to such sub-micron films. Zhuang recently reported the alignment of a cylinder-

forming PS-PI diblock, confined between two polished silicon wafers, during annealing under pressure inside a platen press [89], and suggested that shear was the likely cause of the observed alignment. The work had to be done inside a high-quality cleanroom in order to eliminate any dust that may have prevented the two wafers from coming into conformal contact. Recently, we have developed a much simplified shear-alignment method better suited for applying controlled shear stresses and measuring the strain response [90]. An unpatterned elastomer (PDMS) pad was placed on a monolayer film of randomly ordered cylinder-forming PS-PEP block copolymer coated onto a substrate and supported on a hotplate. With the temperature maintained between the glass and ordering transitions ( $T_g < T < T_{ODT}$ ) the pad was slid forward by applying a controlled and constant force; this caused the shearing of the underlying block copolymer film. The result was complete alignment of the pattern under the pad, which had a 1 cm<sup>2</sup> area, as shown in Fig. 1.16. Though this method did not produce any alignment when applied to a monolayer of



1.16 Shear-aligned sample of PS-PEP diblock copolymer. The shear direction is indicated by the arrow. The alignment indicated in this atomic force microscope image persisted throughout the cm<sup>2</sup> sheared region (scale bar = 250 nm). Reproduced with permission from reference [90].

a sphere-forming block copolymer, shearing films two or more (integral) layers thick resulted in a fully ordered hexagonal pattern [91].

## 1.5 Conclusion

Block copolymer lithography has come a long way in a relatively short time, born of necessity at a time when technology on the nanoscale holds great promise just out of our reach. Although the feature sizes that can be accessed through standard photolithographic techniques have continued to grow ever smaller, the efforts required to attain them have grown ever more complex, and there has been a growing sense in the research community that the end of the line may be close at hand for the shrinking of conventional photolithographic processes. Block copolymer lithography represents an attractive, economical alternative for those seeking the next order of magnitude down in scale – provided that they require nothing more complex than large-area, dense arrays of simple periodic patterns.

Looking into the future, we expect that in the short term, the kinds of techniques we have discussed here will continue to evolve rapidly: long-range ordering of copolymer films will improve, and new processes for selective domain removal will be developed for an ever-growing palette of polymer block chemistries. In the long term, we take a broader view, and see block copolymer lithography as the first of what we hope will be a much wider array of lithographic techniques based on the self-assembly of polymers, inorganic nanostructures, and biologically based molecules. The self-assembly of block copolymers has been fundamentally limited to simple periodic structures because the selectivity in the interaction of their blocks is based only on their amphiphilic nature, describable by a single interaction parameter  $\chi$ . We believe that self-assembly based on molecules whose interactions are more selective, such as between specific proteins and enzymes in biological systems, will ultimately allow for more complex structures to be attained. In the future, we see the simplicity of block copolymer nanostructures enhanced by more specific interactions between other components, to produce patterns ranging from the very simple to the very complex. Finally, we envision these ‘bottom-up’ self-assembly processes being used in conjunction with ‘top-down’ approaches, such as conventional photolithography as well as other approaches discussed in the remaining chapters of this book, to produce structures with complexity that spans many length scales [92]. In summary, block copolymer lithography will continue to be in the future what it is today: one of many excellent tools at our disposal to bring to bear on a variety of lithographic patterning problems.

## 1.6 Acknowledgments

We gratefully acknowledge the support of the National Science Foundation, through the Princeton Center for Complex Materials (DMR-0213706), for our research efforts in this area and during the preparation of this review. We also thank Dr Christopher Harrison for the previously unpublished micrographs in Fig. 1.3.

## 1.7 References

1. Park M., Harrison C., Chaikin P.M., Register R.A. and Adamson D.H., 'Block copolymer lithography: Periodic arrays of  $\sim 10^{11}$  holes in 1 square centimeter', *Science*, 1997 **276**(5317) 1401–4.
2. Kim H.C., Jia X.Q., Stafford C.M., Kim D.H., McCarthy T.J., Tuominen M., Hawker C.J. and Russell T.P., 'A route to nanoscopic SiO<sub>2</sub> posts via block copolymer templates', *Adv. Mater.*, 2001 **13**(11) 795–7.
3. Guarini K.W., Black C.T., Zhang Y., Kim H., Sikorski E.M. and Babich I.V., 'Process integration of self-assembled polymer templates into silicon nanofabrication', *J. Vac. Sci. Technol. B.*, 2002 **20**(6) 2788–92.
4. Park M., Chaikin P.M., Register R.A. and Adamson D.H., 'Large area dense nanoscale patterning of arbitrary surfaces', *Appl. Phys. Lett.*, 2001 **79**(2) 257–9.
5. Li R.R., Dapkus P.D., Thompson M.E., Jeong W.G., Harrison C., Chaikin P.M., Register R.A. and Adamson D.H., 'Dense arrays of ordered GaAs nanostructures by selective area growth on substrates patterned by block copolymer lithography', *Appl. Phys. Lett.*, 2000 **76**(13) 1689–91.
6. Cheng J.Y., Ross C.A., Chan V.Z.H., Thomas E.L., Lammertink R.G.H. and Vancso G.J., 'Formation of a cobalt magnetic dot array via block copolymer lithography', *Adv. Mater.*, 2001 **13**(15) 1174–8.
7. Naito K., Hieda H., Sakurai M., Kamata Y. and Asakawa K., '2.5-inch disk patterned media prepared by an artificially assisted self-assembling method', *IEEE Trans. Magn.*, 2002 **38**(5) 1949–51.
8. Lopes W.A. and Jaeger H.M., 'Hierarchical self-assembly of metal nanostructures on diblock copolymer scaffolds', *Nature*, 2001 **414**(6865) 735–8.
9. Pelletier V., Angelescu D., Waller J., Adamson D., Register R. and Chaikin P., 'Shear-aligned diblock copolymer to fabricate polarizing nanogratings', *Bull. Am. Phys. Soc.*, 2004 **49**(1) 1277.
10. Guarini K., Black C., Zhang Y., Babich I., Sikorski E. and Gignac L., 'Low voltage, scalable nanocrystal FLASH memories fabricated by templated self-assembly', presented at the IEDM Meeting, Washington DC (December 8, 2003). See also: <http://domino.research.ibm.com/Comm/bios.nsf/pages/selfassembly-iedm.html>
11. Hamley I.W., *The Physics of Block Copolymers*, Oxford: Oxford University Press, 1998.
12. Hamley I.W., ed., *Developments in Block Copolymer Science and Technology*, Chichester: John Wiley & Sons Ltd, 2004.
13. Bates F.S. and Fredrickson G.H., 'Block copolymer thermodynamics: Theory and experiment', *Annu. Rev. Phys. Chem.* 1990 **41** 525–57.
14. Bates F.S. and Fredrickson G.H., 'Block copolymers: Designer soft materials', *Physics Today* February 1999 32–38.

15. Hajduk D.A., Harper P.E., Gruner S.M., Honeker C.C., Kim G., Thomas E.L. and Fetters L.J., 'The gyroid: A new equilibrium morphology in weakly segregated diblock copolymers', *Macromolecules*, 1994 **27**(15) 4063–75.
16. Matsen M.W. and Bates F.S., 'Unifying weak- and strong-segregation block copolymer theories', *Macromolecules*, 1996 **29**(4) 1091–8.
17. Harrison C.K., Chaikin P.M. and Register R.A., unpublished results.
18. Matsen M.W. and Bates F.S., 'Conformationally asymmetric block copolymers', *J. Polym. Sci. B: Polym. Phys.*, 1997 **35**(6) 945–52.
19. Semenov A.N., 'Contribution to the theory of microphase layering in block-copolymer melts' *Sov. Phys. JETP*, 1985 **61**(4) 733–42.
20. Quiram D.J., Register R.A. and Marchand G.R., 'Crystallization of asymmetric diblock copolymers from microphase-separated melts', *Macromolecules*, 1997 **30**(16) 4551–8.
21. Peysen P., 'Glass transition temperatures of polymers', in Brandrup J. and Immergut E.H., *Polymer Handbook*, 3rd edition, New York: John Wiley and Sons, 1989, pp. VI/209–77.
22. Lohse D.J., Fetters L.J., Doyle M.J., Wang H.C. and Kow C., 'Miscibility in blends of model polyolefins and corresponding diblock copolymers: Thermal analysis studies', *Macromolecules*, 1993 **26**(13) 3444–7.
23. Avgeropoulos A., Chan V.Z.H., Lee V.Y., Ngo D., Miller R.D., Hadjichristidis N. and Thomas E.L., 'Synthesis and morphological behavior of silicon-containing triblock copolymers for nanostructure applications', *Chem. Mater.*, 1998 **10**(8) 2109–2115.
24. Harrison C., Dagata J.A. and Adamson D.H., 'Lithography with self-assembled block copolymer microdomains', Chapter 9 in Hamley I.W., ed., *Developments in Block Copolymer Science and Technology*, Chichester: John Wiley & Sons Ltd, 2004, pp. 295–323.
25. Matsen M.W., 'Self-assembly of block copolymers in thin films', *Curr. Opin. Coll. Interface Sci.*, 1998 **3**(1) 40–7.
26. Fasolka M.J. and Mayes A.M., 'Block copolymer thin films: Physics and applications', *Annu. Rev. Mater. Res.*, 2001 **31** 323–55.
27. Krausch G. and Magerle R., 'Nanostructured thin films via self-assembly of block copolymers', *Adv. Mater.*, 2002 **14**(21) 1579–83.
28. Harrison C., Park M., Chaikin P.M., Register R.A., Adamson D.H. and Yao N., 'Layer by layer imaging of diblock copolymer films with a scanning electron microscope', *Polymer*, 1998 **30**(13) 2733–44.
29. Harrison C., Park M., Chaikin P., Register R.A., Adamson, D.H. and Yao N., 'Depth profiling block copolymer microdomains', *Macromolecules*, 1998 **31**(7) 2185–9.
30. Knoll A., Horvat A., Lyakhova K.S., Krausch G., Sevink G.J.A., Zvelindovsky A.V. and Magerle R., 'Phase behavior in thin films of cylinder-forming block copolymers', *Phys. Rev. Lett.*, 2002 **89**(3) 035501.
31. Hashimoto T. and Hasegawa H., 'Morphology of block copolymers and mixtures of block copolymers at free surfaces', *Polymer*, 1992 **33**(3) 475–87.
32. Xu T., Hawker C.J. and Russell T.P., 'Interfacial energy effects on the electric field alignment of symmetric diblock copolymers', *Macromolecules*, 2003 **36**(16) 6178–82.
33. Mansky P., Liu Y., Huang E., Russell T.P. and Hawker C., 'Controlling polymer-surface interactions with random copolymer brushes', *Science*, 1997 **275**(5305) 1458–60.
34. Lee J.S., Hirao A. and Nakahama S., 'Polymerization of monomers containing

- functional silyl groups. 7. Porous membranes with controlled microstructures', *Macromolecules*, 1989 **22**(6) 2602–6.
35. Smith D.R. and Meier D.J., 'New techniques for determining domain morphologies in block copolymers', *Polymer*, 1992 **33**(18) 3777–82.
  36. Mansky P., Harrison C.K., Chaikin P.M., Register R.A. and Yao N., 'Nanolithographic templates from diblock copolymer thin films', *Appl. Phys. Lett.*, 1996 **68**(18) 2586–8.
  37. Harrison C., Park M., Chaikin P.M., Register R.A. and Adamson D.H., 'Lithography with a mask of block copolymer microstructures', *J. Vac. Sci. Technol. B*, 1998 **16**(2) 544–52.
  38. Hashimoto T., Tsutsumi K. and Funaki Y., 'Nanoprocessing based on bicontinuous microdomains of block copolymers: Nanochannels coated with metals', *Langmuir*, 1997 **13**(26) 6869–72.
  39. Zalusky A.S., Olayo-Valles R., Wolf J.H. and Hillmyer M.A., 'Ordered nanoporous polymers from polystyrene-poly lactide block copolymers', *J. Am. Chem. Soc.*, 2002 **124**(43) 12761–73.
  40. Liu G.J., Ding J.F., Hashimoto T., Kimishima K., Winnik F.M. and Nigam S., 'Thin films with densely, regularly packed nanochannels: Preparation, characterization, and applications', *Chem. Mater.*, 1999 **11**(8) 2233–40.
  41. Ndoni S., Vigild M.E. and Berg R.H., 'Nanoporous materials with spherical and gyroid cavities created by quantitative etching of polydimethylsiloxane in polystyrene-polydimethylsiloxane block copolymers', *J. Am. Chem. Soc.*, 2003 **125**(44) 13366–7.
  42. Thurn-Albrecht T., Steiner R., DeRouchey J., Stafford C.M., Huang E., Bal M., Tuominen M., Hawker C.J. and Russell T., 'Nanosopic templates from oriented block copolymer films', *Adv. Mater.*, 2000 **12**(11) 787–91.
  43. Thurn-Albrecht T., Schotter J., Kastle C.A., Emley N., Shibauchi T., Krusin-Elbaum L., Guarini K., Black C.T., Tuominen M.T. and Russell T.P., 'Ultrahigh-density nanowire arrays grown in self-assembled diblock copolymer templates', *Science*, 2000 **290**(5499) 2126–9.
  44. Plummer J.D., Deal M.D. and Griffin P.B., *Silicon VLSI Technology: Fundamentals, Practice and Modeling*, Englewood Cliffs: Prentice-Hall, 2000.
  45. Asakawa K. and Hiraoka T., 'Nanopatterning with microdomains of block copolymers using reactive-ion etching selectivity', *Japan J. Appl. Phys. Part. 1*, 2002 **41**(10) 6112–8.
  46. Reichmanis E. and Smolinsky G., 'Deep UV positive resists for 2-level photoresist processes', *Proc. SPIE*, 1984 **469** 38–44.
  47. Chan V.Z.H., Thomas E.L., Frommer J., Sampson D., Campbell R., Miller D., Hawker C., Lee V. and Miller R.D., 'Curious morphology of silicon-containing polymer films on exposure to oxygen plasma', *Chem. Mater.*, 1998 **10**(12) 3895–901.
  48. Chan V.Z.H., Hoffman J., Lee V.Y., Iatrou H., Avgeropoulos A., Hadjichristidis N., Miller R.D. and Thomas E.L., 'Ordered bicontinuous nanoporous and nanorelief ceramic films from self-assembling polymer precursors', *Science*, 1999 **286**(5445) 1716–9.
  49. Foucher D.A., Tang B.Z. and Manners I., 'Ring-opening polymerization of strained, ring-tilted ferrocenophanes: A route to high-molecular-weight poly (ferrocenylsilanes)', *J. Am. Chem. Soc.*, 1992 **114**(15) 6246–8.
  50. Lammertink R.G.H., Hempenius M.A., van den Enk J.E., Chan V.Z.H., Thomas E.L. and Vancso G.J., 'Nanostructured thin films of organic-organometallic block

- copolymers: One-step lithography with poly(ferrocenylsilanes) by reactive ion etching', *Adv. Mater.*, 2000 **12**(2) 98–103.
51. Zehner R.W., Lopes W.A., Morkved T.L., Jaeger H. and Sita L.R., 'Selective decoration of a phase-separated diblock copolymer with thiol-passivated gold nanocrystals', *Langmuir*, 1998 **14**(2) 241–4.
  52. Zehner R.W. and Sita L.R., 'Electroless deposition of nanoscale copper patterns via microphase-separated diblock copolymer templated self-assembly', *Langmuir*, 1999 **15**(19) 6139–41.
  53. Spatz J.P., Mossmer S., Hartmann C., Moller M., Herzog T., Krieger M., Boyen H.G., Ziemann P. and Kabius B., 'Ordered deposition of inorganic clusters from micellar block copolymer films', *Langmuir*, 2000 **16**(2) 407–15.
  54. Morkved T.L., Wiltzius P., Jaeger H.M., Grier D.G. and Witten T.A., 'Mesoscopic self-assembly of gold islands on diblock copolymer films', *Appl. Phys. Lett.*, 1994 **64**(4) 422–4.
  55. Chou S.Y., 'Patterned magnetic nanostructures and quantized magnetic disks', *Proc. IEEE*, 1997 **85**(4) 652–71.
  56. Shin K., Leach K.A., Goldbach J.T., Kim D.H., Jho J.Y., Tuominen M., Hawker C.J. and Russell T.P., 'A simple route to metal nanodots and nanoporous metal films', *Nano Letters*, 2002 **2**(9) 933–6.
  57. Thurn-Albrecht T., DeRouchey J., Russell T.P. and Jaeger H.M., 'Overcoming interfacial interactions with electric fields', *Macromolecules*, 2000 **33**(9) 3250–3.
  58. Jeong U.Y., Kim H.C., Rodriguez R.L., Tsai I.Y., Stafford C.M., Kim J.K., Hawker C.J. and Russell T.P., 'Asymmetric block copolymers with homopolymers: Routes to multiple length scale nanostructures', *Adv. Mater.*, 2002 **14**(4) 274–6.
  59. Jeong U.Y., Ryu D.Y., Kim J.K., Kim D.H., Wu X.D. and Russell T.P., 'Precise control of nanopore size in thin film using mixtures of asymmetric block copolymer and homopolymer', *Macromolecules*, 2003 **36**(26) 10126–9.
  60. Hamley I.W., 'Nanostructure fabrication using block copolymers', *Nanotechnology*, 2003 **14**(10) R39–54.
  61. Park C., Yoon J. and Thomas E.L., 'Enabling nanotechnology with self-assembled block copolymer patterns', *Polymer*, 2003 **44**(22) 6725–60.
  62. Lazzari M. and Lopez-Quintela M.A., 'Block copolymers as a tool for nanomaterial fabrication', *Adv. Mater.*, 2003 **15**(19) 1583–94.
  63. Harrison C., Adamson D.H., Cheng Z.D., Sebastian J.M., Sethuraman S., Huse D.A., Register R.A. and Chaikin P.M., 'Mechanisms of ordering in striped patterns', *Science*, 2000 **290**(5496) 1558–60.
  64. Harrison C., Cheng Z.D., Sethuraman S., Huse D.A., Chaikin P.M., Vega D.A., Sebastian J.M., Register R.A. and Adamson D.H., 'Dynamics of pattern coarsening in a two-dimensional smectic system', *Phys. Rev. E.*, 2002 **66**(1) 011706.
  65. Harrison C., Angelescu D.E., Trawick M., Cheng Z., Huse D.A., Chaikin P.M., Vega D.A., Sebastian J.M., Register R.A. and Adamson D.H., 'Pattern coarsening in a 2D hexagonal system', *Europhys. Lett.*, 2004 **67**(5) 800–6.
  66. Hashimoto T., Bodycomb J., Funaki Y. and Kimishima K., 'The effects of temperature gradient on the microdomain orientation of diblock copolymers undergoing an order-disorder transition', *Macromolecules*, 1999 **32**(3) 952–4.
  67. Angelescu D.E., *Physics and Applications of Diblock Copolymer Thin Films*, Ph.D. Thesis, Princeton University, 2003.
  68. Kim S.H., Misner M.J., Xu T., Kimura M. and Russell T.P., 'Highly oriented and ordered arrays from block copolymers via solvent evaporation', *Adv. Mater.*, 2004 **16**(3) 226–31.

69. Fasolka M.J., Harris D.J., Mayes A.M., Yoon M. and Mochrie S.G.J., 'Observed substrate topography-mediated lateral patterning of diblock copolymer films', *Phys. Rev. Lett.*, 1997 **79**(16) 3018–21.
70. Rockford L., Liu Y., Mansky P., Russell T.P., Yoon M. and Mochrie S.G.J., 'Polymers on nanoperiodic, heterogeneous surfaces', *Phys. Rev. Lett.*, 1999 **82**(12) 2602–5.
71. Rockford L., Mochrie S.G.J. and Russell T.P., 'Propagation of nanopatterned substrate templated ordering of block copolymers in thick films', *Macromolecules*, 2001 **34**(5) 1487–92.
72. Kim S.O., Solak H.H., Stoykovich M.P., Ferrier N.J., de Pablo J.J. and Nealey P.F., 'Epitaxial self-assembly of block copolymers on lithographically defined nanopatterned substrates', *Nature*, 2003 **424**(6947) 411–4.
73. Trawick M., Angelescu D., Chaikin P., Sebastian J., Register R., Adamson D. and Harrison C., 'Tracking topological defects in arrays of block copolymer spherical microdomains', *Bull. Am. Phys. Soc.*, 2002 **47**(1) 970.
74. Segalman R.A., Yokoyama H. and Kramer E.J., 'Graphoepitaxy of spherical domain block copolymer films', *Adv. Mater.*, 2001 **13**(15) 1152–5.
75. Segalman R.A., Hexemer A. and Kramer E.J., 'Effects of lateral confinement on order in spherical domain block copolymer thin films', *Macromolecules*, 2003 **36**(18) 6831–9.
76. Cheng J.Y., Ross C.A., Thomas E.L., Smith H.I. and Vancso G.J., 'Fabrication of nanostructures with long-range order using block copolymer lithography', *Appl. Phys. Lett.*, 2002 **81**(19) 3657–9.
77. Amundson K., Helfand E., Davis D.D., Quan X., Patel S.S. and Smith S.D., 'Effect of an electric field on block copolymer microstructure', *Macromolecules*, 1991 **24**(24) 6546–8.
78. Morkved T.L., Lu M., Urbas A.M., Ehrichs E.E., Jaeger H.M., Mansky P. and Russell T.P., 'Local control of microdomain orientation in diblock copolymer thin films with electric fields', *Science*, 1996 **273**(5277) 931–3.
79. De Rosa C., Park C., Thomas E.L. and Lotz B., 'Microdomain patterns from directional eutectic solidification and epitaxy', *Nature*, 2000 **405**(6785) 433–7.
80. Park C., De Rosa C. and Thomas E.L., 'Large area orientation of block copolymer microdomains in thin films via directional crystallization of a solvent', *Macromolecules*, 2001 **34**(8) 2602–6.
81. Keller A., Pedemonte E. and Willmouth F.M., 'Macro-lattice from segregated amorphous phases of a 3 block copolymer', *Nature*, 1970 **225**(5232) 538–40.
82. Sundrani D. and Sibener S.J., 'Spontaneous spatial alignment of polymer cylindrical nanodomains on silicon nitride gratings', *Macromolecules*, 2002 **35**(22) 8531–9.
83. Kimura M., Misner M.J., Xu T., Kim S.H. and Russell T.P., 'Long-range ordering of diblock copolymers induced by droplet pinning', *Langmuir*, 2003 **19**(23) 9910–3.
84. Morrison F.A. and Winter H.H., 'Effect of unidirectional shear on the structure of triblock copolymers. 1. Polystyrene-polybutadiene-polystyrene', *Macromolecules*, 1989 **22**(9) 3533–40.
85. Hadziioannou G., Mathis A. and Skoulios A., 'Synthesis of 3-block styrene-isoprene-styrene copolymer single-crystals via plane shear-flow', *Colloid. Polym. Sci.*, 1979 **257**(2) 136–9.
86. Hadziioannou G., Picot C., Skoulios A., Ionescu M.L., Mathis A., Duplessix R., Gallot Y. and Lingelser J.P., 'Low-Angle neutron scattering study of the lateral extension of chains in lamellar styrene-isoprene block copolymers', *Macromolecules*, 1982 **15**(2) 263–7.

87. Almdal K., Koppi K.A. and Bates F.S., 'Dynamically sheared body-centered-cubic ordered diblock copolymer melt', *Macromolecules*, 1993 **26**(15) 4058–60.
88. Chen Z.R., Kornfield J.A., Smith S.D., Grothaus J.T. and Satkowski M.M., 'Pathways to macroscale order in nanostructured block copolymers', *Science*, 1997 **277**(5330) 1248–53.
89. Zhuang L., *Controlled Self-Assembly in Homopolymer and Diblock Copolymer*, Ph.D. Thesis, Princeton University, 2002.
90. Angelescu D.E., Waller J.H., Adamson D.H., Deshpande P., Chou S.Y., Register R.A. and Chaikin P.M., 'Macroscopic orientation of block copolymer cylinders in single-layer films by shearing', *Adv. Mater.*, 2004 **16**(19) 1736–9.
91. Angelescu D.E., Waller J.H., Register R.A. and Chaikin P.M., 'Shear-induced alignment in thin films of spherical microdomains', *Adv. Mater.*, 2005, posted on Early View.
92. Du P., Li M.Q., Douki K., Li X.F., Garcia C.R.W., Jain A., Smilgies D.M., Fetters L.J., Gruner S.M., Wiesner U. and Ober C.K., 'Additive-driven phase-selective chemistry in block copolymer thin films: The convergence of top-down and bottom-up approaches', *Adv. Mater.*, 2004 **16**(12) 953–7.

## Surface-induced structure formation of polymer blends

---

R J COMPOSTO and H-J CHUNG,  
University of Pennsylvania, USA

### 2.1 Introduction

Polymer thin films containing mixtures of different polymers and sometimes (nano)particles can provide precise control over processing pathways leading to unique morphologies that have many applications including biomedical scaffolds, electro-optical devices, porous membranes and automotive coatings. Because these components are typically incompatible and confined between surfaces, phase growth is hindered and the wetting behavior at surfaces grows in importance due to the high surface to volume ratio. The complex interplay between wetting and phase separation in thin film polymer blends provides an opportunity to vary the morphology in a systematic fashion over length scales ranging from tens of nanometers to tens of microns. Although these features are larger than those possible with conventional lithographic methods, manipulating wetting and phase separation to control feature size is more facile, requiring only one or two steps to make well-defined, complex structures, and much less expensive. Moreover, combining polymer film technology with soft-lithographic methods provides a simple route for pattern replication. Thus, patterning of thin film polymer blends has the potential to replace conventional lithographic methods to create meso-scale structures.

The greatest hurdle to control pattern formation in thin film polymer blends is in understanding the dynamic interplay between phase separation, wetting and dewetting. Because of the slow dynamics of polymers, non-equilibrium patterns can be frozen during morphology evolution leading to unstable structures. Thus, the dynamics of phase separation and wetting will be considered in this chapter. For example, after quenching into a thermodynamically unstable regime of temperature-composition, a homogeneous polymer mixture will undergo a spontaneous demixing process, which is called a spinodal decomposition<sup>1</sup>. This process leads to isotropic pattern development in bulk with a periodicity that follows dynamic scaling analysis<sup>2</sup>. However, if the mixture is confined to a film, preferential wetting

of one component at the surface is dynamically coupled with phase separation, causing the formation of alternating layers with oscillating concentrations, i.e., surface-directed spinodal decomposition<sup>3</sup>. When the phase size approaches the film thickness, domain growth changes from 3D to pseudo-2D, followed by the growth of a well defined lateral pattern<sup>4,5,6</sup>. As an additional complication, films can rupture by dewetting leading to roughened surfaces<sup>7,8</sup>. In summary, pattern formation in thin film polymer blends requires an understanding of the complex dynamic interplay between phase separation, wetting and dewetting.

The purpose of this chapter is to consolidate in one place the most recent developments in the area of surface-induced pattern formations in thin film polymer blends. Because it is the technologically most useful geometry, the chapter will be limited to films deposited on a substrate with a free surface (i.e., polymer/air). Because of its practical use, phase morphologies occurring at deep quenches will be considered rather than those near criticality, such as wetting transitions. We limit our scope to the studies of lateral pattern formation, which have the potential to compete with conventional lithography. Consequently, experimental studies of wetting and dewetting will receive limited attention in this chapter. Pattern evolution in blends containing one or more crystallizing components<sup>9,10,11,12,13</sup> is also beyond the scope of this chapter. The content of this chapter is related to other chapters including Chapter 1 which describes how copolymer ordering produces patterns and Chapter 5 where dewetting of confined polymer films is used to create topographic features.

Several reviews related to the subject of this chapter fill in several of the topics not covered. For example, the dynamic properties of phase separation are reviewed by Gunton *et al.*<sup>1</sup> This book provides a comprehensive review of the fundamentals of phase separations with an in-depth discussion of dynamics. A recent review by Binder<sup>14</sup> covers the theory describing the interplay between surface and finite size effects, the key topics underpinning thin film phase behavior. Surface segregation and wetting phenomena are extensively covered in the review by Budkowski<sup>15</sup>. This work includes an extensive review of experimental studies along with related theories. A comparison with an earlier review by Krausch<sup>16</sup> shows how rapidly this field developed. Theories of phase transitions in polymer blends under confinement are reviewed by Binder<sup>17</sup>. This review is particularly interesting because it compares theories and experiments from the point of view of a theorist; we note that the theories are limited to planar boundaries (i.e. no surface roughening). A recent review by Geoghegan and Krausch<sup>18</sup> summarizes developments in thin film polymer blends, including wetting, phase separation, and dewetting. This review also presents studies of lateral pattern formation in polymer blends. Finally, the role of hydrodynamics in pattern evolution of polymer solutions and melts are reviewed by Tanaka<sup>4</sup>. Because hydrodynamics

has been found to play a role even in the demixing of viscous polymer melts, this review is particularly relevant.

This chapter is organized as follows. Section 2.2 provides a brief theoretical introduction to the key phenomena relevant to surface-induced pattern formation in thin film polymer blends, namely phase separation, wetting, their interplay in a confined system, and dewetting. Section 2.3 will review experimental techniques typically used to characterize the structure of thin film polymer blends. Techniques are classified as either depth profiling or lateral imaging; an introduction to the next generation of techniques such as those that provide 3D information is provided. In section 2.4, pattern formation is differentiated by the mechanism of morphology evolution. First, pattern evolutions under symmetric wetting conditions (ABA) are discussed. Here, the dynamic interplay between wetting and phase separation plays a crucial role and eventually thin films rupture by dewetting. Secondly, pattern evolutions under asymmetric wetting conditions (AB) are discussed. Here, growing wetting layers eventually form a bilayer structure, and eventually dewetting may occur. Thirdly, morphology evolutions on chemically or structurally patterned substrates are discussed. Alternating boundary conditions cause a phase confinement, resulting in pattern replication. Finally, solvent-induced structure formation is discussed. Although the resulting structures are difficult to control and are unstable, this method of structure formation deserves attention because co-solvents that equally solubilize all polymer components are difficult to achieve in practice. Thus, this method may have the broadest practical application of all previously mentioned processing routes. In section 2.5, future research directions will be suggested and in section 2.6, a short summary of this chapter is given.

## 2.2 Background

### 2.2.1 Phase separation

In thin film processing, one can deposit multicomponent polymer mixtures in one phase and change external parameters (temperature  $T$ , pressure  $P$ , etc.) inside a miscibility gap in the (thermodynamic) equilibrium phase diagram of the system. In this case, thermodynamics determines whether the mixture develops co-existing phases whereas kinetics predicts time-dependent phase development. Thermodynamically, phase behaviors can be defined from the free energy density of mixing,  $F(c)$ . Inside the miscibility gap, phase separation can be distinguished between metastable states,  $\partial^2 F(c)/\partial c^2 > 0$ , and unstable states,  $\partial^2 F(c)/\partial c^2 < 0$ . In metastable states, phase separation is initiated by externally formulated nucleus. In unstable states, on the other hand, random thermal fluctuations cause instability of the system, followed by amplification of the composition fluctuations. This spontaneous phase separation is called

spinodal decomposition. In the simplified linear theory, all concentration wavelengths whose wavelength  $\lambda$  exceeds a critical value  $\lambda_c$  grow exponentially with time, whereas a single maximum wavelength,  $\lambda_m = \sqrt{2}\lambda_c$ , becomes dominant<sup>19,20</sup>. However, recent theoretical development points out that the linear theory is incorrect due to the nonlinear coupling between waves and thus  $\lambda_m$  increases with time<sup>14</sup>. When the compositional fluctuation develops to fully co-existing phases, interfaces between phases become sharp. Correspondingly, well-defined phase domains continue to grow, characterizing the late stage of spinodal decomposition.

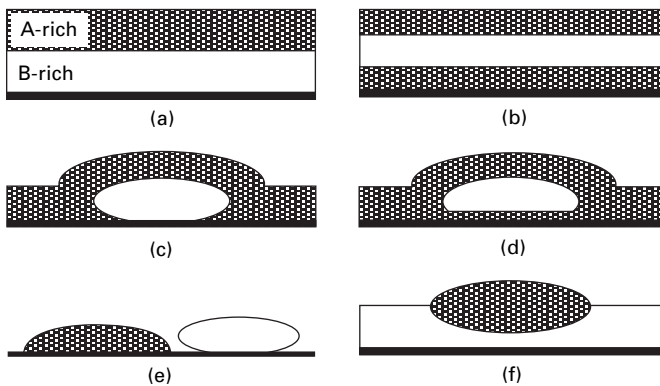
Kinetics of the late stage of spinodal decomposition is described using a dynamic scaling hypothesis, which proposes that a dominant length scale characterizes domain growth at the late stage<sup>1</sup>. The dominant length scale  $R(t)$  is defined as  $2\pi \int S(k, t)dk / \int kS(k, t)dk$ , where  $S(k, t)$  is the density autocorrelator<sup>21</sup>, and follows a power growth law with time,  $R(t) \sim t^\alpha$ . Scaling arguments predict that the growth exponent  $\alpha$  indicates the mechanisms of domain growth. In 3D bulk systems, a well-known Lifshitz-Slyozov theory, otherwise known as the evaporation-condensation mechanism, predicts  $\alpha = 1/3$  when larger domains grow at the expense of smaller ones driven by local minority component solubility gradients in the majority phase<sup>22</sup>. In this case, molecular diffusion of the minority component in the majority phase controls the growth. Alternatively, Binder and Stauffer<sup>23</sup> predicted that domains migrate as a Brownian motion and occasional coalescence drives domain growth. This theory, as well as a recent hydrodynamics-included model by Tanaka<sup>24</sup>, predicts  $\alpha = 1/3$ . In polymer mixtures, however, in-phase material flow becomes important when minority phases are percolated (i.e. co-continuous domain structure). In this case, local domain curvature drives material flow from ‘neck’ to ‘bulges’, causing a rapid growth of domains. When the flow is limited by viscosity, a simple scaling argument by Siggia<sup>25</sup> predicts  $\alpha = 1$ , and it was confirmed for binary polymer mixtures in bulk<sup>26</sup>.

For thin film polymer blends, however, confinement induces many complications in phase separation. For example, the phase diagram of a confined system differs from the bulk<sup>17</sup>. In addition, thickness confinement induces a dimensional change of phase separation from 3D to pseudo-2D, causing a change in the growth mechanism<sup>4,5,6</sup>. Most importantly, morphology development is greatly perturbed by wetting phenomena because of a large surface to volume ratio in thin film geometry. A dramatic example is the surface-directed spinodal decomposition (SDSD)<sup>3</sup>, where spinodal decomposition acquires anisotropy due to the surface effect, resulting in a formation of layered structure parallel to the surface. Naturally, transient and final morphology cannot be interpreted without understanding wetting phenomena.

### 2.2.2 Wetting

Wetting phenomena always play important roles because the surface tension between polymer components is different. Preferential wetting attracts one of the components to substrate or free surface and consequently impacts transient and final morphologies of thin film polymer blends. Thermodynamically, wetting in a phase separating binary blend AB in contact with a surface (or a substrate) is defined using a spread coefficient  $S_A = \gamma_{WB} - \gamma_{WA} - \gamma_{AB}$ , where  $\gamma_{WB}$ ,  $\gamma_{WA}$ , and  $\gamma_{AB}$  are the interfacial tensions between the wall and B-rich phase, the wall and A-rich phase, and the A-rich and B-rich phases, respectively. For partial wetting, the resulting contact angle is  $\cos \theta = (\gamma_{WB} - \gamma_{WA}) / \gamma_{AB}$ . Therefore, a finite contact angle is expected in equilibrium morphology of phase separating blends due to the difference between  $\gamma_{WB}$  and  $\gamma_{WA}$ . In theory, infinite wetting layer growth (i.e., complete wetting) is to be found above a wetting transition temperature located near the critical point of spinodal decomposition (i.e., shallow quench)<sup>15,17,27,28</sup>. In practice, however, surface and substrate serve as a nucleation site for phase separation and infinite enriching of the wetting layer is commonly found in thin film polymer blends at deep quenches<sup>3,4,29</sup>.

Figure 2.1 shows some possible examples of equilibrium morphologies for phase-separating binary polymer blend films on a substrate. Assuming that the A-rich phase is preferred at the top surface, one can hypothesize six equilibrium morphologies: (a) A- and B-rich phases completely wet the surface and substrate respectively, (b) A-rich completely wets both surfaces and B-rich is located in the middle, (c) A-rich completely wets the surface and B-rich partially wets the substrate, (d) A-rich completely wets both surfaces and B-rich is broken as droplets, (e) Both A- and B-rich dewets from substrate, and (f) A-rich partially wets the surface and B-rich completely



2.1 Six equilibrium morphologies of thin film polymer blends which demonstrate how the interplay between phase separation, wetting, and dewetting produces different structures. See text for further details.

wets the substrate. Among the hypothesized morphologies, (a) and (b) are not likely to persist because they contain a large interfacial area between A- and B-rich phases. These stratified morphologies tend to rupture by the dewetting process. Besides the suggested equilibrium morphologies, various transient morphologies are also possible due to kinetic competition among phase separation, wetting, and dewetting. These transient morphologies may also persist for a long time or even become fixed when there is no direct kinetic route towards equilibrium.

### 2.2.3 Dewetting

Dewetting is a breakup of film to achieve minimization of free energy of the system by reducing surface or interface energy. An enormous amount of work has been done on this theoretically and practically important problem. In this section, we will introduce the most relevant problems to the morphology evolutions of polymer blend thin films. Specifically, we will consider the condition of spontaneous breakup of thin films by thermal fluctuations, known as spinodal dewetting.

Spinodal dewetting is driven by the long-range van der Waals force between interfaces. For the simplest case, one can imagine a thin film of a single component between a substrate and a surface (vacuum). When the long-range attractive interaction between two surfaces is large enough to overcome short-range forces at interfaces, the film will spontaneously break up by growing thermal fluctuations<sup>30</sup>. The attractive energy between two planar surfaces can be expressed as  $V(h) = -A_H / 12\pi d^2$ , where  $A_H$  is the Hamaker constant between two surfaces through the medium of film and  $d$  is film thickness<sup>31</sup>. A linear stability analysis shows that the fastest-growing wavelength and the time constant for rupture are  $\Lambda_c = 2\pi d_0^2 (\pi\gamma/A_H)^{1/2}$  and  $\tau_m = 96\pi^2 \gamma \eta d_0^5 A_H^{-2}$ , respectively, where  $d_0$ ,  $\gamma$ , and  $\eta$  are initial thickness, surface tension, and viscosity, respectively<sup>32</sup>. This implies two important features for thin film morphology control. First, one can control the periodicity of patterns using spinodal dewetting. Secondly, thick films are less prone to dewet, meaning that stratified patterns can be stable for long time when the films are thick.

## 2.3 Experimental techniques

### 2.3.1 Depth-profiling techniques

Depth profiling is used to explore the composition variation of films as a function of depth. It is particularly important to investigate wetting phenomena quantitatively, which is necessary to understand the mechanism of pattern development. Typically, hydrogen atoms in one of the polymer components

are replaced by deuterium to achieve compositional labeling with minimal change in polymer properties. In practice, ion-scattering techniques and reflectivity measurements are primarily used for depth profiling.

Elastic recoil detection (ERD), also known as forward recoil spectrometry (FREs), has probably been the most standard ion-scattering technique to investigate depth profiles in polymer films<sup>33</sup>. Here,  $^4\text{He}^+$  or  $^4\text{He}^{++}$  ion beams scatter hydrogen and deuterium in the sample to forward direction. The incident ions and scattered atoms lose kinetic energy mainly due to the interactions between the particles and electrons in the sample, which is called straggling. Hence, kinetic energy of detected hydrogen or deuterium can be converted directly into the depth where atomic collision occurs. To shield the detector from recoiled helium ions, mylar foils are typically placed in front of the detector, which degrades depth resolution. One of the advantages of using ERD is rapid data acquisition. However, poor depth resolution of  $\sim 80$  nm in conventional ERD (3 MeV,  $^4\text{He}^{++}$ , 10  $\mu\text{m}$  mylar) can be problematic<sup>33</sup>. Efforts have been made to improve the depth resolution. For example, the optimization of beam energy and incident angle (LE- or low-energy ERD<sup>34</sup>) achieved the depth resolution of  $\sim 12$  nm. However, probe depth needs to be compromised ( $\sim 70$  nm compared to  $\sim 700$  nm of the conventional ERD) to obtain the high depth resolution. The use of time-of-flight (ToF) apparatus enables the depth resolution of  $\sim 20$  nm by eliminating the use of mylar foil<sup>35</sup>, but the use of ToF is limited by complicated and vulnerable instrumentation.

Rutherford backscattering (RBS) detects recoiled incident ions, typically  $^4\text{He}^{++}$ , from elastic collision with atoms in the sample. Like ERD, incident ions lose energy mainly due to straggling, enabling a direct conversion of kinetic energy to depth profiles. However, this technique is rarely used in polymer research because it requires heavy atoms in the sample. Selective staining of one of components may be applied to use RBS in polymer wetting studies<sup>36</sup>.

Nuclear reaction analysis (NRA) is another powerful ion-beam method to investigate depth profiling in polymer blends<sup>37,38</sup>. Using  $^3\text{He}$  as an incident atom, nuclear reaction with deuterium produces  $^4\text{He}$  atom and a proton, denoted as  $^2\text{H}(^3\text{He}, ^1\text{H})^4\text{He}$ . Because the reaction is quite endothermic ( $Q = 18.352$  MeV), the outgoing  $^4\text{He}$  and  $^1\text{H}$  atoms have high kinetic energy, well separated from incident atoms. Therefore, no mylar foils are needed and a depth resolution better than 20 nm is routinely obtained. The major drawback of NRA is that only deuterium profiles are obtainable. Other nuclear reactions with 1H atoms, such as  $^1\text{H}(^{15}\text{N}, ^4\text{He} \gamma)^{12}\text{C}$ , are suggested<sup>39</sup>, but this suffers from practical difficulties for polymer research so that implementation has not been successful. Another drawback of NRA is that data acquisition is much slower than ERD due to the low cross-section for the nuclear reaction.

The last ion beam technique to mention is dynamic secondary ion mass spectrometry (dynamic SIMS)<sup>40</sup>. In this technique, a beam of ions, typically  $O_2^+$  or  $Ar^+$  etches the film, and the emitted fragments from the sample are analyzed with a mass spectrometer. With controlled etching rate, time is converted to distance from the surface and it enables depth profiling. The major advantage of dynamic SIMS is its capability to detect various elements or molecular species other than hydrogen and deuterium with an excellent depth resolution ( $\sim 10$  nm). However, depth calibration is very difficult and sample dependent, making dynamic SIMS difficult to use in heterogeneous films. Another drawback is slow data acquisition.

As mentioned above, X-ray and neutron reflectivity (XR and NR, respectively) also offer depth information in reciprocal space<sup>41,42</sup>. In these techniques, a collimated monochromatic beam is scattered from the sample, and then structural information is deduced from the intensity of reflected beams. The reflected intensity distribution is determined by the interference of waves at the interfaces between layers of different scattering cross-sections (i.e., refractive indices). Because atomic density is nearly constant in polymer films, the reflected intensity distribution is a function of the refractive indices of layers. It is well known that hydrogen and deuterium have large differences in refractive indices. Thus, NR is more suited for polymer blends than XR, which requires a large deviation in atomic numbers. For depth profiling, specular reflectivity (i.e., incident beam has the same angle as reflected beam) is used whereas off-specular reflectivity provides information on interface roughness. The reflectivity measurements provide exceptional spatial resolution ( $\sim 0.5$  nm). However, interpretation of the raw spectrum is model dependent and often results in a misleading conclusion. Therefore, simultaneous use of both techniques is ideal to obtain the best depth profile<sup>43</sup>.

### 2.3.2 Lateral imaging techniques

Lateral patterns in thin film polymer blends can be visualized using imaging techniques, such as optical microscopy (OM), surface force microscopy (SFM), scanning near-field optical microscopy (SNOM), scanning or transmission electron microscopy (SEM or TEM), and near-edge X-ray absorption fine structure (NEXAFS). When the lateral length scale is sufficiently large and optical contrast between phases exists, OM provides the most convenient way to examine lateral patterns. However, one should note that a variation in thickness can also provide optical contrast therefore the optimal way to study lateral patterns is the combined use of topography and composition profiling techniques.

SFM is the most widely used technique to study nanometer scale features. For example, surface topography can easily be profiled by controlling tip-surface interactions. Local deviations in surface mechanical properties, such

as viscosity and stiffness, can also be quantitatively mapped simultaneously<sup>44,45</sup>. This technique can be used to differentiate lateral compositional profiles at a surface. Here, surface indentation should be taken into account while investigating heterogeneous samples<sup>46</sup>. In addition, selective etching of one of the components can be utilized to investigate internal phase structures<sup>5</sup>.

SNOM combines the merits of SFM and optical probes. By using a nanometer-sized optical aperture and keeping tip-surface distance constantly at some nanometers, SNOM enables optical imaging as well as spectroscopy at sub-wavelength lateral resolution<sup>47,48</sup>. Surface topography can also be profiled by 'shear-force' distance control between tip and sample surface. Despite its versatility, SNOM has not been widely used for thin film polymer blends due to technical problems. However, SNOM has recently drawn attention as one of the major tools to investigate conjugated polymer blends<sup>49,50</sup>.

The last technique that is worth mentioning is NEXAFS, an X-ray microscope from a synchrotron source. Despite the demanding equipment requirements, NEXAFS provides lateral chemical profiles with a spatial resolution of about 45 nm<sup>51,52</sup>.

### 2.3.3 Three-dimensional mapping techniques

The most ideal experimental method to study the morphology of thin film polymer blends is, of course, a direct 3D visualization. Here, we introduce some of recent developments on the methodologies. The first technique to mention is laser scanning confocal microscopy (LCSM)<sup>53</sup>. LCSM provides a fast and non-destructive method for 3D imaging. Although low spatial resolution ( $\sim 1 \mu\text{m}$ ) hampers its use on thin film polymer blends, LCSM is certainly a powerful method for fundamental studies of the interplay between wetting and phase separation<sup>54</sup>. Another interesting technique comes from the combination of SFM and plasma etching, named 'nanotomography'<sup>55</sup>. Followed by layer-by-layer plasma etching, topographic and mechanical property profiles on the respective plane are obtained by SFM, and then combined and reconstructed into a 3D-rendered image with a superb spatial resolution of some few nanometers. A similar approach has been reported using dynamic SIMS with scanning abilities<sup>56,57</sup>. Using focused ion beam, lateral and vertical resolutions are improved up to  $\sim 120 \text{ nm}$  and  $\sim 10 \text{ nm}$ , respectively<sup>56</sup>. Although the usage of these techniques is currently limited by operational difficulties and strict material selections, we believe that these 3D imaging techniques will eventually revolutionize studies on the structures of thin films.

To conclude this section, we note that one should keep in mind that pattern evolution occurs underneath the film surface as a complex interplay among phase separation, wetting and dewetting. In other words, observations of both surface topological change (such as film roughening) and compositional

change (such as phase coarsening) are necessary to understand lateral pattern development in thin film polymer blends. Compositional information on depth direction should also be studied to understand the role of wetting. In short, erroneous conclusions can be drawn if one relies only on topological or compositional analyses.

## 2.4 Surface-induced patterns of binary polymer blends

In this section, we will discuss experimental investigations of the binary polymer mixtures. Motivated by the developments of the characterization tools mentioned in the previous section, the understanding of pattern formation of binary mixtures is reaching maturity from a decade of extensive research. Here, we will summarize the major findings with representative images and introduce underlying mechanisms of pattern development.

### 2.4.1 Morphology development in symmetrically wetting (ABA) blends

In phase-separating binary polymer blend thin films, a trilayer-like structure develops when one of the components (denoted as ‘A’) segregates at both the free surface and substrate. Here, we denote this symmetric wetting situation as ABA blends. In ABA blends, roughly three cases of wetting scenario can be considered depending on the kinetic competition between phase separation and wetting. First, columnar domains connecting surface and substrate can be formed when A phase partially wets surface and substrate (type I). This case is possible if the kinetics of phase separation are much faster than wetting or if the wettability at the surface and substrate is weak. In this case, pattern development kinetics will be limited by diffusion, leading to a Lifshitz-Slyozov growth ( $\sim t^{1/3}$ )<sup>22</sup>. Secondly, a trilayer structure as drawn in Fig. 2.1(b) can be formed when wetting kinetics dominates (type II). In this case, rapid wetting depletes the A phase from the mid-layer, leading to a complete trilayer formation. This structure may rupture by dewetting or be kinetically stabilized, as explained in section 2.2.3. Thirdly, probably the most common case is having wetting layers at both surface and substrate with phase co-existing mid-layer (type III). Hydrodynamics becomes important for pattern growth because of the phase connectivity<sup>4</sup>. This case has been of interest for most quantitative studies on pattern development and is the main topic of this section.

In this section, we will concentrate on the morphology development mechanisms, as well as pattern growth kinetics. Kinetics of wetting will be mentioned only when related to with lateral pattern development, which comes after the wetting-dominated regime. We limit our scope to the case of

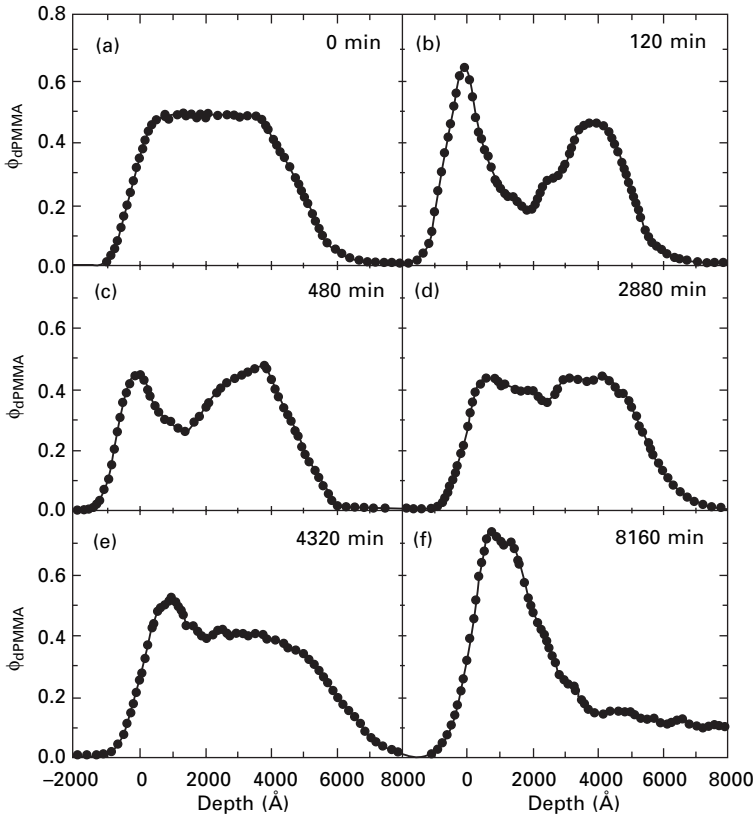
compositionally homogeneous films at deposition to ensure a well-controlled starting point. Pattern development is affected by thermodynamic properties, such as annealing temperature (difference from the critical point), miscibility  $\chi$ , and composition ratio. Akpalu *et al.*<sup>58</sup> studied temperature dependence on the equilibrium morphologies of polyolefin blend films. With NR and XR, almost identical depth profiles were obtained from a wide range of annealing temperatures, suggesting that temperature has only a weak effect on the pattern development of polymer blend films. Affrossman *et al.*<sup>59</sup> studied the dependence of polymer compatibility on pattern development using the blend of deuterated polystyrene (dPS) and poly(styrene-*co*-bromostyrene) (PBr<sub>x</sub>S), where  $x$  is the degree of bromination ( $0.076 < x < 1$ ). With reducing  $x$ , polymer compatibility increases, leading to a suppression of topographical features. In this section, we will first introduce important experimental findings in chronological order. Then, we will explain three distinct regimes of 'type III' morphology development of polymer blends at critical compositions<sup>5,60</sup> and expand this understanding to off-critical mixtures. Quantitative analyses on pattern development as a function of annealing time will also be discussed.

Since the discovery of SDSD by Jones *et al.*<sup>3</sup> using the mixture of hydrogenated and deuterated poly(ethylenepropylene) (PEP and dPEP) in 1991, the complicated interplay between wetting and phase separation has been realized. Studies by Bruder and Brenn<sup>61</sup> qualitatively showed that the interplay can result in a lateral pattern development. Using blends of PS and poly(vinylmethylether) (PVME) in symmetrically confined geometry, Tanaka<sup>62</sup> showed that wetting layers induce a novel domain ordering and coarsening mechanism, suggesting the importance of hydrodynamic flow. The first attempt to quantitatively decouple the kinetics of wetting and phase separation was from Straub *et al.*<sup>63</sup> Using ToF-ERD and SNOM to observe wetting layer and lateral pattern growth, respectively, the growth kinetics of dPS/PBr<sub>0.097</sub>S blend was shown to follow the well-known power law growth,  $t^{1/3}$ , for both directions. However, a comprehensive morphology development scenario was not possible mainly because the authors were not able to explore the internal morphology. Using OM as an imaging tool, the first study of film thickness dependence on the lateral pattern growth was by Sung *et al.*<sup>64</sup> They found a varied range of transient power law growth,  $t^\alpha$ , where  $\alpha$  ranges from 1/3 to 1. However, this work was later criticized by Binder<sup>17</sup> because the effective composition shift due to preferential wetting was not considered. He also pointed out that the mechanism of morphology quenching is also not completely understood. The morphology quenching may stem from solidification of dPS because the annealing temperature (25°C) is far below the glass transition temperature of dPS (90°C for Mw = 1000) Karim *et al.*<sup>65,66</sup> and Slep *et al.*<sup>67</sup> continued to investigate the later pattern developments, but the kinetic origin of the growth was not explained. Heier *et al.*<sup>68</sup> performed

a thorough kinetics study on the wetting layer and lateral pattern growth in off-critical compositions of dPEP/PEP blends. Interestingly, they found a  $t^1$  growth in the off-critical compositions ( $\phi_{\text{dPEP}} = 0.64$  and  $0.69$ ) whereas  $t^{1/3}$  growth was previously found in critical composition ( $\phi_{\text{dPEP}} = 0.5$ )<sup>69</sup>. A rather interesting growth exponent for lateral pattern growth,  $t^{0.8}$ , was also observed from surface topography by SFM. However, these growth exponents could not be directly interpreted by the context of phase separation because they did not examine internal morphologies of dPEP and PEP phases, where the phase separation actually occurs.

In the research on the morphology development of thin film polymer blends, the main difficulties arise from the complexity of the interplay between phase separation, wetting, and dewetting. The complexity can be resolved only if one can differentiate the dominant mechanism for each stage of morphology development. Using the blends of deuterated poly(methyl methacrylate) and poly(styrene-ran-acrylonitrile) (dPMMA and SAN), the entire phase evolution was revealed for 'Type III' thin film polymer blends by a series of research from Composto's group<sup>5,6,7,60,70,71,72,73,74</sup>. By studying evolutions of the dPMMA depth profiles using LE-ERD and surface and internal topographies using SFM from critical blends ( $\phi_{\text{dPMMA}} = 0.47$ ) with 495 nm film thickness, they identified three distinct stages of morphology development. Figure 2.2 shows the dPMMA volume fraction depth profiles from sample deposition to equilibrium structures. The as-cast film is homogeneous in Fig. 2.2(a) and stratifies to trilayers during the early stage up to 120 minutes of annealing, shown in Fig. 2.2(b). From 120 to 2,880 minutes (Figs 2.2(b–d)), the surface and substrate peak diminish until  $\phi_{\text{dPMMA}}$  becomes homogeneous. After 4,320 min (Figs 2.2(e) and (f)), reconstruction of surface peak and a drastic increase in film roughness (i.e., broad tail of  $\phi_{\text{dPMMA}}$ ) become imminent.

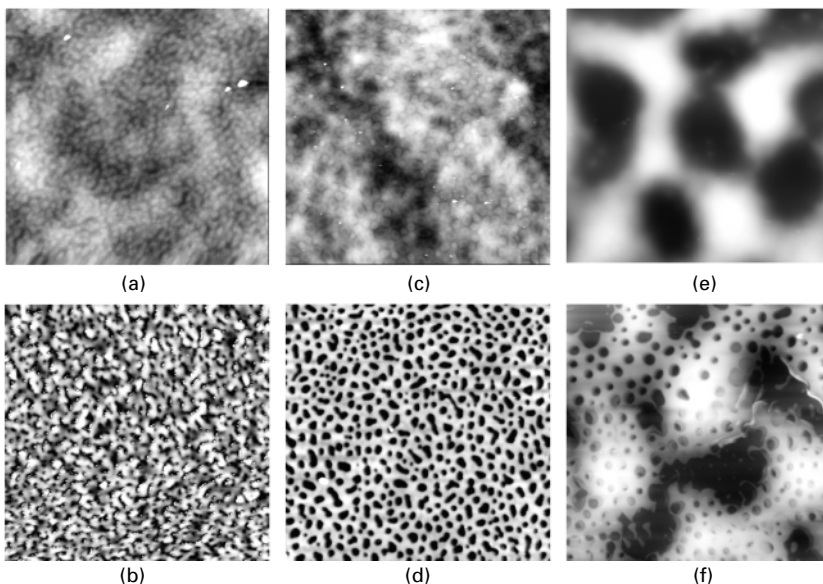
The physical meaning of depth profile evolution can be understood when we study topological evolutions simultaneously. Figure 2.3 shows the corresponding surface and internal morphologies. Here, the internal morphologies of SAN-rich/PMMA-rich interfaces were scanned by SFM after selective etching of PMMA. Upon annealing, short-range fluctuations develop on the surface in Fig. 2.3(a) whereas internal morphology exhibits interconnected structure in Fig. 2.3(b), characterizing the early stage. During the intermediate stage, short- and long-range fluctuations grow in amplitude and wavelength in Fig. 2.3(c) whereas internal morphology reveals that discrete, PMMA-rich domains form in the mid-layer and grow as 2D disks in Fig. 2.3(d). During the late stage, long-range fluctuations grow to rupture the surface and internal structures in Figs 2.3(e) and (f), respectively. Corresponding surface roughness evolution is shown in Fig. 2.4. Upon annealing, surface rapidly roughens in Fig. 2.3(a) during the early stage. After ca. 120 min, surface roughness reaches a plateau (12 nm) up to ca.



2.2 Depth profiles of dPMMA, as measured by LE-ERD, for a  $\sim 500$  nm thick dPMMA/SAN film after various annealing times at  $185^\circ\text{C}$ . The blend undergoes ABA trilayer formation (b), a reduction in the surface and interfacial excess of dPMMA (c–d), and the re-appearance of surface enrichment (e–f). Reprinted from *J. Chem. Phys* 2000; 113; 10386 [5].

2,880 min, which spans the intermediate stage. During the late stage, surface roughness greatly increases due to the rapid growth of the long-ranged fluctuations, followed by film rupture. The details of each stage and the universality of these findings will be discussed in the rest of this section.

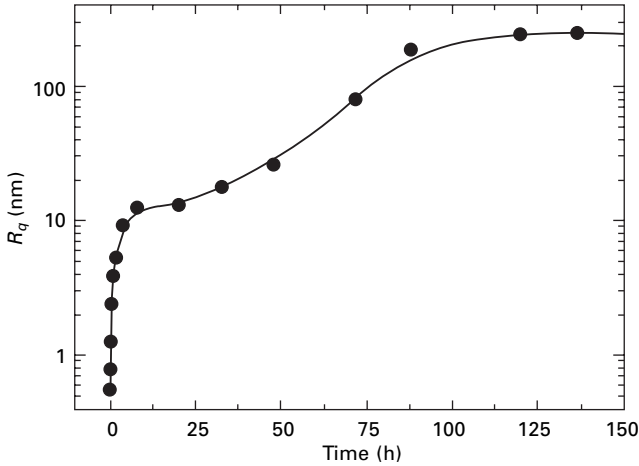
In the early stage, spinodal decomposition produces a bicontinuous morphology, which provides a pathway for the hydrodynamic-flow-driven wetting ( $t^1$ ) of dPMMA to the surface and substrate<sup>70</sup>. This rapid wetting kinetics was also observed from various polymer blend systems, such as critical blends of PVME/water<sup>75</sup>, off-critical blends of dPEP/PEP<sup>68</sup>, and critical blends of dPS/PBr<sub>0.23</sub>S<sup>76,77</sup>. Interestingly, a bicontinuous internal morphology was observed, providing a self-consistent picture for hydrodynamic pumping mechanism<sup>25</sup>. This morphology-kinetics relation was also observed



2.3 SFM images of dPMMA/SAN ( $\phi_{\text{dPMMA}} = 0.47$ , 495 nm thick) blend films showing the (a, c, e) surface and (b, d, f) internal morphology annealed at 185 °C. The annealing time and size scale of images are (a, b) 20 min, 10  $\mu\text{m} \times 10 \mu\text{m}$  (c, d) 1,200 min, 50  $\mu\text{m} \times 50 \mu\text{m}$ , and (e, f) 5,280 min, 50  $\mu\text{m} \times 50 \mu\text{m}$ , respectively. Each image corresponds to the (a, b) early, (c, d) intermediate, and (e, f) late stages, respectively.

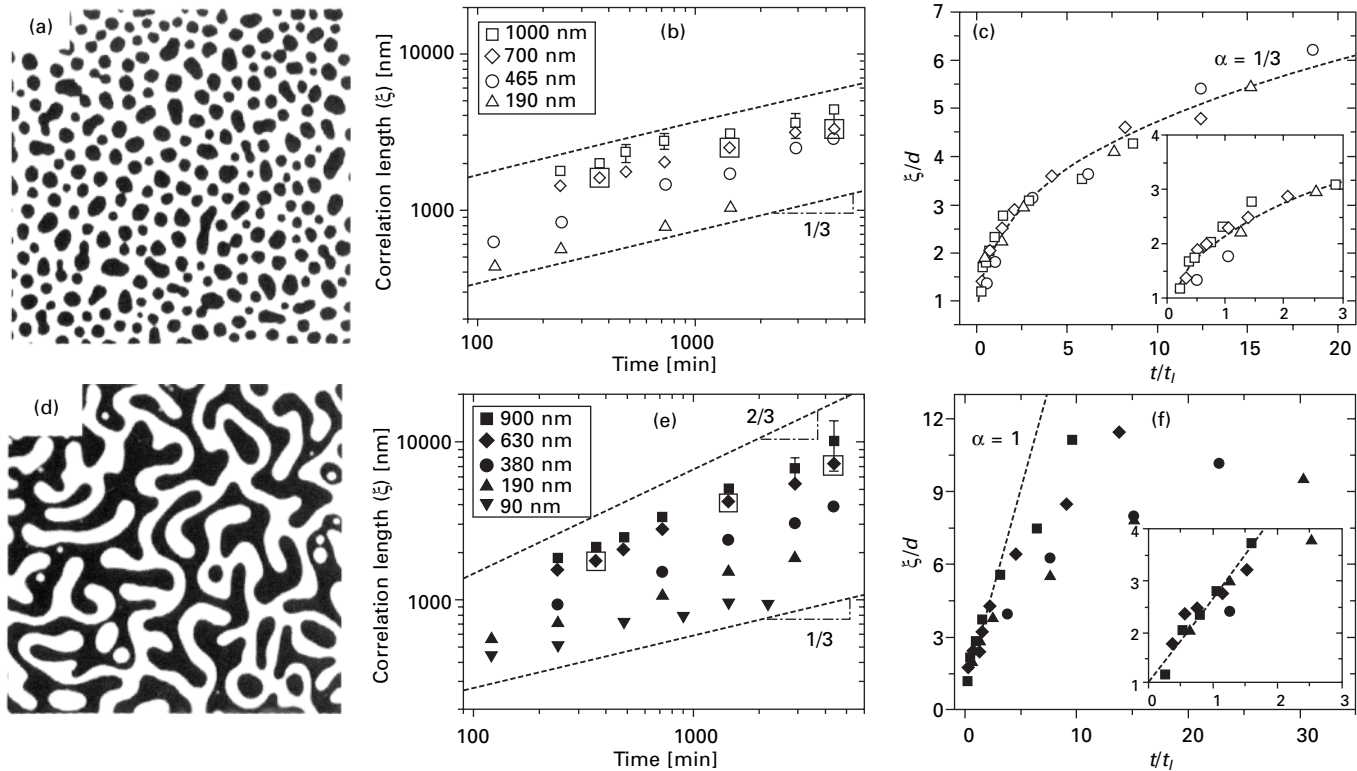
later in dPS/PBr<sub>0.23</sub>S blends by 3D SIMS profiling<sup>76</sup>. In addition, surface roughening was also observed in response to capillary-force-driven-flow of PMMA towards the surface<sup>70</sup>.

The wetting-dominated early stage ends with a decrease of wetting layer, as observed from various other systems<sup>61,63,75,76,78</sup>, which defines the onset of the intermediate stage. This ‘back-flow’ of dPMMA from wetting layers to bulk can be explained as follows<sup>4,75</sup>. During the early stage, hydrodynamic pumping from 3D-bicontinuous phases supply dPMMA to surface and substrate to produce a pressure gradient from bulk to surface, resulting in surface roughening<sup>5,77</sup>. As phase coarsens, 3D isotropic dPMMA-rich domains undergo a dimensional change to 2D, which bridges the two wetting layers. Once the lateral domain (actually, tubes) diameter becomes larger than the mid-layer thickness, the Laplace pressure in domains becomes lower than that in the wetting layer. Therefore, wetting layers thin due to the ‘back-flow’ of materials generated by Laplace pressure. Wang and Composto<sup>5</sup> observed formation and collapse of surface ‘hills’ in the early and the intermediate stages, respectively, which is strong evidence of reversal of the pressure gradient which results in a build up and decay of wetting layers.



2.4 Root-mean-square surface roughness of dPMMA ( $\phi_{\text{dPMMA}} = 0.47$ )/SAN films annealed at 185 °C. Roughness increases rapidly at early times and then reaches a plateau with a roughness value of 12 nm. After 1440 min, macroscopic roughness grows rapidly and reaches a final plateau value of 245 nm. The solid line is to guide the eye. Reprinted from *Europhys. Lett.*; 50; 622 [60].

The growth of 2D domains can be explained in the context of the late stage of spinodal decomposition in pseudo-2D geometry. Chung and Composto<sup>6</sup> explored the kinetics of lateral pattern formation during the intermediate stage using PMMA/SAN blend at bulk critical ( $\phi_{\text{PMMA}} = 50$ ) and off-critical ( $\phi_{\text{PMMA}} = 70$ ) compositions at the thickness range between 90 nm to 1,000 nm. In Figs 2.5(a) and (d), discrete and bicontinuous morphologies are observed, which are characteristic patterns for critical and off-critical quenches, respectively. This conundrum can be explained by the shift of critical composition due to the wetting layer, as pointed out by Binder<sup>17</sup>. From the images, the area fractions of PMMA (i.e., effective compositions) were determined as 0.25 and 0.5 for Figs 2.5(a) and (d), respectively. The growth kinetics was determined by the correlation length,  $\xi(t) = 2\pi / k_{\text{max}}(t)$ , where  $k_{\text{max}}(t)$  is the dominant peak wave vector of  $S(k, t)$ . Figure 2.5(b) and (e) show how  $\xi(t)$  increases with time during the intermediate stage for the discrete and bicontinuous morphologies, respectively. From the plots, the growth exponent  $\alpha$  is 1/3 for discrete growth, whereas  $\alpha$  decreases from 0.62 to 0.28 as  $d$  decreases from 900 to 90 nm for bicontinuous growth. In addition, a coalescence model accurately captures the scaling exponent for film thickness,  $d$ , and annealing time,  $t$ , for the discrete morphology. Modifying the approach by Tanaka<sup>4,62</sup>, originally developed to explain the coalescence dynamics between two domains, scaling analysis of the non-compressive Navier-Stokes equation gives an expression for the correlation length,  $\xi \sim (\sigma / \eta)^{1/3} d^{2/3} t^{1/3}$ , where  $\sigma$  and  $\eta$  are the interfacial tension between PMMA-rich and SAN-rich



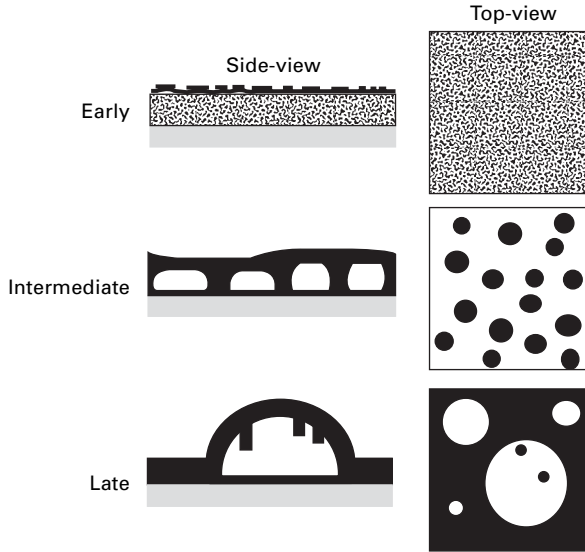
2.5 Lateral pattern growth of PMMA/SAN films annealed at 185 °C for two volume fractions ((a) – (c)  $\phi_{\text{PMMA}} = 0.5$ , (d)–(f)  $\phi_{\text{PMMA}} = 0.7$ ). SFM images of the internal structure after 720 min are shown in (a) and (d). The correlation length,  $\xi$ , as a function of time is plotted in (b) and (e) for a range of thickness values. Reduced correlation length,  $\xi/d$ , as a function of reduced time,  $t/t_i$  are also plotted in (c) and (f), where  $t_i$  ( $\ll d$ ) is the onset of the intermediate stage. Insets expand early time behavior. Here, universal growth is found for discrete growth (c) whereas the universality fails for the bicontinuous case (f). See text for further details. Reprinted from *Phys. Rev. Lett.*; 92; 185704 [6].

phases and viscosity of the more viscous phase, respectively. The universal fitting using the scaling relation is shown in Fig. 2.5(c). However, the universality fails for the bicontinuous growth in Fig. 2.5(f), suggesting suppression of lateral hydrodynamic pumping due to confinement. This requires further theoretical investigations.

During the late stage, the SAN-rich mid-layer ruptures and the film roughens drastically<sup>7,71</sup>. An interesting feature of this film roughening is that the lateral scales of the fluctuation are much larger than those of lateral domain growth. Therefore, there are two length scales for the surface deformation modes: the smaller length scale due to lateral domain growth by phase separation and the larger one due to capillary fluctuation from the long-range interactions between dPMMA-rich layers across the SAN-rich mid-layer. The interfacial roughening mechanism by phase separation<sup>79</sup> cannot explain the rupturing mechanism with multiple length scales. Hoppe *et al.*<sup>78</sup> proposed scaling relations of rupture time and wavelength with the minimization of interfacial tension. However, this does not provide an answer to the kinetic origin of the film-rupturing mechanism. Although simple capillary wave theory based on simple liquid films<sup>30,32</sup> does not accurately predict the rupturing kinetics, it is notable that the multiple length scale fluctuations are frequently found when spinodal dewetting occurs at embedded layers<sup>18,80</sup>. In conclusion, further studies are needed to elucidate the rupturing mechanism of polymer blend thin films.

A brief summary of the ‘type III’ morphology is shown in Fig. 2.6. Here, an early stage is dominated by preferential wetting of A phase to surface and substrate, often accelerated by hydrodynamic flow. Phase separation then undergoes a transition from 3D to pseudo-2D growth, defining the onset of the intermediate stage. During the intermediate stage, self-assembly of nano- or meso-scale lateral pattern is observed with well-defined growth kinetics. During the late stage, the ABA trilayer may rupture due to interfacial fluctuations resulting in a roughened, dewetted film.

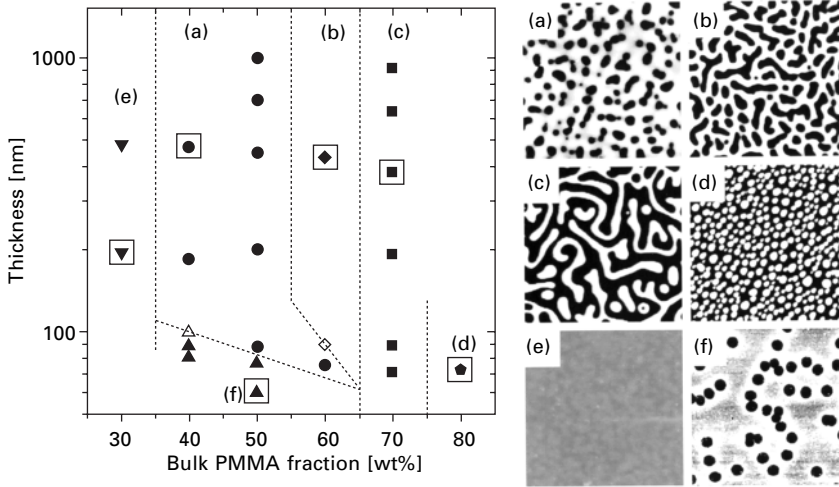
Variations of blend composition<sup>66,67,81,82</sup> and film thickness<sup>73,81</sup> offer various controls in lateral patterns, however, a comprehensive understanding of morphology development requires a systematic study of the growth mechanism. Recently, Chung and Composto<sup>74</sup> have studied the effect of composition and thickness on morphology development mechanisms using PMMA/SAN blends annealed at 185 °C. Figure 2.7 shows six distinct regimes of the intermediate stage pattern development. Regimes (a)–(d) correspond to the ‘type III’ growth, where the lateral pattern growth is governed by phase separation kinetics in the mid-layer. Here, regimes (a) and (c) correspond to the discrete and bicontinuous pattern growth described above<sup>6</sup>. Regime (b) shows a hybrid growth behavior between (a) and (c). In regime (d), the SAN-rich phase is a minority component in the mid-layer, showing a discrete droplet structure. Here, the growth of droplets is controlled either via diffusion of the SAN



**2.6** Three stage model for thin film phase separation and symmetric wetting (Type III). The black and white regions represent A and B phases, respectively. The side view shows layering and small-wavelength surface roughening (early stage), A domains which span the wetting layers and long-wavelength fluctuations (intermediate), and B droplets encapsulated by A wetting layers (late). The top view shows the interconnected morphology below the surface wetting layer (early), the 2D domains of A phase (intermediate), and the encapsulated B droplets (late). Reprinted from *J. Chem. Phys.* 2000; 113; 10386 [5].

molecules across PMMA-rich matrix phase (evaporation-condensation mechanism)<sup>22</sup> or by Brownian motion of the droplets followed by collision leading to a coarsening<sup>23,24</sup>. The lateral domain growth is found to be extremely slow and the film surface remained smooth even after a long annealing time<sup>74,81</sup>. In regimes (e) and (f), thin films form trilayer structures without co-existing PMMA-rich phase in the SAN-rich mid-layer after the early stage, which corresponds to the ‘type II’ growth. However, a collapse of SAN-rich mid-layer sandwiched by PMMA-rich wetting layer (i.e., spinodal dewetting) is observed from regime (f) whereas trilayers in regime (e) are observed to be stable after up to 72 hours of annealing. This is consistent with the spinodal dewetting theory, which predicts that film stability is a strongly increasing function of thickness ( $\tau_m \propto d^5$ )<sup>30,32</sup>.

In conclusion, various patterns can be made from symmetrically wetting (ABA) thin film polymer blends. Morphology development is a result of the interplay among phase separation, wetting, and dewetting, and the first step to design-controlled patterns is to understand the kinetic mechanism. The patterns can be controlled by the compatibility of blending components,



2.7 Left: intermediate stage phase-morphology map of PMMA/SAN blends as a function of composition and film thickness. The morphology development is classified into six distinct regimes. Right: Representative internal images from each regime after selective removal of PMMA. See text for details. Taken from ref. [74]

composition ratio, film thickness, and thermal history. Although the underlying mechanism is mostly understood, it is worthwhile to mention a long-standing debate from an anomalous pattern growth behavior. Wiltzius and Cumming<sup>83,84</sup> performed light scattering studies on thick film ( $\sim 1$  mm) blends of PEP/PI (polyisoprene) and found a fast-growth mode ( $r^{3/2}$ ) near the film walls. This fast growth has attracted great attention among theoreticians<sup>85,86,87,88,89</sup>, but the physical origin is still unclear even now<sup>4</sup>. Therefore, the interplay between phase separation and wetting has not been solved completely, requiring further theoretical and experimental studies.

#### 2.4.2 Morphology development in asymmetrically wetting (AB) blends

When a homogeneous polymer blend thin film undergoes phase separation with an asymmetric wetting condition (A preferred at the surface and B at the substrate), a bilayer structure results. However, the bilayer structure can be unstable due to the large interfacial layer between A and B phases, followed by dewetting process to achieve equilibrium morphologies. This phenomenon is first observed from ultrathin (less than  $2R_g$ ) PS/PVME films, which display droplets of PVME on PS layer covering silicon oxide substrate just after a dip-coating of toluene solution at room temperature<sup>90</sup>. For thicker films, A and B phases stratify upon annealing. For example, dPEP/PEP films spun-

cast on hydrophobic silicon substrate (i.e., oxide layer removed) undergo surface-directed spinodal decomposition, resulting in a bilayer of dPEP and PEP from the surface<sup>91</sup>. Here, transient surface patterns with a lateral lengthscale of hundreds of nanometers were observed as a response to hydrodynamic flow of dPEP from bulk to surface, and the patterns disappear at longer times of annealing.

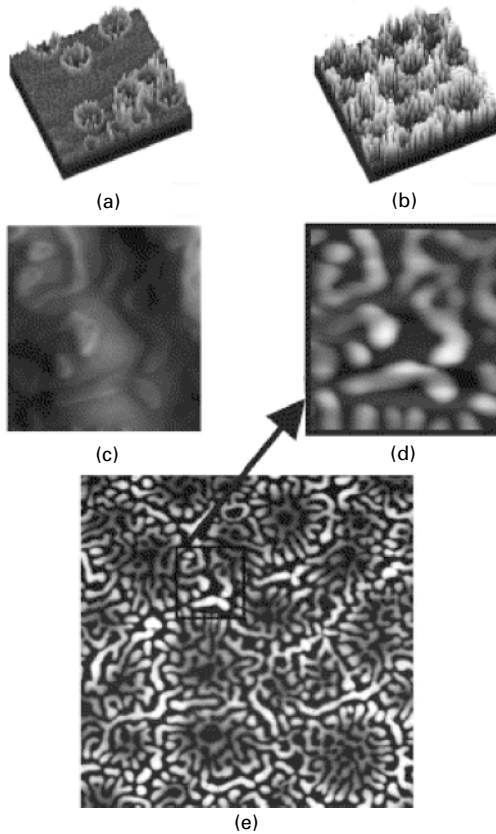
The bilayer structure induced by asymmetric wetting may rupture via dewetting as shown by Klein *et al.*<sup>8,92,93</sup>. Homogeneous mixture of deuterated oligomeric styrene (dOS) and oligomeric ethylene-propylene (OEP) immediately forms a bilayer on silicon oxide substrate where dOS is preferred at the surface. However, the dOS layer dewets from the OEP layer, where the dewetting process is accelerated by Marangoni instability<sup>8</sup>. Consequently, the dewetting front starting at the sample edges propagates inward, leaving droplets on the dewetted area. The droplets continue to move inward, where larger ones move faster, explained by the surface tension gradient of the partially miscible mixtures<sup>92</sup>.

Liquid-liquid bilayer dewetting is a well-studied subject. Most studies consider the case where the top layer dewets from the stable lower one<sup>94,95,96,97</sup>. Alternatively, the lower layer may rupture before the top layer, as shown in Fig. 2.8. Here, the lower PS layer (15 nm) undergoes spinodal dewetting between the top PMMA layer (30 nm) and silicon oxide substrate, resulting in a complex morphology with two characteristic lengthscales<sup>18</sup>. Another interesting example is layer inversion of bilayer films when initial bilayer sequence is against what is thermodynamically favored<sup>98</sup>. For example, poly(2-vinylpyridine) (PVP) layer on top of PS substrate initially creates dewetting holes on PS. Once the dewetting rims merge, PS starts to flow on PVP domains and eventually inverts the layers. This phenomenon was also observed from spun-cast polymer blends of PS/PMMA and PS/PCL (poly( $\epsilon$ -caprolactone)) upon annealing<sup>99</sup>.

### 2.4.3 Solvent-induced patterns

Although most of the fundamental work on the phase separation and wetting of polymer blend films has been done on initially homogeneous systems, it is very difficult to find a ternary system (polymer/polymer/solvent), whereby the solvent is equally good for both the polymers. Moreover, most of the practically important polymer blends, including conjugated ones, phase-separate at room temperature. Therefore, solvent-induced patterns are important subjects to investigate.

Most challenges in studying solvent-induced patterns come from the difficulty in controlling the evaporation rate of the solvent. Because phase separation occurs during solvent evaporation, major changes in morphology happen at very short intervals of time while the composition of solvent



**2.8 Dewetting of PMMA (~30 nm) film from PS (~15 nm) on silicon.** The SFM images ((a), (b), (d), and (e)) were taken after PMMA was selectively removed with acetic acid. The dewetting structure was obtained after annealing for (a) 15 min and (b)–(e) 24 h at 170°C. The lateral scales are (a, b) 10  $\mu\text{m} \times 10 \mu\text{m}$ , (e) 20  $\mu\text{m} \times 20 \mu\text{m}$  (d) is an expansion of the squared region in (e). (c) is the same region as (d), but prior to acetic acid etching. Reprinted from *Prog. Polym. Sci.* 2003; 28; 261 [18].

quickly reduces at the evaporation front. For thick films, solvent evaporation rate can be controlled in closed chambers and the formation of surface patterns is attributed to Marangoni instability, where the temperature gradient from the bulk to the surface of polymer films induces convection of evaporating solutions<sup>100,101</sup>. However, such control is extremely difficult in thin film systems, where most films are prepared by spin-coating<sup>102,103</sup>. Evaporation rate can be controlled by spinning rate, but is not linear with time and is also strongly influenced by the environment, such as relative humidity<sup>104</sup>. Recently, the importance of solvent selection in controlling roughness of spun-cast polymer films has been realized<sup>105</sup> but the solubility differences between

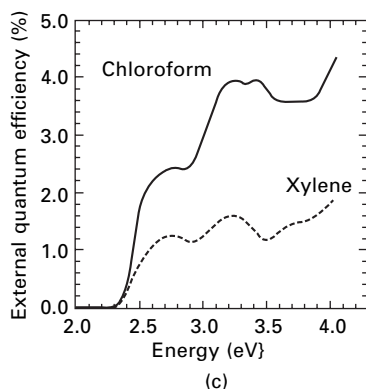
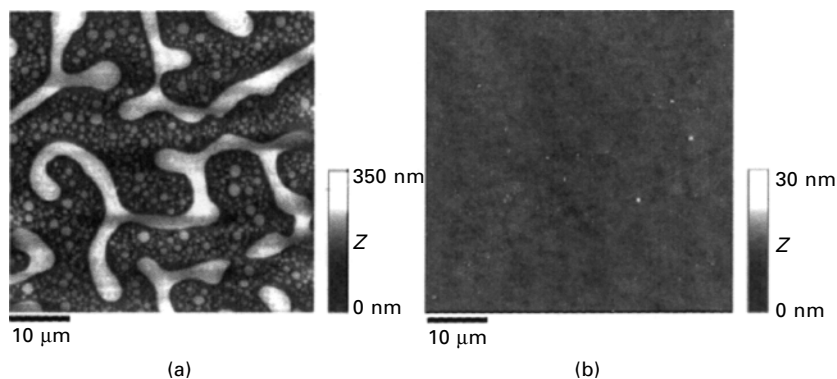
polymer components profoundly complicates the problem in blends. Therefore, quantitative studies of solvent-induced patterns in polymer blend films are intrinsically extremely challenging.

Parameters influencing spun-cast morphologies can be categorized as blend compositions<sup>106,107,108,109,110</sup>, polymer-polymer and polymer-substrate interfacial tensions<sup>111,112,113,114</sup>, molecular weight<sup>115,116</sup> and solubility of polymer components in solution<sup>111,117</sup>, solvent evaporation rate<sup>118,119</sup> and overall film thickness<sup>120,121</sup>, although it is very difficult to systematically decouple the influences. The influence of composition, interfacial tension and film thickness is qualitatively similar to the ABA polymer blends in section 2.4.1. Specifically, percolated structures are typically seen near the critical compositions whereas discrete domains of minority phases appear in continuous majority phase at the off-critical compositions<sup>110</sup>. Interfacial segregation at the surface and the substrate causes a depletion of wetting component in the 'bulk' of the thin film, shifting the composition ratio<sup>108</sup>, and it may even cause a bilayer formation without lateral features<sup>111</sup>. Lateral feature sizes are larger for thicker films<sup>120,121</sup>. However, it should be considered that the solvent-quenched films typically have very rough surfaces where the domains either protrude or depress, distorting composition ratio and thickness.

For the same species of blends, topographical features can be either larger<sup>116</sup> or smaller<sup>115</sup> for the lower molecular weight. This is because the changes in molecular weight affect both the viscosity of polymer and phase diagram of the blends. A slow solvent evaporation rate gives a longer time for phase separation and wetting, thus larger features are obtained<sup>101,118</sup>. However, the evaporation rate is controlled by spin rate in spin-coating, changing the overall thickness<sup>102,103</sup>. It is also reported that the evaporation rate affects the topographic profiles of domains (i.e., convex or concave)<sup>113</sup>. Finally, solubility difference is coupled with surface tension difference, affecting the interfacial properties between two phases<sup>111</sup>. In short, morphology development in the solvent evaporation process is very fast and determining parameters are coupled, making quantitative analysis extremely difficult.

Morphologies of conjugated polymer blends deserve a special interest here. Due to their flexibility, adaptability, high performance, and low cost, today light-emitting polymers (LEPs)<sup>117,122,123</sup> and photovoltaics<sup>124,125,126</sup> are at the point of commercialization in full-color active matrix displays. Moreover, solution casting from a co-solvent enables a one-step process, reducing the cost significantly. The relations between film morphology and performance of LEPs and photovoltaics are discussed in an excellent review by Moons<sup>127</sup> and are beyond the scope of this chapter. However, we will discuss the general features of this subject. For photovoltaics, a large interfacial area is important because excitons generated by light are easily dissociated at the interfaces. Sharp interfaces are advantageous because it will ensure that the dissociated electron-hole pair arrive at the n-type and p-type phases,

respectively, before recombination. It is also important to have percolated morphologies to the electrodes. Spinodal decomposition structures with wetting layers have optimal morphology for photovoltaics. As shown in Fig. 2.9, finer structures in a spun-cast mixture of poly(9,9'-dioctylfluorene-co-bis-N,N'-(4-butylphenyl)-bis-N,N'-phenyl-1,4-phenylenediamine) (PFB) and poly(9,9'-dioctylfluorene-co-benzothiadiazole) (F8BT) prepared by chloroform shows a higher quantum efficiency than larger structures in xylene solutions<sup>124</sup>. For LEPs, diffused interfaces are shown to be more effective<sup>128</sup>, but the optimal structures are still unknown<sup>18</sup>. In conclusion, conjugated polymer blends can be prepared from co-solvent as a one-step process, and the study of the relations between morphology and performance is crucial, yet the optimal structures are still not achieved.



2.9 Topographical SFM image of PFB/F8BT (50/50 by weight) films spun-cast from (a) xylene and (b) chloroform. (c) Short-circuit EQE action spectra of photovoltaic devices prepared from chloroform (solid line) and xylene (dashed line) solutions. Chloroform solution provides a finer (less than 100 nm) structure, leading to a better photovoltaic performance. Reprinted from *Macromolecules* 2001; 34: 6005 [124].

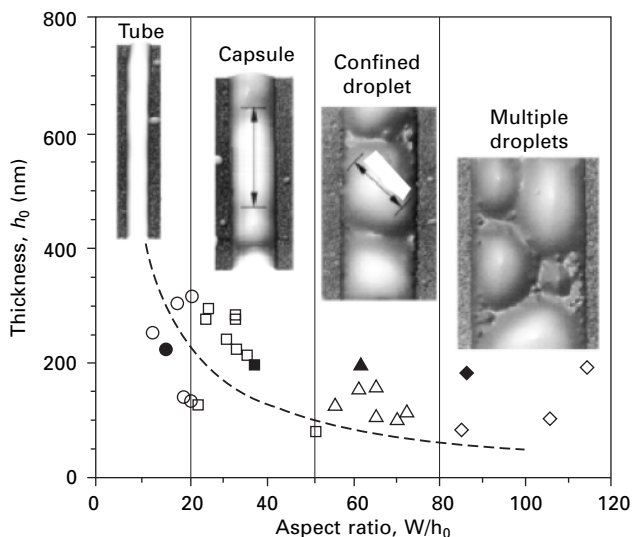
#### 2.4.4 Effects of chemical and topographical confinement

In previous sections we reviewed how the interplay among phase separation, wetting, and dewetting generates various morphologies in polymer blend films deposited on homogeneous substrates. When the substrate has variations of surface energies, on the other hand, morphology of thin films can be guided into well-defined structures. For example, one can confine A and B phases in binary blends into arbitrary substrate domains by alternating wetting preference. Thus, substrate modulation enables highly reproducible polymer films, which can be applied to the formation of photonic bandgap materials, patterned polymer surfaces with selective molecular recognition capabilities, and optical devices<sup>129</sup>.

Patterned substrate has been generated by conventional lithographic techniques to deposit metal wires on semiconductor surfaces<sup>130,131</sup>, adsorption of block copolymer brushes<sup>132</sup>, and microcontact printing of self-assembled monolayers<sup>129,133,134,135,136,137,138</sup>. Among these techniques, the microcontact printing technique provides patterns with high fidelity at low processing cost compared to the conventional ones.

Phase separation may occur during solvent evaporation or by thermal treatment. Solvent-induced pattern replication, especially spin-coating, is a one-step process, and has shown to be effective in many cases<sup>129,130,131,137,138</sup>. However, solvent drying is too fast to control and easily influenced by environment, therefore quantitative control of parameters is extremely difficult. Naturally, quantitative models to describe the substrate pattern replications have been deduced from initially homogeneous films undergoing phase separation and wetting upon annealing. Ermi *et al.*<sup>135,136</sup> examined film morphology evolution kinetics using 2D FFT analysis of the height fluctuations, and concluded that the coupling between phase separation and spinodal dewetting directs the film development leading to the replication of substrate patterns. In addition, Newby and Composto<sup>134</sup> predicted equilibrium structures by the ratio between original film thickness and substrate pattern width as shown in Fig. 2.10, providing a theoretical guide to tailor morphologies.

In addition to the chemical confinement from the substrate, topological confinement can induce intriguing morphologies. Newby and Composto<sup>139</sup> investigated the morphology development kinetics of isolated polymer blend strips. After a long time, an elliptical nonwetting phase core encapsulated by wetting layers was found. Yoo *et al.*<sup>140</sup> put an elastomer mold on top of spun-coat film to generate a negative replica using capillary force but the morphology development was complicated by the mobility of polymer components used in the experiment.



2.10 The experimental phase-morphology map as a function of original film thickness ( $h_0$ ) and OTS stripe width ( $W$ ). Equilibrium domain morphologies are predicted with an aspect ratio  $W/h_0$ . The dashed line represents the morphology transition at constant  $W$ . Reprinted from *Phys. Rev. Lett* 2001; 87; 0983302 [134].

## 2.5 Future trends

In this section, we point out some important future directions for research on pattern development of thin film polymer blends. The first direction to pursue is the addition of nanoparticles in polymer blends. It is well known that the optical, mechanical, and thermal properties of polymers can be improved by adding low concentrations of nanoparticles<sup>141</sup>. Despite the potential advantages of polymer nanocomposites, a fundamental understanding of their phase separation and wetting behavior is currently not well understood<sup>142</sup>. For thin film polymer blends, the addition of nanoparticles generally induces an apparent phase stabilization of the blends<sup>143,144</sup> and a significant retardation of pattern development<sup>145,146,147,148</sup>, yet the mechanism is still unclear. Recently, Chung *et al.*<sup>149</sup> studied the pattern development kinetics for binary polymer blends with mobile nanoparticles that preferentially partition into one of the phases. They captured the retardation of phase separation by a coalescence model, which incorporates an increase in viscosity due to nanoparticle partitioning. For large immobile particles, transient ‘target patterns’ are found to grow at the periphery of the particles<sup>150</sup>. Studies of the nanoparticle-containing polymer blend thin films are beginning, and many of the fundamental issues are not understood. Technological applications are also wide open.

Similarly, addition of the third polymeric component in the binary blends is also of interest. For example, block copolymer or amphiphilic compatibilizer

reduces the interfacial tension between two polymer species, making the spun-cast features smaller or even vanish<sup>151,152</sup>. Ternary polymer blends also enable richer and more complex morphologies<sup>153,154,155,156</sup>. We believe that recent fundamental studies on the interplay between phase separation, wetting, and dewetting makes it possible to understand pattern development on the complex multicomponent systems.

Electric stimuli have recently been employed in manipulating patterns in polymer blend films<sup>157,158</sup>. The electric stimuli have been quite successful in getting ordered structures in block copolymers<sup>159</sup> and polymer nanocomposites<sup>160</sup>. In addition, electrohydrodynamic instabilities are proven to be an excellent way to fabricate patterns in polymer films. We believe that the electric stimuli will provide an effective way to obtain desired morphologies in thin film polymer blends. Another possibility is to manipulate the polymer miscibility with electric stimuli. Then, patterns may reversibly dissolve by the electric stimuli, making the reversal 'responsive' materials. Such responsive materials may be sensitive to surroundings, such as moisture or chemicals, possibly applied to the sensors.

To make practical and robust patterns, two new directions can be suggested. The first one is to use an inorganic precursor as one of the components, making organic-inorganic hybrid materials from thin film polymer blends. Jinnai *et al.* recently fabricated bicontinuous or pillar-like morphologies by controlling the spinodal decomposition of silica precursors and solvents<sup>161,162,163</sup>. This method can be utilized for various organic-inorganic hybrids. The second possibility is to use reactive blending, where polymer chains contain functional groups that associate each other<sup>164,165</sup>. In reactive blending, one can quench the desired morphology by cross-linking the polymer chains.

As a new methodology, combinatorial study developed by National Institute of Standards and Technology (NIST) provides a quick and efficient way to investigate pattern development<sup>166,167,168</sup>. By making a gradient on the governing parameters of pattern development, such as temperature, composition, and thickness, combinatorial study enables a large library of information at a single sample preparation. Recently, this method has been employed in polymer blend thin films to generate a phase diagram on one sample plate<sup>167</sup>. We believe this sample preparation method will soon be commercialized, and become a standard tool for polymer scientists.

## 2.6 Conclusion

In this chapter, we reviewed the recent experimental developments on the pattern formation in thin film polymer blends. A decade of extensive studies has established the fundamental understanding on the essentials of the interplay between phase separation, wetting, and dewetting, which determines pattern

formations. We note that quantitative investigation is still underway for the subject, especially when the mobility difference between two components of a mixture is large<sup>169</sup>. For future studies, quantitative understanding of complex systems, such as solvent-induced patterns or multicomponent blends, may be of interest. In conclusion, surface-induced structures of thin film polymer blends will replace the conventional lithographic methods, especially at the electronic, optical, and biomedical applications.

## 2.7 References

1. Gunton J.D., San Miguel M. and Paramdeep S., Sahni., The dynamics of First-order Phase Transitions, in *Phase Transitions and Critical Phenomena*, London, Academic Press, 267–465.
2. Hiroshi Furukawa, 'A dynamic scaling assumption for phase separation', *Advances in Physics*, 1985, 34(6) 703–750.
3. Richard A.L. Jones, Laura J. Norton, Edward J. Kramer, Frank S. Bates and Pierre Wiltzius, 'Surface-directed spinodal decomposition', *Physical Review Letters*, 1991, 66(10–11) 1326–1329.
4. Hajime Tanaka, 'Interplay between wetting and phase separation in binary fluid mixtures: roles of hydrodynamics', *Journal of Physics: Condensed Matter*, 2001, 13(21) 4637–4674.
5. Howard Wang and Russell J. Composto, 'Thin film polymer blends undergoing phase separation and wetting: Identification of early, intermediate, and late stages', *Journal of Chemical Physics*, 2000, 113(22) 10386–10397.
6. Hyun-joong Chung and Russell J. Composto, 'Breakdown of dynamic scaling in thin film binary liquids undergoing phase separation', *Physical Review Letters*, 2004, 92(18) 185704/1–185704/4.
7. Howard Wang and Russell J. Composto, 'Kinetics of Surface and Interfacial Fluctuations in Phase Separating Polymer Blend Films', *Macromolecules*, 2002, 35(7) 2799–2809.
8. Rachel Yerushalmi-Rozen, Tobias Kerle and Jacob Klein, 'Alternative dewetting pathways of thin liquid films', *Science*, 1999, 285(5431) 1254–1256.
9. Howard Wang, Katsumi Shimizu, Hongdoo Kim, Erik K. Hobbie, Zhi-Gang Wang and Han C.C., 'Competing growth kinetics in simultaneously crystallizing and phase-separating polymer blends', *Journal of Chemical Physics*, 2002, 116(16) 7311–7315.
10. Laszlo Granasy, Tamas Pusztai, James Warren, Douglas J.F., Tamas Borzsonyi and Vincent Ferrero, 'Growth of 'dizzy dendrites' in a random field of foreign particles', *Nature Materials*, 2003, 2(2) 92–96.
11. Mingtai Wang, Hans-Georg Braun and Evelyn Meyer, 'Crystalline structures in ultrathin poly(ethylene oxide)/poly(methyl methacrylate) blend films', *Polymer*, 2003, 44(17) 5015–5021.
12. Stanley Affrossman, Thomas Kiff, Scott A. O'Neill, Richard A. Petrick and Randal W. Richards, 'Topography and Surface Composition of Thin Films of Blends of Poly(methyl methacrylate) and Poly(ethylene oxide)', *Macromolecules*, 1999, 32(8) 2721–2730.

13. Vincent Ferriero, Douglas J.F., James Warren and Alamgir Karim, 'Growth pulsations in symmetric dendritic crystallization in thin polymer blend films', *Physical Review E*, 2002, 65(5) 051606/1–051606/16.
14. Kurt Binder, 'Spinodal Decomposition in Confined Geometry', *Journal of Non-Equilibrium Thermodynamics*, 1998, 23(1) 1–44.
15. Andrzej Budkowski, 'Interfacial phenomena in thin polymer films: phase coexistence and segregation', *Advances in Polymer Science*, 1999, 148(1–112).
16. Georg Krausch, 'Surface induced self assembly in thin polymer films', *Materials Science and Engineering R: Reports*, 1995, 14(1–2) 1–94.
17. Kurt Binder, 'Phase Transitions of Polymer Blends and Block Copolymer Melts in Thin Films', *Advances in Polymer Science*, 1999, 138(1) 1–89.
18. Mark Geoghegan and Georg Krausch, 'Wetting at polymer surfaces and interfaces', *Progress in Polymer Science*, 2003, 28(2) 261–302.
19. Cahn J.W. and Hilliard J.E., 'Free energy of a nonuniform system. I – Interfacial free energy', *Journal of Chemical Physics*, 1958, 28(258–267).
20. Cahn J.W., 'On spinodal decomposition', *Acta Metallurgica*, 1961, 9(795–801).
21. Wagner A.J. and Cates M.E., 'Phase ordering of two-dimensional symmetric binary fluids: A droplet scaling state', *Europhysics Letters*, 2001, 56(4) 556–562.
22. Lifshitz I.M. and Slyozov V.V., 'The kinetics of precipitation from supersaturated solid solutions', *Journal of Physical Chemistry of Solids*, 1961, 19(1–2) 35–50.
23. Kurt Binder and Stauffer D., 'Theory for the Slowing Down of the Relaxation and Spinodal Decomposition of Binary Mixtures', *Physical Review Letters*, 1974, 33(17–21) 1006–1009.
24. Hajime Tanaka, 'Coarsening mechanisms of droplet spinodal decomposition in binary fluid mixtures', *Journal of Chemical Physics*, 1996, 105(22) 10099–10114.
25. Eric D. Siggia, 'Late stages of spinodal decomposition in binary mixtures', *Physical Review A*, 1979, 20(2) 595–605.
26. Takeji Hashimoto, Masahiko Itakura and Nobuyuki Shimidzu, 'Late stage spinodal decomposition of a binary polymer mixture. II. Scaling analyses on  $Q_m(\tau)$  and  $\text{Im}(\tau)$ ', *Journal of Chemical Physics*, 1986, 85(11) 6773–6786.
27. Cahn J.W., 'Critical point wetting', *Journal of Chemical Physics*, 1977, 66(8) 3667–3672.
28. de Gennes P.G., 'Wetting: statics and dynamics', *Review of Modern Physics*, 1985, 57(3) 827–863.
29. Richard A.L. Jones and Randal W. Richards, *Polymers at surfaces and interfaces*, Cambridge, 1999.
30. Brochard-Wyart F. and Dailant J., 'Drying of solids wetted by thin liquid films', *Canadian Journal of Physics*, 1990, 68(8) 1084–1088.
31. Jacob Israelachvili, *Intermolecular and Surface Forces*, New York, 1992.
32. Vrij A. and Overbeek, J.Th.G. 'Rupture of thin liquid films due to spontaneous fluctuations in thickness', *Journal of the American Chemical Society*, 1968, 90(12) 3074–3078.
33. Russell J. Composto, Russel M. Walters and Jan Genzer, 'Application of ion scattering techniques to characterize polymer surfaces and interfaces', *Materials Science and Engineering R: Reports*, 2002, 38(3–4) 107–180.
34. Jan Genzer, Rothman J.B. and Russell J. Composto, 'Improved hydrogen and deuterium depth profiling in polymers using low energy forward recoil spectrometry', *Nuclear Instruments and Methods in Physics Research Section B: Beam Interactions with Materials and Atoms*, 1994, 86(3–4) 345–354.

35. Sokolov J., Rafailovich M.H., Jones R.A.L. and Kramer E.J. 'Enrichment depth profiles in polymer blends measured by forward recoil spectrometry', *Applied Physics Letters*, 1989, 54(6) 590–592.
36. Mark Geoghegan, Richard A.L. Jones, Clough A.S. and Penfold J., 'The morphology of as-cast films of a polymer blend: Dependence on polymer molecular weight', *Journal of Polymer Science Part B: Polymer Physics*, 1995, 33(8) 1307–1311.
37. Payne R.S., Clough A.S., Murphy P. and Mills P.J., 'Use of the  $D(^3\text{He},P)^4\text{He}$  reaction to study polymer diffusion in polymer melts', *Nuclear Instruments and Methods in Physics Research Section B: Beam Interactions with Materials and Atoms*, 1989, 42(1) 130–134.
38. Chaturvedi U.K., Steiner U., Zak O., Georg Krausch, Schatz G. and Jacob Klein, 'Structure at polymer interfaces determined by high-resolution nuclear reaction analysis', *Applied Physics Letters*, 1990, 56(13) 1228–1230.
39. Lanford W.A., Trautvetter H.P., Ziegler J.F. and Keller J., 'New precision technique for measuring the concentration versus depth of hydrogen in solids', *Applied Physics Letters*, 1976, 28(9) 566–568.
40. Schwarz S.A., Wilkens B.J., Pudensi M.A.A., Rafailovich M.H., Sokolov J., Zhao X., Zhao W., Zheng X., Russell T.P. and Jones R.A.L., 'Studies of surface and interface segregation in polymer blends by secondary ion mass spectrometry', *Molecular Physics*, 1992, 76(937–950).
41. Russell T.P., 'X-ray and neutron reflectivity for the investigation of polymers', *Materials Science Reports*, 1990, 5(4–5) 171–271.
42. Russell T.P., 'On the reflectivity of polymers: Neutrons and X-rays', *Physica B*, 1996, 221(1–4) 267–283.
43. Edward J. Kramer, 'Depth profiling methods that provide information complementary to neutron reflectivity', *Physica B*, 1991, 173(1–2) 189–198.
44. Georg Krausch, Hipp M., Boltau M., Mlynek J. and Marti O., 'High-Resolution Imaging of Polymer Surfaces with Chemical Sensitivity', *Macromolecules*, 1995, 28(1) 260–263.
45. Cleveland J.P., Anczykowski B., Schmid A.E. and Elings V.B., 'Energy dissipation in tapping-mode atomic force microscopy', *Applied Physics Letters*, 1998, 72(20) 2613–2615.
46. Knoll W., Magerle R. and Georg Krausch, 'Tapping Mode Atomic Force Microscopy on Polymers: Where Is the True Sample Surface?', *Macromolecules*, 2001, 34(12) 4159–4165.
47. Pohl D.W., Denk W. and Lanz M., 'Optical stethoscopy: Image recording with resolution  $\lambda/20$ ', *Applied Physics Letters*, 1984, 44(7) 651–653.
48. Betzig E. and Trautmann J.K., 'Near-Field Optics: Microscopy, Spectroscopy, and Surface Modification Beyond the Diffraction Limit', *Science*, 1992, 257(5067) 189–195.
49. Jeesung Hwang, Lori S. Goldner, Alamgir Karim and Connie Gettinger, 'Imaging phase-separated domains in conducting polymer blend films with near-field scanning optical microscopy', *Applied Optics*, 2001, 40(22) 3737–3745.
50. Stevenson R., Granstrom M. and Richards D. 'Fluorescence scanning near-field optical microscopy of conjugated polymer blends', *Applied Physics Letters*, 1999, 75(11) 1574–1576.
51. Ade H., Zhang X., Cameron S., Costello C., Kirz J. and Williams S., 'Chemical Contrast in X-ray Microscopy and Spatially Resolved XANES Spectroscopy of Organic Specimens', *Science*, 1991, 258(5084) 972–975.

52. Ade H., Winesett D.A., Smith A.P., Qu S., Ge S., Sokolov J. and Rafailovich M.H., 'Phase segregation in polymer thin films: Elucidation by X-ray and scanning force microscopy', *Europhysics Letters*, 1999, 45(4) 526–532.
53. Hiroshi Jinnai, Tsuyoshi Koga, Yukihiro Nishikawa, Takeji Hashimoto and Stephen T. Hyde, 'Curvature Determination of Spinodal Interface in a Condensed Matter System', *Physical Review Letters*, 1997, 78(11) 2248–2251.
54. Hiroshi Jinnai, Hitoshi Kitagishi, Kauki Hamano, Yukihiro Nishikawa and Masaoki Takahashi, 'Effect of confinement on phase-separation processes in a polymer blend observed by laser scanning confocal microscopy', *Physical Review E*, 2003, 67(2) 021801/1-021801/7.
55. Magerle R., 'Nanotomography', *Physical Review Letters*, 2000, 85(13) 2749–2752.
56. Andrzej Bernasik, Jakub Rysz, Andrzej Budkowski, Kazimierz Kowalski, Jozef Camra and Jerzy Jedlinski, 'Three-Dimensional Information on the Phase Domain Structure of Thin Films of Polymer Blends Revealed by Secondary Ion Mass Spectrometry', *Macromolecular Rapid Communications*, 2001, 22(11) 829–834.
57. Gray K.H., Gould S., Leasure R.M., Musselman I.H., Lee J.J., Meyer T.J. and Linton R.W., 'Three-dimensional characterization of conducting polymer arrays using secondary ion mass spectrometry', *Journal of Vacuum Science and Technology A*, 1992, 10(4) 2679–2684.
58. Akpalu Y.A., Karim A., Satija S.K. and Balsara N.P., 'Suppression of Lateral Phase Separation in Thin Polyolefin Blend Films', *Macromolecules*, 2001, 34(6) 1720–1729.
59. Stanley Affrossman, Scott A.O'Neill and Manfred Stamm, 'Topography and Surface Composition of Thin Films of Blends of Polystyrene with Brominated Polystyrenes: Effects of Varying the Degree of Bromination and Annealing', *Macromolecules*, 1998, 31(18) 6280–6288.
60. Howard Wang and Russell J. Composto, 'Understanding morphology evolution and roughening in phase-separating thin-film polymer blends', *Europhysics Letters*, 2000, 50(5) 622–627.
61. Bruder F. and Brenn R., 'Spinodal decomposition in thin films of a polymer blend', *Physical Review Letters*, 1992, 69(4) 624–627.
62. Hajime Tanaka, 'Interplay between phase separation and wetting for a polymer mixture confined in a two-dimensional capillary: Wetting-induced domain ordering and coarsening', *Europhysics Letters*, 1993, 24(8) 665–671.
63. Straub W., Bruder F., Brenn R., Georg Krausch, Bielefeldt H., Kirsch A., Marti O., Mlynek J. and Marko J.F., 'Transient wetting and 2D spinodal decomposition in a binary polymer blends', *Europhysics Letters*, 1995, 29(5) 353–358.
64. Sung L., Karim A., Douglas J.F. and Han C.C., 'Dimensional Crossover in the Phase Separation Kinetics of Thin Polymer Blend Films', *Physical Review Letters*, 1996, 76(28) 4368–4371.
65. Alamgir Karim, Slawcki T.M., Kumar S.K., Douglas J.F., Satija S.K., Han C.C., Russell T.P., Liu Y., Overney R., Sokolov J. and Rafailovich M.H., 'Phase-Separation-Induced Surface Patterns in Thin Polymer Blend Films', *Macromolecules*, 1998, 31(3) 857–862.
66. Brett D. Ermi, Alamgir Karim and Douglas J.F., 'Formation and dissolution of phase-separated structures in ultrathin blend films', *Journal of Polymer Science Part B: Polymer Physics*, 1998, 36(1) 191–200.
67. Slep D., Asselta J., Rafailovich M.H., Sokolov J., Winesett D.A., Smith A.P., Ade H., Strzhemechny Y., Schwarz S.A. and Sauer B.B., 'Phase Separation of Polystyrene

- and Bromo-Polystyrene Mixtures in Equilibrium Structures in Thin Films', *Langmuir*, 1998, 14(17) 4860–4864.
68. Jakob Heier, Edward J. Kramer, Peter Revesz, Gabor Battistig and Frank S. Bates, 'Spinodal Decomposition in a Subsurface Layer of a Polymer Blend Film', *Macromolecules*, 1999, 32(11) 3758–3765.
  69. Georg Krausch, Chi-An Dai, Edward J. Kramer and Frank S. Bates, 'Real space observation of dynamic scaling in a critical polymer mixture', *Physical Review Letters*, 1993, 71(22) 3669–3672.
  70. Howard Wang and Russell J. Composto, 'Hydrodynamic-flow-driven wetting in thin film polymer blends: Growth kinetics and morphology', *Physical Review E*, 2000, 61(2) 1659–1663.
  71. Howard Wang, Russell J. Composto, Hobbie E.K. and Han C.C. 'Multiple Lateral Length Scales in Phase-Separating Thin-Film Polymer Blends', *Langmuir*, 2001, 17(9) 2857–2860.
  72. Howard Wang, Douglas J.F., Satija S.K., Russell J. Composto and Han C.C., 'Early-stage compositional segregation in polymer-blend films', *Physical Review E*, 2003, 67(6) 061801/1-061801/6.
  73. Howard Wang and Russell J. Composto, 'Wetting and phase separation in polymer blend films: Identification of four thickness regimes with distinct morphological pathways', *Interface Science*, 2003, 11(3) 237–248.
  74. Hyun-joong Chung, Howard Wang and Russell J. Composto, Submitted *Macromolecules*, 2005.
  75. Hajime Tanaka, 'Wetting dynamics in a confined symmetric binary mixture undergoing phase separation', *Physical Review Letters*, 1993, 70(18) 2770–2773.
  76. Andrzej Bernasik, Jakub Rysz, Andrzej Budkowski, Brenn R., Kowalski K., Camra J. and Jedlinski J. 'Evolution of 3D structures in a phase-separating polymer blend film confined by symmetric flat walls', *Eur. Phys. J.E*, 2003, 12(2) 211–214.
  77. Jakub Rysz, Ermer H., Andrzej Budkowski, Andrzej Bernasik, Lekki J., Juengst G., Brenn R., Kowalski K., Camra J., Lekka M. and Jedlinski J., 'Hydrodynamic-flow-driven phase evolution in a polymer blend film modified by diblock copolymers', *Eur. Phys. J.E*, 2001, 5(2) 207–219.
  78. Harald Hoppe, Marcus Heuberger and Jacob Klein, 'Self-Similarity and Pattern Selection in the Roughening of Binary Liquid Films', *Physical Review Letters*, 2001, 86(21) 4863–4866.
  79. Pawel Koblinski, Kumar S.K., Amos Maritan, Koplik J. and Banavar J.R., 'Interfacial Roughening Induced by Phase Separation', *Physical Review Letters*, 1996, 76(7) 1106–1109.
  80. Yoo P.J. and Lee H.H., 'Evolution of a Stress-Driven Pattern in Thin Bilayer Films: Spinodal Wrinkling', *Physical Review Letters*, 2003, 91(15) 154502/1-154502/4.
  81. B. Zhang Newby, Wakabayashi K. and Russell J. Composto, 'Confinement induced stabilization in polymer blend thin films', *Polymer*, 2001, 42(21) 9155–9162.
  82. P. Muller-Buschbaum, Gutmann J.S. and Manfred Stamm, 'Influence of Blend Composition on Phase Separation and Dewetting of Thin Polymer Blend Films', *Macromolecules*, 2000, 33(13) 4886–4895.
  83. Andrew Cumming, Pierre Wiltzius, Frank S. Bates and Jeffrey H. Rosedale, 'Light-scattering experiments on phase-separation dynamics in binary fluid mixtures', *Physical Review A*, 1992, 45(2) 885–897.
  84. Pierre Wiltzius and Andrew Cumming, 'Domain growth and wetting in polymer mixtures', *Physical Review Letters*, 1991, 66(23) 3000–3003.

85. Hajime Tanaka, 'Simple hydrodynamic model of fast-mode kinetics in surface-mediated fluid phase separation', *Physical Review E*, 1996, 54(2) 1709–1714.
86. Hajime Tanaka and Araki T., 'Surface effects on spinodal decomposition of incompressible binary fluid mixtures', *Europhysics Letters*, 2000, 51(2) 154–160.
87. Marko J.F. 'Influence of surface interactions on spinodal decomposition', *Physical Review E*, 1993, 48(4) 2861–2879.
88. Pawel Keblinski, Wen-Jong Ma, Maritan A., Koplik J. and Banavar J., 'Molecular dynamics of phase separation in narrow channels', *Physical Review E*, 1993, 47(4) R2265-R2268.
89. Sandra M. Troian, 'Coalescence induced domain growth near a wall during spinodal decomposition', *Physical Review Letters*, 1993, 71(9) 1399–1402.
90. Keiji Tanaka, Jeong-Sik Yoon, Atsushi Takahara and Tisato Kajiyama, 'Ultrathinning-Induced Surface Phase Separation of Polystyrene/Poly(vinyl methyl ether) Blend Film', *Macromolecules*, 1995, 28(4) 934–938.
91. Klaus D. Jandt, Jakob Heier, Frank S. Bates and Edward J. Kramer, 'Transient Surface Roughening of Thin Films of Phase Separating Polymer Mixtures', *Langmuir*, 1996, 12(15) 3716–3720.
92. Matti Oron, Tobias Kerle, Rachel Yerushalmi-Rozen and Jacob Klein, 'Persistent Droplet Motion in Liquid-Liquid Dewetting', *Physical Review Letters*, 2004, 92(23) 236104/1-236104/4.
93. Tobias Kerle, Jacob Klein and Rachel Yerushalmi-Rozen, 'Accelerated Rupture at the Liquid/Liquid Interface', *Langmuir*, 2002, 18(26) 10146–10154.
94. Alessandro Faldi, Russell J. Composto and Karen I. Winey, 'Unstable Polymer Bilayers. 1. Morphology of Dewetting', *Langmuir*, 1995, 11(12) 4855–4861.
95. Lambooy P., Phelan K.C., Haugg O. and Georg Krausch, 'Dewetting at the Liquid-Liquid Interface', *Physical Review Letters*, 1996, 76(7) 1110–1113.
96. Martin P., Buguin A. and Brochard-Wyart F. 'Bursting of a liquid-film on a liquid substrate', *Europhysics Letters*, 1994, 28(6) 421–426.
97. Qi Pan, Karen I. Winey, Howard H. Hu and Russell J. Composto, 'Unstable Polymer Bilayers. 2. The Effect of Film Thickness', *Langmuir*, 1997, 13(6) 1758–1766.
98. Huiman Kang, Seung-Heon Lee, Sangcheol Kim and Kookheon Char, 'Dewetting and Layer Inversion of Inverted PVP/PS Bilayer Films', *Macromolecules*, 2003, 36(23) 8579–8583.
99. Zong Q., Li Z. and Xie X.M., 'Inversion of phase morphology in polymer-blend thin films on glass substrates', *Macromolecular Chemistry and Physics*, 2004, 205(8) 1116–1124.
100. Eugenia Kumacheva, Lin Li, Mitchell A. Winnik, Doug M. Shinozaki and Cheng P.C. 'Direct Imaging of Surface and Bulk Structures in Solvent Cast Polymer Blend Films', *Langmuir*, 1997, 13(9) 2483–2489.
101. Zdravko Mitov and Eugenia Kumacheva, 'Convection-Induced Patterns in Phase-Separating Polymeric Fluids', *Physical Review Letters*, 1998, 81(16) 3427–3430.
102. Lawrence C.J., 'The mechanics of spin coating of polymer films', *Physics of Fluids*, 1988, 31(10) 2786–2795.
103. Dietrich Meyerhofer, 'Characteristics of resist films produced by spinning', *Journal of Applied Physics*, 1978, 49(7) 3993–3997.
104. Birnie D.P., 'Rational solvent selection strategies to combat striation formation during spin coating of thin films', *Journal of Materials Research*, 2001, 16(4) 1145–1154.
105. Kenneth E. Strawhecker, Sanat K. Kumar, Douglas J.F. and Alamgir Karim, 'The

- Critical Role of Solvent Evaporation on the Roughness of Spin-Cast Polymer Films', *Macromolecules*, 2001, 34(14) 4669–4672.
106. Stanley Affrossman, Henn G., O'neill S.A., Pethrick R.A. and Manfred Stamm, 'Surface Topography and Composition of Deuterated Polystyrene-Poly(bromostyrene) Blends', *Macromolecules*, 1996, 29(14) 5010–5016.
  107. Ton-That C., Shard A.G., Teare D.O.H. and Bradley R.H. 'XPS and AFM surface studies of solvent-cast PS/PMMA blends', *Polymer*, 2001, 42(3) 1121–1129.
  108. Stanley Affrossman, Jerome R., O'neill S.A., Schmitt T. and Manfred Stamm, 'Surface structure of thin film blends of polystyrene and poly(n-butyl methacrylate)', *Colloid and Polymer Science*, 2000, 278(10) 993–999.
  109. Chunyan Chen, Jie Wang, Sara E. Woodcock and Zhan Chen, 'Surface Morphology and Molecular Chemical Structure of Poly (n-butyl methacrylate)/Polystyrene Blend Studied by Atomic Force Microscopy (AFM) and Sum Frequency Generation (SFG) Vibrational Spectroscopy', *Langmuir*, 2002, 18(4) 1302–1309.
  110. Dalnoki-Veress K., Forrest J.A., Stevens J.R. and Dutcher J.R., 'Phase separation morphology of thin films of polystyrene/polyisoprene blends', *Journal of Polymer Science Part B: Polymer Physics*, 1996, 34(17) 3017–3024.
  111. Stefan Walheim, Martin Boltau, Jurgen Mlynek, Georg Krausch and Ullrich Steiner, 'Structure Formation via Polymer Demixing in Spin-Cast Films', *Macromolecules*, 1997, 30(17) 4995–5003.
  112. Raczkowska J., Jakub Rysz, Andrzej Budkowski, Lekki J., Lekka M., Andrzej Bernasik, Kowalski K. and Czuba P., 'Surface Patterns in Solvent-Cast Polymer Blend Films Analyzed with an Integral-Geometry Approach', *Macromolecules*, 2003, 36(7) 2419–2427.
  113. Andrzej Budkowski, Andrzej Bernasik, Cyganik P., Raczkowska J., Penc B., Bergues B., Kowalski K., Jakub Rysz and Janik J., 'Substrate-Determined Shape of Free Surface Profiles in Spin-Cast Polymer Blend Films', *Macromolecules*, 2003, 36(11) 4060–4067.
  114. Bergues B., Lekki J., Andrzej Budkowski, Cyganik P., Lekka M., Andrzej Bernasik, Jakub Rysz and Postawa Z., 'Phase decomposition in polymer blend films cast on homogeneous substrates modified by self-assembled monolayers', *Vacuum*, 2001, 63(1–2) 297–305.
  115. Stanley Affrossman and Manfred Stamm, 'The effect of molecular weight on the topography of thin films of blends of poly (4-bromostyrene) and polystyrene', *Colloid and Polymer Science*, 2000, 278(9) 888–893.
  116. Stefan Walheim, Erik Schaffer, Jurgen Mlynek and Ullrich Steiner, 'Nanophase-Separated Polymer Films as High-Performance Antireflection Coatings', *Science*, 1999, 283(5401) 520–522.
  117. Ji-Seon Kim, Peter K.H. Ho, Craig E. Murphy and Richard H. Friend, 'Phase Separation in Polyfluorene-Based Conjugated Polymer Blends: Lateral and Vertical Analysis of Blend Spin-Cast Thin Films', *Macromolecules*, 2004, 37(8) 2861–2871.
  118. Dalnoki-Veress K., Forrest J.A., Stevens J.R. and Dutcher J.R., 'Phase separation morphology of spin-coated polymer blend thin films', *Physica A*, 1997, 239(1-3) 87–94.
  119. Andrzej Budkowski, Andrzej Bernasik, Cyganik P., Raczkowska J., Penc B., Bergues B., Kowalski K., Jakub Rysz and Janik J., 'Substrate-Determined Shape of Free Surface Profiles in Spin-Cast Polymer Blend Films', *Macromolecules*, 2003, 36(11) 4060–4067.

120. Keiji Tanaka, Atsushi Takahara and Tisato Kajiyama, 'Film Thickness Dependence of the Surface Structure of Immiscible Polystyrene/Poly(methyl methacrylate) Blends', *Macromolecules*, 1996, 29(9) 3232–3239.
121. Muller-Buschbaum P. and Manfred Stamm, 'Film thickness dependence of the domain size in weakly incompatible thin polymer blend films', *Colloid and Polymer Science*, 2001, 279(4) 376–381.
122. John Chappell, David G. Lidzey, Paul C. Jukes, Anthony M. Higgins, Richard L. Thompson, Stephen O'Connor, Ilaria Grizzi, Robert Fletcher, Jim O'Brien, Mark Geoghegan and Richard A.L. Jones, 'Correlating structure with fluorescence emission in phase-separated conjugated-polymer blends', *Nature Materials*, 2003, 2(8) 616–620.
123. Franz P. Wenzl, Peter Pachler, Christian Suess, Anja Haase, Emil J.W. List, Peter Poelt, Dieter Somitsch, Peter Knoll, Ullrich Scherf and Gunther Leising, 'The Influence of the Phase Morphology on the Optoelectronic Properties of Light-Emitting Electrochemical Cells', *Advanced Functional Materials*, 2004, 14(5) 441–450.
124. Arias A.C., MacKenzie J.D., Stevenson R., Halls J.J.M., Inbasekaran M., Woo E.P., Richards D. and Friend R.H., 'Photovoltaic Performance and Morphology of Polyfluorene Blends: A Combined Microscopic and Photovoltaic Investigation', *Macromolecules*, 2001, 34(17) 6005–6013.
125. Henry J. Snaith, Ana C. Arias, Arne C. Morteani, Carlos Silva and Richard H. Friend, 'Charge Generation Kinetics and Transport Mechanisms in Blended Polyfluorene Photovoltaic Devices', *Nano Letters*, 2002, 2(12) 1353–1357.
126. Arias A.C., Corcoran N., Banach M., Friend R.H., MacKenzie J.D. and Huck W.T.S., 'Vertically segregated polymer-blend photovoltaic thin-film structures through surface-mediated solution processing', *Applied Physics Letters*, 2002, 80(10) 1695–1697.
127. Ellen Moons, 'Conjugated polymer blends: linking film morphology to performance of light emitting diodes and photodiodes', *Journal of Physics: Condensed Matter*, 2002, 14(47) 12235–12260.
128. Ho P.K.H., Ji-Seon Kim, Burroughes J.H., Becker H., Li S.F.Y., Brown T.M., Cacialli F. and Friend R.H., 'Molecular-scale interface engineering for polymer light-emitting', *Nature*, 2000, 404(6777) 481–484.
129. Martin Boltau, Stefan Walheim, Jurgen Mlynek, Georg Krausch and Ullrich Steiner, 'Surface-induced structure formation of polymer blends on patterned substrates', *Nature*, 1998, 391(6670) 877–879.
130. Georg Krausch, Edward J. Kramer, Rafailovich M.H. and Sokolov J., 'Self-assembly of a homopolymer mixture via phase separation', *Applied Physics Letters*, 1994, 82(12) 2655–2657.
131. Rockford L., Liu Y., Mansky P. and Russell T.P., 'Polymers on Nanoperiodic, Heterogeneous Surfaces', *Physical Review Letters*, 1999, 82(12) 2602–2605.
132. Kenji Fukunaga, Hubert Elbs and Georg Krausch, 'Thin Film Phase Separation on a Nanoscopically Patterned Substrate', *Langmuir*, 2000, 16(7) 3474–3477.
133. Alamgir Karim, Douglas J.F., Lee B.P., Glotzer S.C., Rogers J.A., Jackman R.J., Amis E.J. and Whitesides G.M., 'Phase separation of ultrathin polymer-blend films on patterned substrates', *Physical Review E*, 1998, 57(6) R6273–R6276.
134. Bi-min Zhang Newby and Russell J. Composto, 'Phase-Morphology Map of Polymer-Blend Thin Films Confined to Narrow Strips', *Physical Review Letters*, 2001, 87(9) 098302/1–098302/4.

135. Brett D. Ermi, Giovanni Nisato, Douglas J.F., John A. Rogers and Alamgir Karim, 'Coupling between Phase Separation and Surface Deformation Modes in Self-Organizing Polymer Blend Films', *Physical Review Letters*, 1998, 81(18) 3900–3903.
136. Giovanni Nisato, Brett D. Ermi, Douglas J.F. and Alamgir Karim, 'Excitation of Surface Deformation Modes of a Phase-Separating Polymer Blend on a Patterned Substrate', *Macromolecules*, 1999, 32(7) 2356–2364.
137. Cyganik P., Andrzej Bernasik, Andrzej Budkowski, Bergues B., Kowalski K., Jakub Rysz, Lekki J., Lekka M. and Postawa Z. 'Phase decomposition in polymer blend films cast on substrates patterned with self-assembled monolayers', *Vacuum*, 2001, 63(307–313).
138. Xue Li, Rubo Xing, Ying Zhang, Yanchun Han and Lijia An, 'Molecular weight effects on the phase morphology of PS/P4VP blend films on homogeneous SAM and heterogeneous SAM/Au substrates', *Polymer*, 2004, 45(5) 1637–1646.
139. Bi-min Zhang Newby and Russell J. Composto, 'Influence of Lateral Confinement on Phase Separation in Thin Film Polymer Blends', *Macromolecules*, 2000, 33(9) 3274–3282.
140. Pil Jin Yoo, Suh K.Y. and Lee H.H., 'Short- and Long-Range Interactions in Thin Films of Polymer Blends in Microchannels', *Macromolecules*, 2002, 35(8) 3205–3212.
141. Schmidt G. and Malwitz M.M., 'Properties of polymer/ nanoparticle composites', *Current Opinion in Colloid and Interface Science*, 2003, 8(1) 103–108.
142. Anna C. Balazs, 'Interactions of nanoscopic particles with phase-separating polymeric mixtures', *Current Opinion in Colloid and Interface Science*, 1999, 4(6) 443–448.
143. Alamgir Karim, Liu D.-W., Douglas J.F., Nakatani A.I. and Amis E.J., 'Modification of the phase stability of polymer blends by fillers', *Polymer*, 2000, 41(23) 8455–8458.
144. Koray Yurekli, Alamgir Karim, Amis E.J. and Ramanan Krishnamoorti, 'Phase Behavior of PS-PVME Nanocomposites', *Macromolecules*, 2004, 37(2) 507–515.
145. Yimin Zhang, Ge S., Tang B., Koga T., Rafailovich M.H., Sokolov J., Peiffer D.G., Li Z., Dias A.J., McElrath K.O., Lin M.Y., Satija S.K., Urquhart S.G., Ade H. and Nguyen D., 'Effect of Carbon Black and Silica Fillers in Elastomer Blends', *Macromolecules*, 2001, 34(20) 7056–7065.
146. Koray Yurekli, Alamgir Karim, Eric J. Amis and Ramanan Krishnamoorti, 'Influence of Layered Silicates on the Phase-Separated Morphology of PS-PVME Blends', *Macromolecules*, 2003, 36(19) 7256–7267.
147. Hajime Tanaka, Andrew J. Lovinger and Don. D. Davis, 'Pattern evolution caused by dynamic coupling between wetting and phase separation in binary liquid mixture containing glass particles', *Physical Review Letters*, 1994, 72(16) 2581–2584.
148. Zhang W., Ge S., Wang Y., Rafailovich M.H., Dhez O., Winesett D.A., Ade H., Shafi K.V.P.M., Ulman A., Popovitz-Biro R., Tenne R. and Sokolov J., 'Use of functionalized WS<sub>2</sub> nanotubes to produce new polystyrene/polymethylmethacrylate nanocomposites', *Polymer*, 2003, 44(7) 2019–2115.
149. Hyun-joong Chung, Taubert A., Deshmukh R.D. and Russell J. Composto, 'Mobile nanoparticles and their effect on phase separation dynamics in thin film polymer blends', *Europhysics Letters*, 2004, 68(2) 219–225.
150. Alamgir Karim, Douglas J.F., Giovanni Nisato, Liu D.-W. and Amis E.J., 'Transient Target Patterns in Phase Separating Filled Polymer Blends', *Macromolecules*, 1999, 32(18) 5917–5924.

151. Wenhua Zhang, Bruce X. Fu, Seo Y., Eric Schrag, Hsiao B., Partick T. Mather, Nan-Loh Yang, Dayi Xu, Harold Ade, Rafailovich M.H. and Sokolov J., 'Effect of Methyl Methacrylate/Polyhedral Oligomeric Silsesquioxane Random Copolymers in Compatibilization of Polystyrene and Poly(methyl methacrylate) Blends', *Macromolecules*, 2002, 35(21) 8029–8038.
152. Sung L., Douglas J.F., Han C.C. and Alamgir Karim, 'Suppression of phase-separation pattern formation in blend films with block copolymer compatibilizer', *Journal of Polymer Science Part B: Polymer Physics*, 2003, 41(14) 1697–1700.
153. Stefan Walheim, Marcus Ramstein and Ullrich Steiner, 'Morphologies in Ternary Polymer Blends after Spin-Coating', *Langmuir*, 1999, 15(14) 4828–4836.
154. Cyganik P., Andrzej Budkowski, Ullrich Steiner, Jakub Rysz, Andrzej Bernasik, Stefan Walheim, Postawa Z. and Raczkowska J., 'Substructure formation during pattern transposition from substrate into polymer blend film', *Europhysics Letters*, 2003, 62(6) 855–861.
155. Cyganik P., Andrzej Budkowski, Raczkowska J. and Postawa Z., 'AFM/LFM surface studies of a ternary polymer blend cast on substrates covered by a self-assembled monolayer', *Surface Science*, 2002, 507–510(1) 700–706.
156. Monika Sprenger, Stefan Walheim, Claudia Schafle and Ullrich Steiner, 'Hierarchical Pattern Replication by Polymer Demixing', *Advanced Materials*, 2003, 15(9) 703–706.
157. Tsutomu Kikuchi, Masato Kudo, Chengjun Jing, Takao Tsukada and Mitsunori Hozawa, 'Electrohydrodynamic Effect on Phase Separation Morphology in Polymer Blend Films', *Langmuir*, 2004, 20(4) 1234–1238.
158. Qui Tran-Cong-Miyata, Shinsuke Nishigami, Tetsuo Ito, Satonori Komatsu and Tomohisa Norisuye, 'Controlling the morphology of polymer blends using periodic irradiation', *Nature Materials* 2004, 3(6) 448–451.
159. Yoav Tsori, Francois Tournilhac and Ludwik Leibler, 'Orienting Ion-Containing Block Copolymers Using AC Electric Fields', *Macromolecules*, 2003, 36(15) 5873–5877.
160. Koerner H., Jacobs J.D., Tomlin D.W., Busbee J.D. and Vaia R.A., 'Tuning Polymer Nanocomposite Morphology: AC Electric Field Manipulation of Epoxy-Montmorillonite (Clay) Suspensions', *Advanced Materials*, 2004, 16(4) 297–302.
161. Kazuyoshi Kanamori, Kazuki Nakanishi, Kazuyuki Hirao and Hiroshi Jinnai, 'Interface-Directed Web-to-Pillar Transition of Microphase-Separated Siloxane Gels', *Langmuir*, 2003, 19(22) 9101–9103.
162. Kazuyoshi Kanamori, Kazuki Nakanishi, Kazuyuki Hirao and Hiroshi Jinnai, 'Three-Dimensional Observation of Phase-Separated Silica-Based Gels Confined between Parallel Plates', *Langmuir*, 2003, 19(14) 5581–5585.
163. Elizabeth A. Wilder, Michael B. Braunfeld, Hiroshi Jinnai, Carol K. Hall, David A. Agard and Richard J. Spontak, 'Nanofibrillar Networks in Poly(ethyl methacrylate) and Its Silica Nanocomposites', *Journal of Physical Chemistry B*, 2003, 107(42) 11633–11642.
164. Helene Pernot, Martin Baumert, Francois Court and Ludwik Leibler, 'Design and properties of co-continuous nanostructured polymers by reactive blending', *Nature Materials*, 2002, 1(1) 54–58.
165. Alamgir Karim, Douglas J.F., Satija S.K., Han C.C. and Goyette R.J., 'Frustrated Coalescence in a Chemically Reactive Polymer Blend Film', *Macromolecules*, 1999, 32(4) 1119–1127.

166. Archie P. Smith, Douglas J.F., Carson Meredith J., Amis E.J. and Alamgir Karim, 'Combinatorial Study of Surface Pattern Formation in Thin Block Copolymer Films', *Physical Review Letters*, 2001, 87(1) 015513/1-015513/4.
167. Carson Meredith J., Alamgir Karim and Amis E.J., 'High-Throughput Measurement of Polymer Blend Phase Behavior', *Macromolecules*, 2000, 33(16) 5760–5762.
168. Marlon L. Walker, Archie P. Smith and Alamgir Karim, 'Combinatorial Approach for Studying the Effects of 4-Biphenyl Carboxylic Acid on Polypropylene Films', *Langmuir*, 2003, 19(17) 6582–6585.
169. Hajime Tanaka, 'Viscoelastic phase separation', *Journal of Physics: Condensed Matter*, 2000, 12(15) R207–R264.

## Rapid prototyping of functional microfabricated devices by soft lithography

---

D B WOLFE and G M WHITESIDES,  
Harvard University, USA

### 3.1 Introduction

Microfabricated devices are integral to electronics (e.g., transistors and integrated circuits), optics (e.g., polarizers and light-emitting diodes), microelectromechanical systems (MEMS) (e.g., accelerometers and micromirrors), and microfluidics (e.g., systems for protein crystallization and for bioassays). There are four general steps in the fabrication of such devices: (i) fabrication of a master (i.e., the pattern from which replicas are made), (ii) replication of the master, (iii) transfer of the pattern present in the replica into a functional material (polymer, ceramic, metal, or semiconductor) to form a functional microstructure, and (iv) registration of a master (the same one, or a different one) with the functional microstructure to form multi-layered structures. Photolithography – the exposure of a photosensitive material through a photomask – is the conventional technique used to replicate patterns. This technique is highly developed and well-suited for applications in microelectronics.<sup>1</sup> It is, however, limited to materials that are photosensitive, and is only suitable for fabrication on planar surfaces. Soft lithography provides an alternative set of techniques for microfabrication (steps 2–4) that does not have these limitations (although it has others).

Soft lithography is a suite of techniques that uses physical contact between a topologically patterned stamp (or mold) and a substrate for pattern transfer. There are two broad classes of soft-lithographic techniques, those that use a soft (elastomeric) stamp to transfer a pattern into organic materials and onto the surface of metals and ceramics and those that use a hard (rigid) stamp to transfer a pattern into thin layers of (soft) organic materials. This chapter will focus on the first of the two classes, and, more specifically, on the uses of soft stamps (or molds) made of elastomeric organic polymers.

Reviews published previously<sup>2–5</sup> have discussed the details of soft lithography. These techniques have five characteristics that are useful for the microfabrication of functional devices:

1. They are rapid. It often takes less than 24 hours to go from a concept to a prototype device.
2. They are inexpensive – they do not require the use of expensive equipment or infrastructure (e.g., cleanrooms).
3. They allow the patterning of a range of functional materials – metals, polymers, molecules, and biological organisms – directly onto surfaces.
4. They can be used to pattern non-planar surfaces.
5. They are simple to use, and do not require specialized training.

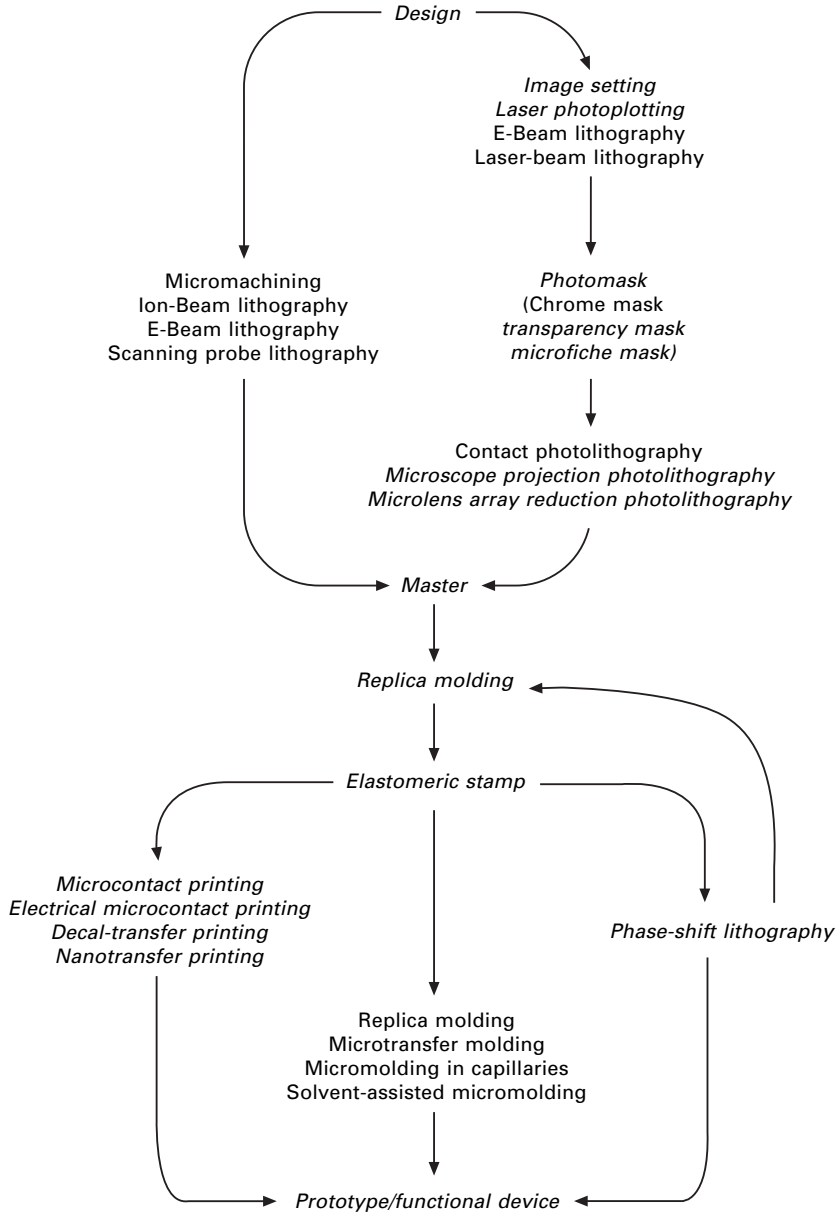
Figure 3.1 diagrams the flow of the process of microfabrication by soft lithography, from the design of the pattern to the generation of the functional device. This chapter will discuss developments in each stage of this process and will also provide examples of devices microfabricated using soft lithography in the period 1999–2004. Examples of the use of soft lithography in biology,<sup>6–8</sup> biochemistry,<sup>6–8</sup> and microfluidics<sup>8–15</sup> are discussed elsewhere. Here we limit the examples to optical and electronic microdevices fabricated by printing or phase-shifting photolithographic techniques.

## 3.2 Developments in soft lithographic techniques

During the period 1999–2004, there have been a number of developments in each stage of the process of fabrication by soft lithography outlined in Fig. 3.1. This chapter emphasizes those developments that have improved the ability to fabricate functional microdevices by soft lithography.

### 3.2.1 Methods of fabricating masters

A master contains the pattern in bas-relief that is replicated into an elastomeric stamp. The ability to design and fabricate these masters quickly and at low cost facilitates the rapid prototyping of microdevices by soft lithography. The pattern for a master is generated by computer-aided design (CAD). These designs are translated into topographically patterned masters by micromachining<sup>16</sup> or serial lithographic techniques (e.g., e-beam, scanning probe, or ion-beam lithographies) or into photomasks by serial lithographic or photographic (e.g., image setting or laser photoplotting)<sup>17, 18</sup> techniques. Photomasks are used in photolithography to make topologically patterned masters. The processes (e.g., electron-beam and laser-beam lithographies) used to fabricate topographically patterned masters and conventional photomasks (i.e., chromium-coated float glass, also referred to as a ‘chrome mask’) directly from the CAD design can be slow (days to weeks) and expensive (> \$100/in<sup>2</sup>), and thus the total number of designs that can be translated into masters using these techniques is limited by time and cost. In contrast, photomasks prepared by image setting or photoplotting provide alternatives to chrome masks that can be produced rapidly (< 24 hours) and



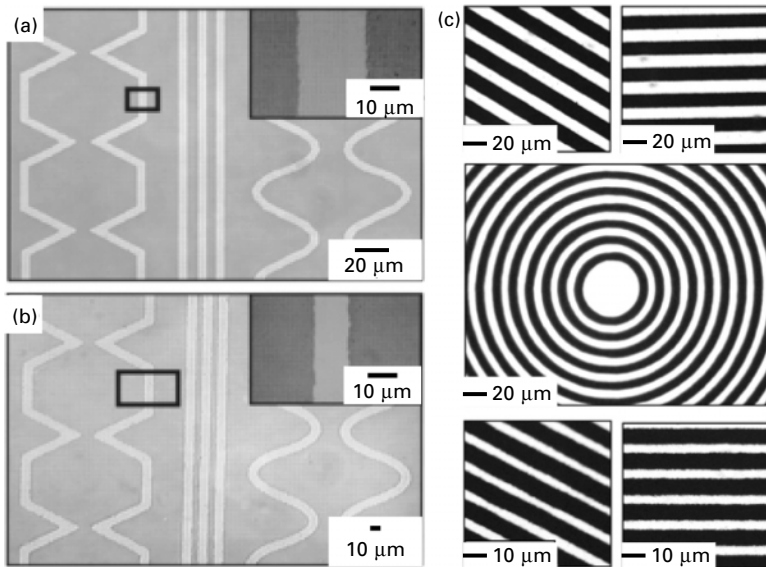
3.1 Diagram of the flow of the process of microfabrication by soft lithography. The elements and techniques of this process that will be discussed in this chapter are shown in italics.

at low cost ( $\sim \$1/\text{in}^2$ ), albeit with feature sizes limited to  $\geq 8 \mu\text{m}$ . These qualities are attractive for the fabrication of masters in a number of areas (for example, microfluidics, biology, and optics), and make soft lithography an

especially attractive method for research and development because prototyping usually involves multiple iterative cycles of the process of fabrication from design to prototype. This discussion describes the characteristics of photomasks that can be fabricated by these techniques.

### *Fabrication of transparency-based photomasks*

Photomasks prepared by laser image setting (5,080 dots/inch (dpi); Linotype-Hell Co) have been an important part of soft lithography since their introduction in 1996.<sup>19</sup> The original demonstration of this capability included photomasks prepared on transparency film with features of lateral dimensions  $\geq 20 \mu\text{m}$  and edge resolution of  $\sim 1\text{--}2 \mu\text{m}$  (Fig. 3.2(a)).<sup>19</sup> These photomasks can prepare integrated designs over areas of  $> 500 \text{ cm}^2$  and enable large-area, modest-resolution microfabrication. The minimum lateral dimension was reduced further to  $\sim 10 \mu\text{m}$ , and the edge resolution to  $\sim 1 \mu\text{m}$ , through photographic reduction of the pattern on the transparency<sup>18</sup> (or on paper)<sup>20</sup> onto microfiche (Fig. 3.2(b)). This two-step process yielded small features at the cost of the area that could be patterned. In one experiment, for example, the area of the



3.2 (a) Optical micrograph of a transparency mask produced by image setting. (b) Optical micrograph of a microfiche mask produced by photographic reduction of (a) by a factor of  $\sim 25$ . (c) Optical micrographs of a transparency mask produced by laser photoplotting. The images in (a) and (b) are reproduced with permission from reference 20 (Copyright 2000, American Chemical Society), and the images in (c) are from ref. 17 (Copyright 2003, American Chemical Society).

original transparency was  $\sim 560 \text{ cm}^2$  (with minimum feature size of  $25 \text{ }\mu\text{m}$ ) and the area of the microfiche was  $19\text{--}25 \text{ cm}^2$  (with minimum feature size of  $10 \text{ }\mu\text{m}$ ). A problem with microfiche is poor contrast between the opaque and transparent regions of the microfiche masks, due to the granular nature of the silver grains in the film.<sup>17</sup>

Photomasks prepared by laser photoplotting can have features with lateral dimensions ( $\geq 8 \text{ }\mu\text{m}$ ) and edge roughness ( $\sim 1 \text{ }\mu\text{m}$ ) similar to, or better than, those of microfiche, over large areas ( $> 500 \text{ cm}^2$ ) (Fig. 3.2(c)).<sup>17</sup> Laser photoplotting is similar to image setting; each technique is a specialized form of photography. Photoplotters are built for high accuracy and have resolutions of 20,000 dpi; this resolution is four times greater than that of image setters. The cost of photomasks prepared by photoplotting is similar to the cost of those produced by image setting (i.e.,  $< \$0.16/\text{cm}^2$ ). Laser photoplotters are available at commercial printing companies in most major cities, and turnaround time for such services is short ( $\sim 1 \text{ day}$ ).<sup>21</sup> This one-step process has provided a significant improvement in the time and cost required to fabricate high-quality photomasks with sub- $20\text{-}\mu\text{m}$  features for use in soft lithography.

Table 3.1 compares the properties of chrome masks to those of transparency-based masks. The ultimate limit of resolution of photomasks prepared by laser photoplotting is determined by two factors, the cross-sectional size of the laser beam and the resolution of the photosensitive films.<sup>17</sup> The wavelength (and thus, the size of the diffraction-limited beam spot) of electron beams is much smaller than that used for laser photoplotting. In addition, the photosensitive materials used in electron-beam lithography (e.g., poly(methylmethacrylate) (PMMA)) have resolutions that are much higher than those of the silver-halide films used in laser photoplotting.

Table 3.1 Properties of chrome and transparency-based masks

	Chrome mask	Transparency-based masks		
		Image setting	Microfiche	Photoplotting
Minimum lateral dimensions ( $\mu\text{m}$ )	$< 0.5$	25	15	8
Edge roughness ( $\mu\text{m}$ )	$< 0.1$	1–2	1	$< 1$
Advantages	High resolution	Low cost, short turnaround ( $\sim 1 \text{ day}$ )		
Disadvantages	High cost, long turnaround (1–2 weeks)	Medium resolution		

Electron-beam lithography, therefore, is capable of resolutions ( $< 20$  nm) and edge roughness ( $< 10$  nm) that are superior to those of laser photoplotters. Many applications for microfabricated devices (e.g., biology, sensors, microfluidics, and some microelectronics), however, do not require this resolution. Generation of photomasks by laser photoplotting, therefore, provides an attractive, low-cost, and rapid alternative to conventional techniques for the fabrication of masters for use in soft lithography.

### *Fabrication of photoresist-based masters using transparency masks*

Transparency-based photomasks can be used to prepare topographically-patterned masters made of photoresist by three types of photolithography: (i) contact photolithography, (ii) microscope projection photolithography (MPP),<sup>22</sup> and (iii) microlens array reduction photolithography (MAP).<sup>23–25</sup> MPP and MAP are alternatives to contact photolithography that are especially useful in making repetitive micropatterns.

#### Contact photolithography

Contact photolithography is widely used both in industrial and research settings. This technique generates a master comprising an array of photoresist-based features that form by parallel replication of the features in the photomask in a single exposure over areas as large as  $\sim 2 \times 10^4$  mm<sup>2</sup> (150-mm-diameter wafer). It is useful for microfabricating masters with features as large as 10–15 cm (for example, those used to fabricate microfluidic channels). In this technique, a photomask is placed in physical contact with a photoresist-coated substrate, and the photoresist is exposed with UV-light through the photomask. The pattern is developed by dissolving the photoresist in the area that was exposed (positive resist) or the area that was not exposed (negative resist). The use of transparency masks in this process is not operationally different from using conventional chrome masks, so transparency masks integrate easily into existing photolithographic equipment and processes. It is a 1:1 technique and does not provide size reduction, and damage or contamination of the resist layer or the mask are concerns.

#### Microscope projection photolithography (MPP)

Microscope projection photolithography (MPP)<sup>22</sup> is useful for the fabrication of features smaller than those available by contact photolithography with transparency-based masks (i.e., features with lateral dimensions of  $\sim 1$ – $10$   $\mu\text{m}$ ), albeit over small areas ( $\sim 4 \times 10^4$   $\mu\text{m}^2$ ) per exposure. Features on this scale are useful in cell biology,<sup>26, 27</sup> microfluidics,<sup>14</sup> and microelectronics.<sup>28</sup> The technique requires only a standard upright microscope equipped with a

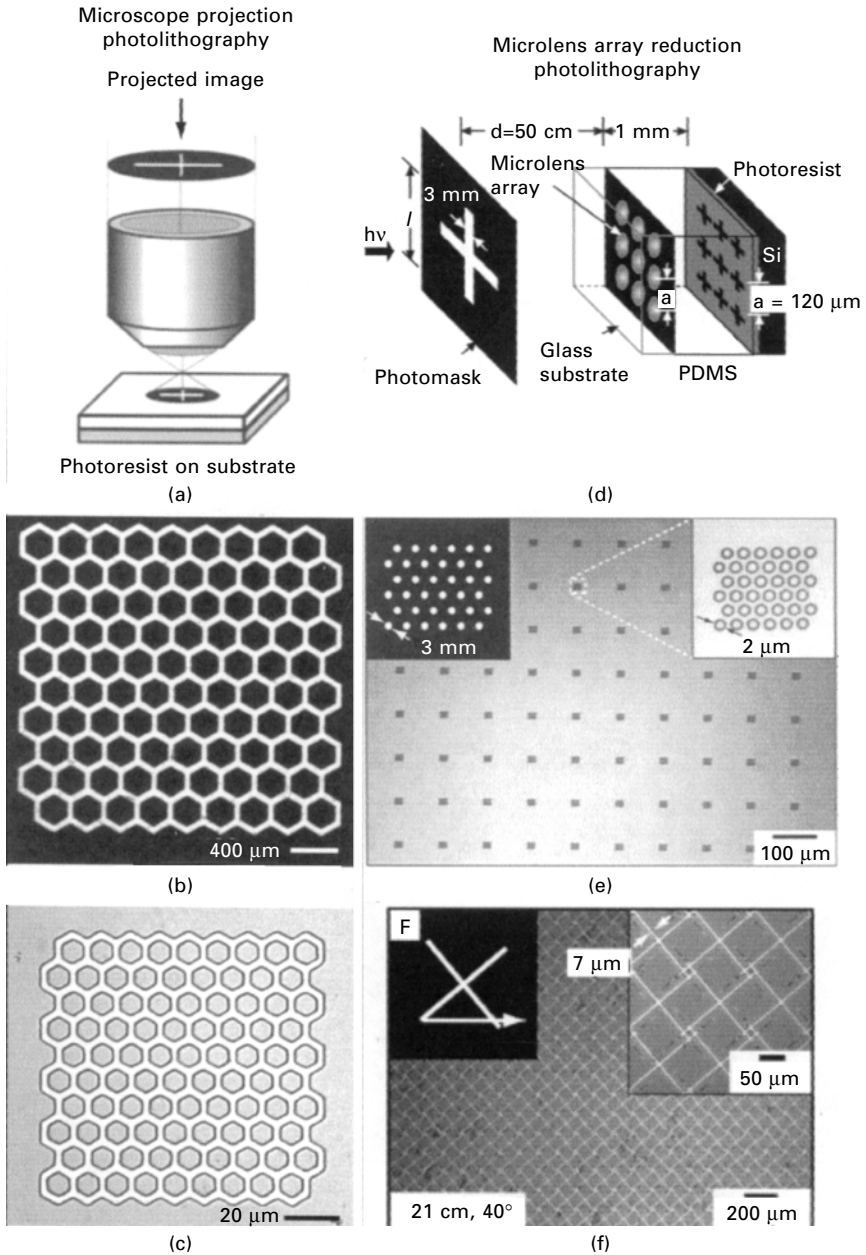
mercury-arc lamp; it is therefore accessible to most research laboratories. MPP includes two features that are common to photolithographic steppers used commercially. First, the translation stage of the microscope allows for accurate registration ( $< 0.35 \mu\text{m}$ ) of the pattern for multi-level fabrication. Second, multiple copies of the same pattern can be generated on a single substrate by translating (i.e., stepping) the sample and repeating the exposure.

In MPP (Fig. 3.3(a)), a transparency photomask is placed in the light path of an upright microscope at the conjugate image plane to the image plane of the substrate so the two images are in focus at the same vertical location of the translation stage. The optics of the microscope (i.e., the objectives and lenses) reduce the lateral dimensions of the pattern on a transparency photomask projected onto a photoresist-coated substrate.<sup>29</sup> The minimum resolution of the technique,  $R$ , is limited by diffraction – that is,  $R = K\lambda/2NA$ , where  $K \approx 1$  for a single-layer resist on a reflective substrate,  $\lambda$  is the wavelength of light, and  $NA$  is the numerical aperture of the objective.<sup>30</sup> Figure 3.3(c) shows an example of features prepared by this technique.

#### Microlens array reduction photolithography (MAP)

Microlens array reduction photolithography (MAP) is capable of producing a periodic array of patterns with  $\mu\text{m}$ -sized features over  $\text{cm}^2$  areas.<sup>23–25</sup> The types of patterns generated by MAP are useful for applications in media for data storage and in patterned substrates for biological assays. MAP produces this array in a single exposure, whereas commercial step-and-repeat lithographic techniques require multiple exposures to pattern similar areas. The microlenses are capable of reducing the lateral dimensions of features in a photomask by a factor of  $\sim 10^3$  in a single step, to yield features with minimum lateral dimensions of  $\sim 500 \text{ nm}$ .<sup>31</sup> The position of the lens with respect to the light source, as well as the size and shape of the pattern on the transparency-based photomask, determine the extent of distortion in the features produced at the edges of the lens array. These distortions due to edge effects are relatively small for areas of  $\sim 4 \text{ cm}^2$ .

The technique uses an array of microlenses prepared by contact photolithography and reflow of the photoresist,<sup>32</sup> or an array of transparent microspheres,<sup>33</sup> to reduce the pattern from a transparency-based photomask onto a photoresist-coated substrate (Fig. 3.3(d)). The photoresist-coated substrate is positioned at a distance equal to the focal length of the lenses by coating the substrate with a thin layer of poly(dimethylsiloxane) (PDMS) of the appropriate thickness. The conformal contact between the PDMS and the substrate reduces distortions due to tilting of the array with respect to the substrate. The surface that contacts the photoresist is a soft, elastomeric polymer, so neither surface is damaged by contact. Because the PDMS has a low interfacial free energy ( $\tau = 21.6 \text{ dyn/cm}^2$ ), its surface resists contamination



3.3 (a) Schematic diagram of the reduction of an image on a photomask onto a photoresist-coated substrate by MPP. (b) Optical micrograph of a transparency mask prepared by image setting. (c) Optical micrograph of a photoresist pattern produced by MPP using the mask in (b). (d) Schematic diagram of the process of MAP. (e)–(f) Optical micrographs of patterns produced by MPP. The insets are optical micrographs of the masks used to pattern the features in the respective images. The images in figures (a)–(c) are reproduced with permission from ref. 22, the images in (d) and (e) from ref. 23, and the image in (f) from ref. 24 (Copyright 2001 and 2002, American Chemical Society).

and is easy to clean. The exposure of the photoresist through the microlenses can be carried out on a standard overhead projector (or other inexpensive source of diffuse illumination); no additional infrastructure or equipment is necessary for this technique. The features in the array can be discrete<sup>24, 25</sup> or connected<sup>23</sup> depending on the size of the features on the original photomask (Fig. 3.3(e) and (f)). Arrays of features with variable topography and shape can be generated by MAP using grey-scale transparencies.<sup>24</sup> Changing the orientation of the pattern being imaged with respect to the array of microlenses can produce an array of different images from a single pattern.<sup>24</sup>

### 3.2.2 Types of elastomeric materials used for stamps

#### *Polydimethylsiloxane (PDMS)*

PDMS is the elastomeric material most commonly used to make stamps or molds for soft lithography. These stamps are made by replica molding of topographically patterned masters by techniques discussed previously (Fig. 3.4(a)).<sup>2, 3, 5</sup> In principle, any elastomeric material that replicates the topology of a master may be useful as a stamp.<sup>34</sup> Sylgard 184 (184-PDMS) is an inexpensive commercial brand of PDMS<sup>35</sup> that is used commonly as the material for the stamps.<sup>2, 3</sup> This material works well for most applications in microfabrication requiring replication of masters with features with lateral dimensions of  $> 500$  nm. The replication of features with lateral dimensions  $< 500$  nm with 184-PDMS yields stamps with deformed, buckled, or collapsed features resulting from lateral and/or roof collapse.<sup>36</sup> Deformation and rounding of the edges of the features also occurs due to surface tension (Fig. 3.4(c)).<sup>36</sup> Most of these problems reflect the low elastic modulus of 184-PDMS (1.8 MPa). The development of formulations of PDMS that have elastic moduli greater than that of 184-PDMS – e.g., *h*-PDMS<sup>37</sup> and *hv*-PDMS<sup>38</sup> – have enabled replication of sub-100-nm features. Composite stamps made of a thin layer of *h*-PDMS (40  $\mu$ m) and a thick layer of 184-PDMS (3 mm) have the ability to replicate sub-100-nm features with the same fidelity as *h*-PDMS, but are not as fragile as pure *h*-PDMS replicas (Fig. 3.4(d)).<sup>36</sup> These materials can replicate features with lateral dimensions as small as 30 nm,<sup>36, 37</sup> and vertical dimensions as small as 2 nm (Fig. 3.4(f)).<sup>39</sup> Table 3.2 summarizes the physical properties of these types of PDMS.

#### *Block co-polymers*

The use of block co-polymer thermoplastics – e.g., polyolefins,<sup>40</sup> poly(styrene-*block*-butadiene-*block*-styrene) (SBS),<sup>41</sup> and poly(styrene-*block*-ethylene-*co*-butylene-*block*-styrene) (SEBS)<sup>41</sup> – as materials for elastomeric stamps has also been explored. These materials have an elastic modulus higher than that

of 184-PDMS (Table 3.2),<sup>42</sup> and thus replicas of these materials are less susceptible to deformations of the features due to roof or lateral collapse. These stamps are also less fragile (more ductile) than those made of *h*-PDMS. The replicas using these materials, however, are more difficult to prepare than those of PDMS because they require the use of hot embossing techniques that use temperatures of 150–200 °C and loads of 200 g. These conditions are not compatible with most photoresist-based masters.

### *Hydrogels*

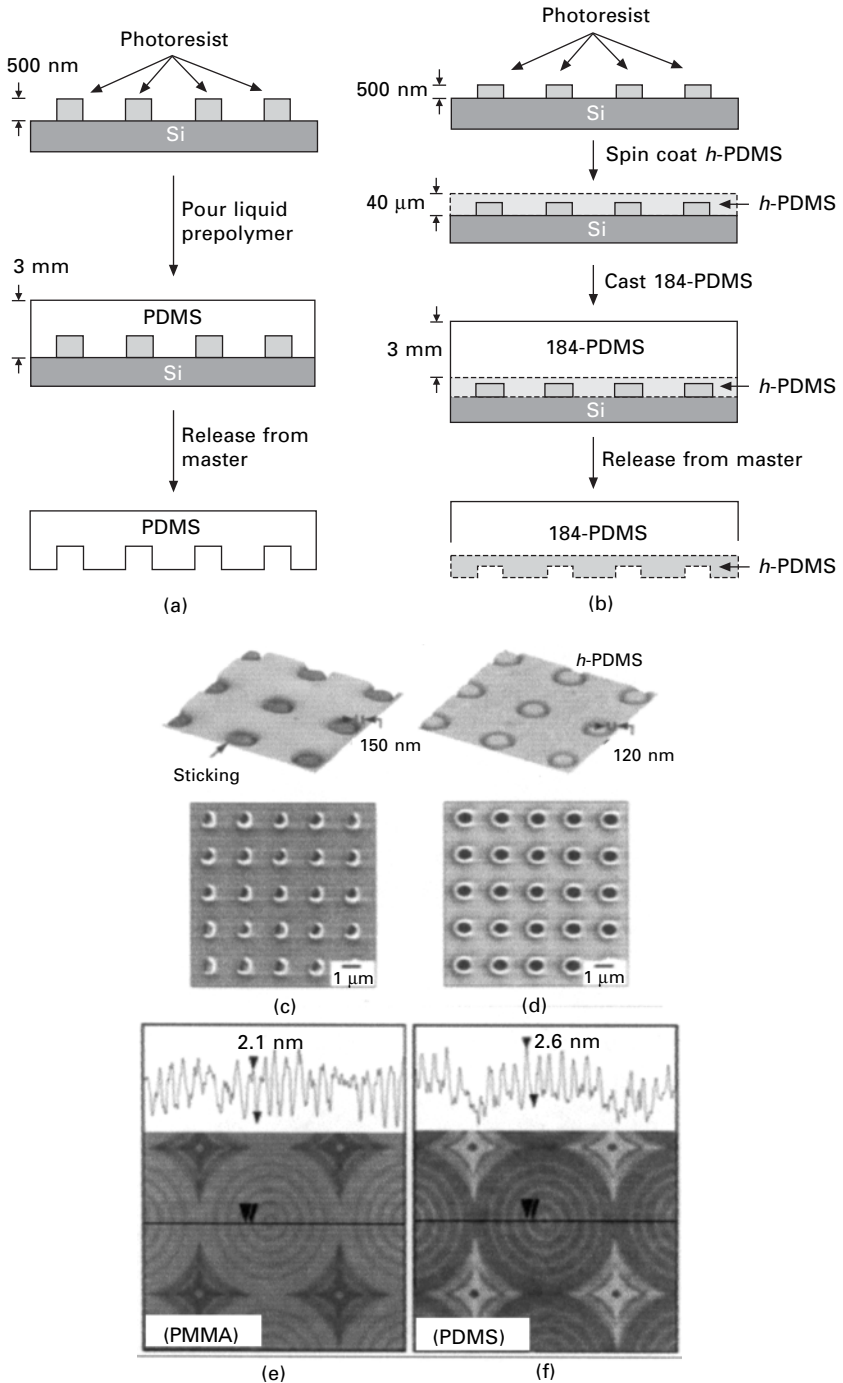
Hydrogel stamps are useful as an alternative to PDMS stamps because they are inherently hydrophilic. They are, of course, mechanically fragile, and useful only for certain applications, especially the patterning of proteins and other biologically relevant molecules that are sensitive to their environment. Mayer, *et al.* demonstrated the fabrication of topographically patterned agarose gels by replica molding of a photoresist-based master and of a 184-PDMS replica of this master.<sup>43</sup> Martin, *et al.* formed hydrogels of poly(6-acryloyl- $\beta$ -*O*-methylcalactopyranoside-*co*-methylele bis(acrylamide) through similar techniques.<sup>44</sup> Hydrogel stamps differ from those made of PDMS or block copolymers in that hydrophilic molecules dissolve into the bulk of the stamps. This property is useful for uniform patterning of hydrophilic molecules by printing.<sup>43</sup> Hydrophilic molecules also diffuse readily through these stamps. Mayer *et al.* used this capability to create a gradient in the concentration of a protein in the hydrogel stamp and transferred this gradient to a glass slide by printing.<sup>43</sup> Hydrogel stamps must be kept in an aqueous environment to prevent cracking or distortions of the topologically defined features that form as a result of drying out of the stamps.

### 3.2.3 Replication using elastomeric stamps (soft lithography)

The suite of techniques in soft lithography includes three general types of replication: printing, molding, and phase-shifting lithography. A number of developments in the areas of printing and phase-shifting lithography have extended the capabilities of each of these techniques to include the patterning of hydrophilic and hydrophobic molecules, polymers, proteins, metals, and electrostatic charge on a surface, and the fabrication of features with lateral dimensions < 100 nm.

#### *Microcontact printing (mCP)*

Microcontact printing is the process of transferring a material ('ink') from the elastomeric stamp to a substrate when the two are in conformal contact



3.4 (a)–(b) Scheme for replica molding of a master into PDMS (a) and into a composite stamp (b). (c)–(d) (top) Atomic force micrograph of

Table 3.2 Physical properties of elastomers used in soft lithography

Material	Tensile modulus (MPa)	Tensile strength (MPa)	Surface free energy (dyn/cm <sup>2</sup> )	Coeff. of linear expansion (ppm/°C)	Method of curing	Comm. avail.
PDMS						
184-PDMS	1.8 <sup>38</sup>	4.77 <sup>38</sup>	21.6	260–310	Heat	Yes
<i>h<sub>v</sub></i> -PDMS	3.4 <sup>38</sup>	0.13 <sup>38</sup>	~20	450 <sup>38</sup>	UV-light	No
<i>h</i> -PDMS	8.2 <sup>38</sup>	0.02 <sup>38</sup>	~20	300 <sup>38</sup>	Heat	Yes
Co-Polymers						
SBS	14.2 <sup>41</sup>	~32 <sup>42</sup>			N/A	Yes
SEBS	46.7 <sup>41</sup>	~31 <sup>42</sup>			N/A	Yes

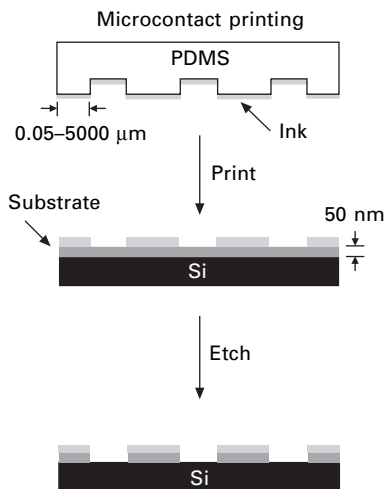
(Fig. 3.5). The ink forms a self-assembled monolayer (SAM) on the surface of the substrates; this transfer is controlled spatially by the topography of the stamp. The combination of  $\mu$ CP of SAMs and wet-chemical etching is used to generate patterns of electronically and optically relevant metals (e.g., Au, Pd, Pt, Ti, Cu, Ag), semiconductors (e.g., Si, GaAs), and insulators (e.g., SiO<sub>2</sub>, glass). The details of  $\mu$ CP have been discussed previously.<sup>2,3</sup> Developments in this technique include the modification of the surface of PDMS stamps to enable the patterning of hydrophilic inks, the use of high-molecular weight inks for nanofabrication, the ability to pattern and attach molecules covalently to SAMs, the improvement of etch chemistries for Au and Cu, and the patterning of Pd<sup>45–47</sup> and indium-tin-oxide (ITO).<sup>48, 49</sup>

### Hydrophilic PDMS stamps

The patterning of hydrophobic molecules (e.g., alkanethiols) by  $\mu$ CP with PDMS stamps made of Sylgard 184 works well because the stamp is hydrophobic, and thus the molecular ‘ink’ is soluble in the stamp and is distributed uniformly on the surface. Recently, there has been substantial interest in the patterning of hydrophilic inks (e.g., water containing DNA,<sup>50, 51</sup> proteins,<sup>52–55</sup> and polar molecules).<sup>56–60</sup> The use of hydrophobic PDMS stamps to pattern hydrophilic inks by  $\mu$ CP yields poor results because the ink does

*(Caption continued from previous page)*

the topography of a replica pattern of rings in 184-PDMS (c) and in a composite stamp (d). (bottom) Scanning electron micrographs of polyurethane replicas of stamps. (e)–(f) Atomic force micrograph of the topography of a PMMA master and a composite stamp replica of this master measured by atomic force microscopy. The images in (c) and (d) are reproduced with permission from ref. 37, and the images in (e) and (f) from ref. 40 (Copyright 2002 and 2003, American Chemical Society).

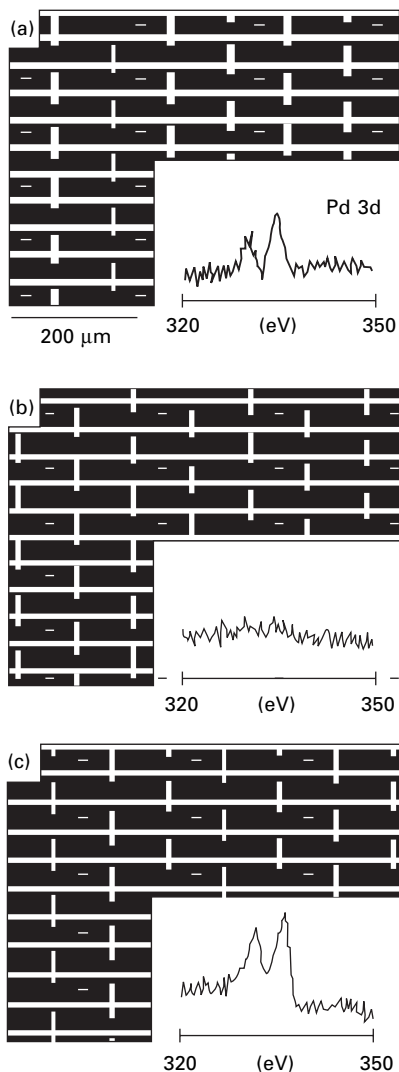


3.5 Scheme for microcontact printing and transfer of the pattern into a substrate by etching.

not coat the surface of the stamp evenly or dissolve into the stamp.<sup>61</sup> Exposure of the PDMS stamps to an oxygen plasma makes the surface of the stamp hydrophilic (by oxidizing Si-CH<sub>3</sub> groups to Si-OH, and perhaps Si-CH<sub>2</sub>-OH groups.<sup>62-64</sup> Reorganization of the surface of oxidized stamps, however, occurs over ~30 min; this reorganization (sometimes called 'reconstruction') causes the surface to revert from hydrophilic to hydrophobic (Fig. 3.6(b)).<sup>61</sup> It probably originates in the migration of mobile, uncrosslinked siloxane molecules from the interior of the polymer to its surface. This reversion can be slowed and minimized by immersing the stamps in water immediately after oxidation.<sup>61-64</sup> Grafting hydrophilic molecules (aminoalkylsilanes)<sup>65</sup> and polymers (e.g., poly(ethyleneoxide)<sup>66</sup> and poly(ethylene glycol)<sup>61</sup> to the surface of oxidized PDMS stamps results in hydrophilic stamps that are stable for > 7 days (Fig. 3.6(c)).

### Molecular 'inks'

The ability to control the wettability of the surface of PDMS stamps has expanded the number and types of molecules that can be patterned by μCP. Table 3.3 contains a list of these molecules, and of compatible substrates, for use in μCP.<sup>67-107</sup> Whereas microfabrication of features with lateral dimensions > 500 nm with these inks is relatively simple, fabrication of features < 200 nm is difficult because low molecular-weight (< 0.3 kD) inks (e.g., alkanethiols) diffuse laterally during printing. Li *et al.* addressed this problem by using dendrimer-based inks.<sup>108</sup> Liebau *et al.* used high-molecular weight (> 1000 kD) inks based on thioether-calixarene derivatives.<sup>105</sup> These inks exhibit low



**3.6** Patterning using hydrophilic PDMS stamps. A catalyst for the electroless deposition of Cu was patterned by mCP using a freshly oxidized stamp (a), an oxidized stamp 3 h after the plasma treatment (b), and a 20-day-old stamp with a grafted layer of poly(ethylene glycol) (c). The images are scanning electron micrographs of Cu that were electrolessly deposited onto the patterned catalyst. The insets are X-ray photoelectron spectra of the Pd<sup>2+</sup> catalyst present on the stamp before printing. The images are reproduced with permission from ref. 62 (Copyright 2001, Wiley-VCH).

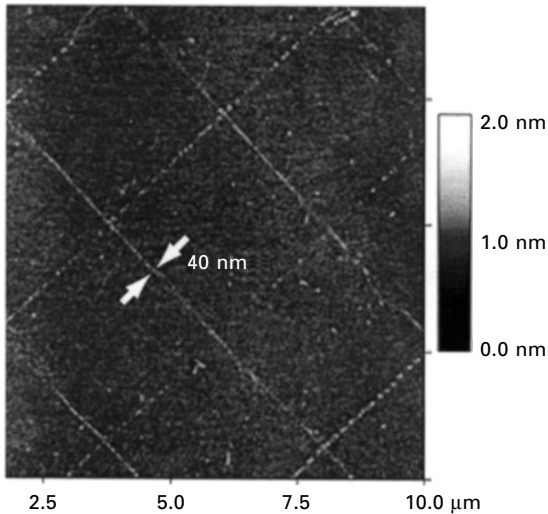
diffusivity, and thus allow the fabrication of features as small as 40 nm by  $\mu$ CP with composite PDMS stamps (Fig. 3.7).

Table 3.3 Types of ink molecules used in  $\mu$ CP

Ink (headgroup)	Substrates	References
ROH	Si-H	67, 68
	Si	69
RNH <sub>2</sub>	Stainless Steel 316L	70
	Mica	71
RSH	Au	72
	Ag	73
	Cu	74
	Pd	75
	Pt	76
	Ni	77
	Stainless Steel 316L	78, 70
	Zn	79
	ZnSe	80
	GaAs	81, 82
	InP	83
RSeH	Au	84, 85
	Ag	86
RS <sub>2</sub> O <sub>3</sub> <sup>-</sup> Na <sup>+</sup>	Au	87
	Cu	88
RCOO <sup>-</sup> /RCOOH	$\alpha$ -Al <sub>2</sub> O <sub>3</sub>	89
	Ti/TiO <sub>2</sub>	90
RSiX <sub>3</sub> X=H, Cl, OCH <sub>2</sub> CH <sub>3</sub>	Al/Al <sub>2</sub> O <sub>3</sub>	91
	Si/SiO <sub>2</sub>	92
	TiO <sub>2</sub>	93–95
	ZrO <sub>2</sub>	93, 95
	HfO <sub>2</sub>	95
	PtO	96
	Indium tin oxide (ITO)	48
RPO <sub>3</sub> <sup>2-</sup> /RP(O)(OH) <sub>2</sub>	Al	97, 98
	Al-OH	99
	TiO <sub>2</sub>	94, 90
	ZrO <sub>2</sub>	100, 101
	GaAs	102
	GaN	102
	Mica	103
	Tooth enamel	104, 105
	Indium tin oxide (ITO)	49
	Indium zinc oxide (IZO)	49
RPO <sub>3</sub> <sup>2-</sup>	TiO <sub>2</sub>	106–108
	Nb <sub>2</sub> O <sub>5</sub>	108
	Al <sub>2</sub> O <sub>3</sub>	108

### Conductive substrate materials

SAMs patterned by  $\mu$ CP can act as resists to wet-chemical etchants; this capability is the basis for patterning thin films of metals, semiconductors, and insulators for use in microelectronic devices; examples include wires or



3.7 Atomic force micrograph of lines of dendrimers printed by two separate mCP steps; the stamp was rotated by  $90^\circ$  for the second step. These lines do not appear to be continuous. The image is reproduced with permission from ref. 106 (Copyright 2003, American Chemical Society).

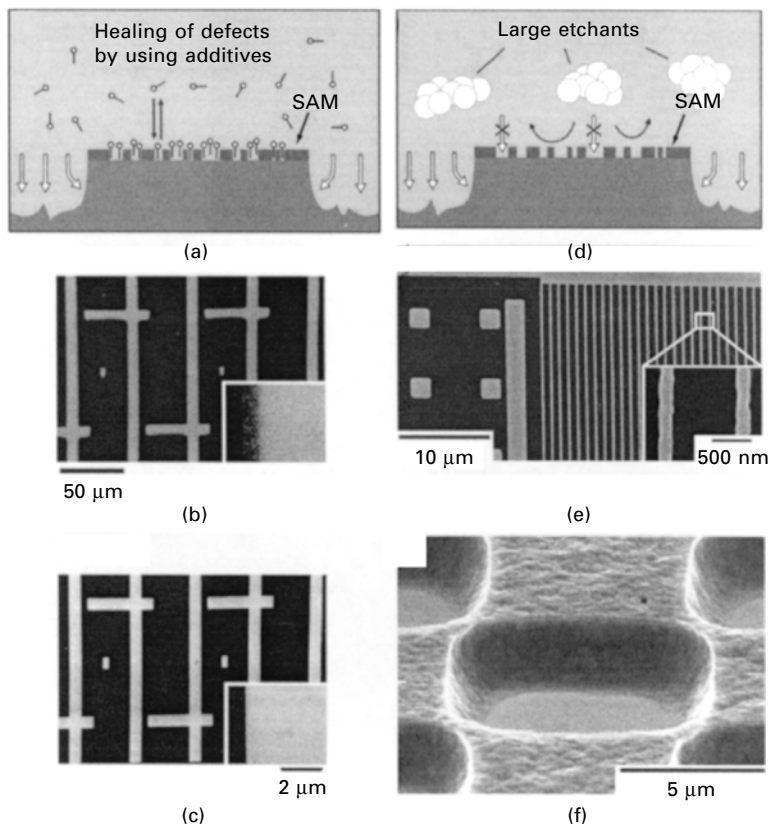
contacts.<sup>2,3</sup> Table 3.4 lists metals and conductive oxides used for this purpose along with wet-chemical etchants that are compatible with SAMs for microfabrication.<sup>94, 106, 107, 109–112</sup> The coinage metals (Au, Ag, and Cu) are used commonly as substrates for this purpose.<sup>2,3</sup>

Defects in the metallic film after etching is a problem common to patterning by  $\mu$ CP on these metals, and can hinder performance of microelectronic

Table 3.4 Types of conductive films, and etchants used with these films

Surface	Etchant	References
Au	$K_3Fe(CN)_6/K_4Fe(CN)_6/Na_2S_2O_3/KOH$	107
	$FeNO_3$ /thiourea	94
Ag	$K_3Fe(CN)_6/K_4Fe(CN)_6/Na_2S_2O_3$	107
	$FeNO_3$ /thiourea	94
Cu	$FeCl_3/HCl$ or $NH_4Cl$	109
	$H_2O_2/HCl$	110
	$KCN/NaOH/KCl$	106
	3-nitrobenzene sulfonic acid/ poly(ethylene imine)	106
	$FeNO_3$ /thiourea	94
Pd	$FeCl_3$	45, 46, 111
	$FeNO_3$	94
Pt	$HCl/Cl_2$	94, 112
Indium tin oxide	Oxalic acid	49
Indium zinc oxide	Oxalic acid	49

devices fabricated by these techniques. Geissler *et al.* used two techniques to decrease the number of defects in patterns of Au and Cu formed by  $\mu$ CP and wet-chemical etching.<sup>106</sup> First, they added octan-1-ol to the etch solution for Au to fill in defects in the SAM of alkanethiolates formed by  $\mu$ CP (Fig. 3.8(a)). Use of this additive significantly reduced the density of etched pits in the patterned thin film of Au (Figs. 3.8(b) and (c)). Secondly, they used a solution containing 3-nitrobenzenesulfonic acid (NBSA) and branched polyethylenimine (PEI) to etch copper patterned by  $\mu$ CP with a SAM of alkanethiolates. They hypothesized that the large molecules of the etch solution could not penetrate through the defects in the SAM, and etching thus produced high-quality patterns of Cu (Figs 3.8d–f).



3.8 (a) Schematic diagram of the 'healing' of defects in SAMs using additive molecules such as octanol that have high affinity for the SAM, but not for the surface. (b)–(c) Au surface patterned by  $\mu$ CP of ECT and etched without (b) and with (c) octanol in the etch solution. (d) Schematic diagram of the use of large wet-chemical etchants that cannot fit into the defects in the SAM. (e)–(f) Cu surface patterned by  $\mu$ CP of ECT and etched with the PEI/NBSA solution. All of the images are reproduced with permission from ref. 108 (Copyright 2002, American Chemical Society).

Love *et al.*, showed that Pd features generated by  $\mu$ CP of alkanethiols and wet-chemical etching were less rough (by a factor of five) and had fewer defects (by a factor of  $\sim 100$ ) than those produced on gold (Fig. 3.9(b)).<sup>45–47</sup> These improvements in the quality of the metallic features result in part from the presence of a thin PdS layer below the SAM of alkanethiolates (Fig. 3.9(a)). This layer acts as an added resist to wet-chemical etchants. Pd has four additional properties useful for microfabrication of functional devices: (i) It resists oxidation in air below 400 °C. (ii) It absorbs 900 times its volume (at STP) in hydrogen – this property is the basis for hydrogen sensors (Figs 3.9(d)–(f)).<sup>45</sup> (iii) It is compatible with materials used in CMOS processing. (iv) It has a wide variety of useful activities as a catalyst.

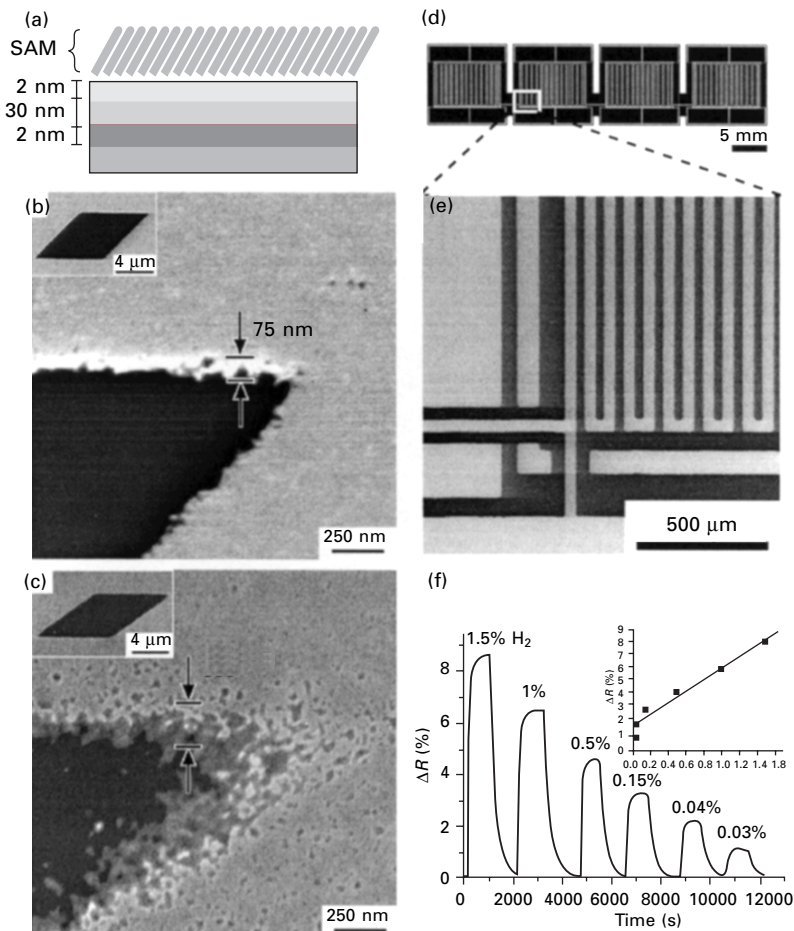
Two groups have extended  $\mu$ CP techniques to the patterning of transparent conductive oxides,<sup>48,49</sup> these materials are used commonly in light-emitting devices and liquid-crystal displays as a transparent electrode. Breen *et al.* used alkanephosphonic acids as the ink in  $\mu$ CP to pattern indium-tin-oxide (ITO) and indium-zinc-oxide (IZO).<sup>49</sup> Although this system was capable of patterning features with lateral dimensions as small as 2  $\mu\text{m}$ , there were numerous etched pits present throughout the sample. Koide *et al.* improved the quality of these features by printing alkyltrichlorosilanes on ITO at elevated temperatures (50 °C).<sup>48</sup> The elevated temperature was necessary to increase the rate of reaction of the silane with the ITO. These SAMs were used as insulating layers in organic light-emitting display (OLED) devices with pixels of 1  $\mu\text{m}$  diameter.<sup>48</sup> They do not etch the unprotected regions of the ITO, and thus a direct comparison of the limits of resolution of this technique to that of Breen *et al.* is not possible.

### *New variations on $\mu$ CP*

There are a number of variations of  $\mu$ CP that provide new capabilities, such as transferring metallic films, storing of charge, and bleaching of dyes. These abilities and developments are the basis for the microfabrication of a number of devices included in this discussion.

### Patterning of reactive SAMs

Lahiri, *et al.* developed a method to pattern ligands onto self-assembled monolayers formed on Au by  $\mu$ CP.<sup>113</sup> This technique is useful for patterning biologically relevant ligands onto surfaces that resist protein adsorption. These patterned surfaces are useful for bio- and cell-based assays.<sup>6</sup> In this technique, a ligand that contains a nucleophilic amine is transferred to a SAM formed on Au that has a reactive terminal group. The SAM comprised a small mole fraction ( $< 0.1$ ) of a pentafluorophenol-activated, terminal carboxylic acid group and a terminal tri(ethyleneglycol) group; the triethylene



**3.9** (a) Schematic diagram of SAMs of alkanethiolates formed on Pd. (b)–(c) Scanning electron micrographs of features patterned in Pd (b) and Au (c) by mCP of octadecanethiol. (d) Design of a 2-m long serpentine wire with electrical contacts positioned along the length of the wire to facilitate measurement of the electrical properties as a function of length. (e) Scanning electron micrograph of a section of the wire fabricated by mCP and wet-chemical etching. (f) Plot of the change in resistance as a function of time on exposure of a microfabricated wire to concentrations of H<sub>2</sub> ranging from 0.03–1.5% vol. in N<sub>2</sub>. The inset is a plot of the change in resistance as a function of the concentration of H<sub>2</sub>. The images in (b) and (c) are reproduced with permission from ref. 47 (Copyright 2002, American Chemical Society) and the images in (d)–(f) from ref. 46 (Copyright 2002, American Institute of Physics).

glycol was present to resist the non-specific adsorption of proteins on the surface. An oxidized stamp was inked with a ligand and placed in contact with the mixed-SAM-coated Au substrate. The reaction of amine-terminated

ligands with the activated carboxylic acid group occurred with high yield (~75–90%).<sup>113</sup> This technique is one example of the patterning of reactive SAMs. Reviews by Kane *et al.*,<sup>7</sup> Sullivan and Huck<sup>114</sup>, and Chechik *et al.*<sup>115</sup> describe additional examples of work in this area.

#### *Positive microcontact printing ((+)- $\mu$ CP)*

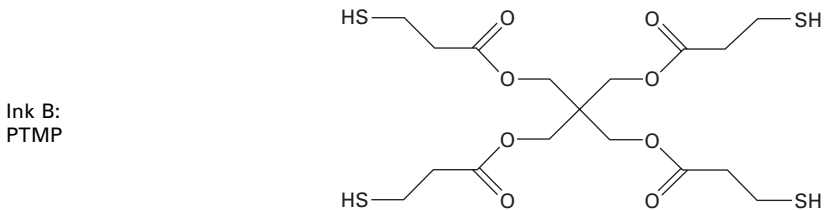
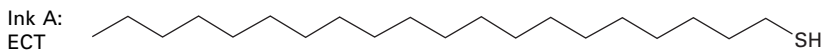
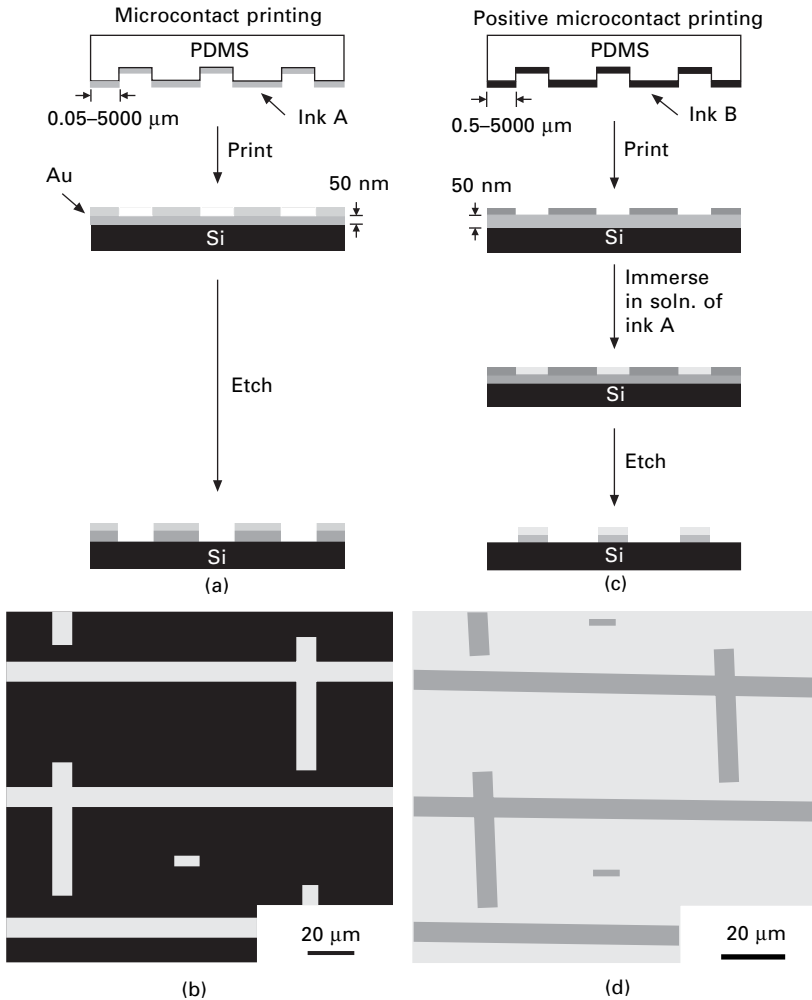
Delamarche *et al.* developed a technique for generating a positive replica in metal of the master from which the PDMS stamp was prepared (Fig. 3.10(c)); that is, this technique is used to produce the inverse pattern of that generated by standard  $\mu$ CP (Figs 3.10(a) and (b)).<sup>116</sup> This process is useful for generating metallic replicas of features with lateral dimensions  $< 1 \mu\text{m}$ . By contrast, the use of 184-PDMS stamps with raised features of these dimensions in  $\mu$ CP results in unwanted contact of the stamp with the substrate because of roof collapse.<sup>36</sup> In (+)- $\mu$ CP, pentaerythritol-tetrakis(3-mercaptopropionate) (PTMP), which is used as the ink, is printed onto the surface of Au and Cu. This monolayer passivated the surface of the metal and prevented binding of other alkanethiols. A SAM of eicosanethiol (ECT) was formed in the unpatterned region. The SAM of ECT acted as a barrier to wet-chemical etchants, whereas the SAM of PTMP was not resistant because it does not form a well-packed monolayer. Figure 3.10(d) shows features generated in Au thin films by (+)- $\mu$ CP.

#### Chemically-amplified soft lithography

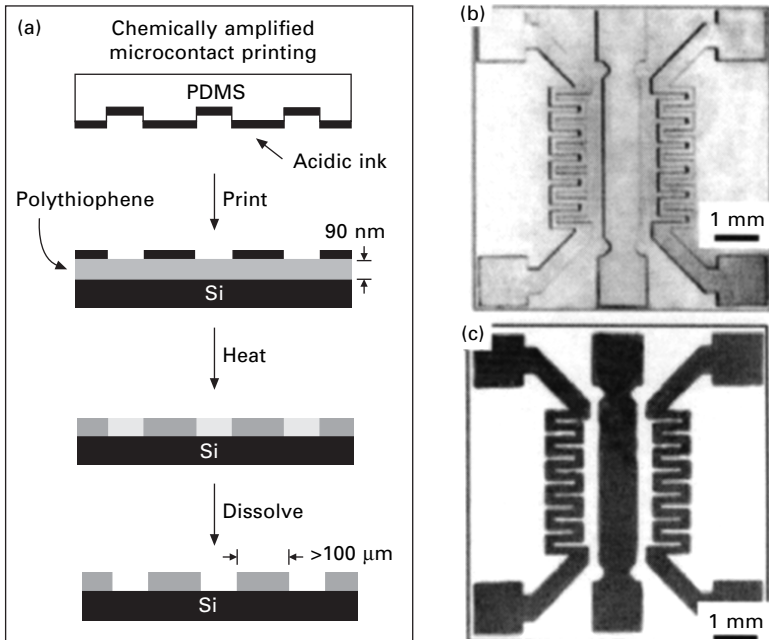
Yu *et al.* described a technique for patterning a conductive polymer by  $\mu$ CP that is useful for fabricating polymer-based microelectronic devices.<sup>117</sup> In this technique, camphorsulfonic acid was used as the ink and was transferred by  $\mu$ CP using a topographically patterned 184-PDMS stamp onto the surface of a thin film (90 nm) of a poly(thiophene)-derivative containing tetrahydropyranyloxyalkyl side chains (Fig. 3.11(a)). An acid-catalyzed reaction occurred in the regions of contact between the stamp and the polymer film (where the ink was deposited) when the sample was heated to 130 °C for ten seconds. This reaction removed the tetrahydropyran group from the poly(thiophene) to make the solubility of these regions orthogonal. This approach was used to pattern polymeric wires of  $\sim 100 \mu\text{m}$  in width (Fig. 3.11(c)); it may be difficult to pattern features of  $< 5 \mu\text{m}$  in width because of diffusive spreading of the acidic ink. The ultimate limit of resolution of this technique has not been defined.

#### Elastomeric membrane printing (EMP)

Lift-off is a technique that is used commonly to pattern metals in the



**3.10 Comparison of patterning Au by standard mCP ((a) and (b)) and by (+)-mCP ((c) and (d)). The image in (b) is reproduced with permission from ref. 108, and (d) from ref. 117. Copyright 2002, American Chemical Society.**



3.11 (a) Scheme for chemically amplified soft lithography. (b) Optical micrograph of the topographically patterned PDMS stamp used to pattern the polymer. (c) Optical micrograph of the polymer after patterning and dissolution of the unpatterned regions. The images in (b) and (c) are reproduced by permission of The Royal Society of Chemistry from ref. 118.

semiconductor industry. This process involves three steps: (i) fabrication of a patterned surface of photoresist by photolithography; (ii) evaporation of metal onto this patterned surface; (iii) removal of the photoresist, and the metal deposited on top of the features defined in the resist, using organic solvents. Many materials (e.g., biological organisms, proteins, and some polymers) are not compatible with these solvents, and thus cannot be patterned by lift-off. EMP uses PDMS membranes both as a dry resist (for electrodepositing metals, reactive ion etching of silicon, and fabricating hydrogel and sol-gel structures) and as a template for dry lift-off (for patterning metals by evaporation, biological materials by nonspecific adsorption, and conductive polymers by chemical vapor deposition) (Fig. 3.12(a)).<sup>118</sup> The entire process is dry because no solvents are necessary to deposit or remove the membrane from the surface. In EMP, the membrane must be continuous (or at least continuous in sections) and mechanically stable. There are, therefore, limitations to the types of pattern that EMP can produce: they must have lateral dimensions  $> 1 \mu\text{m}$ , and continuous patterns.

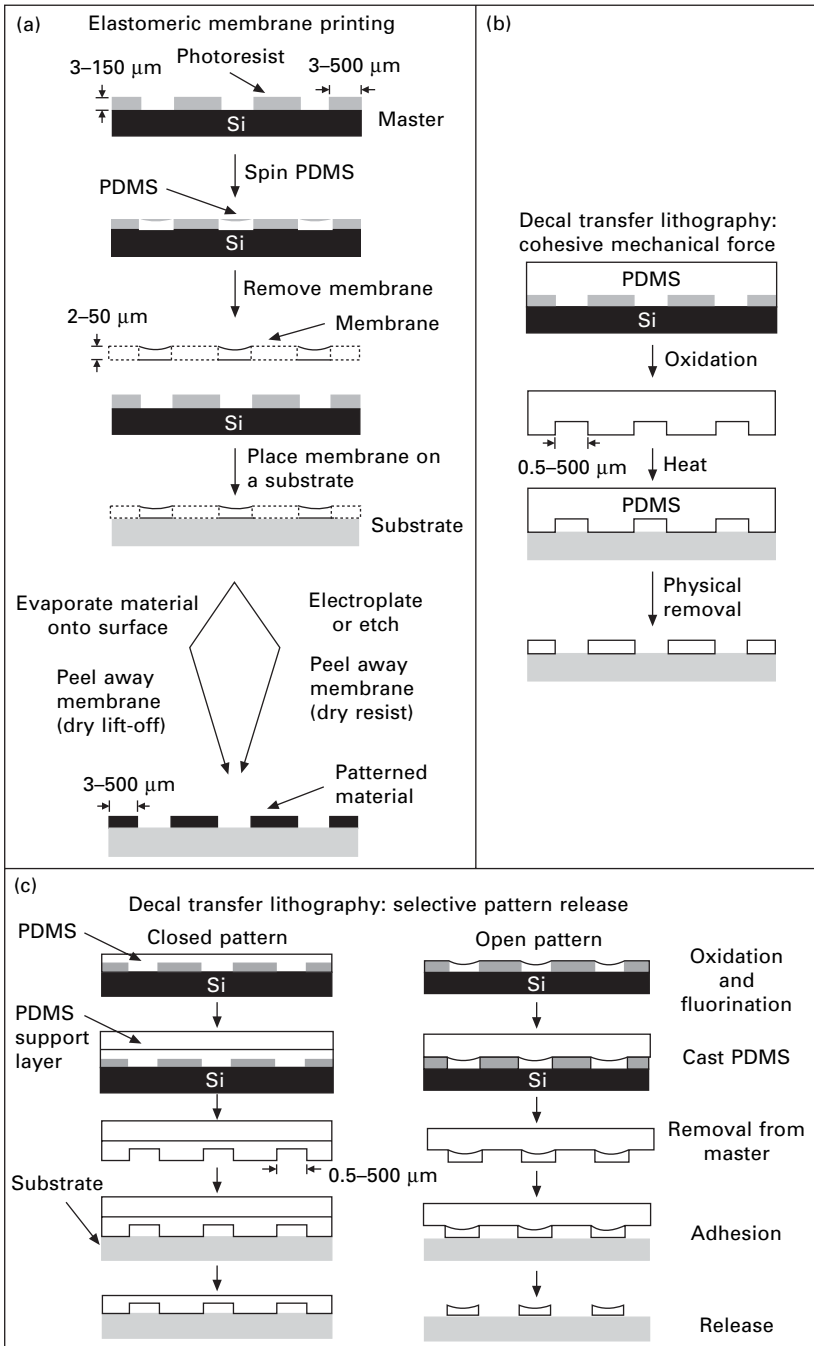
### Decal-transfer microlithography (DTM)

Decal-transfer microlithography<sup>119</sup> is a technique that prints the topographically patterned features of a PDMS stamp onto a substrate. This technique is useful for the transfer to surfaces of PDMS-based features that can not be transferred using EMP techniques, e.g., features with lateral dimensions  $< 1 \mu\text{m}$  and with discontinuous designs. There are two types of process used to facilitate this transfer, cohesive mechanical failure (CMF) and selective pattern release (SPaR). In CMF (Fig. 3.12(b)), an oxidized PDMS stamp is placed in contact with a silicon, glass, quartz, PDMS, or metal oxide substrate. The surface of the oxidized PDMS stamp bonds irreversibly to these substrates. The PDMS stamp is physically torn from the surface, leaving behind the PDMS that was bound to the surface in the pattern of the topology of the stamp. This technique fabricates patterns that are ‘open’ – i.e., the individual pieces of PDMS need not be connected by a continuous top layer. Open features are useful as resists to etching of the underlying substrate.

In SPaR (Fig. 3.12(c)), a two-layer PDMS stamp is prepared that has a bottom layer containing the topographical pattern and a top surface that is a removable support layer. The layers can be separated without causing damage to either layer because they are sealed reversibly by van der Waals interactions. This technique can be used to fabricate both ‘open’ and ‘closed’ features. Closed features are useful as microfluidic channels or for patterning by micromolding in capillaries (MIMIC).<sup>14</sup> SPaR is less destructive than CMR to the PDMS stamp, but requires two steps of curing PDMS in order to prepare the transfer element. Either process can be repeated to fabricate 3D structures, such as microfluidic networks.<sup>119</sup>

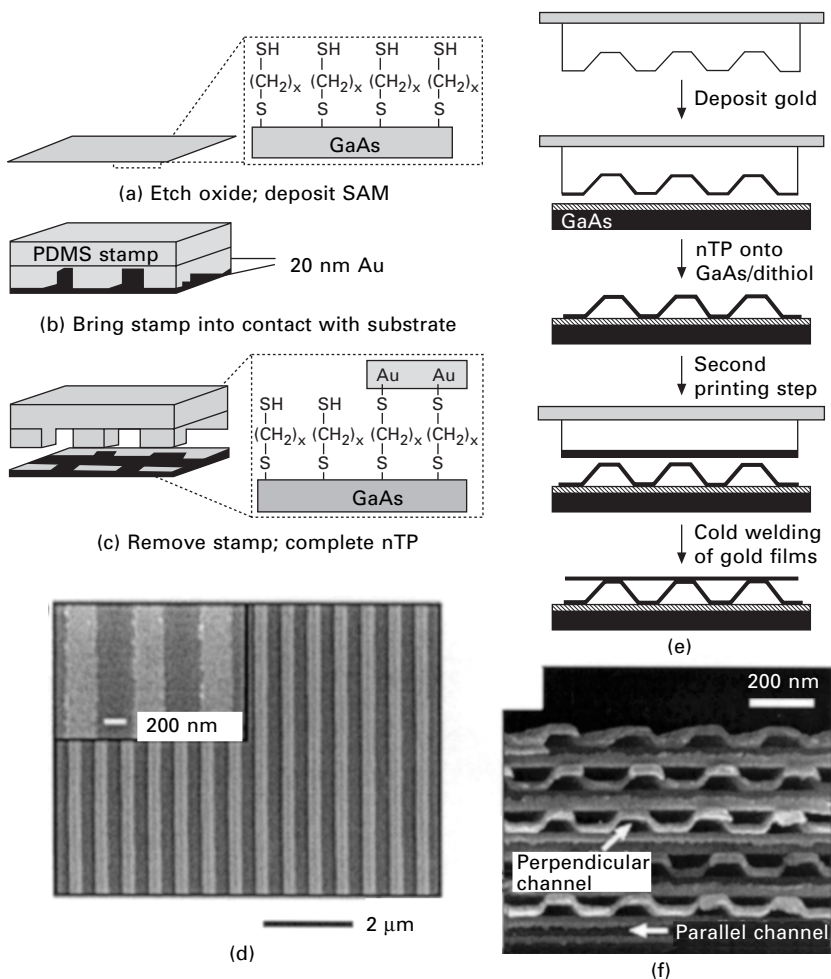
### Nanotransfer printing (nTP)

Nanotransfer printing is a method for depositing thin films of gold from a topographically patterned stamp onto the surface of metals, semiconductors, and insulators (Figs 3.13(a) and (b)).<sup>120–123</sup> This technique is additive, that is, the gold features are transferred directly from the PDMS to the substrate, and no additional steps (e.g., wet-chemical etching or dissolving of photoresist) are necessary. Such conditions are useful for the fabrication of contacts for plastic electronics because nTP does not subject the substrate to conditions that may damage the polymer. In this technique, a thin (20 nm) gold film is deposited directly onto a PDMS stamp by physical vapor deposition. The substrate is functionalized with mercaptopropyltrimethoxysilane (MPTMS) (for metal oxides or silicon)<sup>120</sup> or 1,8 octadecanedithiol (for non-oxide forming metals or semiconductors, e.g., Au or GaAs);<sup>123</sup> these molecules form a monolayer on the surface that present a terminal thiol group. A covalent bond forms between the gold and the thiol group when the gold-coated stamp is placed in conformal contact with the thiol-presenting surface. The



3.12 Schematic diagrams for (a) elastomeric membrane patterning and ((b) and (c)) the two types of decal transfer lithography.

thin film of gold transfers easily to the substrate because the strength of interaction between it and the thiol-presenting SAM on the substrate is much greater than that of the Au and the PDMS. This technique yields high-quality gold features with lateral dimensions as small as  $\sim 100$  nm, and edge roughness of  $\sim 15$  nm (Fig. 3.13(c)). The topology of the stamp can be designed such that a continuous gold film is formed on the surface by physical vapor



3.13 (a)–(c) Schematic diagram outlining the fabrication of metallic contacts on GaAs by nTP. (d) Scanning electron micrograph of lines of Au patterned on GaAs by nTP. (e) Schematic diagram showing fabrication of three-dimensional structures by nTP. (f) Scanning electron micrograph of a three-dimensional structure fabricated by nTP. The images in (a)–(d) are reproduced with permission from ref. 123, and the images in (e) and (f) from ref. 121. Copyright 2003, American Chemical Society.

deposition. The subsequent transfer of this film by nTP yields a pattern of gold with 3D topology (Fig. 3.13(d)).<sup>103</sup> This technique was used to prepare electrical contacts for high-mobility transistors and inverter circuits.<sup>120, 122</sup>

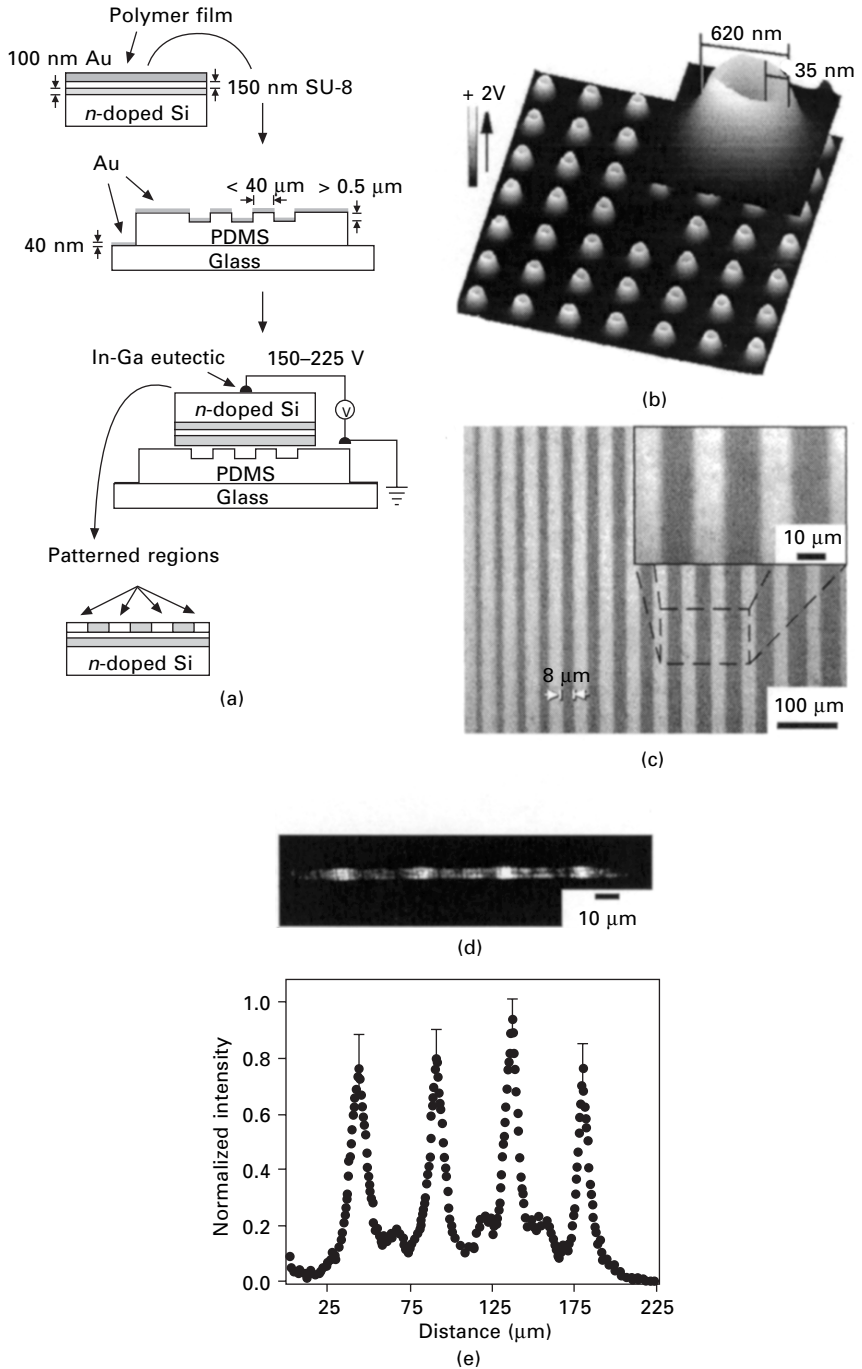
### Electrical microcontact printing (E-mCP)

This technique uses a metal-coated, topographically patterned PDMS stamp to define regions of charge<sup>124</sup> or of bleached dyes<sup>125</sup> in polymeric thin films. The patterns generated by this technique may be useful in data storage, and in the fabrication of optical waveguides. Figure 3.14(a) illustrates this process. The metal-coated stamp was prepared by physical vapor deposition of Au onto the PDMS stamp. The stage holding the stamp must be cooled to prevent unwanted thermal expansion of the PDMS during deposition, because this behavior can induce cracks and waves in the thin metallic films upon cooling.<sup>126</sup> The metallic stamp was placed in contact with the surface of a polymer film supported by a conductive substrate (e.g., Au-coated silicon wafer). A DC-bias was applied between the stamp and the substrate such that current flowed through the polymer film. Jacobs, *et al.* used this technique to pattern charge in thin films of poly(methylmethacrylate) (Fig. 3.14(b)).<sup>124</sup> We described the use of this technique to bleach selectively a dye, phloxine B, doped in a thin film (3–5  $\mu\text{m}$ ) of poly(vinylphenol) (Fig. 3.14(c)).<sup>125</sup> The bleaching of the dye results in a decrease of the refractive index of these regions. This work is the basis for the fabrication of planar optical waveguides and a  $1 \times 4$  optical splitter (Figs 3.14(d) and (e)).

### *Phase-shifting photolithography*

Features with lateral dimensions of  $< 100$  nm are useful for applications in data storage and subwavelength optics. It is difficult to produce features of this size by standard photolithographic techniques because of limits determined by the numerical aperture of imaging optics. Phase-shifting lithography is a specialized type of photolithography that uses the modulation of the intensity of light in the near field at the edges of features defined in a photomask to pattern features with lateral dimensions of  $< 100$  nm.<sup>127,128</sup> The use of rigid masks in phase-shifting lithography is difficult because the distance between the phase mask and the photoresist layer must be controlled precisely, and because accidental contact between the mask and the layer of resist damages both.

Elastomeric phase masks are a useful alternative to rigid phase masks because the distance between the mask and the substrate is controlled by the height of the features rather than by specialized positioning equipment (Fig. 3.15(a)), and because physical contact is ‘soft’, and non-damaging. The conformal physical contact between the PDMS mask and the resist also



3.14 (a) Scheme for E-mCP using metal-coated PDMS stamps. (b) Kelvin force micrograph of charge in a film of

minimizes diffractive broadening of features, and allows the generation of small ( $< 50$  nm) features. Rogers *et al.* demonstrated that topographically patterned 184-PDMS stamps can be used as phase masks in photolithography to produce features with lateral dimensions of  $\sim 100$  nm over large areas ( $> \text{cm}^2$ ) rapidly ( $< 1$  s/exposure).<sup>127, 128</sup> Odom *et al.* used an elastomeric phase mask made of a composite 184-PDMS/h-PDMS stamp to extend the resolution of this technique to  $\sim 30$  nm (Figs. 3.15(c) and (d)).<sup>36, 129</sup> Phase-shifting photolithography has been used to fabricate transistors (Fig. 3.15(d))<sup>130</sup> and polarizers (Fig. 3.15(e)).<sup>131</sup>

### 3.2.4 Approaches to registration

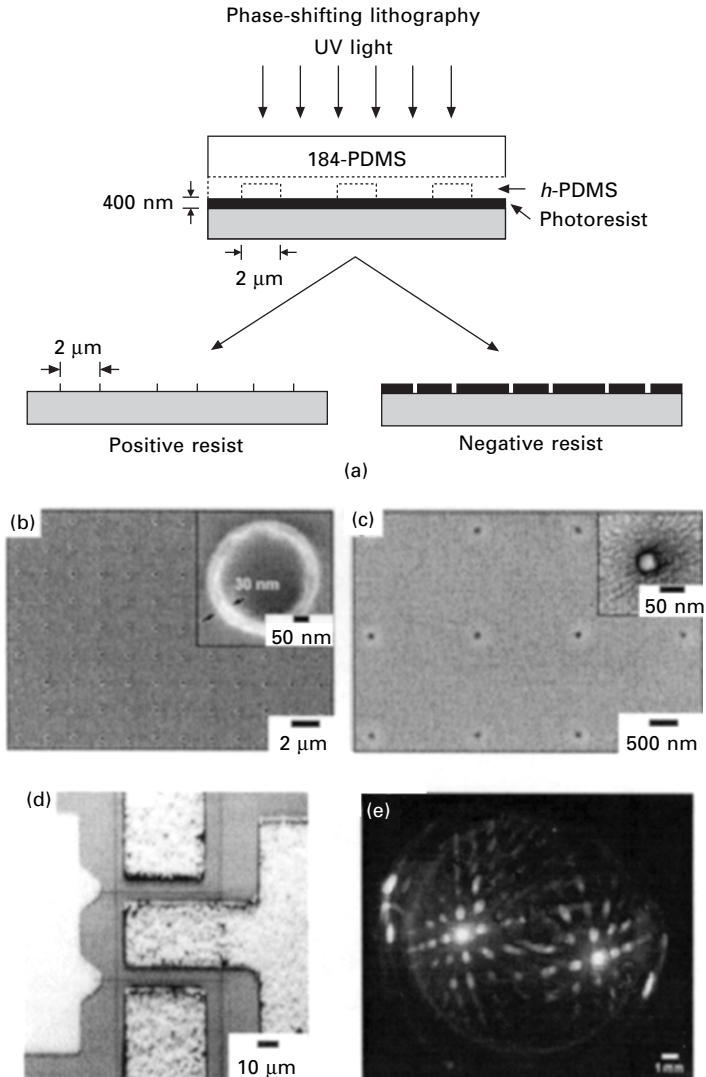
The fabrication of complex microdevices requires multiple steps of lithography where the pattern in each layer is aligned precisely in register with the previous ones. Many microelectronic, microfluidic, and microelectromechanical systems require the multilevel fabrication of two or more types of structure. In soft lithography, it is difficult to register multiple layers with high accuracy ( $< 1$   $\mu\text{m}$  over 1 mm) because of the elastomeric nature and the high coefficient of thermal expansion of the materials used for the stamps. These properties can result in deformation of the features in the stamp when placed in contact with a rigid substrate. The low contrast between the raised and recessed regions of the stamp also makes it difficult to register patterns optically. These difficulties in registering multiple layers of patterning using PDMS stamps have limited the use of soft lithography to those applications where one, or at most two, levels of patterning are necessary.

#### *Multilevel stamping*

In an effort to overcome this limitation, Tien *et al.* developed a technique for registering multiple steps of patterning using a single PDMS stamp that contains multilevel topology.<sup>132</sup> The details of the technique are described elsewhere.<sup>132</sup> Briefly, each level of the stamp was inked with different molecules. When the stamp was placed in contact with a rigid substrate, only

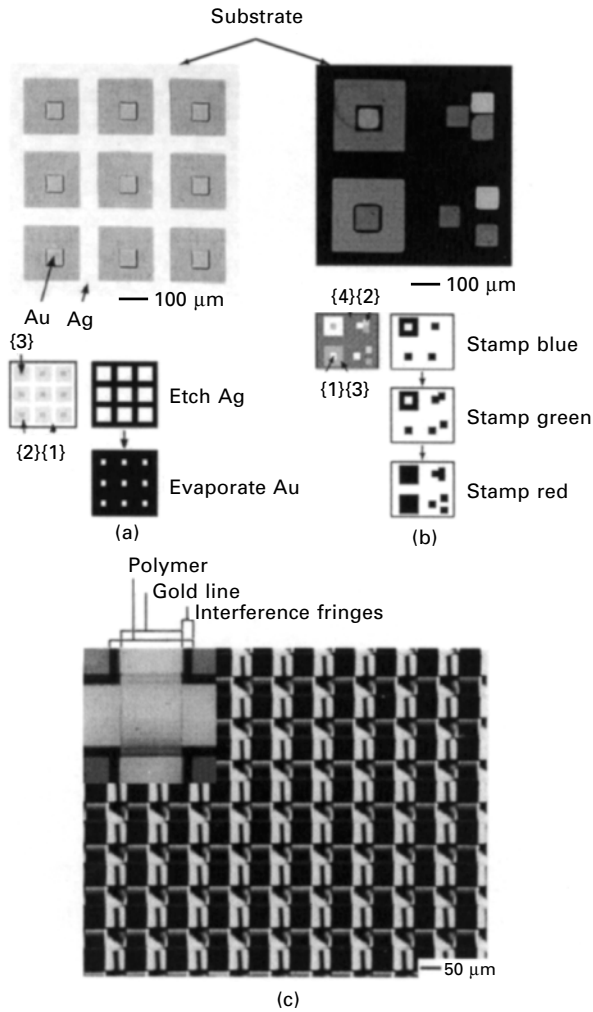
*(Caption continued from previous page)*

poly(methylmethacrylate) patterned by this technique. (c) Optical micrograph of patterned bleaching of a thin film of phloxine B-doped poly(vinylphenol). (d) Optical micrograph of the output of light from a  $1 \times 4$  optical splitter fabricated in the film described in (c). (e) Plot of the intensity versus position along the edge of the waveguides. The scheme and images in (a) and (c)–(e) are reproduced with permission from ref. 126 (Copyright 2004, American Institute of Physics) and the image in (b) from ref. 125 (Copyright 2001, American Association for the Advancement of Science).



3.15 (a) Scheme for phase-shifting lithography using conformal phase masks. (b) and (c) Scanning electron micrographs of features in photoresist (rings (b) and holes (c)) fabricated by this technique. (d) Scanning electron micrograph of a HEMT GaAs/AlGaAs-based transistor. The gates in this device were patterned using this technique. (e) Photograph of the diffraction of light from a spherical surface with surface features patterned by phase-shifting lithography using a conformal phase mask. This photograph shows an example of patterning sub-200-nm features on non-planar surfaces (1-cm-diameter steel spheres coated with photoresist) by soft lithography. The images in (b) and (c) are reproduced with permission from ref. 130 (Copyright 2002, American Chemical Society), the image in (d) from 131 (Copyright 2000, Elsevier B.V.), and the image in (e) from 132 (Copyright 2003, Wiley-VCH).

the tallest raised features were in conformal contact so patterning occurred only in these regions. Subsequent levels of the stamp were placed in contact with the substrate by applying pressure to the stamp. This technique was used to pattern a surface with regions of Au and Ag (Fig. 3.16(a)) and fluorescently labeled proteins (Fig. 3.16(b)) in register.



3.16 (a) and (b) Optical micrograph and scheme of fabrication for a patterned substrate generated by a combination of etching and evaporation using a three-level membrane. The numbers in the brackets represent the different levels of the multi-level stamp with the highest number as the most recessed feature. (c) Scanning electron micrographs of a crossed wire array fabricated by microcontact printing and patterned self-assembly. The images in (a) and (b) are reproduced with permission from ref. 133 (Copyright 2002, National Academy of Sciences, USA). The images in (c) are reproduced with permission from ref. 134 (Copyright 2000, Elsevier B.V.).

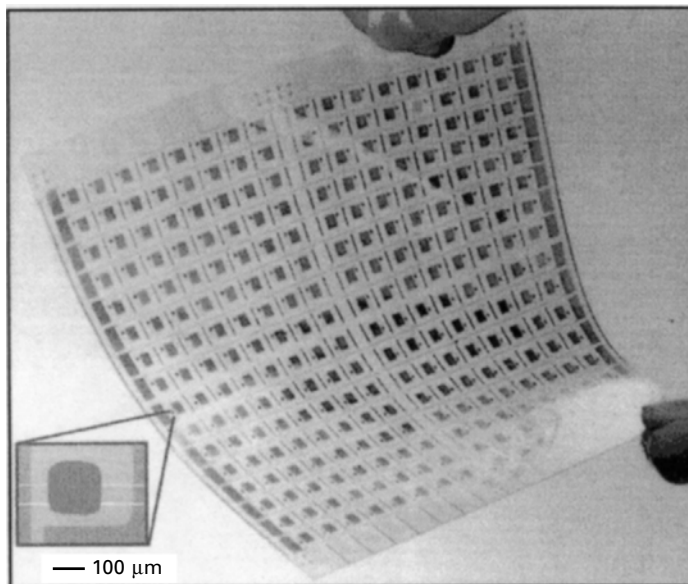
*Patterned self-assembly of polymers*

Crossed wires that are electrically isolated from one another are integral components of microelectronic devices. The standard techniques to prepare arrays of crossed wires include multiple steps of pattern transfer and registration. Black *et al.* used  $\mu$ CP and patterned self-assembly to pattern such a system without the need for complex steps of registration.<sup>133</sup> The details of the technique are discussed in the original manuscript.<sup>133</sup> SAMs of carboxylic acid-terminated alkanethiolates patterned by  $\mu$ CP on Au made those regions hydrophilic. The unpatterned regions were rendered hydrophobic by washing the surface with a solution of methyl-terminated alkanethiolates. Hydrophilic, insulating polymers (e.g., polyurethanes, epoxies, or some photoresists) deposited by spin coating or dip coating stuck only to the regions patterned with the hydrophilic SAM. The regions of the gold not coated with polymer were removed by wet-chemical etching. This process was repeated to produce an array of electrically isolated, crossed wires (Fig. 3.16(c)) with only one step of registration necessary (i.e., a simple 90° rotation of the stamp with respect to the orientation of the first set of wires).

### 3.3 Conclusions and outlook

Soft lithography is not meant to replace the high-resolution tools (i.e., electron-beam and laser lithographies and photolithography) used to generate masters for micro- and nanofabrication of integrated circuits. The combination of the two sets of techniques enables routine and cost-effective microfabrication – and potentially of nanofabrication – of functional devices. Soft lithography has six advantages over conventional techniques (e.g., photolithography and electron-beam lithography).

1. It is well suited for fabricating low-cost, disposable devices, and tools for analysis, because the fixed costs are low.
2. It can generate prototype devices rapidly – the time from design to prototype can be less than 24 hours.
3. It can pattern features smaller than those by photolithography because it is not subject to the limits of optical diffraction.
4. It can pattern features on both planar and non-planar surfaces.
5. It can be integrated easily into existing manufacturing processes and facilities.
6. It may be possible to pattern large areas ( $> 1 \text{ m}^2$ ) in a single step; this limit is dictated by the size of the stamp rather than the size of the beam spot, uniformity of the intensity, and variations in focus. Initial efforts towards the patterning of these large areas have been successful (Fig. 3.17).<sup>134</sup>



3.17 Photograph of a backplane for an active-matrix TFT display prepared using soft lithographic techniques. The inset is a photograph of an individual organic transistor. This image was reproduced from ref. 135 (Copyright 2001, National Academy of Sciences, USA).

There are three disadvantages of the use of soft lithography in the fabrication of functional microdevices. First, the optical (e.g., low contrast of the features) and physical (e.g., high coefficient of thermal expansion and low elastic modulus) properties of the elastomeric stamp make it difficult to register multiple lithographic steps with accuracy of  $< 1 \mu\text{m}$ . Secondly, the stamps are subject to distortion of the features because of their elastomeric nature and because of their high coefficient of thermal expansion; these properties of the stamp limit the use of soft lithographic techniques to applications where small distortions or defects do not affect device performance. It is therefore unlikely that soft lithography will replace photolithography as the technique used most commonly to fabricate complex microelectronic devices such as microprocessors. Thirdly, the PDMS-based stamps are not stable to many organic solvents<sup>135</sup> or at high ( $> 200 \text{ }^\circ\text{C}$ ) temperatures.

A wide range of disciplines (e.g., biology, chemistry, engineering, and physics) have adopted soft lithography. The interdisciplinary use of soft-lithographic techniques has enabled the development of new capabilities in each of the aforementioned areas of science; examples include the patterning of cells on surfaces for cell-based assays<sup>27</sup> and the rapid turnaround of prototype and single-use devices in microfluidics<sup>14</sup> and biology.<sup>6</sup> The continued development of soft-lithographic techniques through interdisciplinary research

may enable methods of microfabrication for which the extension of conventional techniques is not straightforward, such as large-area, macroelectronic devices<sup>134, 136, 137</sup> and non-planar electronic and optical devices.<sup>138–143</sup> It is also unclear how conventional techniques will successfully pattern features having sizes < 50 nm over large areas rapidly and cost-effectively. The combination of soft lithography and patterned self-assembly may be a solution to this problem.

### 3.4 Further information

The examples of functional microdevices fabricated by soft lithography that are listed in this chapter are only a subset of those described and demonstrated in the literature. Below we list reviews that describe the use of soft lithography in electronics, optics, microfluidics, and cell biology; these reviews provide an introduction to the larger literature.

The use of soft lithographic printing techniques for microelectronics and optical devices is discussed in detail by Rogers in ‘Rubber Stamping for Plastic Electronics and Fiber Optics’.<sup>144</sup> Gates *et al.* review soft lithographic techniques for nanofabrication in ‘Unconventional Nanofabrication’.<sup>145</sup>

The use of soft lithography to fabricate microfluidic devices is discussed in detail by Whitesides and Stroock in ‘Flexible Methods for Microfluidics’<sup>12</sup>, Ng *et al.* in ‘Components for Integrated Poly(dimethylsiloxane) Microfluidic Systems’,<sup>9</sup> McDonald *et al.* in ‘Fabrication of Microfluidic Systems in Poly(dimethylsiloxane)’,<sup>14</sup> and Quake and Scherer in ‘From Micro- to Nanofabrication with Soft Materials’.<sup>146</sup> The use of PDMS-based microfluidic channels in biology and biochemistry is described by Sia and Whitesides in ‘Microfluidic Devices Fabricated in Poly(dimethylsiloxane) for Biological

*Table 3.5* Examples of PDMS-based microfluidic components and devices

	Reference
Components	
Valves	146–153
Mixers	154–158
Functional Devices	
Dilutor	159
Immunoassay systems	160–165
DNA and protein separators	166–170
Cell sorters	171–174
Combinatorial screening devices	175–179
Tools for cell biology	180–183
Gradient generators	184–185
Bubble generators	186–190
Maze solver	191
Analog computer	192

Studies',<sup>15</sup> by Jiang and Whitesides in 'Engineering Microtools in Polymers to Study Cell Biology',<sup>8</sup> and by Whitesides *et al.* in 'Soft Lithography in Biology and Biochemistry'.<sup>6</sup> Table 3.5 is a list of examples of PDMS-based, microfluidic components and devices along with their respective references.<sup>146–192</sup> Microfluidic systems fabricated in PDMS and in other materials (e.g., glass and silicon) are discussed in further detail in Chapters 10 and 11.

Reviews of the use of soft lithography for applications in cell biology are described by Whitesides *et al.* in 'Soft Lithography in Biology and Biochemistry'<sup>6</sup> and by Jiang and Whitesides in 'Engineering Microtools in Polymers to Study Cell Biology.'<sup>8</sup>

### 3.5 Acknowledgements

The authors thank the National Science Foundation (CHE-0101432), the National Institutes of Health (GM065364), and DARPA for financial support.

### 3.6 References

1. Madou M.J., *Fundamentals of microfabrication*. ed., CRC Press: Boca Raton, 1997.
2. Xia Y. and Whitesides G.M., 'Soft lithography', *Angew. Chem. Int. Ed.*, 1998 **37**(5) 550–75.
3. Xia Y. and Whitesides G.M., 'Soft lithography', *Annu. Rev. Mater. Sci.*, 1998 **28** 153–84.
4. Xia Y., Rogers J.A., Paul K.E. and Whitesides G.M., 'Unconventional methods for fabricating and patterning nanostructures', *Chem. Rev.*, 1999 **99**(7) 1823–48.
5. Michel B., Bernard A., Bietsch A., Delamarche E., Geissler M., Juncker D., Kind H., Renault J.P., Rothuizen H., Schmid H., Schmidt-Winkel P., Stutz R. and Wolf H., 'Printing meets lithography: Soft approaches to high-resolution printing', *IBM J. Res. Dev.*, 2001 **45**(5) 697–719.
6. Whitesides G.M., Ostuni E.S., Takayama S., Jiang X. and Ingber D.E., 'Soft lithography in biology and biochemistry', *Annu. Rev. Biomed. Eng.*, 2001 **3** 335–73.
7. Kane R.S., Takayama S., Ostuni E., Ingber, D.E. and Whitesides G.M., 'Patterning proteins and cells using soft lithography', *Biomaterials*, 1999 **20**(23/24) 2363–76.
8. Jiang X. and Whitesides G.M., 'Engineering microtools in polymers to study cell biology', *Eng. Life Sci.*, 2003 **3**(12) 475–80.
9. Ng J.M.K., Gitlin I., Stroock A.D. and Whitesides G.M., 'Components for integrated poly(dimethylsiloxane) microfluidic systems', *Electrophoresis*, 2002 **23**(20) 3461–73.
10. Kane R.S., Stroock A.D., Jeon N.L., Ingber D.E. and Whitesides G.M., 'Soft lithography and microfluidics', *Opt. Biosens.*, 2002 571–95.
11. McDonald J.C. and Whitesides G.M., 'Poly(dimethylsiloxane) as a material for fabricating microfluidic devices', *Acc. Chem. Res.*, 2002 **35**(7) 491–99.
12. Whitesides G.M. and Stroock A.D., 'Flexible methods for microfluidics', *Phys. Today*, 2001 **54**(6) 42–48.

13. Kenis P.J.A., Ismagilov R.F., Takayama S., Whitesides G.M., Li S. and White H.S., 'Fabrication inside microchannels using fluid flow', *Acc. Chem. Res.*, 2000 **33**(12) 841–47.
14. McDonald, J.C., Duffy D.C., Anderson J.R., Chiu D.T., Wu H. and Whitesides G.M., 'Fabrication of microfluidic systems in poly(dimethylsiloxane)', *Electrophoresis*, 2000 **21** 27–40.
15. Sia S.K. and Whitesides G.M., 'Microfluidic devices fabricated in poly(dimethylsiloxane) for biological studies', *Electrophoresis*, 2003 **24**(21) 3563–76.
16. Holmes A.S., 'Laser processes for mems manufacture', *RIKEN Rev.*, 2002 **43** 63–69.
17. Linder V., Wu H., Jiang X. and Whitesides G.M., 'Rapid prototyping of 2d structures with feature sizes larger than 8  $\mu\text{m}$ ', *Anal. Chem.*, 2003 **75**(10) 2522–27.
18. Deng T., Tien J., Xu B. and Whitesides G.M., 'Using patterns in microfiche as photomasks in 10- $\mu\text{m}$ -scale microfabrication', *Langmuir*, 1999 **15**(16) 6575–81.
19. Qin D., Xia Y. and Whitesides G.M., 'Rapid prototyping of complex structures with feature sizes larger than 20  $\mu\text{m}$ ', *Adv. Mater.*, 1996 **8**(11) 917–19.
20. Deng T., Wu H., Brittain S.T. and Whitesides G.M., 'Prototyping of masks, masters, and stamps/molds for soft lithography using an office printer and photographic reduction', *Anal. Chem.*, 2000 **72**(14) 3176–80.
21. Cad/art services, inc., ([www.Outputcity.Com](http://www.Outputcity.Com)) is an example of a company with laser photoplotting capabilities.
22. Love J.C., Wolfe D.B., Jacobs H.O. and Whitesides G.M., 'Microscope projection photolithography for rapid prototyping of masters with micron-scale features for use in soft lithography', *Langmuir*, 2001 **17**(19) 6005–12.
23. Wu H., Odom T.W. and Whitesides G.M., 'Connectivity of features in microlens array reduction photolithography: Generation of different patterns using a single photomask', *J. Am. Chem. Soc.*, 2002 **124**(25) 7288–89.
24. Wu H., Odom T.W. and Whitesides G.M., 'Reduction photolithography using microlens arrays: Applications in grayscale photolithography', *Anal. Chem.*, 2002 **74**(14) 3267–73.
25. Wu H., Odom T.W. and Whitesides G.M., 'Generation of chrome masks with micrometer-scale features using microlens lithography', *Adv. Mater.*, 2002 **14**(17) 1213–16.
26. Chen C.S., Mrksich M., Huang S., Whitesides G.M. and Ingber D.E., 'Geometric control of cell life and death', *Science*, 1997 **276**(5317) 1425–28.
27. Ostuni E., Kane R., Chen C.S., Ingber D.E. and Whitesides G.M., 'Patterning mammalian cells using elastomeric membranes', *Langmuir*, 2000 **16**(20) 7811–19.
28. Rogers J.A., Bao Z., Meier M., Dodabalapur A., Schueller O.J.A. and Whitesides G.M., 'Printing, molding, and near-field photolithographic methods for patterning organic lasers, smart pixels and simple circuits', *Synth. Met.*, 2000 **115**(1–3) 5–11.
29. In most commercial microscopes there is a lens that precedes the objective in the path of light from the bulb to the substrate. This lens increases the diameter of the light by a factor of 4 to fill completely the back aperture of the objective. The presence of this lens reduces the linear reduction of the pattern by a similar factor; that is, a 100 $\times$  objective reduces the linear dimensions by a factor of 25 $\times$ .
30. Moreau W.M., *Semiconductor lithography: Principles, practices, and materials*. ed. Plenum Publishing Corporation: New York, 1988.

31. Wu M.-H., Paul K.E., Yang J. and Whitesides G.M., 'Fabrication of frequency-selective surfaces using microlens photolithography', *Appl. Phys. Lett.*, 2002 **80**(19) 3500–02.
32. Hutley M., Stevens R. and Daly D., 'Correlation between surface free energy and surface constitution', *Phys. World*, 1991 **4**(7) 27–32.
33. Wu M.H. and Whitesides G.M., 'Fabrication of arrays of two-dimensional micropatterns using microspheres as microlenses for projection lithography', *Appl. Phys. Lett.*, 2001 **78**(16) 2273–75.
34. Harper C.A., *Handbook of plastics and elastomers*. ed.; McGraw-Hill: New York, 1975.
35. Sylgard 184 is available from Dow Corning; equivalent materials are available from other manufacturers.
36. Odom T.W., Love J.C., Wolfe D.B., Paul K.E. and Whitesides G.M., 'Improved pattern transfer in soft lithography using composite stamps', *Langmuir*, 2002 **18**(13) 5314–20.
37. Schmid H. and Michel B., 'Siloxane polymers for high-resolution, high-accuracy soft lithography', *Macromolecules*, 2000 **33**(8) 3042–49.
38. Choi K.M. and Rogers J.A., 'A photocurable poly(dimethylsiloxane) chemistry designed for soft lithographic molding and printing in the nanometer regime', *J. Am. Chem. Soc.*, 2003 **125**(14) 4060–61.
39. Gates B.D. and Whitesides G.M., 'Replication of vertical features smaller than 2 nm by soft lithography', *J. Am. Chem. Soc.*, 2003 **125**(49) 14986–87.
40. Csucs G., Kuenzler T., Feldman K., Robin F. and Spencer N.D., 'Microcontact printing of macromolecules with submicrometer resolution by means of polyolefin stamps', *Langmuir*, 2003 **19**(15) 6104–09.
41. Trimbach D., Feldman K., Spencer N.D., Broer D.J. and Bastiaansen C.W.M., 'Block copolymer thermoplastic elastomers for microcontact printing', *Langmuir*, 2003 **19**(26) 10957–61.
42. www.Kraton.Com
43. Mayer M., Yang J., Gitlin I., Gracias D.H. and Whitesides G.M., 'Micropatterned agarose gels for stamping arrays of proteins and gradients of proteins', Submitted.
44. Martin B.D., Brandow S.L., Dressick W.J. and Schull T.L., 'Fabrication and application of hydrogel stampers for physisorptive microcontact printing', *Langmuir*, 2000 **16**(25) 9944–46.
45. Wolfe D.B., Love J.C., Paul K.E., Chabinyk M.L. and Whitesides G.M., 'Fabrication of palladium-based microelectronic devices by microcontact printing', *Appl. Phys. Lett.*, 2002 **80**(12) 2222–24.
46. Love J.C., Wolfe D.B., Haasch R., Chabinyk M.L., Paul K.E., Whitesides G.M. and Nuzzo R.G., 'Formation and structure of self-assembled monolayers of alkanethiolates on palladium', *J. Am. Chem. Soc.*, 2003 **125**(9) 2597–609.
47. Love J.C., Wolfe D.B., Chabinyk M.L., Paul K.E. and Whitesides G.M., 'Self-assembled monolayers of alkanethiolates on palladium are good etch resists', *J. Am. Chem. Soc.*, 2002 **124**(8) 1576–77.
48. Koide Y., Such M.W., Basu R., Evmenenko G., Cui J., Dutta P., Hersam M.C. and Marks T.J., 'Hot microcontact printing for patterning into surfaces. Methodology, morphology, microstructure, and OLED charge injection barrier imaging', *Langmuir*, 2003 **19**(1) 86–93.
49. Breen T.L., Fryer P.M., Nunes R.W. and Rothwell M.E., 'Patterning indium tin oxide and indium zinc oxide using microcontact printing and wet etching', *Langmuir*, 2002 **18**(1) 194–97.

50. Lange S.A., Benes V., Kern D.P., Hoerber J.K.H. and Bernard A., 'Microcontact printing of DNA molecules', *Anal. Chem.*, 2004 **76**(6) 1641–47.
51. Xu C., Taylor P., Ersoz M., Fletcher P.D.I. and Paunov V.N., 'Microcontact printing of DNA-surfactant arrays on solid substrates', *J. Mater. Chem.*, 2003 **13**(12) 3044–48.
52. Renault J.P., Bernard A., Bietsch A., Michel B., Bosshard H.R., Delamarche E., Kreiter M., Hecht B. and Wild U.P., 'Fabricating arrays of single protein molecules on glass using microcontact printing', *J. Phys. Chem. B*, 2003 **107**(3) 703–11.
53. Inerowicz H.D., Howell S., Regnier F.E. and Reifengerger R., 'Multiprotein immunoassay arrays fabricated by microcontact printing', *Langmuir*, 2002 **18**(13) 5263–68.
54. Graber D.J., Zieziulewics T.J., Lawrence D.A., Shain W. and Turner J.N., 'Antigen binding specificity of antibodies patterned by microcontact printing', *Langmuir*, 2003 **19**(13) 5431–34.
55. Bernard A., Renault J.P., Michel B., Bosshard H.R. and Delamarche E., 'Microcontact printing of proteins', *Adv. Mater.*, 2000 **12**(14) 1067–70.
56. Runge A.F. and Saavedra S.S., 'Comparison of microcontact-printed and solution-adsorbed cytochrome c films on indium tin oxide electrodes', *Langmuir*, 2003 **19**(22) 9418–24.
57. Shin H.S., Yang H.J., Jung Y.M. and Kim S.B., 'Direct patterning of silver colloids by microcontact printing: Possibility as sers substrate array', *Vib. Spectrosc.*, 2002 **29**(1–2) 79–82.
58. Kind H., Bonard J.-M., Forro L., Kern K., Hernadi K., Nilsson L.-O. and Schlapbach L., 'Printing gel-like catalysts for the directed growth of multiwall carbon nanotubes', *Langmuir*, 2000 **16**(17) 6877–83.
59. Shin H., Im H., Hong S., Lee K., Lim G., Jeon J.U., Kim E.S. and Pak Y.E., 'Selective depositions of Fe-containing oxide films on mixed self-assembled organic monolayers using microcontact printing', *Mater. Res. Soc. Symp. Proc.*, 1999 **576** 191–96.
60. Kind H., Geissler M., Schmid H., Michel B., Kern K. and Delamarche E., 'Patterned electroless deposition of copper by microcontact printing palladium(II) complexes on titanium-covered surfaces', *Langmuir*, 2000 **16**(16) 6367–73.
61. Donzel C., Geissler M., Bernard A., Wolf H., Michel B., Hilborn J. and Delamarche E., 'Hydrophilic poly(dimethylsiloxane) stamps for microcontact printing', *Adv. Mater.*, 2001 **13**(15) 1164–67.
62. Chaudhury M.K. and Whitesides G.M., 'Correlation between surface free energy and surface constitution', *Science*, 1992 **255**(5049) 1230–32.
63. Chaudhury M.K. and Whitesides G.M., 'Direct measurement of interfacial interactions between semispherical lenses and flat sheets of poly(dimethylsiloxane) and their chemical derivatives', *Langmuir*, 1991 **7**(5) 1013–25.
64. Morra M., Occhiello E., Marola R., Garbassi F., Humphrey P. and Johnson D., 'On the aging of oxygen plasma-treated polydimethylsiloxane surfaces', *J. Colloid Interface Sci.*, 1990 **137**(1) 11–24.
65. Tan J.L., Tien J. and Chen C.S., 'Microcontact printing of proteins on mixed self-assembled monolayers', *Langmuir*, 2002 **18**(2) 519–23.
66. Delamarche E., Donzel C., Kamounah F.S., Wolf H., Geissler M., Stutz R., Schmidt-Winkel P., Michel B., Mathieu H.J. and Schaumburg K., 'Microcontact printing using poly(dimethylsiloxane) stamps hydrophilized by poly(ethylene oxide) silanes', *Langmuir*, 2003 **19**(21) 8749–58.

67. Zharnikov M., Kueller A., Shaporenko A., Schmidt E. and Eck W., 'Aromatic self-assembled monolayers on hydrogenated silicon', *Langmuir*, 2003 **19**(11) 4682–87.
68. Joy V.T. and Mandler D., 'Surface functionalization of h-terminated silicon surfaces with alcohols using iodoform as an *in situ* iodinating agent', *ChemPhysChem*, 2002 **3**(11) 973–75.
69. Niederhauser T.L., Lua Y.-Y., Jiang G., Davis S.D., Matheson R., Hess D.A., Mowat I.A. and Linford M.R., 'Arrays of chemomechanically patterned patches of homogeneous and mixed monolayers of 1-alkenes and alcohols on single silicon surfaces', *Angew. Chem. Int. Ed.*, 2002 **41**(13) 2353–56.
70. Ruan C.-M., Bayer T., Meth S. and Sukenik C.N., 'Creation and characterization of n-alkylthiol and n-alkylamine self-assembled monolayers on 316l stainless steel', *Thin Solid Films*, 2002 **419**(1–2) 95–104.
71. Benitez J.J., Kopta S., Ogletree D.F. and Salmeron M., 'Preparation and characterization of self-assembled monolayers of octadecylamine on mica using hydrophobic solvents', *Langmuir*, 2002 **18**(16) 6096–100.
72. Laibinis P.E., Whitesides G.M., Allara D.L., Tao Y.T., Parikh A.N. and Nuzzo R.G., 'Comparison of the structures and wetting properties of self-assembled monolayers of n-alkanethiols on the coinage metal surfaces, copper, silver, and gold', *J. Am. Chem. Soc.*, 1991 **113**(19) 7152–67.
73. Li Z., Chang S.-C. and Williams R.S., 'Self-assembly of alkanethiol molecules onto platinum and platinum oxide surfaces', *Langmuir*, 2003 **19**(17) 6744–49.
74. Mekhalif Z., Laffineur F., Couturier N. and Delhalle J., 'Elaboration of self-assembled monolayers of n-alkanethiols on nickel polycrystalline substrates: Time, concentration, and solvent effects', *Langmuir*, 2003 **19**(3) 637–45.
75. Laffineur F., Couturier N., Delhalle J. and Mekhalif Z., 'Effect of the solvent on the formation of n-dodecanethiol films on a polycrystalline ag90ni10 substrate', *Appl. Surf. Sci.*, 2003 **212–213** 452–57.
76. Sinapi F., Forget L., Delhalle J. and Mekhalif Z., 'Self-assembly of (3-mercaptopropyl)trimethoxysilane on polycrystalline zinc substrates towards corrosion protection', *Appl. Surf. Sci.*, 2003 **212–213** 464–71.
77. Noble-Luginbuhl A.R. and Nuzzo R.G., 'Assembly and characterization of sams formed by the adsorption of alkanethiols on zinc selenide substrates', *Langmuir*, 2001 **17**(13) 3937–44.
78. Ye S., Li G., Noda H., Uosaki K. and Osawa M., 'Characterization of self-assembled monolayers of alkanethiol on GaAs surface by contact angle and angle-resolved xps measurements', *Surf. Sci.*, 2003 **529**(1–2) 163–70.
79. Baum T., Ye S. and Uosaki K., 'Attenuated total reflection fir studies of self-assembled monolayers of alkanethiols on gallium arsenide', *Proc. Electrochem. Soc.*, 2002 **99**(15) 149–54.
80. Schvartzman M., Sidorov V., Ritter D. and Paz Y., 'Passivation of inp surfaces of electronic devices by organothiolated self-assembled monolayers', *J. Vac. Sci. Technol. B*, 2003 **21**(1) 148–55.
81. Protsailo L.V., Fawcett W.R., Russell D. and Meyer R.L., 'Electrochemical characterization of the alkaneselenol-based sams on au(111) single crystal electrode', *Langmuir*, 2002 **18**(24) 9342–49.
82. Han S.W. and Kim K., 'Self-assembled monolayers of organoselenium compounds on gold: Surface-enhanced raman scattering study', *J. Colloid Interface Sci.*, 2001 **240**(2) 492–97.

83. Han S.W., Lee S.J. and Kim K., 'Self-assembled monolayers of aromatic thiol and selenol on silver: Comparative study of adsorptivity and stability', *Langmuir*, 2001 **17**(22) 6981–87.
84. Lee M.-T., Hsueh C.-C., Freund M.S. and Ferguson G.S., 'Electrochemical self-assembly of monolayers from alkylthiosulfates on gold', *Langmuir*, 2003 **19**(13) 5246–53.
85. Lusk A.T. and Jennings G.K., 'Characterization of self-assembled monolayers formed from sodium s-alkyl thiosulfates on copper', *Langmuir*, 2001 **17**(25) 7830–36.
86. Taylor C.E. and Schwartz D.K., 'Octadecanoic acid self-assembled monolayer growth at sapphire surfaces', *Langmuir*, 2003 **19**(7) 2665–72.
87. Chen H.-G., Wu X.-D., Yu Q.-Q., Yang S.-R., Wang D.-P. and Shen W.-Z., 'Self-assembled monolayers of n-hexadecanoic acid and a-hydroxyl n-hexadecanoic acid on titanium surfaces', *Chin. J. Chem.*, 2002 **20**(12) 1467–71.
88. Jeon N.L., Finnie K., Branshaw K. and Nuzzo R.G., 'Structure and stability of patterned self-assembled films of octadecyltrichlorosilane formed by contact printing', *Langmuir*, 1997 **13**(13) 3382–91.
89. Marcinko S., Helmy R. and Fadeev A.Y., 'Adsorption properties of sams supported on tio2 and zro2', *Langmuir*, 2003 **19**(7) 2752–55.
90. Helmy R. and Fadeev A.Y., 'Self-assembled monolayers supported on tio2: Comparison of c18h37six3 (x = h, cl, och3), c18h37si(ch3)2cl, and c18h37po(oh)2', *Langmuir*, 2002 **18**(23) 8924–28.
91. Fadeev A.Y., Helmy R. and Marcinko S., 'Self-assembled monolayers of organosilicon hydrides supported on titanium, zirconium, and hafnium dioxides', *Langmuir*, 2002 **18**(20) 7521–29.
92. Long Y.-T., Herrworth S., Eck W. and Grunze M., 'Synthesis and characterization of self-assembled monolayers based on redox-active compounds on platinum surfaces', *Phys. Chem. Chem. Phys.*, 2002 **4**(3) 522–26.
93. Pellerite M.J., Dunbar T.D., Boardman L.D. and Wood E.J., 'Effects of fluorination on self-assembled monolayer formation from alkanephosphonic acids on aluminum: Kinetics and structure', *J. Phys. Chem. B*, 2003 **107**(42) 11726–36.
94. Geissler M., Wolf H., Stutz R., Delamarche E., Grummt U.-W., Michel B. and Bietsch A., 'Fabrication of metal nanowires using microcontact printing', *Langmuir*, 2003 **19**(15) 6301–11.
95. Lewington T.A., Alexander M.R., Thompson, G.E. and McAlpine, E., 'Characterisation of alkyl phosphonic acid monolayers self assembled on hydrated surface of aluminum', *Surf. Eng.*, 2002 **18**(3) 228–32.
96. Pawsey S., Yach K. and Reven L., 'Self-assembly of carboxyalkylphosphonic acids on metal oxide powders', *Langmuir*, 2002 **18**(13) 5205–12.
97. Yim C.T., Pawsey S., Morin F.G. and Reven L., 'Dynamics of octadecylphosphonate monolayers self-assembled on zirconium oxide: A deuterium nmr study', *J. Phys. Chem. B*, 2002 **106**(7) 1728–33.
98. Hughes W.C., Koh S.E., Augustine B.H. and Polefrone J.M., 'Self-assembly of phosphonate monolayers on gaas and gan', *Proc. Electrochem. Soc.*, 2001 **2001**(1) 213–17.
99. Neves B.R.A., Salmon M.E., Russell P.E., and Troughton E.B., Jr., 'Spread coating of opa on mica: From multilayers to self-assembled monolayers', *Langmuir*, 2001 **17**(26) 8193–98.
100. D'Andrea S.C., Iyer K.S., Luzinov I., and Fadeev A.Y., 'Self-assembled monolayers of organophosphonic acids supported on teeth', *Colloids Surf. B*, 2003 **32**(3) 235–43.

101. Fadeev A. Y., D'Andrea S., Iyer K.S. and Luzinov I., 'Organic monolayers supported on tooth enamel surfaces', *Polym. Mater. Sci. Eng.*, 2003 **89** 155.
102. Zwahlen M., Tosatti S., Textor M. and Haehner G., 'Orientation in methyl- and hydroxyl-terminated self-assembled alkanephosphate monolayers on titanium oxide surfaces investigated with soft X-ray absorption', *Langmuir*, 2002 **18**(10) 3957–62.
103. Tosatti S., Michel R., Textor M. and Spencer N.D., 'Self-assembled monolayers of dodecyl and hydroxy-dodecyl phosphates on both smooth and rough titanium and titanium oxide surfaces', *Langmuir*, 2002 **18**(9) 3537–48.
104. Haehner G., Hofer R. and Klingenfuss I., 'Order and orientation in self-assembled long chain alkanephosphate monolayers adsorbed on metal oxide surfaces', *Langmuir*, 2001 **17**(22) 7047–52.
105. Liebau M., Huskens J. and Reinhoudt D.N., 'Microcontact printing with heavyweight inks', *Adv. Funct. Mater.*, 2001 **11**(2) 147–50.
106. Geissler M., Schmid H., Bietsch A., Michel B. and Delamarche E., 'Defect-tolerant and directional wet-etch systems for using monolayers as resists', *Langmuir*, 2002 **18**(6) 2374–77.
107. Xia Y., Zhao X.-M., Kim E. and Whitesides G.M., 'A selective etching solution for use with patterned self-assembled monolayers of alkanethiolates on gold, silver and copper', *Chem. Mater.*, 1995 **7**(12) 2332–37.
108. Li H.-W., Muir B. V.O., Fichet G. and Huck W.T.S., 'Nanocontact printing: A route to sub-50-nm-scale chemical and biological patterning', *Langmuir*, 2003 **19**(6) 1963–65.
109. Xia Y., Kim E., Mrksich M., and Whitesides G.M., 'Microcontact printing of alkanethiols on copper and its application in microfabrication', *Chem. Mater.*, 1996 **8**(3) 601–3.
110. Moffat T.P., and Yang H., 'Patterned metal electrodeposition using an alkanethiolate mask', *J. Electrochem. Soc.*, 1995 **142**(11) L220-L22.
111. Carvalho A., Geissler M., Schmid H., Michel B. and Delamarche E., 'Self-assembled monolayers of eicosanethiol on palladium and their use in microcontact printing', *Langmuir*, 2002 **18**(6) 2406–12.
112. Geissler M., Chen J. and Xia Y., 'A comparative study of monolayers self-assembled from octadecylisocyanide and oca-decaethiol on polycrystalline pt substrates', Submitted.
113. Lahiri J., Ostuni E. and Whitesides G.M., 'Patterning ligands on reactive sams by microcontact printing', *Langmuir*, 1999 **15**(6) 2055–60.
114. Sullivan T.P. and Huck W.T.S., 'Reactions on monolayers: Organic synthesis in two dimensions', *Eur. J. Org. Chem.*, 2003 **2003**(1) 17–29.
115. Chechik V., Crooks R.M. and Stirling C.J.M., 'Reactions and reactivity in self-assembled monolayers', *Adv. Mater.*, 2000 **12**(16) 1161–71.
116. Delamarche E., Geissler M., Wolf H. and Michel B., 'Positive microcontact printing', *J. Am. Chem. Soc.*, 2002 **124**(15) 3834–35.
117. Yu J. and Holdcroft S., 'Chemically amplified soft lithography of a low band gap polymer', *Chem. Commun.*, 2001 (14) 1274–75.
118. Jackman R.J., Duffy D.C., Cherniavskaya O. and Whitesides G.M., 'Using elastomeric membranes as dry resists and for dry lift-off', *Langmuir*, 1999 **15**(8) 2973–84.
119. Childs W.R. and Nuzzo R.G., 'Decal transfer microlithography: A new soft-lithographic patterning method', *J. Am. Chem. Soc.*, 2002 **124**(45) 13583–96.
120. Loo Y.-L., Willett R.L., Baldwin K.W. and Rogers J.A., 'Additive, nanoscale patterning of metal films with a stamp and a surface chemistry mediated transfer process: Applications in plastic electronics', *Appl. Phys. Lett.*, 2002 **81**(3) 562–64.

121. Loo Y.-L., Someya T., Baldwin K.W., Bao Z., Ho P., Dodabalapur A., Katz H.E. and Rogers J.A., 'Soft, conformable electrical contacts for organic semiconductors: High-resolution plastic circuits by lamination', *Proc. Natl. Acad. Sci. U.S.A.*, 2002 **99**(16) 10252–56.
122. Loo Y.-L., Lang D.V., Rogers J.A. and Hsu J.W.P., 'Electrical contacts to molecular layers by nanotransfer printing', *Nano Lett.*, 2003 **3**(7) 913–17.
123. Loo Y.-L., Willett R.L., Baldwin K.W. and Rogers J.A., 'Interfacial chemistries for nanoscale transfer printing', *J. Am. Chem. Soc.*, 2002 **124**(26) 7654–55.
124. Jacobs H.O. and Whitesides G.M., 'Submicrometer patterning of charge in thin-film electrets', *Science*, 2001 **291**(5509) 1763–66.
125. Wolfe D.B., Conroy R.S., Love J.C., Gates B.D., Prentiss M.G. and Whitesides G.M., 'Fabrication of planar optical waveguides by electrical microcontact printing', *Appl. Phys. Lett.*, 2004 **84**(10) 1623–25.
126. Bowden N., Brittain S., Evans A.G., Hutchinson J.W. and Whitesides G.M., 'Spontaneous formation of ordered structures in thin films of metals supported on an elastomeric polymer', *Nature*, 1998 **393**(6681) 146–49.
127. Rogers J.A., Paul K.E., Jackman R.J. and Whitesides G.M., 'Using an elastomeric phase mask for sub-100 nm photolithography in the optical near field', *Appl. Phys. Lett.*, 1997 **70**(20) 2658–60.
128. Rogers J.A., Paul K.E., Jackman R.J. and Whitesides G.M., 'Generating ~90 nanometer features using near-field contact-mode photolithography with an elastomeric phase mask', *J. Vac. Sci. Technol. B*, 1998 **16**(1) 59–68.
129. Odom T.W., Thalladi V.R., Love J.C. and Whitesides G.M., 'Generation of 30–50 nm structures using easily fabricated, composite pdms masks', *J. Am. Chem. Soc.*, 2002 **124**(41) 12112–13.
130. Hu J., Deng T., Beck R.G., Westervelt R.M., Maranowski K.D., Gossard A.C. and Whitesides G.M., 'Fabrication of GaAs/AlGaAs high electron mobility transistors with 250 nm gates using conformal phase shift lithography', *Sens. Actuators, A*, 2000 **86** 122–26.
131. Paul K.E., Prentiss M.G. and Whitesides G.M., 'Patterning spherical surfaces at the two-hundred-nanometer scale using soft lithography', *Adv. Funct. Mater.*, 2003 **13**(4) 259–63.
132. Tien J., Nelson C.M. and Chen C.S., 'Fabrication of aligned microstructures with a single elastomeric stamp', *Proc. Natl. Acad. Sci. U.S.A.*, 2002 **99**(4) 1758–62.
133. Black A.J., Nealey P.F., Thywissen J.H., Deshpande M., El-Zein N., Maracas G.N., Prentiss M. and Whitesides G.M., 'Microfabrication of two layer structures of electrically isolated wires using self-assembly to guide the deposition of insulating organic polymer.' *Sens. Actuators, A*, 2000 **86**(1–2) 96–102.
134. Rogers J.A., Bao Z., Baldwin K., Dodabalapur A., Crone B., Raju V. R., Kuck V., Katz H., Amundson K., Ewing J. and Drzaic P., 'Paper-like electronic displays: Large-area rubber-stamped plastic sheets of electronics and microencapsulated electrophoretic inks', *Proc. Natl. Acad. Sci. U.S.A.*, 2001 **98**(9) 4835–40.
135. Lee N., J., Park C. and Whitesides G.M., 'Solvent compatibility of poly (dimethylsiloxane)-based microfluidic devices', *Anal. Chem.*, 2004 **75**(23) 6544–54.
136. Rogers J.A., Bao Z., Makhija A. and Braun P., 'Printing process suitable for reel-to-reel production of high-performance organic transistors and circuits', *Adv. Mater.*, 1999 **11**(9) 741–45.
137. Rogers J.A., Baldwin K., Bao Z., Dodabalapur A., Raju V.R., Ewing J. and Amundson K., 'Large area, rubber stamped plastic circuits for electronic paper', *Mater. Res. Soc. Symp. Proc.*, 2001 **660** JJ7 1/1-JJ7 1/8.

138. Jackman R.J., Brittain S.T., Adams A., Wu H., Prentiss M.G., Whitesides S. and Whitesides G.M., 'Three-dimensional metallic microstructures fabricated by soft lithography and microelectrodeposition', *Langmuir*, 1999 **15**(3) 826–36.
139. Jackman R.J. and Whitesides G.M., 'Electrochemistry and soft lithography: A route to 3-d microstructures', *CHEMTECH*, 1999 **29**(5) 18–30.
140. Brittain S.T., Schueller O.J.A., Wu H., Whitesides S. and Whitesides G.M., 'Microorigami: Fabrication of small, three-dimensional, metallic structures', *J. Phys. Chem. B.*, 2000 **105**(2) 347–50.
141. Wu H., Brittain S.T., Anderson J.R., Grzybowski B., Whitesides S. and Whitesides G.M., 'Fabrication of topologically complex three-dimensional microstructures: Metallic microknots', *J. Am. Chem. Soc.*, 2001 **122**(51) 12691–99.
142. Wu H., Odom T.W., Chiu D.T. and Whitesides G.M., 'Fabrication of complex three-dimensional microchannel systems in pdms', *J. Am. Chem. Soc.*, 2003 **125**(2) 554–59.
143. Wu H., Whitesides S. and Whitesides G.M., 'Fabrication of micro-chain mail by simultaneous, patterned electrodeposition on a plane and multiple cylinders', *Angew. Chem. Int. Ed.*, 2001 **40**(11) 2059–60.
144. Rogers J.A., 'Rubber stamping for plastic electronics and fiber optics', *Mater. Res. Bull.*, 2001 **26**(7) 530–34.
145. Gates B.D., Xu Q., Love J.C., Wolfe D.B. and Whitesides G.M., 'Unconventional nanofabrication', *Annu. Rev. Mater. Sci.*, Submitted.
146. Quake S.R. and Scherer A., 'From micro- to nanofabrication with soft materials', *Science*, 2000 **290**(5496) 1536–40.
147. Grover W.H., Skelley A.M., Liu C.N., Lagally E.T. and Mathies R.A., 'Monolithic membrane valves and diaphragm pumps for practical large-scale integration into glass microfluidic devices', *Sens. Actuators, B*, 2003 **89**(3) 315–23.
148. Beebe D.J., Mensing G.A. and Walker G.M., 'Physics and applications of microfluidics in biology', *Annu. Rev. Biomed. Eng.*, 2002 **4** 261–86.
149. Unger M.A., Chou H.-P., Thorsen T., Scherer A. and Quake S.R., 'Monolithic microfabricated valves and pumps by multilayer soft lithography', *Science*, 2000 **288**(5463) 113–16.
150. Ismagilov R.F., Rosmarin D., Kenis P.J.A., Chiu D.T., Zhang W., Stone H.A. and Whitesides G.M., 'Pressure-driven laminar flow in tangential microchannels: An elastomeric microfluidic switch', *Anal. Chem.*, 2001 **73**(19) 4682–87.
151. Beebe D.J., Moore J.S., Bauer J.M., Yu Q., Liu R.H., Devadoss, C. and Jo B.-H., 'Functional hydrogel structures for autonomous flow control inside microfluidic channels', *Nature*, 2000 **404**(6778) 588–90.
152. Hua S.Z., Sachs F., Yang D.X., and Chopra H.D., 'Microfluidic actuation using electrochemically generated bubbles', *Anal. Chem.*, 2002 **74**(24) 6392–96.
153. Griss P., Andersson H. and Stemme G., 'Expandable microspheres for the handling of liquids', *Lab on a Chip*, 2002 **2**(2) 117–20.
154. Stroock A.D., Dertinger S.K.W., Ajdari A., Mezit I., Stone H.A. and Whitesides G.M., 'Chaotic mixer for microchannels', *Science*, 2002 **295**(5555) 647–51.
155. Seong G.H. and Crooks R.M., 'Efficient mixing and reactions within microfluidic channels using microbead-supported catalysts', *J. Am. Chem. Soc.*, 2002 **124**(45) 13360–61.
156. Song H., Tice J.D. Ismagilov R.F., 'A microfluidic system for controlling reaction networks in time', *Angew. Chem. Int. Ed.*, 2003 **42**(7) 768–72.
157. Johnson T.J., Ross D. and Locascio L.E., 'Rapid microfluidic mixing', *Anal. Chem.*, 2002 **74**(1) 45–51.

158. He B., Burke B.J., Zhang X., Zhang R. and Regnier F.E., 'A picoliter-volume mixer for microfluidic analytical systems', *Anal. Chem.*, 2001 **73**(9) 1942–47.
159. Jiang X., Ng J.M.K., Stroock A.D., Dertinger S.K.W. and Whitesides G.M., 'A miniaturized, parallel, serially diluted immunoassay for analyzing multiple antigens', *J. Am. Chem. Soc.*, 2003 **125**(18) 5294–95.
160. Hatch A., Kamholz A.E., Hawkins K.R., Munson M.S., Schilling E. A., Weigl B.H. and Yager P., 'A rapid diffusion immunoassay in a t-sensor', *Nature Biotechnol.*, 2001 **19**(5) 461–65.
161. Chiem N.H. and Harrison D.J., 'Microchip systems for immunoassay: An integrated immunoreactor with electrophoretic separation for serum theophylline determination', *Clin. Chem.*, 1998 **44**(3) 591–98.
162. Linder V., Verpoorte E., De Rooij N.F., Sigrist H. and Thormann W., 'Application of surface biopassivated disposable poly(dimethylsiloxane)/glass chips to a heterogeneous competitive human serum immunoglobulin g immunoassay with incorporated internal standard', *Electrophoresis*, 2002 **23**(5) 740–49.
163. Rossier J.S., Girault H.H., 'Enzyme linked immunosorbent assay on a microchip with electrochemical detection', *Lab on a Chip*, 2001 **1**(2) 153–57.
164. Ismagilov R.F., Ng J.M.K., Kenis P.J.A. and Whitesides G.M., 'Microfluidic arrays of fluid-fluid diffusional contacts as detection elements and combinatorial tools', *Anal. Chem.*, 2001 **73**(21) 5207–13.
165. Bernard A., Michel B., Delamarche E., 'Micromosaic immunoassays', *Anal. Chem.*, 2001 **73**(1) 8–12.
166. Harris C.M., 'Shrinking the lc landscape', *Anal. Chem.*, 2003 **75**(3) 64A–69A.
167. Slentz B.E., Penner N.A., Lugowska E. and Regnier F., 'Nanoliter capillary electrochromatography columns based on collocated monolithic support structures molded in poly(dimethyl siloxane)', *Electrophoresis*, 2001 **22**(17) 3736–43.
168. Jiang Y., Wang P.-C., Locascio L.E. and Lee C.S., 'Integrated plastic microfluidic devices with esi-ms for drug screening and residue analysis', *Anal. Chem.*, 2001 **73**(9) 2048–53.
169. Kim J.S., and Knapp D.R., 'Microfabrication of polydimethylsiloxane electrospray ionization emitters', *J. Chromatogr. A*, 2001 **924**(1-2) 137–45.
170. Huikko K., Oestman P., Grigoras K., Tuomikoski S., Tiainen V.M., Soininen A., Puolanne K., Manz A., Franssila S., Kostiaainen R. and Kotiaho T., 'Poly(dimethylsiloxane) electrospray devices fabricated with diamond-like carbon-poly(dimethylsiloxane) coated su-8 masters', *Lab on a Chip*, 2003 **3**(2) 67–72.
171. Fu A.Y., Chou H.-P., Spence C., Arnold F.H. and Quake S.R., 'An integrated microfabricated cell sorter', *Anal. Chem.*, 2002 **74**(11) 2451–57.
172. Deng T., Prentiss M. and Whitesides G.M., 'Fabrication of magnetic microfiltration systems using soft lithography', *Appl. Phys. Lett.*, 2002 **80**(3) 461–63.
173. Cho B.S., Schuster T.G., Zhu X., Chang D., Smith G.D. and Takayama, S., 'Passively driven integrated microfluidic system for separation of motile sperm', *Anal. Chem.*, 2003 **75**(7) 1671–75.
174. Beebe D., Wheeler M., Zeringue H., Walters E. and Raty S., 'Microfluidic technology for assisted reproduction', *Theriogenology*, 2002 **57**(1) 125–35.
175. Hansen C.L., Skordalakes E., Berger J.M. and Quake S.R., 'A robust and scalable microfluidic metering method that allows protein crystal growth by free interface diffusion', *Proc. Natl. Acad. Sci. U.S.A.*, 2002 **99**(26) 16531–36.
176. Monahan J., Gewirth A.A. and Nuzzo R.G., 'A method for filling complex polymeric microfluidic devices and arrays', *Anal. Chem.*, 2001 **73**(13) 3193–97.

177. Liu J., Enzelberger M. and Quake S., 'A nanoliter rotary device for polymerase chain reaction', *Electrophoresis*, 2002 **23**(10) 1531–36.
178. Mao H., Holden M.A., You M. and Cremer P.S., 'Reusable platforms for high-throughput on-chip temperature gradient assays', *Anal. Chem.*, 2002 **74**(19) 5071–75.
179. Chiu D.T., 'A microfluidics platform for cell fusion', *Curr. Opin. Chem. Bio.*, 2001 **5**(5) 609–12.
180. Takayama S., McDonald J.C., Ostuni E., Liang M.N., Kenis P.J.A., Ismagilov R.F., and Whitesides G.M., 'Patterning cells and their environments using multiple laminar fluid flows in capillary networks', *Proc. Natl. Acad. Sci. U.S.A.*, 1999 **96**(10) 5545–48.
181. Chiu D.T., Li Jeon, N., Huang S., Kane R.S., Wargo C.J., Choi I.S., Ingber D.E. and Whitesides G.M., 'Patterned deposition of cells and proteins onto surfaces by using three-dimensional microfluidic systems', *Proc. Natl. Acad. Sci. U.S.A.*, 2000 **97**(6) 2408–13.
182. Takayama S., Ostuni E., LeDuc P., Naruse K., Ingber D.E. and Whitesides G.M., 'Subcellular positioning of small molecules', *Nature*, 2001 **411**(6841) 1016.
183. Sawano A., Takayama S., Matsuda M. and Miyawaki A., 'Lateral propagation of egf signaling after local stimulation is dependent on receptor density', *Dev. Cell*, 2002 **3**(2) 245–57.
184. Jeon N.L., Baskaran H., Dertinger S.K.W., Whitesides G.M., Van De Water L. and Toner M., 'Neutrophil chemotaxis in linear and complex gradients of interleukin-8 formed in a microfabricated device', *Nature Biotechnol.*, 2002 **20**(8) 826–30.
185. Dertinger S.K.W., Jiang X., Li Z., Murthy V.N. and Whitesides G.M., 'Gradients of substrate-bound laminin orient axonal specification of neurons', *Proc. Natl. Acad. Sci. U.S.A.*, 2002 **99**(20) 12542–47.
186. Kumacheva E., Garstecki P., Wu H. and Whitesides G.M., 'Two-dimensional colloid crystals obtained by coupling of flow and confinement', *Phys. Rev. Lett.*, 2003 **91**(12) 128301/1–01/4.
187. Thorsen T., Roberts R.W., Arnold F.H. and Quake S.R., 'Dynamic pattern formation in a vesicle-generating microfluidic device', *Phys. Rev. Lett.*, 2001 **86**(18) 4163–66.
188. Tice J.D., Lyon A.D., and Ismagilov R.F., 'Effects of viscosity on droplet formation and mixing in microfluidic channels', *Anal. Chim. Acta*, 2004 **507**(1) 73–77.
189. Tice J.D., Song H., Lyon A.D. and Ismagilov R.F., 'Formation of droplets and mixing in multiphase microfluidics at low values of the reynolds and the capillary numbers', *Langmuir*, 2003 **19**(22) 9127–33.
190. Hua Susan Z., Sachs F., Yang David X. and Chopra Harsh D., 'Microfluidic actuation using electrochemically generated bubbles', *Anal. Chem.*, 2002 **74**(24) 6392–96.
191. Fuerstman M.J., Deschatelets P., Kane R., Schwartz A., Kenis P.J.A., Deutch J.M., Whitesides G.M., 'Solving mazes using microfluidic networks', *Langmuir*, 2003 **19**(11) 4714–22.
192. Chiu D.T., Pezzoli E., Wu H., Stroock A.D., and Whitesides G.M., 'Using three-dimensional microfluidic networks for solving computationally hard problems', *Proc. Natl. Acad. Sci. U.S.A.*, 2001 **98**(6) 2961–66.

## Chemomechanical surface modification of materials for patterning

---

M LINFORD,<sup>1</sup> R DAVIS, S MAGLEBY, L HOWELL,  
G JIANG, and C THULIN  
Brigham Young University, USA

### 4.1 Introduction

In chemomechanical modification of surfaces and materials a mechanical agitation or perturbation is applied to a surface or material, which leads to a modification of its surface or near surface by an external chemical reagent. This method is ideally suited for patterning surfaces at the micron and nanometer scales because modification takes place wherever a tip makes contact with the surface or material, and (ideally) nowhere else.

#### 4.1.1 Background

Perhaps the earliest example of this approach to surface modification was in 1992 by Abbot, Folkers and Whitesides, who mechanically scribed a thiol-coated gold surface with a scalpel or a carbon fiber, creating 0.1 to 1  $\mu\text{m}$  lines.<sup>1</sup> They then showed that immersion of the scribed surface into a solution of a thiol (different from the first) led to thiol deposition in the exposed area. In 1994 they published three additional papers on this subject. In one,<sup>2</sup> they showed that this method could be used to produce 0.1–1  $\mu\text{m}$  gold lines on glass or silicon by scribing into a monolayer of  $\text{HO}(\text{CH}_2)_2\text{SH}$  on gold to expose a fresh gold surface, immersing the surface into a solution of  $\text{CH}_3(\text{CH}_2)_{15}\text{SH}$  to create a monolayer in the scribed region, and then chemically etching away the  $\text{HO}(\text{CH}_2)_2\text{SH}$ -coated gold. It was then shown that these miniature gold lines could be used as microelectrodes.<sup>3</sup> They also demonstrated that corrals of hydrophobic lines on a hydrophilic background on gold would confine droplets of water, and that finite element analysis could be used to estimate  $\gamma_{\text{sv}}-\gamma_{\text{sl}}$ .<sup>4</sup>

In their 1994 *Chemistry of Materials* paper Abbot, Kumar, and Whitesides noted that, in theory, an AFM (atomic force microscope) or SEM (scanning electron microscope) could be used to pattern monolayers on gold with their method.<sup>2</sup> In 1997 Liu and Xu<sup>5</sup> confirmed and improved upon this idea by demonstrating that mechanical writing with an AFM on a thiol-on-gold

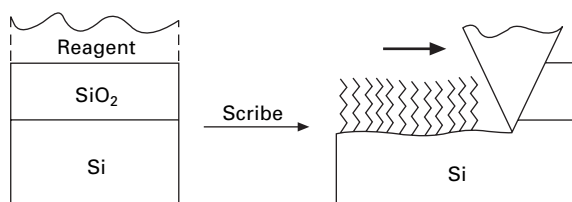
monolayer could be performed while the substrate was immersed in a solution of another thiol. Thus, formation of a new monolayer took place in regions of a monolayer surface as they were exposed by the AFM. An important difference between the Liu and Whitesides approaches is that the underlying substrate does not appear to be significantly damaged in the Liu work, i.e., the AFM appears to apply only enough force to the monolayer to shave off the alkyl chains on it, thus their term ‘nanoshaving’.

Liu’s seminal work on nanoshaving took place at about the same time Linford made another advance in chemomechanical materials modification. Linford (before leaving graduate school in mid-1996) showed that alkyl monolayer-coated silicon particles could be made by grinding silicon that was immersed in 1-hexadecene. A provisional patent was filed on this work after he left in 1997 and a patent was ultimately issued in 2000.<sup>6</sup> This work extended the chemomechanical approach to a semiconductor (a covalent solid). Because bare, unpassivated silicon readily reacts with oxygen, it was necessary to immerse the silicon in the reagent it was to be coated with prior to grinding – in the original study the 1-alkene was degassed and grinding was performed manually in a glove box.

The literature contains other related examples of surface patterning by mechanical means, especially by AFM.<sup>7</sup> AFM-based methods include modification of self-assembled monolayers by conductive AFM,<sup>8,9</sup> dip-pen nanolithography,<sup>10</sup> and field enhanced oxidation of silicon followed by chemical modification of the oxidized patterns.<sup>11</sup> Mechanical surface modification by AFM has also been applied to make oxidized patterns on silicon,<sup>12</sup> but not to covalently bind organic molecules to surfaces.

#### 4.1.2 The chemistry of scribed silicon ( $\text{Si}_{\text{scr}}$ )

In 2001, the Linford grinding work on bulk silicon was extended to planar silicon. In the first paper on this subject<sup>13</sup> it was shown (i) that monolayer-coated features on silicon surfaces could be produced by wetting silicon with a reactive compound, and then scribing (see Fig. 4.1), (ii) that alkynes, in addition to alkenes, would chemomechanically modify silicon in this manner, (iii) that silicon could be chemomechanically patterned in an open laboratory



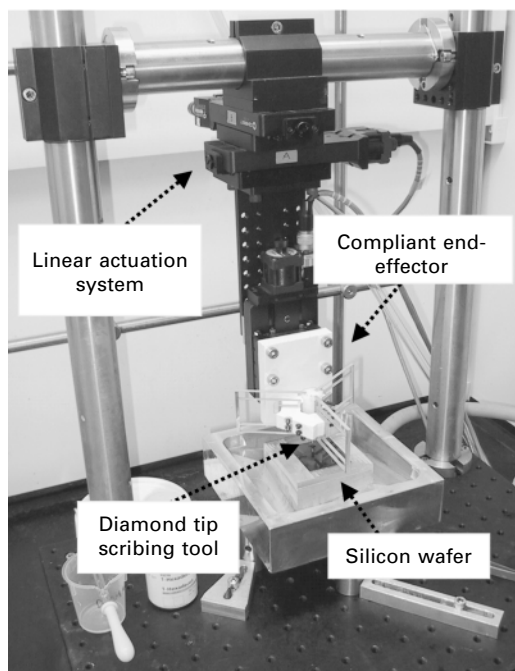
4.1 Chemomechanical production of a monolayer made on silicon by scribing.

with liquids that had not been degassed or otherwise specially treated, and (iv) that enclosures of scribed lines (hydrophobic corrals) could hold water and other liquids with relatively high surface tensions. Later, it was shown that scribed silicon would also react with alkyl halides<sup>14</sup> (chlorides, bromides, and iodides), alcohols,<sup>15</sup> epoxides,<sup>16</sup> and aldehydes.<sup>17</sup> In all of these studies it was hypothesized that scribed silicon is chemically similar to Si(100) –  $2 \times 1$  and Si(111) –  $7 \times 7$ , which are the two most important reconstructions of silicon, and which have been extensively studied under ultra-high vacuum conditions.<sup>18–22</sup> The alkyl chains in these monolayers, especially those that are believed to be bonded through carbon-silicon bonds, are found to be very stable to a variety of conditions, such as hot solvents, or extended immersions in water or exposures to the laboratory environment.<sup>23</sup> Time of flight secondary ion mass spectrometry (ToF-SIMS) provided evidence for the surface structures that had been hypothesized for 1-alkenes, 1-alkynes, and alkyl halides.<sup>24</sup> A mechanistic study of silicon that was ground in the presence of alkyl halides provided direct evidence for radicals in monolayer formation,<sup>25</sup> as had previously been proposed.<sup>14</sup> Mixed monolayers<sup>15,16</sup> and functionalized monolayers<sup>14,16</sup> were also prepared.

#### 4.1.3 Chemomechanical patterning of silicon

Because surface patterning is a critically important topic in modern science and technology, a primary focus of the chemomechanical modification of silicon has been to develop methods and instruments for finely and accurately patterning its surface. At first, silicon was scribed by hand using a diamond-tipped stylus and a ruler. Later, a more sophisticated device was developed, which consisted of three computer-controlled translation stages that held a diamond tip in a spring-loaded tool.<sup>13</sup> However, in spite of this improvement, the tip holder was found to be unsatisfactory for making fine ( $< 50 \mu\text{m}$ ) features. For such lines to be precisely made the tip would need to be rigidly attached to a device that would act as a very flexible spring out of the plane, but simultaneously be extremely stiff in the plane. Using the principles of advanced compliant mechanisms<sup>26</sup> such an ‘end-effector’ was designed (see Fig. 4.2) and shown to indeed produce very narrow features.<sup>27,28</sup>

As might be imagined, the nature of the tip strongly influences the size and depth of surface features. For example, when hydrogen-terminated silicon<sup>29</sup> was scribed with a miniature tungsten carbide ball lines could be made that were *ca.*  $20 \mu\text{m}$  wide, but only *ca.*  $2 \text{ nm}$  deep.<sup>30</sup> Another significant advance in the chemomechanical surface patterning of silicon was the production of nanometer features (as small as *ca.*  $20 \text{ nm}$ ) on hydrogen-terminated silicon with an AFM tip.<sup>31</sup> In this study it was shown that changing the force on the tip changes the width of the lines that are produced. Scanning electron microscopy (SEM) and ToF-SIMS confirmed surface modification and patterning by AFM.



4.2 A scribing system, including the scribing tool, end-effector, and motion system.

## 4.2 The chemistry of scribed silicon

Scribed silicon has now been shown to react with a variety of reactive compounds, including 1-alkenes,<sup>13,15,24</sup> 1-alkynes,<sup>13,24</sup> alkyl halides (chlorides, bromides, and iodides),<sup>14,24</sup> epoxides,<sup>16</sup> alcohols,<sup>15</sup> and aldehydes.<sup>17</sup> There are, no doubt, other functional groups that will also react with this surface. It has been hypothesized that scribed silicon reacts similarly to bare, reconstructed silicon. Indeed, the reactions of reconstructed silicon ( $\text{Si}(100) - 2 \times 1$  and  $\text{Si}(111) - 7 \times 7$ )<sup>18-22</sup> with 1-alkenes,<sup>32-36</sup> 1-alkynes,<sup>37-41</sup> alkyl halides,<sup>42-44</sup> alcohols,<sup>45-48</sup> and aldehydes<sup>46,49-51</sup> have been reported. We are unaware of any published results of the reactivity of epoxides with reconstructed silicon.

### 4.2.1 General properties of silicon scribed under monofunctional compounds

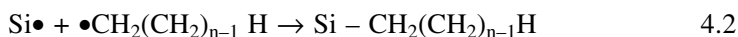
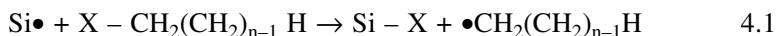
All of the monofunctional, reactive compounds that have been investigated to date on scribed silicon produce similar surfaces, where the most important factor influencing the properties of the resulting surfaces is the number of carbon atoms in the adsorbate. For example, it is found that adsorbates with

shorter alkyl chains produce surfaces with smaller water contact angles (they are more hydrophilic) and surfaces prepared with reactive compounds that have longer alkyl chains have higher water contact angles (they are more hydrophobic). In particular, for a homologous series of compounds the water contact angles rise fairly constantly with chain length for the smaller adsorbates (up to *ca.* 8 carbon atoms) after which they approach a constant value.<sup>15,16</sup> Analogous behavior has also been found<sup>52</sup> for alkyl monolayers of thiols on gold,<sup>53,54</sup> silanes on silicon oxide,<sup>55,56</sup> and 1-alkenes on hydrogen-terminated silicon.<sup>57,58</sup>

The wetting results for silicon scribed under homologous series of reactive compounds (see above) imply that the amount of hydrocarbon on the surfaces increases with increasing alkyl chain length of the adsorbate. XPS provides direct evidence for this hypothesis in the form of increasing C1s/Si2p ratios from silicon scribed with adsorbates that have more carbon atoms (longer alkyl chains).<sup>13–17</sup> ToF-SIMS also shows this same general trend, which is that fragments that contain carbon and hydrogen, or carbon, hydrogen and silicon generally become more intense as the number of carbons in the adsorbate increases.<sup>24</sup> Thus, wetting, XPS, and ToF-SIMS results suggest alkyl monolayer formation on silicon when it is scribed in the presence of a variety of reactive compounds.

#### 4.2.2 The reaction of Si<sub>scr</sub> with alkyl halides

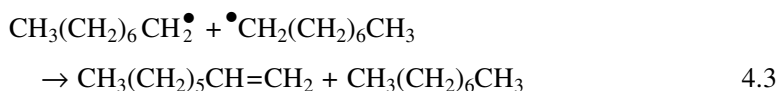
Of all of the functional groups that react with scribed silicon, the mechanism of adsorption of alkyl halides and the properties of the resulting surfaces are perhaps best understood. In the first report of this chemistry<sup>14</sup> it was hypothesized that monolayer formation would be driven by the stronger silicon-halogen bond, compared to the weaker carbon-halogen bond.<sup>59,60</sup> Thus, in monolayer formation surface halogen abstraction (eqn 4.1 below) could be followed by diffusion of the resulting radical back to the surface to tether the alkyl chain (eqn 4.2),



where  $-\text{X}$  could be  $-\text{Cl}$ ,  $-\text{Br}$ , or  $-\text{I}$ . Bronikowski and Hamers had previously proposed a nearly identical mechanism to explain the reactivity of methyl chloride with  $\text{Si}(100) - 2 \times 1$  under ultra-high vacuum conditions.<sup>42</sup> If eqns 4.1 and 4.2 are truly operative, one would expect halogen to be present at the surface of silicon after scribing. XPS confirms the presence of the halogens, and ToF-SIMS shows  $\text{SiX}^+$  species in their correct isotopic abundances.<sup>14</sup> ToF-SIMS of silicon scribed under  $\text{CH}_3\text{I}$  and  $^{13}\text{CH}_3\text{I}$  shows strong  $\text{SiCH}_3^+$  and  $\text{Si}^{13}\text{CH}_3^+$  peaks, respectively.<sup>24</sup>

Stability tests on monolayers on scribed silicon prepared from alkyl halides are consistent with surface reactions that would tether alkyl chains through robust carbon-silicon bonds and also produce hydrolysable silicon-halogen surface species.<sup>23</sup> For example, after two 1 h immersions in boiling 0.1 M H<sub>2</sub>SO<sub>4</sub>, the C1s/Si2p XPS ratio from a monolayer prepared with 1-chlorooctane was unchanged or increased slightly, i.e., the alkyl monolayer was stable to these harsh conditions. In addition, while the C1s/Si2p XPS ratio remained constant or rose slightly during 1800 h of exposure to the air, the I3d<sub>5/2</sub>/Si2p ratio steadily decreased, indicating a loss of iodine. Similar steady decays in the I3d<sub>5/2</sub>/Si2p ratio are observed for scribed silicon prepared from 1-iodododecane, 1-iodopentane, and iodomethane immersed in water for 1700 h. That surface iodine remains on scribed silicon after tens of hours of exposure to air or water is somewhat surprising given the highly reactive nature of the Si-I bond. However, in support of these results we note that chlorine-terminated Si(111) has also been found to hydrolyze slowly under water.<sup>61</sup> The stability of surface halogen on silicon against hydrolysis is attributed to steric hindrance from the silicon surface, steric hindrance of any alkyl chains in the immediate vicinity of the halogen, the hydrophobic nature of alkyl chains in the immediate vicinity of the halogen, and the constraining effect of substrate Si-Si bonds on possible Si<sub>3</sub>Si-X surface species.

A recent set of experiments provides additional, direct evidence for the mechanism in eqns 4.1 and 4.2 of monolayer formation from alkyl halides.<sup>62</sup> In this study silicon was ground in the presence of octyl chloride, bromide, or iodide, and gas chromatography-mass spectrometry (GC-MS) was performed on the liquid that remained after grinding. This analysis revealed the presence of octane, 1-octene, and hexadecane, which are the disproportionation (eqn 4.3) and dimerization products (eqn 4.4)<sup>63</sup> of the octyl radical that would be expected from eqns 4.1–2:



An even more compelling experiment consisted of grinding silicon in the presence of heptyl iodide and octyl iodide. The resulting scribing liquid similarly showed the expected disproportionation products (heptane, 1-heptene, octane, and 1-octene) and dimerization products (tetradecane, pentadecane, and hexadecane in a *ca.* 1:2:1 ratio).

#### 4.2.3 The reaction Si<sub>scr</sub> with alkenes and alkynes

The most important and studied reagents for monolayer formation on hydrogen-terminated and bare (reconstructed) silicon are the alkenes and alkynes.

These reagents also react readily with  $\text{Si}_{\text{scr}}$  to form monolayers, and they exhibit the general wetting, XPS, and ToF-SIMS behavior mentioned above.<sup>13,15,24</sup> It was proposed that these reagents would react with scribed silicon as they do with unpassivated silicon, i.e., to form four-membered rings that contain two silicon and two carbon atoms. This mechanism has important implications. First, it suggests a direct reaction between the reagent and the surface, which means that no species would need to diffuse back to the surface for monolayer formation, and no additional species besides the alkyl chain would add to the surface, as is the case for the alkyl halides. The complete stability of monolayers on scribed silicon prepared from 1-octene and 1-decene to boiling 0.1 M  $\text{H}_2\text{SO}_4$  for as long as they were studied (2 h and 1 h immersions, respectively)<sup>23</sup> is in accord with the robust carbon-silicon bonds that were proposed.

#### 4.2.4 The reaction of $\text{Si}_{\text{scr}}$ with alcohols

Alcohols are another important class of compounds that react with scribed silicon, and they too exhibit the general wetting and XPS behavior of all monolayers on scribed silicon.<sup>15</sup> A dissociative mechanism of RO–H bond cleavage was proposed to yield Si–OR and Si–H surface species, as is the case for chemisorption of alcohols onto  $\text{Si}(100) - 2 \times 1$ .<sup>64–66</sup> However, high resolution C1s XPS scans of silicon scribed under alcohols also indicate some complications in monolayer formation, showing not only the expected C–O bonds in the adsorbates, but also indicating small, but significant, amounts of –C=O and –COOH species. (The adsorption of alcohols on  $\text{Si}(111) - 7 \times 7$  is also complicated, i.e., C–O bond cleavage is observed.<sup>20,65</sup>) ToF-SIMS provides the strongest evidence for monolayer formation on scribed silicon from alcohols to date.<sup>15</sup> Silicon scribed under 1-propanol yields  $\text{C}_3\text{H}_7^+$ ,  $\text{C}_3\text{H}_7\text{OSi}^+$ ,  $\text{C}_3\text{H}_5\text{O}^-$ , and  $\text{C}_3\text{H}_7\text{O}^-$  fragments, and silicon scribed under 1-butanol and 1-octanol yield  $\text{C}_4\text{H}_9^+$ ,  $\text{C}_4\text{H}_9\text{OSi}^+$ ,  $\text{C}_4\text{H}_7\text{O}^-$ ,  $\text{C}_4\text{H}_9\text{O}^-$ , and  $\text{C}_8\text{H}_{15}\text{O}^-$  and  $\text{C}_8\text{H}_{17}\text{O}^-$ , respectively. These results are unlike those of monolayers prepared from 1-alkenes, 1-alkynes, and alkyl halides, which do not generally yield molecular or quasi-molecular ions.

#### 4.2.5 The reaction of $\text{Si}_{\text{scr}}$ with epoxides

The reaction of epoxides with scribed silicon is unique in that no precedent for this chemistry on bare silicon (reconstructed) existed. To the extent that they have been studied, monolayers of monoepoxides on scribed silicon exhibit the same general wetting, XPS, and ToF-SIMS properties as the other monolayers (see above).<sup>16</sup> The mechanism by which epoxides react with the surface is unknown, although the authors favor a radical mechanism that ultimately leads to a five-membered ring that contains two silicon, two carbon, and one oxygen atom.

#### 4.2.6 The reaction of Si<sub>scr</sub> with aldehydes

Aldehydes react with unpassivated<sup>46,49,50</sup> and scribed silicon.<sup>17</sup> They exhibit the same general wetting, XPS, and ToF-SIMS behavior of the other reactive species that have been studied. The mechanism of monolayer formation is probably similar to aldehyde chemisorption onto Si(100) –  $2 \times 1$  and Si(111) –  $7 \times 7$ .<sup>46,49,50</sup> The ToF-SIMS data of the homologous series of aldehydes on scribed silicon suggests an even-odd effect, which is indicative of a degree of ordering and uniformity of attachment of alkyl chains on the surface.<sup>17</sup>

#### 4.2.7 Preparation of mixed monolayers on Si<sub>scr</sub>

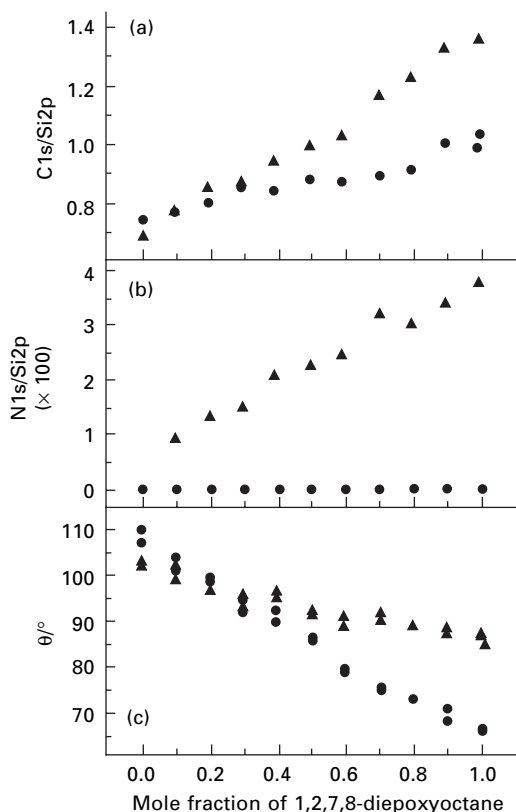
An important goal of materials chemistry is the preparation of materials with finely tuned properties, and the physical and chemical properties of surfaces can be varied by making mixed monolayers from two different adsorbates.<sup>52,67,68</sup> In the case of scribed silicon, mixed monolayers of 1-decene and 1-octadecene,<sup>15</sup> 1-decene and 1-decanol,<sup>15</sup> and 1,2-epoxyoctane and 1,2,7,8-diepoxyoctane<sup>16</sup> have been prepared. In contrast to results for thiols on gold,<sup>67</sup> in all of these systems it appears that there is close to a linear relationship between surface composition and solution composition, suggesting kinetic, and not thermodynamic control over monolayer formation.

#### 4.2.8 Preparation of functionalized monolayers on Si<sub>scr</sub>

Another significant goal of surface modification is the preparation of surfaces with reactive functional groups. The general strategy for creating reactive monolayers on Si<sub>scr</sub> has been to employ bifunctional compounds of the form Z(CH<sub>2</sub>)<sub>n</sub>Z. Two such compounds (1,4-dibromobutane (Br(CH<sub>2</sub>)<sub>4</sub>Br)<sup>14</sup> and 1, 2, 7, 8-diepoxyoctane<sup>16</sup>) have been investigated. Characterization of the monolayer prepared from 1, 4-dibromobutane by high resolution XPS showed two carbon signals in a 1:3 ratio. The smaller signal was chemically shifted to lower kinetic energy (higher binding energy), indicating that the carbon from this signal is bonded to a species more electronegative than itself, i.e., bromine – under the conditions used to analyze the monolayer, the chemical shift due to silicon would be difficult to detect. The Br3d signal also showed two forms of bromine, consistent with bromine bonded to carbon, and bromine bonded to silicon. Peak positions from comparison spectra of a monolayer made from 1-bromopentane confirmed these assignments.

A surface modified by scribing under 1,2,7,8-diepoxyoctane was similarly compared to silicon scribed under 1,2-epoxyoctane. Consistent with formation of a functionalized (epoxide-terminated) surface from 1,2,7,8-diepoxyoctane were a lower water contact angle, more chemically shifted carbon by XPS, and a slightly higher C1s/Si2p XPS ratio (the density of reactive functional

groups is higher in the diepoxide than in the monoepoxide). More significantly, it was shown that a monolayer prepared from 1,2,7,8-diepoxyoctane, as well as a series of mixed monolayers of 1,2,7,8-diepoxyoctane and 1,2-epoxyoctane were amine-reactive (see Fig. 4.3). Thus, a reactive surface on scribed silicon can be prepared in one step from a single, or simple mixture, of reagents.



**4.3 Physical properties of mixed monolayers prepared by scribing silicon under binary solutions of 1,2-epoxyoctane and 1,2,7,8-diepoxyoctane before (circles) and after (triangles) reaction with 1-amino-octane: (a) C1s/Si2p XPS uncorrected area ratio, (b) N1s/Si2p XPS uncorrected area ratio, and (c) sessile water contact angles. Figure used with permission from *Angewandte Chemie International Edition* (2003, 42, 4046–4049).**

## 4.3 Chemomechanical nanopatterning of silicon<sup>31</sup>

### 4.3.1 Introduction

Extending chemomechanical surface functionalization to nanometer scale features is realized by using an atomic force microscope (AFM) to scribe a

hydrogen-terminated silicon surface.<sup>31</sup> Chemomechanical patterning by AFM uses small forces ( $\mu\text{N}$  down to  $\text{pN}$ ) on small probes ( $<10$  nm tip radii) to strain or break a small number of chemical bonds. Using this technique we have created lines with widths down to 20 nm. This method employs an AFM fluid cell to immerse the AFM probe and silicon surface in a reactive liquid. The AFM uses tips that are much smaller than other chemomechanical probes that have been employed.<sup>13,30</sup> It also provides improved force regulation so that surface damage can be minimized and feature size carefully controlled. In addition, *in-situ* characterization can be performed with the same AFM tip used to create the features.

The steps of chemomechanical surface functionalization with an AFM are (i) preparation of a flat hydrogen-terminated silicon substrate (the AFM tip struggles to penetrate through a layer of oxide on silicon), (ii) wetting the surface with a reactive compound, and (iii) scribing the surface with an AFM probe. After scribing, the patterns are characterized by AFM, lateral force microscopy (LFM), scanning electron microscopy (SEM), and time-of-flight secondary ion mass spectroscopy (ToF-SIMS).

### 4.3.2 Experimental

#### *Instrumentation*

A Digital Instruments (Santa Barbara, CA, USA) Dimension 3100 AFM, equipped with a motorized optical microscope, a motorized stage, a fluid cell, a Nanoscope IIIa controller, and Nanoscope III version 4.42r8 software, were used for the AFM work.

#### *Surface preparation*

All preparations were performed under ambient conditions without any special treatment or degassing of chemicals. Prime, phosphorus-doped, n-type Si (111) wafers (1.0–5.6  $\text{m}\Omega\text{-cm}$  resistivity) were cleaved into chips approximately  $1/2$  inch square. The chips were cleaned and etched to produce a flat, hydrogen-terminated silicon surface.<sup>69</sup> This was done by rinsing with acetone, drying with  $\text{N}_2$ , immersing in 3:7  $\text{H}_2\text{O}_2\text{:H}_2\text{SO}_4$ , for ten minutes at 100–130 °C to remove contaminants, rinsing for  $\sim 1$  minute with Milli-Q-water and drying with  $\text{N}_2$ . The chips were finally dipped in 40%  $\text{NH}_4\text{F}$  for seven minutes to remove the native oxide from the surface, rinsed for  $\sim 10$  seconds with Milli-Q-water, and blown dry with  $\text{N}_2$ . Warning: the  $\text{H}_2\text{O}_2\text{:H}_2\text{SO}_4$  and  $\text{NH}_4\text{F}$  solutions are extremely dangerous.

#### *Scribing the patterns*

Within an hour after the  $\text{NH}_4\text{F}$  etch, the silicon wafers were wet with a

reactive liquid and scribed with an AFM probe. The surface was wet with a scribing liquid. We used either 3,3,4,4,5,5,6,6,7,7,8,8,9,9,10,10,10-heptafluoro-1-decene ( $\text{CF}_3(\text{CF}_2)_7\text{CH}=\text{CH}_2$ ), (Aldrich, 99%), 1-hexadecene ( $\text{CH}_3(\text{CH}_2)_{13}\text{CH}=\text{CH}_2$ ), (Aldrich, 92%), 1-Octanol ( $\text{CH}_3(\text{CH}_2)_6\text{CH}_2\text{OH}$ ), (Fisher Scientific, Certified), or 1,8-dibromooctane (Aldrich, 98%). Compounds were used as received. Lines and patterns were scribed by executing programmed movements of the AFM tip with feedback turned off. z-direction movements were used to control the loading force, and x-y movements generated the pattern. Square patches of functionalized regions were scribed in silicon by engaging the tip in imaging mode. In this case, feedback was used and the engagement force was increased by adjusting the feedback voltage set point. The x,y-dimensions of the patch were determined by the scan size of the image. Immediately after scribing, the chips were rinsed with ethanol (~1 min), then with Milli-Q-water (~1 min), and blown dry with  $\text{N}_2$ .

#### *Force characterization*

The force the tip exerts on the surface was determined using  $F = -kz$ , where  $k$  is the spring constant of the cantilever and  $z$  is the vertical displacement. When scribing was performed under feedback control,  $z$  was determined using  $z = S\Delta V$ , where  $S$  is the AFM detector sensitivity and  $\Delta V$  is the voltage difference between the set point voltage and the pre-engage vertical deflection voltage of the cantilever. We used high spring constant ( $k = 23$  to  $91/\text{m}$ ) silicon-based AFM tips coated with a 10-nm wear resistive silicon nitride coating, purchased from  $\mu\text{masch}$  (Tallinn, Estonia). The spring constant of each cantilever was determined using  $k = \frac{Ewt^3}{2l^3}$ , which incorporates the parallel beam approximation.<sup>70</sup> The length  $l$  and width  $w$  of the cantilevers were defined lithographically to within 5% variation, but the thickness  $t$  of the cantilevers varied by 15%. To obtain a more accurate cantilever thickness, the resonant frequency  $f$  was measured and the thickness of the cantilever was determined using  $t \approx 2\pi fl^2 \sqrt{\frac{\rho}{E}}$  where  $E$  and  $\rho$  are the Young's modulus and the density of silicon.<sup>70</sup>

### 4.3.3 Results and discussion

#### *AFM scribing*

Lines and patches were first characterized *in situ* by AFM with the same tip used to scribe them. The samples were then analyzed with a Philips (Hillsboro, OR, USA) XL 30 S-FEG SEM with a low acceleration voltage (1–5 kV). All

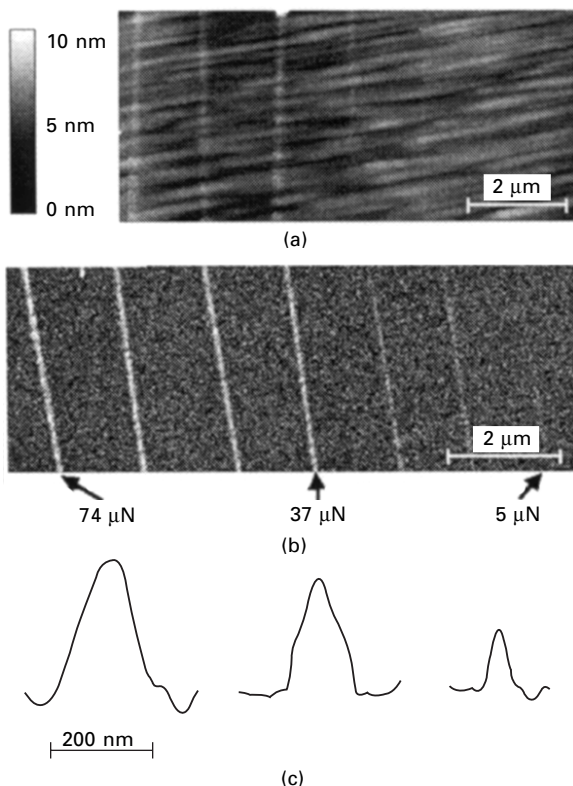
images are secondary electron images taken with an annular through-the-lens detector. Patches scribed under  $\text{CF}_3(\text{CF}_2)_7\text{CH}=\text{CH}_2$  were analyzed with a Physical Electronics (Eden Prairie, MN, USA) TRIFT II ToF-SIMS. Ion images were acquired in negative and positive ion modes using a primary ion beam potential of 28 kV and a beam current of 600 pA. The beam size was 0.2  $\mu\text{m}$ . Data were acquired over the mass range  $m/z$  5 to  $m/z$  1200, and the primary ion beam was rastered over a 75  $\mu\text{m}$  by 75  $\mu\text{m}$  area to cover the areas patterned with the AFM. Ion images were acquired for a four-minute period from each patterned area.

#### *Feature characterization by AFM and SEM*

Two major factors that control the dimensions of scribed lines are the force applied by the AFM tip and the tip shape. In Fig. 4.4 we show an AFM image, an SEM image, and profile plots derived from the SEM data of lines scribed on silicon while it was wet with  $\text{CF}_3(\text{CF}_2)_7\text{CH}=\text{CH}_2$ . These lines were patterned at various forces yielding wider lines at higher forces. By AFM, the five widest lines are discernable (Fig. 4.4(a)), but surface roughness (1 nm rms) did not allow resolution of the finer lines. However, all seven of the lines can be resolved by SEM (Fig. 4.4(b)). This contrast points to a difference in work function between scribed and unscribed regions on silicon. Line widths were measured by taking the full width at half maximum of the profile plots (see Fig. 4.4(c)). The line widths were 110 nm (74  $\mu\text{N}$  tip force), 85 nm (37  $\mu\text{N}$  tip force), and 30 nm (5  $\mu\text{N}$  tip force). A comparison of the AFM and SEM images in Fig. 4.4 shows that the *in situ* AFM imaging of the patterns at a tip force of 0.25  $\mu\text{N}$  can be nondestructive.

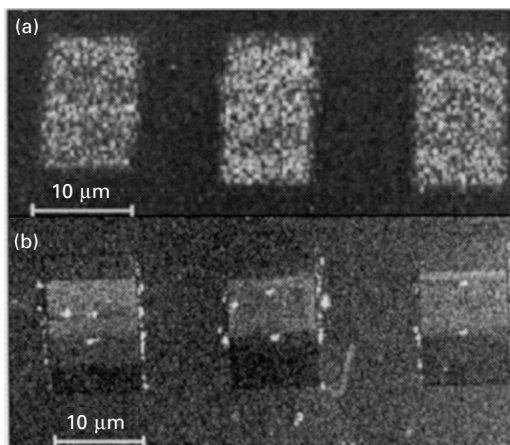
#### *Feature characterization by ToF-SIMS*

To verify chemical functionalization of the patterned features, we analyzed scribed patches with ToF-SIMS. In its scanning mode this instrument acts as a chemical microscope. Figure 4.5(a) shows a ToF-SIMS image of the  $\text{F}^-$  ion of a sample prepared by scribing rectangular patches on silicon that was wet with  $\text{CF}_3(\text{CF}_2)_7\text{CH}=\text{CH}_2$ . This image shows a clear enhancement of  $\text{F}^-$  in the scribed regions over the unscribed background. It was anticipated that good ion yields would be obtained from  $\text{F}^-$  because of fluorine's high electronegativity. There was also positive contrast between the scribed and unscribed regions in negative and positive spectra from  $\text{SiF}^+$ ,  $\text{SiF}^-$ ,  $\text{C}^+$ , and  $\text{O}^-$  (not shown). The  $\text{SiF}^+$  and  $\text{SiF}^-$  ions may be the result of sputter-induced decomposition (followed by recombination) in the near-surface region. The  $\text{O}^-$  ion suggests that more oxidation of the silicon substrate occurred in the scribed than unscribed regions. Oxidation of the silicon substrate following scribing was also observed in macroscopic scribing studies.<sup>15,23,30</sup> Negative contrast,



4.4 (a) *In situ* AFM and (b) corresponding SEM images of seven lines scribed on silicon in the presence of  $\text{CF}_3(\text{CF}_2)_7\text{CH}=\text{CH}_2$ . Forces were, starting from the left, 74, 62, 49, 37, 25, 12, and 5  $\mu\text{N}$ , and the tip speed was 10  $\mu\text{m/s}$ . (c) Profile plots of three of the lines in part (b). The arrows indicate the line that each of the plots were made from and the labels refer to the force used to scribe the lines. The vertical axis is the grayscale value. Figure used with permission from *Applied Physics Letters* (2003, **82**, 808–810).

meaning that fewer ions were produced from the scribed regions, was observed in the  $\text{Si}^+$  and  $\text{SiH}^+$  images. These latter results are consistent with monolayer quantities of material covering the silicon substrate and removal of surface Si-H moieties by scribing. Figure 4.5 also contains an SEM image of the same array of patches to demonstrate that the SEM contrast is consistent with the functionality of the regions as determined by ToF-SIMS. The variation in contrast of the patches in the SEM images is due to the fact that the AFM tip passed over the surface more than once in some regions of the patch as the surface was scribed.



4.5 (a) A ToF-SIMS image of the  $F^-$  ion and (b) a SEM image of the same array of patches produced by scribing in the presence of  $CF_3(CF_2)_7CH=CH_2$  with a force of 13 mN, a scan size of 10 mm, a scan rate of 5 Hz, 256 lines per frame. Figure used with permission from *Applied Physics Letters* (2003, 82, 808–810).

#### 4.3.4 Conclusion

Patterns scribed with an AFM in the presence of  $CF_3(CF_2)_7CH=CH_2$  have been shown. Similar AFM and SEM results were also obtained using the same procedure with  $CH_3(CH_2)_{13}CH=CH_2$ ,  $CH_3(CH_2)_6CH_2OH$  and 1,8-dibromooctane.

We expect that all of the chemistry that has previously been developed in macroscopic scribing studies will be applicable to AFM patterning of silicon. Although patterning with an AFM tip is slow, combining this approach with parallel AFM tip operation<sup>71</sup> could allow large areas to be patterned rapidly.

### 4.4 Patterning silicon at the micron scale

#### 4.4.1 Introduction

Mechanical characteristics that affect scribed feature attributes include the shape and hardness of the scribing tool, the force applied during etching, and the scribing speed.<sup>27</sup> A scribing system consists of a scribing tool, end-effector, and motion control mechanism, as shown in Fig. 4.2. Diamond tips are common scribing tools for the scribing process, but other materials have also been demonstrated, including tungsten carbide balls.<sup>30</sup> The end-effector holds the scribing tool and applies the force to the surface to be scribed. Several types of end-effectors have been employed, including spring-loaded diamond tips, which can also be employed in the apparatus shown in

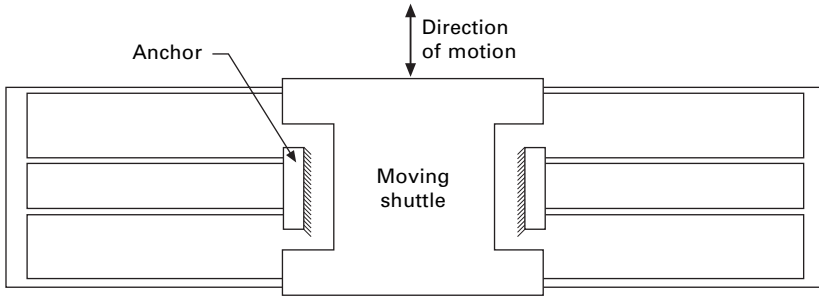
Fig. 4.2.<sup>13</sup> The end-effector is connected to a motion control system that controls translation in three axes.

This section describes an end-effector that was developed to achieve improved performance over early designs.<sup>13</sup> Three primary characteristics were considered in the development of a precision end-effector for chemomechanical scribing (i) It should be passively controlled. Passive control is desirable because active control of small forces is often difficult and a passively controlled device is easily implemented. (ii) It should have low axial stiffness. The axial direction is perpendicular to the scribed surface and the axial force is the force applied to the scribed surface. A low stiffness is required to produce a low force from a relatively large deflection. (iii) It should have high lateral stiffness, i.e., be stiff in the direction parallel to the scribed surface. The end-effector should remain stiff in this direction throughout its motion.

A 'compliant mechanism' end-effector was designed to achieve these three major characteristics. A compliant mechanism transfers or transforms motion, force, or energy through the deflection of flexible members.<sup>26</sup> A compliant mechanism was used for the end-effector design for three reasons. First, compliant mechanisms achieve their motion without conventional hinges which makes them inherently frictionless. This feature makes it possible to obtain low axial stiffness. Second, compliant mechanisms are ideal for adverse environments. Scribing is performed in the presence of reactive chemicals that may damage hinges that are used in a kinematic linkage design. Since a compliant mechanism has no hinges, it is less likely that it will be damaged by chemicals. Finally a compliant mechanism was used because performance can be passively controlled. Compliant mechanism analysis methods allow the end-effector to be designed with the desired performance requirements.

#### 4.4.2 Results and discussion

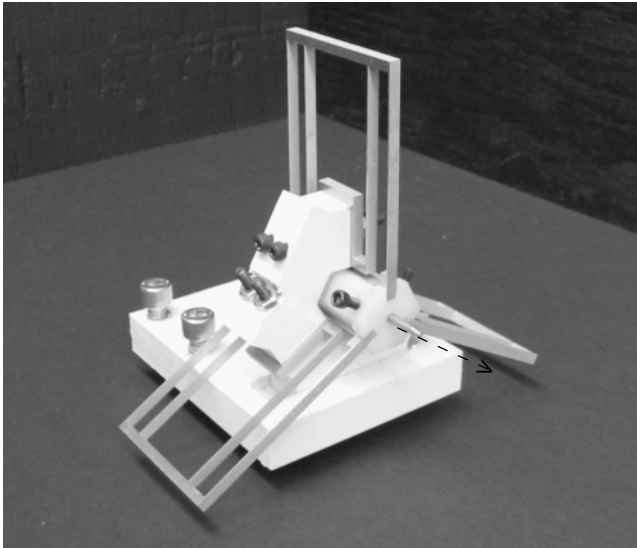
Several compliant mechanism configurations were considered for potential use as an end-effector, and a folded-beam linear motion mechanism was ultimately found to be most satisfactory. This mechanism (Fig. 4.6) provides the following advantages. (i) It has one degree-of-freedom that allows the scribing tool to translate, but it constrains motion in other directions. (ii) The configuration can be designed for low force output. The force applied to the surface is controlled by deflecting the mechanism to a prescribed displacement, e.g., a small deflection is applied to achieve a small force. This also allows one mechanism to apply a range of forces. (iii) The folded-beam linear motion mechanism can be designed to create a near-constant axial stiffness over the range of motion. This allows the device to apply low axial forces while being relatively insensitive to displacement.



4.6 A folded beam mechanism with two beam segments in a single plane.

The compliant end-effector was constructed of three folded-beam segments positioned at an angle of  $120^\circ$  to each other, as shown in Fig. 4.7. This configuration was chosen because it provides a high lateral stiffness and low axial stiffness.

Linear-elastic beam theory can be used to predict the force-deflection relationships for beams with relatively small deflections. The analysis assumes that the curvature of the beam can be approximated by the second derivative of the deflection. This assumption is valid when the slope of a deflected beam is negligible. The resulting force-deflection equation is



4.7 The compliant end-effector for scribing. Three folded beam segments are combined  $120^\circ$  apart to provide high lateral stiffness and low axial stiffness. The dashed arrow indicates the axial movement of the end-effector.

$$F = \frac{nEbh^3}{L^3} \delta \quad 4.5$$

where  $F$  is the axial scribing force,  $\delta$  is the end-effector deflection, and  $n$  is the number of folded beam segments in the system. The other parameters represent the material properties and geometry of the flexible beams, including their out-of-plane width ( $b$ ), thickness ( $h$ ), length ( $L$ ), and Young's modulus ( $E$ ). This linear relationship between the axial force and the axial deflection allows the desired force magnitude to be selected by providing the corresponding displacement to the end-effector. Parameter values used for the end-effector design were as follows:  $n = 3$ ,  $L = 50.8$  mm,  $b = 3.18$  mm,  $h = 0.38$  mm, and  $E = 71.7$  GPa (aluminum). A nonlinear, large deflection analysis of the device has also been completed.<sup>28</sup> Finite element analysis predicts the ratio of lateral stiffness to axial stiffness to be nearly 1000:1. A fatigue analysis predicted that the mechanism could achieve approximately 1 billion cycles without failure.

Testing showed that the device can achieve low forces, is inherently frictionless, and can keep the tip movement linear. Low forces produce lines that are smooth, uniform and that exhibit little chipping. The end-effector is passively controlled, has a high axial/lateral stiffness ratio, and can be designed for a range of force magnitudes.

## 4.5 Applications I: Preparation of surfaces for matrix-assisted laser desorption/ionization (MALDI) mass spectrometry

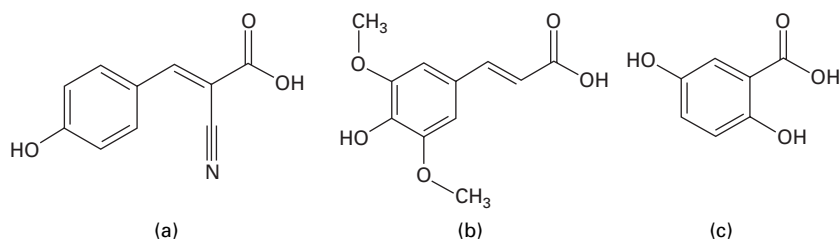
### 4.5.1 Introduction

The matrix-assisted laser desorption/ionization (MALDI) technique was developed in 1987 for the ionization of relatively large polypeptides and proteins.<sup>72</sup> To date, MALDI TOF has been successfully used for the analysis of a wide range of different analyte molecules including peptides, proteins, oligosaccharides, oligonucleotides, lipids, complex carbohydrates, complexes of metal ions with biomolecules,<sup>73-79</sup> synthetic polymers,<sup>80-86</sup> etc. A great advantage of MALDI TOF mass spectrometry is that the process of soft-ionization causes little or no fragmentation of analytes,<sup>87</sup> allowing the molecular ions of analytes to be identified, even within mixtures. Furthermore, if relatively pure material is available, unequivocal identification of that material can be achieved by a process known as mass-mapping.<sup>88-90</sup>

The mechanism of MALDI is not fully understood yet.<sup>91</sup> It is believed that the laser-light absorbing matrix molecules are excited by high-intensity, short-duration laser pulses. The absorbed energy is then transferred to the analyte molecules, causing them to be desorbed and ionized. Since the analyte

does not directly absorb the energy of the laser, it generally does not undergo fragmentation, which is important for determining the mass of intact molecular ions of the analyte. Intact analyte masses facilitate their identification.

The key aspect of MALDI-MS is to mix the analyte with a large excess of highly absorbing small organic molecules (the matrix), such as  $\alpha$ -cyano-4-hydroxycinnamic acid (CHCA), sinapinic acid (SA), or 2,5-dihydroxybenzoic acid (DHB) (Fig. 4.8), and to then allow the mixture droplet to dry on a MALDI sample support into a crystalline deposit.<sup>91</sup> Typically, a conventional MALDI-MS sample plate is made of stainless steel, on which  $10 \times 10$  sample supports (100 2 mm diameter circles) are etched. Usually, 0.5–2.0  $\mu\text{L}$  of 0.1–10 pmol/ $\mu\text{L}$  peptide or protein solution and the same volume of a 10 g/L matrix solution are applied on each sample support. As soon as the dried analyte-matrix co-crystallization mixture is loaded into the mass spectrometer, a spectrum can be generated within seconds.



4.8 Structures of (a)  $\alpha$ -cyano-4-hydroxycinnamic acid (CHCA), (b) sinapinic acid (SA), and (c) 2,5-dihydroxybenzoic acid (DHB).

MALDI TOF mass spectrometry is one of the most important tools for the analysis of the proteome, i.e., proteomics.<sup>92</sup> In addition, it is the major tool for the analysis of the products of peptide synthesis.<sup>93–96</sup> However, because the crystallization of the analyte-matrix mixture on a sample plate is heterogeneous, large variations in signal and noise often occur inside a sample support and from support to support. As mentioned, typically, the size of a sample support is over 100 times that of the cross-section of the ionization laser beam (*ca.* 200  $\mu\text{m}$  diameter). That is, the laser beam hits only a small part of a sample support, and the signal intensity varies significantly and data reproducibility between supports is usually poor. Thus the need to search for ‘hot spots,’ which are regions in an analyte/matrix spot that give significant signals. These problems also limit analysis sensitivity, which is a critical issue for the analysis of many biomolecules. Accordingly, if the cross-section of the ionization laser beam could be increased to the size of the sample supports, or, on the contrary, if the size of the sample supports could be decreased down to that of the cross-section of the laser beam, both reproducibility and sensitivity of MALDI-MS analysis might be improved significantly.

It has previously been shown that the idea of decreasing the size of MALDI-MS sample supports does work.<sup>97-102</sup> One such approach is to etch directly *ca.* 200  $\mu\text{m}$  diameter nanovials on a single crystal silicon wafer or another material by using micromachining methods, which usually consist of multi-step photolithography.<sup>97-99,101</sup> This pathway is usually coupled with a microdispenser for handling analyte-matrix mixture solutions because of the nanoliter scale capacities of these nanovials. The other approach is to use hydrophobic-hydrophilic interactions to focus the analyte-matrix droplets onto the hydrophilic anchors of *ca.* 200  $\mu\text{m}$  diameter. These hydrophilic anchors are created on a hydrophobic polymer layer coated on a conventional sample plate,<sup>100</sup> or on a gold-coated silicon wafer with hydrophobic monolayers grown on it.<sup>102</sup> In the case of the gold-coated substrate, this pathway also uses complicated micromachining methods to make a mask or a stamp for transferring the patterns of anchors to the substrate. Gold-sputtering equipment is also required. Thus, although designs of the miniaturized MALDI-MS sample supports have been successful in research, they may not be applicable for routine MALDI-MS analysis because of the time and cost required to make them. It is apparent that a more straightforward, miniaturized MALDI-MS sample support that can be made by MALDI-MS operators or made commercially at low cost would be very valuable for MALDI-MS analyses.

Here it is shown that a chemomechanical approach to silicon surface modification can be used to create the desired substrates for MALDI. Briefly, miniaturized MALDI-MS sample supports were made on silicon by (i) silanizing a silicon chip with a neat silane<sup>103</sup> in a common laboratory oven to obtain a very hydrophobic surface, and (ii) scribing a pattern on this silanized surface in the presence of water. Water is believed to react chemomechanically with silicon during scribing to create hydrophilic Si-OH groups on the scribed area. This patterning can be completed in a few minutes. Once droplets of a peptide-DHB water solution are loaded onto these sample supports, they gradually dry in the air and finally focus and crystallize on top of the sample supports (hydrophilic anchors) that were scribed on the hydrophobic substrate. An important finding from these studies is that the shape of the scribed feature (cross, circle, or round patch) influences the intensity and reproducibility of the MALDI signal.

## 4.5.2 Experimental

### *Surface silanization*

Silicon chips were cleaned and dried,<sup>13,23</sup> and then silanized<sup>103</sup> with neat trichloro(1H, 1H, 2H, 2H-perfluorooctyl)silane in a common laboratory oven at 90 °C for 15 minutes. After this treatment the advancing water contact angle of the surface was 120° or higher.

### *Scribing the silanized surface*

The silanized silicon chip was wet with deionized water and a pattern of *ca.* 200  $\mu\text{m}$  diameter hydrophilic regions (round patches, single circles and single crosses) was scribed on it using a diamond tip loaded in the end-effector attached to the three translation stages shown in Fig. 4.2.

### *Sample handling*

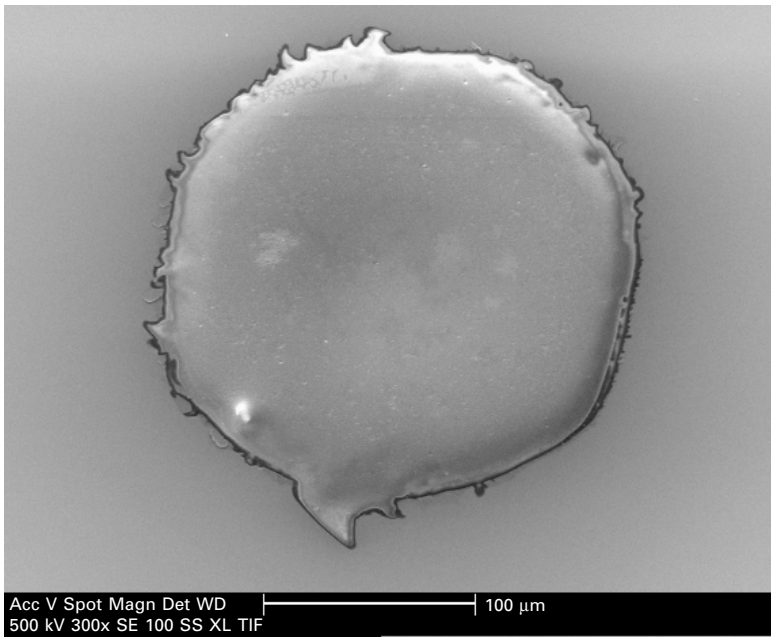
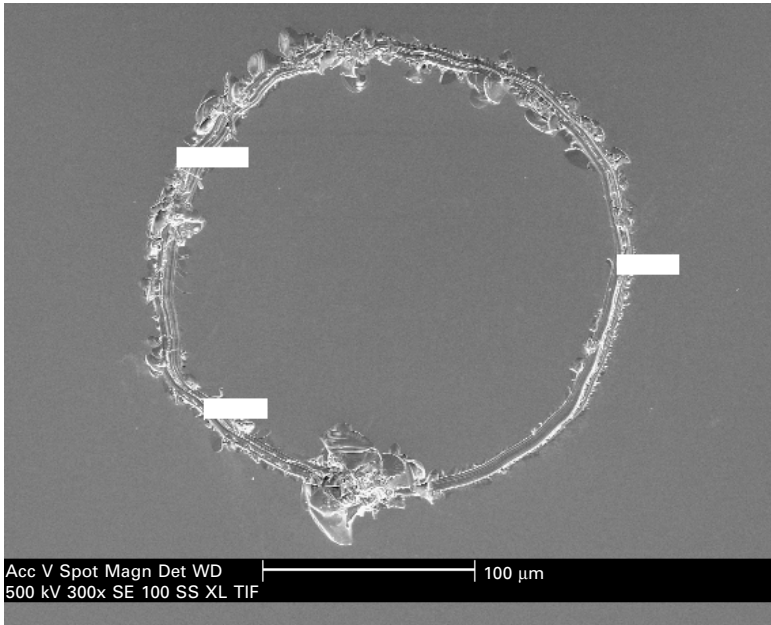
Specific sample handling equipment, e.g., a microdispenser, is usually required for handling very small volumes of solutions onto miniaturized MALDI-MS sample supports. However, in the designs considered here, because much more solution can be loaded onto each sample support, a manual micro-syringe was sufficient for the sample handling. This method is very similar to that used in conventional MALDI-MS. The silicon substrate with a scribed pattern of sample supports was attached to a homebuilt MALDI plate, similar to a commercially available PAGE gel MALDI plate that has a recessed area in its center. The attachment was made with single-sided tape over the edge of plate, and not with double-sided tape, which would electrically insulate it. MALDI-MS analysis was then performed, except there is no need to search for 'sweet spots'.

It was found that only limited amounts of analyte-matrix mixture could be focused and crystallized on each sample support for the three different shapes. Thus, for each sample support, only 0.3  $\mu\text{l}$  of analyte-matrix mixture solution (50:50, v/v) is loaded, which is the minimum volume that a manual micro-syringe (1  $\mu\text{l}$ ) can handle for the hydrophobic silicon chips. A watch glass placed over the surface was usually used to slow down the drying speed of the loaded sample droplets for better focusing effects.

### 4.5.3 Results and discussion

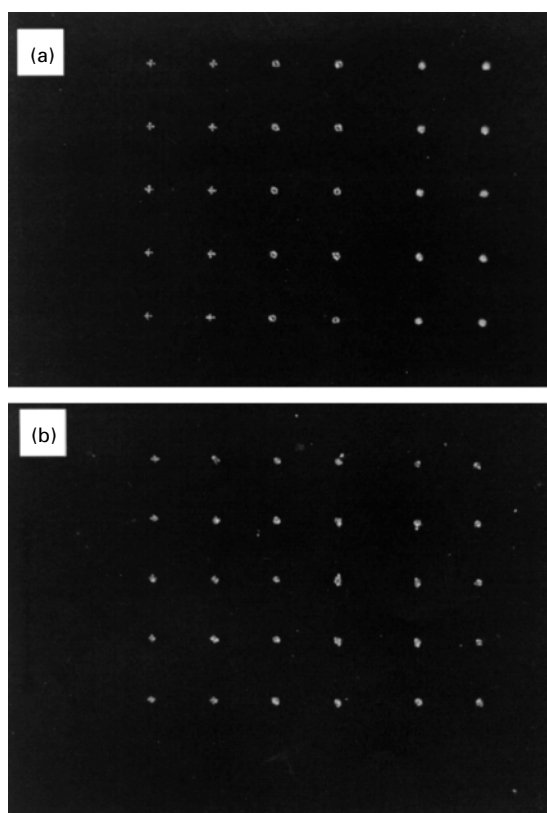
SEM and optical microscope pictures of circular miniaturized MALDI-MS sample supports (Fig. 4.9) show that annular sample supports have good focusing capability. Unfortunately, MALDI-MS analysis showed no signal for the analyte focused in the circles in Fig. 4.9 because the sample mixture and matrix ( $\alpha$ -CHC) did not crystallize.  $\alpha$ -CHC is a less than ideal matrix for this application because it is not soluble in water and an organic cosolvent must be used. The presence of this organic material lowers the surface tension of the droplet and makes focusing more difficult. Thus, DHB (see Fig. 4.8), a water soluble matrix material, was chosen as the matrix for these studies. 20 mM DHB was used as the matrix solution in subsequent studies because it produced better signals than 10 mM or 5 mM DHB.

In order to investigate the influence that the geometry of the scribed feature might have on the MALDI signal, a silicon surface was scribed with

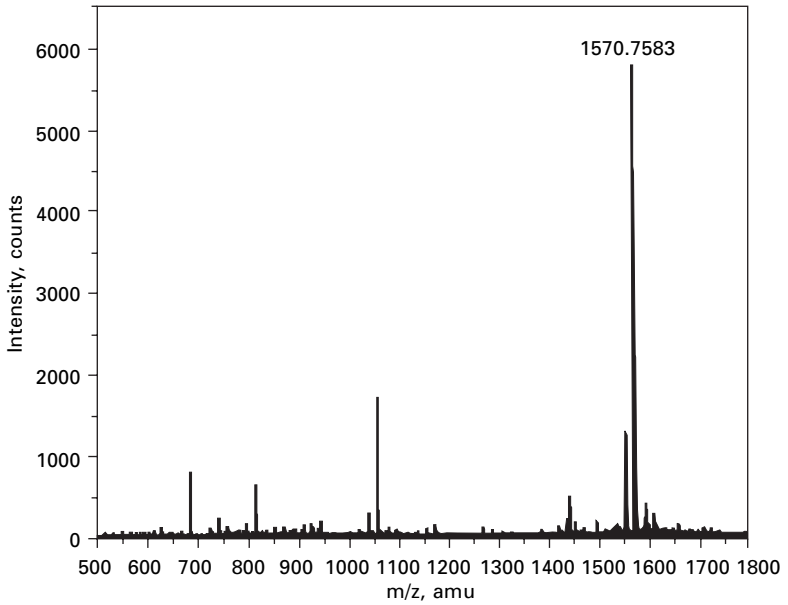


4.9 SEM pictures of a bare circular sample support (top) and a circular sample support loaded with 0.3  $\mu\text{l}$  1.0 pmol/ $\mu\text{l}$  Glufibrinopeptide B plus 0.3  $\mu\text{l}$  1 mg/ml  $\alpha$ -CHC (bottom).

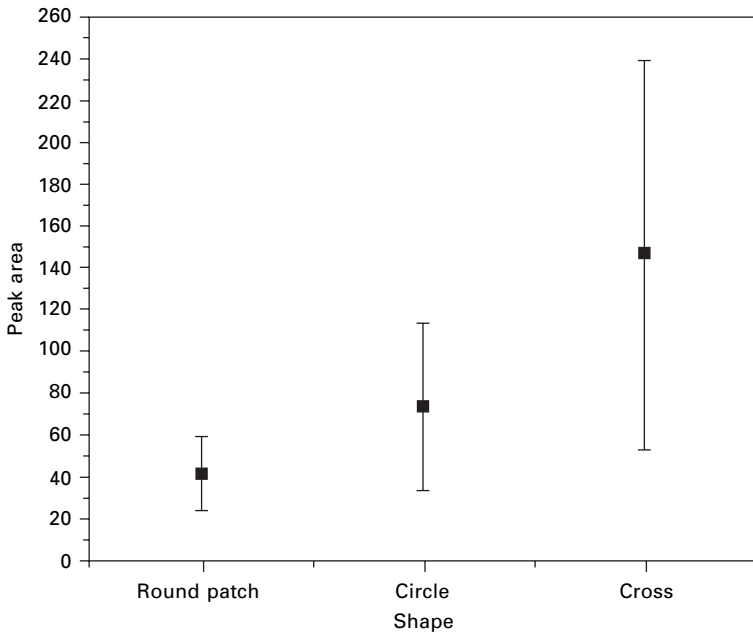
ten crosses, ten circles and ten round patches (see Fig. 4.10(a)). Figure 4.10(b) shows this same sample plate loaded with sample droplets of DHB and a peptide (glufibrinopeptide B) that focused and dried/crystallized on the surface. MALDI-MS of the focused spots showed good mass spectra for the peptide (Fig. 4.11). Interestingly, the most intense signals were obtained from the crosses, followed by the circles, which were followed by the round patches (see Fig. 4.12). It is also of interest that the standard deviation of the measurements (the error bars) increase with increasing signal intensity, although in all cases the results are far more reproducible than those typically obtained with conventional MALDI. These results correlate well with the signal-to-noise (S/N) ratios for these data. The average S/N ratios and standard deviations for the crosses, circles, and round patches were  $194.6 \pm 102.1$ ,  $113.2 \pm 48.2$ , and  $89.4 \pm 23.3$ . A possible explanation for these results is that the smooth, hydrophobic monolayer releases the matrix and analyte more readily than



4.10 A pattern of ten crosses (left), ten circles (middle) and ten round patches (right) sample supports on a hydrophobic silicon chip (a) as scribed, and (b) after droplets of  $0.3 \mu\text{l}$  Glufibrinopeptide B and DHB matrix had focused/dried.



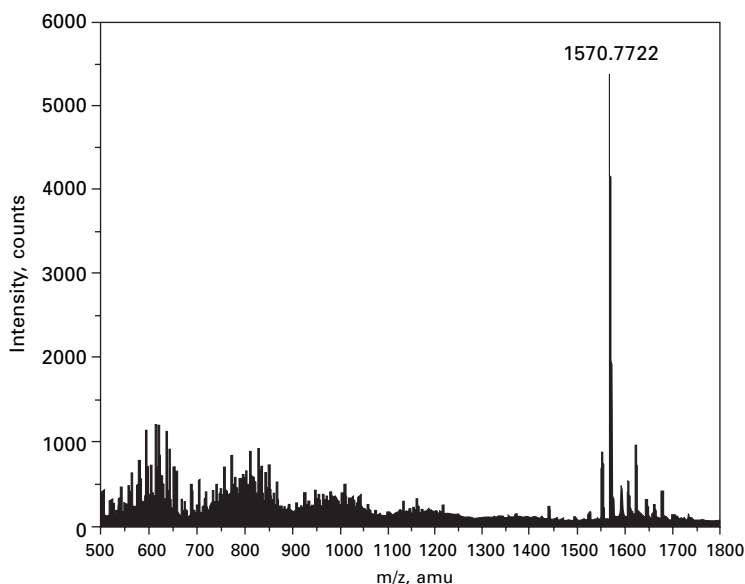
4.11 A MALDI-MS spectrum of a 50:50 mixture (v/v) of 0.3  $\mu\text{L}$  1.0 pmol/ $\mu\text{L}$  glufibrinopeptide B solution and 20 mM DHB solution dried on a miniaturized MALDI-MS cross-shaped sample support on silicon.



4.12 Sensitivity and reproducibility of the glufibrinopeptide B data collected with the miniaturized MALDI-MS sample supports.

the hydrophilic scribed regions. Indeed, we have observed that dried droplets of matrix and analyte on anchor regions with little hydrophilic area under them are fairly easily knocked free by the laser beam.

Because glass slides are much cheaper and more readily available to most researchers than silicon wafers, and silane chemistry should work equally as well on glass slides as on silicon's native oxide layer,<sup>104</sup> the same chemistry that has been described in this section (surface silanization to make the silicon surface hydrophobic, followed by scribing under water) was also performed with glass slides. Figure 4.13 shows data that were obtained using a functionalized glass slide. The spectrum obtained from silicon wafers (see, for example, Fig. 4.11) is very similar to that obtained using a conventional (metal) MALDI sample plate, while the spectra obtained using glass sample supports differs from (is not as clean as) those taken with metal or silicon. We attribute this difference to the insulating nature of glass.



4.13 A MALDI-MS spectrum of a 50:50 mixture (v/v) of 0.3 mL 1.0 pmol/mL glufibrinopeptide B solution and 20 mM DHB solution dried on a miniaturized MALDI-MS cross-shaped sample support on glass.

#### 4.5.4 Conclusion

These preliminary studies show that miniaturized MALDI-MS sample supports can be made on silanized, hydrophobic silicon chips by scribing. These sample supports focus analyte-matrix water droplets on them. The MALDI-MS data collected with these sample supports showed good signal sensitivity

and reproducibility compared to conventional MALDI. These results point the way to a simple, readily fabricated sample support for MALDI.

## 4.6 Applications II: Preparation of masters for microcontact printing ( $\mu$ CP) by scribing<sup>105</sup>

Microcontact printing ( $\mu$ CP)<sup>106</sup> and replica molding (REM)<sup>106,107</sup> are powerful methods for surface modification and pattern transfer. In  $\mu$ CP an elastomeric stamp is cast from a patterned surface (a master). This master is typically made in a clean room using semiconductor processing equipment and techniques. Surface patterning is performed by coating the stamp with a compound of interest (an 'ink') and then pressing it against a surface to transfer the 'ink'. In REM a replica of a surface is made by first transferring its pattern to a polymer, to make its negative, and then transferring the pattern from the negative to another polymer. These two methods have been combined by Whitesides and coworkers who generated masters for  $\mu$ CP by laser ablation, cast poly(dimethylsiloxane) (PDMS) stamps (negatives) from these masters, and then cast replica PDMS stamps from these negatives.<sup>108</sup>

It has recently been shown that scribing can be used to make masters for  $\mu$ CP with 1–12  $\mu$ m features.<sup>105</sup> These masters can be rapidly made with high precision over large (many centimeter) areas using only a computer numerical controlled milling machine (a CNC), a diamond tip, and a tip holder (an end-effector). The CNC takes the place of the translation stages shown in Fig. 4.2.

Patterns are transferred from scribed glass microscope slides to poly(methylmethacrylate) (PMMA) by embossing. Elastomeric stamps in poly(dimethylsiloxane) (PDMS) are then cast<sup>109</sup> from the PMMA negatives.<sup>106</sup> The entire process of scribing the glass, embossing the PMMA, and casting the PDMS takes only a few hours. Microcontact printing is confirmed using ToF-SIMS. Because CNCs are readily available to a much larger number of researchers than the clean rooms, clean room equipment, or lasers that to date have been needed to prepare masters for  $\mu$ CP, this development<sup>105</sup> should make microcontact printing, and especially rapid prototyping with this method, much more accessible to the technical community.

## 4.7 Future trends

### 4.7.1 Chemistry

There are clearly many unexplored frontiers in the chemomechanical modification of surfaces and materials. Some of these include the functionalization of new substrates, the reaction between gas phase reagents and scribed surfaces, the reaction of other functional groups with scribed silicon, and the immobilization of biologically important molecules.

### *New substrates*

Because the chemistries of germanium and silicon are so similar, germanium, which was employed in semiconductor devices before silicon, is the next logical choice as a substrate for chemomechanical surface modification. And while it has the drawback of being considerably more expensive than silicon, germanium also has certain electronic advantages, including a higher hole mobility, and closer hole and electron mobilities than any other common semiconductor.

### *New functional groups*

In addition to those mentioned here, a number of other functional groups should react with  $\text{Si}_{\text{scr}}$ . We are particularly interested in the acid chlorides because bifunctional molecules of the form  $\text{ClC(O)(CH}_2)_2\text{C(O)Cl}$  are commercially available. These compounds may react with silicon at one end of the molecule to produce amine-, hydroxyl-, and sulfhydryl-reactive monolayers in a single step. Peptides, proteins, and DNA could then be tethered to these surfaces through known bioconjugate chemistry.<sup>110</sup>

## 4.7.2 AFM patterning

We do not believe that the 20 nm line widths that have been obtained by chemomechanical nano-patterning of silicon represent the smallest features that can be made with this technique. The probes used so far were hard silicon nitride coated tips with tip radii ranging from 20 to 30 nanometers and large force constants. Tips with smaller radii are commercially available and will be used in future studies. Ultimately AFM probes made of very short, mechanically attached carbon nanotubes<sup>111</sup> may be ideal scribing tools for producing the finest lines, but scribing of softer materials, like germanium, may be required with these scribes. The forces studied to date are also much larger than the minimum achievable by AFM. The extension to smaller forces will also be pursued in future work to determine the ultimate linewidth limit of this technique.

## 4.7.3 End-effector development

Future work in scribing systems will build on our experience at the macro level and with AFM tips to design and prove concepts for new mechanisms and tips that simplify the micro-scribing process. Scribing has been researched extensively at the macro-scale using a special compliant end-effector attached to an X-Y-Z positioner. It was specifically designed to be very flexible in the axial direction and stiff in the lateral directions in order to vary the scribing

force while maintaining alignment in the X-Y plane. Similarly, scribing using AFM tips has been studied.

While the use of AFM systems to perform scribing has been successful, the AFM tip was not designed for scribing and does not enjoy many of the operational and performance advantages of the specially designed macro-level scribing systems. In addition, the AFM machine is expensive and incorporates many features that are unnecessary for scribing.

The objective of this new work is to design and prove a concept for a mechanism to replace existing AFM cantilever suspension and probe tip systems. Four categories of specifications for this new system have been developed and compiled.

### *Passive mechanisms*

The first category, passive, relates to a desired improvement over the current system. The current process using an AFM relies on a number of time-consuming steps. In order to eliminate some of these steps the mechanism should be passive. It should maintain the desired scribing force with little need for feedback and initial measurements of surface contours. The user should also be able to vary the scribing force within a range without difficulty.

### *Precision*

The second group of characteristics relates to the mechanism's precision, which should be very precise and accurate. In order to achieve this the scribe mechanism should limit movement of the tip to an axis perpendicular to the surface being scribed. Therefore lateral forces should only deflect the tip a negligible amount. The mechanism must be able to operate at a fast scribing speed and maintain performance when dynamically loaded. Also the mechanism should be simple to calibrate and repeatable, with little or no hysteresis.

### *Fabrication requirements*

The third category, fabrication, groups together characteristics that are important from a fabrication standpoint. The mechanism must be reasonably possible to construct, and its materials must not react with chemicals used in chemo-mechanical scribing. The fabrication of the mechanism must also be capable of producing sufficiently sharp tips for scribing.

### *Array compatibility*

The final category relates to the future use of the scribing mechanism as part of an array. Researchers working with chemo-mechanical scribing predict

that many similar scribing mechanisms will be joined in an array to scribe multiple features simultaneously. Therefore it is important that the mechanisms have a small footprint and that it be possible to join it with other mechanisms into an array.

#### 4.7.4 MALDI

Here we identify four future directions for this research.

##### *Immobilization of a protease enzyme on a scribed patch*

The groundwork for protein immobilization onto scribed silicon has been laid.<sup>16</sup> Thus, it should be possible to immobilize protease enzymes onto silicon. It may then be possible to perform on-chip proteolytic digestions of some proteins and the subsequent MALDI-MS analyses of the digestion products for identification of unknown proteins of interest. This capability would be of great utility in proteomics.

##### *A study of the effect of line thickness and the effect of pattern shape (other than those tested) on signal*

It has been shown in this chapter that the shape of the scribed pattern strongly influences the intensity and reproducibility of the MALDI signal. Thus, other patterns will be investigated. These initial results also suggest that narrowing the line width will increase the signal.

##### *A study of other materials (other water-soluble matrices and peptides)*

Other water-soluble matrices and analytes, including peptides, proteins, DNA, synthetic polymers, etc., need to be investigated. The procedure for evaluating other analytes and matrices will be the same as that used with glufibrinopeptide B and DHB.

##### *A determination of the work life of the sample supports*

Long work life, i.e., reusability, is obviously preferred for the miniaturized sample supports. However, preliminary work indicates that the sample supports gradually lose their hydrophilicity so that their work life is limited. The work life of the sample supports will be measured as a function of the time they are left out in an open laboratory to contaminate. Attempts will be made to improve their work life by immobilizing a hydrophilic monolayer on the scribed patches that might be expected to release contamination better than

SiO<sub>2</sub>. Monolayers of polyethylene glycol on scribed silicon will be investigated for this purpose.

#### 4.7.5 Microcontact printing

The primary goal of research in this area would be to demonstrate the production and transfer of smaller (few micron to submicron) features.

### 4.8 References

1. Abbott N.L., Folkers J.P. and Whitesides G.M., Manipulation of the Wettability of Surfaces on the 0.1 to 1 Micrometer Scale Through Micromachining and Molecular Self-Assembly. *Science* 1992, **257**, 1380–1382.
2. Abbott N.L., Kumar A. and Whitesides G.M., Using Micromachining, Molecular Self-Assembly, and Wet Etching to Fabricate 0.1–1  $\mu\text{m}$ -Scale Structures of Gold and Silicon. *Chem. Mater.* 1994, **6**, 596–602.
3. Abbott N.L., Rolison D.R. and Whitesides G.M., Combining Micromachining and Molecular Self-Assembly To Fabricate Microelectrodes. *Langmuir* 1994, **10**, 2672–2682.
4. Abbott N.L., Whitesides G.M., Racz L.M. and Szekely J., Using Finite Element Analysis to Calculate the Shapes of Geometrically Confined Drops of Liquids on Patterned, Self-Assembled Monolayers: A New Method to Estimate Excess Interfacial Free Energies  $\gamma_{sv}-\gamma_{sl}$ . *Journal of the American Chemical Society* 1994, **116**, 290–294.
5. Xu S. and Liu G.-y., Nanometer-Scale Fabrication by Simultaneous Nanoshaving and Molecular Self-Assembly. *Langmuir* 1997, **13**, 127–129.
6. Linford M.R., Producing coated particles by grinding in the presence of reactive species. Patent no. 6,132,801. United States, 2000.
7. Snow E.S., Campbell P.M. and Perkins F.K. Nanofabrication with proximal probes. *Proc. IEEE* 1997, **85**, 601–611.
8. Lercel M.J., Redinbo G.F., Craighead H.G., Sheen C.W. and Allara D.L. Scanning tunneling microscopy based lithography of octadecanethiol on Au and GaAs. *Appl. Phys. Lett.* 1994, **65**, 974–976.
9. Perkins F.K., Dobisz E.A., Brandow S.L., Koloski T.S., Calvert J.M., Rhee K.W., Kosakowski J.E. and Marrian C.R.K., Proximal probe study of self-assembled monolayer resist materials. *J. Vac. Sci. Technol. B* 1994, **12**, 3725–3730.
10. Piner R.D., Zhu J., Xu F., Hong S. and Mirkin C.A., ‘Dip-Pen’ Nanolithography. *Science* 1999, **283**, 661–663.
11. Ara M., Graaf H. and Tada H., Nanopatterning of alkyl monolayers covalently bound to Si (111) with an atomic force microscope. *Appl. Phys. Lett.* 2002, **80**, 2565–2576.
12. Lee H.T., Oh J.S., Park S.-J., Park K.-H., Ha J.S., Yoo H.J. and Koo J.-Y., Nanometer-scale lithography on H-passivated Si(100) by atomic force microscope in air. *J. Vac. Sci. Technol., A* 1997, **15**, 1451–1454.
13. Niederhauser T.L., Jiang G., Lua Y.-Y., Dorff M.J., Woolley A.T., Asplund M.C., Berges D.A. and Linford M.R., A New Method of Preparing Monolayers on Silicon and Patterning Silicon Surfaces by Scribing in the Presence of Reactive Species. *Langmuir* 2001, **17**, 5889–5900.

14. Niederhauser T.L., Lua Y.-Y., Sun Y., Jiang G., Strossman G.S., Pianetta P. and Linford M.R., Formation of (Functionalized) Monolayers and Simultaneous Surface Patterning by Scribing Silicon in the Presence of Alkyl Halides. *Chemistry of Materials* 2002, **14**, 27–29.
15. Niederhauser T.L., Lua Y.-Y., Jiang G., Davis S.D., Matheson R., Hess D.A., Mowat I.A. and Linford M.R., Arrays of Chemomechanically Patterned Patches of Homogeneous and Mixed Monolayers of 1-Alkenes and Alcohols on Single Silicon Surfaces. *Angew. Chem., Int. Ed. Engl.* 2002, **13**, 2353–2356.
16. Lua Y.-Y., Lee M.V., Fillmore W.J.J., Matheson R., Sathyapalan A., Asplund M.C., Fleming S.A. and Linford M.R., Amine-Reactive Monolayers on Scribed Silicon with Controlled Levels of Functionality: Reaction of a Bare Silicon Surface with Mono- and Diepoxides. *Angew. Chem. Int. Ed. Eng.* 2003, **42**, 4046–4049.
17. Lua Y.-Y., Fillmore W.J.J. and Linford M.R., Aldehydes React with Scribed Silicon to form Alkyl Monolayers. Characterization by ToF-SIMS Suggests an Even-Odd Effect. *Applied Surface Science*. 2004, **231–232**, 323–327.
18. Hamers R.J. and Wang Y., Atomically-Resolved Studies of the Chemistry and Bonding at Silicon Surfaces. *Chemical Reviews* 1996, **96**, 1261–1290.
19. Buriak J.M., Organometallic Chemistry on Silicon and Germanium Surfaces. *Chem. Rev.* 2002, **102**, 1271–1308.
20. Buriak J.M., Organometallic chemistry on silicon surfaces: formation of functional monolayers bound through Si-C bonds. *Chemical Communications* 1999, 1051–1060.
21. Bent S.F., Attaching Organic Layers to Semiconductor Surfaces. *J. Phys. Chem. B* 2002, **106**, 2830–2842.
22. Bent S.F., Organic functionalization of group IV semiconductor surfaces: principles, examples, applications, and prospects. *Surface Science* 2002, **500**, 879–903.
23. Jiang G., Niederhauser T.L., Davis S.D., Lua Y.-Y., Cannon B.R., Dorff M.J., Howell L.L., Magleby S.P. and Linford M.R., Stability of Alkyl Monolayers on Chemomechanically Scribed Silicon to Air, Water, Hot Acid, and X-rays. *Colloids and Surfaces A* 2003, **226**, 9–16.
24. Lua Y.-Y., Niederhauser T.L., Matheson R., Bristol C., Mowat I.A., Asplund M.C. and Linford M.R., Static Time-of-Flight Secondary Ion Mass Spectrometry of Monolayers on Scribed Silicon derived from 1-Alkenes, 1-Alkynes and 1-Haloalkanes. *Langmuir* 2002, **18**, 4840–4846.
25. Jiang G., Niederhauser T.L., Fleming S.A., Asplund M.C. and Linford M.R., Evidence for a Radical Mechanism in Monolayer Formation on Silicon Ground (or Scribed) in the Presence of Alkyl Halides. *Langmuir* 2004, **20** (5), 1772–1774.
26. Howell L.L., *Compliant Mechanisms*, John Wiley & Sons: New York, NY, 2001.
27. Cannon B.R., Magleby S.P., Howell L.L., Jiang G., Niederhauser T.L. and Linford M.R., Influence of Scribe Speed and Force on Chemomechanical Nanofunctionalized Features. *ASME International Mechanical Engineering Congress and Exposition*: New Orleans, LA, 2002.
28. Cannon B.R., Lillian T.D., Magleby S.P., Howell L.L. and Linford M.R., A Compliant End-effector for Microscribing. *Precision Engineering* 2003.
29. Higashi G.S., Chabal Y.J., Trucks G.W. and Raghavachari K., Ideal hydrogen termination of the Si (111) surface. *Applied Physics Letters* 1990, **56**, 656–658.
30. Lua Y.-Y., Niederhauser T.L., Wacaser B.A., Mowat I.A., Woolley A.T., Davis R.C., Fishman H.A. and Linford M.R., Chemomechanical Production of Submicron Edge Width, Functionalized, ~20  $\mu\text{m}$  Features on Silicon. *Langmuir* 2003, **19**, 985–988.

31. Wacaser B.A., Maughan M.J., Mowat I.A., Niederhauser T.L., Linford M.R. and Davis R.C., Chemomechanical Surface Patterning and Functionalization of Silicon Surfaces Using an Atomic Force Microscope. *Applied Physics Letters* 2003, **82**, 808–810.
32. Cheng C.C., Choyke W.J. and Yates J.T., Jr., Thermal stability of the carbon-carbon bond in ethylene adsorbed on Si(100): An isotopic mixing study. *Surface Science* 1990, **231**, 289–296.
33. Liu H. and Hamers R.J., Stereoselectivity in Molecule-Surface Reactions: Adsorption of Ethylene on the Silicon(001) Surface. *Journal of the American Chemical Society* 1997, **119**, 7593–7594.
34. Lu X., Diradical Mechanism for the [2 + 2] Cycloaddition of Ethylene on Si(100) Surface. *J. Am. Chem. Soc.* 2003, **125**, 6384–6385.
35. Yoshinobu J., Tsuda H., Onchi M. and Nishijima M., The adsorbed states of ethylene on Si(100)c(4 × 2), Si(100)(2 × 1), and vicinal Si(100)9°: Electron energy loss spectroscopy and low-energy electron diffraction studies. *Journal of Chemical Physics* 1987, **87**, 7332–7340.
36. Lopinski G.P., Moffatt D.J., Wayner D.D.M. and Wolkow R.A., How Stereoselective Are Alkene Addition Reactions on Si(100)? *Journal of the American Chemical Society* 2000, **122**, 3548–3549.
37. Liu Q. and Hoffmann R., The Bare and Acetylene Chemisorbed Si(001) Surface, and the Mechanism of Acetylene Chemisorption. *J. Am. Chem. Soc.* 1995, **117**, 4082–4092.
38. Nishijima M., Yoshinobu J., Tsuda H. and Onchi M., The Adsorption and Thermal Decomposition of Acetylene on Si(100) and Vicinal Si(100)9°. *Surface Science* 1987, **192**, 383–397.
39. Taylor P.A., Wallace R.M., Cheng C.C., Weinberg W.H., Dresser M.J., Choyke W.J. and Yates J.T., Jr., Adsorption and Decomposition of Acetylene on Si(100) – (2 × 1). *Journal of the American Chemical Society* 1992, **114**, 6754–6760.
40. Yoshinobu J., Tsuda H., Onchi M. and Nishijima M., Rehybridization of acetylene on the Si(111) (7 × 7) Surface – A vibrational study. *Chemical Physics Letters* 1986, **30**, 170–174.
41. Chen Y., Liu Z., Zhang Q., Feng K. and Lin Z., Effect of atomic hydrogen on the acetylene adsorbed Si(100)(2 × 1) surface. *Appl. Phys. Lett.* 1995, **67**, 2936–2938.
42. Bronikowski M.J. and Hamers R.J., Atomically Resolved Scanning Tunneling Microscopy Study of the Adsorption and Dissociation of Methylchloride on Si(001). *Journal of Vacuum Science & Technology, A: Vacuum, Surfaces, and Films* 1995, **13**, 777–781.
43. Keeling L.A., Chen L., Greenlief C.M., Mahajan A. and Bonser D., Direct Evidence for β-hydride elimination on Si(100). *Chemical Physics Letters* 1994, **217**, 136–141.
44. Brown K.A. and Ho W., The interaction of methyl chloride and Si(100) 2 × 1. *Surface Science* 1995, **338**, 111–116.
45. Zhang L., Carman A.J. and Casey S.M., Adsorption and thermal decomposition chemistry of 1-propanol and other primary alcohols on the Si(100) surface. *Accepted J. Phys. Chem. B* 2003 **107** (33), 8424–8432.
46. Lu X., Zhang Q. and Lin M.C., Adsorption of methanol, formaldehyde and formic acid on the Si(100) – 2 × 1 surface: A computational study. *Phys. Chem. Chem. Phys.* 2001, **3**, 2156–2161.
47. Casaletto M.P., Zanoni R., Carbone M., Piancastelli M.N., Aballe L., Weiss K. and

- Horn K., Methanol adsorption on Si(1 0 0) $2 \times 1$  investigated by high-resolution photoemission. *Surface Science* 2002, **505**, 251–259.
48. Casaletto M.P., Zanoni R., Carbone M., Piancastelli M.N., Aballe L., Weiss K. and Horn K., High-resolution photoemission study of ethanol on Si(100) $2 \times 1$ . *Surface Science* 2000, **447**, 237–244.
  49. Bu Y., Breslin J. and Lin M.C., Adsorption and Thermal Decomposition of Acetaldehyde on Si(111) –  $7 \times 7$ . *J. Phys. Chem. B* 1997, **101**, 1872–1877.
  50. Tanaka K., Matsuzaki S. and Toyoshima I., Photodecomposition of Adsorbed Methoxy Species by UV Light and Formaldehyde Adsorption on Si(111) Studied by XPS and UPS. *J. Phys. Chem.* 1993, **97**, 5673–5677.
  51. Armstrong J.L., White J.M. and Langell M., Thermal decomposition reactions of acetaldehyde and acetone on Si(100). *J. Vac. Sci. Technol. A* 1997, **15**, 1146.
  52. Ulman A., *An Introduction to Ultrathin Organic Films: from Langmuir-Blodgett to Self-Assembly*, Academic Press: Boston, 1991.
  53. Bain C.D., Troughton E.B., Tao Y.-T., Evall J., Whitesides G.M. and Nuzzo R.G., Formation of Monolayer Films by the Spontaneous Assembly of Organic Thiols from Solution onto Gold. *J. Am. Chem. Soc.* 1989, **111**, 321–335.
  54. Offord D.A., John C.M. and Griffin J.H., Contact Angle Goniometry, Ellipsometry, XPS, and TOF-SIMS Analysis of Gold-Supported, Mixed Self-Assembled Monolayers Formed from Mixed Dialkyl Disulfides. *Langmuir* 1994, **10**, 761–766.
  55. Tillman N., Ulman A., Schildkraut J.S. and Penner T.L., Incorporation of Phenoxy Groups in Self-Assembled Monolayers of Trichlorosilane Derivatives. Effects on Film Thickness, Wettability, and Molecular Orientation. *J. Am. Chem. Soc.* 1988, **110**, 6136–6144.
  56. Offord D.A. and Griffin J.H., Kinetic Control in the Formation of Self-Assembled Mixed Monolayers on Planar Silica Substrates. *Langmuir* 1993, **9**, 3015–3025.
  57. Linford M.R., Fenter P., Eisenberger P.M. and Chidsey C.E.D., Alkyl Monolayers on Silicon Prepared from 1-Alkenes and Hydrogen-Terminated Silicon. *Journal of the American Chemical Society* 1995, **117**, 3145–3155.
  58. Sieval A.B., Demirel A.L., Nissink J.W.M., Linford M.R., van der Maas J.H., de Jeu W.H., Zuilhof H. and Sudhölter E.J.R., Highly Stable Si-C Linked Functionalized Monolayers on the Silicon (100) Surface. *Langmuir* 1998, **14**, 1759–1768.
  59. Dean J.A., *Lange's Handbook of Chemistry*; 15th edn; McGraw-Hill, Inc.: New York, 1999.
  60. *Handbook of Chemistry and Physics*, 81 edn., CRC Press: Boca Raton, 2000.
  61. Linford M.R., *Chemical Functionalization of Hydrogen-Terminated Silicon Surfaces: The First Self-Assembled Monolayers on Silicon*; Stanford University, 1996.
  62. Jiang G., Niederhauser T.L., Fleming S.A., Asplund M.C. and Linford M.R., Evidence for a Radical Mechanism in Monolayer Formation on Silicon Ground (or Scribed) in the Presence of Alkyl Halides. *Langmuir* 2004, **20**, 1772–1774.
  63. Gibian M.J. and Corley R.C., Organic radical-radical reactions. Disproportionation vs. combination. *Chem. Rev.* 1973, **73**, 441–464.
  64. Carbone M., Piancastelli M.N., Paggel J.J., Weindel C. and Horn K., A high-resolution photoemission study of ethanol adsorption on Si(111) – ( $7 \times 7$ ). *Surface Science* 1998, **412/413**, 441–446.
  65. Carbone M., Piancastelli M.N., Zanoni R., Comtet G., Dujardin G. and Hellner L., Methanol adsorption on Si(111) – ( $7 \times 7$ ), investigated by core-line photoemission and mass spectrometry of photodesorbed ions. *Surface Science* **1997**, **370**, L179–L184.

66. Casaletto M.P., Zanoni R., Carbone M., Piancastelli M.N., Aballe L., Weiss K. and Horn K., High-resolution photoemission study of ethanol on Si(100) $2 \times 1$ . *Surface Science* 2000, **447**, 237–244.
67. Laibinis P.E., Nuzzo R.G. and Whitesides G.M., Structure of Monolayers Formed by Coadsorption of Two *n*-Alkanethiols of Different Chain Lengths on Gold and Its Relation to Wetting. *J. Phys. Chem.* 1992, **96**, 5097–5105.
68. Chapman R.G., Ostuni E., Yan L. and Whitesides G.M., Preparation of Mixed Self-Assembled Monolayers (SAMs) That Resist Adsorption of Proteins Using the Reaction of Amines with a SAM That Presents Interchain Carboxylic Anhydride Groups. *Langmuir* 2000, **16**, 6927–6936.
69. Sakaue H., Fujiwara S., Shingubara S. and Takahagi T., Atomic-scale defect control on hydrogen-terminated silicon surface at wafer scale. *Appl. Phys. Lett.* 2001, **78**, 309–311.
70. Gibson C.T., Watson G.S. and Myhra S., Scanning Force Microscopy—Calibrative Procedures for ‘Best Practice’. *Scanning* 1997, **19**, 564–581.
71. Wilder K., Soh H.T., Atalar A. and Quate C.F., Nanometer-scale Patterning and Individual Current-controlled Lithography Using Multiple Scanning Probes. *Review of Scientific Instruments* 1999, **70**, 2822–2827.
72. Karas M., Bachmann D., Bahr U. and Hillenkamp F., Matrix-Assisted Ultraviolet Laser Desorption of non-Volatile Compounds. *Int. J. Mass Spectrom. Ion Process.* 1987, **78**, 53–68.
73. Linnemayr K., Rizzi A. and Allmaier G., Characterization of Modified Cyclodextrins Applied in Capillary Electrophoresis and High-Performance Liquid Chromatography as Chiral Selectors by Matrix-Assisted Laser Desorption Curved Field Reflectron Mass Spectrometry. *J. of Chromatography A.* 1997, **791**, 299–306.
74. Overberg A., Karas M., Bahr U., Kaufmann R. and Hillenkamp F., Matrix-Assisted Infrared-Laser (2.49  $\mu\text{m}$ ) Desorption/Ionization Mass Spectrometry of Large Biomolecules. *Rapid Commun Mass Spectrom.* 1990, **4**, 293–296.
75. Overberg A., Karas M. and Hillenkamp F., Matrix-Assisted Laser Desorption of Large Biomolecules with a TEA-CO<sub>2</sub>-Laser. *Rapid Commun Mass Spectrom.* 1991, **5**, 128–131.
76. Spengler B., Pan Y., Cotter R.J. and Kan L.-S., Molecular Weight Determination of Underivatized Oligodeoxyribonucleotides by Positive-Ion Matrix-Assisted Ultraviolet Laser-Desorption Mass Spectrometry. *Rapid Commun. Mass Spectrom.* 1990, **4**, 99–102.
77. Yamagaki T., Maeda M., Kanazawa K., Ishizuka Y. and Nakanishi H., Structures of Caulerpa Cell Wall Microfibril Xylan with Detection of b-1,3-Xylo-Oligosaccharides as Revealed by Matrix-Assisted Laser Desorption/Ionization Time-of-Flight Mass Spectrometry. *Biosci. Biotechnol. Biochem.* 1996, **60**, 1222–1228.
78. Kaltashov I.A., Doroshenko V., Cotter R.J., Takayama K. and Qureshi N., Confirmation of the Structure of Lipid A Derived from the Lipopolysaccharide of *Rhodobacter sphaeroides* by a Combination of MALDI, LSIMS, and Tandem Mass Spectrometry. *Anal. Chem.* 1997, **69**, 2317–2322.
79. Okamoto M., Takahashi K., Doi T. and Takimoto Y., High-Sensitivity Detection and Postsource Decay of 2-Aminopyridine-Derivatized Oligosaccharides with Matrix-Assisted Laser Desorption/Ionization Mass Spectrometry. *Anal. Chem.* 1997, **69**, 2919–2926.
80. Lloyd P.M., Scrivener E., Maloney D.R., Haddleton D.M. and Derrick P.J., Cation Attachment to Synthetic Polymers in Matrix-Assisted Laser Desorption/Ionisation Mass Spectrometry. *Polymer Preprints* 1996, **37**, 847–848.

81. Kassis C.M., Belu A.M., DeSimone J.M., Linton R.W., Lange G.W. and Friedman R.M., Polymer Characterisation Using Matrix-Assisted Laser Desorption Ionisation Mass Spectrometry. *Polymer Preprints* 1996, **37**, 833.
82. Mandal H. and Hay A.S., Synthesis Characterisation and Cross-Linking Study of Some Novel Polycyclic Carbonates of 4-Alkyl Substituted Phenol-Formaldehyde Resin. *Polymer Preprints* 1997, **38**, 193–194.
83. Kassis C.M., DeSimone J.M., Linton R.W., Remsen E.E., Lange G.W. and Friedman R.M., A Direct Deposition Method for Coupling Matrix-Assisted Laser Desorption/Ionization Mass Spectrometry with Gel Permeation Chromatography for Polymer Characterization. *Rapid Commun. Mass Spectrom.* 1997, **11**, 1134–1138.
84. Kassis C.M., DeSimone J.M., Linton R.W., Lange G.W. and Friedman, R.M., An Investigation into the Importance of Polymer-Matrix Miscibility Using Surfactant Modified Matrix-assisted Laser Desorption/Ionization Mass Spectrometry. *Rapid Commun. Mass Spectrom.* 1997, **11**, 1462–1466.
85. Yoshida S., Yamamoto S. and Takamatsu T., Detailed Structural Characterisation of Modified Silicone Copolymers by Matrix-Assisted Laser Desorption/Ionisation Time-of-flight Mass Spectrometry. *Rapid Commun. Mass Spectrom.* 1998, **12**, 535–544.
86. Mandal H. and Hay A.S., Synthesis and Characterization by MALDI-TOF MS of Polycyclic Siloxanes Derived from p-Substituted Novolac Resins by MALDI-TOF MS. *J. Poly. Sci.* 1998, **36**, 2429–2437.
87. Spengler B. and Kaufmann R., Gentle Probe for Tough Molecules: Matrix-assisted Laser Desorption Mass Spectrometry. *Analysis* 1992, **20**, 91–101.
88. Zhang W., Czernik A.J., Yungwirth T., Aebersold R. and Chait B.T., Matrix-Assisted Laser Desorption Mass Spectrometric Peptide Mapping of Proteins Separated by Two-Dimensional Gel Electrophoresis: Determination of Phosphorylation in synapsin I. *Protein Sci.* 1994, **3**, 677–686.
89. Zhang W. and Chait B.T., Profound: an Expert System for Protein Identification Using Mass Spectrometric Peptide Mapping Information. *Anal Chem.* 2000, **72**, 2482–2489.
90. Jensen O.N., Podtelejnikov A.V. and Mann M., Identification of the Components of Simple protein Mixtures by High-Accuracy Peptide Mass Mapping and Database Searching. *Anal Chem.* 1997, **69**, 4741–4750.
91. Zenobi R. and Knochenmuss R., Ion Formation in MALDI Mass Spectrometry. *Mass Spectrometry Reviews* 1998, **17**, 337–366.
92. Lewis J.K., Wei J. and Siuzdak G., Matrix-Assisted Laser Desorption/Ionization Mass Spectrometry in Peptide and Protein Analysis. *Peptide and Protein Analysis*. John Wiley & Sons Ltd: Chichester, 2000; pp 5880–5894.
93. Moren A., Hellman U., Inada Y., Imamura T., Heldin C.-H. and Moustakas, A. Differential Ubiquitination Defines the Functional Status of the Tumor Suppressor Smad4. *J. Biol. Chem.* 2003, **278**, 33571–33582.
94. Hellman U. and Bhikhabhai R., Easy Amino Acid Sequencing of Sulfonated Peptides Using Post-Source Decay on a Matrix-Assisted Laser Desorption/Ionization Time-of-Flight Mass Spectrometer Equipped with a Variable Voltage Reflector. *Rapid Commun Mass Spectrom.* 2002, **16**, 1851–1859.
95. Persson C., Engström U., Mowbray S.L. and Östman A., Primary Sequence Determinants Responsible for Site-Selective Dephosphorylation of the PDGF beta-Receptor by the Receptor-Like Protein Tyrosine Phosphatase DEP-1. *FEBS Lett.* 2002, **517**, 27–31.
96. Grönroos E., Hellman U., Heldin C.-H. and Ericsson J., Control of Smad7 Stability

- by Competition Between Acetylation and Ubiquitination. *Mol. Cell.* 2002, **10**, 483–493.
97. Little D.P., Cornish T.J., O'Donnell M.J., Braun A., Cotter R.J. and Köster H., MALDI on a Chip: Analysis of Arrays of Low-Femtomole to Subfemtomole Quantities of Synthetic Oligonucleotides and DNA Diagnostic Products Dispensed by a Piezoelectric Pipet. *Anal. Chem.* 1997, **69**, 4540–4546.
  98. Ekström S., Ericsson D., Önnerrfjord P., Bengtsson M., Nilsson J., Marko-Varga G. and Laurell T., Signal Amplification Using 'Spot-on-a-Chip' Technology for the Identification of Proteins via MALDI-TOF MS. *Anal. Chem.* 2001, **73**, 214–219.
  99. Ekström S., Önnerrfjord P., Bengtsson M., Nilsson J., Laurell T. and Marko-Varga, G. Integrated Microanalytical Technology Enabling Rapid and Automated Protein Identification. *Anal. Chem.* 2000, **72**, 286–293.
  100. Schuereberg M., Luebbert C., Eickhoff H., Kalkum M., Lehrach H. and Nordhoff E., Prestructured MALDI-MS sample supports. *Analytical Chemistry* 2000, **72**, 3436–3442.
  101. Marko-Varga G., Ekström S., Helldin G., Nilsson J. and Laurell T., Disposable Polymeric High-Density Nanovial Arrays for Matrix Assisted Laser Desorption/Ionization-Time of Flight-Mass Spectrometry: I. Microstructure Development and Manufacturing. *Electrophoresis.* 2001, **22**, 3978–3983.
  102. Xu Y., Watson J.T. and Bruening M.L., Patterned monolayer/polymer films for analysis of dilute or salt-contaminated protein samples by MALDI-MS. *Analytical Chemistry* 2003, **75**, 185–190.
  103. Husseini G., Peacock J., Sathyapalan A., Zilch L.W., Asplund M.C., Sevy E.T. and Linford M.R., Alkyl Monolayers on Silica Surfaces Prepared Using Neat, Heated Dimethylmonochlorosilanes with Low Vapor Pressures. *Langmuir* 2003, **19**, 5169–5171.
  104. Plueddemann E.P., *Silane Coupling Agents*; Plenum Press: New York, 1991.
  105. Zilch L.W., Husseini G.A., Lua Y.-Y., Lee M.V., Gertsch K.R., Cannon B.R., Perry R.M., Sevy E.T., Asplund M.C., Woolley A.T. and Linford M.R., A rapid and convenient method for preparing masters for microcontact printing with 1–12  $\mu\text{m}$  features. *Rev. Sci. Instr.* 2004, **75** (9), 3065–3067.
  106. Xia Y. and Whitesides G.M., Soft Lithography. *Annu. Rev. Mater. Sci.* 1998, **28**, 153–184.
  107. Xia Y., Kim E., Zhao X.-M., Rogers J., Prentiss M. and Whitesides G.M., Complex Optical Surfaces Formed by Replica Molding Against Elastomeric Masters. *Science* 1996, **273**, 347–349.
  108. Grzybowski B.A., Haag R., Bowden N. and Whitesides G.M., Generation of Micrometer-Sized Patterns for Microanalytical Applications Using a Laser Direct-Write Method and Microcontact Printing. *Anal. Chem.* 1998, **70**, 4645–4652.
  109. Terris B.D., Manim H.J., Best M.E., Logan J.A., Rugar D. and Rishton S.A., Nanoscale replication for scanning probe data storage. *Appl. Phys. Lett.* 1996, **69**, 4262–4264.
  110. Hermanson G.T., *Bioconjugate Techniques*; Academic Press: San Diego, 1996.
  111. Whittaker J.D., Brink M., Husseini G., Linford M.R. and Davis R.C., Self-Aligned Mechanical Attachment of Carbon Nanotubes to Silicon Dioxide Structures by Selective Silicon Dioxide Chemical Vapor Deposition. *Applied Physics Letters* 2003, **83**, 5307–5309.

---

P J YOO, K Y SUH, Y S KIM, D-Y KHANG and  
H H LEE, Seoul National University, Korea

## 5.1 Introduction

Thin polymer films provide a fertile ground for uncovering interesting physical phenomena. The basic forces governing the behavior of the thin films are capillarity, dewetting, dispersion force, and stress. These fundamentals have been fully explored for free thin films. When the film is confined, an unexpected landscape often emerges and as such, the subject has recently drawn much interest. Our interests have been in utilizing the basic forces for the purposes of patterning the polymer films and of inducing self-organization to ordered polymeric structures by imposing a physical confinement to the film. The unique feature of the methods described here is that they are simple, efficient and cost-effective in fabricating nano- and micro-structures.

In this chapter, we describe these techniques in detail in four sections: (i) patterning by capillary force; (ii) influence of dispersion force on patterning; (iii) patterning by dewetting, and (iv) patterning by stress for metal/polymer bilayer. These methods can provide one not only with a useful tool for simple replication of original patterns but also with various strategies for fabricating unique structures that cannot be readily accessed by conventional lithographic techniques, as in the fabrication of complicated three-dimensional structures, oval-shaped dot arrays and sinusoidal wave structures. These patterning techniques can be utilized in various fields, including microelectronics, optics, microelectromechanical systems (MEMS) and biological systems.

## 5.2 Patterning by capillary lithography

Capillarity is one of the useful concepts that can be used in patterning polymeric materials. When a liquid wets a capillary tube and if the wetting results in lowering the free energy, it will cover much of the wall, resulting in the capillary rise of the liquid.<sup>1,2</sup> Capillary lithography is the collective name for a set of lithographic techniques based on capillarity: capillary force

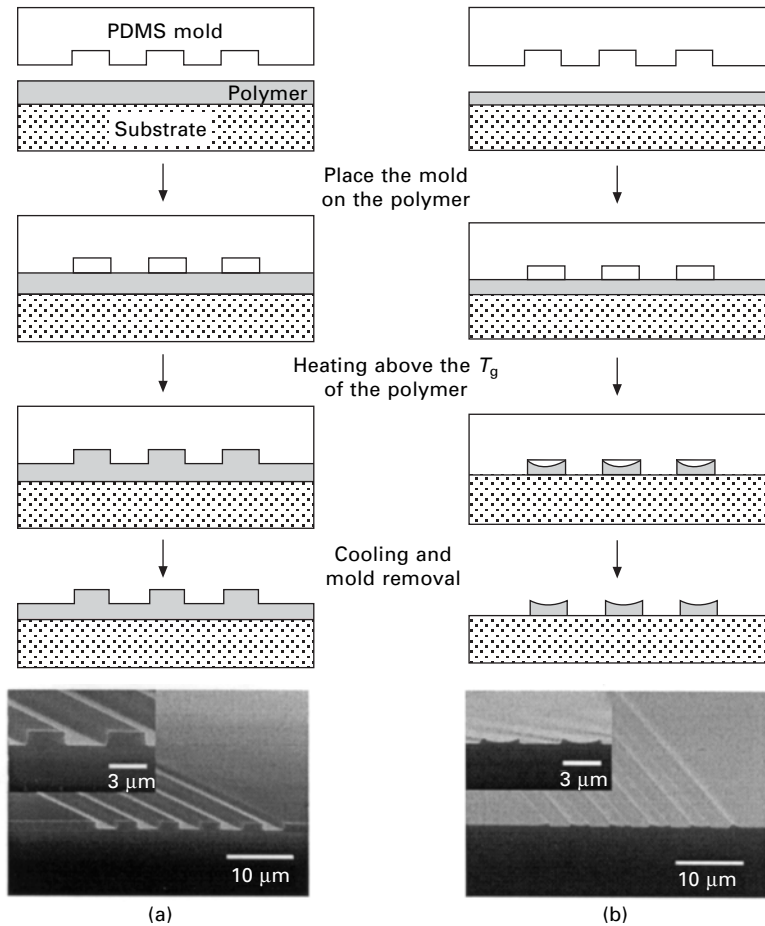
lithography (CFL)<sup>3</sup>, soft molding (SOMO),<sup>4,5</sup> and pressure-assisted CFL (PACFL).<sup>6</sup>

### 5.2.1 CFL by thermally-induced capillarity

The CFL presented in this section is a simple and yet robust method for patterning complex and large area structures by utilizing thermally induced capillarity in confined channels.<sup>3</sup> In CFL, the essential feature of nanoimprint lithography – molding a polymer melt – is combined with the prime element of soft lithography – use of an elastomeric mold.<sup>7–9</sup> As a result, the advantage of imprint lithography over soft lithography is retained in meeting stringent pattern fidelity requirements as in the fabrication of integrated circuits while eliminating the need to use an extremely high pressure that is a requirement of nanoimprint lithography.

When a patterned (positive or negative) polydimethylsiloxane (PDMS) mold is placed on a polymer surface and heated above the polymer's glass transition temperature ( $T_g$ ), capillarity forces the polymer melt into the void space of the channels formed between the mold and the polymer surface, thereby generating a negative replica of the mold as shown in Fig. 5.1. The high gas permeability of a PDMS mold allows the air trapped in the channel void to diffuse out of the mold during the capillary rise.<sup>10</sup> When the polymer film is thick enough to fill the cavity of the mold completely, a residual polymer layer remains on the substrate as shown in Fig. 5.1(a). However, if the polymer film is thin and the interactions between the polymer and the substrate are sufficiently weak, the substrate surface can be exposed as depicted in Fig. 5.1(b). The bottom part of Fig. 5.1 shows the scanning electron microscopy (SEM) images of the typical polymer patterns realized by CFL. In the case of Fig. 5.1(b), a meniscus is observed at the protruding end of the polymer, which is the signature of the capillary rise.

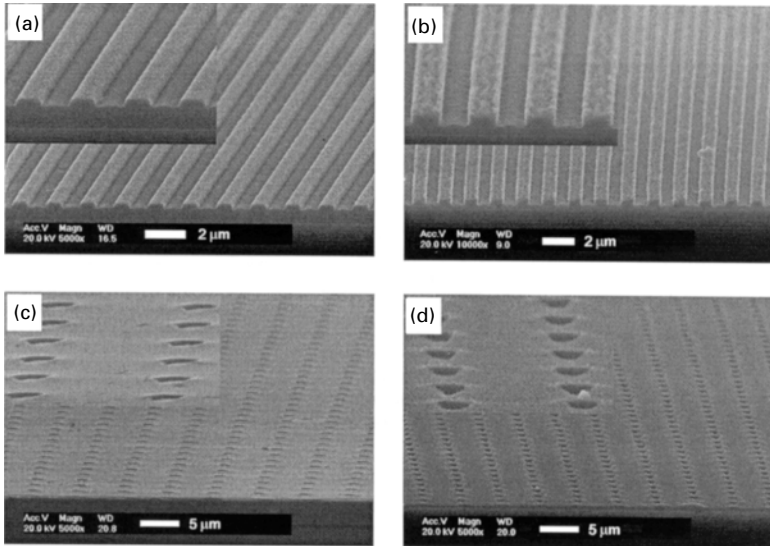
CFL can preserve the fidelity of the original structure without causing any distortions or defects. Furthermore, the edge definition, which is an important characteristic for the subsequent etching step, is also satisfactory. The transfer of a polymer pattern to an underlying  $\text{SiO}_2$  substrate by reactive ion etching (RIE) can be carried out in one step when the substrate surface is exposed. Such results are shown in Fig. 5.2 for a 800 nm line-and-space pattern. To examine the etching characteristics of the polymer resist, the etching time was varied from 5 min (Fig. 5.2(a)) to 15 min (Fig. 5.2(b)) for the line-and-space pattern. As shown, the shape of the etched structure is dependent on the etching time due to the meniscus in the original polymer structure. Because of the presence of a meniscus, the minimum point of the meniscus is vulnerable to RIE in that the underlying substrate can be exposed first at that point as the etching time increases. Once the substrate is exposed, both polymer and  $\text{SiO}_2$  are etched simultaneously, thus leading to a rough surface structure as



5.1 Schematic diagram of CFL when the film thickness is relatively thick with respect to the mold step height (a) and when it is thin (b) and scanning electron microscopy (SEM) images for each case. When the initial film thickness is about 1.5  $\mu\text{m}$ , the channel is completely filled up. When it is thin (about 180 nm), the substrate surface can be completely exposed. Reproduced from ref. 3.

shown in Fig. 5.2(b). The transfer of a 1  $\mu\text{m}$  dot pattern was also carried out as shown in Figs 5.2(c) (before etching) and 5.2(d) (after etching). Although the substrate surface was not exposed in this case, one-step RIE was carried out. The roughness in the transferred pattern would have been eliminated if conventional two-step etching had been used.

CFL is a powerful method for patterning polymers on a large area. As the PDMS mold spontaneously wets the surface and makes conformal contact with the substrate without any external force, an area as large as needed can be patterned in one step with high pattern fidelity. With further development,



5.2 Examples of the pattern transfer to  $\text{SiO}_2$  substrate by RIE in one step for 800 nm line-and-space pattern (5 min etching (a) and 15 min etching (b)) and 1  $\mu\text{m}$  dot pattern (before etching (c) and after etching (d)). For the line-and-space pattern, a relatively thin film (60 nm) was used while a relatively thick film (170 nm) was used for the dot pattern. Reproduced from ref. 16.

the technique could become a strong candidate for an alternative to photolithography in fabricating large-scale integrated circuits.

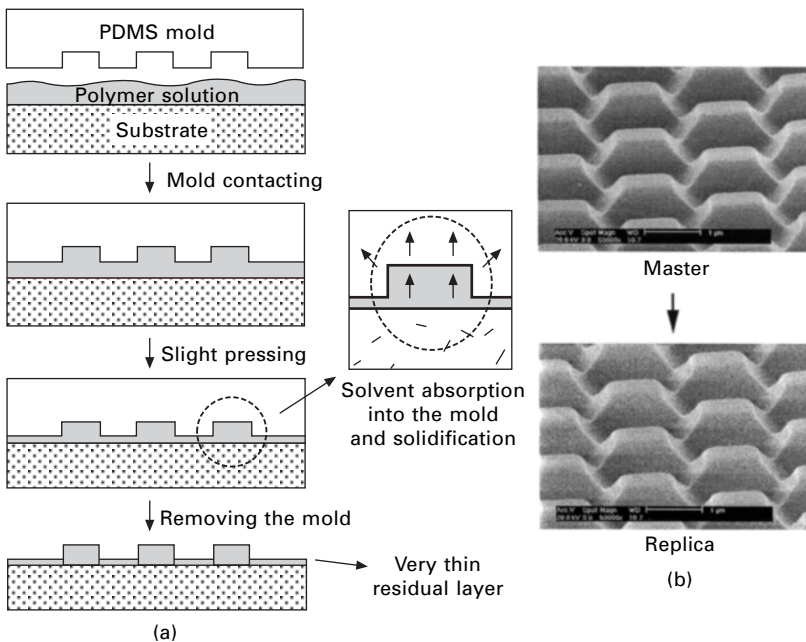
### 5.2.2 Soft molding (SOMO) by solvent-induced capillarity

The soft molding process presented in this section is another method for patterning three-dimensional structures by capillarity, which is induced by the solvent.<sup>4,5</sup> Soft molding was motivated by our earlier work on imprint lithography by solvent vapor treatment.<sup>11</sup> We wanted to reduce substantially the high pressure still needed by the solvent vapor treatment by making the polymer-film laden with a sufficient amount of solvent. Use of a hard mold for such a film led to failure. The idea was then to use a soft mold that is capable of absorbing the solvent such that by the time the polymer is molded, the film does not contain much solvent. Figure 5.3(a) illustrates the soft molding process. A PDMS mold with the desired pattern is placed onto a polymer film, without baking, immediately after the film is spin-coated onto a substrate and then pressed slightly (just enough for conformal contact) at a pressure less than  $1 \text{ N/cm}^2$ . After releasing the pressure, the mold and the substrate are allowed to remain undisturbed for a period of time, which is of

the order of ten minutes. During the soft molding, the solvent contained in the polymer film diffuses toward the interface due to the concentration gradient and is absorbed into the mold. The solvent then permeates through the mold and finally evaporates into the air. After the evaporation is completed, the mold is removed, thus finishing the soft molding.

In one form of soft molding, the residual layer remaining after patterning can be made very thin (typically less than 10 nm) such that one-step etching is possible. In this case, the solvent is present in an amount sufficient for continuous movement of polymer into the void space by solvent-assisted capillarity. For this modified SOMO, the solvent and polymer pair should be chosen in such a way that the solvent would be removed slowly by absorption into the mold. In other words, the rate of absorption should be less than the rate of removal of solvent from film or the rate of solvent evaporation from the polymer surface. An optimum pair of polymer and solvent are 2-polyvinylpyridine (P2VP) and methanol.

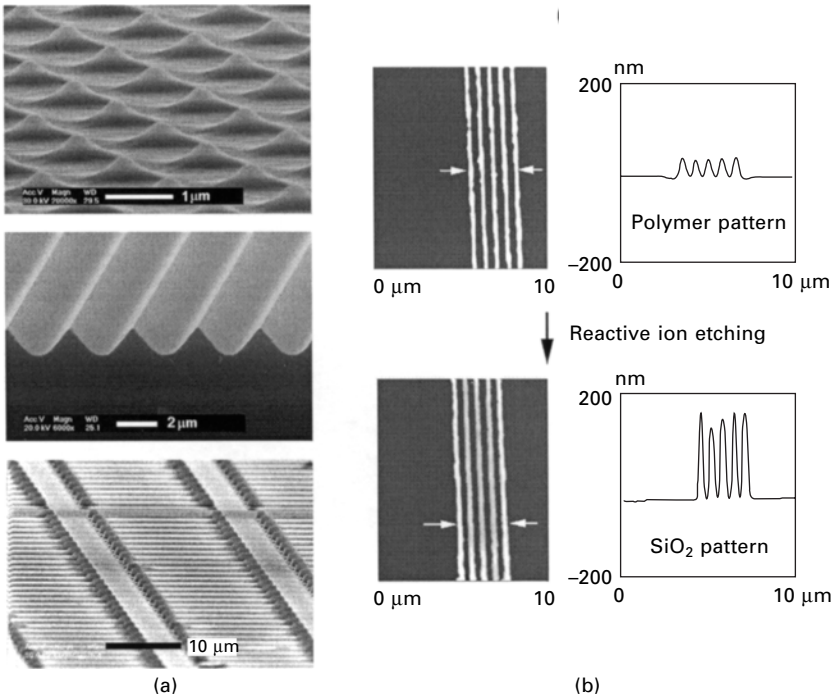
Figure 5.3(b) shows SEM images of a three-dimensional structure that was formed by soft molding. Comparison of the master (top) from which the mold was prepared with the polymer replica (bottom) obtained by soft molding reveals that the original three-dimensional structure is well transferred to the polymer film without any distortions or defects in a single step. In soft



5.3 (a) Schematic diagram of the experimental procedure of soft molding method. (b) SEM images of the master (top) used for soft molding and the replica fabricated (bottom). Reproduced from ref. 4.

molding, the solvent in the molded polymer is continuously removed by absorption into the PDMS mold at the interface between the mold and the molded polymer and replenished by solvent diffusion to the interface. The gradual and continuous replenishment of solvent and accompanying polymer to the interface assures the fidelity of the molded polymer structure.

Figure 5.4(a) shows several three-dimensional structures formed by soft molding. Circular cones fabricated to have a base diameter of  $1\ \mu\text{m}$  are shown in the top part of Fig. 5.4(a). Rounded triangular channels with a period of approximately  $3\ \mu\text{m}$  are given in the middle of the figure. A three-level fabricated structure is shown at the bottom. These results demonstrate the effectiveness of soft molding in fabricating three-dimensional structures. Figure 5.4(b) shows a  $400\ \text{nm}$  line structure that was transferred into  $\text{SiO}_2$  layer (bottom) by one step RIE after forming the same structure in P2VP film by soft molding (top). Soft molding is an efficient and low-cost technique for the patterning of three-dimensional and nano-scale features.



5.4 (a) Tilted SEM images of several three-dimensional structures fabricated by soft molding. (b) AFM images of  $400\ \text{nm}$  line-and-space polymer pattern by soft molding (top) and transferred pattern into underlying  $\text{SiO}_2$  layer by one step RIE (bottom). Reproduced from refs. 4 and 5.

### 5.2.3 Self-organized polymeric microstructures by CFL

Structures with micro-scale ( $1 \sim 50 \mu\text{m}$ ) features have extensively been studied because they bridge the molecular and the macroscopic systems.<sup>12</sup> Therefore, fabrication and study of these systems have become active areas of research.<sup>13,14</sup> In this section, we introduce a concept of self-organization on a micro-scale, involving self-organization of an existing microsystem into a new microstructure that is driven by capillarity.<sup>15,16</sup>

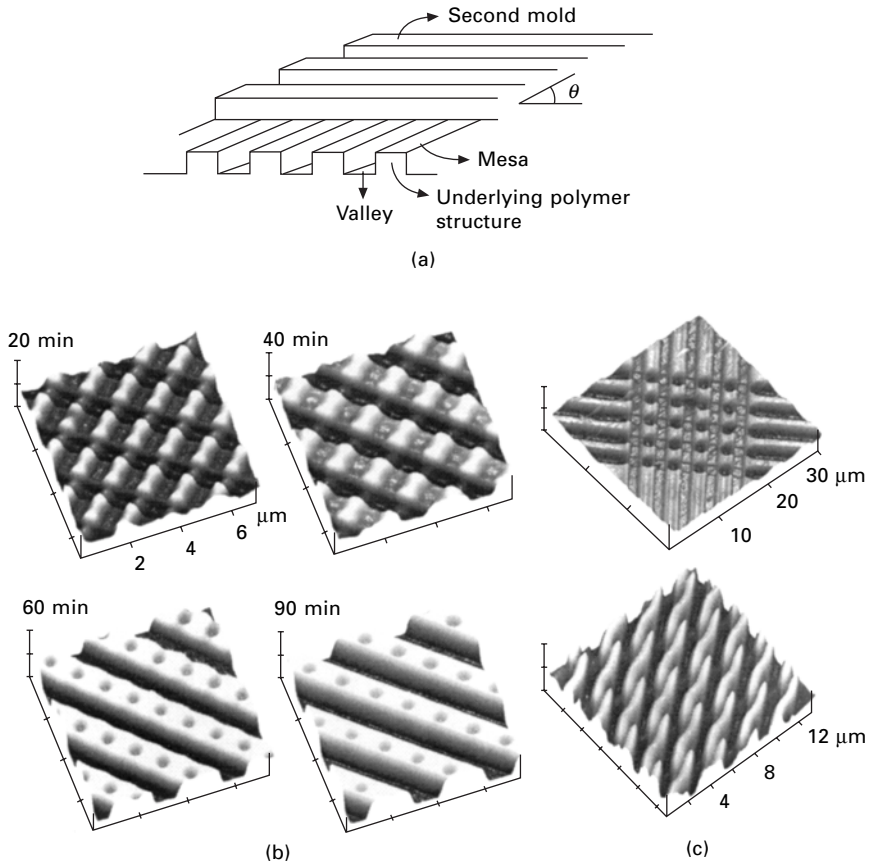
This method is based on the fact that the pattern formation by CFL is driven by a natural force of capillarity, which does not involve any external modification or force. A simple meniscus forms when the capillarity is applied to a flat surface. On the other hand, unexpected structures would result when the capillarity is made to act upon an underlying polymer structure, since then the dynamics of reorganization of the underlying structure could lead to self-organized, ordered polymer microstructures.

A schematic diagram of the two-step method is shown in Fig. 5.5(a). Typically a PDMS mold is placed on the surface of a polymer layer spin-coated onto a silicon substrate. After forming the underlying structure by CFL, the first mold is removed and the second mold is placed on the patterned polymer film with the second mold rotated with respect to the first at an angle  $\theta$  and the sample is heated to another annealing temperature.

Figure 5.5(b) shows the transient morphology of the polymer microstructures (PS,  $MW = 2.3 \times 10^5$ ) formed with a  $1 \mu\text{m}$  line-and-space pattern second mold as a function of annealing time (20, 40, 60, and 90 min) at  $130^\circ\text{C}$ . Eventually, one row of holes forms along the pattern direction of the second mold, as seen in Fig. 5.5(b), when the angle  $\theta$  is  $90^\circ$ . The holes are located at the valleys between two adjacent mesas (Fig. 5.5(a)) of the underlying polymer structure that were originally formed with the first mold. In the initial stage, the polymer on the mesa, which is in contact with the void of the second mold, selectively wets the mold walls, leading to the formation of the first meniscus within the void channel. The polymer rises continuously until it reaches the ceiling of the mold. Note in this regard that the second mold has a finite step height of 220 nm. In the meantime, a uniformly curved surface develops at the mesa position due to Laplace pressure. A second meniscus starts forming when the mold makes contact with the valley (40 min annealing in Fig. 5.5(b)). In the final stage, the height of the first meniscus becomes almost flattened and the lowest part of the second meniscus keeps rising due to capillarity, which leads to the formation of regularly spaced holes (60 min and 90 min annealing in Fig. 5.5(b)). If the annealing time increases further to 3 h, the holes become completely filled.

In the process of self-organization, the step height of the underlying pattern acts as an important factor for pattern formation. For instance, no hole formation occurs if the step height is relatively large. One example is shown in the top part of Fig. 5.5(c), where the step height of the second mold is 600 nm. In

this case, the second meniscus cannot begin forming as seen from the figure such that an isolated line structure results. Furthermore, the underlying structures are not completely destroyed even with a long annealing time. Shown at the bottom of Fig. 5.5(c) is the microstructure that results from the self-organization when the second mold is oriented  $45^\circ$  with respect to the first. In this case, a twisted microstructure forms with an apparent directionality. The directionality of the polymer along the wall is quite surprising in that the polymer is expected to move freely in every direction. As the polymer



5.5 (a) Schematic diagram of the experimental procedure, where  $\theta$  is the angle of mold rotation. (b) AFM images of transient microstructures obtained when the underlying structure of  $1\ \mu\text{m}$  line-and-space patterns was annealed at  $130^\circ\text{C}$  as a function of annealing time. The mold was rotated  $90^\circ$ . (c) Morphologies that result when the step height of the underlying structure is relatively large: transient microstructure obtained when the underlying structure is  $1\ \mu\text{m}$  line-and-space pattern (top). The rotation angle of the mold is  $45^\circ$  (bottom). Reproduced from ref. 15.

tends to decrease the wetting angle in the obtuse angle direction, the rate of mass flow along the obtuse angle direction is much faster than along the acute angle direction, which leads to the morphology shown at the bottom of Fig. 5.5(c).

Various microstructures for different purposes can be obtained including regular arrays of holes and twisted microstructures simply by changing the rotation angle of the second mold with respect to the first, the shape and pattern of the second mold, and that of the underlying polymer structure. These structures would be useful for a variety of applications in biomedical, electronic and optical areas.

#### 5.2.4 Pressure-assisted capillary force lithography (PACFL)

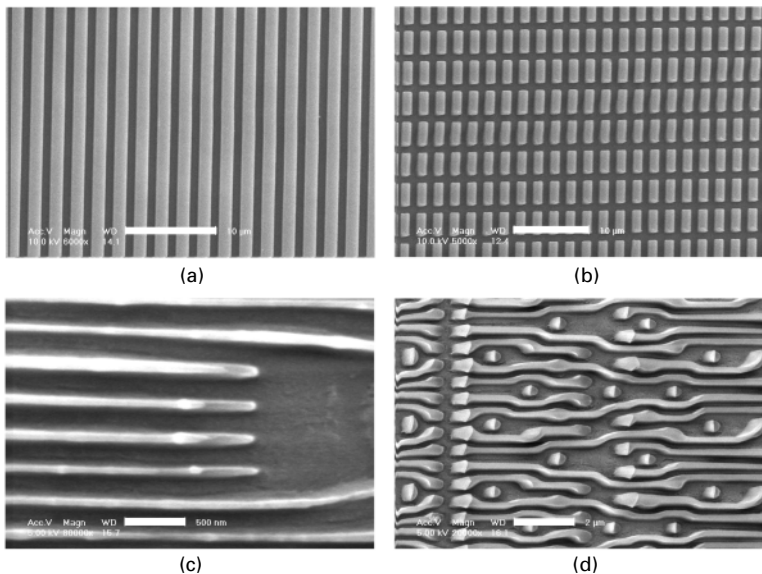
Although the CFL is a powerful patterning technique, deformation problems of PDMS molds impose a resolution limit on the CFL process. Sub-100 nm high-density and high-aspect-ratio features cannot be realized with the conventional elastomeric mold (Sylgard 184, Dow Corning) in the CFL process, as in any other soft lithographic technique because of mold deformation problems, such as pairing, lateral buckling, roof-collapsing, or rounding by surface tension.<sup>17-19</sup>

In this section, we introduce PACFL using a permeable fluoropolymer mold.<sup>6</sup> Compared with conventional CFL, where no pressure is required for the conformal contact of PDMS mold with polymer, PACFL requires a slight pressing (2~3 bar) to achieve the conformal contact of the stiff (tensile modulus ~ 1.6 GPa) fluoropolymer mold with the polymeric layer. The permeable nature of the fluoropolymer mold material is one of the key factors of this PACFL process. Another useful property of the fluoropolymer mold material is its very low surface energy (15.6 dyne/cm), which makes it possible to remove the mold cleanly from the patterned polymer without any mold surface treatment and without surface deterioration over many patterning cycles.

The mold material used in this work is an amorphous fluoropolymer, Dupont Teflon® AF 2400 that is a copolymer of 2,2-bistrifluoromethyl-4,5-difluoro-1,3-dioxole (PDD) and tetrafluoroethylene (TFE).<sup>20</sup> The polymer has a large gas permeability, which is thought to originate from the microvoids (~ 1 nm) generated by loose chain packing that is caused by the high energy for rotation and reorientation of the dioxole-ring-containing polymer chain. This large permeability enables the capillary filling of polymeric melt without any limiting action of entrapped air between the mold and the polymer layer, because the air can diffuse out through the permeable mold during the capillary filling.<sup>6</sup>

The mold was prepared by compression molding of amorphous fluoropolymer powder on a master mold (patterned  $\text{SiO}_2/\text{Si}$  wafer fabricated by conventional photolithography and reactive ion etching) that was placed between the platens of a hydraulic press with heating elements, at  $T \sim 350^\circ\text{C}$ ,  $P \sim 2000$  psi, and time  $\sim 10$  min. After the compression molding of the fluoropolymer powder, the molded samples were cooled to room temperature while maintaining pressure to prevent mold deformation. Then the compression-molded part was manually separated from the master mold. The easy separation from the master mold is due to the low surface energy. To ensure capillary action, the fluoropolymer mold used in this work has recessed patterns on its surface.

For successful PACFL, the uniformity of applied pressure is essential, which ensures conformal contact and thus the capillary action. For this purpose we used a rounded polydimethylsiloxane (PDMS) block as a deformable buffer layer between the weighting block and the mold. Shown in Fig. 5.6 are the scanning electron microscopy (SEM) images of various features patterned by PACFL process. The PACFL was carried out at a temperature of  $160^\circ\text{C}$  for ten minutes with a slight pressing ( $2\sim 3$  bar). As can be seen from the images, these features were well patterned on the polymer surface.



**5.6** SEM images of various features patterned by PACFL process with a permeable fluoropolymer mold. (a) regular line-and-space pattern ( $\sim 1.5 \mu\text{m}$  line-width, bar scale  $\sim 10 \mu\text{m}$ ), (b) regular square pattern ( $\sim 1 \mu\text{m} \times 2 \mu\text{m}$ , bar scale  $\sim 10 \mu\text{m}$ ), (c) dense lines ( $\sim 80$  nm line-width, bar scale  $\sim 500$  nm), and (d) dense, meandering lines and dots ( $\sim 250$  nm wide, bar scale  $\sim 2 \mu\text{m}$ ). Reproduced from ref. 6.

In summary, the PACFL technique introduced in this section has two advantages; high resolution ( $\sim 80$  nm) due to the stiff nature of the mold material and clean mold release or de-molding without any surface treatment due to its low surface energy and inertness. While the smallest feature size demonstrated is about 80 nm because of unavailability of a master with a smaller feature size, there is in principle no reason that PACFL cannot be applied to smaller feature sizes.

### 5.3 Influence of dispersion force on patterning

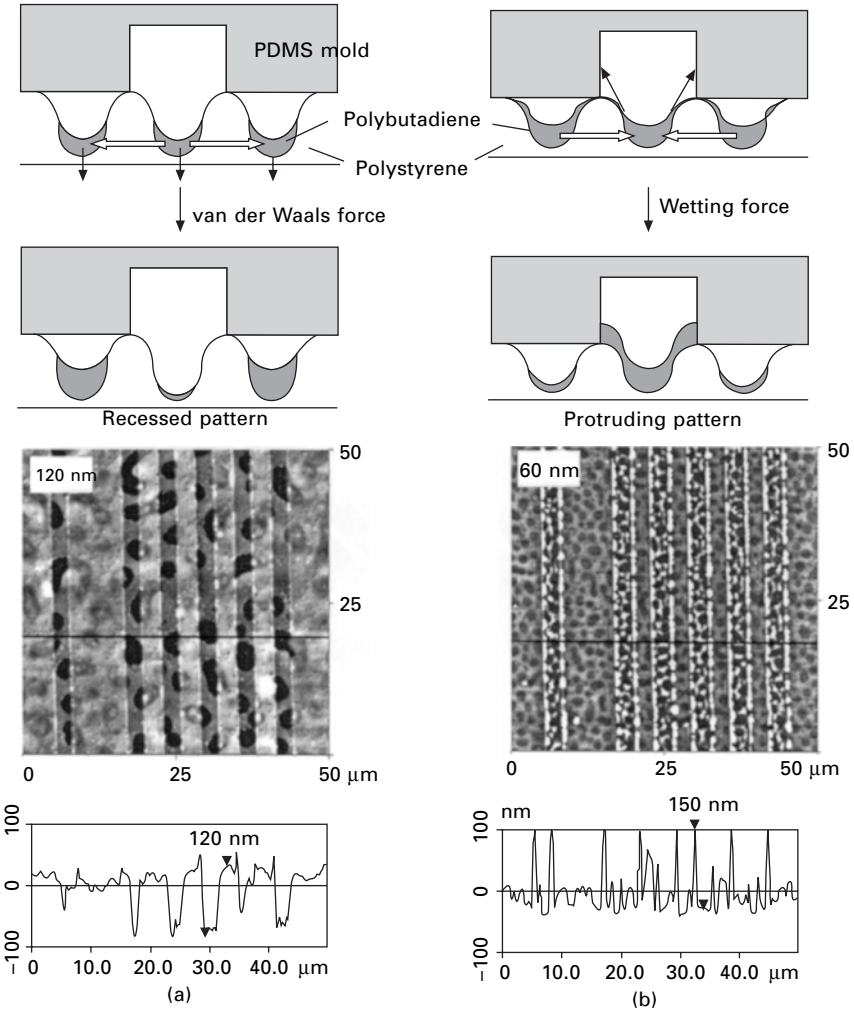
#### 5.3.1 Pattern formation in polymer blend system

While the short-range interactions of capillarity have been exploited in the previous section, the long-range interactions of dispersion force also come into play when the film is thin enough.<sup>21–23</sup> There have been numerous studies in which the short- or long-range interactions alone play the major role in thin films. However, there are not many studies in which both interactions interplay.

In a blend film system of polystyrene (PS) and polybutadiene (PB), PB phase is surrounded by PS phase and the blending results in an isolated island-like morphology. The PS phase protrudes due to its relatively high surface tension and therefore a small gap exists between the two phases.<sup>24,25</sup> Therefore, an application of CFL process to the thin films of polymer blends could provide a unique system in which the direct capillarity is retarded due to this small height gap if one anneals the system at a selected temperature that only makes the underlying PB phase soften ( $T_{g, PB} < T_{g, PS}$ ).<sup>3,26</sup>

The surface morphologies of PS/PB blend films that are 120 nm thick and 60 nm thick are shown in Figs 5.7(a) and (b). The darker island-like domain is the PB phase and the brighter sea-like domain the PS phase. If the PDMS mold with a stripe pattern is placed on the film and the sample is heated at 95 °C, which is slightly below the  $T_g$  of PS (PB is mobile but PS is glassy), the opposite pattern behavior emerges depending on the film thickness. Figure 5.7(a) for 120 nm thick film shows that the stripe-like region under the void of the microchannels of the mold has receded as if it has been pressed. For 60 nm thick film, however, PB rises into the void of the microchannel such that protruding stripes result, as one would observe in the usual CFL.

This difference arises due to the fact that the capillarity competes with the dispersion force, which acts as a dominant force in films thinner than 100 nm.<sup>23,26</sup> The gap between the PS and PB phases is in the range between 30 and 70 nm, so that the dispersion force can participate in the interaction. The case of making the contact is referred to as ‘complete wetting’ in the figure (Fig. 5.7(b)) and that of not making the contact as ‘partial wetting’ (Fig. 5.7(a)). When the rise of PB by capillarity is sufficient to result in



5.7 (a) Idealized schematic diagram for the case where the dispersion force dominates under partial wetting conditions, leading to the recessed pattern (top) and AFM images of PS/PB blend film 120 nm thick with recessed stripes (bottom). (b) Idealized diagram for the case where the capillarity dominates under complete wetting condition, leading to the protruding pattern (top) and AFM images of 60 nm thick film with protruding stripes (bottom). Reproduced from ref. 26.

complete wetting, the PDMS mold picks up the risen PB and also draws PB from the adjacent contact regions for the capillary rise into the mold void, leading to the protruding pattern in Fig. 5.7(b). When partial wetting occurs, however, the capillary force in the void region is counterbalanced by that in the mold contact region and cannot draw the PB phase. Therefore, only the

dispersion force comes into play, which causes the PB in the void region to move into the contact region, resulting in the recessed pattern depicted in Fig. 5.7(a). As presented in this section, a competition between dispersion force and capillary force can lead to interesting pattern formation.

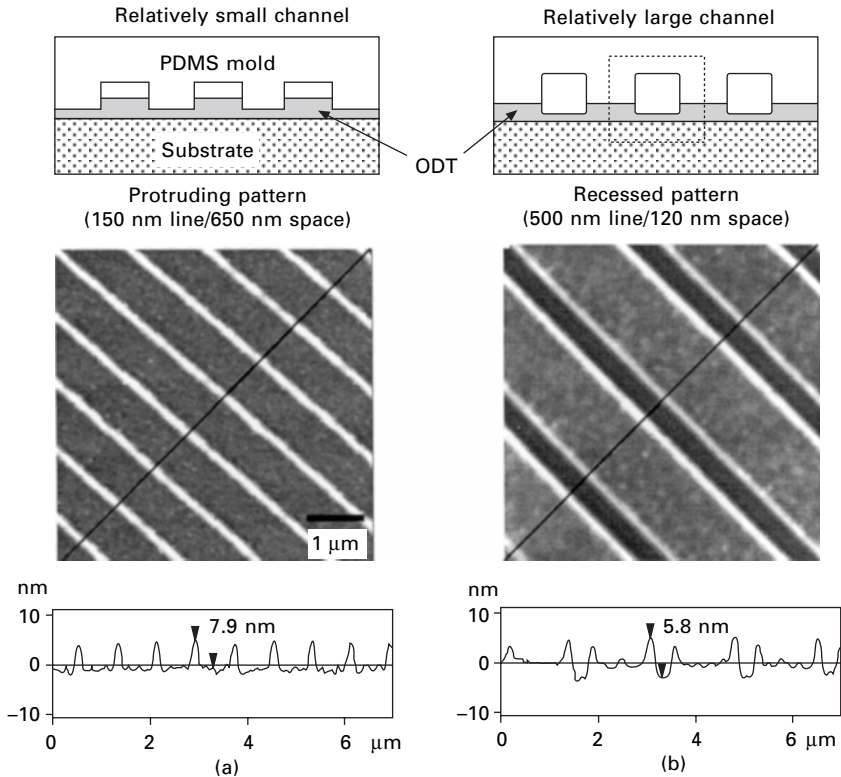
### 5.3.2 Pattern formation in ultra-thin liquid films

Thermal stability of thin liquid films on solid substrates involving dewetting phenomena has been extensively studied.<sup>27–29</sup> Generally, there are two competing factors that dominate the thermodynamic and kinetic behavior of the instability. One is the dispersion force, which promotes the instability, and the other the surface tension, which suppresses the instability.<sup>1,2</sup> As a result, the stability problem is primarily determined by the balance between these two factors.

Introducing capillarity into the picture has the significance of altering the balance between dispersion force and surface energy and of shifting the focus from undesirable dewetting to stable ultrathin film formation.<sup>30</sup> Ordinarily, Laplace pressure overwhelms disjoining pressure when microcapillaries are used. Therefore, the film should be thinner than 10 nm to elucidate clearly the interplay between Laplace and disjoining pressures. For the purpose, self-assembled monolayer (SAM) materials can be used in CFL, such as octadecanethiol (ODT,  $\text{CH}_3-(\text{CH}_2)_{17}-\text{SH}$ ).<sup>30</sup> In the experimental results shown in Fig. 5.7, a PDMS mold with a pattern was placed on the surface of the ODT layer formed on a silicon substrate and then heated well above the melting temperature ( $31 \sim 35^\circ\text{C}$ ) of ODT to  $150^\circ\text{C}$ .<sup>31</sup> A considerable amount of ODT film is immediately absorbed into the PDMS mold when the mold is placed on the surface. As there exist van der Waals interactions between the substrate and the liquid film, however, an ultrathin film (less than 10 nm) always remains on the surface.

Figure 5.7 shows the AFM images of a 3.7 nm ODT film for (a) 150 nm line/650 nm space and (b) 500 nm line/1200 nm space patterns. The depth of the mold cavity is 27 nm for (a) and 97 nm for (b), respectively. As shown in the figure, contrasting behavior emerges depending on the channel width.

The film fills the cavity of the mold to a thickness of about 5.4 nm for a relatively small channel width (150 nm) as shown in Fig. 5.8(a), which results from capillary rise. However, about 2.7 nm thick film remains on the substrate under the regions that were in contact with the mold. On the other hand, for a relatively large channel width (500 nm) shown in Fig. 5.8(b), the film under the void of the channel recedes, thus leading to a thickness difference of about 2.1 nm between the recessed region (valley) and the adjacent region that was in contact with the mold. This result can be viewed as a simple system in which two competing forces exist within the channel confinement; one is the Laplace pressure or capillary force, the first derivative of which is



**5.8** Schematic diagram of the experimental procedure and planar ( $5\ \mu\text{m} \times 5\ \mu\text{m}$ ) and cross-sectional AFM images for (a) 150 nm line/650 nm space and (b) 500 nm line/1,200 nm space patterns. The solid line in the figure indicates the original film height. The samples were annealed at  $150\ ^\circ\text{C}$  for 24 hrs. Reproduced from ref. 30.

negative so that it is stabilizing, and the other is the intermolecular interactions of dispersion force, the first derivative of which is positive so that it is a destabilizing term. The negative Laplace pressure is forced to equilibrate with the positive disjoining pressure, thus making the film stable even at a film thickness less than 10 nm.<sup>30</sup> Therefore, one can make stable ultrathin ( $< 10\ \text{nm}$ ) liquid films even at temperatures much higher than the melting temperature by introducing Laplace pressure. With the capillarity providing a mass sink, the balance between the Laplace pressure and the dispersion force makes the system stable.

## 5.4 Patterning by polymer dewetting

### 5.4.1 Anisotropic dewetting by physical confinement

Dewetting of a liquid film on a substrate has drawn much attention due to fundamental interests in basic wetting phenomena and potential applications

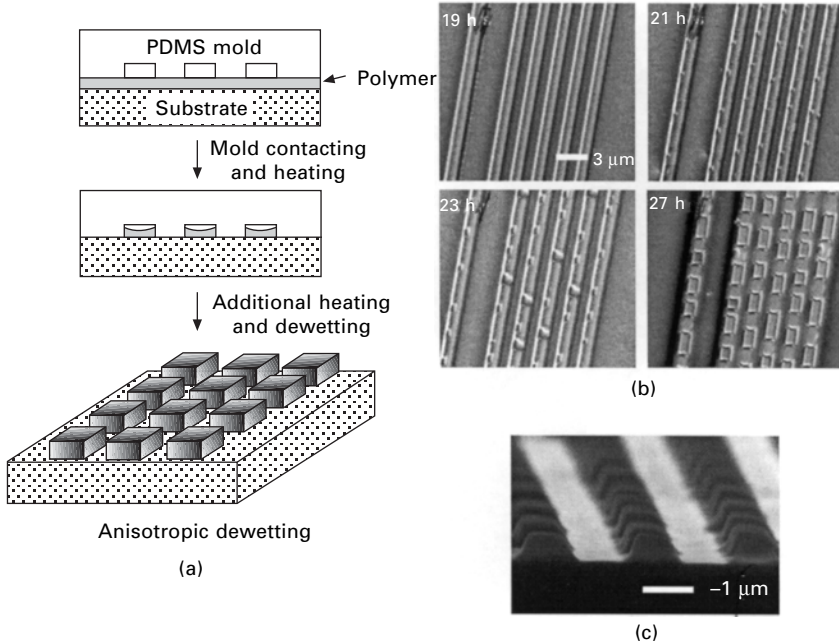
to nano-patterning technology.<sup>27–29,32</sup> Recently, anisotropic spinodal dewetting of polymer films has been reported as a route to patterning surfaces on a nanometer scale.<sup>33,34</sup> To overcome the isotropic nature of spinodal dewetting, chemically or mechanically treated substrates are used, which gives rise to anisotropic behavior. In this section, dewetting behavior of laterally confined polymer films is utilized for patterning with an experimental method specifically devised for the purpose. As a result of physical confinement, the dewetting wave propagates only along the stripe direction and it results in the formation of a directly observable, regular structure.<sup>35</sup>

For the experimental setup, we utilized the CFL method for relatively thin polymer films (42 nm to 127 nm thickness of PS or symmetric styrene-butadiene-styrene (SBS) block copolymer).<sup>3</sup> As shown in Fig. 5.9(a), the PDMS mold with a pattern is placed on the surface of a polymer layer and then heated above the  $T_g$  of the polymer. Due to capillary force, the polymer melt fills up the void space of the channels and each of the polymer stripes formed in each of the channels is confined by silicon substrate and two PDMS walls. The whole setup is then left undisturbed at a chosen heating temperature for a period of time for the dewetting to take place. The PDMS mold is then removed after cooling to room temperature.

If the film is thick enough so that the mold void is completely filled, no dewetting takes place. When the film is thin such that the mold void is partially filled as in Fig. 5.9(a), however, the hole formation occurs above the  $T_g$ . Figure 5.9(b) shows optical microscopy images of the typical transient morphologies of laterally confined SBS films for a 1  $\mu\text{m}$  line-and-space pattern that result from the dewetting. Up to 19 hours, there is no observable change on the polymer surface. However, regularly spaced holes are detected after 21 hours and some holes grow across the stripe after 23 hours. Finally, all the holes propagate to the edge in the lateral direction, which leads to the regularly separated block formation (after 27 hours). The magnified cross-sectional SEM image of the final state is shown in Fig. 5.9(c), which clearly shows the periodic block formation along the stripe.

The existence of PDMS walls is a critical factor for the formation of separated polymer blocks. Without the walls, the nucleated holes could not laterally grow across the wall direction, thereby leading to isolated hole structures. In addition, the confining walls give rise to anisotropic hole growth by suppressing wave propagation in one direction.<sup>38</sup> We found that the anisotropic nature is destroyed as the stripe width increases. The critical value above which the anisotropy is destroyed is about 8  $\mu\text{m}$ .

One important finding in our experiment is that the wavelength of the instability is of the order of  $\mu\text{m}$ . However, the conventional capillary wave model gives a wavelength of the order of several hundred  $\mu\text{m}$  for the conditions used in our experiment. One possible cause of this discrepancy is the viscoelastic properties of the polymer films. As the molecular weight of the polymer



5.9 (a) Schematic diagram of the experimental setup for the anisotropic dewetting and illustration of separated block formation. (b) Optical microscopy images of transient morphologies of SBS thin films for  $1\ \mu\text{m}$  line-and-space pattern. The film thickness is about  $67\ \text{nm}$  and the samples were annealed at  $120\ ^\circ\text{C}$  for various annealing times. (c) Cross-sectional SEM images of the final state of dewetting (after 27 hours). Reproduced from ref. 35.

(MW of PS =  $2.3 \times 10^5$ , MW of SBS =  $3 \times 10^5$ ) used in our experiment is sufficiently high, it would show a more solid-like behavior such that elastic effects may come into play.<sup>36</sup>

We have shown that laterally confined polymer film dewets from the substrate anisotropically along the stripe direction. The dewetting results in the formation of distinctly observable, periodically separated blocks of polymer film. The simple experimental method proposed in this section would be quite useful for the study of polymer films with anisotropic geometry.

#### 5.4.2 Drop patterning by confinement-controlled dewetting

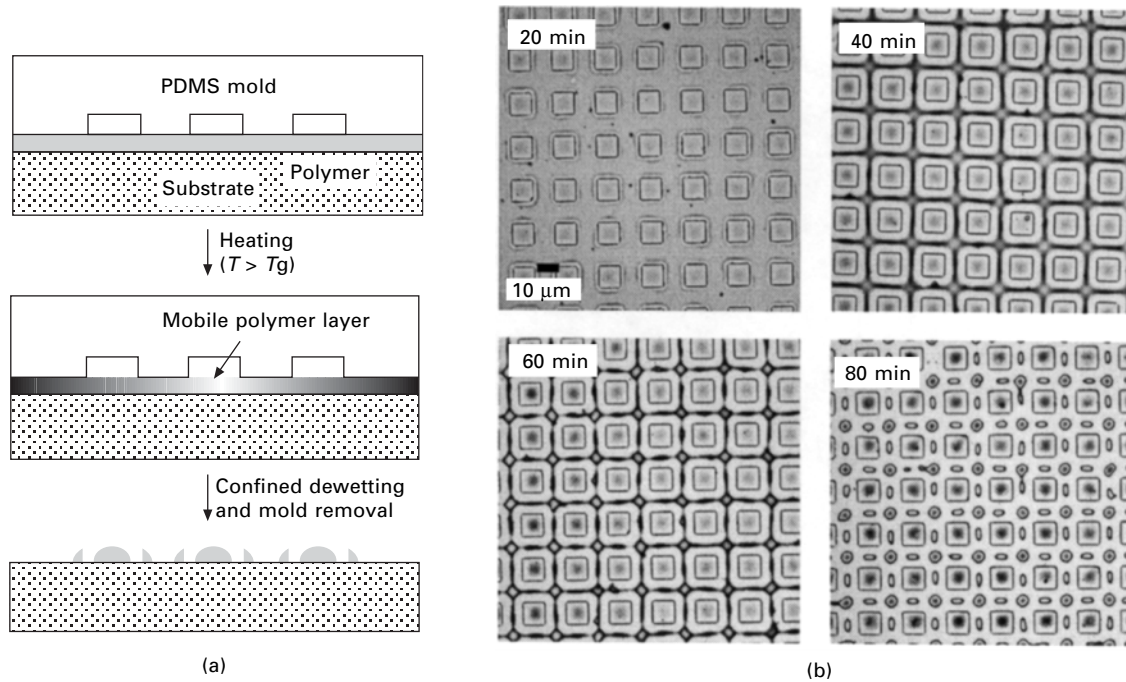
Micro- or nanostructures of polymer can be fabricated easily by the CFL technique, which is treated in section 5.1.1.<sup>3,16</sup> If one hopes to obtain an exact replica of the mold, a high molecular weight polymer should be used as the dewetting of the polymer is suppressed throughout the annealing

process due to its high viscosity. On the other hand, if one hopes to utilize the dewetting phenomenon of the polymer film, a low molecular weight polymer would be useful. As an extension of the previous subject in this section, the controlled polymer dewetting is treated in physically confined systems, in which low molecular weight polymers are used.<sup>37</sup>

Thin films are prepared by spin coating a polymer (PS, MW = 3900,  $T_g = 98^\circ\text{C}$ ) onto a silicon substrate. The film thickness ranges from 23 to 75 nm. The mold with a pattern is placed on the surface of a polymer and then heated above the  $T_g$  of the polymer. During the dewetting process, the PDMS walls act as a boundary, thereby generating a three-dimensionally confined system. A schematic diagram of an experimental setup is shown in Fig. 5.10(a).

To investigate the transients of the regular drop formation, dewetting experiments were carried out with 23 nm PS films using a positive mold for various annealing times (20, 40, 60, and 80 min) at  $130^\circ\text{C}$ , the results of which are shown in Fig. 5.10(b). Both the box size and the space between two adjacent boxes in the figure are  $10\ \mu\text{m}$ . After 20 minutes, the mass climbs up the walls due to capillarity, leading to the thin square lines defining the boxes. Hole formation, which is frequently observed in the conventional dewetting experiments, was not detected in this initial stage. Instead, the polymer recedes from the confining walls both inside and outside the box such that outside the box a large circular rim surrounding the box is observed but a flat and circular drop forms inside the box. Note in this regard that the box in contact with the polymer acts as a defect-like site from which the mass is driven away. The circular rim outside the box is formed by the mass accumulation from the walls, which has the same origin as in the hill formation around the holes in the conventional dewetting. In this initial stage, no distinct ordering is observed. Then, the polymer merges into a thick, square ribbon outside the box. Spherical drops form at four corners due to mass accumulation (after 40 min). The drops continuously grow in size at the expense of the ribbons and finally the ribbons break up after about 60 minutes. When the annealing time exceeds 60 minutes, the drops further merge into larger ones that are located at four corners and four center lines around a box (after 80 min), which resembles the two-dimensional projection of a face-centered cubic (FCC) structure. No further transient morphology was observed even after one day such that the structure after 80 min appears to be at equilibrium.

One notable finding in Fig. 5.10(b) is that the shape of the drops located at the mid points between corners is oval rather than circular whereas the drops at four corners are circular. This fact reveals that kinetic rather than thermodynamic factors could govern the drop shape. Although a perfectly spherical drop may be thermodynamically stable, the drop cannot change overall shape once the oval shape forms. This fact is readily understood in



5.10 (a) Illustration of experimental procedure for controlled dewetting. (b) Optical micrographs of the transient morphologies of polymer drops for a  $10\ \mu\text{m} \times 10\ \mu\text{m}$  positive box pattern. Samples were annealed at  $130\ ^\circ\text{C}$  for 20, 40, 60, and 80 minutes, respectively. Reproduced from ref. 37.

that the polymer should migrate in an excessive amount to change the overall shape, which may be kinetically hindered because of its high kinetic barrier.<sup>37</sup> Further study would be required to elucidate the effect of physical confinement on the drop shape.

It has been shown that polymer films form ordered drops under the physical confinement of PDMS mold. The shape of the drop located at the mid points between the corners of boxes is determined by kinetic factors. As a result, an oval rather than the expected circular shape is observed, which opens up a new possibility of controlling the drop shape. Since the findings should be equally applicable to a number of polymers, the results reported here could provide a convenient way of studying the dewetting behavior of thin polymer films under confined geometry and also of fabricating ordered polymer microstructures.

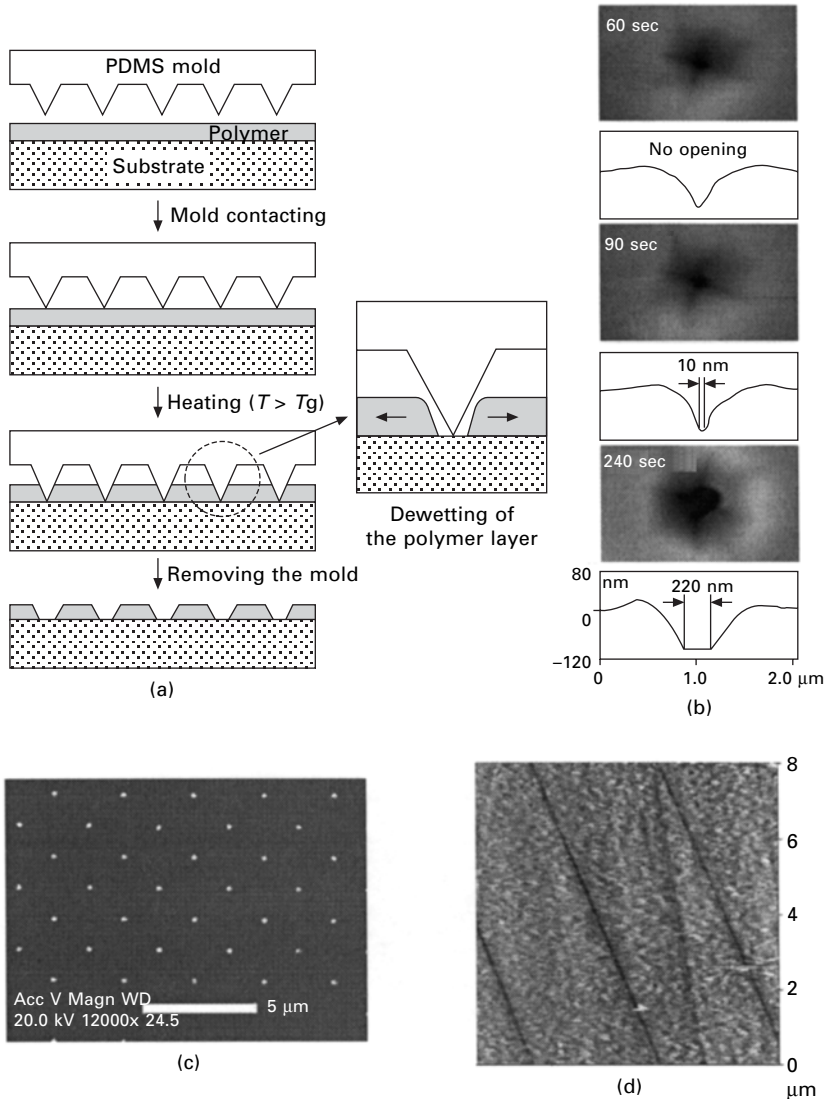
#### 5.4.3 Pattern formation by selective dewetting

London force involving a very thin layer has been utilized as a means for patterning surfaces on a nanometer scale through anisotropic spinodal dewetting.<sup>34</sup> However, this route to patterning by dewetting cannot provide one with the capability of patterning a surface only on desired locations. In this section, a simple method is presented that allows for patterning a surface only at desired locations through selective dewetting.<sup>38</sup>

The procedure involved in the self-generation of a pattern with a template and the coated polymer is schematically illustrated in Fig. 5.11(a). The PDMS mold with a desired pattern is simply placed on the polymer film and heated to a temperature higher than the  $T_g$  of the polymer and then allowed to remain undisturbed for a specified period of time. During this annealing process, the mold sinks into the polymer melt. When the sharp edges of the mold approach the substrate surface close enough that London force comes into play, dewetting starts taking place, which in turn breaks up the film, opening holes or lines depending on whether the pattern on the mold consists of sharp points or lines. After the specified time has elapsed, it is cooled with the mold still in place and then the mold is simply removed.

The instability causing the film to break up occurs at the location where the film thickness is the smallest which allows for selective dewetting and hole formation.<sup>27</sup> Once the dry spots (holes) form, the hole radius grows with time, which in turn allows for control of the hole size by simply manipulating the annealing time. The time progression of hole formation and its subsequent growth of the hole size is given in Fig. 5.11(b). Shown in the figure are AFM images obtained as a function of annealing time along with the sectional thickness profiles across the developing holes. After one minute of annealing of 75 nm thick PS ( $MW = 1.1 \times 10^4$ ) film, the hole has not yet formed as the sharp edge at the center indicates in the cross-sectional

profile. A flat portion starts appearing after 1.5 minutes and the length of this portion or the hole radius begins to grow rather quickly with time. The key here is that the feature size can be controlled down to 10 nm level.



5.11 (a) Illustration of the procedure for the self-generation of desired pattern by selective dewetting. (b) Temporal progression of hole opening in 75 nm thick PS film on Si wafer (image size  $2 \times 2 \mu\text{m}^2$ ). (c) SEM images of dot (180 nm) pattern formed by selective dewetting and then depositing copper by electroless plating. (d) AFM image of the lines formed by the technique and then wet etching: lines with  $\sim 50$  nm width (image size  $8 \times 8 \mu\text{m}^2$ ). Reproduced from ref. 38.

To confirm the presence of dry spots, we carried out an electroless copper deposition. If the underlying silicon surface is exposed, a treatment with HF of the surface followed by placing the whole structure in a copper sulfate solution (HF: CuSO<sub>4</sub>: H<sub>2</sub>O = 2: 5: 93) should result in the growth of copper only on the exposed surface of the holes but not on the surface covered with the polymer.<sup>4</sup> It can be verified in Fig. 5.11(c) that 180 nm size copper dots deposited. These results demonstrate not only the patterning capability of the desired features but also the utilization of the patterning for film deposition. To show a fine pattern that can be etched, a line pattern obtained by the selective dewetting was etched through the native oxide of the substrate by dipping in a dilute HF solution and then removing the polymer by washing in toluene. Figure 5.11(d) shows the fine lines thus obtained, the width of which is about 50 nm.

Dewetting has been a subject much studied for its dynamics and instability. Its use as a means for general-purpose patterning or lithography has never been shown to be possible, presumably due to the complexity of the dewetting process. As presented in this section, a selective dewetting technique can be used for general-purpose patterning. We have shown that the desired pattern size ranging from the 10 nm level to hundreds of nanometers can be obtained with the same mold simply by changing the duration of dewetting.<sup>38</sup> This unique capability of the technique is due to the nature of dewetting. In contrast, other techniques require a different mold whenever a different size is needed.<sup>7-9</sup> As the technique is a simple method applicable to large-area patterning, the extension to larger areas should be quite possible.

## 5.5 Patterning by stress for metal/polymer bilayer

### 5.5.1 Spinodal wrinkling in metal/polymer bilayer

Wrinkle formation in thin film systems by buckling is a well known phenomenon. The wrinkles are believed to form spontaneously by the abrupt compressive stress due to the misfit strain from the mismatch in thermal expansion coefficients.<sup>39,40</sup> However, the thin bilayer system being considered here is a thin polymer layer capped with a thin metal layer and the stress at work on the metal layer during the heating process is tensile.

In this system, a viscoelastic property of polymer induces the instability and forms an isotropically buckled surface. Bilayers of aluminum on PS are used in experiments, in which aluminum is thermally deposited on the coated PS film. Then the samples are heated above the  $T_g$  of PS. Final wavy surface structures are examined by AFM in the contact mode.

Temporal evolution of the surface pattern is shown in Fig. 5.12(a) along with Fast Fourier Transform (FFT) shown in the inset of each frame. There are two distinct transitions. One is the transition from an island-like pattern

to a labyrinthine pattern as apparent in going from the first to the second. This early stage, which is to be called Stage I, is characterized by the constancy of the dominant wavelength of buckled waves. The other transition is marked by the appearance of a second wave, as typified in the third FFT in Fig. 5.12(a), i.e., the emergence of a second ring or a larger wave than the first in Stage I. As time progresses, the larger wave starts exerting itself and becomes dominant over the initial wave. This period is to be called Stage II.<sup>41</sup>

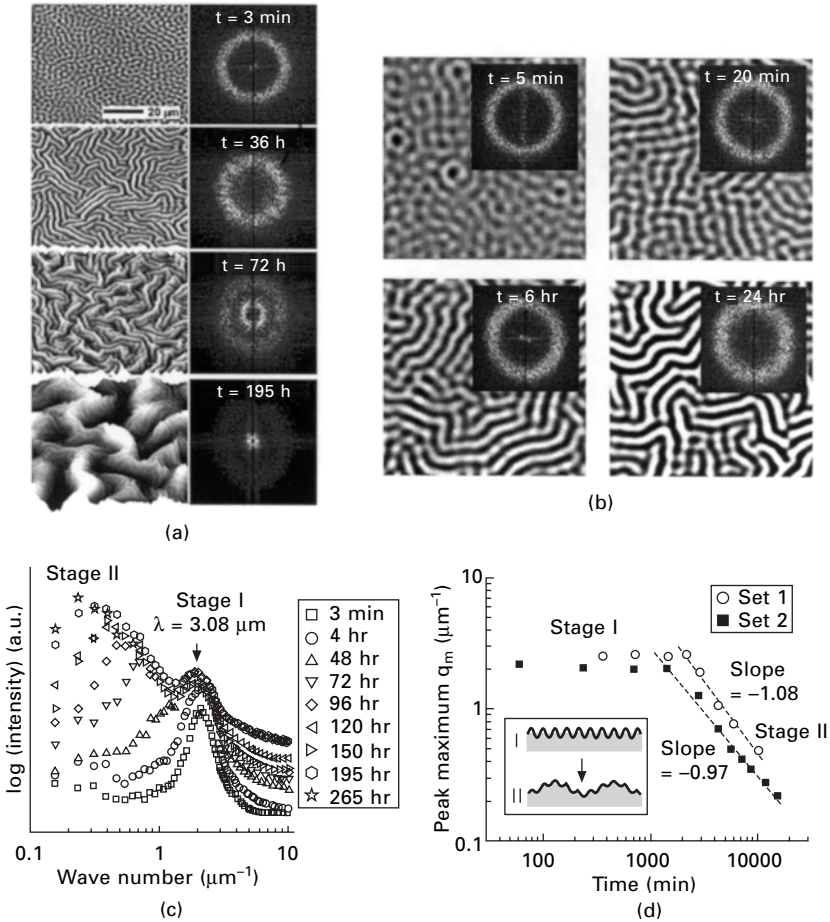
The shape transition in Stage I is detailed in Fig. 5.12(b). The island-like pattern is seen to evolve to a textured and to a fully-developed labyrinthine pattern in about one day.<sup>42</sup> During this early stage, the wave amplifies continuously but the wavelength remains the same. The characteristic wavelength is determined by minimizing the system free energy of the bilayer with respect to wave number and is in effect the result of a competition between metal bending energy and elastic polymer deformation energy.<sup>43,44</sup> The result predicts well the wavelength dependence on thickness and temperature variations.

The dynamics of these two stages can be understood more precisely by an analysis of power spectra of the resulting patterns shown in Fig. 5.12(c). It uncovers the fact that initial waves are still retained even in the late stage. Thus, initial small waves are imbedded in the larger waves. However, once the second maximum peak emerges after about two days of heating, the larger waves become dominant and grow with time. Figure 5.12(d) shows the wave number plotted against time. As mentioned earlier, the wave number remains the same in Stage I. In Stage II of interest here, it is seen that the wave number is inversely proportional to time.<sup>40</sup> It is notable that this growth rate dependence is identical with that found in the late coarsening stage of spinodal decomposition.<sup>45,46</sup>

As a result, spinodal wrinkling can be summarized as one in which the wavelength remains constant and the magnitude increases with time in Stage I (elasticity-induced wave), but the magnitude remains constant in Stage II (viscosity-induced wave) while the wavelength increases with time. Spinodal wrinkling also have many similarities with spinodal decomposition in morphological characteristics.<sup>44,45,47</sup>

## 5.5.2 Pattern formation by anisotropic buckling

The basic idea in this section is that a certain order could be imposed on the buckling if an elastomeric mold with a desired pattern is placed on the metal surface of a bilayer of metal on polymer, prior to heating. During the buckling process, then, the wrinkles generated to relieve the stress could self-organize into the contour of the mold surface.<sup>48</sup> As discussed in the previous section, the early stage of the spinodal wrinkling has a characteristic constant wavelength so that it can provide us a good processing window for this self-organization



5.12 (a) AFM images of temporal evolution of stress-driven surface wave pattern. A bilayer of 580 nm thick polymer and 30 nm thick aluminum was used. (b) AFM images of the initial stage of wave development. (c) Power spectra intensity of evolving patterns as a function of wave number. (d) Dominant wave number-time relation. Reproduced from ref. 41.

of buckling wave in the confined environment of PDMS/metal/polymer system.<sup>41</sup>

The procedure involved in the physical self-organization by anisotropic buckling is illustrated schematically in Fig. 5.13(a). As shown in first step of the figure, a PDMS mold with a pattern is simply placed on the metal surface of the bilayer on a substrate. With the mold in place without any external force, the temperature is raised above the  $T_g$  of the polymer. After the buckling takes place, the mold is simply removed, finishing the self-organization.

To quantify the experimental results, an estimation of the characteristic

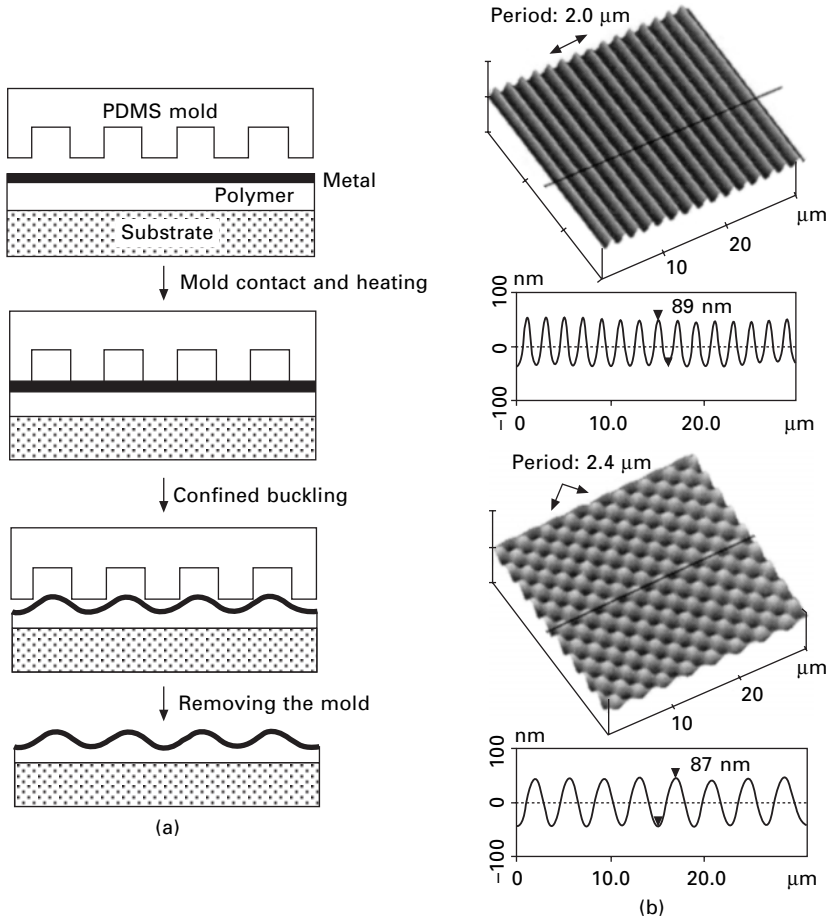
wavelength of a buckling wave is needed. For the system being considered, the film thickness of the underlying polymer is finite and of the same order of magnitude as the metal layer. To take into account the effects of the thin underlying layer, a free energy approach based on an elastic theory for polymer layer can be adopted.<sup>43,44</sup> For a buckled bilayer of thin film, the total free energy is given by the sum of the bending energy of the metal layer and the deformation energy of the underlying polymer layer. Then, the intrinsic buckling wavelength can be obtained by minimizing the free energy with respect to the wave number. After determining the characteristic wavelength of buckling, we can apply the PDMS mold that has a similar pattern size for the self-organization.

Figure 5.13(b) shows ordered bilayer structures obtained by this anisotropic buckling. It is seen that the random wrinkles such as those in Fig. 5.12(b) have self-organized themselves into ordered structures. PDMS molds with protruding lines and spaces between them were used for the result in the top part of Fig. 5.13(b); the molds with a protruding cylinder-shaped dot pattern were used for the result in the bottom part of Fig. 5.13(b). In the case of the line-and-space pattern, a sinusoidal line structure forms that is the negative replica of the PDMS mold pattern. In Fig. 5.13(b), the period of the line-and-space pattern on the mold is  $2\ \mu\text{m}$  and the intrinsic buckling wavelength is  $2.6\ \mu\text{m}$ . Although the intrinsic buckling wavelength is somewhat larger than the period of the mold pattern in this case, the wrinkles conform to the period dictated by the mold, the period of the self-assembled bilayer being  $2\ \mu\text{m}$ . As long as the difference is not too large between the intrinsic buckling wavelength and the period of the mold pattern, a sinusoidal surface structure results. The compliance with the mold pattern period is also apparent in the checkerboard pattern in Fig. 5.13(b) that is obtained with a cylinder-shaped dot pattern. A checkerboard-like self-organization is seen to have resulted in which the intrinsic wavelength is  $2.6\ \mu\text{m}$  and the pattern period is  $2.4\ \mu\text{m}$ .<sup>48</sup>

In summary, we have presented a form of physical self-organization in which stress relief is the driving force for the self-organization. When a bilayer of metal on polymer is heated above the glass transition temperature of the polymer, directionally random wrinkles are generated. However, an elastomeric mold with a periodic pattern, when placed on the metal surface, guide the random wrinkles to self-organize into an ordered sinusoidal structure.

### 5.5.3 Microshaping metal surfaces by self-organized buckling

Controlling the wrinkles by buckling so as to produce a desired pattern or shape has been a key issue in surface wrinkling and yet only recently have



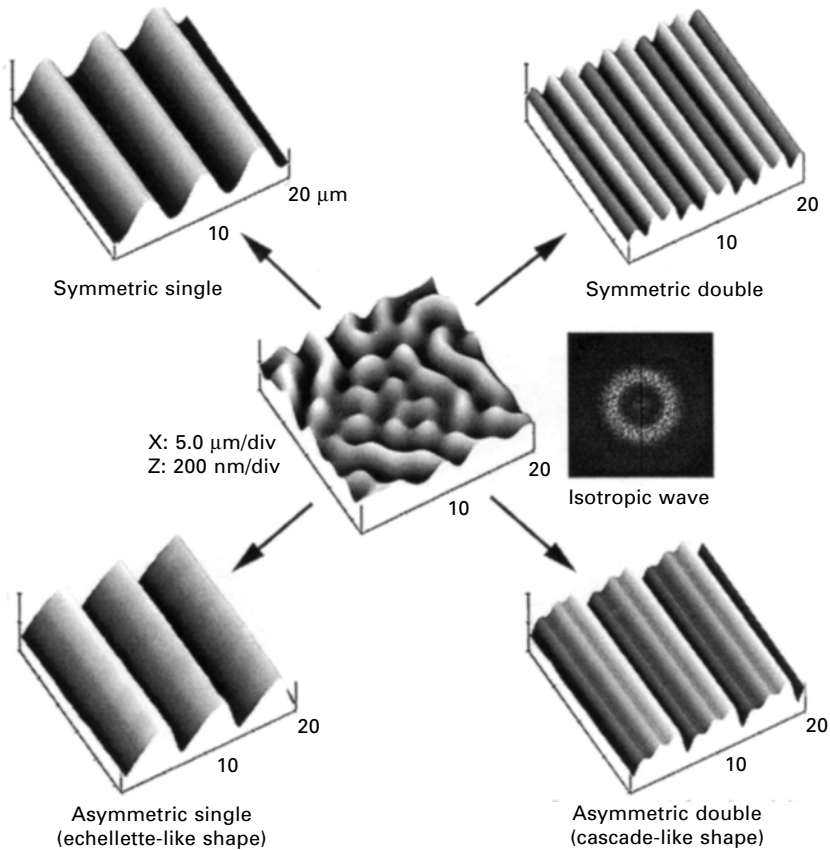
5.13 (a) Schematic illustration of the procedure involved in self-organized buckling. (b) AFM images of ordered structures resulting from self-organization of the random wrinkles. Top pattern is the structure resulting from applying a line-and-space mold with a period of  $2.0\ \mu\text{m}$  ( $t_m = 60\ \text{nm}$ ,  $t_p = 180\ \text{nm}$ ,  $\lambda_i = 2.6\ \mu\text{m}$ ), where  $t_m$ ,  $t_p$  are the metal and polymer layer thickness, respectively, and  $\lambda_i$  is the intrinsic buckling wavelength. Bottom pattern is the structure resulting from applying a cylindrical dot mold with a period of  $2.4\ \mu\text{m}$  under the same experimental conditions. Reproduced from ref. 48.

there been studies on utilizing the wrinkling for the purpose of generating regular patterns.<sup>49–51</sup> In the previous section, it was shown that anisotropic buckling can be realized by introducing external confinement.<sup>48</sup>

When a patterned PDMS mold is placed on the bilayer, it makes a strong conformal contact with the underlying metal surface, which makes the edges of the pattern act as nodes. These nodes dictate the nodal condition to be

satisfied, i.e., creation of nodal waves within the period of the mold pattern (see Fig. 5.13(a)). The question is how these nodal waves created by the externally imposed wave interact with the internal, intrinsic wave. In general, the mold wave number is not equal to the intrinsic wave number as was the case in the previous section. If there is a mismatch, therefore, the system must adjust its wave number so as to satisfy the imposed nodal condition.

A specific question raised in this section is how an externally imposed periodic wave causes the surface of a bilayer to evolve into different shapes by self-organization. As shown in the center of Fig. 5.14, the usual isotropic wrinkles are created in the absence of an external mold.<sup>52</sup> When a mold with



**5.14** AFM images of metal surface formed by self-organization. For all the shapes formed, one and the same PDMS mold ( $3\ \mu\text{m}$  line-and-space) was used. Isotropic waves in the absence of the mold (center). Symmetric single-mode (left up:  $t_m = 80\ \text{nm}$ ,  $t_p = 520\ \text{nm}$ ,  $\lambda_i = 4.68\ \mu\text{m}$ ). Asymmetric single-mode (left down:  $t_m = 60\ \text{nm}$ ,  $t_p = 600\ \text{nm}$ ,  $\lambda_i = 3.92\ \mu\text{m}$ ). Asymmetric double-mode (right down,  $t_m = 50\ \text{nm}$ ,  $t_p = 350\ \text{nm}$ ,  $\lambda_i = 2.96\ \mu\text{m}$ ). Symmetric double-mode (right up,  $t_m = 30\ \text{nm}$ ,  $t_p = 220\ \text{nm}$ ,  $\lambda_i = 1.68\ \mu\text{m}$ ). Reproduced from ref. 53.

a periodic pattern is placed onto the bilayers with a different intrinsic wavelength, however, the bilayers are made to self-organize into the various ordered shapes even with the same mold.<sup>53</sup> This self-organization does not lead to a surface with a simple sinusoidal structure or shape. One notable finding in these experimental results is that asymmetric waves form as shown in the bottom part of Fig. 5.14. This symmetry breaking originates from the system's desire to minimize its free energy. This accommodation of the symmetry-breaking harmonic gives rise to an echellette-like or cascade-like shape, which is very useful for optical applications, as in shallow gratings.

To explain the various wave formations, the free energy approach that takes into account the confinement state can be used for analysis.<sup>43,44,54</sup> The free energy minimization can also be utilized to determine the fraction of magnitude that each allowed harmonic mode contributes to the overall surface shape, thereby permitting shape engineering of the metal surface.<sup>53</sup> The ability to tailor the shape of a solid surface would find potential applications in many areas. In particular, the advantage of tunability for an optical surface can be utilized as a promising method for making an optical device with other techniques that have been proposed.<sup>55–57</sup>

## 5.6 References

1. Adamson A.W. and Gast A.P., *Physical Chemistry of Surfaces*, New York, John Wiley & Sons, 1997.
2. Israelachvili J.N., *Intermolecular and Surface Forces*, London, Academic Press, 1992.
3. Suh K.Y., Kim Y.S. and Lee H.H., 'Capillary force lithography', *Adv. Mater.*, 2001 **13**(18) 1386–1389.
4. Kim Y.S., Suh K.Y. and Lee H.H., 'Fabrication of three-dimensional microstructures by soft molding', *Appl. Phys. Lett.*, 2001 **79**(14) 2285–2287.
5. Kim Y.S., Park J. and Lee H.H., 'Three-dimensional pattern transfer and nanolithography: modified soft molding', *Appl. Phys. Lett.*, 2002 **81**(6) 1011–1013.
6. Khang D.Y. and H.H., 'Pressure-assisted capillary force lithography', *Adv. Mater.*, 2004 **16**(2) 176–179.
7. Chou S.Y., Krauss P.R. and Renstrom P.J., 'Imprint lithography with 25-nanometer resolution', *Science*, 1996 **272**(5258) 85–87.
8. Xia Y.N. and Whitesides G.M., 'Soft lithography', *Angew. Chem. Int. Ed.*, 1998 **37**(5) 551–575.
9. Xia Y.N., Rogers J.A., Paul K.E. and Whitesides G.M., 'Unconventional methods for fabricating and patterning nanostructures', *Chem. Rev.*, 1999 **99**(7) 1823–1848.
10. Mark J.E., *Polymer Data Handbook*, New York, Oxford University Press, 1999.
11. Khang D.Y. and H.H., 'Room-temperature imprint lithography by solvent vapor treatment', *Appl. Phys. Lett.*, 2000 **76**(7) 870–872.
12. Imry Y., *Introduction to Mesoscopic Physics*, New York, Oxford University Press, 1997.
13. Aizenberg J., Black A.J. and Whitesides G.M., 'Control of crystal nucleation by patterned self-assembled monolayers', *Nature*, 1999 **398**(6727) 495–498.

14. Choi I.S., Bowden N. and Whitesides G.M., 'Macroscopic, hierarchical, two-dimensional self-assembly', *Angew. Chem. Int. Ed.*, 1999 **38**(20) 3078–3081.
15. Suh K.Y. and Lee H.H., 'Self-organized polymeric microstructures', *Adv. Mater.*, 2002 **14**(5) 346–351.
16. Suh K.Y. and Lee H.H., 'Capillary force lithography: large-area patterning, self-organization, and anisotropic dewetting', *Adv. Funct. Mater.*, 2002 **12**(6+7) 405–413.
17. Delamarche E., Schmid H., Michel B. and Biebuyck H., 'Stability of molded polydimethylsiloxane microstructures', *Adv. Mater.*, 1997 **9**(9) 741–746.
18. Schmid H. and Michel B., 'Siloxane polymers for high-resolution, high-accuracy soft lithography', *Macromolecules*, 2000 **33**(8) 3042–3049.
19. Hui C.Y., Jagota A., Lin Y.Y. and Kramer E.J., 'Constraints on microcontact printing imposed by stamp deformation', *Langmuir*, 2002 **18**(4) 1394–1407.
20. Resnick P.R. and Buck W.H., in *Fluoropolymers* (eds: Hougham G.G., Cassidy P.E., Johns K. and Davidson T.), Vol. 2, Kluwer Academic Publisher, New York, 1999.
21. Bruder F. and Brenn R., 'Spinodal decompositions in thin films of a polymer blend', *Phys. Rev. Lett.*, 1992 **69**(4) 624–627.
22. Martin P. and Brochard-Wyart F., 'Dewetting at soft interfaces', *Phys. Rev. Lett.*, 1998 **80**(15) 3296–3299.
23. David M.O., Reiter G., Sitthai T. and Schultz J., 'Deformation of a glassy polymer film by long-range intermolecular forces' *Langmuir*, 1998 **14**(20) 5667–5672.
24. Tanaka K., Takahara A. and Kajiyama T., 'Film thickness dependence of the surface structure of immiscible polystyrene/poly(methyl methacrylate) blends' *Macromolecules*, 1996 **29**(9) 3232–3239.
25. Dalnoki-Veress K., Forrest J.A. and Dutcher J.R., 'Mechanical confinement effects on the phase separation morphology of polymer blend thin films', *Phys. Rev. E.*, 1998 **57**(5) 5811–5817.
26. Yoo P.J., Suh K.Y. and Lee H.H., 'Short- and long-range interactions in thin films of polymer blends in microchannels', *Macromolecules*, 2002 **35**(8) 3205–3212.
27. Reiter G., 'Dewetting of thin polymer films', *Phys. Rev. Lett.*, 1992 **68**(1) 75–78.
28. Reiter G. and Khanna R., 'Real-Time Determination of the Slippage Length in Autophobic Polymer Dewetting', *Phys. Rev. Lett.*, 2000 **85**(13) 2753–2756.
29. Suh K.Y. and Lee H.H., 'Dynamic Instability of Strongly Confined Thin Polymer Films in Spinodal Dewetting', *Phys. Rev. Lett.*, 2001 **87**(13) 135502.
30. Suh K.Y. and Lee H.H., 'Ultrathin liquid films under alternating intermolecular potential fields and capillary force', *J. Chem. Phys.*, 2002 **117**(13) 6266–6270.
31. Calistri-Yeh M., Kramer E.J., Sharma R., Zao W., Rafailovich M.H., Sokolov J. and Brock J.D., 'Thermal stability of self-assembled monolayers from alkylchlorosilanes', *Langmuir*, 1996 **12**(11) 2747–2755.
32. Herminghaus S., Jacobs K., Mecke K., Bischof J., Fery A., Ibn-Elhaj M and Schlagowski S., 'Spinodal dewetting in liquid crystal and liquid metal films', *Science*, 1998 **282**(5390) 916–919.
33. Higgins A.M. and Jones R.A.L., 'Anisotropic spinodal dewetting as a route to self-assembly of patterned surfaces', *Nature*, 2000 **404**(6777) 476–478.
34. Gleiche M., Chi L.F. and Fuchs H., 'Nanosopic channel lattices with controlled anisotropic wetting', *Nature*, 2000 **403**(6766) 173–175.
35. Suh K.Y. and Lee H.H., 'Anisotropic hole formation in thin polymer films confined by walls', *J. Chem. Phys.*, 2001 **115**(17) 8204–8208.
36. Wang J., Tolan M., Seeck O.H., Sinha S.K., Bahr O., Rafailovich M.H. and Sokolov J., 'Surfaces of Strongly Confined Polymer Thin Films Studied by X-Ray Scattering', *Phys. Rev. Lett.*, 1999 **83**(3) 564–567.

37. Suh K.Y., Park J. and Lee H.H., 'Controlled polymer dewetting by physical confinement', *J. Chem. Phys.*, 2002 **116**(17) 7714–7718.
38. Kim Y.S. and Lee H.H., 'Selective dewetting for general purpose patterning', *Adv. Mater.*, 2003 **15**(3) 332–334.
39. Timoshenko S.P. and Gere J.M., *Theory of Elastic Stability*, New York, McGraw-Hill, 1961.
40. Allen H.G., *Analysis and Design of Structural Sandwich Panels*, New York, Pergamon, 1969.
41. Yoo P.J. and Lee H.H., 'Evolution of stress-driven pattern in thin bilayer films: spinodal wrinkling', *Phys. Rev. Lett.*, 2003 **91**(15) 154502.
42. Gunaratne G.H., Ratnaweera A. and Tennekone K., 'Emergence of order in textured patterns', *Phys. Rev. E.*, 1999 **59**(5), 5058–5064.
43. Landau L.D. and Lifshitz E.M., *Theory of Elasticity*, Oxford, Pergamon, 1970.
44. Fredrickson G.H., Ajdari A., Leibler L. and Carton J., 'Surface modes deformation energy of a molten polymer brush', *Macromolecules*, 1992 **25**(11) 2882–2889.
45. Cahn J.W., 'Spinodal decomposition', *Trans. Metall. Soc. AIME.*, 1968 **242** 166–180.
46. Bates F.S. and Wiltzius P., 'Spinodal decomposition of a symmetric critical mixture of deuterated and protonated polymer', *J. Chem. Phys.*, 1989 **91**(5) 3258–3274.
47. Herminghaus S., 'Dynamical Instability of Thin Liquid Films Between Conducting Media', *Phys. Rev. Lett.*, 1999 **83**(12) 2359–2361.
48. Yoo P.J., Suh K.Y., Park S.Y. and Lee H.H., 'Physical self-assembly of microstructures by anisotropic buckling', *Adv. Mater.*, 2002 **14**(19) 1383–1387.
49. Bowden N., Brittain S., Evans A.G., Hutchinson J.W. and Whitesides G.M., 'Spontaneous formation of ordered structures in thin films of metals supported on an elastomeric polymer', *Nature*, 1998 **393**(6681) 146–149.
50. Bowden N., Huck W.T.S., Paul K.E. and Whitesides G.M., 'The controlled formation of ordered, sinusoidal structures by plasma oxidation of an elastomeric polymer', *Appl. Phys. Lett.*, 1999 **75**(17) 2557–2559.
51. Chua D.B.H., Ng H.T. and Li S.F.Y., 'Spontaneous formation of complex and ordered structures on oxygen-plasma-treated elastomeric polydimethylsiloxane', *Appl. Phys. Lett.*, 2000 **76**(6) 721–723.
52. Dalnoki-Veress K., Nickel B.G. and Dutcher J.R., 'Dispersion-driven morphology of mechanically confined polymer films' *Phys. Rev. Lett.*, 1999 **82**(7) 1486–1489.
53. Yoo P.J., Park S.Y., Kwon S.J., Suh K.Y. and Lee H.H., 'Microshaping metal surfaces by wave-directed self-organization', *Appl. Phys. Lett.*, 2003 **83**(21) 4444–4446.
54. Groenewold J., 'Wrinkling of plates coupled with soft elastic media', *Physica A*, 2001 **298**(1–2) 32–45.
55. Hutley M.C., *Diffraction Gratings*, New York, Academic Press, 1982.
56. Loewen E.G. and Popov E., *Diffraction gratings and applications*, New York, Marcel Dekker Inc., 1997.
57. Xia Y.N., Kim E., Zhao X., Rogers J.A., Prentiss M. and Whitesides G.M., 'Complex optical surfaces formed by replica molding against elastomeric masters', *Science*, 1996 **273**(5273) 347–349.

## 6.1 Introduction

The interactions between beams of accelerated positively charged nuclei or ions and the atoms of a workpiece can modify the material in such a way that it can be patterned, either because the material is removed directly by the interaction (sputtering or ablation) or because the properties of the material are changed by the interaction. Most commonly the solubility of the material is modified, allowing the pattern to be developed in a solvent, but other properties such as refractive index or optical absorption may be modified to create functional devices. Compared with other forms of pattern transfer, the use of ion beams can offer important advantages in terms of minimum feature size, structure depth or aspect ratio, depending on the details of the application.

This chapter aims to present an overview of ion beam techniques of micro-fabrication, commencing with a review of the important aspects of ion-solid interactions and moving on to a description of the three most important techniques: reactive ion etching, focused ion beam and the newly emerging proton beam machining using MeV ions. For each technique an outline of the equipment and methods will be given, together with examples of applications using the techniques. Finally an overview of the future trends of the development of the techniques will be given.

## 6.2 Ion-solid interactions

### 6.2.1 General introduction and terminology

Ions are the electrically charged particles formed by adding or removing one or more electrons to or from a neutral atom or molecule. Although negative ions (more electrons than protons) can exist, they are not used in patterning applications, and we will consider only positive ions, which have a deficit of electrons. The simplest positive ion is the proton (the nucleus of a hydrogen

atom), but atomic and molecular ions can be created with a wide spectrum of charge and mass.

Ions can be generated by exciting the electron shells of an atom or molecule so that one or more of the electrons is ejected from the shell structure. The minimum energy required to do this is the ionisation potential of the electron, and ranges from a few electron volts for the outer electrons of atoms to tens of kilo-electron volts for the inner electrons of heavy atoms. Ions are commonly created by applying a constant or radio-frequency electric field to a low-pressure gas of the atoms to be ionised, but more complex techniques involving electron bombardment or photo-ionisation are also used.

### *Ion beams distinguished from plasmas*

Ions can be accelerated in electric fields, and it is the kinetic energy of the moving ions which is exploited in the modification of the properties of the workpiece. We need to distinguish two cases. In a plasma the ions exist in the same volume as their associated free electrons. The relative concentration of positive ions relative to neutral atoms and electrons is a dynamic equilibrium between continuous ionisation and recombination and the velocity of the particles is randomly distributed, or there may be a relatively small drift velocity in one direction. In order to modify a workpiece it must be immersed in the plasma, where it is subjected to essentially random bombardment by the ions in the plasma. In an ion beam the positive ions are separated completely from the electrons and neutrals by relatively strong directional electrostatic fields, and there is a very large component of velocity in one direction (the beam direction) compared with the others. Ion beams can be steered and focused using both magnetic and electrostatic fields, so that the particles can be transported over long distances and delivered to a sample with any desired shape.

### *Ion species and energy regimes*

The way in which the properties of a material are modified by ion bombardment is critically dependent on both the energy and the atomic species of the ions. In the field of lithography there are two regimes which are of importance: the low-energy regime, in which the ions employed are usually singly charged positive ions of heavy atoms (e.g. O, Ar, Ga, Xe) and the energy is typically between 1 keV and 100 keV, and the high-energy regime in which positive ions of light atoms (H, He) with energies of 1–3 MeV are used.

All the ion-solid interactions encountered in materials modification arise from the electrostatic (Coulomb) forces between the positively charged ions and the charged nuclei and electrons of the sample atoms. The way in which this is felt is different in each regime, and is determined primarily

by the velocity of the ion relative to the velocity of the electrons in the atomic shells.

### *Low-energy ion-atom collisions*

In the low-energy regime the ion velocity is slow compared with the electron velocity and so the effective atomic charge distribution felt by the ion is averaged over the entire atomic volume. At a large distance the atom appears to be neutral (equal amounts of positive and negative charge) and no force is felt. As the ion penetrates the outer electron shells, the forces due to negative charge at radii beyond the ion position average to zero, and so effectively the charge felt by the ion becomes increasingly positive. Hence there is an increasing repulsive force between the ion and the centre of mass of the atom, i.e., the nucleus.

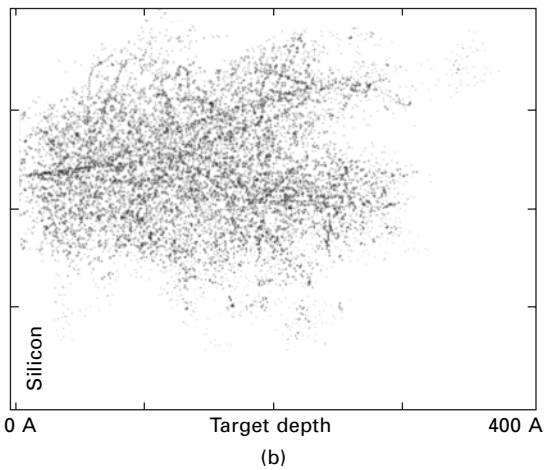
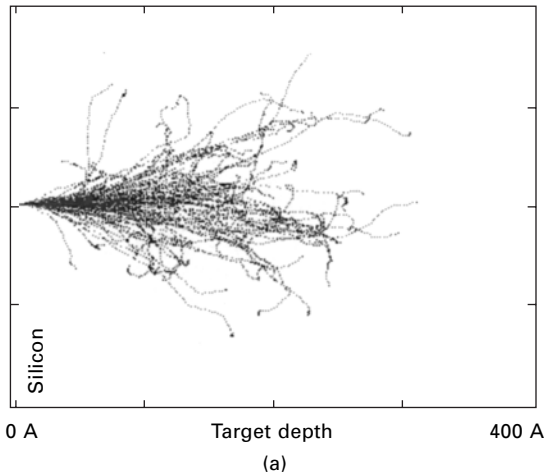
This means that low-energy ion-electron collisions can effectively be treated as classical particle (billiard ball) collisions in which the momentum of the ion is transferred to the entire atom according to the principles of conservation of energy and momentum. The effects of this are:

- The incident ion loses a large fraction of its energy in each collision and can be deflected through large angles. The ion rapidly loses all its energy and comes to rest; the typical range (maximum penetration depth) of low energy ions in solids is of the order of 1 to 100 nm.
- The target atom suffers a large impulse and may be displaced if the transferred energy is greater than its lattice binding energy. If the target atom is close to the surface it may be ejected from the surface. This process is called sputtering, and forms the basis of many low-energy ion patterning techniques. Displaced atoms which lie deeper in the material can displace other atoms, leading to 'collision cascades' in which all the energy of the incident ion is dissipated in ion displacements or lattice heating.

Figure 6.1(a) shows simulations of the paths of 10 keV argon ions in silicon, while Fig. 6.1(b) shows the paths of silicon atoms displaced in the collision cascade.

### *High-energy ion-atom interactions*

In the high-energy regime, the velocity of the ions is high compared with the electron velocity. This means that during the very short time of the collision (typically  $10^{-18}$  s) of the collision the electrons are effectively 'frozen' in their positions and the interactions can be considered to take place between the point charges on individual electrons (or the nucleus) and the ion and not with the entire atom. Thus we need to consider electronic and nuclear interactions separately.



6.1 SRIM 2003 simulations showing (a) the paths of 100 10 keV argon ions incident from the left on a silicon surface, and (b) the same diagram with the paths of displaced silicon atoms superimposed as points. Horizontal and vertical scale 40 nm.

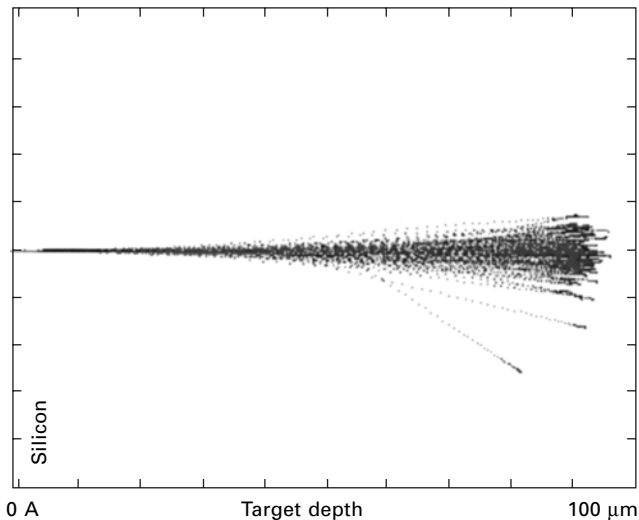
### Electronic interactions

Ion-electron interactions in the high-energy regime result in energy being transferred to individual electrons in the atom according to the laws of kinematics. These show that the maximum energy that can be transferred to an electron (in a head-on collision) is  $\sim E(4m_e/M)$ , where  $E$  and  $M$  are the energy and mass of the incident ion and  $m_e$  is the electron mass. Thus for a 3 MeV  $H^+$  ion, the maximum energy transferred to an electron will be around 6 keV, and for the majority of collisions (at glancing angles) it will be much less than this. This shows that a high-energy ion passing through

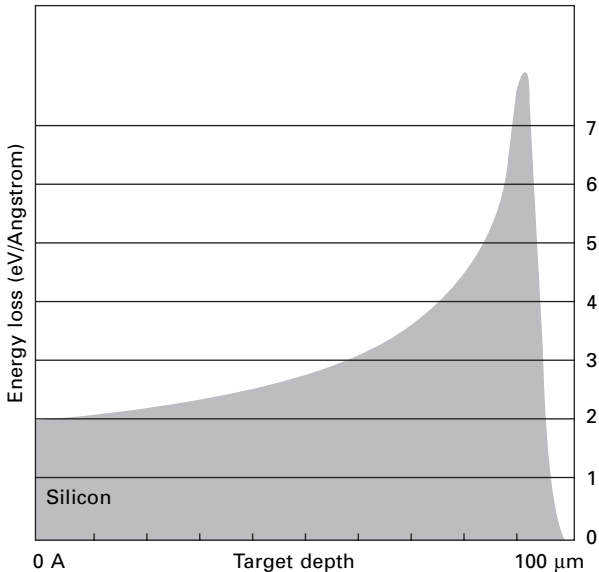
matter can undergo many thousands of electron ‘collisions’ before it loses all its energy.

High-energy ion-electron interactions affect both the atom and the ion:

- The ion is slowly deflected from its original straight path. Each electron interaction introduces a small lateral deflection (typically milliradians) and these accumulate randomly along the path of the ion. For the majority of the range, the lateral scattering is very small, but at the end of range, the energy of the ion falls to the point where it moves into the low-energy regime and the scattering and energy loss increase significantly. This gives the ion distribution a characteristic ‘trumpet’ shape (see Fig. 6.2).
- The ion gradually loses energy as it passes through matter. The rate of energy loss is called the stopping power and is typically  $10\text{--}20\text{ keV }\mu\text{m}^{-1}$ . The typical range (total depth of penetration before all kinetic energy is lost) of MeV light ions in matter is of the order of  $50\text{--}100\text{ }\mu\text{m}$  and because of the random nature of the multiple electron scattering stopping process, there is an uncertainty on the range called straggling, which can be as much as 10% of the range. Once the ions move into the low energy range, they lose energy very rapidly and one feature of ion interactions with solids is that a large fraction of the incident energy is deposited around the end of range (see Fig. 6.3, which shows the rate of energy loss of 3 MeV protons as a function of depth in a polymer). The end-of-range energy deposition can be exploited in some forms of materials modification using MeV ions.



6.2 SRIM 2003 simulations of the paths of 100 3 MeV protons incident on a silicon surface. Horizontal and vertical scale  $100\text{ }\mu\text{m}$ .



6.3 A graph showing the ionisation energy deposited in silicon by 3 MeV protons at different depths below the surface. (Vertical axis units electron volts per Angstrom).

- The electron can be excited within the shell structure of the atom. This can have a number of effects. If the electron is excited to a bound state then the subsequent relaxation of the electron structure will result in the emission of electromagnetic radiation in the visible, ultraviolet or X-ray region of the spectrum. (This emission can be used for chemical characterisation of the sample.) If the energy transferred to the electron is greater than its ionisation potential, then it can be completely ejected, leaving the atom in an ionised state. If the excited atom is part of a molecule, then the molecular bonding can be disrupted by the excitation and the molecule can be dissociated. This can modify, for instance, the refractive index or the solubility of the material and this forms the basis of many of the high-energy ion patterning techniques.

The amount of energy transferred to the material is called the linear energy transfer (LET) of the ion in the material, and is usually expressed as  $\text{keV } \mu\text{m}^{-1}$ . The distinction between LET and stopping power is that LET is energy deposited in the lattice whereas stopping power is energy lost by the ion, which also includes energy which escapes from the lattice through the emission of radiation. In practice these values are very similar.

### Nuclear interactions

For the vast majority of high-energy ion-atom interactions, the charge of the

nucleus is screened by electrons, and in fact the nucleus plays very little part in ion-solid interactions in the high-energy regime. A very small fraction of the incident ions do penetrate close enough to the nucleus to undergo a full coulomb collision, often resulting in high-angle 'backscattering' of the incident ion. This is the technique used by Rutherford to confirm the nuclear model of the atom in 1906 and is now widely used for materials characterisation. However, Rutherford backscattering is not significant for lithography and we will not discuss it further.

Contrasting Fig. 6.2 with Fig. 6.1 highlights the differences between high-energy and low-energy ions in solids, especially the huge difference in range and the virtual absence of lateral scattering over the majority of the ion range for high-energy ions.

### *Ion tracks*

The combined effect of the passage of a high-energy ion through matter is to create a short-lived region of highly excited atoms called the ion track. This region is effectively a high-temperature plasma of ionised atoms, dissociated molecular fragments and free electrons with a diameter of a few nanometres (depending on ion and energy) and a length equal to the ion range. The effect of the ion on the material then depends on how the excited atoms in the track condense.

### *Lattice damage in crystals*

Both high-energy and low-energy ion bombardment can create damage in crystalline materials. This occurs as a result of atomic displacements either through low-energy collisions with heavy ions or through high-energy Rutherford type collisions with high-energy ions. The results can range from low densities of defects or interstitials through to complete amorphisation of the lattice. This can be desirable (where, for instance, it can be used to modify locally the refractive index of a material) or undesirable, in which case it may be possible to anneal the material thermally after processing to re-form the lattice structure.

### *Calculating the effect of ions in solids*

All types of ion patterning of solids requires a detailed knowledge of the interactions between the ions and the target atoms. It is desirable to be able to calculate not only the effects of the beam on the target (to know, for example, the distribution of deposited energy and induced damage) but also the effect on the beam, so that the depth of penetration and the location of implanted ions can be calculated. For many years now the industry standard

tool for carrying out these calculations has been the SRIM (Stopping and Range of Ions in Matter) suite developed by Ziegler and Biersack (Ziegler and Biersack, 2003). This program, which is freely available for non-commercial applications, uses a quantum mechanical treatment of ion-atom collisions with a Monte-Carlo treatment of the jumps between collisions. SRIM can make predictions for all projectiles and target atoms over a wide energy range.

## 6.2.2 Interactions resulting in direct removal of material

Surface patterning relies on the removal of material in well-defined regions of the workpiece. Certain ion-solid interactions result in the direct removal of material and can be used for patterning with no further processing stages.

### *Sputter etching*

As described on page 186, sputtering results from the displacement of near-surface sample atoms as a result of collisions with low-energy heavy ions, usually achieved by immersing the workpiece in a plasma. The process of sputtering has been known for many years and is widely used as a technique for producing vapours of solid materials for preparing thin film surface coatings. The efficiency of sputtering is described by the sputtering yield, which is defined as the number of target atoms ejected by each incident ion. Sputtering yields vary over a wide range depending on the incident ion species and energy and the atomic number of the target atom.

Table 6.1 shows the sputtering yield with target atomic number for selected bombarding ions. The choice of ions in this table reflects the fact that inert gas ions are used for sputtering since this reduces the likelihood of chemical contamination of the workpiece or the deposited film. To put this in perspective, for a silicon surface bombarded with an ion current density of  $1 \text{ mA cm}^{-2}$  (typical plasma sputtering conditions), a sputtering yield of 1 corresponds to a material etch rate of  $0.12 \text{ } \mu\text{m sec}^{-1}$ .

*Table 6.1* Sputtering yields for pure solid elements bombarded with argon and xenon ions of different energy. The values are presented as atoms per incident ion. (Values calculated using SRIM 2003)

Element	2 keV Ar	10 keV Ar	10 keV Xe	100 keV Xe
C	0.4	0.9	1.2	2.5
Al	1.5	2.4	3.5	6.7
Si	1.1	1.7	2.5	5.3
Cr	3	4.7	4.4	9.2
Cu	5.3	8.5	7.8	13.1
Ag	5.1	8	10.2	16.5
Au	5.7	8.7	16.2	26.9

Sputtering yields also depend strongly on the nature of the surface (chemical state, texture, etc.) and whether the material immediately below the surface is crystalline. Sputtering may take place preferentially along particular crystallographic directions, and this can sometimes be exploited to form angular structures with very sharp edges, and is commonly used for revealing the microstructure of surfaces prior to electron microscopy.

Sputter etching can be used to fabricate microstructures by depositing a patterned resist layer onto the surface of the workpiece. The disadvantages of this method are that sputtering will erode the resist layer at a comparable rate to the workpiece material and that the sputtered material may be re-deposited at neighbouring sites on the workpiece, leading, for example, to the build-up of a cone of material surrounding a hole or the deposition of material from the bottom of the structure onto the sides. These effects limit the application of the technique in forming deep structures with lateral dimensions less than a few micrometres.

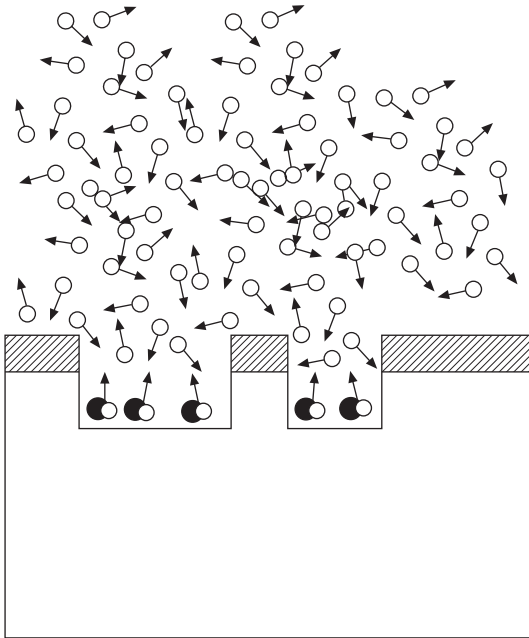
### *Reactive ion etching*

Sputtering yields can be enhanced or degraded by using chemically reactive gases (e.g. SF<sub>6</sub>, CF<sub>4</sub>, CHF<sub>3</sub>, O<sub>2</sub>, etc.) in the plasma, and this can be exploited to create selective high rate etching conditions for specific materials. This process is indicated schematically in Fig. 6.4. This means that the etching of the workpiece can be enhanced relative to that of the mask material and that the chemically active component of the plasma can be selected so as to create stable volatile reaction products so that the material removed from the workpiece diffuses into the gas and there is a greatly reduced probability of re-deposition, leading to very clean etching.

When the chemically active component is part of the plasma the technique is known as reactive ion etching (RIE) or dry etching. The effect of the etching can be controlled by varying the energy of the ions in the plasma (for instance by applying a DC or radio-frequency potential to the workpiece), the density of ions in the plasma (by changing the gas pressure and electrical power applied to form the plasma) and also choosing whether or not the workpiece is immersed within the plasma or is outside the plasma volume with the ions extracted by an electric field. Certain plasma conditions can enhance the penetration of the ions into surface structures, and this process is known as deep reactive ion etching (DRIE). Figure 6.5 shows schematically the layout of a system for lithography using reactive ion etching. Further details of this wide topic can be found in books such as Sugawara (1998).

### *Chemical decomposition*

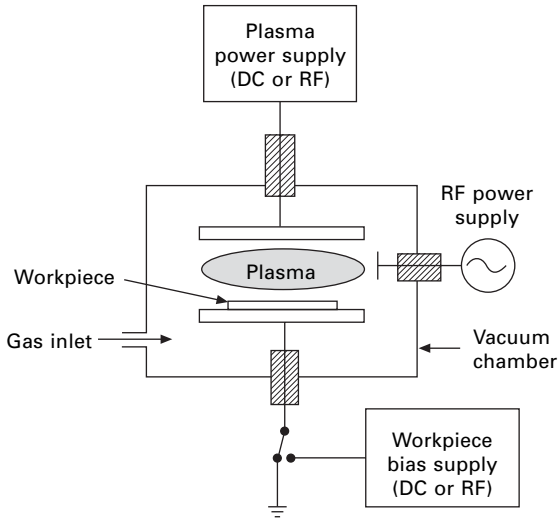
Some materials decompose directly into gaseous products under ion



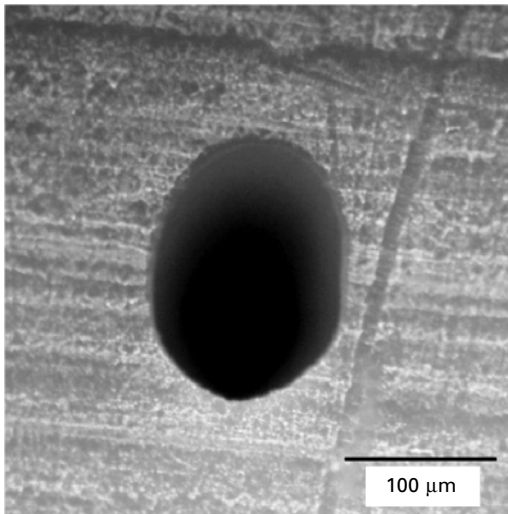
6.4 Schematic diagram of reactive ion etching. Chemically reactive ions in the plasma (open circles) react with the surface of the workpiece to form stable gaseous molecules (open/black circles) which diffuse into the plasma to remove material from the surface. Careful selection of gas species and resist material (shaded layers) ensures that the applied resist pattern is not etched, leading to a potentially high aspect ratio.

bombardment, and provided these can be extracted efficiently from the structure, this results in a very efficient removal of material. This effect is in some ways similar to reactive ion etching, but does not rely on chemical reactions to cause the initial breakdown of the workpiece material.

One example is the decomposition of polytetrafluoroethylene when bombarded with MeV light ions. The  $(-CF_2-)_N$  molecule is readily dissociated in the ion tracks and on condensation forms gaseous  $C_nF_m$  products. If these can escape from the hole then the material can be rapidly eroded and very deep high aspect ratio structures can be formed. Preliminary studies have demonstrated that the etch rate is maximised in the presence of oxygen, presumably due to the formation of stable gaseous compounds such as carbonyl fluoride ( $CF_2O$ ) (Gomez-Morilla *et al.*, 2005, Grime *et al.*, 2005). The etch rates achieved can be very high. Figure 6.6 shows a hole etched in bulk PTFE by a 1 nA beam of 2.8 MeV protons focused to 100  $\mu\text{m}$  diameter. The depth etched in two minutes was 2 mm. This process offers a novel method of micromachining PTFE.



**6.5** Schematic diagram of plasma chamber for reactive ion etching. The ionised plasma is created between two electrodes by applying a DC or radio-frequency potential to the upper electrode. Additional RF energy may be used to increase the plasma density. The workpiece is mounted on the lower electrode which can be grounded or biased with a DC or RF potential to vary the energy of the ions impinging on the surface. The gas pressure and composition can be controlled using an automated gas handling system.



**6.6** Optical micrograph of a hole etched into a stack of 100  $\mu\text{m}$  thick sheets of PTFE by a 1 nA beam of 2.8 MeV protons in air focused to 100  $\mu\text{m}$  diameter. The hole shown is from a depth of 600  $\mu\text{m}$  below the surface. The total depth of the hole was 2 mm and this was etched in less than four minutes. (Reprinted from Gomez-Morilla *et al.* 2005 ©2005 with permission from Institute of Physics).

### 6.2.3 Interactions resulting in modification of material properties

The ‘cooling’ of the highly excited material in high-energy ion tracks may leave the material in a different chemical or physical state from the original bulk workpiece and this can be exploited to form patterns. The most important application of this effect is changing the solubility of the material to allow differential etching, but other properties such as refractive index or crystallinity may also be important.

#### *Modification of solubility*

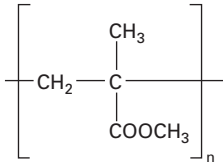
The use of certain polymers as light, electron or X-ray sensitive resist materials is well known and underpins the majority of current microlithography. The same materials have been found to respond in much the same way to ion bombardment. In this case the major interest is in the high-energy regime, since the sputtering and lateral scattering that occurs in the low-energy regime is undesirable. High-energy ions allow us to exploit their long range and low lateral scattering to create structures with a very high aspect ratio. The majority of conventional resist materials are polymers, but sensitised glasses can also be used, and both can be exposed by high-energy ions.

#### Positive and negative polymer resist materials

Polymer materials are available both as positive and negative resists. In positive resist materials, the exposed regions of the material become soluble, so that following development the exposed areas are removed. In negative resists, the opposite happens, the material becomes insoluble, and exposed regions remain after development.

These two types of response arise from chain scission and cross-linking. Chain scission is the irreversible breaking of covalent bonds within the polymer, which reduces the mean molecular weight of the material and increases the solubility leading to a positive resist response. Cross-linking involves the formation of additional covalent bonds between adjacent chains or the growth of other molecular structures such as carbon aromatic rings. Under these conditions the polymer mean molecular weight increases and the material becomes less susceptible to solvents, giving a negative resist behaviour. Some materials may show either positive or negative behaviour depending on the total radiation dose.

One common positive resist material is poly-methyl methacrylate (PMMA). This has the molecular structure indicated in Fig. 6.7, and when it is exposed to relatively low doses of radiation, scission can occur both on the main chain and of the pendent  $\text{COOCH}_3$  groups, leaving low molecular weight



6.7 The structure of one monomer unit of the poly-methyl methacrylate molecule.

fragments which are soluble in a developer typically based on methyl isobutyl ketone or diethylene glycol monobutyl ether.

The most common negative resist material for lithography applications is SU-8, an epoxy-based UV-sensitive resin developed by IBM for microfabrications and MEMS applications. The precursor material cross links on exposure to radiation forming a hard resin with high resistance to most chemical solvents.

#### Photosensitive glasses

Certain glasses are available as UV-sensitive resist materials. These include Foturan originally developed by Schott Glaswerk, Germany and PEG-3 from Hoya Corporation, Japan. These glasses are doped with metal ions (typically silver) which when ionised form nuclei which induce the formation of crystalline regions when the material is thermally annealed. The differential solubility of the crystals relative to the surrounding glass (a factor of 10–20) allows the exposed material to be removed by etching. Recent experiments at the Universities of Oxford and Surrey (Gomez-Morilla, 2003) have shown that these photosensitive glasses are extremely sensitive to exposure with MeV ions and this allows complex direct-write structures to be formed in a relatively short time.

#### *Modification of optical properties*

The refractive index of optical materials is very sensitive to the chemical composition and in crystalline materials, the lattice quality. This allows us to modify the refractive index in a controlled way by either inducing impurity ions or by creating localised crystal damage. Using MeV ions gives the possibility of controlling the location of the refractive index change both laterally, and by selecting the beam energy, in depth. This allows the formation of a range of complex optical devices such as buried waveguides (Buchal, 1992).

#### *Modification of electrical properties*

In the same way the electrical properties of materials, especially semiconductors, can be modified by implantation or lattice damage resulting

from ion bombardment. This technique is called ion implantation, which is now a well established and vital part of modern technology. All modern integrated circuit chips now go through at least one step of ion implantation to introduce dopant atoms at well controlled depths, and the provision of ion implantation services and equipments is a major industry. This is taking us away from the topic of surface patterning, and is really outside the scope of this chapter. Readers who wish to know more about ion implantation are referred to the many textbooks and web resources relating to this e.g., Rimini (1995) or Ryssel *et al.*, (1986).

#### 6.2.4 Ion beam deposition

The techniques described so far are all aimed at removing material to create a patterned surface. Low-energy focused ion beams can additionally be used to deposit solid material onto a substrate and so build up or repair microstructures. This process uses the energy from the ion beam to decompose a complex molecule into the required solid material and a volatile gaseous component. The precursor material is usually introduced as a jet of gas which is adsorbed onto the surface of the workpiece and then under ion bombardment, the precursor decomposes and solid material builds up under the beam position (see Fig. 6.8).

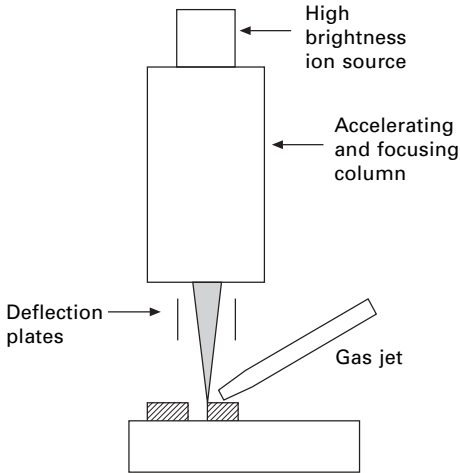
A wide range of precursor gases is now available, allowing many solids to be deposited. Some examples are shown in Table 6.2. Ion beam deposition (IBD) or chemically assisted ion beam deposition (CAIBD) as it is sometimes known, is essentially a surface chemical reaction, and ions in the low-energy regime are required to ensure that all the beam energy is deposited within the thin layer of precursor material. By replacing the precursor gas with a reactive etching gas, the same equipment can be used for spatially resolved reactive ion etching, allowing both removal and deposition of material. This variant is sometimes referred to as gas assisted etching (GAE).

### 6.3 The use of ion beams for microfabrication

In order to exploit ion bombardment to create surface patterns the spatial extent of the ions on the surface of the workpiece must be defined. There are two basic approaches to this, masked processes and direct-write processes.

#### 6.3.1 Masked processes

In masked processes, the workpiece is exposed to the ion beam through a thin membrane into which the desired pattern has been cut, as in Fig. 6.4. The mask membrane is selected so that the ion beam is blocked or scattered by the material, and the workpiece is only exposed to the beam in the open areas.



6.8 Schematic diagram showing the use of a low-energy focused ion beam to deposit solid material by the decomposition of a gaseous precursor material. Since the decomposition takes place only at the beam impact point the extent of the deposited material is defined by the diameter of the beam allowing direct write fabrication of complex structure. By replacing the precursor gas with a reactive gas such as oxygen or chlorine the same system can be used for spatially resolved reactive ion etching to remove material from highly localised regions of the workpiece.

Table 6.2 Examples of precursor gases for the deposition of solid materials by ion beam deposition

Precursor	Deposit
$\text{WF}_6$	W
$\text{W}(\text{CO})_6$	W, WC
$\text{Mo}(\text{CO})_6$	Mo, MoC
$\text{Fe}(\text{CO})_5$	Metal, oxide, carbide
$\text{Ni}(\text{CO})_4$	
$\text{C}_7\text{H}_{10}\text{AuF}_3\text{O}_2$ (tfac)	Au metal and compounds
$\text{C}_7\text{H}_7\text{AuF}_6\text{O}_2$ (DMGhfac)	
$\text{Cu}(\text{hfac})_2$	Cu oxide
$\text{Cr}(\text{C}_6\text{H}_6)_2$	Cr carbide
$\text{C}_5\text{H}_5\text{Pt}(\text{CH}_3)_3$	Pt metal and compounds
Styrene	Carbon
Methyl isobutyl ketone	
Isopropyl alcohol	

### Advantages and disadvantages

The major advantage of masked lithography is that the entire surface of the workpiece can be exposed to the ion beam in a single operation, and since

masks can be created with relatively large areas (which can be further increased using step and repeat techniques), this means that large numbers of two-dimensional features can be produced very quickly, making the process ideal for mass production. In addition, since the feature dimensions are determined by the mask and not by the beam, the design of the ion beam equipment is much simplified (a broad beam can be used). The disadvantage is that mask fabrication may become very complex and expensive.

### *Mask materials and fabrication*

The selection of mask materials depends very much on the details of the ion lithography process employed. In many cases the mask can be prepared directly on the surface of the workpiece using conventional photolithography or electron lithography processes. The final mask material can either be the original resist polymer or can be etched into an underlying layer of metal or oxide material. Directly deposited masks can only be used once and are most suitable for RIE processing.

Alternatively, the mask can be formed in a thick self-supporting film material which may or may not be supported on a thin transparent support membrane. In this case the mask is reusable and can either be mounted in contact with the surface of the workpiece or used to project a 'shadow' onto the surface (see next section). For ion beam applications, especially in the low-energy regime, it may not be possible to find a thin support membrane which does not stop or degrade the beam, and in this case it is necessary to form the mask in a self-supporting film of material with true holes. This is a stencil mask and the design of the hole pattern is constrained by the need to ensure that the solid material is continuous so that all parts of the pattern are supported.

### *Projection mask processes*

The problem of fabricating stencil masks with very small feature size can be alleviated by using a projection system in which the ion optical system is used to create a demagnified image of the mask on the workpiece (Lawes, 2000). In this way the mask can be fabricated with dimensions many times larger than the final feature size. The design of focused ion beam lens columns lends itself conveniently to this technique.

## 6.3.2 Direct-write processes

In direct-write processes, the ion beam is focused to a very small diameter and the beam is scanned using electrostatic or magnetic fields across the surface of the sample to create the desired pattern, as in Fig. 6.8. In the low-

energy regime, this technique is commonly used and is known as the focused ion beam (FIB). In the high-energy regime, the technique is still emerging and is becoming known as proton beam writing (PBW) or ion beam lithography (IBL). The minimum feature size is determined primarily by the diameter of the focused ion beam on the sample surface (as well as by the effects of scattering processes in the material below the impact point) and so the use of direct-write lithography in the micro- and nano-metre regions is linked directly to the development of microfocusing technology for high-energy ions.

### *Advantages and disadvantages*

Direct-write processes have a great advantage in flexibility, since any changes to the pattern can be made simply by modifying software, and it is not necessary to go through the long process of creating a new mask. The major disadvantage is that in general, direct-write processes are significantly slower than masked processes, since the focused beam must cover the entire pattern sequentially. This makes direct-write operations generally unsuitable for high-volume production, and at present it is used primarily for fabricating specialised or prototype devices, although high-energy proton beam writing can be used to fabricate masters which could be used to make many replicates for instance by microstamping.

One important exception to this is the use of FIB to repair minor faults in expensive large-scale structures such as masks for X-ray lithography. In this case, since it is not necessary to cover the entire surface of the workpiece, the slow speed of direct writing is not an issue. A further disadvantage of direct-write processes is that the feature size is determined essentially by the beam diameter, which places severe constraints on the design of the focusing and scanning system.

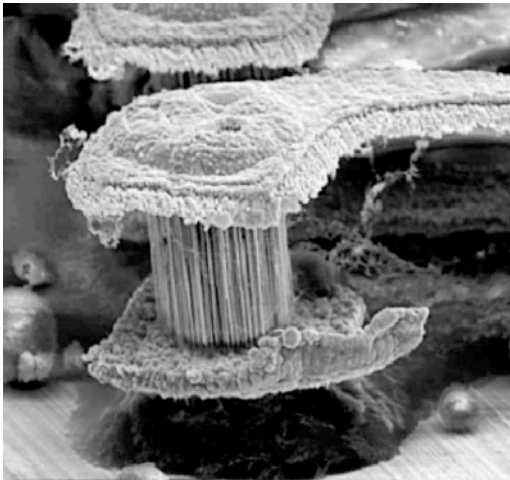
### *Pattern-generation techniques*

In direct-write systems, the beam is deflected across the surface of the workpiece using either magnetic or electrostatic deflection fields. The voltages or currents used to generate these fields are controlled by pattern-generation software. In general, the area that can be covered without distortion or loss of spatial resolution (broadening of the beam spot) is limited by aberrations in the lenses to a few millimetres, and so to cover larger areas, mechanical motion of the sample in a 'step and repeat' pattern is required. Another requirement of direct-write exposure is the ability to blank the beam to allow disconnected regions to be exposed. This is done either by modulating the voltages in the ion source or lens, or more commonly (and exclusively in high-energy systems) by using a pulsed electrostatic deflector positioned before the lens as a fast beam switch.

### 6.3.3 Ion track lithography

A newly emerging form of ion beam patterning is ion track lithography, in which the volume of single MeV ion tracks (see page 190) in polymer materials is removed by etching to give nanometre diameter capillaries which can be used for filtration or diffusion applications or as plating moulds to form nanometre wires. Ion track lithography can be created by exposing the workpiece to a flux of MeV ions generated either by an accelerator or a radioactive source. Provided the total number of ions is low (i.e. with an average density of less than one ion within the area of an ion track) isolated tracks will be formed. By exposing through lithographically defined masks, clusters of capillaries or wires can be used to form larger structures (see Fig. 6.9). Although it is still at an early stage of development, ion track lithography could be used to make significant advances in areas such as the fabrication of polymer filters with precisely defined channels, sensitive magnetic field sensors based on magnetic nanowires and nano and micro fluidic channels (Thornell *et al.*, 1999, Lindberg, 2003, Toulemonde *et al.*, 2004).

The logical development of ion track lithography will be the use of precisely positioned single ions (PPSI) to form structures of accurately defined single nanotubes or wires. Single ion lithography has already been demonstrated on the micrometre scale (Fischer, 1988), but important new capabilities will arise when MeV ion focusing technology develops the ability to position single ions with nanometre targeting accuracy.



6.9 Via consisting of a bundle of nanowires created by metal plating through the pores created by etching ion tracks in polymer. Such a connection will have very low impedance at microwave frequencies (Reprinted from Toulemonde *et al.* 2004. © 2004 with permission from Elsevier).

## 6.4 Ion beam equipment

### 6.4.1 Low energy systems

#### *Reactive ion etching*

Reactive ion etching or dry etching is now a key technology for mainstream Si and GaAs semiconductor fabrication and the worldwide market for RIE equipment is worth several billion US dollars and is growing at about 10% per annum. This growth has been driven by the steady trend in IC fabrication toward smaller line geometries and feature sizes. RIE may be the only high-volume etch technology capable of working consistently below 500 nm ('sub half-micron' manufacturing) and very high-performance dry etch equipment is required to work in this region.

This equipment is compact enough to fit into a normal laboratory, and consists at its simplest of a vacuum chamber in which the gas pressure and composition can be controlled and some method of creating a plasma, for example an electrode to which a DC or radio-frequency voltage can be applied (see Fig. 6.5). Further details of RIE equipment can be found in references such as Sugawara (1998).

#### *Focused ion beam (FIB)*

Focused ion beam equipment requires the additional technological complexity of an ion focusing and scanning column. The focusing elements used are cylindrical electrostatic lenses which, since their focusing strength is independent of the mass of the ions, allow ions of different masses to be focused. The focusing column is usually combined with the acceleration system. At very small beam diameters, angle-dependent imaging aberrations in the lens introduce broadening, and in order to limit this, the divergence of the beam entering the lens must be drastically reduced. In order to avoid an unacceptable loss of beam current, this means that the ion sources used must have a very high brightness, and FIB is critically dependent on the use of either the liquid metal ion source which can produce very high brightness beams of low melting point metals such as gallium, lithium or indium, or field ionisation ion sources in which gases such as oxygen, argon or xenon are ionised in the very high electrostatic field close to a charged metal tip of atomic dimension (Orloff, 1993) (Orloff *et al.*, 2002).

The focusing column incorporates scanning plates to deflect the beam and may also have facilities to place a stencil mask at the intermediate focus to allow projection ion lithography. At the time of writing, the smallest usable beam diameters that have been reported are of the order of 5 to 10 nm. A FIB instrument has much in common with an electron microscope (and may even incorporate a scanning electron microscope for visualising the sample – the

so-called dual-beam instrument), and externally their size and appearance are very similar. This technology is evolving rapidly and current information can be obtained from the web sites of groups such as the European Focused Ion Beam Users Group (<http://www.imec.be/efug/>) or from manufacturers.

### 6.4.2 High-energy systems

The major component of any high-energy ion beam facility is the particle accelerator. This must generate ions of the species and energy required to carry out the applications (usually protons and alpha particles with energies of a few MeV), but the requirement of operating with a focusing system may also impose additional constraints on the energy spread and brightness of the beam.

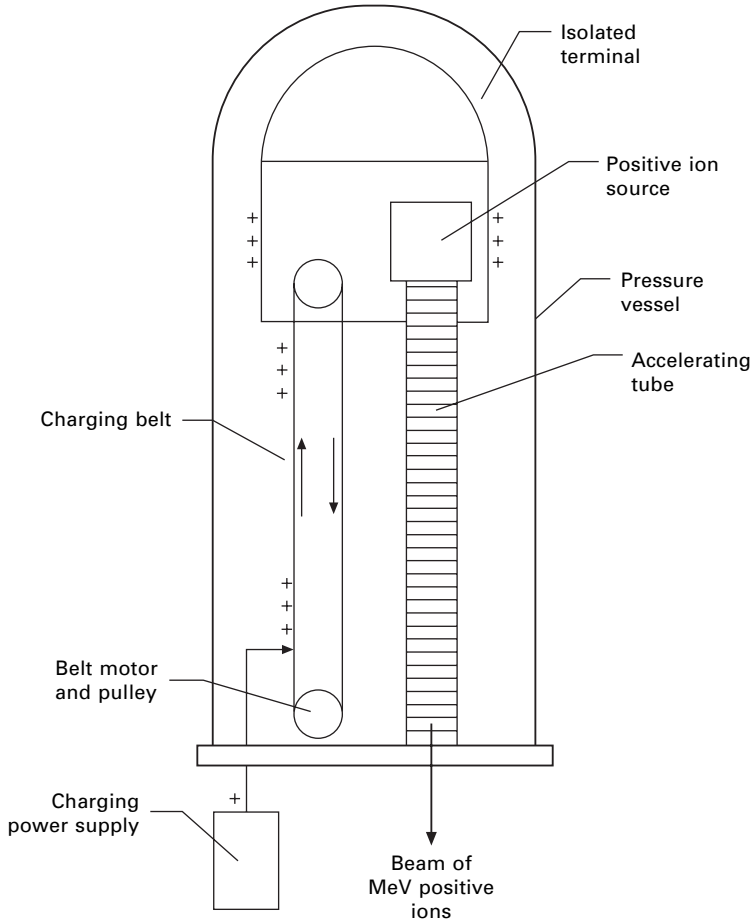
The accelerators most suitable for focused ion beam systems are the electrostatic type, in which a static voltage equal to the beam energy required is generated, and the particles are accelerated in a single step (or two steps if the 'tandem' principle is used). The voltage may be generated either by an electrostatic system such as the popular 'van de Graaff' system, or by a voltage multiplier stack, in which an alternating voltage is rectified in such a way as to generate a DC voltage many times greater than the amplitude of the applied voltage. Figure 6.10 shows schematically the principle of electrostatic accelerators.

Traditionally, a nuclear accelerator has formed part of a major facility and many groups still share beam time at a nuclear physics accelerator institute. In contrast, modern small accelerators represent a relatively modest investment in capital and support costs and increasingly now, new small accelerators are being purchased specifically for applications in research institutes or industrial organisations.

#### *MeV ion microbeams*

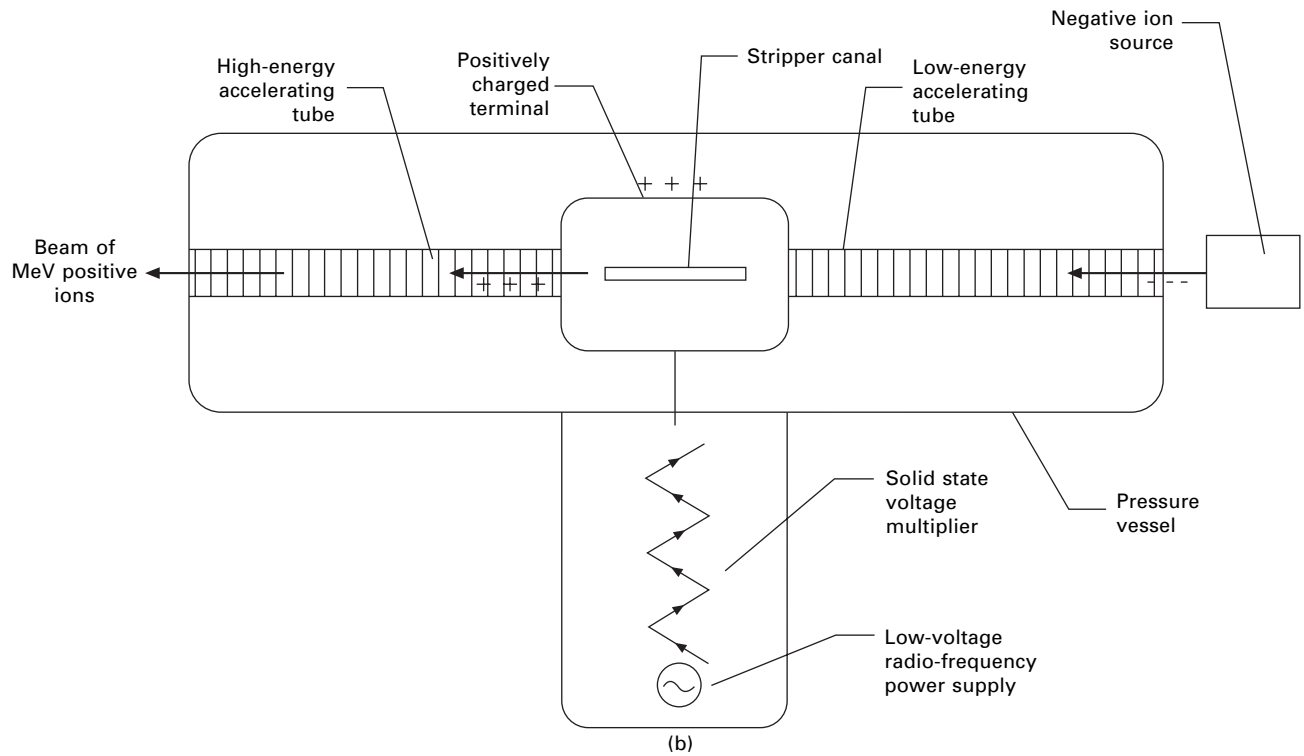
The high momentum of MeV ions which gives them their advantage for lithography also makes them difficult to focus. In particular the standard cylindrical magnetic and electrostatic lenses used in electron or low-energy ion focusing columns are too weak to be used with MeV ions, and alternative technologies must be sought. Many different arrangements of apertures and electromagnetic fields have been proposed, but the system which has shown consistently the best performance is the magnetic quadrupole multiplet (Grime and Watt, 1984).

Quadrupole lenses have four magnetic poles arranged symmetrically N-S-N-S around the beam axis. They have a strong focusing action on charged particle beams but because of the anti-symmetry a single quadrupole lens converges the beam in only one plane and diverges in a plane normal to this.

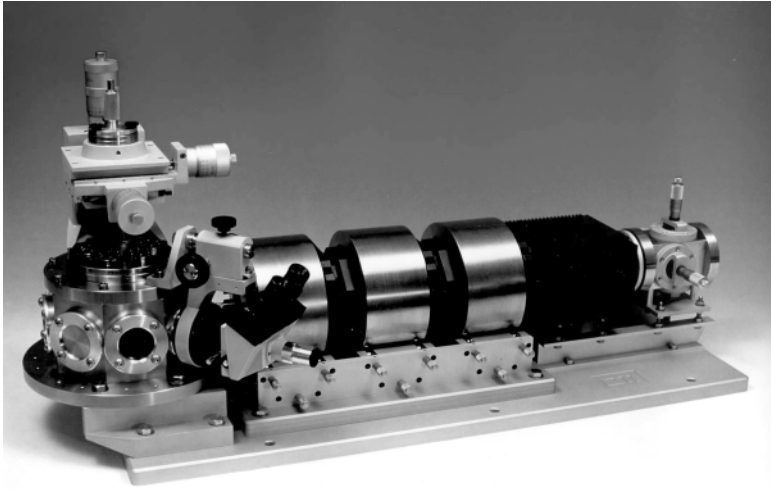


(a)

6.10 Schematic diagram of (a) single-ended accelerator and (b) tandem accelerator. The terminal voltage may be generated either by a moving belt or chain (the van de Graaff or Pelletron principle) or by rectifying a high-frequency alternating voltage (the Tandatron). In the single-ended accelerator a positive ion source is mounted in the terminal and the beam energy is equal to the terminal voltage. In the tandem accelerator an external negative ion source injects ions into the accelerator where they are accelerated toward the positive terminal. In the terminal they pass through a region of low-pressure gas (the stripper) where collisions with the gas molecules remove some or all of the electrons. The resulting positive ion is further accelerated. The final energy is given by  $V(1+q)$  where  $V$  is the terminal voltage and  $q$  is the charge state after stripping. The accelerator assembly is normally enclosed in a pressure vessel containing several atmospheres of an insulating gas such as  $\text{SF}_6$  to avoid the possibility of electrical discharges.



6.10 Continued



6.11 Photograph of the endstage of a commercially available microbeam focusing system using a triplet of magnetic quadrupoles. The beam enters the system from the right and passes through the collimator aperture, magnetic deflection coils to sweep the beam across the sample and the three quadrupole magnets before entering the target chamber where the sample is mounted on a micrometer-controlled positioning stage Reprinted with permission ©1998, Oxford Microbeams Ltd., Oxford U.K.).

For this reason two or more quadrupoles of alternating polarity are required to form a point focus. Combinations of two, three and four lenses have been used (see Fig. 6.11). Like lenses for FIB systems, quadrupole lenses suffer from significant angle-dependent aberrations which increase the beam diameter and these set a limit to the smallest usable beam diameter that can be achieved. This technology is still evolving, but the most successful systems can now achieve resolutions of less than 100 nm with beam currents suitable for lithography (Watt *et al.*, 2003) and several research groups are working to reduce the beam diameter into the sub-10 nm range.

## 6.5 Specific techniques and examples

Ion beam patterning is set to grow in importance as the semiconductor industry moves toward device feature sizes which are smaller than the diffraction limit of conventional masked contact photolithography. Already the industry is planning 45 nm features and this is posing a serious challenge to fabrication technology. A recent report on the industry (ITRS, 2003; M. Arden, 2002) accepts that the next generation lithographies will have to include direct-write ion beam techniques. However, the capability of fabricating three-dimensional structures with a scale of nanometres is still very novel and ion

beam techniques are poised to make a major contribution in areas of nanotechnology other than semiconductor fabrication.

### 6.5.1 Low-energy techniques

#### *Focused ion beam*

Because direct-write focused ion beam patterning is very slow, the technique is not used for volume production applications and for many years the major application was in the preparation of samples for analysis using transmission electron microscopy by selectively removing material to expose the structures of interest (Giannuzzi and Stevie, 1999). In recent years the cost and complexity of masks for X-ray and ultraviolet lithography have grown to the point where it is economically viable to use focused ion beams for mask repair. The ability both to remove and deposit material in very precise areas means that both clear and opaque mask defects can be repaired and so rescue a mask which could have a cost of \$100,000. The global market in high-resolution lithography masks is now approaching \$3 billion and FIB is now firmly established as a mask repair technique (Liang *et al.*, 2000).

FIB deposition is increasingly being used for fabricating complex three-dimensional micro- and nanostructures in a variety of materials. In a now famous demonstration (Matsui *et al.*, 2000) a wine glass with a diameter of less than 3  $\mu\text{m}$  has been fabricated in diamond-like carbon using a focused beam of 30 keV gallium ions and a hydrocarbon precursor gas (see Fig. 6.12). The same technique has been used to make ‘nano-manipulators’ with micron scale fingers which can be opened or closed by varying the electrostatic charge on the structure (Kometani *et al.*, 2004) (Fig. 6.13).

#### *Reactive ion etching*

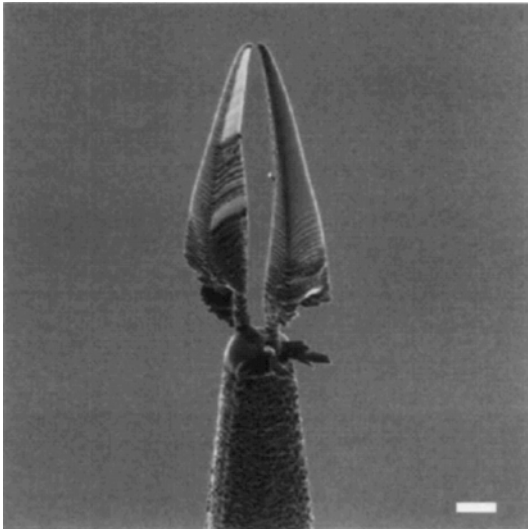
Reactive ion etching and its variants are commonly used for volume production of microcircuits and other similar devices, but they can also be used for creating complex three-dimensional structures such as micro-electromechanical structures (MEMS), especially in ‘difficult’ materials which cannot be etched chemically. Figure 6.14 shows refractive lenses for use in focusing synchrotron X-rays fabricated in both silicon and diamond using an oxygen plasma (Nohammer *et al.*, 2003).

### 6.5.2 High-energy ion lithography using resist materials

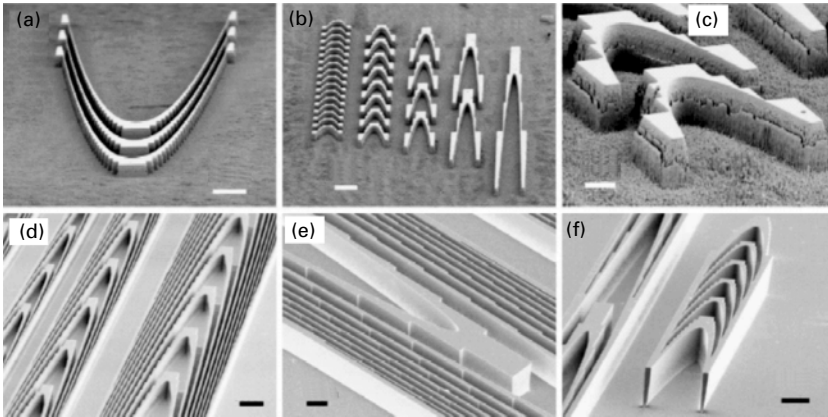
As noted on page 188 MeV ions follow virtually straight paths for the majority of their range in matter. This fact is the basis for the newly emerging field of MeV ion lithography or proton beam writing (PBW). Studies have found that the majority of materials which are sensitive to other forms of radiation



6.12 A diamond-like carbon wine glass with an outside diameter of 2.75 μm and height of 12 μm fabricated by direct writing with a 30 keV focused gallium beam in a hydrocarbon atmosphere (Reprinted with permission from Matsui *et al.*, 2000 ©2000, American Institute of Physics).



6.13 A nano-manipulator with three 'fingers' fabricated by direct-write chemical vapour deposition with a 30 keV focused gallium beam. The material is diamond-like carbon deposited from a phenanethrene precursor (Reprinted with permission from Kometani *et al.*, 2004 ©2004, American Institute of Physics).



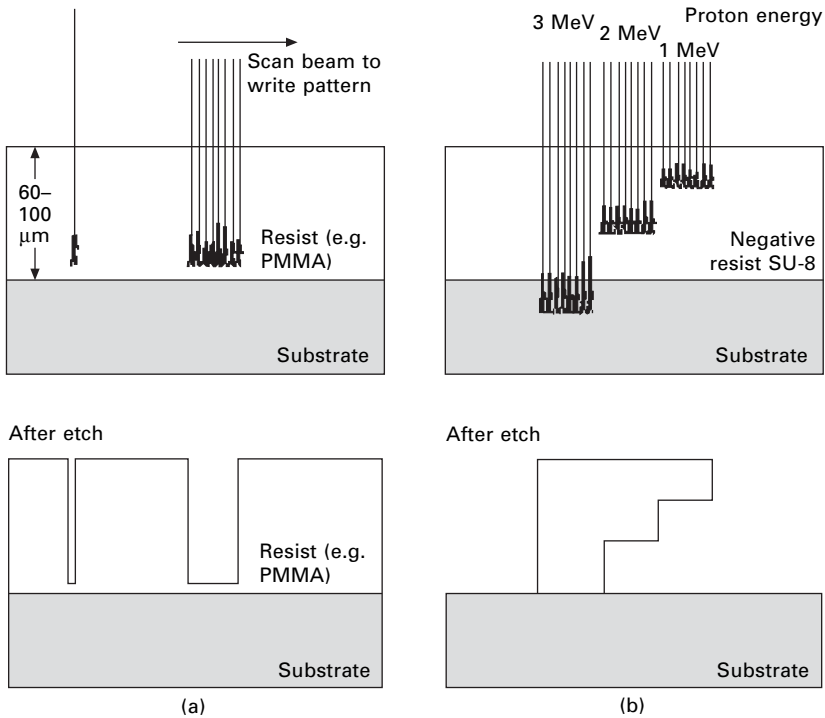
6.14 Refractive X-ray lenses fabricated in diamond (a–c) and silicon (d–f) using masked reactive ion etching in an oxygen plasma. (Reprinted from Nohammer *et al.*, 2003 ©2003 with permission from Elsevier).

(e.g. photoresist, electron beam resists) respond in a similar way to MeV ion irradiation, although in some cases the total deposited energy required to expose the material may be different (in most cases, less). The technique was first demonstrated in poly methylmethacrylate (PMMA) (Breese *et al.*, 1993), but is being extended to other materials including negative working SU-8 resist, UV-sensitive etchable glasses and semiconductors.

PBW can create structures with depths of tens of micrometres with a sidewall angle very close to 90 degrees and very low roughness (1–10 nm) and is at present the only single-step direct-write lithography capable of fabricating three-dimensional structures with sub-micron feature sizes and could become a significant tool in the development of semiconductor and other devices in the sub-100nm range.

Figure 6.15 shows the processes involved in proton beam writing using positive and negative resist materials. Negative resists (Fig. 6.15(b)) give the unique possibility of exposing the material at different energies to create overhanging structures or buried channels. The development of proton beam writing is being pioneered at the National University of Singapore in a wide range of application areas. At the time of writing the full potential of PBW is still being explored, and the quality of the demonstration structures which can be formed are indicated in Fig. 6.16.

Specific areas of application for PBW will include microfluidics, where the three-dimensional capability of the technique can be exploited to fabricate buried micro channels in a single exposure step (Tay *et al.*, 2001) (see Fig. 6.17), the fabrication of MEMS using masters formed by PBW to create electroplating moulds by stamping (van Kan *et al.*, 2001) (Fig. 6.18), complex surface texturing for tissue engineering and surface biotechnology applications



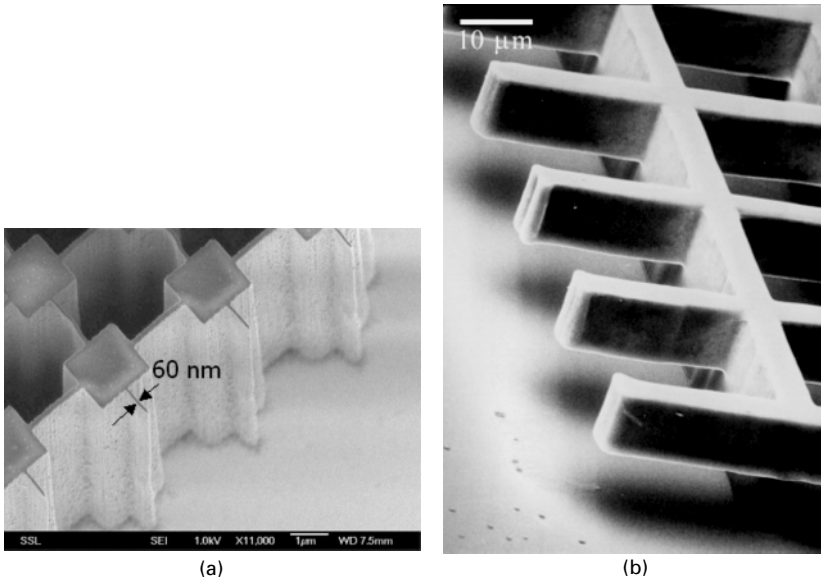
6.15 Schematic diagram showing the principles of proton beam writing in (a) positive resist material (material becomes soluble in the beam) and (b) negative resist material showing how a negative material can be exposed at different energies to fabricate cantilevered structures with controlled thickness.

and the fabrication of micro-optical structures such as waveguides, couplers, photonic bandgap filters, etc.

A key role for PBW is expected to be in the fabrication of stamp masters for nano-imprint lithography, which can then be used to replicate many devices, including masks for X-ray (LIGA) and extreme ultraviolet (EUV) lithography (Ansari *et al.*, 2004). This group of technologies will combine the high aspect ratio, small feature size and short development cycle of PBW with the volume production capabilities of conventional techniques.

## 6.6 Future trends

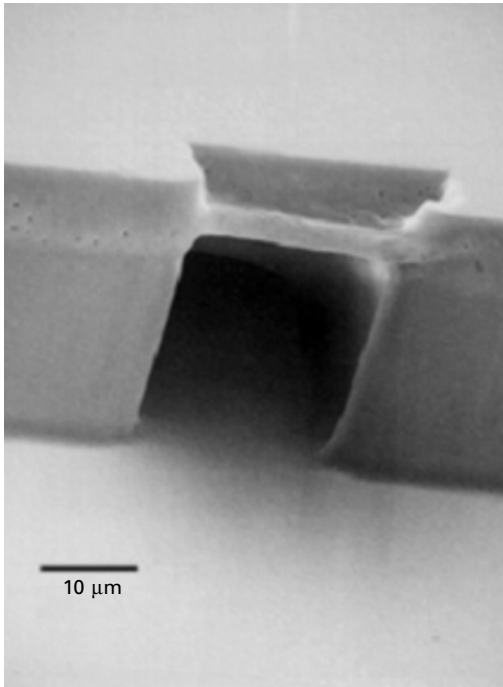
The aim of this chapter has been to provide a brief overview of the use of ion beam techniques for patterning surfaces and structures. These are summarised in Table 6.3. Of the techniques described, reactive ion etching and focused ion beam techniques are already well established in niche applications in the semiconductor industry and indeed are being driven by the need of this



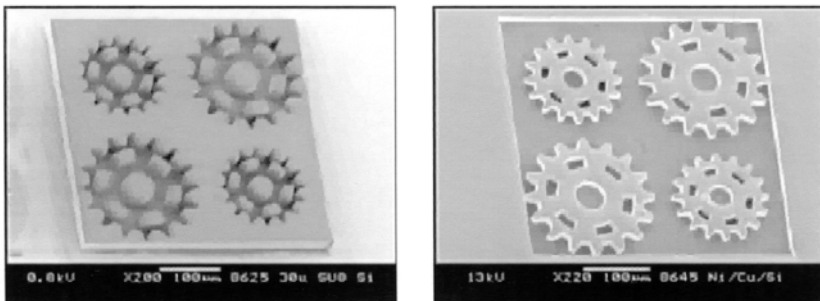
**6.16** Demonstration structures formed at the National University of Singapore in SU-8 negative photoresist using proton beam writing with beams of MeV protons. (a) Pillars 1  $\mu\text{m}$  in diameter and 10  $\mu\text{m}$  high joined by walls with a thickness of 60 nm formed using a beam of 1 MeV protons focused to a diameter of 60 nm. (b) Cantilevered structured formed by exposing SU-8 with protons of 2 MeV to form the walls and 1 MeV protons to form the cantilevers (Reprinted with the permission of CIBA, National University of Singapore).

industry to reduce the feature size below the diffraction limit of conventional photolithography. Low-energy ion beams can already be focused to nanometre dimensions using existing technology and so it is unlikely that substantial reductions in effective feature size will emerge – at this level one is working at the dimensions of single molecules and other techniques in nanotechnology may be more appropriate for this. However the range of solid materials that can be deposited using chemically assisted ion beam deposition is expanding, and with improvements in the control of the beam and the gas environment one can envisage the direct fabrication of complex multi-material three-dimensional functional nanostructures using focused ion beam techniques.

The development of lithographic techniques in the high-energy regime is still in its infancy and several research groups are working to improve both the ion beam focusing equipment and the range of ion-solid interactions which can be exploited for patterning. The smallest effective feature size that can be formed at present using PBW is of the order of 50 nm, though there is no fundamental physical reason why MeV protons should not be focused to a diameter of 10 nm or less and the factors limiting the resolution



6.17 A buried channel for use in a microfluidic network formed in a SU-8 negative photoresist by dual-energy proton beam exposure: 2.5 MeV to form the walls and 1 MeV for the channel cap (Reprinted with the permission of CIBA, National University of Singapore).



6.18 Nickel gear wheels (right) formed at the National University of Singapore by electroplating through the mould (left) created by proton beam writing in SU-8 negative resist (Reprinted with the permission of CIBA, National University of Singapore).

at present are associated with precision engineering at the nanometre scale and the issues associated with interfacing a large mechanically, acoustically and electrically noisy structure (the nuclear accelerator) to a nanometre scale instrument.

Table 6.3 Summary of patterning techniques using ion beams

Technique	Other names or variants	Acronyms	Ion species and energy	Masked or direct-write	Feature size and depth		Typical applications
Sputtering	Plasma etching	PE	Inert gas plasmas, few keV	Masked	$\mu\text{m}$	$< \mu\text{m}$	Surface cleaning
Reactive ion etching	Dry etching Deep reactive ion etching	RIE, DRIE	Mixtures of inert and reactive gases, few keV	Masked (reactive gas selected to have low etch rate for mask)	$< 100 \text{ nm}$	$> \mu\text{m}$	High-volume etching High-aspect ratio structures in chemically resistant materials.
Focused ion beam	Gas assisted etching	FIB, GAE	Li, Ga, O 10–50 keV	Direct-write (with or without etch gas)	nm	$> \mu\text{m}$	Sample preparation for TEM Complex microstructures Mask repair
Focused ion beam	Chemically assisted ion beam deposition	FIB, IBD, CAIBD	Li, Ga, O 10–50 keV	Direct-write (with precursor gas)	nm	$> \mu\text{m}$	Fabrication of complex structures Mask repair
Proton beam writing	Deep ion beam lithography	PBW, DIBL	Proton 1–4 MeV	Direct-write	$< 100 \text{ nm}$	$> 10 \mu\text{m}$	Complex high-aspect ratio 3-D microstructures in many materials. Buried channels. Patterned physical properties
Ion track lithography	Precisely positioned single ions	ITL PPSI	Heavy ion $> 1 \text{ MeV}$	Masked or direct-write (single ion)	$< 10 \text{ nm}$	$> 100 \mu\text{m}$	Structures assembled from nanotubes and nanowires
Proton beam induced decomposition			Protons 1–10 MeV	Masked or direct-write	$< 1 \mu\text{m}$	$> 1 \text{ mm}$	High-aspect-ratio structures formed in PTFE and other polymers

MeV ion interactions can be used to modify many properties of a wide range of solids (Toulemonde *et al.*, 1994), giving the possibility of creating functional structures with various physical properties patterned on the nanometre scale. One current example of this is the use of single ions to create nanometre scale magnetic domains in magnetic materials (Toulemonde *et al.*, 2004). Another example is the use of the crystal damage induced by localised MeV irradiation to pattern crystalline semiconductors by altering the rate of electrochemical etching. This has already been demonstrated in silicon and gallium arsenide (Teo *et al.*, 2004, Mistry *et al.*, 2004) (Fig. 6.19) and this could be a route for the integration of functional microstructures directly into electronic circuits.



**6.19** Scanning electron micrograph of the University of Surrey logo etched into the surface of a p-type gallium arsenide crystal by proton beam writing. The region of the letters was scanned using a 2 MeV beam of protons focused to 2  $\mu\text{m}$  diameter. After exposure the structure was electrochemically etched in a solution of hydrofluoric acid. The localised crystal damage induced by the beam inhibits the etching process leading to the formation of the pattern as a step of approximately 20  $\mu\text{m}$  depth.

These developments combined with other nanoscale techniques are likely to open up new areas of nanotechnology by permitting the fabrication of complex three-dimensional functional structures in materials including polymers, glasses, ceramics, semiconductors and metals.

## 6.7 Sources of further information and advice

Reactive ion etching and focused ion beam techniques are now maturing technologies and there are a number of books describing the principles, equipment and techniques in detail. Examples include Sugawara (1998) for RIE and Orloff *et al.* (2002) for FIB. High-energy ion beam techniques are still emerging and the only sources of information at present are the research papers and websites of the key groups (see Table 6.4). Although proton beam writing is not routinely available as a commercial service at the time of writing, all research groups will be happy to consider a commercial application

**Table 6.4** A list of selected research institutions active in the development of high-energy proton beam writing techniques at the time of writing. (Web addresses correct at the time of going to press)

Centre for Ion Beam Applications, National University of Singapore, Singapore	<a href="http://www.ciba.nus.sg">www.ciba.nus.sg</a>
Ion Beam Centre, University of Surrey, Guildford, U.K.	<a href="http://www.ee.surrey.ac.uk">www.ee.surrey.ac.uk</a>
Centre for Ion Beam Analysis (CAFI), University of Applied Sciences of the Jura, Le Locle, Switzerland	<a href="http://www.eiaj.ch/cafi">www.eiaj.ch/cafi</a>
LIPSION laboratory, Division of Nuclear and Solid State Physics, University of Leipzig, Germany	<a href="http://www.uni-leipzig.de/%7EEnfp">www.uni-leipzig.de/%7EEnfp</a>
Microanalytical Centre, Institute 'Jozef Stefan', Ljubljana, Slovenia	<a href="http://www.rcp.ijs.si/~mic">www.rcp.ijs.si/~mic</a>
Division of Nuclear Physics, University of Lund, Sweden	<a href="http://nuclearphysics.pixe.lth.se">nuclearphysics.pixe.lth.se</a>
Microanalytical Research Centre University of Melbourne, Australia	<a href="http://www.ph.unimelb.edu.au/marc">www.ph.unimelb.edu.au/marc</a>
Louisiana Accelerator Centre, Lafayette, Louisiana, U.S.A.	<a href="http://lac.louisiana.edu">lac.louisiana.edu</a>
Gesellschaft für Schwerionenfysik (GSI), Darmstadt, Germany	<a href="http://www-w2k.gsi.de/mr">www-w2k.gsi.de/mr</a>
Institute of Nuclear Research (ATOMKI), Debrecen, Hungary	<a href="http://www.atomki.hu/atomki/vdg">www.atomki.hu/atomki/vdg</a>

programme, and those wishing to investigate the use of these techniques should approach any of the laboratories in this list.

The general principles of forming MeV ion microbeams and reviews of their analytical applications can be found in books such as Grime and Watt (1984), Watt and Grime (1987) and Grime (1999).

## 6.8 References

- Ansari K., van Kan J.A., Bettiol A.A. and Watt F., (2004), 'Fabrication of high aspect ratio 100 nm metallic stamps for nanoimprint lithography using proton beam writing', *Applied Physics Letters*, **85**, 476–478.
- Breese M.B.H., Grime G.W., Watt F. and Williams D., (1993), 'MeV ion-beam lithography of pmma', *Nucl. Instr. and Meths. B.*, **77**, 169–174.
- Buchal C., (1992), 'Ion implantation of optical devices', *Nuclear Instruments and Methods in Physics Research Section B: Beam Interactions with Materials and Atoms*, **68**, 355–360.
- Fischer B.E., (1988), 'The heavy-ion microprobe at GSI -- Used for single ion micromechanics', *Nuclear Instruments and Methods in Physics Research Section B: Beam Interactions with Materials and Atoms*, **30**, 284–288.

- Giannuzzi L.A. and Stevie F.A., (1999), 'A review of focused ion beam milling techniques for TEM specimen preparation', *Micron*, **30**, 197–204.
- Gomez-Morilla I., Sofield C.J., Grime G.W. and Gwilliam R., (2005), 'Rapid deep Micromachining of polytera fluoroethylene by MeV ion bombardment in oxygen-rich atmospheres'. *J. Micromech. Microeng.* **15** 698–701
- Gomez-Morilla I., (2003), 'An investigation of novel processes for, microlithography using MeV ion beams', D. Phil. Thesis, University of Oxford.
- Grime G.W., (1999), In *Encyclopedia of Spectroscopy and Spectrometry* (eds, Lindon, J.C., Tranter, G.E. and Holmes, J.L.) Academic Press, Chichester, pp. 1901–1905.
- Grime G.W., Sofield C.J., Gomez-Morilla I., Gwilliam R.M., Ynsa M.D. and Enguita O., (2005), 'Rapid direct micromachining of PTFE using MeV ions in an oxygen rich atmosphere', *Nuclear Instruments and Methods in Physics Research Section B: Beam Interactions with Materials and Atoms*, **231**, 378–383.
- Grime G.W. and Watt F., (1984), *Beam Optics of Quadrupole Probe-Forming Systems*, Hilger, Bristol.
- ITRS (2003), *Report 'Lithography'*, International Technology Roadmap for Semiconductors. <http://public.itrs.net>
- Kometani R., Morita T., Watanabe K., Hoshino T., Kondo K., Kanda K., Haruyama Y., Kaito T., Fujita J.I., Ishida M., Ochiai Y. and Matsui S., (2004), 'Nanomanipulator and actuator fabrication on glass capillary by focused-ion-beam-chemical vapor deposition', *Journal of Vacuum Science & Technology B*, **22**, 257–263.
- Lawes R.A., (2000), 'Future trends in high-resolution lithography', *Applied Surface Science*, **154-155**, 519–526.
- Liang T., Stivers A., Livengood R., Yan P.-Y., Zhang G. and Lo F.-C., (2000), 'Progress in extreme ultraviolet mask repair using a focused ion beam', *Journal of Vacuum Science & Technology B-Microelectronics Processing and Phenomena*, **18**, 3216–3220.
- Lindberg M., (2003), 'High aspect ratio microsystem fabrication by ion track lithography, Ph.D. thesis, University of Uppala, Uppsala, Sweden.
- M. Arden W. (2002), 'The International Technology Roadmap for Semiconductors – Perspectives and challenges for the next 15 years', *Current Opinion in Solid State and Materials Science*, **6**, 371–377.
- Matsui S., Kaito T., Fujita J., Komuro J., Kanda K. and Haruyama Y., (2000), 'Three-dimensional nanostructure fabrication by focused-ion-beam chemical vapor deposition', *Journal of Vacuum Science & Technology B-Microelectronics Processing and Phenomena*, **18**, 3181–3184.
- Mistry P., Gomez-Morilla I., Webb R.P., Kirkby K.J., Grime G.W., Jeynes C., Gwilliam R.M., Merchant M.J. and Clough A.S., (2004), 'The development of proton beam machining at the University of Surrey', *Nucl. Instr. and Meths. B*, **231**, 428–432.
- Nohammer B., David C., Rothuizen H., Hoszowska J. and Simionovici A., (2003), 'Deep reactive ion etching of silicon and diamond for the fabrication of planar refractive hard X-ray lenses', *Microelectronic Engineering*, **67-68**, 453–460.
- Orloff J., (1993), 'High-resolution focused ion beams', *Review of Scientific Instruments*, **64**, 1105–1130.
- Orloff J., Swanson L. and Utlaut M., (2002), *High Resolution Focused Ion Beams: FIB and Applications*, Kluwer Academic/Plenum Publishers.
- Rimini E., (1995), *Ion Implantation: Basics to Device Fabrication*, Kluwer Academic Publishers.
- Ryssel H., Ruge I. and Goodman J.E., (1986), *Ion Implantation*, John Wiley and Sons Ltd.

- Sugawara M., (1998) *Plasma Etching: Fundamentals and Applications*, Oxford University Press, Oxford.
- Tay F.E.H., van Kan J.A., Watt F. and Choong W.O., (2001), 'A novel micro-machining method for the fabrication of thick-film SU-8 embedded micro-channels', *J Micromech Microeng*, **11**, 27–32.
- Teo E.J., Tavernier E.P., Breese M.B.H., Bettiol A.A., Watt F., Liu M.H. and Blackwood D.J., (2004), 'Three-dimensional micromachining of silicon using a nuclear microprobe', *Nucl. Instr. and Meths. B*, **222**, 513–517.
- Thornell G., Spohr R., van Veldhuizen E.J. and Hjort K., (1999), 'Micromachining by ion track lithography', *Sensors and Actuators A: Physical*, **73**, 176–183.
- Toulemonde M., Bouffard S. and Studer F., (1994), 'Swift heavy-ions in insulating and conducting oxides – tracks and physical properties', *Nucl. Instr. and Meths. B*, **91**, 108–123.
- Toulemonde M., Trautmann C., Balanzat E., Hjort K. and Weidinger A., (2004), 'Track formation and fabrication of nanostructures with MeV-ion beams', *Nuclear Instruments and Methods in Physics Research Section B: Beam Interactions with Materials and Atoms*, **216**, 1–8.
- van Kan J.A., Bettiol A.A. and Watt F., (2001), 'High precision 3D metallic microstructures produced using proton beam micromachining', *Nuclear Instruments and Methods in Physics Research Section B: Beam Interactions with Materials and Atoms*, **181**, 258–262.
- Watt F. and Grime G.W., (1987), *Principles and Applications of High Energy Ion Microbeams*, Hilger, Bristol.
- Watt F., van Kan J.A., Rajta I., Bettiol A.A., Choo T.F., Breese M.B.H. and Osipowicz T., (2003), 'The National University of Singapore high energy ion nano-probe facility: Performance tests', *Nuclear Instruments and Methods in Physics Research Section B: Beam Interactions with Materials and Atoms*, **210**, 14–20.
- Ziegler J.F. and Biersack J.P., (2003), *SRIM-2003*. <http://www.srim.org>.

## Nanofabrication by shadow deposition through nanostencils

---

J BRUGGER, Ecole Polytechnique Fédérale de Lausanne,  
Switzerland and

G KIM, Kyungpook National University, Korea

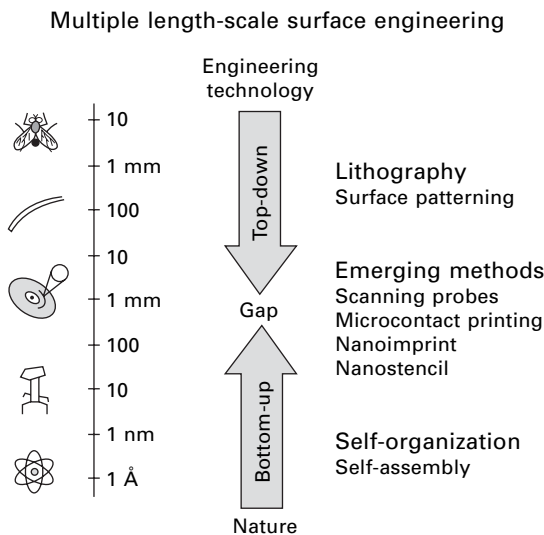
### 7.1 Introduction

Both microelectronic fabrication and micromachining start with lithography, the technique used to transfer copies of a master pattern onto the surface of a solid material, such as a silicon wafer (e.g. Madou 2002). In recent years, due to the continuous miniaturization and integration of devices, lithography techniques have been pushed into the sub-100-nm scale for industrial applications (ITRS roadmap 2003). For meeting the specifications of micrometer and nanometer scale devices, photolithographic techniques associated with pattern transfer methods rely on well defined and tight process parameters. Surface patterning using lithography is a subtractive method. This means that the material is first deposited everywhere and then reduced to the desired shape by lithography and etching methods. This procedure involves a series of processing steps and associated sub-steps such as thin film deposition, photo-resist spinning, exposure, development, etching, and finally resist removal. All these steps need to be performed for each layer in the process. In the case of materials that are difficult or impossible to etch, a so-called ‘lift-off’ process is used. Here, first a photoresist is deposited and structured by lithography, and then the thin film is deposited over the substrate that is partially covered with resist. Finally, the resist layer is dissolved whereby unwanted material is lifted off the surface.

While the described standard lithography methods form the workhorse methods for large-volume manufacturing in semiconductor applications, they have fundamental limitations when considered for the fabrication of advanced micro/nanosystems (MEMS/NEMS). The conception of MEMS and NEMS increasingly requires the use of ‘soft’ materials such as polymers and functional chemical layers that are incompatible with standard semiconductor spin-coating, baking and etch processing methods. MEMS also often include 3D surface topography or mechanically fragile parts such as thin membranes for pressure sensors and particle filters, or micro-cantilevers for scanning probes and other beam deflection sensors. In those cases spin-coating of resist can

not be applied as the fragile micromechanical parts would be damaged. Other important examples of increasing relevance are MEMS with surfaces containing sensitive (bio-) chemical coatings. Last but not least, advanced high-resolution photolithography based on semiconductor processes does not allow for rapid prototyping, as it involves high equipment and operational costs. These technological and economic barriers prevent efficient progress in research and development in many application fields of micro and nanosystems.

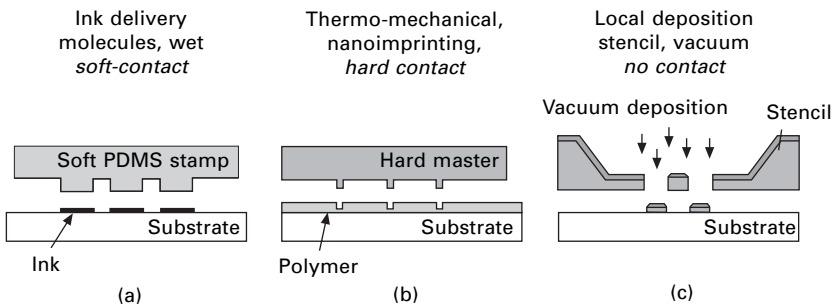
To overcome this bottleneck, a series of alternative micro- and nanopatterning methods have been developed in recent years. They are complementary to standard lithography processes and include, e.g., scanning probe methods (Quate, 1997; Piner, 1999), soft-lithography or microcontact printing (mCP) (Xia, 1998; Michel, 2001), and nanoimprint lithography (NIL) (Chou, 1995). They allow for versatile, flexible, and multi-material patterning with high throughput and are promising candidates for low-cost manufacturing. The newly emerging patterning methods have the capability to cover multiple length-scales from molecular scale to sub-centimeters. Consequently they are considered to be good candidates to bridge between the classical top-down miniaturization methods with central control by lithographic engineering and the bottom-up self-organization strategies with distributed control by nature driven self-assembly (see Fig. 7.1).



**7.1** Top-down engineering methods versus bottom-up self-assembly approaches. The emerging methods, e.g. scanning probes, microcontact printing, nanoimprinting and nanostencil, are good candidates to bridge the gap.

Soft-lithography or micro-contact printing ( $\mu$ CP) as well as nano-imprint lithography (NIL) is well documented (see Chapter 3). Both methods rely on a local physical contact between a master surface (stamper) and the surface to be patterned as shown schematically in Figs 7.2(a) and (b). In the case of  $\mu$ CP the contact between the elastic stamp and the surface is soft and is only used to transmit a thin molecular layer at the contact points. In the case of NIL, the physical contact is typically accompanied by a thermal process to heat a polymer over the glass transition temperature in order to indent the micro and nanoscale features into the polymer film.

In contrast to  $\mu$ CP and NIL, local deposition via nanostencils is a potentially contact-less method (Brugger, 2000). Therefore, nanofabrication using stencils offers promising alternatives to define micro and nanoscale surface structures without actually touching the substrate (Fig. 7.2(c)). This obviously makes the method extremely interesting for patterning on fragile surfaces. In the rest of this chapter, we will describe details of the nanofabrication method using nanostencils.



7.2 Comparison of replication methods (a) soft-lithography with elastic contact (b) nano-imprint with hard contact and temperature (c) nanostencil method which is the only one not relying on a local mechanical contact for pattern creation.

## 7.2 Surface patterning by deposition through stencils

### 7.2.1 Physical vapor deposition (PVD)

This section summarizes some basics on physical vapor deposition (PVD) (Sze, 1988) that are relevant for understanding the mechanism of shadow mask or stencil patterning. The rate of evaporation of metal from a melt is estimated by using the Hertz Knudsen equation

$$N_e = (2\pi mkT)^{-1/2} P_e \quad 7.1$$

where  $N_e$  is the number of molecules per unit area per time,  $m$  is the molecular (atomic) mass,  $k$  is Boltzmann's constant,  $T$  is the surface temperature in

Kelvin, and  $P_e$  is the equilibrium vapor pressure of the evaporated material. This vapor pressure may be written as a rate of mass loss per unit area from the source

$$R = 4.43 \times 10^{-4} \left[ \frac{M}{T} \right]^{1/2} P_e \text{ g/cm}^2 \cdot \text{s} \tag{7.2}$$

where  $M$  is the gram-molecular mass and  $P_e$  is in Pa. For example the equilibrium vapor pressure  $P_e$  of Aluminum at 1,500 K is  $\sim 1.5$  Pa.

The total loss  $R_T$  per unit time from the source may be found by integrating over the source area

$$R_T = \int R dA_s \tag{7.3}$$

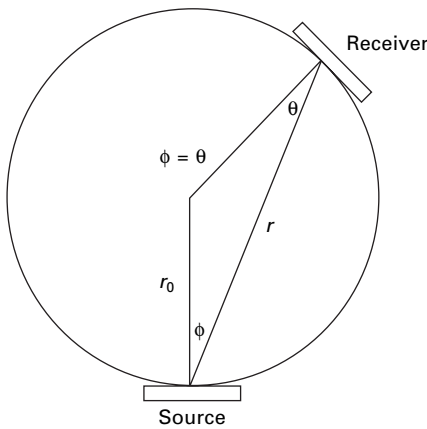
The flux of material to the receiving substrate is dependent on the cosine of the angle,  $\phi$  between the normal to the source surface and the direction of the receiving surface a distance  $r$  away. If  $\theta$  is an angle between the receiving surface normal and the direction back to the source, then

$$D = \frac{R_T}{\pi r^2} \cos \phi \cos \theta \tag{7.4}$$

where  $D$  is the deposition rate in  $\text{g/cm}^2 \cdot \text{s}$ .

When the receiving surface is spherical and has a radius  $r_0$ , and the source is on the surface as shown in Fig. 7.3, then

$$\cos \phi = \cos \theta = \frac{r}{2r_0}$$



7.3 Idealized view of the method using evaporated material from a source that is deposited on a surface mounted on a sphere of radius  $r_0$ .

and eqn 7.4 can be written as

$$D = \frac{R_T}{4\pi r_0^2}$$

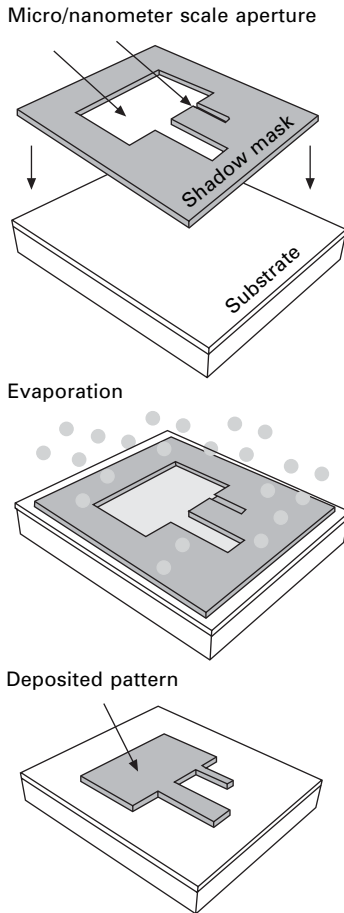
Therefore the deposition rate  $D$  is the same for all points on the spherical surface. This is the principle behind the planetary substrate supporting systems with rotating spherical sections typically used in deposition chambers.

### 7.2.2 Local physical vapor deposition through stencil membranes

As shown above, evaporation is done by heating a source material under high vacuum conditions ( $<10^{-3}$  Pa) to its melting temperature. Under high vacuum conditions the mean free path of the vaporized material is much larger than the distance of the source to the substrates, so that the vaporized material streams in straight lines from the source to the substrate, also called line-of-sight deposition. If a shadow mask or stencil is brought between the source of evaporated material and the substrate a shadow pattern is created on the surface as illustrated schematically in Fig. 7.4. Stencil patterning can be compared to the well-known lift-off method. The essential difference is the use of a thin mechanical, solid-state membrane instead of a photoresist layer to mask the surface. Since no organic photoresist is used, the stencil approach is potentially cleaner and can be applied also on fragile surfaces.

Yet, in contrast to the resist-based lift-off technique where the intimate contact between the resist and the surface provides excellent edge definition, shadow-mask patterning suffers from some error sources that prevent precise pattern definition. For instance, one drawback of mechanical shadow-masks is the insufficient control of the distance between the stencil-membrane and the substrate surface. The gap may be caused initially by substrate bending or contamination particles on the surface. The gap may also appear during the deposition process due to stress-induced bending of thin, micromechanical parts in the stencil membrane. Besides blurring the pattern, it will also be shifted from its designated position, if the substrate and shadow mask are not placed exactly perpendicular to the vapor stream. A simple calculation shows that at the angle of  $1^\circ$  a point pattern shifts laterally  $2\ \mu\text{m}$  for a gap of  $0.1\ \text{mm}$  between the shadow mask and the substrate (assuming a large source distance and small source size). As a consequence the positioning of the shadow mask must be controlled precisely for accurate pattern definition (Burger, 1996).

Another reason for spreading is due to the back-scattering of material from the stencil pore as well as from the substrate surface. For instance, if the sticking coefficient of the vapor atoms is lower than unity, they will



7.4 Principle of shadow evaporation through a thin mechanical solid-state membrane or nanostencil.

scatter at the mask edge and the substrate (Gray, 1959). These scattered atoms may be deposited under the shadow mask. This results in an undesired thin skin layer in the shadow regions. However, since this spreading is much thinner than the desired pattern, it can be removed by subsequent appropriate etching process.

Despite all these limitations, shadow masking techniques have long been used in thin-film processing of components. Due to their extreme simplicity and efficiency, they have been employed for the fabrication of millimeter and micrometer scale devices for a variety of applications in the field of information technology. It is hence interesting and important to study the resolution limit of the stencil-method. In particular, we have seen that stencil-based nanofabrication can be contact-free, and atomically clean. Thus, it

forms an ideal candidate for template formation at the micro-to-nano interface, and for directed molecular assembly in molecular electronics applications (Joachim, 2000) where extremely clean surface interfaces are required. In the following section, we will focus on the fabrication of micro and nanostencils and discuss the materials that can be used to form thin solid-state membranes with apertures in the sub-micrometer range.

## 7.3 Ultra-thin solid-state membranes

### 7.3.1 Materials

Using membranes as shadow masks for high-resolution patterning purposes requires that they can be made (i) very thin, (ii) with a uniform thickness, (iii) with low or no stress, (iv) with micro and nanometer scale pores, and (v) from a mechanically stable and chemically inert material. In the past the stencil masks were realized in metal or graphite sheets by milling, arc erosion or laser cutting. The smallest aperture using these methods was around 50  $\mu\text{m}$  with a tolerance of 5  $\mu\text{m}$  (Glang, 1970). More recently, semiconductor processing associated with precise etch-stop techniques has allowed the control of the shape and thickness of free-standing membranes down to micrometer dimensions and below. Possible membrane materials include doped silicon, low-stress silicon nitride (SiN) or single-crystal silicon (Si), e.g., made on a silicon-on-insulator (SOI) wafer. Low-stress silicon nitride (SiN) is often used as the material for free-standing membrane due to its superb material properties such as stability and chemical inertness. By using a well-controlled low-pressure chemical vapor deposition (LPCVD) process, an inherently low stress around 200 MPa can be achieved, which is the major prerequisite for flat, unbuckled membranes. Silicon-on-insulator (SOI) wafers (e.g. SIMOX<sup>®</sup>, SDB, or Poly SOI) can also be used for stencil fabrication (Butschke, 1999). The advantage of using SOI material is that the single crystal silicon is initially totally stress free, which provides flat, unbuckled membranes over large areas. An additional advantage is that the buried silicon dioxide insulator layer acts as a stop layer for the membrane etching.

Polymer layers were also used as material for thin stencil membranes. The elasticity of the material allows approaching the stencil conformal to the substrate and thereby reduces the gap. For instance, elastomer membranes were fabricated by spin-coating a liquid poly(dimethylsiloxane) (PDMS) pre-polymer onto a master consisting of high-aspect ratio features of silicon or SU-8 on a silicon wafer (Jackman, 1999). Because the elastomer membrane conforms and seals tightly to surfaces with which it is in contact, no air gap exists between the mask and substrate and it is impermeable to the reagents used in deposition. Also, since the elastomer is chemically inert, a variety of materials including metals, sol-gels, hydrogels, biological macromolecules,

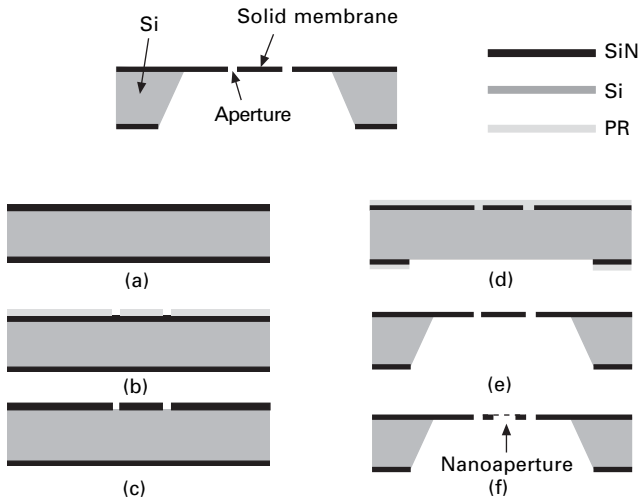
and organo-metallic molecules can be patterned. In another approach, thin shadow-mask membranes have been made directly from photostructurable epoxy-based SU-8 polymer by lithography and sacrificial layer etching (Kim 2003b). The advantage here is that a 5  $\mu\text{m}$  thick membrane and 200  $\mu\text{m}$  thick rim part can be fabricated on the sacrificial layer by a simple process of lithography and development of the cross-linked SU-8 polymer.

### 7.3.2 Fabrication of nanostencils

In addition to the choice of the appropriate material for the stencil membrane, a convenient method for micron and submicron apertures needs to be derived. Here, we benefit from extended know-how in MEMS technology related to thin-membrane fabrication processes (van Rijn, 1998). Membrane apertures can be defined by microfabrication processes using standard UV photolithography and thin film etching, followed by wafer-through etching to release the membrane (Kim, 2003a). Sub-micron scale periodic structures were obtained by laser interference lithography and etching (van Rijn, 1999). Arbitrary sub-micron patterns can be obtained by direct milling of silicon nitride using a focused ion beam (FIB) (Köhler, 1999; Deshmukh, 1999; Kim 2003a). Here, a focused beam of gallium ions at a high energy ( $\sim 30$  KeV) removes the material physically at a desired region on the membrane. The shape of the apertures can be controlled by choosing the appropriate scan range of the focused beam. Very small apertures down to  $\sim 10$  nm were realized in SiN films that were locally thinned down to a few nanometers only (Deshmukh, 1999). Such thin membranes cannot be made very large as they cannot sustain the mechanical stress induced by handling and/or processed thin films. One remedy is to use rib-supported membranes (Hammer, 1977) for increased vertical stability. Another way is to support the thin membrane by thicker parts at positions with lower demands on pattern resolution. On the other hand, an important parameter for high-resolution deposition through mechanical membranes is the aspect ratio of the aperture. For example, an aspect ratio of 5 (e.g. a 100-nm aperture in a 500-nm thick membrane), reduces the deposition rate in a typical deposition equipment drastically due to the shadow effect of the aperture sidewall itself. As a rule of thumb we assume that a convenient aspect ratio between membrane thickness and aperture is about 1.

A solution is to use membranes that are locally thin around the apertures, but thick enough elsewhere for increased mechanical stability. Such membranes have been made by a combination of MEMS processes and local FIB milling (Kim, 2003a). Here the FIB milling has been used as post processing after the conventional MEMS fabrication with micron-scale pores. Thereby, an initially 500 nm thick and stable SiN membrane with micrometer scale apertures made by a UV MEMS process has been thinned down locally to 100 nm by

FIB. Then the 100-nm scale apertures were fabricated in the thinned membrane portion as shown in Figs 7.5 and 7.6. In such a case, low-density sub-micron apertures can be made over millimeter areas.

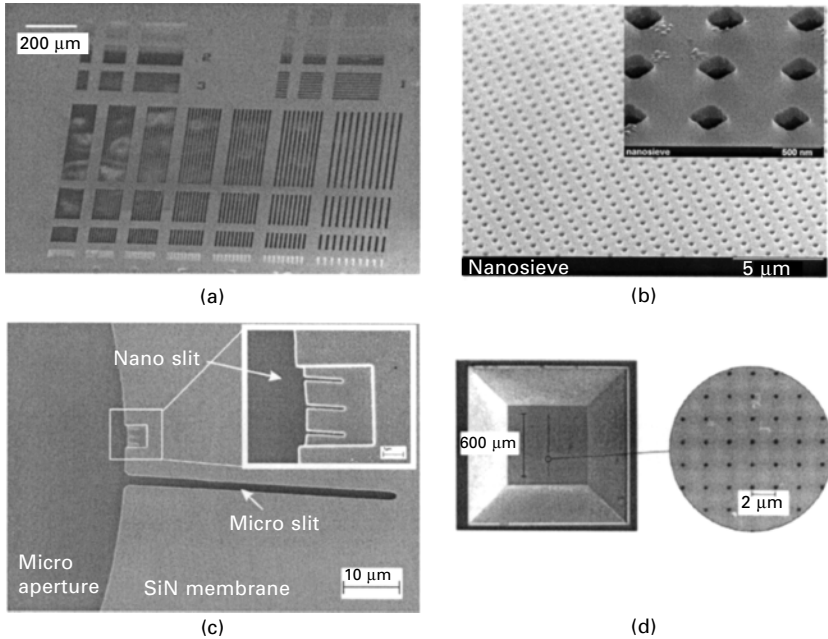


7.5 MEMS fabrication of shadow mask membrane (schematic).

(a) SiN layer deposition (b) aperture patterning by photolithography (c) pattern transfer into SiN layer on topside (d) membrane window definition by photolithography on reverse (e) bulk Si wet etching to make membrane. (f) FIB milling for nanoaperture fabrication (including membrane thinning).

### 7.3.3 Full-wafer nanostencil for high-throughput nanopatterning (incl. DUV)

To overcome the inherent through-put limitations by using FIB as nanoscale milling tool, a high-resolution deep ultraviolet (DUV) lithography technique can be combined with a MEMS process for the high-throughput fabrication of large stencils. Here, an industry-standard DUV lithography was used to create patterns in a photoresist layer down to 250 nm on full-wafer scale. After development, the resist patterns were transferred into a 500 nm-thick low-stress-SiN by means of reactive ion etching. Finally the membrane is etched by wafer-through etching using KOH to release the nanostencil membranes. A variety of structure geometries down to 250 nm length-scale can be produced by the combined DUV/MEMS method on a full-wafer scale with high throughput as shown in Fig. 7.7 (van den Boogaart, 2004).

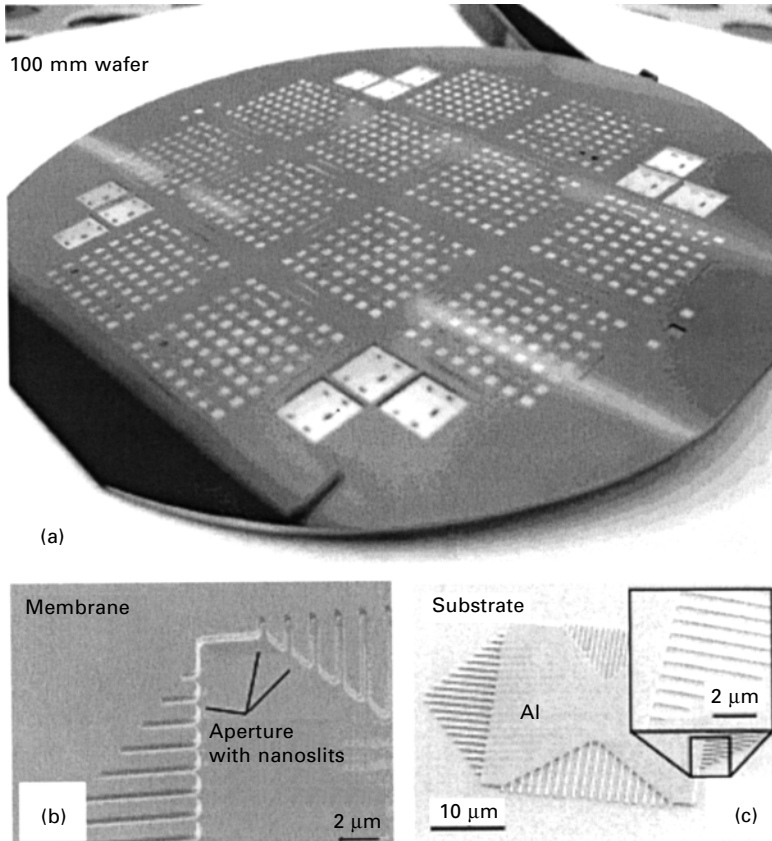


7.6 SEM photos of shadow masks: (a) microstencil made by photolithography; (b) nanostencil made by Laser interference lithography (LIL); (c) multiple length scale stencil made by the combination of photolithography and FIB; (d) nanostencil made by FIB milling (Köhler, 1999).

## 7.4 Nanofabrication using nanostencils

### 7.4.1 Patterning on planar surfaces

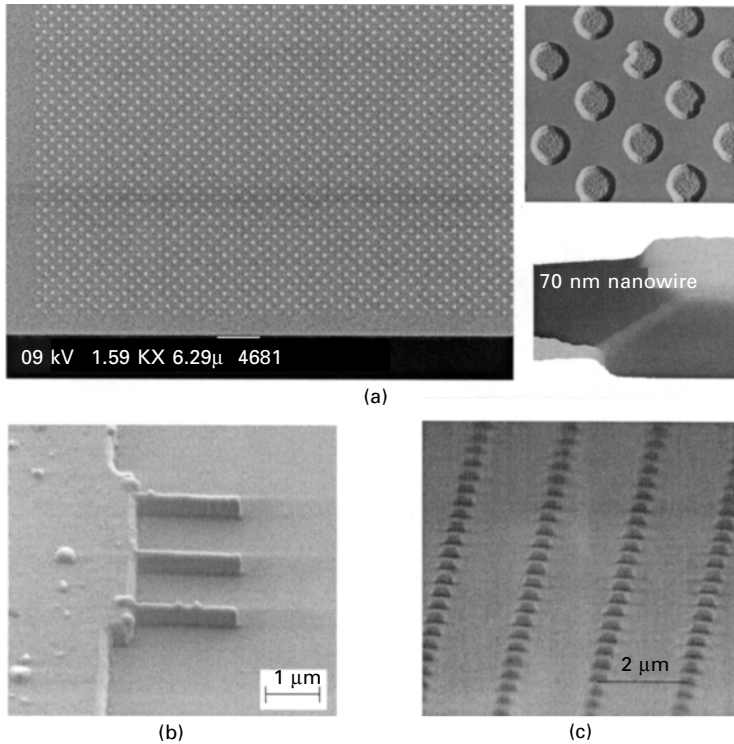
In general, the thin film material of choice can be deposited through the stencil by evaporation, sputtering, chemical vapor deposition (CVD), pulsed laser deposition (PLD) or molecular beam epitaxy (MBE). Evaporation of metal is the most simple way of stencil based nanofabrication because the mean free path of the evaporated metal is very long in high vacuum conditions. This results in an excellent shadow effect which is important for high-resolution stenciling. Figure 7.8 shows some typical examples of nanoscale metal patterns made by evaporation through the nanostencils shown in Fig. 7.6. Figure 7.8 (a) shows a SEM image and AFM image of part of an area containing millions of 300 nm gold dots that were created by thermal evaporation of a 30 nm thick Au layer through the nanosieve shown in Fig. 7.6(b). In addition, a 70 nm wide gold nanowire connecting two 700 nm gold dots was fabricated by the same method. Other typical nanostructures in thin metal layers based on FIB fabricated stencils are shown in Figs 7.8(b) and (c) (Kim, 2003a; Köhler, 1999). Other work showed that metal contacts can be fabricated to



7.7 Full-wafer nanostencil: (a) photo of a 100 mm full wafer nanostencil containing various membranes with numerous geometrical apertures; (b) released SiN membrane with nano-slits (200 nm); (c) metal (Al) patterns made by local deposition through the nanostencil.

DNA molecular circuits or single-walled carbon nanotube (SWNT) (Zhou, 2003). The metal contacts can be fabricated on as-grown molecular wires that would be contaminated or destroyed by chemicals and heat treatments associated with conventional lithographic techniques. Also, massive arrays of carbon nanotubes can be synthesized by chemical vapor deposition of iron template made through shadow mask (Fan, 1999).

Local deposition through shadow mask or stencils is not limited to methods based on thermal evaporation of metal. Organic light emitting diode (OLED) can be fabricated by vacuum deposition of organic materials between indium tin oxide (ITO) and metal cathode through stencil (Tian, 1999). High-quality thickness-tapered semiconductor waveguides were fabricated based on controlling in-plane thickness during MOVPE by using a comb-shaped silicon



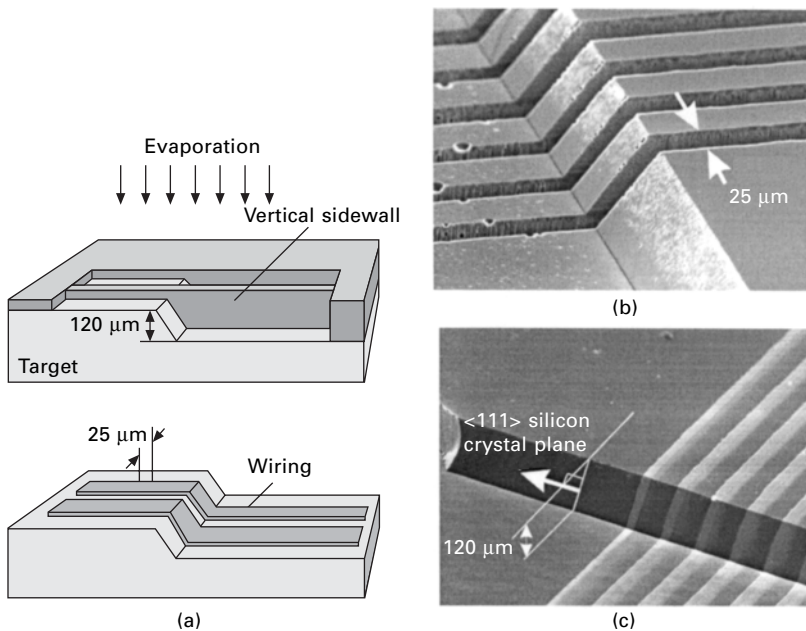
7.8 Examples of typical micro/nanostencil patterns: (a) scanning electron microscope image of an array of 300 nm size gold dots made using the nanostencil shown in Fig. 7.6 (left), atomic force microscope (AFM) image of 700 nm size gold dots (top right) and AFM image of 70 nm wide gold nanowire (bottom right); (b) nanoscale cantilever pattern made by using FIB milled nanostencil; (c) nanoscale dot pattern made by stencil in 7.6(d) (Köhler, 1999).

shadow mask (Aoki, 1996). Sub-micron patterning using pulsed laser deposition (PLD) through stencils was also investigated (Vroegindeweij, 2004). For the PLD method, stencils with circular and elliptical patterns were used, with pore sizes ranging from 1  $\mu\text{m}$  down to 500 nm. Strontium titanate ( $\text{SrTiO}_3$ ), silicon (Si), and self-assembled monolayers (SAM) on gold were used as substrate materials, whereas nickel (Ni), nickel oxide (NiO), and gold (Au) have been deposited. Other examples of the selective molecular beam epitaxial growth technique using shadow mask (Beam, 1991) can be found in many articles for selective doping (Gulden, 1993) and for fabrication of many devices, e.g., monolithically integrated smart pixels (Hilburger, 1999), single two-dimensional (2D) atomically thick magnetic particles of cobalt and iron (Stamm, 1998), InGaAsP/InP strained MQW laser with integrated mode size converter (Moerman, 1995), and InAs/GaAs self-organized quantum dots (Songmuang, 2001).

### 7.4.2 Patterning on recessed surfaces

When the shadow masking technique is applied for the patterning of materials in deep holes or a recessed non-planar surface, the increased gap between stencil and surface will compromise the resolution due to the large distance between the aperture and the target plane. In order to overcome these limitations, three-dimensional shadow masks that approach the aperture close to the surface were proposed (Brugger, 1999). Figure 7.9(a) shows a schematic illustration of the 3D shadow mask required for metal wiring across step and the corresponding results. The 3D shadow mask allows the aperture of the shadow to be approached within a few micrometers to the target plane for a better pattern resolution. Figures 7.9(b) and (c) show the fabricated 3D shadow mask and the 500 nm thick aluminum wires on a step evaporated with the 3D shadow mask, respectively.

Another application is metal patterning on the tip of a scanning probe (Champagne, 2003). Recently, advanced types of scanning probe systems have used nanofabricated structures that serve as scanning sensors or functional probes, e.g., scanning thermal microscopy and magnetic force microscopy.



7.9 Three-dimensional (3D) shadow mask for patterning on recessed surface (Brugger, 1999): (a) Schematic illustration of the 3D shadow mask required for metal wiring across step (top) and the target result (bottom); (b) SEM image of the 3D shadowmask for step wiring seen from the recessed side; (c) 500 nm aluminum wires on a step evaporated with the 3D shadow mask.

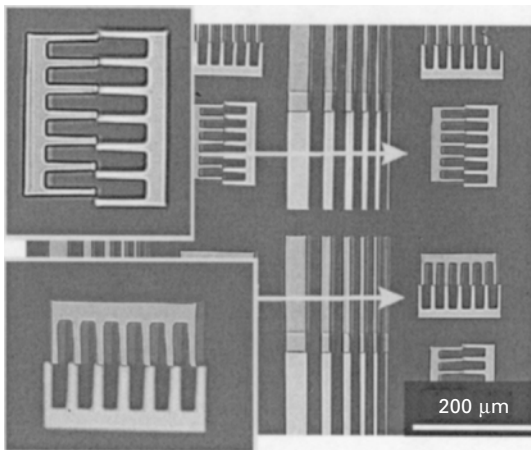
In order to achieve high sensitivity and spatial resolution, functional nanostructures must be built near the apex of a tip in order to allow the sensor to be scanned close to the sample surface. By employing the stencil mask technique, a wide variety of devices can be fabricated at the apex of SPM tips with spatial resolution down to 10 nm.

### 7.4.3 Multi-layer patterning with alignment

So far only single-layer fabrication has been discussed. In most practical cases, multiple layers of material patterns need to be fabricated with precise alignment to each other. In order to pattern multi-layers, the shadow mask has to be aligned accurately to the target wafer. The stencil can either be aligned using a mechanical tool, or it can rely on some sort of self-alignment. Mechanical self-alignment structures were made by deep etching of Si (Tixier, 2000), or by SU-8 structuring (Kim, 2003b). Self-aligning can be also exploited by using Si crystal plane resulting from KOH etching of Si and 3D shadow mask (Brugger, 1999). Figure 7.10 shows an example of multilayer micrometer size patterns of Al and Au using two subsequent evaporation steps through complementary shadow masks with precise mechanical alignment within  $\sim 10 \mu\text{m}$ .

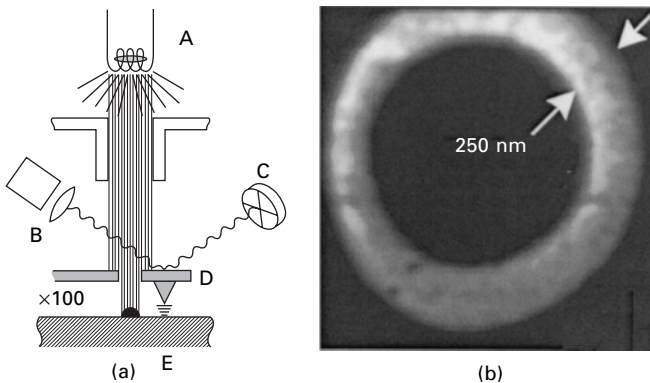
### 7.4.4 Scanned AFM nanostencil

A dynamic stencil is based on a combination of shadow mask and scanning probe methods (Lüthi, 1999). The method represents a resistless lithography technique, i.e., a local and variable direct patterning of thin film structures



7.10 An example of multilayer patterns of 100 nm thick Al and 200 nm thick Au layers manually aligned under an optical microscope with  $10 \mu\text{m}$  precision (Kim, 2003b).

on wafers. Figure 7.11(a) shows the principle of a scanning nanostencil. Instead of fixing the stencil to the substrate, the sample is moved underneath a AFM cantilever with an aperture during the deposition of the material. With this technique arbitrary patterns can be written on the surface, like rings (Figure 7.11(b)), wires and intersecting lines with dimensions of less than 100 nm. After the deposition the thin film structures can be characterized using the same AFM tip. Thus this technology is extremely interesting for depositing nanoscale combinatorial libraries. In this context, recently a related method has been presented for forming nanometer-scale metal features based on evaporation onto a substrate through a moving stencil mask. The stencil mask is laterally translated by a piezoflexure stage, between evaporations of different metals. The metals are chosen based on their etch chemistry to allow one material to be lifted off with respect to another. In this way, sidewall features are formed with dimensions and spacing controlled by moving the translation stage, which has 1 nm resolution (Racz, 2004).



7.11 Scanned AFM nanostencil (Lüthi, 1999): (a) schematic view of the principle. Material is deposited through a nanoaperture on scanning AFM cantilever; (b) a ring shape can be patterned by moving the AFM probe in a circular way.

## 7.5 Limitations of stencil technology

### 7.5.1 Clogging

Deposited material is deposited not only on the substrate but also on the membrane and inside the apertures of the stencil. This leads to clogging and constitutes the major limitation of the stencil method. Remedies to overcome this problem are being investigated. The simplest way is to clean the stencil by selectively etching the deposited material away. Another approach is to prevent or slow down the clogging effect by tuning the adhesion properties of the membrane material. For instance, the clogging problem can be reduced

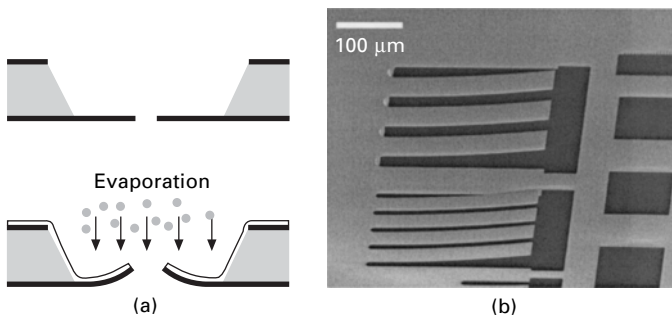
by coating an organic self-assembled monolayer (SAM) on the nanostencil as an anti-adhesion layer. The SAM layer prevents adhesion of material to the aperture walls and thus increases the performance and throughput of the nanostencil technique (Koebel, 2003).

### 7.5.2 Bending

Another limitation on the use of thin mechanical films as solid-state shadow mask membranes is due to bending from mechanical stress induced by the deposited thin film on the membrane itself (Fig. 7.12). The amount of bending depends on the geometry of the free-standing thin membrane portions. Many efforts are being made to study stress on membranes and to measure their residual stress, e.g., using dependency of membrane resonance frequency on membrane residual stress (Degen, 2001). To overcome the stability limitation, mechanical reinforcement structures can be integrated into the membrane to stabilize it locally, e.g., by rib-supported structures (Hammer, 1977; van den Boogaart, 2005).

## 7.6 Conclusion

In summary we have described details of a novel surface nanopatterning method that is based on the local physical vapor deposition through miniaturized shadow masks, called nanostencils. By using a combination of advanced MEMS processing with high-resolution lithography and well-controlled etching, large, stable ultra-thin membranes can be made on a wafer scale. Applying the stencils as shadow mask allows the creation of surface patterns in the micron to sub-100 nm length scale. The absence of processing steps other than deposition makes the technique very interesting for patterning



7.12 Stress-induced bending of the membrane resulting from metal deposition; (a) schematic view; (b) bending of 500 nm SiN membrane after an evaporation of 700 nm aluminum. Bending of free-ending cantilever on the left is clearly seen compared to the double clamped part on the right.

arbitrary material (metal, dielectrics, organic molecules) on conventional (silicon wafer, glass plates) as well as on unconventional surfaces (polymer, PDMS, SU-8, 3D-topography). The ability to pattern sub-100 nm scale patterns in a vacuum-clean fashion makes the nanostencil an interesting candidate for the combination with bottom-up chemical self-assembly, where clean molecular interfaces are needed for future molecular electronic applications. Last but not least, the availability of nanostencils will allow advancing basic and applied research nanoscience and nanotechnology in laboratories where expensive exposure tools are not accessible.

## 7.7 Acknowledgements

We are very pleased to acknowledge our colleagues Ing. M.A.F. van den Boogaart, Dr. Lianne Doeswijk and our colleagues from the EPFL Center of Micro and Nanotechnology as well as Rudy Pellins from ASML, for their contribution to the nanostencil work. Many thanks also to the MESA+ Research Institute for Nanotechnology, University of Twente, The Netherlands, where the membrane nanostencil work started. Financial support for part of the work described here came from the European Union 5th Framework project ATOMS, the Swiss CTI Top-Nano 21 project ‘Melode’, and from the Swiss Federal Institute of Technology, EPFL, Lausanne.

We gratefully acknowledge permission to reprint several figures and pictures from the following publications:

Figure 7.6(d) and Fig. 7.8(c): Reprinted from *Physica E: Low-dimensional Systems and Nanostructures*, 4 (3), 196–200, Köhler J, Albrecht M, Musil C R, Bucher E., ‘Direct growth of nanostructures by deposition through an  $\text{Si}_3\text{N}_4$  shadow mask’, Copyright 1999, with permission from Elsevier.

Figure 7.9: reprinted from *Sensors and Actuators A*, Vol. 76, No 1-3, 1999, pages 329–334.: J. Brugger *et al.*, ‘Self-aligned 3D shadow mask technique for patterning deeply recessed surfaces of micro-electro-mechanical systems devices’, Copyright 1999, with permission from Elsevier.

Figure 7.10: reprinted from *Sensors and Actuators A*, 107, 132–136, Kim G M, Kim B J, Brugger J, (2003b), ‘All-photoplastic microstencil with self-alignment for multiple layer shadow-mask patterning’, copyright 2003, with permission from Elsevier.

Figure 7.11: reprinted from *Applied Physics Letter* Vol. 75, Number 9 (1999) 1314–1316., Roli Luethi, *et al.*, ‘Parallel nanodevice fabrication using a combination of shadow mask and scanning probe methods’, with permission from the American Institute of Physics.

## 7.8 References

- Aoki M., Komori M., Suzuki M., Sato H., Takahashi M., Ohtoshi T., Uomi K. and Tsuji S., (1996), 'Wide-temperature-range operation of 1.3- $\mu\text{m}$  beam expander-integrated laser diodes grown by in-plane thickness control MOVPE using a silicon shadow mask', *Photonics Technology Letters*, 8 (4), 479–481.
- Beam E.A., Kao Y.C. and Yang J.Y., (1991), 'A cantilever shadow mask technique for reduced area molecular beam epitaxial growth', *Applied Physics letters*, 58 (2), 152–154.
- Brugger J., Andreoli C., Despont M., Drechsler U., Rothuizen H. and Vettiger P., (1999), 'Self-aligned 3D shadow mask technique for patterning deeply recessed surfaces of micro-electro-mechanical systems devices', *Sensors and Actuators*, 76, 329–334.
- Brugger J., Berenschot J.W., Kuiper S., Nijdam W., Otter B. and Elwenspoek M., (2000), 'Resistless patterning of sub-micron structures by evaporation through nanostencils', *Microelectron. Eng.*, 53, 403–405.
- Burger G.J., Smulders E.J.T., Berenschot J.W., Lammerink T.S.J., Fluitman J.H.J. and Imai S., (1996), 'High-resolution shadow-mask patterning in deep holes and its application to an electrical wafer feed through', *Sensors Actuators A*, 54, 669–673.
- Butschke J., Ehrmann A., Höfflinger B., Irmscher M., Käismaier R., Letzkus F., Löschner H., Mathuni J., Reuter C., Schomburg C. and Springer R., (1999), 'Companion of silicon stencil mask distortion measurements with finite element analysis', *Microelectronic engineering*, 46 (1-4), 473–476.
- Champagne A.R., Couture A.J., Kuemmeth F. and Ralph D.C., (2003), 'Nanometer-scale scanning sensors fabricated using stencil lithography', *Appl. Phys. Lett.*, 82(7), 1111–1113.
- Chou S.Y., Krauss P.R. and Renstrom P.J., (1995), 'Imprint of sub-25nm vias and trenches in polymers', *Appl. Phys. Lett.*, 76, 3114–3116.
- Degen A., Abedinov N., Gotszalk T., Sossna E., Kratzenberg M. and Rangelow I.W., (2001), 'Stress analysis in Si membranes for open stencil masks and mini-reticles using double bulging and resonance methods,' *Microelectronic Engineering*, 57–58, 425–432.
- Deshmukh M., Ralph D.C., Thomas M. and Silcox J., (1999), 'Nanofabrication using a stencil mask', *Appl. Phys. Lett.*, 75, 1631–1633.
- Fan S., Chapline M.G., Franklin N.R., Tomblor T.W., Cassell A.M. and Dai H., (1999), 'Self-oriented regular arrays of carbon nanotubes and their field emission properties', *Science*, 283, 512–514.
- Glang R. and Gregor L.V., (1970), 'Generation of patterns in thin films', *Handbook of Thin-film Technology*, New York, McGraw-Hill.
- Gray S. and Weimer P.K., (1959), 'Production of fine patterns by evaporation,' *RCA Review*, 20, 413–425.
- Gulden K.H., Wu X., Smith J.S., Kiesel P., Hofler A., Kneissl M., Riel P. and Doehler G.H., (1993), *Appl. Phys. Lett.*, 62, 3180–3182.
- Hammer R., (1977), 'Solving the "stencil" problem in vacuum deposition masks using rib-supported structures', *J. Vac. Sci. Technol.*, Vol. 14, No. 5, Sept./Oct. 1977, 1208–1210.
- Hilburger U., Fix W., Mayer R., Geisselbrecht W., Malzer S., Velling P., Prost W., Tegude F.J. and Döhler G.H., (1999), 'Extension of the epitaxial shadow mask MBE technique for the monolithic integration and *in situ* fabrication of novel device structures,' *Journal of crystal growth*, 201–202, 574–577.

- ITRS roadmap (2003) at <http://public.itrs.net/>
- Jackman R.J., Duffy D.C., Cherniavskaya O. and Whitesides G.M., (2003), 'Using elastomeric membranes as dry resists and for dry lift-off', *Langmuir*, 15, 2973–2984.
- Joachim C., Gimzewski J.K. and Aviram A., 'Electronics using hybrid-molecular and mono-molecular devices', *Nature*, Vol. 408, 30 November 2000, p. 541–546.
- Kim G.M., van den Boogaart M.A.F. and Brugger J., (2003a), 'Fabrication and application of a full wafer size micro/nanostencil for multiple length-scale surface patterning', *Microelectronic Engineering*, 67–68, 609–614.
- Kim G.M., Kim B.J. and Brugger J., (2003b), 'All-photoplastic microstencil with self-alignment for multiple layer shadow-mask patterning', *Sensors and Actuators A*, 107, 132–136.
- Koelbel M., Tjerkstra R.W., Kim G.M., Brugger J., van Rijn C.J.M., Nijdam W., Huskens J. and Reinhoudt D.N., (2003), 'Self-assembled monolayer coating on nanostencils for the reduction of materials adhesion', *Advanced Functional Materials*, 13, 210–224.
- Köhler J., Albrecht M., Musil C.R. and Bucher E., (1999), 'Direct growth of nanostructures by deposition through an Si<sub>3</sub>N<sub>4</sub> shadow mask', *Physica E: Low-dimensional Systems and Nanostructures*, 4 (3), 196–200.
- Lüthi R., Schlittler R.R., Brugger J., Vettiger P., Welland M.E. and Gimzewski J.K., (1999), 'Parallel nanodevice fabrication using a combination of shadow mask and scanning probe methods', *Appl. Phys. Lett.*, 75 (9), 1314–1316.
- Madou M.J., (2002), *Fundamentals of Microfabrication: The Science of Miniaturization* 2nd edn, CRC Press.
- Michel B., Bernard A., Bietsch A., Delamarche E., Geissler M., Juncker D., Kind H., Renault J-P., Rothuizen H., Schmid H., Schmidt-Winkel P., Stutz R. and Wolf H., (2001), 'Printing meets lithography: soft approaches to high-resolution patterning', *IBM J. Res. Develop.* 45, 697–719.
- Moerman I., D'Hondt M., Vanderbauwhede W., Van Daele P., Demeester P. and Hunziker W., (1995), 'InGaAsP/InP strained MQW laser with integrated mode size converter using the shadow masked growth technique,' *Electronics Letters*, 31 (6), 452–454.
- Piner R.D., Zhu J., Xu F., Hong S. and Mirkin C.A., (1999), 'Dip-Pen Nanolithography', *Science*, 283 (29), 661–663.
- Quate C.F., (1997), 'Scanning probes as a lithography tool for nanostructures', *Surface Science* 386 (1-3), 259–264 Oct.
- Racz Z., He J., Srinivasan S., Zhao W., Seabaugh A., Han K., Ruchhoeft P. and Wolfe J., (2004), 'Nanofabrication using nanotranslated stencil masks and lift off', *J. Vac. Sci. Technol. B* 22(1), 74–76.
- Stamm C., Marty F., Vaterlaus A., Weich V., Egger S., Maier U., Ramsperger U., Fuhrmann H. and Pescia D., (1998), 'Two-Dimensional Magnetic Particles', *Science*, 282, 449–451.
- Schallenberg T., Schumacher C., Gundel S. and Faschinger W., (2002), 'Shadow mask technology', *Thin solid films*, 412 (1-2), 24–29.
- Songmuang R., Kiravittaya S., Thainoi S., Changmuang P., Sopotpan S., Ratanathammaphan S., Sawadsaringkarn M. and Panyakeow S., (2001), 'Selective growth of InAs/GaAs self-organized quantum dots by shadow mask technique', *Journal of crystal growth*, 227–228, 1053–1056.
- Sze S.M., (1988), *VLSI Technology*, New York: McGraw-Hill.
- Tian P.F., Bulovic V., Burrows P.E., Gu G., Forrest S.R. and Zhou T.X., (1999), 'Precise, scalable shadow mask patterning of vacuum-deposited organic light-emitting devices,' *Journal of vacuum science and technology*, 17 (5), 2975–2981.

- Tixier A., Mita Y., Gouy J.P. and Fujita H., (2000), 'A silicon shadow mask for deposition on isolated areas', *J. Micromech. Microeng.*, 10, 157–162.
- van den Boogaart M.A.F., Kim G.M., Pellens R., van den Heuvel J-P. and Brugger J., (2004), 'Deep-ultraviolet-microelectromechanical systems stencils for high-throughput resistless patterning of mesoscopic structures', *Journal of Vacuum Science and Technology B*, 22(6) 3174–3177.
- van den Boogaart M.A.F., Lishchynska M., Doeswijk L.M., Greer J.C. and Brugger J., (2005), *In-situ* 'Stabilization of membranes for improved large-area and high-density nanostencil lithography'. Conference proceedings of 13<sup>th</sup> International Conference on Solid State Sensors, Actuators and Microsystems in Seoul, Korea, 5–9.
- van Rijn C.J.M., Veldhuis G.J. and Kuiper S., (1998), 'Nanosieves with microsystem technology for microfiltration applications', *Nanotechnology* (9) 343–345.
- van Rijn C.J.M., Nijdam W., Kuiper S., Veldhuis G.J., van Wolferen H. and Elwenspoek M., (1999), 'Microsieves made with laser interference lithography for micro-filtration applications', *J. Micromech. Microeng.* (9), 170–172.
- Vroegindewij F., Speets E.A., Steen J.A.J., Brugger J. and Blank D.H.A., (2004), 'Exploring microstencils for sub-micron patterning using pulsed laser deposition', accepted for publication in *Applied Physics A*.
- Xia Y. and Whitesides G.M., (1998), 'Soft Lithography', *Angew. Chem. Int. Ed.*, 37, 550–575 and the references therein.
- Zhou Y.X., Alan J.T., Hone J. and Walter S.F., (2003), 'Simple fabrication of molecular circuits by shadow mask evaporation', *Nano letters*, 3 (10), 1371–1374.

## 8.1 Introduction

Photolithography is the workhorse of the semiconductor chip manufacturing industry. It provides a rapid route to the parallel fabrication of dense arrays of electronic devices using tried-and-trusted techniques. Until comparatively recently, photolithography has been amply capable of keeping pace with the demands for decreasing device size that have followed from the relentless progress of the chip manufacturing industry along the path charted by Moore's law. However, all conventional optical techniques are subject to a lower resolution limit, known as the diffraction limit. When light is constrained to pass through an aperture smaller than approximately one half of its wavelength,  $\lambda$ , diffraction occurs. In the context of lithography, this means that unlimited reduction of feature sizes is not possible in a mask-based process: when the gaps in the mask become so small that they are equal to  $\lambda/2$  in size, the resulting structures will no longer be clearly defined because diffraction will occur. The semiconductor chip manufacturing industry has begun addressing this fundamental obstacle with great urgency, for without an adequately low-cost solution, capable of being implemented in mass manufacturing operations, current rates of improvement in microprocessor performance will slow significantly. A variety of incremental changes have been explored that would enable manufacturing to continue within the current paradigm, but, for example, with the use of shorter wavelengths to reduce the dimensions at which diffraction becomes a problem. However, there has been limited success and the drive towards ever smaller components challenges the ingenuity of engineers and far UV and X-ray lithography still present significant practical challenges. The only well-established tool for the fabrication of electronic devices with truly nanoscale dimensions is electron beam lithography. While capable of defining structures at the level of a few nm, however, it requires expensive instrumentation, vacuum operation and, moreover, is a serial fabrication technique. There are thus obstacles to its commercial application, especially in the mass-manufacturing of electronic devices.

The central focus of this chapter is not directly to solve the problems of semiconductor chip manufacturing (although some of the work described is applicable to electronic device production); indeed, much of the motivation behind it comes from interest in organising organic and biological molecules. However, the problems of device manufacturing provide a backdrop against which a variety of preconceptions about lithographic techniques have been formed. In particular, photolithography is perceived as a suitable method for mass fabrication of microstructured devices, but one that offers little by comparison with electron beam lithography when it comes to the fabrication of truly nanoscale devices. Other chapters in this volume challenge common preconceptions about lithography. For example, Chapter 3 (Soft lithography) describes simple, low-cost methods for the mass production of microstructured materials that have been pioneered with tremendous effectiveness by Whitesides and co-workers. In the present chapter, however, we are particularly concerned with the notion that electron beam lithography is the benchmark tool for nanometre scale lithography. It will be demonstrated that, unexpectedly, optical methods are capable of rivalling the performance of electron beam lithography, while also offering the capability for utilisation under ambient conditions or even under a fluid medium. These advances open up powerful new capabilities. As a result, photochemical methods may become established as true nanofabrication tools.

In biology, in particular, photochemical reactions offer some flexible and versatile methods for the placement of molecules on surfaces, and have already found widespread application at the micron scale (Blawas and Reichert, 1998). For example, light-directed chemical synthesis has provided a means by which dense arrays of oligonucleotides may be synthesised on solid substrates, base-by-base, by taking advantage of highly efficient chemistry based upon the use of photo-cleavable protecting groups (Fodor *et al.*, 1991). This type of chemistry has become the foundation of a highly successful commercial analytical system in which arrays of spots functionalised by different oligonucleotides are fabricated photolithographically and utilised in high-throughput analysis of DNA. Binding of sample DNA only occurs to spots occupied by complementary sequences, so binding at a given location in the array is positive evidence for the presence of a particular sequence in the sample DNA. Such methods have played an important role in genomics, and promise to continue to play an important role in the future, not only in genomics but also in proteomics and other areas of biology where there is a need for the rapid analysis of large samples. Miniaturisation may play an important role in their future exploitation, with miniaturised arrays offering the potential for increased sensitivity. Other approaches have been demonstrated by Delamarche *et al.* (1996), who attached IgG to benzophenone derivatised monolayers, and Yang *et al.* (2000), who functionalised carboxylic acid terminated thiols with methyl  $\alpha$ -nitropiperonyl oxycarbonyl biotin (MeNPOC-

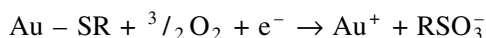
biotin), a caged biotin functionality which may be photochemically deprotected and bound to streptavidin. The ability to selectively immobilise biological molecules on nanometre length scales would be of considerable value in many areas of bioanalytical science, as well as in fundamental studies of biomolecular structure and function, where single molecule investigations by spectroscopic and mechanical (e.g. optical tweezers) methods are of growing importance.

Photochemical methods may thus present valuable and versatile routes to the immobilisation of biological molecules on very small length scales, and the techniques that we shall describe in this chapter present a starting point for this endeavour. The methods we shall review are not restricted to biological systems, however. Photochemical methods may also offer significant capability in many other areas of molecular science, including, for example, molecular electronics, where the fabrication of small structures is required. Conventional photolithography has often been claimed to be on the ropes in recent years, and yet engineers have continued to push the boundaries of its capability ever downwards towards smaller scales, taking advantage of the flexibility and simplicity of optical methods. The unconventional near-field methods that are the subject of this chapter offer the prospect of significant further advance, and suggest that photolithography will continue to have a bright future.

The choice of resist is critical in any application of photolithography. In the extreme photolithography that is our concern here, the choice of resist is of particularly acute significance. To date, self-assembled monolayers (SAMs) have yielded the best resolution in near-field photolithography (13 nm), and they are thus a particular interest in this chapter. The photochemistry of SAMs has perhaps been less well studied than other aspects of their structures and reactivity, but is flexible and versatile and is thus the starting point for our discussion. Once the underlying chemistry has been described, we will proceed to examine the use of near-field methods in more detail and illustrate their applications to a variety of systems including SAMs.

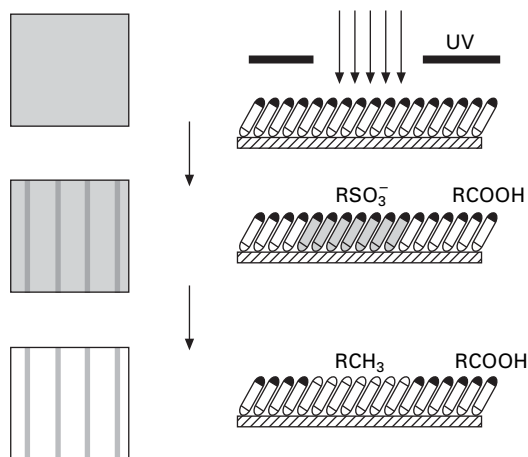
## 8.2 Photochemistry of self-assembled monolayers

SAMs formed by the adsorption of alkanethiols  $\text{HS}(\text{CH}_2)_n\text{X}$  onto gold surfaces may be photopatterned, and form a particular focus of some of the work to be described here. While the majority of interest in SAM patterning has focused on soft lithography, photopatterning offers straightforward routes to clean, well-defined surface chemistries. Li *et al.* (1992) and Tarlov and Newman (1992) first reported the oxidation of alkanethiolates to alkylsulfonates following extended exposure to the air:

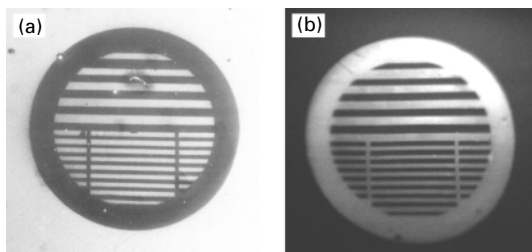


The photo-oxidation of SAMs to yield the same products was reported by Huang and Hemminger (1993), who exposed SAMs of 4-chlorothiophenol to light from a mercury lamp. The formation of the sulfonate oxidation product was verified using laser desorption mass spectrometry, which revealed a strong peak in the mass spectrum corresponding to the molecular sulfonate species) and X-ray photoelectron spectroscopy (XPS), which revealed a transformation of the sulfur oxidation state, reflected in the appearance of a peak at 5 eV higher binding energy than the main component in the S 2p region of the spectrum. Tarlov *et al.* (1993) reported similar XPS data for monolayers of hexanethiol exposed to light from a high-pressure mercury lamp. They found that unlike the adsorbates in the pristine monolayer, the sulfonate oxidation products were only weakly bound, and could be displaced, either by rinsing or by immersion in a solution of a second thiol, to generate a chemical pattern. Using imaging secondary ion mass spectrometry (SIMS), Tarlov *et al.* were able to verify that clean, well-defined patterns with good edge definition could be prepared. The process is illustrated in Fig. 8.1, where a carboxylic acid terminated thiol is photopatterned.

After immersion of the sample in a solution of a methyl-terminated thiol, a chemical pattern is formed that may be imaged using a variety of methods (Fig. 8.2). For example, scanning electron microscopy (SEM) yields dark contrast over hydrophilic regions, due to the accumulation of atmospheric contaminants in these areas, and brighter contrast over methyl terminated regions (Cooper and Leggett, 1999). Using imaging SIMS, it is possible to map the intensity of a molecular fragment characteristic of the carboxylic



8.1 Schematic diagram illustrating the photopatterning of a SAM. A carboxylic acid terminated SAM is formed and then exposed to UV light through a mask. In exposed areas, the adsorbates are oxidised to weakly bound alkylsulfonates, which are displaced by a contrasting solution-phase thiol in the final step.

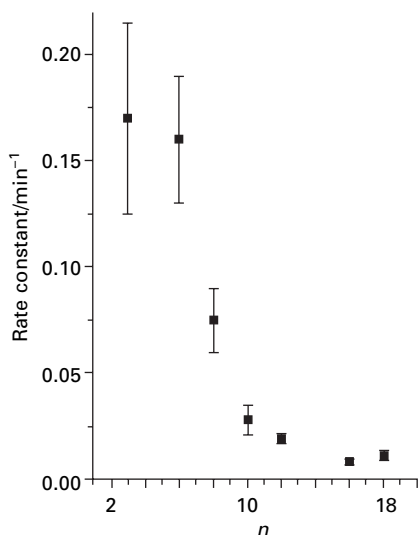


8.2 SEM (a) and SIMS (b) images of a patterned SAM. The mask used was an electron microscope grid consisting of 50 and 110 nm wide bars. The pattern in (a) consists of regions functionalised by  $\text{HS}(\text{CH}_2)_7\text{CH}_3$  (bright contrast) and  $\text{HS}(\text{CH}_2)_2\text{COOH}$  (dark), while that in (b) consists of regions functionalised by  $\text{HS}(\text{CH}_2)_{17}\text{CH}_3$  (dark contrast) and  $\text{HS}(\text{CH}_2)_2\text{COOH}$  (bright contrast, imaged using the  $\text{AuSS}(\text{CH}_2)_2\text{COO}^-$  ion). Reproduced with permission from Cooper and Leggett 1999.

acid-terminated adsorbate, yielding a more structurally specific type of characterisation. SIMS also enables the presence of contamination to be investigated. In general, photopatterned SAMs are very clean. The advantage of depositing both chemistries in a solution-phase self-assembly process is that the entire specimen exhibits well-ordered adsorbates with relatively low defect densities.

The kinetics of the photo-oxidation reaction are influenced by the structures of the adsorbate molecules and the nature of the sulfur-metal bonding. Early studies used mercury arc lamps with broad emission spectra to excite SAM photo-oxidation. Under such conditions, the mechanism of oxidation and the identity of the active species causing oxidation remained difficult to establish. However, a number of useful generalisations could be established. The first is that the rate determining step in the photo-oxidation process was penetration of oxygen species to the S-metal bond. Hutt and Leggett (1996) demonstrated that, for a series of methyl terminated alkanethiols adsorbed on gold, the rate constant for the photo-oxidation reaction decreased sharply with increasing adsorbate chain length from propanethiol to dodecanethiol, and then subsequently decreased rather more slowly with increasing chain length for longer adsorbates (Fig. 8.3). This correlated very well with knowledge of adsorbate packing in SAMs. It is thought that from around  $\text{C}_{12}$  upwards, the adsorbates form an ordered, two-dimensional crystalline structure. The most likely sites of attack for oxygen in such a structure are at domain boundaries, step edges and other discontinuities. For shorter adsorbates, chain mobility increases with decreasing length, meaning that penetration of oxygen to the Au-S bond is increasingly facile.

Similar conclusions were drawn for monolayers of thiols adsorbed on silver (Hutt *et al.*, 1998), which also exhibited pronounced chain-length



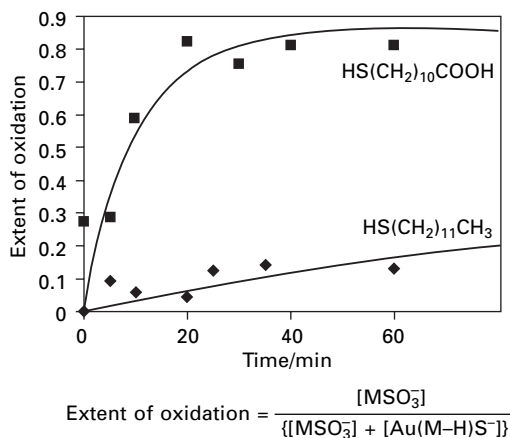
8.3 Variation in the rate constant for the photo-oxidation of alkanethiol SAMs with the number of carbon atoms in the adsorbate molecule  $n$ . Reproduced with permission from Hutt and Leggett 1996.

dependency in the rate of photo-oxidation. However, there were also differences between the two metals (Lewis *et al.*, 1995; Hutt *et al.*, 1998). In particular, on silver, a competing process may occur in which the S-C bond of the adsorbate molecule is broken, leading to the formation of, initially, inorganic silver sulfide. The terminal group of the adsorbate molecule plays a significant role in influencing the kinetics of oxidation. In studies using a mercury arc lamp, Cooper and Leggett (1998) found that for a given chain length, the rate constants for the photo-oxidation of carboxylic acid, hydroxyl and methyl terminated SAMs were in the ratio 1:2:4 respectively. The reduced rate of photo-oxidation of the polar SAMs was attributed to the existence of strong hydrogen bonding between adsorbate terminal groups (Cooper and Leggett, 1999). As will be seen below the influence of the terminal group on the photo-oxidation kinetics is complex.

The nature of the active agent causing SAM photo-oxidation was not explored systematically in any of these studies. Huang and Hemminger (1993) speculated that oxidation was initiated by hot electrons generated in the Au surface following exposure to UV photons. A variety of alternative explanations were also worthy of consideration, including the action of singlet oxygen. One of the problems in these early studies was the reliance upon mercury arc lamps as UV sources; such lamps have broad emission spectra and the emission spectrum also varies substantially depending upon the type of lamp. Zhang *et al.* (1998) and Norrod and Rowlen (1998) separately concluded that the

oxidation of SAMs on exposure to UV light was due to the action of ozone. Norrod and Rowlen exposed SAMs to ozone generated by electrical discharge. Surface enhanced Raman spectroscopy (SERS) was used to characterise the influence on the bonding of decanethiol. They observed a decline in the intensities of the bands attributed to C-C and C-S stretching modes in the SERS spectra.

While this demonstrates that SAMs may react with ozone, it does not shed any light on the mechanism of photo-oxidation, however (despite the assertion by the authors). Ferris and Rowlen (2000) attempted to make this connection in a subsequent paper. They exposed a SAM of decanethiol, sealed in an environmentally controlled cell to prevent exposure to ozone, to light from a UV lamp emitting at 254 nm for a short period of time. They observed no evidence of oxidation and concluded that this demonstrated the requirement for ozone to be present. However, the lamp used emits only weakly and the longest exposure time used was only brief. Importantly, they considered only one SAM, and did not compare adsorbates with different terminal groups. Using the same lamp, which was fitted with a filter to prevent emission of short wavelengths required to initiate ozone formation, Brewer *et al.* (2001) demonstrated, using static SIMS, that carboxylic acid terminated thiols oxidised rapidly (Fig. 8.4) and that full oxidation of methyl terminated SAMs did occur, provided adequate time was allowed for the reaction to proceed. It is thus clear that photochemical oxidation of SAMs does occur. The apparent failure of Rowlen and co-workers to observe oxidation is the consequence of using a weak light source for an inadequately lengthy



8.4 Extent of oxidation as a function of exposure time determined from SIMS data. The extent of oxidation is determined from the relative intensities of ions characteristic of the oxidation product ( $\text{MSO}_3^-$ ) and the unoxidised adsorbate ( $\text{Au}(\text{M}-\text{H})\text{S}^-$ ) in the negative ion SIMS spectrum. Reproduced with permission from Brewer *et al.*, 2001.

period of time, and also of their failure to compare adsorbates with other terminal groups. Similar criticisms may be made of the work of Bohn and co-workers (Zhang *et al.*, 1998), which also focused only on methyl terminated SAMs. Their conclusion that light with a wavelength less than 200 nm is required for SAM oxidation was refuted by the study of Brewer *et al.*

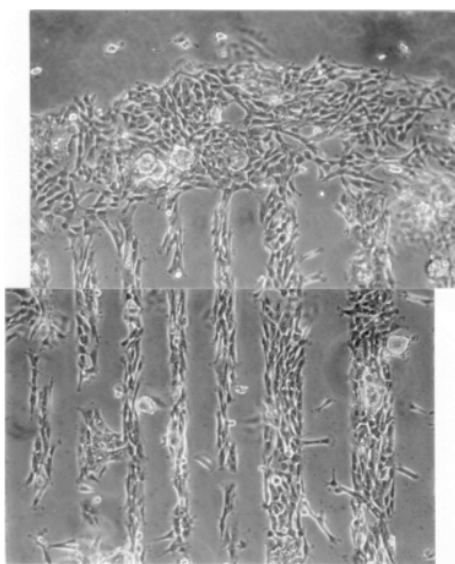
The apparent slowness of photo-oxidation using mercury arc lamps is a consequence of their broad emission spectra and their predominantly weak emission in the relevant regions of the electromagnetic spectrum. Thus, although the criticism has been made that photopatterning of SAMs is slow, it is not justified. Work in the author's laboratory has shown that using a frequency-doubled argon ion laser, emitting at 244 nm, photo-oxidation of SAMs with a variety of terminal groups occurs in a matter of seconds (Sun and Leggett, 2002b). In other words, provided an adequately intense light source with appropriate emission characteristics is used, photooxidation is very rapid. However, the observation that using 254 nm light carboxylic acid terminated adsorbates oxidise faster than methyl terminated ones (Brewer *et al.*, 2001) is perplexing. This is the reverse of the behaviour reported by Cooper and Leggett (1998) in their study using a mercury arc lamp. This problem remains to be resolved. However, it may be concluded that the photochemistry of SAMs is rich and complex.

On irradiation at 254 nm, the suggestion of Huang and Hemminger (1993) that oxidation proceeds via the creation of hot electrons seems to provide the most likely route for initiation of oxidation. On exposure to light from a broad-spectrum source such as an arc lamp, other processes may occur and, depending on the nature of the emission spectrum, these may be statistically more significant. They may include ozonolysis, which the data of Rowlen and Bohn and co-workers certainly suggest occurs, and which Poirier *et al.* (1999) also demonstrated to occur in a study by scanning tunnelling microscopy (STM). If the rate-determining step in such processes was the penetration of oxygen species to the gold-sulfur bond, as suggest by Hutt and Leggett (1996), then the carboxylic acid terminated SAMs, with their strong hydrogen bonds, would be expected to exhibit reduced rates of oxidation. At 254 nm, however, there may be an additional factor – the work function of the SAM-modified gold surface, for example. Work in the author's laboratory has indicated that at 254 nm, the chain length of the adsorbate (i.e. the packing density of the adsorbate molecules) still has a significant effect on the kinetics of oxidation, but it clearly does not provide the entire explanation. Conversely, studies using an ozone generator yield rate constants for the oxidation reaction that reflect the behaviour observed using a broad-spectrum arc lamp source (i.e. carboxylic acid terminated SAMs oxidise the slowest).

There is clearly a good deal more work required to establish fully the details of the SAM photo-oxidation mechanism. However, it may be concluded that photochemical oxidation occurs rapidly on exposure to light with a

wavelength of *c.* 250 nm, providing the basis for a simple and versatile patterning method that yields clean, well-ordered structures with good edge definition.

Photopatterned SAMs have been used in a variety of applications. Some of these depend upon the straightforward replacement of one thiol by another. For example, in the author's laboratory, simple patterned SAMs have been utilised to direct cellular attachment (Fig. 8.5). However, this is not the only route to photopatterned SAMs. The work of Yang *et al.* (2000) described above provides a clear illustration of how photochemical reactions may be used to pattern the end-group chemistry of SAMs for a biological application. Wollman *et al.* (1994) provided the earliest illustration of the use of a SAM terminating in a photoactivatable group. They prepared SAMs that terminated in an aryl azide functionality which, on exposure to UV light, was converted to a nitrene. The nitrene was reactive with primary or secondary amines, yielding 3*H*-azepine and/or hydrazine products. Wollman *et al.* used this chemistry to immobilise a variety of secondary amines including 2-ferrocenylethyl-2',2',2'-trifluoroethylamine leading to the formation of surface-confined ferrocene. In an alternative approach, the same authors used SAMs terminating in a cyclopentadienyl manganese tricarbonyl group to bind phosphine-containing ligands, which are able to displace CO under exposure

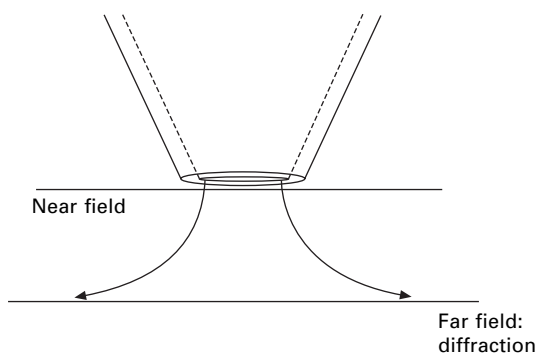


8.5 Optical micrograph showing fibroblasts attached to a photopatterned SAM consisting of carboxylic acid and methyl terminated regions. The pattern used was similar to that shown in Fig. 8.2(a). Here, fibroblasts have attached almost exclusively to carboxylic acid terminated regions of the surface. Reproduced with permission from Cooper *et al.*, 1997.

to UV light. Wolf and Fox (1995) used UV light to switch between *cis*- and *trans*-isomers of 4-cyano-4'-(10-thiodecoxy) stillbene molecules adsorbed to gold surfaces. In the *cis* conformation, the adsorbate is more hydrophobic, exhibiting a contact angle of  $60^\circ$ , while in the *trans* conformation a contact angle of  $44^\circ$  is measured, reflecting greater interaction of the polar CN group with the test liquid. Other illustrations may readily be found in the literature.

### 8.3 Near-field optics and lithography

The preceding discussion has focused on the fabrication of micropatterned structures. The diffraction limit presents a fundamental obstacle to the simplistic reduction of features fabricated using conventional photopatterning techniques, which typically involve the projection of light through apertures in a mask. Thus all of the benefits described above are of little consequence for the fabrication of nanostructures unless we can find a way around the diffraction limit. Near-field techniques present a solution to this problem. The feasibility of conducting optical measurements in the near-field was first conceived early in the 20th century by Synge (1928, 1931, 1932). Synge proposed the formation of a small aperture in an opaque screen, and then irradiating the sample through the aperture. The aperture was to be much smaller than the wavelength of the light used. If the screen was brought close enough to the sample, he argued, then the sample could be illuminated without the light passing through the aperture being able to undergo diffraction (Fig. 8.6). Synge was aware of the practical difficulties associated with the realisation of his idea, and, indeed, it was another 50 years before the feasibility of high-resolution imaging was first demonstrated. Ash and Nichols (1972) passed microwaves, with a wavelength of 3 cm, through a sub-diffraction limit aperture and were able to demonstrate a resolution of  $\lambda/60$  in studies of optical gratings. However, there were significantly greater technical challenges



8.6 By bringing a surface close to a small aperture, it is possible for light to emerge from the aperture without undergoing diffraction

associated with the use of visible light. These were eventually solved in the near-field scanning optical microscope (see below).

The simplest approach based upon near-field optics would be the use of contact masks; simply by ensuring uniform conformal contact between the mask and the surface, it should be possible to generate features very much smaller than the diffraction limit simply by shrinking the dimensions of the gaps in the mask. Simple though this sounds, it proves highly complex in reality because of the difficulty in ensuring conformal contact between a rigid mask and the resist over large enough areas to be useful (for example, small non-uniformities in either the mask or the substrate, or even nanoparticulate specks of dust, will lead to defective operation). Alternative approaches are thus required. One approach is the use of elastomeric phase masks (Aizenberg *et al.*, 1997; Rogers *et al.*, 1998). A transparent mask may be exposed to light, with the consequence that abrupt changes in the phase of the light occur at the edges of relief features formed in the mask. The consequence of this is a pronounced attenuation of the optical transmission along these edges, leading to a sharply defined local minimum in the exposure of the sample. However, there are still problems associated with the maintenance of adequate contact between mask and sample. Usually the mask must be compressed or bent in order to ensure conformality. Whitesides and co-workers have utilised elastomeric masks with great effect to deliver enhanced performance. Relief features are formed in a polydimethylsiloxane (PDMS) by casting a liquid prepolymer against a silicon master and curing, a methodology that forms the basis for soft lithography (see Chapter 3 for a more detailed description). The cured PDMS may be removed from the master and utilised either as a stamp to transfer materials onto a suitable substrate or, in the present case, as a mask. The PDMS is mechanically soft, so gentle pressure ensures conformal contact across the entire area of the stamp. Specks of dust may distort contact locally, but will not prevent contact across the vast majority of the mask surface, representing a significant advance. Irradiation of the transparent PDMS leads to phase-shifting photolithography with a resolution that may be as good as 50 nm (Aizenberg *et al.*, 1997; Rogers *et al.*, 1998).

Several variations on the theme have been reported. For example, fabrication of PDMS masks with ridges having a triangular cross-section enables the exploitation of internal reflections to optimise performance (Qin *et al.*, 1998). If the sidewalls of the ridges meet the flat face of the mask at the dihedral angle of  $54^\circ$ , then the mask selectively blocks the incident light in the regions with a sloping surface. By varying the load during compression of the mask it is possible to vary the cross-sectional area of the sloping regions of the mask, thus adjusting the dimensions of the features mask from the incident light. Another approach is to use polymer microspheres as lenses (Wu *et al.*, 2003). Microlenses with small diameters (less than  $3\ \mu\text{m}$ ) produce

well-defined micrometre-scale features in the near field under flood illumination.

However, in many circumstances where one might wish to use high-resolution photolithographic techniques, the ability to arbitrarily pattern surfaces on very small length scales would be desirable. An illustration of this would be the fabrication of an array of biological molecules organised on length scales close to the molecular dimensions. It may be desirable to initiate photochemical reactions at different locations according to a variable sequence. The methods described previously, while delivering exceptional resolution in many cases, rely upon the excitation of near-field effects in structures that are nevertheless organised on much larger length scales than the nanoscale. For many operations, scanning probe microscopy (SPM) provides a highly desirable model, and there has thus been interest in using the near-field scanning optical microscope as a tool for conducting photolithography.

#### **8.4 Near-field scanning optical microscopy**

The near-field scanning optical microscope (NSOM) was the eventual realisation of Synge's concept for the circumvention of the diffraction limit. NSOM emerged from the explosion of interest in scanning probe microscopy in the wake of the discovery of STM by Binnig and Rohrer. The key to its realisation was the utilisation of an optical fibre, drawn to a narrow aperture (*c.* 50 nm under optimal conditions) as the probe, and coated with aluminium to confine the electric field of the light within the fibre, and the integration of this with suitable feedback mechanisms for the precise control of fibre motion. This latter aspect is critical in order to ensure the aperture remains suitably close to the sample surface during imaging. Betzig and Trautman (1992) claimed a resolution of 12 nm was feasible, but only after deconvolution of the probe geometry. This spatial resolution has not generally been reproduced. Hosaka and Saiki (2001) reported a resolution of 15 nm in studies of single dye molecules, which they attributed to non-radiative energy transfer between the tip and the sample. However, generally speaking, resolution is less good. As a rule of thumb, a resolution matching the fibre internal diameter (at best 50 nm) probably reflects the best levels of performance. Transmission and reflection modes are possible. Collected light may be filtered and projected onto a sensitive detector (such as an avalanche photodiode) or an optical spectrometer.

There have been some attempts to produce microfabricated probes (Zhou *et al.*, 1999a,b). These are now commercially available, at reasonable cost. Generally, however, NSOM probes are fabricated from optical fibres which are prepared by either mechanical pulling or chemical etching followed by the evaporative deposition of an aluminium coating. Pulled probes are prepared by first heating the fibre (for example, using a CO<sub>2</sub> laser) and then pulling it

apart (Harootunian *et al.*, 1986). The probe shape depends on the temperature reached, the pulling rate and other parameters. There are some advantages to mechanical pulling (for example, the exterior of the glass fibre is smooth around the tip, leading to good adhesion of the metal coating (Hecht *et al.*, 2000)). However, unlike microfabricated NSOM probes, it is rarely possible to achieve a large cone angle with the result that the transmission coefficient for fibre probes of a given aperture size is low.

Etched probes may be prepared by immersing the fibre in a solution of HF covered with an organic overlayer. As the fibre is drawn up through the overlayer, tip formation occurs at the interface between the organic layer and the HF solution (Hoffman *et al.*, 1995). The resulting probes tend to have much higher transmission coefficients than pulled fibres. Improved results may be achieved if the polymer coating is left on the fibre during etching, a method termed 'tube etching' (Stockle *et al.*, 1999, Soh and Zenobi, 2000).

Shear-force feedback systems (Betzig *et al.*, 1992a, Toledo-Crow *et al.*, 1992) are commonly used to control the tip-sample separation. Typically, the probe is attached to a tuning fork which causes it to oscillate parallel to the plane of the surface. As the tip approaches the surface, a dramatic reduction in the oscillation amplitude is observed. Other approaches have been developed based upon cantilever systems. For example, one approach utilises a bent optical fibre which functions as a lever, while another uses a microfabricated cantilever, with an aperture at its apex, in an AFM feedback mode. However, an advantage of the tuning fork system is that no secondary light sources are required (detection of the dither motion is not optical). A concern about the high Q factors associated with tuning fork systems is that long response times are expected, meaning that scan rates are, in principle, limited. However, solutions exist to such problems. Recently, Humphris *et al.*, (2003) reported the acquisition of NSOM images at an astonishing 100 frames per second.

There are many applications of NSOM to imaging (Dunn 1999), including, for example, measurements of fluorescence (Rucker *et al.*, 1995; Betzig and Chichester, 1993; Dunn *et al.*, 1994), local Raman spectroscopy (Webster *et al.*, 1998a,b; Zeisel *et al.*, 1998) and investigations of electronic materials (McNeill *et al.*, 2000, 2001; McNeill and Barbara, 2002). The capability to operate in a fluid environment has been demonstrated (Moyer and Kämmer, 1996; De Serio *et al.*, 2003).

## 8.5 Lithography based upon near-field scanning optical microscopy

A fibre-based NSOM essentially consists of a very small light source that is rastered across a sample surface. The potential for application of NSOM to photolithography is thus clear. While NSOM lithography would be subject to the general criticism of SPM-based lithographic techniques, that it would

be a serial process, there are many circumstances that one might envisage where the ability to place molecules one-by-one on a surface, through the initiation of a photochemical coupling reaction, for example, would be desirable. Moreover, in recent years there has been a great deal of excitement about the concept of the 'Millipede', devised by researchers at IBM, in which large numbers of atomic force microscope (AFM) cantilevers, all separately actuated, are used to write nanostructures in a massively parallel process. Similar approaches have been applied to dip-pen nanolithography, (see Bullen *et al.*, 2004). The Millipede thus represents a new paradigm that places SPM lithography techniques in a new context and NSOM lithography acquires a greater significance, besides the fundamental curiosity aroused by the possibility of using light to manipulate matter on length scales beyond the diffraction limit.

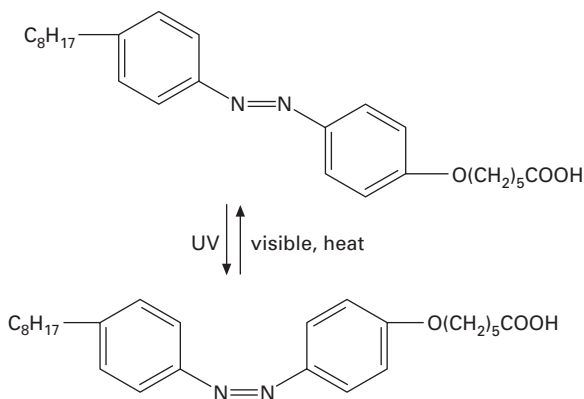
The first attempt to use NSOM as a lithographic tool was reported by Betzig *et al.*, (1992b), who used an optical fibre controlled using a shear-force modulation system to expose selectively regions of a thin film magneto-optic material. Exposure of the film to light passed through the NSOM fibre led to the formation of structures possessing a magnetisation in the opposite direction to that of the surrounding medium. The process was thought to involve localised heating of the sample, with a temperature rise to *c.* 300 °C being required to effect the transformation. The structures were imaged by NSOM, controlling the polarisation of the light from the aperture relative to a detector fitted with a polariser. Different orientations led to different contrast. Using the NSOM as a lithographic tool it was possible to fabricate features with a range of dimensions down to *c.* 60 nm. This remained the best resolution realised by NSOM for approximately a decade.

The early attempts to use NSOM for surface patterning focused on the adaptation of methods used in electronic device fabrication. Krausch and co-workers (Krausch *et al.*, 1995; Krausch and Mlynek, 1995) used an NSOM to expose a standard, multi-purpose photoresist (Hoechst Novolack AZ 6612) to 454 nm light. The resist was diluted in 1-methoxy-2-propyl acetate and thin films (thicknesses in the range 20–50 nm) were spun-cast onto polished silicon wafers. The resist films were annealed to remove traces of residual solvent. A photosensitive complex was incorporated into the resist to render it insoluble in basic solutions. Exposure of the complex to light and water renders it soluble in basic solutions, enabling removal of exposed regions of the film. The samples were developed following exposure to light from a reflection-mode NSOM (i.e. one in which the optical fibre acts both as the source of light and the means of collecting the signal) and imaged by AFM. The features formed in the photoresist represented a mechanical replica of the intensity distribution in the optical near field of the tip. It was found that the features were best fitted with a Gaussian intensity distribution with a width of approximately 100 nm, and a height of *c.* 15 nm. A grating was

fabricated with a period of 164 nm and a linewidth of 82 nm. This represents a performance on the order of  $\lambda/5.5$ , significantly beyond the diffraction limit. A similar response was adopted by Smolyaninov *et al.*, (1995) who also used an NSOM to expose a commercial photoresist, achieving a linewidth of *c.* 100 nm. Clearly the thickness of the resist layer is critical in determining the dimensions of the features created; because of the divergence of the electric field beneath the NSOM aperture (Novotny *et al.*, 1995), the widths of the lines of a grating fabricated this way would increase as the thickness of the resist increased.

It was realised early that the thickness of the resist layer had a strong influence upon the resolutions achievable in lithographic applications of NSOM. Several authors have explored means for restricting the thickness of the resist layer while utilising an NSOM to undertake lithography. For example, Fujihara and co-workers prepared Langmuir-Blodgett films of a photochromic material containing 4-octyl-4'-(5-carboxypentamethyleneoxy)azobenzene. On exposure to UV light ( $\lambda = 350$  nm) this molecule undergoes a *cis-trans* conformational change (Fig. 8.7). The change is reversible on application of heat or exposure to visible light. A resolution of 130 nm was achieved (Jiang *et al.*, 1994; Fujihara *et al.*, 1995). Fujihara *et al.* also explored the use of chloromethylphenyltrimethoxysilane monolayers formed on the native oxide of a silicon wafer for surface modification by near-field methods. On exposure to UV light, they predicted that cleavage of Si-C bonds would occur to yield a surface pattern. Although the features reported were not especially small, the concept was important because a monolayer effectively represents an extremely thin resist layer.

Zenobi and co-workers have examined the ablation of dye molecules and other crystalline organic molecules from surfaces (Zeisel *et al.*, 1996). Anthracene was ablated with a spatial resolution of only 70 nm (Zeisel *et al.*,

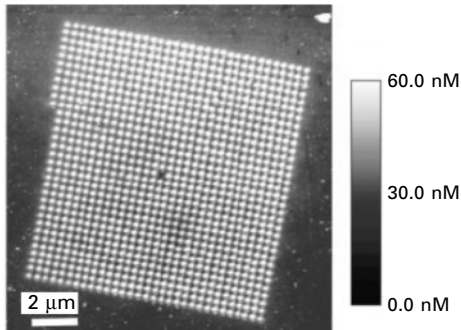


8.7 4-octyl-4'-(5-carboxypentamethyleneoxy)azobenzene undergoes a *cis-trans* conformational change on exposure to UV light.

1996), attributed to a thermal desorption mechanism. Stockle *et al.*, (2001) were able to build upon these advances by carrying out laser ablation mass spectrometry with a spatial resolution of only 200 nm. Thermal modification of materials have been reported by other workers in studies of inorganic materials. Hosaka and co-workers (Imura *et al.*, 1996; Hosaka *et al.*, 1997) have patterned GeSbTe films with NSOM-based methods, yielding features as small as 80 nm, and attributed the lithographic process to localised heating.

Several groups have used NSOM to pattern conjugated polymers. These approaches rely upon the selective photo-oxidation of regions of the sample. Wei *et al.* used thin films of poly(3,4-diphenyl-2,5-thienylene vinylene). Exposure to UV light in the presence of air leads to the oxidation of  $\pi$  bonds to yield carbonyl groups. Oxidative chemistry was also exploited by Buratto and co-workers in detailed studies of poly(2-methoxy, 5-(2'-ethyl hexyloxy)-*p*-phenylene vinylene) (MEH-PPV) films (DeAro *et al.*, 1999, Credo *et al.*, 2000). Exposure of the films to 514 nm light from a fibre-based NSOM system resulted in the local modification of both the polymer topography (a depression results in oxidised regions) and its emission spectrum. The film modification was attributed to a combination of photo-oxidation and localised heating. A line width of 100 nm was reported. Significantly, however, Credo *et al.* (2000) studied the time-dependence of the diameters of features produced using a stationary probe, and reported that the long-time diameter of the oxidised region was significantly larger than the tip diameter. This was attributed to energy migration. Similar behaviour was observed in studies of films of *tris*-8-hydroxyquinoline aluminium and dye-functionalised polyelectrolyte self-assembled layers. These observations provide an explanation for the generally disappointing performance of NSOM-based approaches in these and other studies; the transport of energy through the resist layer, which has a significant thickness on such small length scales, may play a critical role in determining the dimensions of the features that result. The diffuse morphology observed in these and other studies reflects the problems associated with energy transfer in the film.

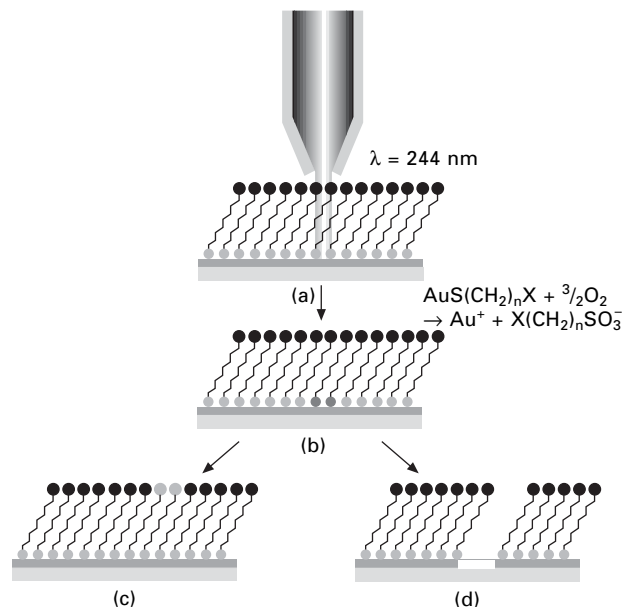
A slightly different approach has been adopted by Riehn *et al.* (2003). They fabricated structures in a film of poly(*p*-phenylene vinylene) (PPV) using an NSOM, including the periodic two-dimensional photonic crystal shown in Fig. 8.8. They found that feature sizes were somewhat larger (*c.* 160 nm) than the aperture in the NSOM probe. Using the Bethe Bouwkamp model, they simulated the near-field illumination intensity. They found that the field intensity was sharply confined within the PPV layer but decreased approximately exponentially outside of the area beneath the aperture. They suggested that if the film thickness is smaller than the aperture radius, the feature size is limited by the aperture size and the tip-sample distance. In their studies, Riehn *et al.* concluded that heating of the sample did contribute significantly to the phenomena observed.



8.8 A tapping mode AFM image of a two-dimensional photonic crystal composed of PPV pillars that are 32 nm tall, have a full width at half maximum height of 200 nm and a pitch of 333 nm. Reproduced with permission from Riehn *et al.*, 2003.

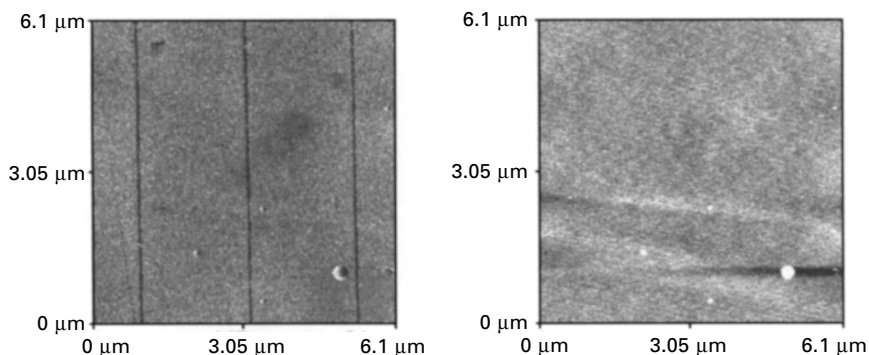
In view of the importance of the resist layer in determining the resolution of near-field photolithographic techniques, self-assembled monolayers represent an extremely attractive system. The hypothesis that ozone was the active agent in SAM photo-oxidation was in principle problematic, because gaseous diffusion of reactive species would be poorly spatially confined. However, the demonstration that photo-oxidation occurs in the absence of ozone, probably via oxidation of thiol sulfur atoms initiated by hot-electron emission, means that the lithographic process may be very effectively contained – in fact, it may be confined to a monatomic layer of sulfur atoms at the monolayer-gold interface. The limited length of the alkyl chains (1–2 nm) and the uniformity of coverage of the adsorbate molecules in SAMs mean that they constitute an idealised resist. Not only should the lithographic process be confined to a region that is of monatomic thickness, but a very close approach of the NSOM aperture to the surface should also be permitted.

Sun *et al.* explored the use of an NSOM to pattern alkanethiol SAMs, coupling a frequency doubled argon ion laser (244 nm) to the NSOM via fused silica fibres. They termed this approach scanning near-field photolithography (SNP). The process is illustrated schematically in Fig. 8.9. They found that exceptionally good spatial resolution could be achieved. Routinely, it proved possible to fabricate features with widths of 30–40 nm. Figure 8.10 provides an illustration. A carboxylic acid terminated monolayer has been formed and three lines traced across the sample using the NSOM source. Where the sample was exposed to UV light, adsorbate molecules were photo-oxidised to yield weakly bound alkylsulfonates. On immersion of the sample in a solution of a methyl terminated thiol, the sulfonate species were displaced. The methyl terminated thiols adsorbed onto the exposed regions of the sample, forming a chemical pattern. A topographical AFM image of the sample reveals no contrast, because the adsorbates have equal



**8.9** A schematic diagram illustrating the application of scanning near-field photolithography. A sample is exposed to UV light from an NSOM, leading to local oxidation and either replacement of the oxidation products by a contrasting thiol, or etching of the gold underlying the oxidised regions. Reproduced with permission from Sun and Leggett 2002a.

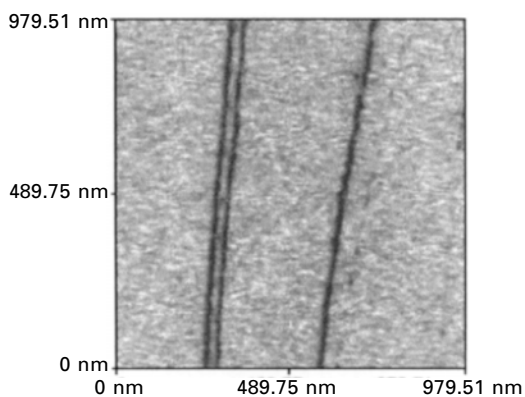
lengths. A friction force microscopy image reveals the formation of a pattern, however, because regions of the surface occupied by adsorbates with different terminal groups exhibit differential contrast. Regions occupied by carboxylic acid terminated adsorbates exhibit bright contrast because they interact strongly with the polar surface of the silicon nitride AFM probe, while methyl terminated



**8.10** Friction force (left) and topographical (right) AFM images of lines of methyl terminated thiols written into a carboxylic acid terminated SAM using SNP. Sun *et al.*, 2002.

adsorbates exhibit dark contrast because they interact more weakly. There is clear contrast between the acid and methyl terminated regions of the surface.

A priori, one might have expected that the spatial resolution achievable using this approach would be limited by the diameter of the aperture in the NSOM fibre. At best this is found to be around 50 nm; the fabrication of smaller apertures is rather challenging and, moreover, they would be expected to exhibit much diminished transmission, rendering them increasingly ineffectual as the diameter decreased below 50 nm. Routinely, and comparatively easily, however, we have found that it is possible to fabricate features significantly smaller than the diameter of the aperture. Figure 8.11 shows three lines of hexadecanethiol written into a monolayer of 3-mercaptopropanoic acid by SNP (Sun and Leggett, 2004a). These lines are only 20 nm full width at half maximum height (FWHM), rivalling the performance of electron beam lithography. The smallest feature we have fabricated to date was only 13 nm FWHM, or  $\lambda/20$  – significantly beyond the diffraction limit. This is a significant length scale, because it corresponds to the dimensions of many protein molecules. It suggests the possibility of being able to use SNP to control the location of single protein molecules under optimal conditions. But what explanation might there be for the formation of such small features? The line width appears to be unconnected with the rate of photo-oxidation (i.e. it does not take longer to write a narrow line than a broad one). It may thus be concluded that this exceptional performance is not the consequence of an unusually small aperture. In support of this, it is possible to obtain an estimate of the aperture size by exposing the sample beneath a stationary probe. Using our experimental configuration, there appears to be little tendency for feature sizes to broaden on extended exposure. Spots formed by stationary illumination exhibit diameters  $\geq 50$  nm, again suggesting

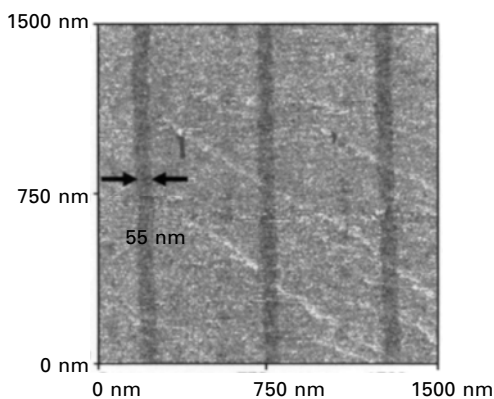


8.11 Matching the performance of electron beam lithography by photochemical means. Lines of methyl terminated thiol only 20 nm wide written into an acid terminated SAM by SNP. Sun and Leggett 2004a.

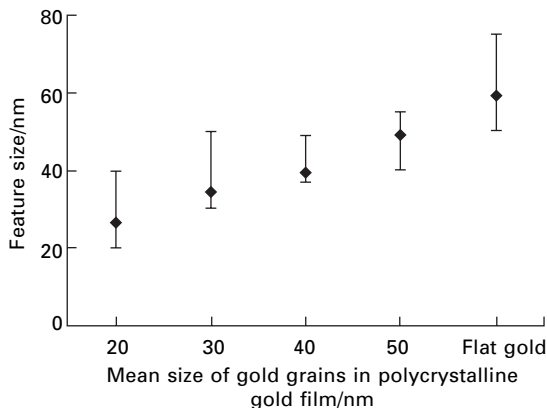
that the best resolution is not simply the result of an unusually small aperture. An alternative explanation is required, therefore.

It was observed that there was a correlation between the line width obtained and the morphology of the underlying substrate. The SAMs used were predominantly formed on polycrystalline gold films. These exhibit a mean grain size (50–80 nm) that is comparable to the aperture diameter. The grain size was also typically similar to the dimensions of an atomic force microscope tip such as might be used to carry out apertureless NSOM. Theoretical work by Novotny *et al.* (1995) indicated that exposure of a metallic asperity to illumination may lead to the excitation of a surface plasmon with a significant near-field enhancement of the electric field. The electric field associated with the plasmon was found to be highly confined. This confinement of the field provides the theoretical foundation for apertureless NSOM. It was hypothesised (Sun and Leggett, 2004a) that in the case of exposure of polycrystalline gold to light from a fibre-based NSOM, a similar effect was occurring but with the sample providing the asperities that focused the electric field. Light from the fibre irradiated the grains in the gold film, which interacted non-radiatively with the fibre leading to a confined electric field. A criticism of this hypothesis is that the wavelength used in these studies was some way from the maximum of the gold plasmon absorption. However, the optical properties of gold are strongly dependent upon its morphology (for example, for gold nanoparticles, the positions of plasmon bands are dependent upon particle size) and, moreover, it is possible that absorption off-maximum may still be significant in certain circumstances. Experimental evidence in support of this hypothesis is shown in Figs 8.12 and 8.13.

When an atomically flat gold substrate was used (Fig. 8.12), it was found that the best resolution was similar to the diameter of the NSOM aperture.



8.12 Lines of methyl terminated adsorbates fabricated in a carboxylic acid terminated SAM formed on an atomically flat gold substrate. Reproduced with permission from Sun and Leggett 2004a.



8.13 The variation in linewidth as a function of the grain size of the underlying gold film in SNP. Reproduced with permission from Sun and Leggett 2004a.

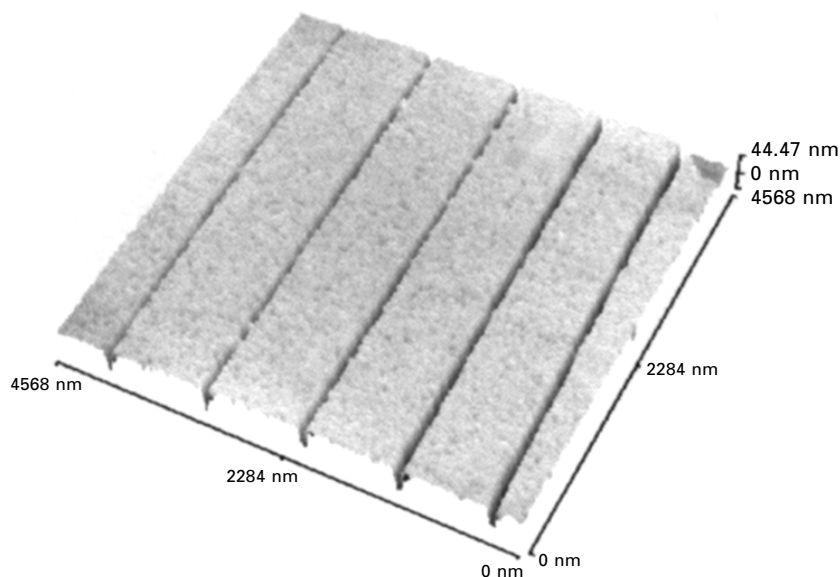
This is exactly what one might have expected for a flat surface in the absence of other effects. Moreover, the linewidth was found to be correlated with the grain size on polycrystalline films (Fig. 8.13).

Although it may be thought that this explanation suggests a restricted field of application for SNP, this is not the case. The confinement of the electric near-field due to such non-radiative interactions is not restricted to gold. Moreover, a broad variety of molecular systems may be envisaged that meet our additional criterion for SNP, that a specific photochemical reaction be excited in a functional group distributed with monolayer coverage on a solid surface. There thus seems to be significant scope for the widespread application of SNP given proper design of the experimental system. Recently it was demonstrated in the author's laboratory that SNP could be utilised to selectively alkylate hydrogen passivated silicon surfaces by exposing them to UV light from an NSOM fibre submerged beneath a layer of liquid alkene (Sun and Leggett, 2004b). UV light initiates reaction between an Si-H bond and the double bond of an alkene molecule. Significantly, this additionally demonstrates that SNP may be carried out under a fluid medium. In the context of the fabrication of biological nanostructures, this is an important result. Not only are biological molecules susceptible to denaturation following drying, but fluid-phase nanolithography offers the possibility of integrating SNP with apparatus for delivering multiple reagents, in a specific sequence, facilitating the fabrication of multiple-component nanostructures. For many biological applications of nanofabrication, it is desirable to be able to fabricate extensive arrays that contain multiple, arbitrarily positioned components. There are few techniques capable of offering such potential.

Nanostructured SAMs formed by SNP may be utilised in a variety of different ways. For example, if the sample is immersed in a solution of a

solution-phase etchant for the underlying substrate in the final step, instead of a contrasting thiol solution, then the gold may be removed to yield nanoscale trenches. In regions where the adsorbate remains intact, the surface is masked and protected from the etchant. The trenches shown in Fig. 8.14 were etched using an aqueous ferri/ferro cyanide reagent (Xia *et al.*, 1995), and the AFM data indicate a width of *c.* 50 nm and a depth of 30 nm (the thickness of the film). Because of the finite size of the tip these dimensions may not be accurate, but the data certainly confirm the efficacy of the approach. Other uses of SAMs patterned by SNP have relied upon the creation of regions with contrasting chemical functionality. For example, aldehyde-functionalised polymer nanoparticles have been attached to amine-terminated regions in carboxylic acid terminated SAMs. Proteins may also be patterned using SNP. In protein patterning on any length scale, the most difficult problem is the prevention of non-specific adsorption, because proteins tend to adhere strongly to most surfaces. On the nanometre scale, any such problems are accentuated. Compared to a region of several  $\mu\text{m}^2$ , a few non-specifically adsorbed protein molecules may be missed; compared to a feature of comparable size to a protein molecule, they will be much more problematic.

One particularly significant contribution to the field of protein adsorption has been the use of oligo(ethylene glycol) (OEG) terminated thiols to resist protein adsorption (Sigal *et al.*, 1998). These are so effective in reducing



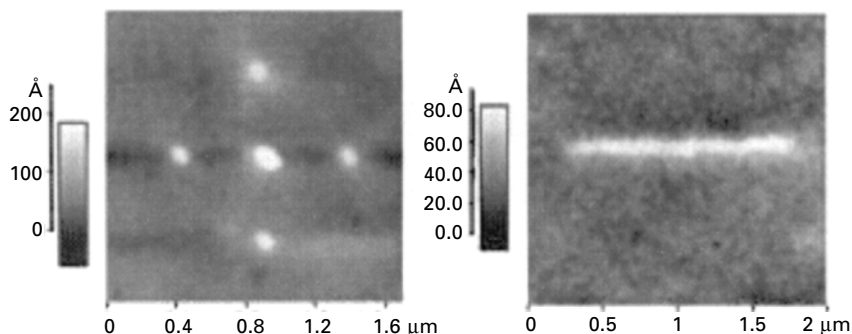
8.14 Trenches etched into a gold film using an SNP-patterned SAM as a resist. Reproduced with permission from Sun and Leggett 2002a.

non-specific adsorption that it becomes insignificant even on molecular length scales. Using SNP, regions in an OEG terminated SAM may be selectively oxidised and replaced either with an adsorbate that does not resist protein adsorption, leading to localised adsorption on transfer to the biological medium, or with an adsorbate to which proteins may be covalently attached. One approach adopted in the author's laboratory is to introduce carboxylic acid terminated adsorbates into regions of an OEG-terminated SAM and then attach IgG using well-established carbodiimide coupling chemistry originally established for use on larger length scales (Patel *et al.*, 1997). In conjunction with SNP, this approach yields protein features with linewidths smaller than 100 nm.

## 8.6 Towards the future: apertureless NSOM

For many years near-field scanning optical microscopy (NSOM) promised to take optical measurement to new levels of spatial resolution, but proved frustratingly incapable of fulfilling its promise. Recently, advances in NSOM, particularly in the area of apertureless NSOM, have reawakened interest in optical measurement beyond the diffraction limit (Frey *et al.*, 2002; Bouhelier *et al.*, 2003a; Diziain *et al.*, 2003). Particularly elegant illustrations of the power of near-field techniques come in the work of Novotny and co-workers, who have recently published astonishing Raman microscopy data from studies of carbon nanotubes, with a resolution of 25 nm (Hartschuh *et al.*, 2003a,b). A number of other groups are active in this field and there is growing evidence that resolution approaching molecular dimensions is feasible using a range of methods including Raman microscopy, fluorescence microscopy and others based on resonant energy transfer between a tip and a sample. Optics appears not to end at the diffraction limit after all. Apertureless methods offer an important avenue for the future exploitation of SNP. Recently, Royer and co-workers have provided intriguing evidence for the superior capabilities of apertureless techniques in lithographic applications. Their motivation was to use photosensitive films as a means of observing the field enhancement beneath an apertureless NSOM probe (Wurtz *et al.*, 2000, H'dhili *et al.*, 2001).

Using azobenzene films spin-coated onto glass with a thickness estimated to be 200 nm, they were able to write lines with a width of *c* 50 nm and dots as small as 30 nm (Fig. 8.15; Bachelot *et al.*, 2003). These are important data, because undoubtedly these samples were subject to the limitations of the resist films employed in previous studies using aperture-based methods. In the apertureless mode, however, the resolution is significantly improved and approaches the performance achieved for SAMs. Extrapolating from this behaviour to the better-optimised SAM system, it may be predicted that significant improvements may be feasible using apertureless approaches.



8.15 Examples of patterns written into azobenzene-containing polymer films using apertureless NSOM. Reproduced with permission from Bachelot *et al.*, 2003.

Moreover, it is significant to note that the thiol-on-gold photochemistry is probably far from optimal. In work conducted to date, there has been no attempt to optimise the optical absorption of the adsorbate molecules (for example, through the incorporation of suitable chromophores). It thus appears that there is a good deal of room for improvement on the initial data we have published.

A drawback associated with apertureless methods is the associated far-field exposure, which may lead to complications in lithographic operation. However, there is again a great deal of scope for optimisation. It is becoming clear that sophisticated optical measurements may be feasible using apertureless probes. For example, Bouhelier *et al.* (2003b) have shown that near-field second harmonic generation is possible. One route of potential value in lithographic applications is the use of multi-photon processes (Sauchez *et al.* (1999). Exposure of the tip-sample combination to light from a pulsed laser system would give rise to far-field exposure to photons with a wavelength unsuitable for initiation of photochemistry, while absorption of two photons in the near-field region leads to a strongly enhanced reactivity and a more favourable ratio between rates of reaction under the tip and elsewhere on the sample – especially if a reaction may be selected that has a threshold exposure. The feasibility of such approaches has been demonstrated by Yin *et al.* (2002) who fabricated features with widths of *c.* 70 nm in a photoresist film.

In conclusion, it may be seen that near-field lithographic methods based upon NSOM are beginning to bear real fruit. For appropriate resist materials and chemistries, a resolution rivalling that of electron beam lithography is possible, but without the requirement for operation in vacuum and at significantly lower cost. Feature sizes approaching the dimensions of single biological molecules have been demonstrated for SAMs, offering the possibility, when combined with fluid operation, for the rapid fabrication of complex,

multi-component arrays. These capabilities are very powerful. Given the synthetic utility of photochemical methods, and the scope for further enhancement of performance through the use of apertureless techniques and enhanced photochemistries, it seems that scanning near-field photolithography has the potential to make important and unique contributions to molecular nanotechnology.

## 8.7 Acknowledgement

The author is grateful to the RSC Analytical Chemistry Trust Fund and the EPSRC for financial support.

## 8.8 References

- Aizenberg J., Rogers J.A., Paul K.E. and Whitesides G.M., (1997), "Imaging the irradiance distribution in the optical near field", *Appl. Phys. Lett.* 71, 3773–3775.
- Ash E.A. and Nicholls G., (1972), "Super-resolution aperture scanning microscope", *Nature* 237, 510–512.
- Bachelot R., H'dhili F., Barchiesi D., Lerondel G., Fikri R. and Royer P., (2003), "Apertureless near-field optical microscopy: a study of the local tip field enhancement using photosensitive azobenzene-containing films", *J. Appl. Phys.* 94, 2060–2072.
- Betzig E. and Chichester R.J., (1993), "Single molecules observed by near-field scanning optical microscopy", *Science* 262, 1422–1425.
- Betzig E. and Trautman J.K., (1992), "Near-field optics: microscopy, spectroscopy and surface modification beyond the diffraction limit", *Science* 257, 189–195.
- Betzig E., Finn P.L. and Weinder J.S., (1992a) "Combined shear force and near-field scanning optical microscopy", *Appl. Phys. Lett.* 60, 2484–2486.
- Betzig E., Trautman J.K., Wolfe R., Gyorgy E.M., Finn P.L., Kryder M.H. and Chang C.H., (1992b), "Near-field magneto-optics and high density data storage", *Appl. Phys. Lett.* 61, 142–144.
- Blawas A.S. and Reichert W.M., (1998), 'Protein patterning', *Biomaterials* 19, 595–609.
- Bouhelier A., Renger J., Beversluis M.R. and Novotny L., (2003a), "Plasmon-coupled tip-enhanced near-field optical microscopy", *J. Microsc.* 210, 220–224.
- Bouhelier A., Beversluis M., Hartschuh A. and Novotny L., (2003b), "Near-field second-harmonic generation induced by local field enhancement", *Phys. Rev. Lett.* 90, 013903.
- Brewer N.J., Rawsterne R.E., Kothari S. and Leggett G.J., (2001), "Oxidation of self-assembled monolayers by UV light with a wavelength of 254 nm", *J. Am. Chem. Soc.* 123, 4089–4090.
- Bullen D., Chung S-W., Wang X., Zou J., Mirkin C.A. and Liu C., (2004), "Parallel dipen nanolithography with arrays of individually addressable cantilevers", *Appl. Phys. Lett.* 84, 789–791.
- Cooper E. and Leggett G.J., (1998), "Static SIMS Studies of Self-assembled Monolayers: the Influence of Adsorbate Chain Length and Terminal Functional Group on Rates of Photo- Oxidation of Alkylthiols on Gold", *Langmuir* 14, 4795–4801.
- Cooper E. and Leggett G.J., (1999), "Influence of Tail-group Hydrogen Bonding on the Stabilities of Self-assembled Monolayers of Alkylthiols on Gold", *Langmuir* 15, 1024–1032.

- Cooper E., Wiggs R., Hutt D.A., Parker L., Leggett G.J. and Parker T.L., (1997), "Rates of attachment of fibroblasts to self-assembled monolayers formed by the adsorption of alkylthiols onto gold surfaces", *J. Mater. Chem.* 7, 435–441.
- Credo G.M., Lowman G.M., deAro J.A., Carson P.J., Winn D.L. and Buratto S.K., (2000), "Probing nanoscale photo-oxidation in organic films using spatial hole burning scanning optical microscopy", *J. Chem. Phys.* 112, 7864–7872.
- DeAro J.A., Gupta R., Heeger A.J. and Buratto S.K., (1999), "Nanoscale oxidative patterning and manipulation of conjugated polymer thin films", *Synth. Met.* 102, 865–868.
- Delemarche E., Sundarababu G., Biebuych H., Michel B., Gerber Ch., Sigrist H., Wolf H., Ringsdorf H., Xanthopoulos N. and Mathieu H.J., "Immobilization of antibodies on a photoactive self-assembled monolayer on gold", *Langmuir* 12, 1997–2006.
- De Serio M., Bader A.N., Heule M., Zenobi R. and Deckert V., (2003), 'A near-field optical method for probing liquid-liquid interfaces', *Chem. Phys. Lett.* 380, 47–53.
- Diziain S., Adam P.M., Bijeon J.L., Lamy de la Chapelle M. and Royer P., (2003), "Development of an apertureless near-field optical microscope for fluorescence imaging and spectroscopy", *Synth. Met.* 139, 557–560.
- Dunn R.C., (1999), "Near-field scanning optical microscopy", *Chem. Rev.* 99, 2891–2927.
- Dunn R.C., Holton G.R., Mets L. and Xie X.S., (1994), "Near-field fluorescence imaging and fluorescence lifetime measurement of light-harvesting complexes in intact photosynthetic membranes", *J. Phys. Chem.* 98, 3094–3098.
- Ferris M.M. and Rowlen K.L., (2000), "Direct evidence of ozone as the active oxidant in 'photooxidation' of alkanethiols on SERS-active silver", *Appl. Spectrosc.* 54, 664–668.
- Fodor S.P.A., Read J.L., Pirrung M.C., Stryer L., Liu A.T. and Solas D., (1991), "Light-directed, spatially addressable parallel chemical synthesis", *Science* 251, 767–773.
- Frey H.G., Keilmann F., Kriele A. and Guckenberger R., (2002), "Enhancing the resolution of scanning near-field optical microscopy by a metal tip grown on an aperture probe", *Appl. Phys. Lett.* 81, 5030–5032.
- Fujihara M., Monobe H., Muramatsu H. and Ataka T., "Near-field optical microscopic recording on Langmuir-Blodgett (LB) films and chemically modified surfaces", *Ultramicrosc.* 57, 176–179.
- Harootunian A., Betzig E., Isaacson M.S. and Lewis A., (1986), "Super-resolution fluorescence near-field scanning optical microscopy", *Appl. Phys. Lett.* 49, 674–676.
- Hartschuh A., Sánchez E.J., Xie X.S. and Novotny L. (2003a), "High-resolution near-field Raman microscopy of single-walled carbon nanotubes", *Phys. Rev. Lett.* 90, 095503.
- Hartschuh A., Pedrosa H.N., Novotny L. and Krauss T.D., (2003b), "Simultaneous fluorescence and Raman scattering from single carbon nanotubes", *Science* 301, 1354–1356.
- H'dhili F., Bachelot R., Lerondel G., Barchiesi D. and Royer P., (2001), "Near-field optics: direct observation of the field enhancement below an apertureless probe using a photosensitive polymer", *Appl. Phys. Lett.* 79, 4019–4021.
- Hecht B., Sick B., Wild U.P., Deckert V., Zenobi R., Martin O.F. and Pohl D.W., (2000), "Scanning near-field optical microscopy with aperture probes: fundamentals and applications", *J. Chem. Phys.* 112, 7761–7773.
- Hoffman P., Dutoit B. and Salthé R-P., (1995), "Comparison of mechanically drawn and protection layer chemically etched optical fiber tips", *Ultramicrosc.* 61, 165–170.

- Hosaka N. and Saiki T., (2001), "Near-field fluorescence imaging of single molecules with a resolution in the range of 10 nm", *J. Microsc.* 202, 362–364.
- Hosaka S., Kikukawa A., Koyanagi H., Shintani T., Miyamoto M., Nakamura K. and Etoh K., (1997), 'SPM-based data storage for ultrahigh density recording', *Nanotechnol* 8, A58-A62.
- Huang J. and Hemminger J.C., (1993), "Photooxidation of thiols in self-assembled monolayers on gold", *J. Am. Chem. Soc.* 115, 2243–3343.
- Humphris A.D.L., Hobbs J.K. and Miles M.J., (2003), "Ultrahigh-speed scanning near-field optical microscopy capable of over 100 frames per second", *Appl. Phys. Lett.* 83, 6–8.
- Hutt D.A. and Leggett G.J., (1996), "Dependence of Rates of Photo-oxidation of Self-assembled Monolayers on Adsorbate Alkyl Chain Length", *J. Phys. Chem.* 100, 6657–6662.
- Hutt D.A., Cooper E. and Leggett G.J., "Structure and Mechanism of Photo-oxidation of Self-assembled Monolayers of Alkylthiols on Silver studied by XPS and Static SIMS", *J. Phys. Chem. B* 102, 174–184.
- Imura R., Shintani T., Nakamura K. and Hosaka S., (1996), "Nanoscale modification of phase change materials with near-field light", *Microelectron Eng.* 30, 387–390.
- Jiang S., Ichihashi J., Monobe H., Fujihara M. and Ohtsu M., (1994), "Highly localised photochemical processes in LB films of photochromic material by using a photon scanning tunnelling microscope", *Optics. Comm.* 106, 173–177.
- Krausch G. and Mlynek J., (1995), "Surface modification in the optical near field", *Microelectron Eng.* 32, 219–228.
- Krausch G., Wegscheider S., Kirsch A., Bielefeldt H., Meiners J.C. and Mlynek J., (1995), "Near field microscopy and lithography with uncoated fibre tips: a comparison", *Optics Comm.* 119, 283–288.
- Lewis M., Tarlov M.J. and Carron K., (1995), "Study of the photooxidation process of self-assembled alkanethiol monolayers", *J. Am. Chem. Soc.* 117, 9574–9575.
- Li Y., Huang J., McIver R.T. and Hemminger J.C., (1992), "Characterization of thiol self-assembled films by laser desorption Fourier transform mass spectrometry", *J. Am. Chem. Soc.* 114, 2428–2432.
- McNeill J.D. and Barbara P.F., (2002), "NSOM investigation of carrier generation, recombination and drift in a conjugated polymer", *J. Phys. Chem. B.* 106, 4632–4639.
- McNeill J.D., O'Connor D.B. and Barbara P.F., (2000), "Imaging organic device function with near-field scanning optical microscopy", *J. Chem. Phys.* 112, 7811–7821.
- McNeill J.D., O'Connor D.B., Adams D.M., Barbara P.F. and Kämmer S.B., (2001), "Field-induced photoluminescence modulation of MEH-PPV under near-field optical excitation", *J. Phys. Chem. B* 105, 76–82.
- Moyer P.J. and Kämmer S.B., (1996), "High-resolution imaging using near-field scanning optical microscopy and shear force feedback in water", *Appl. Phys. Lett.* 68, 3380–3382.
- Norrod K.L. and Rowlen K.L., (1998), "Ozone-induced oxidation of self-assembled decanethiol: contributing mechanism for 'photooxidation'", *J. Am. Chem. Soc.* 120, 2656–2657.
- Novotny L., Pohl D.W. and Hecht B., (1995), "Light confinement in scanning near-field optical microscopy", *Ultramicrosc.* 61, 1–9.
- Patel N., Davies M.C., Hartshorne M., Heaton R.J., Roberts C.J., Tandler S.J.B. and Williams P.M., (1997), "Immobilization of protein molecules onto homogeneous and mixed carboxylate-terminated self-assembled monolayers", *Langmuir*: 13, 6485–6490.

- Poirier G.E., Herne T.M., Miller C.C. and Tarlov M.J., (1999) "Molecular-scale characterization of the reaction of ozone with decanethiol monolayers on Au(111)", *J. Am. Chem. Soc.* 121, 9703–9711.
- Qin D., Black A.J. and Whitesides G.M., (1998), "Photolithography with transparent reflective photomasks", *J. Vac. Sci. Technol. B.* 16, 98–103.
- Riehn R., Charas A., Morgado J. and Cacialli F., (2003), "Near-field optical lithography of a conjugated polymer", *Appl. Phys. Lett.* 82, 526–528.
- Rogers J.A., Paul K.E., Jackman R.J. and Whitesides G.M., (1998), "Generating ~90 nanometer features using near-field contact-mode photolithography with an elastomeric phase mask", *J. Vac. Sci. Technol. B.* 16, 59–68.
- Rucker M., Vanoppen P., De Schryver F.C., Ter Horst J.J., Hotta J. and Masahura H. (1995), 'Fluorescence mapping and photobleaching of dye-labelled latex particles dispersed in poly(vinyl alcohol) matrices with a near-field optical microscope', *Macromol* 28, 7530–7535.
- Sánchez E.J., Novotny L. and Xie X.S., (1999), "Near-field fluorescence microscopy based on two-photon excitation with metal tips", *Phys. Rev. Lett.* 82, 4014–4017.
- Sigal G.B., Mrksich M. and Whitesides G.M., (1998), "Effect of surface wettability on the adsorption of proteins and detergents", *J. Am. Chem. Soc.* 120, 3464–3473.
- Soh Y.D. and Zenobi R., (2000), "Improved probes for scanning near-field optical microscopy", *Adv. Mater.* 12, 1139–1142.
- Smolyaninov I., Mazzoni D.L. and Davis C.C., (1995), "Near-field direct-write ultraviolet photolithography and shear-force microscopy studies of the lithographic process", *Appl. Phys. Lett.* 67, 3859–3861.
- Stockle R., Fokas C., Deckert V., Zenobi R., Sick B., Hecht B. and Wild U.P., (1999), "High-quality near-field optical probes by tube etching", *Appl. Phys. Lett.* 75, 160–162.
- Stockle R., Setz P., Deckert V., Lippert T., Wokaun A. and Zenobi R., (2001), 'Nanoscale atmospheric pressure laser ablation-mass spectrometry', *Anal. Chem.* 73, 1399–1402.
- Sun S. and Leggett G.J., (2002a), "Generation of Nanostructures by Scanning Near-field Photolithography of Self-Assembled Monolayers and Wet Chemical Etching", *Nano. Lett.* 2, 1223–1227.
- Sun S. and Leggett G.J., (2002b), unpublished work, University of Sheffield.
- Sun S. and Leggett G.J., (2004a), "Matching the resolution of Electron Beam Lithography using Scanning Near-field Photolithography", *Nano Lett.* 4, 1381–1384.
- Sun S. and Leggett G.J., (2004b), unpublished work, University of Sheffield.
- Sun S., Chong K.S.L. and Leggett G.J., (2002), "Nanoscale molecular patterns fabricated using scanning near-field optical lithography", *J. Am. Chem. Soc.* 124, 2414–2415.
- Syngé E.H., (1928), "A suggested method for extending microscopic resolution into the ultra-microscopic region", *Phil. Mag.* 6, 356–362.
- Syngé E.H., (1931), "A microscopic method", *Phil. Mag.* 11, 65–80.
- Syngé E.H., (1932), "An application of piezo-electricity to microscopy", *Phil. Mag.* 13, 297–300.
- Tarlov M.J. and Newman J.G., (1992), "Static secondary ion mass spectrometry of self-assembled alkanethiol monolayers on gold", *Langmuir.* 8, 1398–1405.
- Tarlov M.J., Burgess D.R.F. and Gillen G., (1993) "UV photopatterning of alkanethiolate monolayers self-assembled on gold and silver", *J. Am. Chem. Soc.* 115, 5305–5306.
- Toledo-Crow R., Yang P.C., Chen Y. and Vaez-Iravani M., (1992) "Near-field differential scanning optical microscope with atomic force regulation", *Appl. Phys. Lett.* 60, 2957–2959.

- Webster S., Batchelder D.N. and Smith D.A., (1998a), "Submicron resolution measurement of stress in silicon by near-field Raman spectroscopy", *Appl. Phys. Lett.* 72, 1478–1480.
- Webster S., Smith D.A. and Batchelder D.N., (1998b), "Raman microscopy using a scanning near-field optical probe", *Vib. Spectrosc.* 18, 51–59.
- Wolf M.O. and Fox M.A., (1995), "Photochemistry and surface properties of self-assembled monolayers of *cis*- and *trans*-4-cyano-4'-(10-thiodecoxy)stilbene on polycrystalline gold", *J. Am. Chem. Soc.* 117, 1845–1846.
- Wollman E.W., Kang D., Frisbie C.D., Lorkovic I.M. and Wrighton M.S., (1994), "Photosensitive self-assembled monolayers on gold: photochemistry of surface-confined aryl azide and cyclopentadienylmanganese tricarbonyl", *J. Am. Chem. Soc.* 116, 4395–4404.
- Wu M-H., Park C. and Whitesides G.M., (2003), "Generation of submicrometer structures by photolithography using arrays of spherical microlenses", *J. Coll. Interface. Sci.* 265, 304–309.
- Wurtz G., Bachelot R., H'dhili F., Royer P., Triger C., Ecoffet C. and Lougnot D-J., (2000), "Photopolymerisation induced by optical field enhancement in the vicinity of a conducting tip under laser illumination", *Jpn. J. Appl. Phys.* 39, L98-L100.
- Yang Z., Frey W., Oliver T. and Chilkoti A., (2000), "Light-activated affinity micropatterning of proteins on self-assembled monolayers on gold", *Langmuir* 16, 1751–1758.
- Yin X., Fang N., Zhang X., Martini I.B. and Schwartz B.J., (2002), "Near-field two-photon nanolithography using an apertureless optical probe", *Appl. Phys. Lett.* 81, 3663–3665.
- Xia Y., Zhao X-M., Kim E. and Whitesides G.M., (1995), "A selective etching solution for use with patterned self-assembled monolayers of alkanethiolates on gold", *Chem. Mater.* 7, 2332–2337.
- Zeisel D., Nettesheim S., Dutoit B. and Zenobi R., (1996), "Pulsed laser-induced desorption and optical imaging on a nanometer scale with scanning near-field microscopy using chemically etched fiber tips", *Appl. Phys. Lett.* 68, 2491–2493.
- Zeisel D., Deckert V., Zenobi R. and Vo-Dinh T., (1998), "Near-field surface-enhanced Raman spectroscopy of dye molecules adsorbed on silver island films", *Chem. Phys. Lett.* 283, 381–385.
- Zhang Y., Terrill R.H., Tanzer T.A. and Bohn P.W., (1998), "Ozonolysis is the primary cause of UV photooxidation of alkanethiolate monolayers at low irradiance", *J. Am. Chem. Soc.* 120, 2654–2655.
- Zhou H., Midha G., Donaldson L. and Weaver J.M.R., (1999a), "Scanning near-field optical spectroscopy and imaging using nanofabricated probes", *Appl. Phys. Lett.* 75, 1824–1826.
- Zhou H., Midha A., Bruchhaus L., Mills G., Donaldson L. and Weaver J.M.R., (1999b), "Novel scanning near-field optical microscopy/atomic force microscope probes by combined micromachining and electron-beam lithography", *J. Vac. Sci. Technol. B* 17, 1954–1958.

## Ink-jet printing as a tool in manufacturing and instrumentation

---

D WALLACE and D HAYES,  
MicroFab Technologies, Inc., USA

### 9.1 Introduction

In the last twenty years, ink-jet printing has not only come to dominate the small office/home office (SOHO) color printer and the industrial marking markets, it has become accepted as a precision fluid microdispensing technology for use in manufacturing and instrumentation. Taking a broader view of the technologies encompassed by the term 'ink-jet' has led to development of applications in electronics, optics, displays, biomedical instrumentation, and medical diagnostics using these technologies.

#### 9.1.1 Additive processes and flexible manufacturing

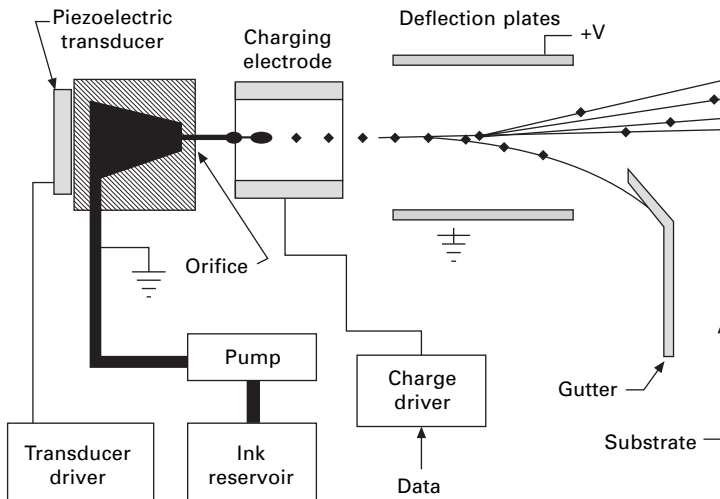
The characteristics of ink-jet printing technology that make it a highly useful fluid microdispensing tool for manufacturing and instrumentation are as follows.

- It is data-driven, requiring no tooling, such as masks or screens. Process information can be created directly from CAD data and then stored digitally. Being data-driven, it is flexible, a highly valuable attribute in today's manufacturing climate. In contrast, screen printing and most photolithographic processes require the use of masks or stencils, which cause delays in both initial process evaluation and changeover time.
- It is an additive process, and thus environmentally friendly, using only the amount of material necessary to perform the required function. In contrast, subtractive methods such as photolithography usually waste over 90%, and sometimes over 99% of the applied material. Many materials employed in subtractive processes are either toxic or contain volatile organic compounds (VOCs), requiring significant handling and cleanup cost. Finally, if the applied materials are expensive, the additive nature of ink-jet can result in very significant cost savings.
- It is non-contact, allowing printing onto non-planar surfaces. Even on planar surfaces, the non-contact and additive characteristics combine to

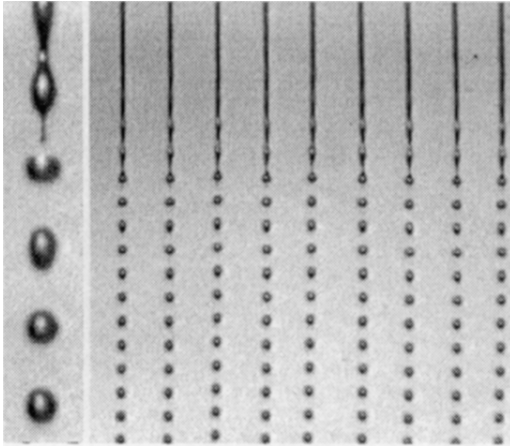
decrease or eliminate the interaction between processes sequentially applied to a substrate. This characteristic is particularly important in applications with a high level of process diversity (i.e., different types of processes), common in MEMS and other applications having a high level of integration.

### 9.1.2 Background on ink-jet printing technology

Ink-jet printing technology is actually not a single technology, but a group of different technologies that have a common end result; the extremely repeatable formation of small fluid droplets that can be directed to a specific location with high accuracy. These technologies fit into two general categories. In continuous mode ink-jet printing technology, a cylindrical jet of liquid is formed by forcing a fluid under pressure through an orifice. Surface tension forces create instabilities in the jet, causing it to break up into drops [1, 2]. By providing a single controlled-frequency disturbance, the jet can be forced to break up at precise time intervals into uniform diameter and velocity droplets. The droplets can be charged by an electrostatic field during their breakup and deflected from a straight trajectory by a second electrostatic field [3]. Charging the drops to different levels allows the drops to be deflected to one of several locations on a substrate, or to be directed into a catcher or gutter for recycling or disposal. Figure 9.1 shows a schematic of a continuous mode ink-jet printing system, and Fig. 9.2 shows a photomicrograph of an array of 70  $\mu\text{m}$  diameter jets of water issuing from a droplet generator device and breaking up into  $\sim 140 \mu\text{m}$  diameter droplets at 40,000 per second.



9.1 Schematic of a continuous ink-jet printer.



9.2 Array of continuous jets with 70  $\mu\text{m}$  diameter breaking up into 140  $\mu\text{m}$  droplets at 40 kHz.

Continuous mode ink-jet printing systems produce droplets that are approximately twice the orifice diameter. Droplet generation rates for commercially available continuous mode ink-jet systems are usually in the 80–100 kHz range, but systems with operating frequencies up to 1 MHz are in commercial use. Droplet sizes can be as small as 20  $\mu\text{m}$  in a continuous system, but 150  $\mu\text{m}$  is more typical. Droplets as large as 1 mm ( $\sim 0.5 \mu\text{l}$ ) have been observed.

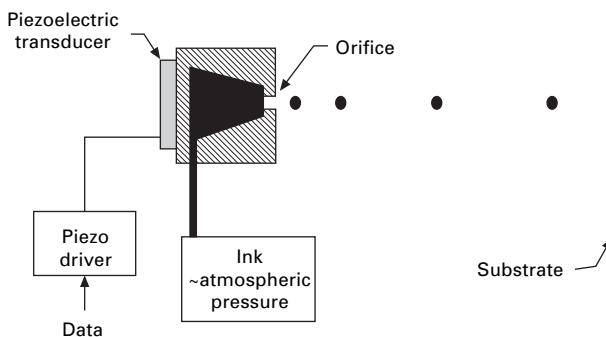
Continuous mode ink-jet systems are currently in widespread use for industrial marking, with product labeling of food and medicines being an important application. These systems have high throughput capabilities and are best suited for very high duty cycle applications. Few continuous mode ink-jet systems are multicolor (i.e., multi-fluid) or use multiple orifices. In almost all cases, multiple fluids and orifices are achieved by the use of multiple discrete printhead assemblies, not by integrating the capability into a single assembly. Continuous mode systems have been employed in novel applications such as rapid prototyping [4], electronics manufacturing [5], uniform sphere or balloon generation [6], and medical diagnostics manufacturing [7].

Although continuous ink-jet systems have been in use for more than three decades, there are a number of practical limitations to their broad use as an unconventional printing technology. Because they generate drops continuously, as the name implies, continuous systems require unused drops to be recirculated or wasted. Recirculation causes a change in fluid properties over time, due to solvent loss, and can change the properties of the jetted material in other ways due to the stress of repeated pumping and filtration. Drop velocities and droplet diameters are generally higher in continuous systems than in

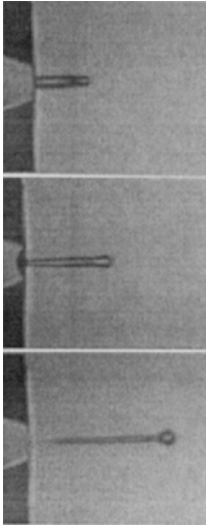
demand mode systems (discussed next), both of which can lead to difficulties in unconventional printing applications.

Demand mode ink-jet technology is employed in all SOHO (small, home office) ink-jet printers. In demand mode systems, a small transducer is used to displace the ink, creating a pressure wave. This pressure wave travels to the orifice [8, 9] where its energy is converted to inertial energy, resulting in the ejection of a droplet. A single drop may be generated, or a group of drops at arbitrary intervals of time. Thus the droplets are created ‘on demand’. Demand mode droplets are usually the same diameter as the orifice diameter. Drop diameters of 15–100  $\mu\text{m}$  (2–500 p $\text{l}$ ) can be achieved with demand mode systems, at droplet generation rates of up to 30 kHz. Demand mode ink-jet systems have no fluid recirculation requirement, and as Fig. 9.3 indicates, they are conceptually less complex than continuous mode systems. On the other hand, demand mode droplet generation requires the transducer to deliver three or more orders of magnitude greater energy to produce a droplet, compared to continuous mode, and there are many ‘elegant’ (i.e., complex) array demand mode printhead designs [10]. Figure 9.4 shows a demand mode ink-jet device generating 60  $\mu\text{m}$  diameter drops of butyl carbitol (an organic solvent) from a device with a 50  $\mu\text{m}$  orifice at 4,000 per second.

The transducer employed in demand mode systems was piezoelectric in early demand mode printers, but in many printers today, a thin film resistor that acts as a heating element is substituted for the piezoelectric transducer. When a high current is passed through this resistor, the ink in contact with it is vaporized, forming a bubble over the resistor [11]. The vapor bubble serves the same functional purpose as the piezoelectric transducer; it displaces the fluid to create a pressure wave. This type of printer is usually referred to as a thermal ink-jet printer. Making the fluid an integral part of the energy input device places additional constraints on the fluid properties. In practice, this means that thermal demand mode ink-jet technology is rarely used for novel (i.e., non-ink) applications, although some researchers have employed it [12].



9.3 Schematic of a demand mode ink-jet printer.



9.4 Demand mode ink-jet device generating 60  $\mu\text{m}$  drops 50  $\mu\text{m}$  orifice at 4 kHz.

Since piezoelectric demand mode ink-jet technology does not require recirculation of the working fluid, does not create thermal stress on the fluid, and does not depend on a thermal process to impart acoustic energy to the working fluid, it is the most adaptable of the ink-jet printing technologies to fluid microdispensing applications. As a non-contact printing process, the volumetric accuracy of ink-jet dispensing is not affected by how the fluid wets a substrate, as is the case when positive displacement or pin transfer systems ‘touch off’ the fluid onto the substrate during the dispensing event. In addition, the fluid source cannot be contaminated by the substrate, or contamination on the substrate, in a non-contact dispensing process. Finally, the ability to free-fly the droplets of fluid over a millimeter or more allows fluids to be dispensed into wells or other substrate features (e.g., features that are created to control wetting and spreading).

## 9.2 Electronics manufacturing applications

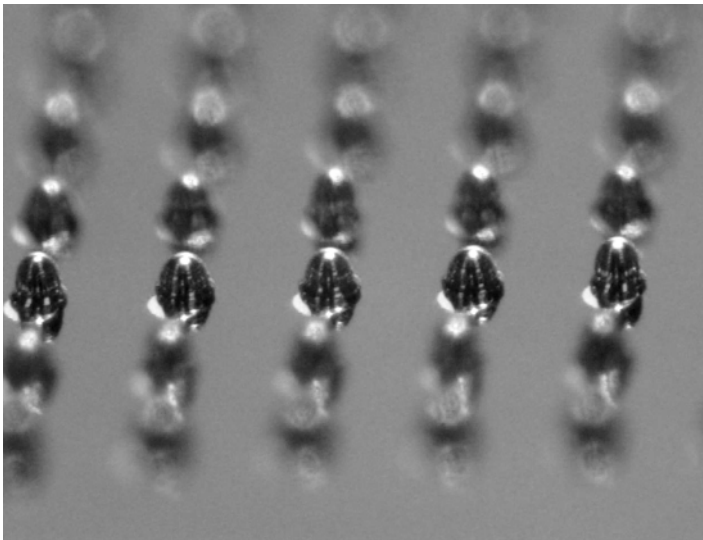
### 9.2.1 Electrical interconnect

Solder for electrical interconnect is commonly printed as a paste, containing flux, onto a circuit board. For many state-of-the-art electronic packages, the solder is applied by a variety of means (plating, evaporation, mechanically placing discrete balls) because of limitations in screen printing processes. Ink-jet printing technology, or Solder Jet<sup>®</sup> technology when used in this case, is also being used as an alternative to screen printing for this application, particularly in cases where three-dimensional interconnects are required and for very small feature sizes.

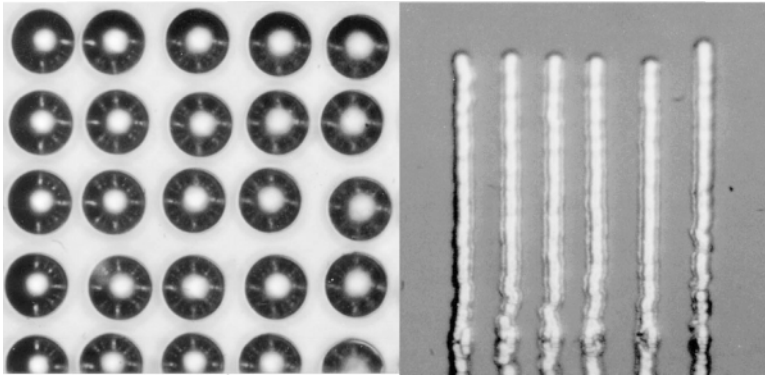
Solders suitable for electrical interconnects have been dispensed using piezoelectric demand mode ink-jet technology [13 14]. Bumping of wafers for flip-chip assembly has been demonstrated, and both Motorola and Delphi have developed and certified bumping and assembly processes based on Solder Jet<sup>®</sup> equipment. Operating characteristics achieved for jetting of solders include: formation of spheres with diameters of 25–125  $\mu\text{m}$ ; drop formation rates (on-demand) up to 1,000 per second; deposition onto pads at up to 600 per second; and operating temperatures to 320  $^{\circ}\text{C}$ . The solder dispensed has been primarily eutectic tin-lead (63% Sn/37% Pb), but a number of other solders have been evaluated, including high lead (95% Pb/5% Sn), no lead (96.5% Sn/3.5% Ag; indium; 52% In/48% Sn), and low temperature bismuth solders.

Figure 9.5 shows results from printing solder onto an 18 by 18 array of pads on a test vehicle, where the pads are 100  $\mu\text{m}$  diameter and on 250  $\mu\text{m}$  centers. The deposited solder volume is equivalent to a drop diameter of 100  $\mu\text{m}$ . The resolution obtainable with ink-jet based deposition of solders is illustrated in Fig. 9.6, where both bumps and towers of solder have been deposited with 25  $\mu\text{m}$  feature size and at pitches as small as 35  $\mu\text{m}$ .

Higher levels of integration of multiple functions, whether or not one uses the MEMS label to describe them, can lead to electrical interconnect requirements that are very difficult to address by conventional means. One example is the read-write head assembly in hard disk drives. Location of the conditioning electronics as close as possible to the ferrite read-write element allows for increased speed and density. However, a three-dimension electrical



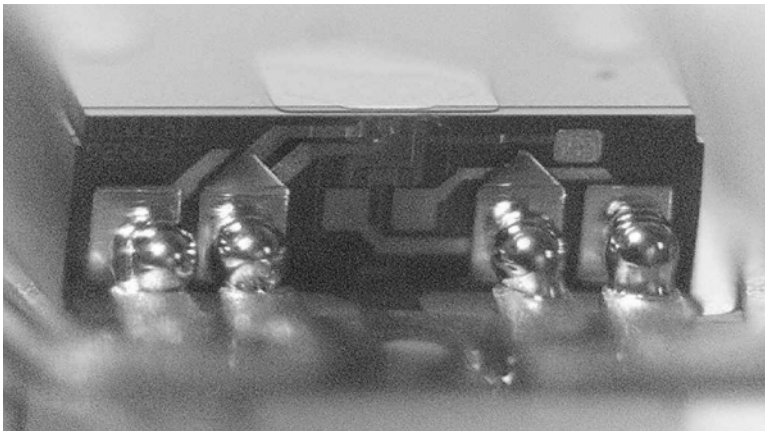
9.5 100  $\mu\text{m}$  pads on 250  $\mu\text{m}$  centers at 400 per second.



9.6 25  $\mu\text{m}$  bumps of solder on 35  $\mu\text{m}$  centers and 25  $\mu\text{m}$  towers printed on 50  $\mu\text{m}$  centers.

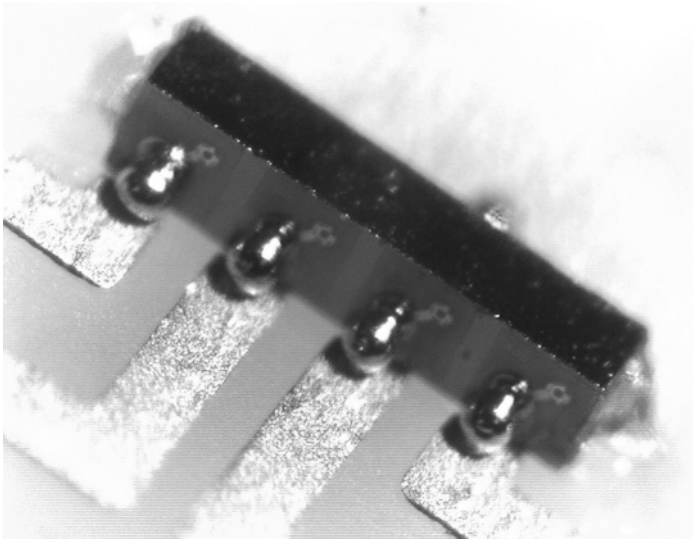
interconnect is required in that a solder ball must be placed in the inside corner formed by the conditioning electronics integrated circuit and the flex circuit that connects to the ferrite read-write element. Figure 9.7 illustrates a three-dimensional interconnect created using Solder Jet<sup>®</sup> technology.

Electrical interconnect for photonic components in an integrated assembly is another area that can lead to three-dimensional assembly requirements. The most popular solid state lasers used today are vertical cavity surface lasers (VCSELs) where the emitter and electrical interconnect pads are located very close to each other on the top surface of a gallium arsenide wafer. To increase the capacity of data transmission devices, VCSELs are using in arrays. To avoid using wire bonding, which is undesirable for reasons of



9.7 Integrated circuit containing signal conditioning electronics for read-write head of a hard disk drive. IC is attached to flex circuit by Solder Jet<sup>®</sup> technology by placing a solder ball in an inside corner. Pads are 100  $\mu\text{m}$ .

reliability, size, and ease of integration, to electrically interconnect a line array of VCSELs, an inside corner three-dimensional interconnect, similar to the disk drive read-write head example above, may be employed. Figure 9.8 shows a VCSEL line array with four emitters electrically connected to a circuit board by an 80  $\mu\text{m}$  solder ball that has been printed into the inside corner using Solder Jet<sup>®</sup> technology.

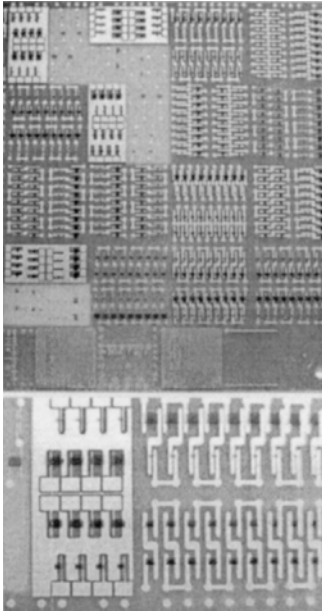


9.8 Array of four VCSEL lasers with 80  $\mu\text{m}$  solder ball for electrical interconnect printed into inside corner using Solder Jet<sup>®</sup> technology.

### 9.2.2 Embedded passives

Using a method to ‘write’ electrical passives (conductors, resistors, capacitors, inductors, antennae, and batteries) has great potential for lowering cost and increasing performance for consumer electronics, particularly high-frequency communications devices. Cost could be reduced by eliminating the need to purchase, stock, and place (onto the circuit board) large numbers and types of discrete passive devices. Performance would be increased by allowing the passives to be embedded into the inner layers of the circuit board, decreasing both the parasitic electrical characteristics associate with discrete passives and the cross-talk with active components. In addition, design flexibility could be increased by enabling conformal antennae and batteries.

Resistors are the simplest of the passives and several approached for embedded and/or direct write resistors have been pursued. Ink-jet printing of embedded resistors has been successfully demonstrated using both filled polymer and conductive polyimide ink as part of an NIST/ATP project [15]. Figure 9.9 shows one of the 4-up 18"  $\times$  12" embedded resistor test



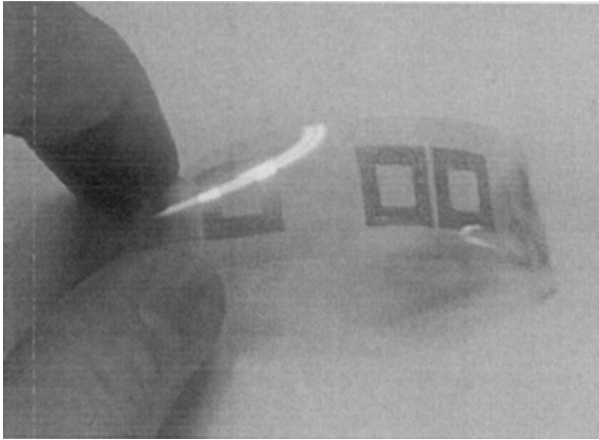
9.9 Embedded conductive polymer resistors printed using ink-jet technology, resistivity  $<200 \Omega/\text{sq}$ . Length of resistors  $\sim 1 \text{ mm}$ . Top, 100 mm square test panel. Bottom, enlarged view.

vehicle panel printed using a DuPont proprietary polyimide ink. Resistors ranging from  $100 \Omega$  to several  $\text{M}\Omega/\text{square}$  have been created using materials with low resistivity. Printed resistors ranged in size from  $125 \mu\text{m}$  to several mm long.

Conductor printing using ink-jet technology is being pursued by a number of organizations, and some initial successes have been demonstrated, most notably in the printing of address lines for organic drive electronics used in active matrix displays [16] and antennae. Figure 9.10 shows an antennae printed at the University of California at Berkeley using ink-jet technology [17]. Direct-write capacitors, inductors, and batteries represent significantly greater materials and process challenges than do resistors, but they are possible in principle, and a number of research organizations have ongoing research in this area.

### 9.2.3 Chip-scale (3D) packaging

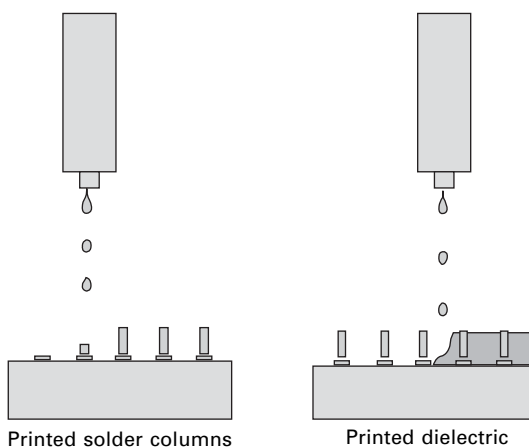
A microelectronic package must satisfy various functional requirements: support the die, protect the die from the environment, provide direct electrical interconnect, form compliant interconnects to allow for thermal expansion mismatch, and allow for easy assembly to printed circuit boards. In state-of-the-art electronics, the package is only slightly larger than the integrated



9.10 Antennae printed using ink-jet technology. Image courtesy of U.C. Berkeley.

circuit itself, and these packages are referred to as chip-scale. Fabrication of chip-scale packages while the integrated circuits are still embedded in the silicon or gallium arsenide wafer (i.e., wafer-scale) is the most economical because a large number of integrated circuits can be packaged at one time and because it eliminates the need to handle very small parts during the processes.

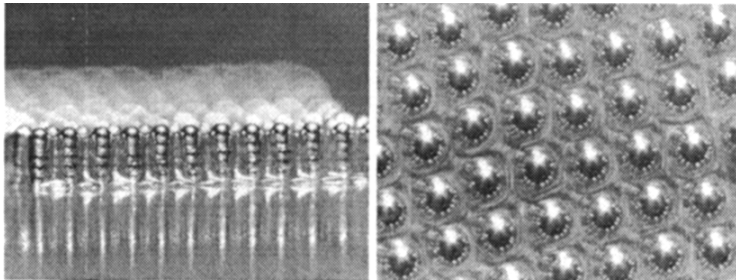
A direct-write chip-scale wafer-level packaging concept, based on both Solder Jet<sup>®</sup> [18] and Polymer Jet<sup>™</sup> technology, is currently under development at MicroFab. Figure 9.11 illustrates the steps in the fabrication process. First, solder columns with an aspect ratio of two or greater and approximately the



9.11 Chip-scale, wafer-level electronic packaging concept utilizing Solder Jet<sup>®</sup> and Polymer Jet<sup>™</sup> technology.

same width as the pads are printed onto each pad. High aspect ratio solder columns are used to eliminate the failures associated with thermal expansion mismatch between the integrated circuit and the circuit board. Second, a dielectric polymer underfill is printed onto the die surface and cured (UV or thermal). The polymer is printed around the solder columns to encapsulate them, but it is not printed onto the wafer in the regions that will be sawn with a diamond saw to singulate the integrated circuits. Unlike the highly filled polymers that are currently injected under an integrated circuit that is flip-chip bonded to a circuit board in order to overcome the thermal expansion mismatch problem, the printed polymer serves only to contain the solder columns so can be a much lower performance material.

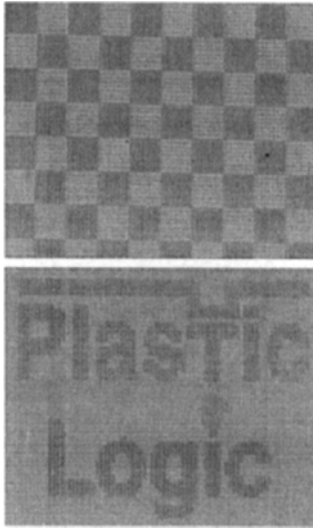
The basic components of the process described above, printing solder columns and dielectric polymers, have been demonstrated. Figure 9.12 shows a prototype with solder printed into 240  $\mu\text{m}$  tall columns that are placed on 150  $\mu\text{m}$  pitch. After printing the columns, a polymer dielectric was printed into the spaces between the columns.



9.12 Chip-scale, wafer-level packaging concept fabricated using ink-jet technology: polymer filled solder column array. Columns are 240  $\mu\text{m}$  tall and 150  $\mu\text{m}$  pitch.

#### 9.2.4 Organic electronics

Organic electronics is being pursued as a low-cost, low-performance alternative to silicon based electronics for such applications as radio frequency identification (RFID) tags and ‘disposable’ consumer electronics. The materials to make organic logic are very similar to the light-emitting polymers used in displays and discussed below. Initial efforts have focused on thin-film transistors (TFTs), used principally as drivers in displays. Figure 9.13 shows a prototype display driver fabricated by Plastic Logic of Cambridge U.K. where the source, drain, and address line for each of 4,800 pixels have been printed using ink-jet technology.



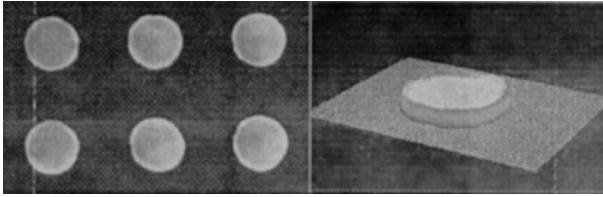
9.13 Ink-jet printed active matrix display electronics with 4,800 pixels operating at 80 Hz. Courtesy of Plastic Logic.

### 9.3 Display manufacturing applications

Ink-jet printing methods have been discussed and demonstrated over the last few years for a variety of applications in the manufacture of flat panel displays. For display technologies that are in wide commercial production today, specific processes for use of ink-jet methods include printing of spacers and color filters for liquid crystal displays (LCDs), and printing phosphor particles for inorganic electroluminescent devices [19]. However, ink-jet printing has come to the forefront for polymer light-emitting diode (PLED) displays, widely viewed as the dominant display technology of the future [20, 21, 22].

#### 9.3.1 PLED displays

Light-emitting polymers [23] are a subset of a broad class of conjugated polymers discovered by Shirakawa, Heger and MacDiarmid, for which they received the Nobel prize. Whether they are deposited in a spin-coating process or by ink-jet deposition, the polymer is usually suspended in low concentrations (0.5–2%) in a volatile organic solvent. To construct light-emitting diodes in the form of pixels for display devices with these materials, a uniform layer of 1  $\mu\text{m}$  or less must be created in a structure, and the structure must create an electric field across the light-emitting polymer layer. An example of PLED printing by ink-jet is shown in Fig. 9.14, where 250  $\mu\text{m}$  diameter spots of a light-emitting polymer (LEP) are printed on 600  $\mu\text{m}$  centers onto a Baytron-P (hole transfer layer material) coated substrate.



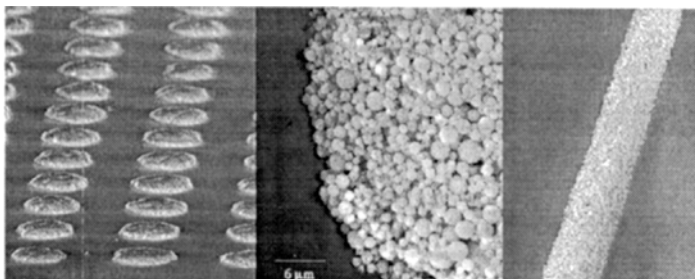
9.14 250  $\mu\text{m}$  diameter spots of a light-emitting polymer (LEP) ink-jet printed on 600  $\mu\text{m}$  centers onto a Baytron-P coated substrate. Left, shown under UV illumination. Right, height profile, nominal thickness of 50  $\mu\text{m}$ .

### 9.3.2 FED displays

Printing phosphors for the anode of field effect device (FED) displays using ink-jet printing would result in a manufacturing cost savings of 20–30%, because of the high-cost of high quality phosphors and the wasteful, subtractive processes currently employed to apply them in the required patterns. However, the performance of currently available phosphors degrades significantly as the particle size decreases and thus the minimum particle size for acceptable performance is in the 1–2  $\mu\text{m}$  range. This presents a significant difficulty both in formulation of a jettable dispersion, and in achieving reliable jetting. Despite these difficulties, the basic feasibility of jetting phosphors for FED displays has been demonstrated [24]. Phosphor ink ( $\text{Zn}_2\text{SiO}_4\text{:Mn}$ ), which included a binder, was dispensed to form arrays of spots and lines on glass substrates. After printing, the binder was burned off in an oven, leaving only the phosphor on the surface. Figure 9.15 illustrates the resulting patterns. These printed features (90  $\mu\text{m}$ ) are smaller than pixels currently used in many phosphor displays, and the high density and uniformity of particles in the pixels, needed for efficient cathodoluminescence, are apparent.

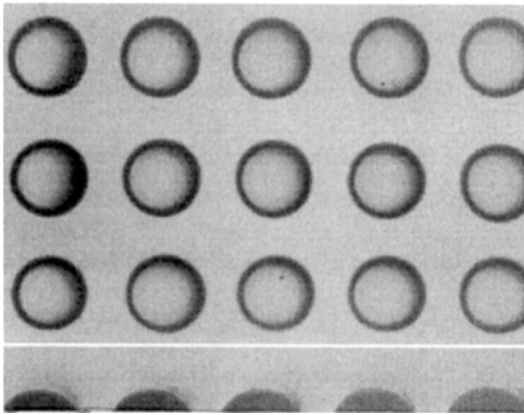
### 9.3.3 LCDs

High-quality and high-cost materials are also required in liquid crystal display (LCD) manufacturing. In this case, the color filter materials represent 20–



9.15 SEM of 90  $\mu\text{m}$  lines and spots of ink-jet printed phosphor.

40% of the manufacturing cost of the display, again because of the use of wasteful subtractive processes. These materials can be formulated so that they can be applied using ink-jet technology, and the feasibility of jetting these materials has been demonstrated. Currently, at least one materials supplier to the LCD industry is actively developing jettable filter materials. In addition to jetting color filter materials, LCD manufacturers have explored using ink-jet technology to deposit the spacers required to create the volume into which the liquid crystal material is deposited. UV-curing polymers can be printed into the required dimensions, with bumps as small as 25  $\mu\text{m}$  diameter and 10  $\mu\text{m}$  high possible. Figure 9.16 shows an example of printed spacer bumps that would meet the physical and thermal (in excess of 200 EC) durability requirements for flat panel displays.



9.16 95  $\mu\text{m}$  diameter, 34  $\mu\text{m}$  high, printed spacer bumps, in substrate plane (top) and in profile (bottom).

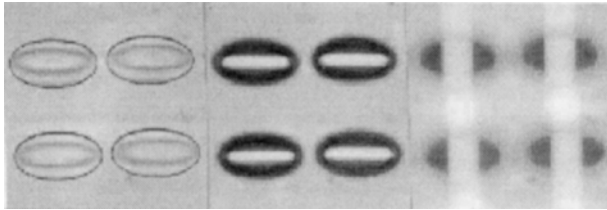
## 9.4 Photonics applications

The information transmission and processing (Datacom and Telecom) markets are pushing component manufacturers toward lower cost and higher performance optical interconnect technologies. To achieve this, organic optical materials are becoming accepted in the fabrication of micro-optical elements. Polymer refractive microlenses and waveguides created by ink-jet printing optical epoxies have a number of advantages [25, 26, 27], including higher thermal durability than PMMA [28], used in photolithographic methods, and the ability to fabricate directly onto optical components of arbitrary geometry.

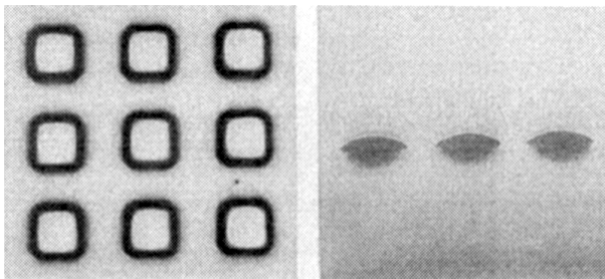
### 9.4.1 Microlens arrays

Refractive microlens configurations that can be printed using ink-jet processes include convex/plano hemispherical, hemi-elliptical and square, and convex-

convex. Printed hemi-elliptical and square lenses are illustrated in Fig. 9.17 and Fig. 9.18. The elliptical and square lens configuration could be useful in edge-emitting diode laser collimation and light-collection for CCD (charged-coupled device), respectfully.

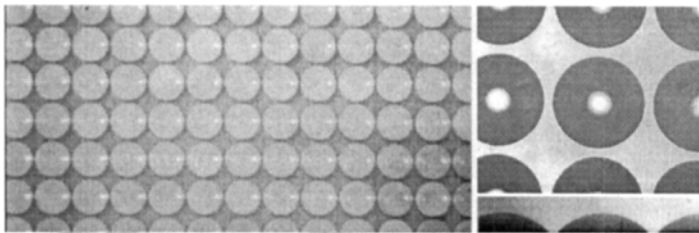


9.17 Printed hemi-elliptical microlenses 284  $\mu\text{m}$  long, shown in substrate, fast-focal and slow-focal planes.



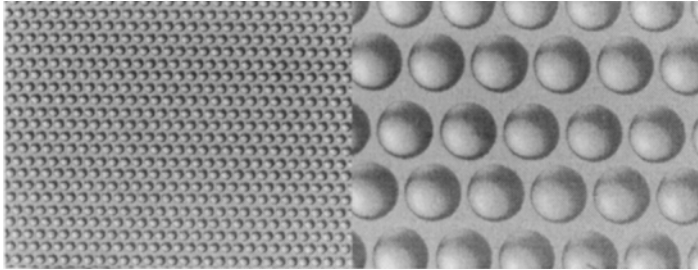
9.18 Printed 300  $\mu\text{m}$  square microlenses shown in focal plane and in profile.

Printed arrays of microlenses, such as that shown in Fig. 9.19, are currently being used in coupling light into and out of optical fibers in micromirror based MEMS optical switches. The array shown in this figure has 400 microlenses of 916  $\mu\text{m}$  diameter on 1 mm centers. The focal length is  $1.10 \pm 0.01\text{mm}$ . Diameter and center variation is  $\pm 1 \mu\text{m}$ . Smaller diameter lenses



9.19 Portion of printed array of 916  $\mu\text{m}$  diameter microlenses on 1 mm centers with focal lengths of  $1.10 \pm 0.01 \text{ mm}$ . Diameter and center variation  $\pm 1 \mu\text{m}$  for the 400 lenses in the array.

at higher packing density and in larger arrays can be used for optical diffusers in LCD displays. Figure 9.20 shows a portion of an array of 200,000 microlenses, 104  $\mu\text{m}$  diameter and 112  $\mu\text{m}$  pitch, printed using ink-jet technology.

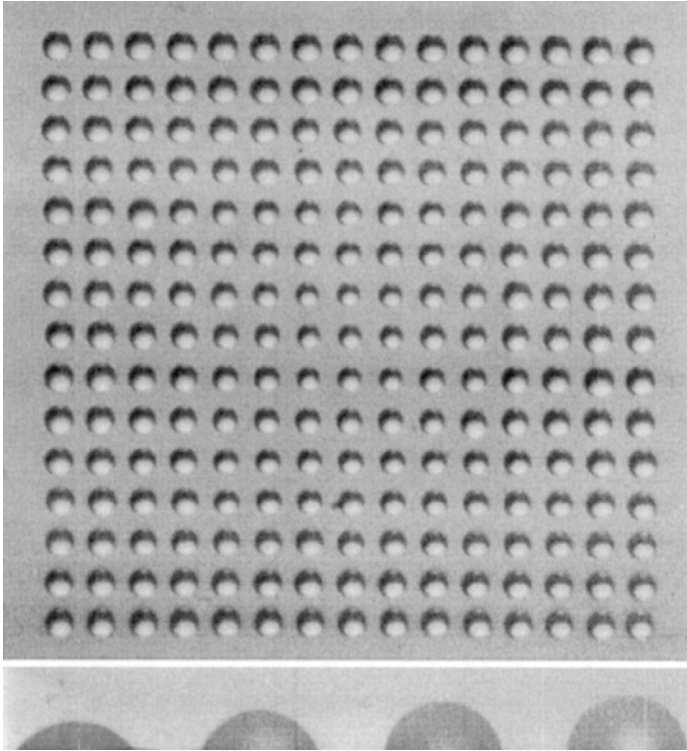


9.20 Portion of printed array of 200,000 microlenses, 104  $\mu\text{m}$  diameter and 112  $\mu\text{m}$  pitch.

The focal lengths for printed microlenses may be varied over wide ranges even within a single array. This can be an important performance enhancing feature for optical assemblies that require free-space optical interconnections over relatively long and variable path lengths different elements of the optical array, as occurs in some micromirror switching devices. Illustrated in Fig. 9.21 are arrays of variable focal length lenses. In the top image is a two-dimensional array with variable lens height and diameter. In the bottom image, constant 700  $\mu\text{m}$  diameter lenses are shown in profile with focal lengths of (left-to-right) of 850, 525, 430 and 405  $\mu\text{m}$ , respectively.

## 9.5 Integrated electro-optic assemblies

Reductions in packaging costs and improved performance may be achieved in the coupling of output beams from VCSELs into optical fibers with microlenses. Packaging cost is decreasing by decreasing alignment accuracy requirements, thus reducing assembly cost. Increased performance is achieved by increasing the optical coupling efficiency. Fabrication of the microlenses over the VCSEL emitters can be accomplished with high quality and at low cost. [29] Since it is optically impossible to collimate or focus the laser output using the spherical-section (versus ball) microlenses that can be achieved by ink-jet printing, an offset of the microlens from the emitter plane is required. One way of achieving this in VCSEL array packaging is to print an array of microlenses onto a glass substrate, where the thickness of the substrate is matched to the radius of curvature of the lenslets such that their back focal points will be at the emitter plane. Then the glass substrate is placed over the VCSEL wafer and microlenses and emitters are aligned. [30, 31] This alignment

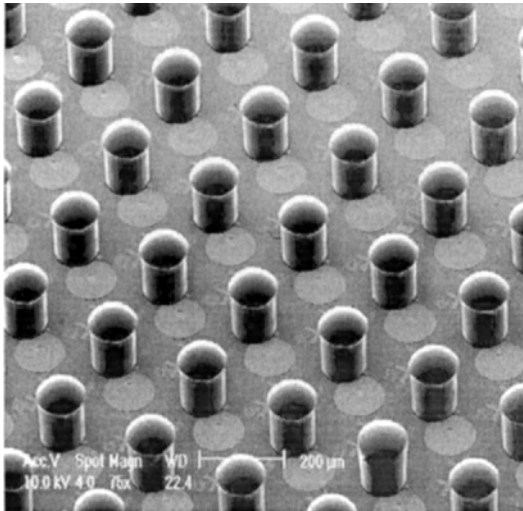


9.21 Arrays of variable focal length lenses. Top, two-dimensional array. Bottom, 700  $\mu\text{m}$  diameter microlenses in profile with focal lengths of (left-to-right) of 850, 525, 430 and 405  $\mu\text{m}$ , respectively.

step may be eliminated by forming individual pedestals of optically transparent material on top of each emitter, then printing a microlens on top of each pedestal, as shown in the photograph of Fig. 9.22. The radius of curvature of the deposited microlenses may be varied over a wide range by varying the number of printed droplets, since the pedestal perimeter stops the fluid flow to a degree determined by the surface tension of the optical material. Optical modeling of this configuration shows that either collimation or focusing of the VCSEL beams at a design distance from the microlenses may be achieved by adjusting pedestal diameter and height and lenslet radius of curvature, taking into account VCSEL numerical aperture and refractive indexes of the pedestal and lenslet materials.

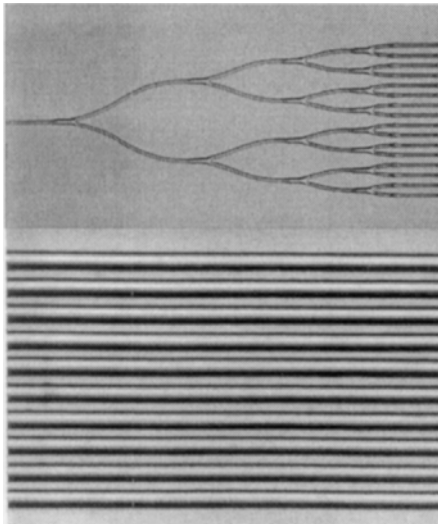
### 9.5.1 Waveguides and photonic circuits

The ability to ‘write’ transmissive optical materials (shown in printed microlens examples above), active optical materials (demonstrated for display manufacturing applications), and dielectrics, conductors, and other electronic



9.22 Microlenses printed onto 100  $\mu\text{m}$  tall pedestals to collimate VCSEL output.

elements, makes it conceptually possible to direct-write photonic circuits, including associated electronics components. Printing transmissive optical materials in the form of multi-mode waveguides has been demonstrated using the optical epoxy material used to form a microlens by ink-jet printing. Figure 9.23 illustrates some of the results that have been obtained. A 1.74-



9.23 Waveguides printed using ink-jet technology. Above, 1.74-index optical thermoplastic printed on glass as 1-16 splitter, 120  $\mu\text{m}$  wide branches. Below, 125  $\mu\text{m}$  Multi-mode waveguides printed on 150  $\mu\text{m}$  centers.

index material is shown printed on glass as 1–16 splitter with 120  $\mu\text{m}$  wide branches, and 125  $\mu\text{m}$  waveguides are shown printed on 150  $\mu\text{m}$  centers. Edge smoothness of the waveguide-substrate interface is of the order of the wavelength of the transmitted light and is superior to etched waveguides. To date, waveguides have been written only with materials with unacceptably high loss (for use in waveguides, but not for lenses), but low loss waveguide materials developed by several materials companies for photolithographic processing can be, and have been in at least one case, formulated to be compatible with ink-jet processes.

## 9.6 Biomedical manufacturing and instrumentation applications

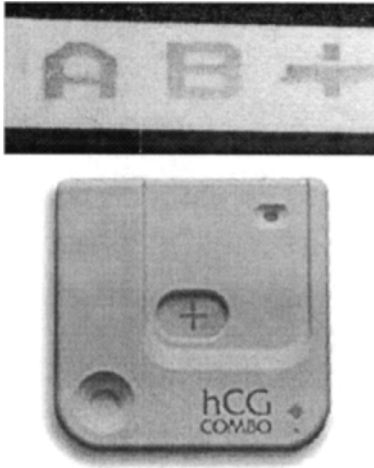
Ink-jet dispensing of bioactive materials has received a great deal of attention in the past two decades because of the rapidly expanding knowledge and capabilities in molecular biology. The key drivers behind the interest in ink-jet dispensing are the minimal use of rare fluids (both sample and diagnostic reagents) and parallel processing of a large number of tests, which drives assay size down and density up. More recently, use of ink-jet technology in biochemical synthesis and analysis has brought ink-jet technology applications into biomedical instrumentation applications.

### 9.6.1 Printing for diagnostics and discovery

#### *Proteins*

Early development in ink-jet printing of bioactive fluids [32] centered on making patterns of antibodies on membrane materials, typically nitrocellulose, that bound the antibody for use in an assay. The pattern was used as a human readable display for the assay. Examples include a prototype blood typing test shown in Fig. 9.24. Here, three blood typing reagents and a control have been printed into the characters A, B, and + (the plus contains both the control and RH positive antibodies), and have been exposed to AB + blood. Another example given in Fig. 9.24 which shows Abbott's TestPack™ product line. Here two antibodies (typically,  $\beta\text{HCG}$  and a control) are printed onto nitrocellulose using ink-jet technology. Over 500 million of these diagnostic test strips have been manufactured to date.

Use of ink-jet printing of antibodies progresses from 'printing' to miniaturization in the 1990s. Miniaturization of antibody assays increases the number of diagnostic tests that can be conducted in parallel and increases the sensitivity of the assay, by minimizing the amount of analyte that is bound to the antibody. [33] In Boehringer Mannheim's (now Boehringer Roche) MicroSpot™ system, as many as 196 distinct reaction sites (i.e., spots)

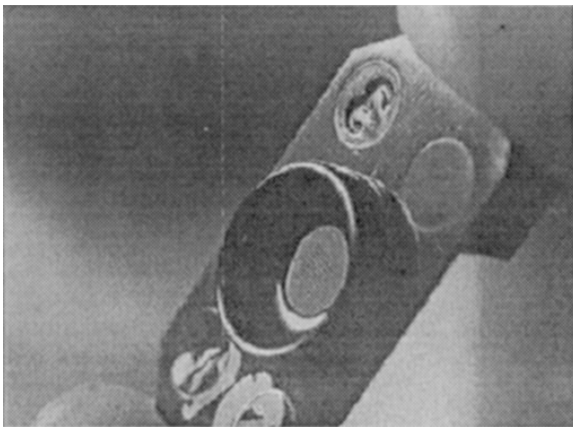


9.24 Antibodies ink-jet printed into human readable characters/symbols. Top, three blood typing antibodies plus a control. Bottom, one antibody and a control.

fit into a disposable reaction well the size of a thumbnail, as shown in Fig. 9.25 [34].

#### *DNA and peptide arrays*

Although the most prevalent DNA array fabrication techniques have been Affymetrix's light-activated DNA fabrication method [35] and pin transfer methods, ink-jet printing has been used by a number of organizations, both for synthesis and for deposition of oligonucleotides into a microarray format.



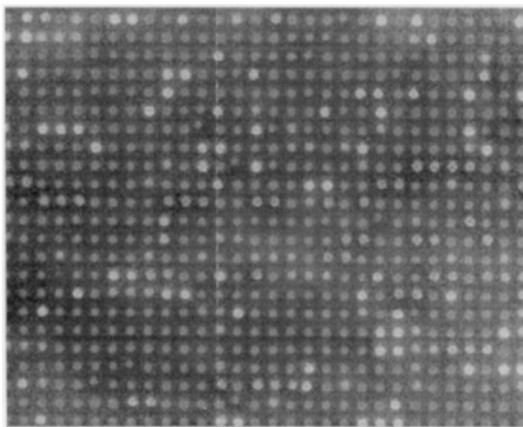
9.25 Disposable diagnostic test 'well' that can contain as many as 100 individual antibodies (tests) printed using ink-jet technology.

Deposition of oligonucleotides that are synthesized and verified off-line has been accomplished by commercially available six color thermal ink-jet printheads [36], conventional fluid robots modified to hold 4, 8, and possibly up to 96 individual piezoelectric demand mode jetting devices [37] and custom piezoelectric demand mode array printheads. Figure 9.26 shows simulated DNA array produced by printing eight different fluorescent dyes from ten channel/ten fluid printheads. Center-to-center distance of the spots is 150  $\mu\text{m}$ .

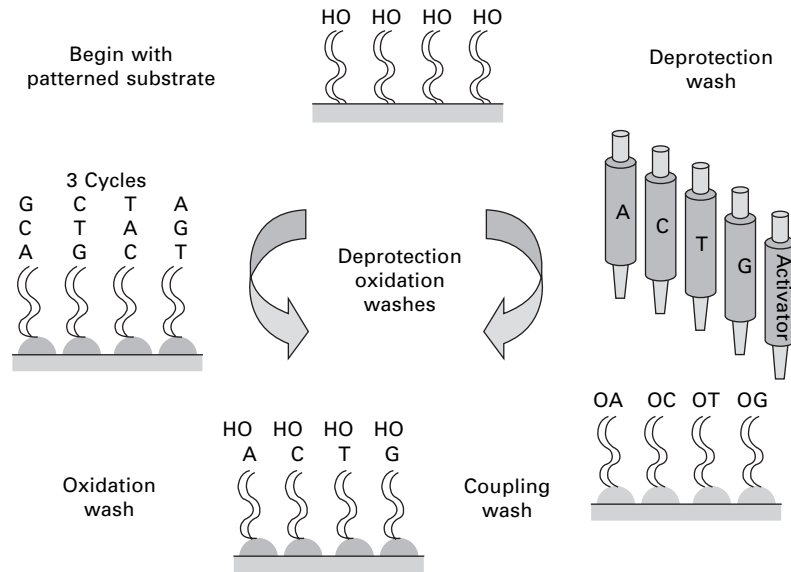
The chief difficulty in deposition of oligonucleotides is the number of fluids to be dispensed. For very specific genetic resequencing applications (i.e., looking for known sequences or mutations), the number of oligonucleotides required can be as few as ten to less than 100. Resequencing applications include clinical diagnostics, SNP (single nucleotide polymorphism) detection, and point mutation detection.

Deposition of bioactive molecules allows known, quality controlled materials to be applied to substrates. If a large number of different molecules is to be deposited, a simpler and more flexible method is to fabricate those molecules *in situ* using ink-jet deposition of precursor materials. Oligomeric materials are most suited to this approach with DNA and peptides being obvious candidates. Although only these two bioactive molecules are discussed, this approach is valid for general combinatorial synthesis [38].

Synthesis of DNA arrays using ink-jet technology greatly decreases the number of different fluids required. Only the precursor solutions of the four constituent bases (A, G, C, T) of DNA, plus an activator (tetrazole), are jetted, as illustrated in Fig. 9.27, along with Protogene's implementation of the concept. Each 'layer' of bases is synthesized with only a single activation



9.26 Simulated DNA array produced by printing eight different fluorescent dyes from a ten channel/ten fluid printhead. Center-to-center distance of the spots is 150  $\mu\text{m}$ .



9.27 Schematic of ink-jet based DNA array synthesis and DNA synthesis printer.

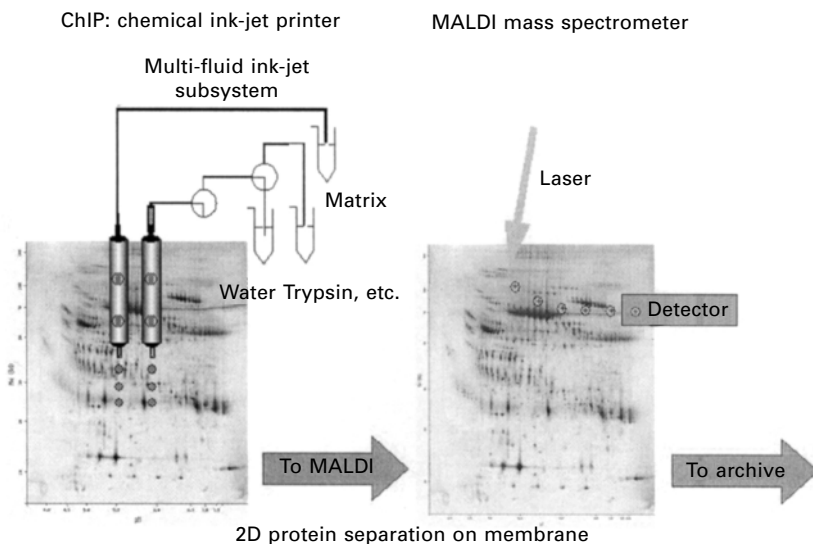


step. This is a considerable simplification compared to light-activated synthesis of DNA arrays [33] which usually requires four activation steps per ‘layer’. The complexity of multi-step chemical synthesis in an anhydrous environment is an added problem, but a number of investigators have overcome this difficulty [39, 40]. DNA arrays manufactured in this way using ink-jet technology are available from Protogene, Agilent, Rosetta Informatics, and Oxford Gene Technologies.

Peptide arrays for drug and expression screening studies [41] can be synthesized using ink-jet can in a manner similar to DNA arrays, except that there are 20 naturally occurring amino acids, making the dispensing system more complex. Initial proof-of-principle peptides are currently being fabricated at MicroFab using an adapted Jetlab® printing system.

### Chemical printing

Ink-jet technology can be used to deliver sample reagents, enzymes, or other sample processing fluids directly to immobilized biological samples, making it a toll for *in situ* microchemistry. The Chemical Ink-jet Printer (ChIP, Shimadzu Biotech [42]) incorporates this capability by delivering small volumes of enzymes and reagents to protein samples immobilized on a membrane, to prepare the protein samples for matrix assisted laser desorption ionization time of flight mass spectrometry (MALDI-TOF MS) analysis performed directly on the membrane. Figure 9.28 schematically illustrates the ChIP process applied to protein identification. The protein on the membrane has been electroblotted from a two-dimensional electrophoretic gel (2-D gel)



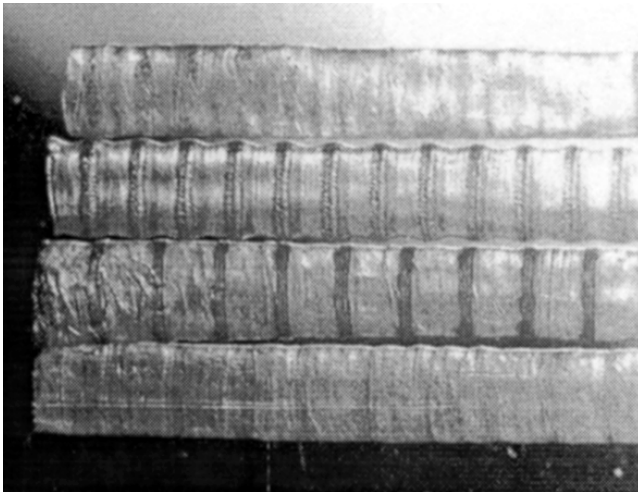
9.28 Schematic of Chemical Ink-Jet Printer (ChIP) for protein analysis.

with the proteins separated in one dimension by charge (isoelectric point) and the other dimension by mass. Use on ink-jet based *in situ* microchemistry eliminates the need to manually perform peptide extraction, digestion, clean-up, and sample transfer to a MALDI-TOF target prior to MS analysis. Conservation of limited/irreproducible samples is achieved by selecting only specific proteins for sub-analysis, allowing the remainder to be archived.

In a CHIP type instrument, ink-jet microdispensing can also be used to microdeposit antibodies specific to specific protein spots in a 2-D separation. This capability can be useful in detecting or analyzing bacteria or viruses in the environment or in human samples for the detection of bacterial infections.

### 9.6.2 Tissue engineering

The ability to ‘write’ biopolymers, cells, and growth factors (stimulants and inhibitors) with nanoliter (and smaller) volume precision opens the possibility of digitally constructing engineered tissue using ink-jet printing technology. Biosorbable polymers (PLGA) can be printed as a three-dimensional structure, using methods currently employed in free-form fabrication, to form scaffolds in the desired tissue shape. Cells seeded into this scaffold would grow into this shape and gradually dissolve the polymer structure after it has been implanted, leaving only the tissue and no ‘foreign’ materials for the body to reject. One application in this very broad area is the fabrication of nerve conduits for regeneration of peripheral nerves. Figure 9.29 shows 1 mm diameter biosorbable conduits for peripheral nerve regeneration, fabricated

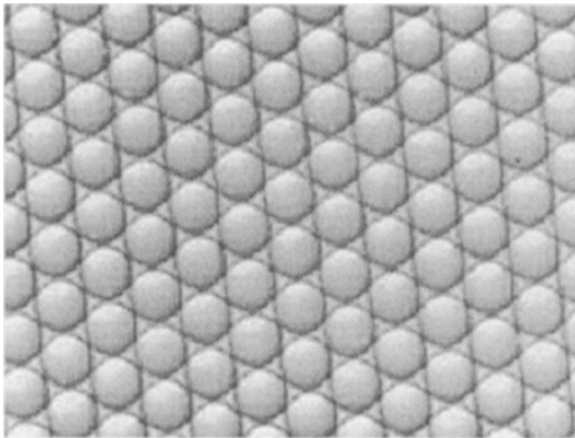


9.29 1 mm diameter biosorbable conduits for peripheral nerve regeneration, fabricated using ink-jet printing methods. Nerve growth factor (NGF) is embedded in the conduit to stimulate direct growth.

using ink-jet printing methods. Nerve growth factor (NGF) is embedded in the conduit to stimulate and direct growth. Directing growth requires that the NGF be printed in a gradient of concentration, a requirement reality met by ink-jet printing's inherently digital control.

### 9.6.3 Drug delivery

The same family of biosorbable polymers used in creating structures for tissue growth can be loaded with small molecules, steroids, proteins, peptides, genetic material, etc., to be used as therapeutic agents (i.e., drugs). Embedding these materials in the polymer allows for controlled release, with the polymer formulation and the geometry controlling the release profile. The simplest shapes useful for drug delivery are spheres, which can be controlled to a very uniform diameter, or generated in a specific diameter distribution. Figure 9.30 shows monodispersed ( $100 \pm 1 \mu\text{m}$ ) PLGA microspheres loaded with an anti-cancer agent, fabricated using ink-jet technology.



9.30 Highly uniform microspheres of biosorbable polymer (PLGA) loaded with an anti-cancer agent,  $60 \pm 1.0 \mu\text{m}$  in diameter.

## 9.7 Implementation considerations

### 9.7.1 Fluid requirements

To be able to use ink-jet methods in an industrial process, the working fluid must be low viscosity (usually  $< 20 \text{ cp}$ ), nearly Newtonian, and free of particles of the order of the orifice diameter. At first glance, these requirements may appear to be so restrictive as to eliminate the possibility of using ink-jet processes in industrial applications. On the other hand, if one looks at the ink used in an offset press, it is hard to imagine how ink-jet printing technology could be possible! By operating at higher or lower temperatures and by

selecting alternative materials and formulations, the number of industrial applications of ink-jet printing can be made surprisingly large.

### 9.7.2 Fluid/substrate interactions

Except for the cases where ink-jet technology is used to meter fluid, as in filing a microwell plate for a high-throughput drug screening application, ink-jet deposition processes are used to produce a desired pattern of material onto a substrate. The interaction between the fluid formulation, jetting parameters (drop size, velocity, frequency), substrate characteristics, printing grid (dots per inch), and printing sequence (interleave, overprinting, color sequence, etc.) is a key aspect in the development of all ink-jet printing systems, whether they use an aqueous ink or solder for electronic assembly. For the case of liquid ink on paper, the porosity of the paper and the low viscosity of the ink represented a major challenge in the initial development of ink-jet printers. Rapid spreading of liquid ink through the fibers can cause the spot size to become much larger than the drop size, decreasing the optical density of the spot and resulting in irregular spots that degrade the quality of characters, lines, etc. Use of ink-jet printing technology for printing onto a non-porous substrate (similar to printing ink onto an overhead transparency) creates a different set of issues.

Control of the spreading is essential if the desired resolution is to be obtained. Phase change inks (Dataproducts, Tektronix printers) were developed for conventional ink-jet printers for precisely this reason, since they solidify quickly after impact. The control of spreading due to solidification is a positive aspect of phase change materials if one is trying to limit spreading and obtain the smallest spot for a given drop size. However, if one is trying for deposition of a uniform layer, solidification into a bump is a problem, not a feature.

Many organic liquids, such as isopropanol, acetone, and acetonitrile, are very low viscosity and highly wetting, making them spread rapidly when printed onto a solid surface. Rapid spreading makes it difficult to achieve small and/or uniform features. In some applications, this problem can be solved by creating features in the surface, such as the wells commonly used in phosphor-based flat panel displays, to provide a barrier to spreading and physically define the feature size. In other applications, surface treatments, such as plasma cleaning or application of a non-wetting coating, can be used to control spreading.

### 9.7.3 Throughput

Droplet generation rates for continuous ink-jet technology are of the order of 80 kHz, and rates for demand mode technology are of the order of 8 kHz. For

office ink-jet printers, the maximum droplet rate, the number of channels in the printhead, and the printing resolution combine to determine the nominal throughput. For many manufacturing applications of ink-jet printing, this is not the case. If multiple drops are required per spot, as is the case with some micro-optics applications, then the printhead will usually move to a new location and stop before dispensing. The acceleration associated with this procedure limits the effective maximum throughput to approximately five dispenses a second, though each dispense may contain tens, hundreds, or thousands of drops. Even when printing while the printhead is in motion, which is how office ink-jet printers work, the effective dispensing rate can be far below the theoretical maximum. If the distance between dispensing sites is fairly large (e.g., 200  $\mu\text{m}$  or more for an electrical interconnect application), the translational speed limits can be encountered before drop generation limits are encountered.

#### 9.7.4 Post-processing

In conventional ink-jet printing, the ink is usually allowed to dry without any active post-printing process. However, UV curing inks have been employed in industrial ink-jet printing applications where the surface is non-absorptive, such as VCR tape cases and pharmaceutical containers. In this case, the post-processing of the printed features (i.e., UV irradiation of the printed characters) is a critical part of the printing process. In non-conventional applications of ink-jet printing, post-processing is frequently important also. UV curing of the optical epoxy used to create microlenses and waveguides was discussed above. Conductive inks for electronics applications are typically heated to sinter the metal particles together and/or convert organometallic solutions to solid metal [43]. Many of these post-processing procedures are applied to the entire substrate, such as heating or UV illuminating an entire circuit board. However, localized application of energy can be required or useful for some applications. One means of accomplishing this is using a laser to 'write' over the printed pattern, either after the printing process has been completed or in real time, with the delay between printing and laser being in the millisecond range [44].

### 9.8 Equipment

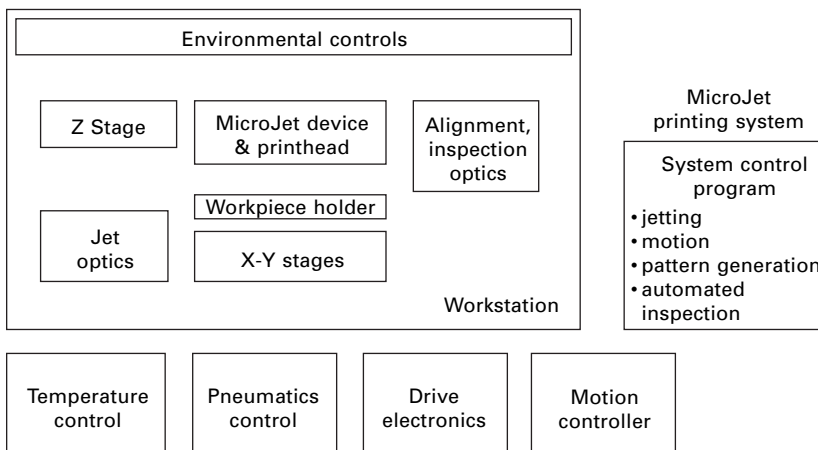
For manufacturing applications of ink-jet printing technology, the substrate to be printed upon determines the machine configuration. In many cases, the substrate will be similar to a silicon wafer, a circuit board, circuit board panel, or other relatively flat, rigid substrate. In other cases, they will be anything but flat. Examples of the latter include printing DNA or protein arrays onto the bottom of a microwell plate, printing solder into corners for

disk drive assemblies, and printing lenses onto pedestals. Manufacturing equipment using ink-jet dispensing will have setup, calibration, alignment, and control functions not generally found in desktop printers. Maintenance functions, which are found in desktop printers, will also be included in ink-jet based manufacturing equipment.

To expand the range of materials that can be jetted, the printhead may require elevated or depressed temperature operation. Also, the substrate may need to be heated or cooled to control the pattern formed by the dispensed fluid after it has landed on the substrate. Environmental control requirements may include particle control, oxygen control, or water vapor control. Curing immediately after printing may require injection of reactive gasses or UV illumination. Figure 9.31 shows a block diagram for a typical ink-jet based dispensing system. In this case, the workpiece is shown mounted onto an X-Y stage, so that the printhead assembly is stationary. A stationary printhead does not have to be designed to account for acceleration effects on the contained fluid, or the motion of service lines if a remote reservoir is utilized.

### 9.9 Future trends

Ink-jet printing technology has become the dominant technology for the home and SOHO (small office/home office) market because of its cost/performance capabilities, the most important of which is color printing of images. However, current and future developments in the conventional ink-jet market are, and remain, highly targeted to consumer products and these developments will not directly affect the applicability of ink-jet printing technology to manufacturing applications, where the ‘printer’ is a tool.



9.31 Block diagram for a typical ink-jet based dispensing system.

Developments in two non-ink applications of ink-jet printing are likely to have significant impact on the overall capabilities and availability of ink-jet based rapid prototyping equipment in the future. The explosion in genetic information from the Human Genome Project has created an ever-growing demand for DNA microarrays for gene expression studies, single nucleotide polymorphism (SNP) detection, clinical diagnostics, and other genetics-based studies [45]. To date, pin transfer methods have dominated the research and low volume commercial markets for DNA microarrays, and Affymetrix's DNA microarrays fabricated using light-activated synthesis [46] have been widely used by drug companies in their research. However, as the market for DNA microarrays becomes larger and more clearly defined, companies such as Agilent and Motorola have begun to develop high-volume DNA microarray production capabilities using ink-jet printing methods. As these and other companies expand their use of ink-jet printing technology for DNA microarrays, standardized and commercially available manufacturing equipment using ink-jet dispensing should become more capable and more generally available. This equipment should be more suitable for, or adaptable to, other rapid prototyping applications than printheads and printers developed for ink deposition.

In the display market there is a broadly held consensus that in the future, light-emitting polymer based displays [47] will displace CRT and LCD displays in many or most existing display products, and will enable a wide range of display products not technically or economically viable today. There is also a broad acceptance that ink-jet printing technology is the most practical method for manufacturing multi-color light-emitting polymer based displays, and many display manufacturers (Philips, Samsung, Sieko-Epson, Siemens, etc.) are developing ink-jet based manufacturing methods and equipment. Again, this should result in standardized and commercially available manufacturing equipment using ink-jet dispensing becoming more capable and more generally available in the future, and this equipment is more suitable for, or adaptable to, other rapid prototyping applications than printheads and printers developed for ink deposition.

## 9.10 Conclusion

The capability of ink-jet printing technology to control and dispense a wide range of materials of interest to many applications has been demonstrated. These materials include optical polymers, solders, thermoplastics, light-emitting polymers, biologically active fluids, and precursors for chemical synthesis. In addition to the wide range of suitable materials, the inherently data-driven nature of ink-jet printing technology makes it highly suited for prototyping applications. Using ink-jet based methods, commercialization of products is in progress for DNA microarrays, color displays, electronics assembly, and

photonic elements. In the future, both the number and type of products fabricated using ink-jet technology should increase, and the availability and capabilities of ink-jet based prototyping and production tools should expand.

## 9.11 References

1. Rayleigh J.W.S., (1892). On the instability of a cylinder of viscous liquid under capillary force. *Phil. Mag.* **34**, 145–154.
2. Pimbley W.T., (1984). Drop formation from a liquid jet: a linear one-dimensional analysis considered as a boundary value problem. *IBM Journ. Res. Dev.* **29**, 148–156.
3. Filmore G.L., Buehner W.L. and West D.L., (1984). Drop Charging and deflection in an electrostatic ink jet printer. *IBM Journ. Res. Dev.* **21**, 37–47.
4. Yoo J., Cima M., Sachs E. and Suresh S., (1995). Fabrication and microstructural control of advanced ceramic components by three dimensional printing. *Ceramic Engineering & Science Proceedings* **16**, 5, 755–762.
5. Muntz E.P., Orme M., Pham-Van-Diep G. and Godin R., (1997). An analysis of precision, fly-through solder jet printing for DCA components. *Proceedings, ISHM 97* (Philadelphia), 671–680.
6. Hendricks C., (1982). Inertial confinement fusion targets. *Proceedings of the 2nd International Colloquium on Drops and Bubbles*. NASA-CR-168848, JPL 82-7. 88–93.
7. Hayes D.J., Wallace D.B., VerLee D. and Houseman K., (1989). Apparatus and process for reagent fluid dispensing and printing. U.S. patent 4, 877, 745.
8. Dijkman J.F., (1984). Hydrodynamics of small tubular pumps. *Journ. Fluid Mech.* **139**, 173–191.
9. Adams R.L. and Roy J., (1986). A one dimensional numerical model of a drop-on-demand ink jet. *J. of Appl. Mech.* **53**, 193–197.
10. Pies J.R., Wallace D.B. and Hayes D.J., (1993). High density ink jet printhead. U.S. patent 5, 235, 352.
11. Aden J.S., Bohorquez J.H., Collins D.M., Crook M.D., Garcia A. and Hess U.E., (1994). The third generation hp thermal inkjet printhead. *Hewlett-Packard Journal* **45**, 1, 41–45.
12. Okamoto T., Suzuki T. and Yamamoto N., (2000). Microarray fabrication with covalent attachment of DNA using bubble jet technology. *Nature Biotechnology* Volume **18**, 4, 438–441.
13. Hayes D.J., Wallace D.B., Boldman M.T. and Marusak R.M., Picoliter solder droplet dispensing, *Microcircuits and Electronic Packaging*. **16**, 3, pp. 173–180, 1993. July 23, 2001.
14. Hayes D.J., Cox W.R. and Grove M.E., Microjet printing of polymers and solder for electronics manufacturing, *J. of Electronics Manuf.* **8**, 3&4, pp. 209–216, 1998.
15. Shah V.G. and Hayes D.J., Trimming and Printing of Embedded Resistors Using Demand-Mode Ink-Jet Technology and Conductive Polymer, *Proc., IPC Printed Circuits Expo 2002*, Long Beach, CA, March 24–28, 2002.
16. Burns S., Active-Matrix Displays Made with Ink-Jet-Printed Polymer TFT, *Proc., SID 2003 International Symposium*, Baltimore, MD, May 20–22, 2003.
17. Inkjetted Passive Components on Plastic Substrate for RFID, Redinger D., Farshchi R. and Subramanian V., *2003 IEEE Device Research Conference Conference Digest*, pp. 187–188, 2003.

18. Hayes D.J. and Wallace D.B., Solder Jet Printing: Wafer Bumping and CSP Applications, *Chip Scale Review*, Vol. 2, No. 4, pp. 75–80, September 1998.
19. Hayes D.J., Cox W.R. and Grove M.E., Low-cost display assembly and interconnect using ink-jet printing technology, *Journal of the Society for Information Display*, Vol. 9, No. 1, pp. 9–13, 2001,
20. Miyashita S., Kanbe S., Kobayashi H., Seki S., Kiguchi, H., Morii K., Shimoda T., Friend R.H., Burroughes J.H. and Towns C.R., (1999). Patterning of light-emitting polymers for full color displays by ink-jetting. *Proceedings, The 1999 International Conference on Display Phosphors and Electroluminescence*.
21. Grove M.E., Shah V., Hayes D.J., Bernkopf J. and Shi Y. Color polymeric light emitting diodes fabricated by ink-jet deposition, *SID International Symposium, Digest of Technical Papers*, Vol. 38, No. 2, p. 1044, June, 2001.
22. Haskal E.I., Buechel M., Dijkman J.F., Duineveld P.C., Meulenkaamp E.A., Mutsaers C.A.H.A., Sempel A., Snijder P., Vulto S.I.E., van de Weijer P. and de Winter S.H.P.M., Ink-jet printing of passive-matrix polymer light emitting displays, *Society for Information Display 2002 International Symposium Digest of Technical Papers*, Vol. 32, 2002.
23. Pei Q., *et al.*, Polymer light-emitting electrochemical cells, *Science*, 269(5227):1086–8, 25 August 1995.
24. Grove M., Hayes D., Cox R., Wallace D., Caruso J., Hampden-Smith M., Kodas T., Kunze K., Ludviksson A., Pennino S. and Skamser D., (1999). Color flat panel manufacturing using ink jet technology. *Proceedings, Display Works >99* (San Jose, CA) 131–134.
25. Cox W.R., Hayes D.J., Chen T., Trost H-J., Grove M.E., Hoenigman R.F. and MacFarlane D.L., 1997. Low cost optical interconnects by micro-jet printing. *IMAPS International Journal of Microcircuits & Electronic Packaging* **20**, 2, 89–95.
26. Baukens V., Goulet A., Thienpont H., Veretennicoff I., Cox W.R. and Guan C., (1998). GRIN-lens based optical interconnection systems for planes of photo-emitters and detectors: Microlens arrays improve transmission efficiency. *Proceedings, OSA Diffractive Optics and Micro-Optics Topical Meeting* (Kailua-Kona, HI).
27. Ishii Y., Koike S., Arai Y. and Ando Y. (2000). Hybrid integration of polymer microlens with VCSEL using drop-on-demand technique. In *Optoelectronic Interconnects VII; Photonics and Integration II* (M.R. Feldman, R.L. Li, W.B. Matkin, S. Tan, Ed.) *Proceedings of SPIE* **3952**, 364–374.
28. Daly D., Stevens R.F., Hutley M.C. and Davies N., (1990). The manufacture of microlenses by melting photo-resist. *Measurement Science & Technology* **1**, 759–766.
29. Ishii Y., Koike S., Arai Y. and Ando Y. Hybrid integration of polymer microlens with VCSEL using drop-on-demand technique, *Proceedings of SPIE*, Vol. 3952, pp. 364–374, 2000.
30. Cox W.R., Chen T. and Hayes D.J., Micro-optics fabrication by ink-jet printing, *OSA Optics & Photonics News*, Vol. 12, No. 6, Fig. 3, p. 33, June, 2001.
31. Liu Y., Johnson K. and Hibbs-Brenner M. Chip-scale integration of VCSEL, photodetector, and microlens arrays, *SPIE Proceedings*, Vol. 4652, pp. 11–18, 2002.
32. Hayes D.J., Wallace D.B., VerLee D. and Houseman K. (1989). Apparatus and process for reagent fluid dispensing and printing. U.S. patent 4, 877, 745.
33. Ekins R., (1994). Immunoassay: recent developments and future directions. *Nucl. Med. Biol.* **21**, 3, 495–521.
34. Eichenlaub U., Berger B., Finckh P., Karl J., Hornauer H., Ehrlich-Weinreich G.,

- Weindel K., Lenz H., Sluka P. and Ekins R., (1998). Microspot - A highly integrated ligand binding assay technology. *Proceedings, Second International Conference on Microreaction Technology* (New Orleans, LA), eds, W. Ehrfeld, I.H. Renard and R.S. Wegeng (The American Institute of Chemical Engineers, New York), 134–138.
35. Chee M., Yang R., Hubbell E., Berno A., Huang X.C., Stern D., Winkler J., Lockhart D.J., Morris M.S. and Fodor S.A., Accessing genetic information with high-density DNA arrays, *Science* **274**, pp. 610–614, 1996.
  36. Okamoto T., Suzuki T. and Yamamoto N., Microarray fabrication with covalent attachment of DNA using bubble jet technology. *Nature Biotechnology* **18**, 4, pp. 438–441, 2000.
  37. James P. and Papen R., A new innovation in robotic liquid handling, *Drug Discovery Today* **3**, 9, pp. 429–430, 1998.
  38. Wallace D.B., Microdispensing for combinatorial synthesis, *Proc. COMBI 2001*, The Knowledge Foundation, San Diego, Jan. 28–30, 2001.
  39. Blanchard A.P., Kaiser R.J. and Hood L.E., High density oligonucleotide arrays, *Biosensors and Bioelectronics* **11**, pp. 687–690, 1996.
  40. Brennan T.M., Apparatus for diverse chemical synthesis using two-dimensional array, U.S. patent 6,00,1311, 1999.
  41. Frank R. and Overwin H., Spot synthesis: Epitope analysis with arrays of synthetic peptides prepared on cellulose membranes, *Meth. Mol. Biol.* **66**, pp. 149–169, 1996.
  42. Sloane A.J., Duff J.L., Wilson N.L., Gandhi P.S., Hill C.J., Hopwood F.G., Smith P.E., Thomas M.L., Cole R.A., Packer N.H., Breen E.J., Cooley P.W., Wallace D.B., William K.L. and Gooley A.A., High throughput Peptide mass fingerprinting and protein macroarray analysis using chemical printing strategies. *Mol. Cell. Proteomics*. **1**: 490–9, 2002.
  43. Chung J., Bieri N.R., Ko S., Grigoropoulos C.P. and Poulidakos D., In-tandem deposition and sintering of printed gold nanoparticle inks induced by continuous Gaussian laser irradiation, *Appl. Phys. A* **79**, 1259B1261 (2004).
  44. Bieri N.R., Chung J., Haferl S.E., Poulidakos D. and Grigoropoulos C.P., Microstructuring by printing and laser curing of nanoparticle solutions, *Applied Physics Letters*, Vol. 84, no. 5, February 2, 2004.
  45. Aschheim K., (2000). Gene detection by array. *Nature Biotechnology* **18**, 1129.
  46. Fodor S.P.A., Read J.L., Pirrung M.C., Stryer L., Tsai Lu A. and Solas D., (1991). Light-directed, spatially addressable parallel chemical synthesis. *Science* **251**, 767–773.
  47. (1999). Philips readies the lines for LEP-based display. *Electronics Times* June 29 issue.

---

A AJDARI and P TABELING, Ecole Supérieure de  
Physique et de Chimie Industrielles, France

## 10.1 Introduction

Microfluidics is about flows of liquids and gases, single or multiphase, through microdevices fabricated by MEMS (i.e. micro electromechanical systems) technology, using hard (silicon or glass) or soft (plastic or elastomer) materials. Microfluidics is fostered by exciting applications, representing important industrial challenges. It also embraces a number of fundamental issues, interesting in their own right: examples are the identification of the boundary conditions in microchannel flows (Tretheway 2002, Joseph 2004), the description of patterns arising in multiphase microflows (Thorsen 2001, Anna 2003, Dreyfus 2003), the behaviour of single molecules in Microsystems [Smith 1999], or the flow of liquids through nanochannels (Giordano 2001). Microfluidics has grown recently, stimulated by progress made on ‘lab-on-a-chip’ devices, i.e., systems able to perform all sorts of chemical and biological analyses in a short time on a chip (Reyes 2002, Beebe 2002, Tabeling 2003). For the future, it is possible to speculate that lab-on-a-chip will increase in complexity, following a trend comparable to that of microelectronic devices. This would lead to systems difficult to imagine today, performing tasks perhaps similar to those achieved in sophisticated natural systems.

Microfluidics represents a major field of application for a number of technologies described in this book. In the present chapter, we concentrate on two aspects which may play an important role for the development of microfluidics over the next few years; the first is actuation and the second patterning. In the lab-on-a-chip of the future, flows will be handled at the microscale through mazes of microchannels. To reach such a level of complexity, it will be crucial to integrate actuators on the chip, since it is hard to conceive that a large number of independent fluid-handling operations could be performed by changing just one or two parameters on external devices. In the meantime, there is a need to increase the functionalities of the surfaces containing the working fluids, whether encapsulated in drops, or simply confined by micro-channel walls. Here we take a particular perspective,

emphasizing the new capabilities surface patterning may provide on the chip; pumping, mixing, sorting, drop handling, etc.

The chapter is thus naturally divided into two parts: The first describes the applications of actuators on the chip, and the second surface patterning. The first part is dedicated to PDMS technology. Actuators made in hard materials have been reported (Maillefer 2001), but their complexity is such that they offer little promise for easy integration on lab-on-a-chip devices. In contrast, PDMS actuators have been shown to be extremely well adapted to integration (this is perhaps the main virtue of PDMS). Since the pioneering work on the subject (Unger 2000, Scherrer 2000), a number of groups have succeeded in developing applications in different directions, and one objective of this chapter is to offer a tentative review of this approach. This part, completed by that related to surface patterning, may represent an updated illustration of microfluidic devices representing applications for a number of technologies described in this book.

## 10.2 PDMS actuators and microfluidics

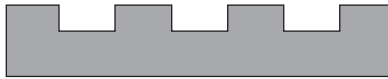
### 10.2.1 PDMS technology

PDMS is a family of polymers of general formula  $-\text{Si}(\text{CH}_3)_2\text{O}-$ ; brought above the reticulation temperature and in the presence of a curing agent, these polymers form elastomers. The main properties of these elastomers are listed in Table 10.1. PDMS is a convenient material for microfluidics (Kim 1995). Microchannels can be rapidly made in this material by using the technique of moulding replication. The microfabrication technique includes three steps, described in Fig. 10.1. One first uses a mould made in hard material (silicon, glass, metal) or in polymer. The fabrication of the mould may require a clean-room environment. The other operations can be done in a room where the temperature and the hygrometry are roughly controlled.

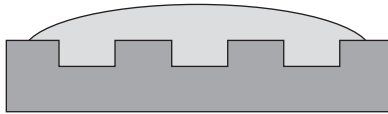
As sketched in Fig. 10.1, the mixture – composed of the PDMS material and a curing agent – is poured into a mould. The system is then heated at a

*Table 10.1* Some physical and chemical properties of PDMS

Properties	Characteristics
Density	Around 0.9
Optical	Transparent, between 300 nm and 2200 nm
Electrical	Insulator, with an electric field breakdown 20 kV/cm
Thermal	Insulator, with thermal conductivity around 0.2 W/m/K
Interfacial	Low surface energy (~20 mN/m)
Permeability	Permeable to gas and organic apolar solvent, low permeability to water
Reactivity	Inert, oxydable by plasma
Toxicity	Non-toxic



1. Fabrication of mould



2. Reticulation



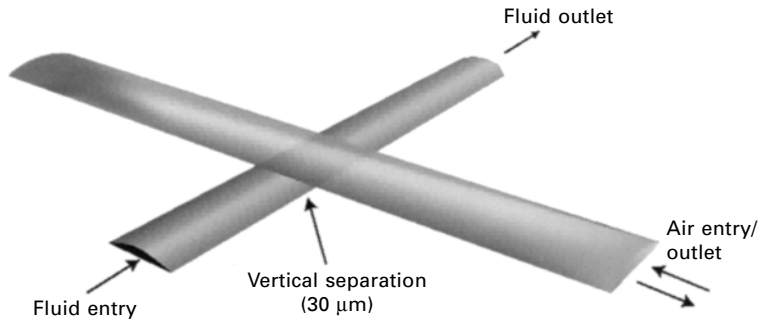
3. Separation

**10.1** Technique of fabrication of a PDMS device. Several steps are needed; a mixture of PDMS and curing agent is poured into a mould. After curing, it is separated from the mould to form the PDMS device.

moderately high temperature (around 70 °C). In this step, the PDMS reticulates, and the mixture becomes solid. After demoulding, one obtains an object that represents the negative of the mould. The accuracy of the structure realized in this way is surprisingly good. Whitesides group has shown that it is possible to obtain structures (posts, grooves, etc.) with a sub-micrometric precision (Kim 1995). One nonetheless currently considers that appropriate sizes of the PDMS microchannels range between 5 and 500  $\mu\text{m}$  because of the elastomeric character of the material and ageing effects. One may outline some characteristics of PDMS relevant to microfluidics:

- Transparency in the visible spectrum allows the visualization of flows.
- The Young modulus of PDMS considerably varies with the ratio curing agent/PDMS.
- The elastomeric properties of PDMS are extremely interesting for the realization of integrated valves and pumps.
- Untreated PDMS is hydrophobic. It becomes hydrophilic after oxidation of the surface by an oxygen plasma, or after immersion in NaOH. Oxidized PDMS adheres well to itself, to glass, silicon, polyethylene, provided that the surfaces have been subjected to plasma oxidation.
- Permeability to gas facilitates the filling of the channels; the permeability to organic solvents is an obstacle for using PDMS in a number of biological or analytical chemistry applications.
- The low surface energy of PDMS is interesting because this facilitates the demoulding.
- The properties of PDMS are not stationary. They continuously evolve in time. PDMS is a generous material, but it is less reliable than glass or silicon.

The method of fabrication of integrated PDMS valves has been described in Unger 2000. It is schematically shown in Fig. 10.2. One uses two moulds, of parallelepiped shapes, forming two channels, placed perpendicularly with respect to the other. One is the working channel (along with the working fluid flows) and the other is the actuation channel. One is on top of the other, and a thin PDMS membrane, located at the intersection, separates both. To close the valve, one pressurizes the actuation channel. The pressure forces distort the membrane separating the working from the actuation channel, thus closing the working channel. The use of a pressure source coupled to electrovalves, monitored by some device, is necessary for imposing pressurization and depressurization cycles. A micro-pump is obtained by putting three valves in series (Scherrer 2000). The opening and closing of the valves follows a peristaltic cycle, suitable to obtain a mean velocity along the working channel.



10.2 Schematic view of a PDMS valve (Scherrer 2000).

## 10.2.2 Application of PDMS actuation technology to microfluidics

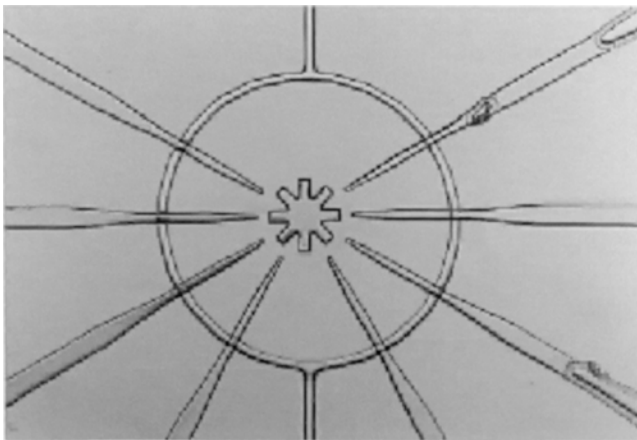
### *Flow switching*

Cell sorting has been reviewed in this book (Ch. 11) and in order to avoid duplication, we shall be brief. Cell sorting was one of the very first applications illustrating the advantage of using PDMS integrated valves. In the work reported in Fu (1999), cell sorting was achieved by using a microfluidic system consisting of a T channel whose arms are equipped with two PDMS micro-valves. The systems to sort consisted of fluorescent and non-fluorescent cells. A video camera equipped with appropriate filters captured the image of the system in real time. Depending on whether the cell is fluorescent or not, the right or left valve was opened, directing the flow to the right or the left part of the system. In this way, fluorescent and non-fluorescent cells could be sorted. For further detail, the reader may refer to Chapter 11.

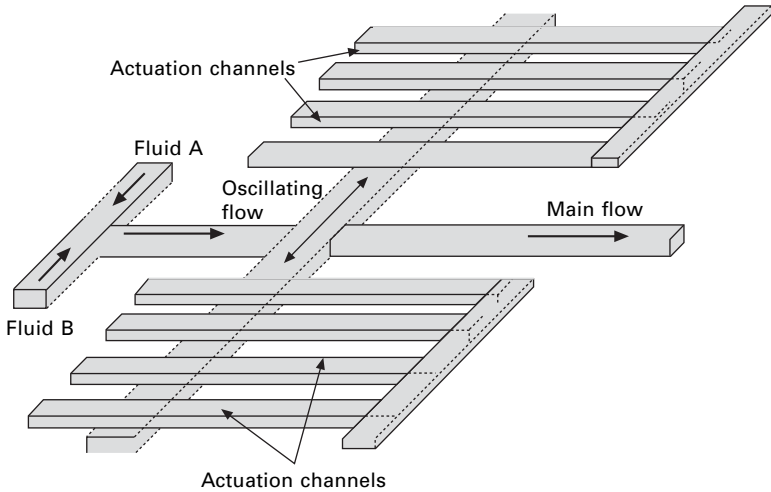
*Mixing and extracting*

Mixing is problematic in microfluidic systems because flows are laminar; if no dedicated flow pattern is imposed, mixing relies on molecular diffusion which is too slow a process for the majority of applications. This issue was recognized by the community, and a number of groups have developed methods to mix efficiently in microsystems over the last ten years. Using PDMS microactuators in this context has led to the realization of efficient micromixers (Chou 2001, Dodge 2004), whose remarkable versatility has recently been underlined (Dodge 2004). In Chou (2001), the micromixer is a circular channel, actuated by a peristaltic pump, made of eight valves in series (see Fig. 10.3). The flow rotates under the action of valves (located in a second layer, placed normally to the ring), actuated in a peristaltic way. Mixing is the result of Taylor-Aris dispersion (Tabeling 2003). The process is completed after a few turnover times, i.e., typically fractions of seconds. The circular mixer operates well in a batch mode. It represents an elementary brick currently used in PDMS lab-on-a-chip developed by Caltech, Fluidigm or others. Examples will be given later in this Chapter.

The second example is a cross-channel flow, composed of a main channel where two streams flow side by side (Dodge 2004, Tabeling 2004) A series of ten integrated PDMS valves are disposed in a comb-shaped fashion onto two channel branches perpendicular to the main flow (see Fig. 10.4). As the comb-disposed valves close on one branch, they create a displacement of fluid at the channel intersection located at the centre of the device. Releasing the pressure applied to one comb and applying pressure on the other comb



**10.3** Micromixer made in PDMS, using MSL technology. The mixing takes place in the ring; the flow rotates under the action of valves (normal to the ring), actuated in a peristaltic mode. Mixing is the result of Taylor-Aris dispersion.



10.4 Scheme of the chaotic micromixer, using PDMS valves to generate the transverse perturbation to the mean stream (Dodge 2004).

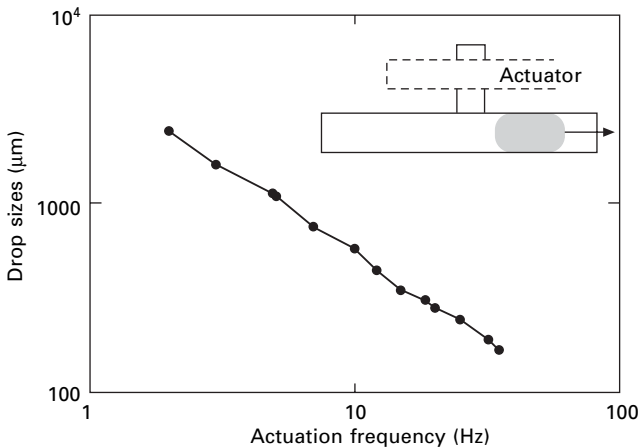
creates a flow in the opposite direction. In this way, one obtains an oscillating flow with prescribed frequency and amplitude at the cross-channel intersection. Theory predicts that, for a certain range of parameters, chaotic mixing is achieved in this system, while, under some ‘resonance’ conditions, a transient, reversible elongation of the interface is obtained (Okkels 2004). The two effects could be demonstrated experimentally by using actuators, as represented in Fig. 10.3 (Dodge 2004). This situation was further exploited to realize an efficient, tunable, particle extraction/chaotic mixer microfluidic device, achieving a versatility well beyond the reach of ordinary fluidic systems (Dodge 2004).

#### *Drop size control in multiphase flows*

The study of liquid-liquid flows in PDMS microsystems has expanded in the last two years. Although most of the studies could have been done in hard material, PDMS technology has played a role in the subject by accelerating the analysis of different geometries, for a problem where geometry plays a crucial role. The very first PDMS studies of two phase flows (Quake) showed that oil/water systems flowing in a microchannel display an unexpectedly rich variety of patterns. The system was a T-junction, where water and hexadecane meet, to form drops. Just downstream from the drop formation region, the channel widens. Thorsen (2001) found that in a range of pressure conditions, several interesting patterns can be obtained, such as isolated drops and pearl-necklace structures. One year later, Anna (2003) investigated

a hydrodynamic focusing type geometry still with water and hexadecane as the working fluid. A number of different states were obtained; single drops, crystals of drops, disordered states. The intrusion of PDMS actuators in this field is more recent. H. Willaime (2005) used an actuator to control the sizes of drops forming in a PDMS T-Channel.

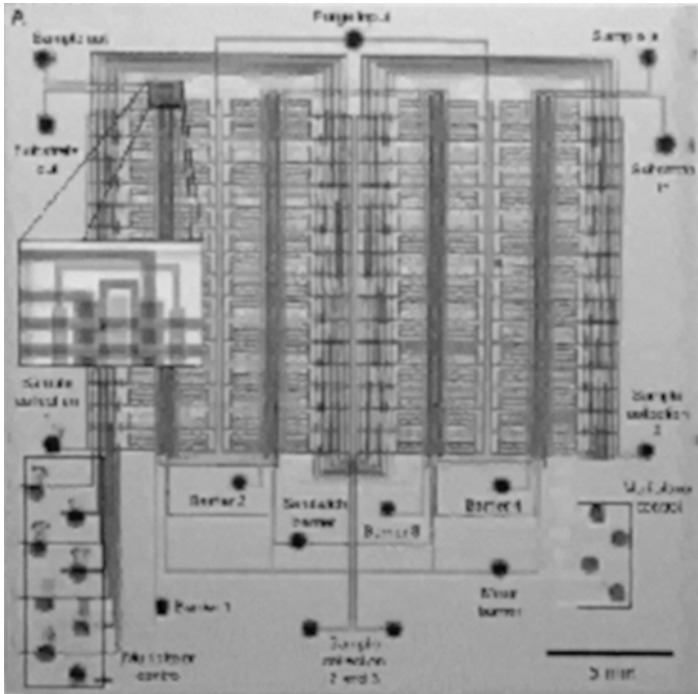
The drops are formed at the intersection of a main and a side channel, sketched in the upper right corner of Fig. 10.5. Their sizes can be varied by one order of magnitude by changing the actuation frequency, without modifying the flow-rates. This is shown in Fig 10.5. Note that the emission frequency of the drop is controlled by the actuator. Recently, H. Willaime revealed the presence of Arnold tongues as the coupling between the actuator and the natural instability leading to drop formation is decreased.



10.5 Evolution of the drop size with actuation frequency in a PDMS system perturbed by a membrane placed close to the drop formation region (the intersection between the side and the main channels).

### *Fluid handling in large integrated microfluidic devices*

It was shown recently that soft lithography allows the realization of large-scale integrated systems, evoking the systems made in the microelectronic industry. The system reported by Thorsen (2002) integrated hundreds of valves on a chip as shown in Fig. 10.6. Each valve connects two wells, filled with two different reagents; by opening the valves, the reagents mix diffusively and develop a chemical reaction or quench a physical process. Filling the whole system without being subjected to the ‘tyranny of large numbers’ is successfully achieved by using a multiplexer unit. The microfluidic platform was used for protein crystallization, a critical step in biology research preceding the determination of protein functionality. It was reported that a number of



10.6 Crystalliser using a large number of chambers, spanning a wide range of conditions leading to crystal formation.

proteins, reputedly hard to crystallize, could be successfully crystallized by using this system.

### *Complex lab-on-a-chip*

At the moment, the most sophisticated lab-on-a-chip devices are made in PDMS; the reason is that this material allows the exploitation of MSL technology for convenient integration of valves and pumps. A first example of a PDMS evolved lab-on-a-chip device was reported in 2002 at Caltech; it was dedicated to DNA analysis. Here we concentrate on a more recent example, dedicated to the preparation of proteic samples, prior to MS analysis (Brunet 2004).

The device combined electro-osmotic pumping with mechanical trapping and pumping. After electrophoretic separation on chip, the selection of the protein of interest is performed by closing integrated trapping valves. A series of three integrated valves activated in series in a peristaltic pump fashion is used to mechanically pump the selected protein into a rotary microreactor, the reactor already containing a solution of trypsin. The enzyme digests the selected protein when full mixing of protein with enzyme is

achieved. Extraction of peptides from the device is performed using a PEEK capillary spotting onto a MALDI target before addition of crystallization matrix. Total analysis time from sample injection to MALDI-TOF analysis is 20 minutes. This represents a gain of one order of magnitude in time compared to the traditional approach. The main problem of such a lab-on-a-chip is not the flow control (remarkably well achieved by using integrated actuators), but the interaction PDMS-proteins. Protein adsorption is typically strong with PDMS, and that is obviously a difficulty when this material is used for proteomic purposes. At the moment, there is no simple surface treatment which may overcome unwanted adsorption for all proteins of interest.

## 10.3 Nanopatterning for microfluidics

### 10.3.1 Small scale patterning within microchannels for flow control

In most situations microfluidic devices consist of 2D networks of microchannels, the length of which is in the mm to cm range, whereas the transverse dimensions are more commonly tens or hundreds of microns. Getting fluids to flow in such small channels is usually achieved by applying a difference of pressure or of electric potential between the ends of the channel generating respectively pressure-driven flow and electro-osmotic flow (EOF) – see, e.g., Stone (2004). Typical velocities achieved run from a few microns/second to cm/s. With these numbers, the hydrodynamic description of the flow lies definitely in the low Reynolds number regime: inertial effects are negligible compared to viscous forces. In this realm the flow velocities are proportional to the driving forces that generate them (pressure drop or electric field), and the flow is laminar (turbulence is absent).

A consequence of this last point is that the flow lines in the channel are parallel to one another and to the channel axis if its section and surface properties are constant. This provides on the one hand the possibility to control and predict the flow pattern, but on the other hand imposes serious limitations on the set of flow geometries achievable, and makes a few things difficult; mixing can become a problem, and relatedly, getting flow streams to cross each other in the usual 2D layout of most microfluidic systems seems a priori impossible.

The general idea explored in this section is the following: for given driving forces, the surfaces usually affect the flow inasmuch as they impose the boundary conditions, so in principle introducing modulations in topography, surface charge or chemical composition on the surface of a channel induces a related modulation of the boundary conditions, and consequently generates features in the flow pattern. The resulting flow patterns should reflect to some extent the features of the surface pattern, wave-length, symmetry, and complexity.

We briefly review here recent studies exploring this strategy. They correspond in most cases to rather simple model geometries, which are sometimes easy to fabricate, but more importantly demonstrate in a clear way the potential power of the method. A few direct applications will also be quoted along the way: mixing, pumping, valving, etc. Practically, we start by recalling the usual description of pressure-driven and electro-osmotic flows in non-patterned microchannels. We then provide a few brief comments about the patterning of the channel walls, before successively examining the influence on the flow of topographic patterns, of surface-charge patterns, and of chemical patterns. We end with a short conclusion pointing out closely related issues.

### 10.3.2 Standard flows

Flows in microchannels can be described by a momentum conservation law which expresses the balance between pressure and viscous forces. The pressure locally adjusts so as to respect the actual incompressibility of the liquid. This results in the following set of two equations:

$$\begin{aligned} -\vec{\nabla} p + \eta \Delta \vec{v} &= \vec{0} \\ \vec{\nabla} \cdot \vec{v} &= 0 \end{aligned} \quad 10.1$$

where  $\eta$  is the viscosity of the liquid.

For pressure-driven flows in microchannels, the driving is imposed by a pressure difference applied between the ends of the channel. This results in a net force on the fluid, that is transmitted to the channel walls by viscous friction. It is common to describe this liquid-wall coupling by a simple no-slip boundary condition on the walls<sup>1</sup>:

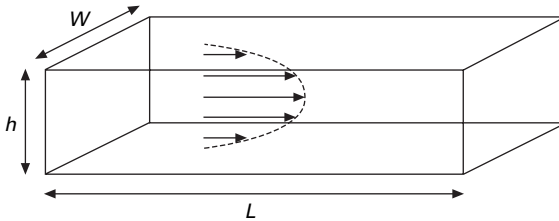
$$\vec{v}|_{\text{wall}} = \vec{0} \quad 10.2$$

For a channel of constant cross-section, the flow then has a so-called Poiseuille profile, with flow lines all parallel to the channel axis, and a velocity profile essentially parabolic in the shortest cross-dimension of the channel (Fig. 10.7). The appreciable difference of velocities between the centre and the sides of the channel leads to hydrodynamic dispersion which can be detrimental for the transport of plugs of solutes in microchannels.

For electro-osmotic flows, a difference of electrostatic potential is applied to the ends of a channel filled with an electrolyte solution. The primary outcome is a simple electric current through the channel as described by

---

<sup>1</sup>The question of the precise conditions of validity of this no-slip boundary condition for specially clean and engineered surfaces is a topic that has recently been revived by experimental studies. However, for most practical applications it seems perfectly suitable.



10.7 Schematic description of the velocity profile in a microchannel for a pressure-driven flow. The velocity is zero on the walls and maximal in the centre. All flow lines are parallel to the channel axis.

Ohm's law. A secondary outcome is a net flow, the electro-osmotic flow (EOF) which occurs if the channel walls are charged. Indeed in such cases, the charge in the electrolyte solution is non-zero in a thin (nanometer thick) region close to the surface, as a result of a balance between the translational entropy of the ions and electrostatic effects. As a consequence the applied field  $\vec{E}$  induces a force on these non-neutral thin fluid layers. The result is that an effective velocity difference is established between the walls and the fluid outside this thin layer. The bulk of the fluid is neutral and is thus not affected by the electric field, so that the Stokes equation 10.1 applies. On a larger scale, the image is such that the fluid slips past the surface at a velocity that in simple cases is proportional to the surface potential  $\zeta$ , and to the local tangent electric field, so that the boundary condition reads<sup>2</sup>:

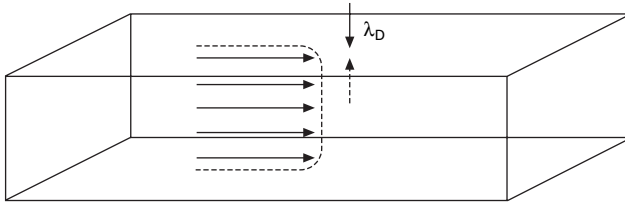
$$\vec{v}|_{\text{wall}} = \mu_{\text{EO}} \vec{E} \quad 10.3$$

with the electro-osmotic mobility  $\mu_{\text{EO}} = -\epsilon\zeta/\eta$  according to the Smoluchowski formula ( $\epsilon$  is the dielectric permittivity of the solvent).

In a channel of constant cross-section and surface potential (see Fig. 10.8), the electric field  $\vec{E}$  is constant and the velocity profile is a plug-flow with again all the field lines parallel to the channel axis, but here with the velocity constant everywhere:  $\vec{v} = \mu_{\text{EO}} \vec{E}$ . There is ideally no hydrodynamic dispersion in this case. This picture holds if there is no pressure difference between the ends of the channel, letting the electrically generated flow exit freely. If such is not the case, then a pressure drops builds up along the channel, so that the total flow is the sum of the plug flow and of a parabolic flow, which restores hydrodynamic dispersion.

Both pressure-driven flow and EOF are widely used in micro-channels, each having their advantages and drawbacks (see e.g. Gitlin (2003) for a

<sup>2</sup>The precise description of this electrohydrodynamic coupling is still a matter of scientific research. The simple scheme used here whereby the slip velocity is simply proportional to the surface potential and to the local electric field is however a rather robust way to get a first-order description of the hydrodynamic effects generated.



**10.8** Schematic representation of electro-osmotic flow (EOF) in a channel of homogeneous surface charge. An electric field along the channel induces shear forces in the liquid only in the very thin charged layers close to the walls (thickness  $\lambda_D$  of a few nanometres). The bulk is not sheared, and flows as a plug 'slipping' on the walls.

summary). As previously mentioned a shared point is the laminarity of the flow and the fact that the flow lines are simply parallel to the axis of the channel. Another important point is that (as long as we consider features larger than the thickness of the charged layer  $\lambda_D$ ), there is no intrinsic length scale in our discussion so far. So many concepts will apply independent of the dimensions, provided that the geometrical ratios of lengths are conserved.

### 10.3.3 Patterning surfaces

We are going to consider situations where one (or a few) of the walls of the channel is (are) patterned, in the sense that it bears a surface pattern with features smaller than the channel lateral dimensions, and therefore typically from a few tens of nanometres to a few tens of microns. The pattern can consist in modulations of the topography, of the surface charge, or of the surface chemistry (and in particular hydrophobicity).

These patterns can be generated at different stages of the fabrication of a microchannel, which is often (but not always) assembled by bonding a flat cover (the ceiling) on an open structure bearing the floor and lateral walls of the channel:

1. The pattern can be realized during the fabrication of the channel. For example, steps can be added to the lithographic process yielding a resin master that will be used to mould channels in PDMS with built-in topological corrugations. (see e.g. Stroock 2002a, b). Various materials can also be deposited through masks at intermediate steps of microfabrication.
2. They can be implemented in the channel after fabrication but before sealing; laser ablation allows the drawing of topological features in plastic microsystems, and under controlled atmosphere the modification locally of surface chemistry and charge (Pugmire 2002), nano-imprint allows the chemical patterning of a glass surface before a channel is realized by bonding it to a piece of moulded PDMS (Whitesides 2001).

3. The pattern can in some cases be realized after the channel has been sealed! For example, one can take advantage of the laminarity of flows to adsorb on specific areas species that are brought there by flowing a solution in the channel. The pattern of chemical composition and charges obtained in such processes consists mostly of domains oriented along the channel axis (Zhao 2001, Kenis 1999, Stroock 2000, Barker 2000, Locascio 2000).

We will not detail here any further patterning methods, and turn to the consequences on the flow geometry inside the channel. Note however that in most cases it is relatively easy to pattern only one of the surfaces of the channel, say the floor or the ceiling, leaving the remaining boundaries flat and featureless. We will consequently focus on this practically relevant situation, rather than exploring exotic things that could be achieved by patterning all walls. In most of the situations explored below the gain in ease of fabrication by far exceeds the loss in performance.

#### 10.3.4 Patterning topography

As the simplest example of topographic patterning let us consider a surface with parallel sinusoidal grooves. For sake of preciseness, we describe the surface location by its height  $z(x, y) = h_0 \cos(qx)$  over a reference plane  $z = 0$ . We then study the flow generated by a pressure drop in a slab consisting of a flat top a distance  $h$  above the sinusoidal floor, and compare it to the case of two flat walls (formally  $h_0 = 0$ ). We focus here on the case where the characteristics of the pattern (height  $h_0$  and wavelength  $2\pi/q$ ) are smaller than the channel thickness  $h$ . Thanks to the linearity of the equations describing fluid motion, the flow then can be obtained as the sum of the parabolic flow one would obtain with flat walls, and corrections due to the patterns on the surface.

If the pressure is applied along  $x$  (perpendicular to the grooves), these additional flow features consist in (i) periodic recirculations localized in the vicinity of the patterned surface (with wavelengths that are integer fractions of the wavelength of the pattern), plus (ii) a net shear flow emanating from the surface that goes against the drive. As a consequence of the Laplacian mathematical nature of the hydrodynamic equations the periodic structures (i) extend only roughly a wavelength away from the surface. However, the net shear term (ii) extends throughout the channel. As a result the hydrodynamic resistance of the slab increases. This effect is proportional to  $(h_0/h)^2$ .

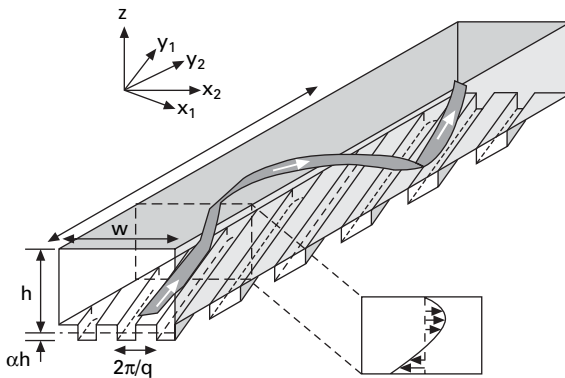
If the pressure is applied perpendicular to  $x$  (along the grooves), the additive corrections to the parabolic flow again consist in (i) periodic features in the vicinity of the bottom patterned surface, and (ii) a net shear flow resisting the driving. This effect is also proportional to  $(h_0/h)^2$  but with a different (weaker) prefactor!

As a consequence, if the pressure gradient is applied at some angle to the grooves, in addition to the parabolic flow along this pressure gradient, there is a net shear flow sideways from this driving, corresponding to the flow turning in the vicinity of the patterned surface towards the ‘easy axis’, i.e., along the grooves! The anisotropy of the surface pattern induces a net transverse hydrodynamic response (i.e. perpendicular to the grooves).

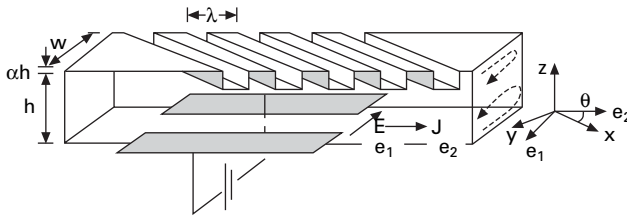
The simplest yet important application of this analysis, is the case of a regular microchannel with a floor bearing topographic modulations (grooves) at an angle with the channel axis. Upon application of a pressure difference at its ends, a 3D helical flow is generated (Fig. 10.9) instead of the simple Poiseuille profile of Fig. 10.7: close to the floor the fluid tends to slide sideways along the grooves, but the lateral wall imposes a transverse recirculation by the build up of a pressure gradient perpendicular to the channel! We recall here that the flow pattern (the geometry of the flow lines) does not depend on the strength of the driving (the applied pressure gradient), only the magnitude of the velocities along the flow lines does. More importantly, this effect is unaffected by the downsizing of the dimensions, as long as the ratios of the various lengths are kept constant.

This simple surface pattern thus induces some stirring in the microchannel and flow lines that wind periodically from one lateral wall of the channel to the other, allowing for example a fluidic ‘crossing’ of the flow lines in the plane of the microsystem, something topologically impossible with 2D networks of channels and simple Poiseuille flow (Stroock 2002b).

More importantly, tailoring the flow in a 3-dimensional way using 2D surface patterns opens up a large toolbox for flow design. For example, a



**10.9** Pressure-driven flow in a channel bearing a topographic pattern of oblique grooves on one wall. Close to this wall, the flow tends to orient along the grooves leading to a lateral motion to the left wall, transverse recirculation then occurs in the middle of the channel (see the schematic representation of the transverse flow in a cross-section). The overall resulting flow pattern consists of helical flow lines, one of which is schematically depicted.



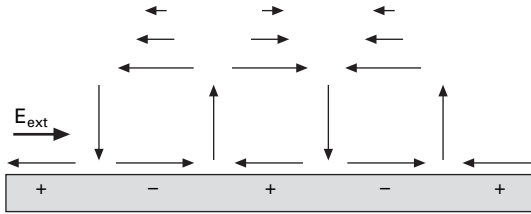
10.10 Scheme of a transverse electro-osmotic pump that uses the same pattern of oblique grooves in Fig. 10.3. An electric field  $E$  applied between the two lateral flat electrodes generates, thanks to the pattern, a net flow  $J$  along the channel axis (Gitlin 2003).

pattern of alternating chevrons on the floor of the channel induces a succession of pairs of counter-rotating helical flow motifs that result in an exponential intermingling of the flow lines along the channel. This permits an efficient ('chaotic') mixing of the fluids in the channel as they flow downstream upon the simple application of a pressure drop, as has been experimentally demonstrated in (Stroock 2002a). Such a passive mixer, with patterns on a single wall, can easily be integrated in a microfluidic system. Channels bearing grooves can also be of interest for electrokinetic effects. The point is that the anisotropy of the pattern induces not only transverse electrical effects (anisotropic conductance) but also transverse electrokinetic effects (coupling of electrical and hydrodynamic effects in perpendicular directions). For example, consider a channel a section of which has a rifled floor channel as in Fig. 10.9, and a homogeneous constant surface charge density. An applied pressure drop between the ends of this channel generates in that section not only a helical flow as described previously but also a net difference of electric potential between the two side walls (transverse streaming potential) that can be used to measure the flow rate in the channel (Ajdari 2002). Conversely, a new possibility for the electro-osmotic generation of flow appears (Fig. 10.10): an electric field applied between the two side walls (by means of embedded electrodes) in the patterned section will induce an electro-osmotic flow along the channel axis. Such a 'transverse electro-osmosis' can be used to realize integrated low-voltage micropumps that allow one to tune locally the flow rate in microfluidic networks, instead of only applying potential differences between the few outlets of the network. Potentialities and limitations are discussed in Gitlin (2003).

### 10.3.5 Patterning surface charges

Patterning of the surface charge can also affect the flow in a microchannel, essentially in the case of electrically driven EOF flows.<sup>2</sup> Here the simplest

<sup>2</sup>Actually this can affect also pressure-driven flows in the case of strong surface charges and low conductivity electrolytes by so-called electro-viscous effects that we will not discuss further here.



**10.11** An electric field applied to the electrolyte solution along a charge-modulated surface induces an effective slip of alternating directions (arrows close to the surface). Mass conservation then imposes recirculation rolls and local pressure gradients that are described by the hydrodynamic eqns 10.1.

model geometry corresponds to a pattern of parallel stripes on the surface resulting in a modulated surface charge density  $\sigma = \sigma_0 \cos(qx)$ . This directly induces a modulation of the electro-osmotic mobility  $\mu_{EO} = \mu_0 \cos(qx)$  that controls the boundary condition for the velocity in EOF (eqn (10.3)). For this geometry (Fig. 10.11), if an electric field is applied along  $x$ , a set of rolls is generated in the vicinity of the surface (again their extension away from the surface is comparable to the wavelength  $2\pi/q$  of the pattern). If the field is applied in the perpendicular direction a set of rows of alternating direction is generated, again only in the vicinity of the surface. It was indeed demonstrated in a microfluidic format that putting stripe motifs on the floor perpendicular or parallel to the axis of a microchannel generates recirculating rolls in the former case, and flows in opposite directions (as in a freeway) in the second case (Stroock 2000; Barker 2000). Here again surface patterns translate into flow patterns. More complex patterns can be envisaged theoretically (Erickson 2002; Ajdari 2002) and realized experimentally.

An important remark is that in many microsystems where electrophoresis is performed, undesired patterns of surface charge form as defects, e.g., due to adsorption of charged species. These will also induce rolls that can induce important dispersion effects of solutes transported in the channel (Anderson 1985; Long 1999).

An interesting application of flow design using surface charges concerns EOF in turning channels, a practically important question for electrophoresis devices. Indeed, a way to store important channel lengths (sometimes necessary for separation purposes) on chips of limited surface area is to use spiral or zigzag microchannels. The numerous resulting turns can, however, have a detrimental effect; the electric field is a turn weaker in the outer part of the channel, whereas the travel distance along flow lines is longer. The outcome is that the fluid at the outside takes more time to go around the turn by electro-osmosis than the fluid at the inside, which results in an important

dispersion of transported solutes to be separated. A possible way to deal with this is to increase the surface charge on the outer side of the channel (e.g. by laser-induced modification (Johnson 2001), so as to increase the electro-osmotic velocity there.

In the study of the model stripe geometry above, the main difference with the topographic patterning described in the previous paragraph is that there is in a linear picture no net effect equivalent to the anisotropic net resistive shear. Such net effects (that concern the whole channel and not only the vicinity of the patterned surface) are recovered if the topography is also modulated, and strong transverse effects can arise if the charge and topography modulations are correlated (Ajdari 1995). For example, an electro-osmotically generated helical flow in the whole channel can result from a short wavelength modulation on the bottom surface (at a finite angle to the channel axis). Patterns of a few diagonal grooves achieved with laser ablation that modify topography and likely surface properties have also been shown to significantly improve mixing in a microchannel after a junction (Johnson 2002).

### 10.3.6 Patterning chemistry and wettability

It is also possible to pattern the surface chemistry of one or some of the microchannel walls, often by deposition, adsorption or ablation. In general, such a modification on a flat wall will not modify the behaviour of the flow in a completely filled channel, as the chemistry does not show up in the boundary conditions, but for the effect of surface charge previously described. The difference in surface energy between the different wet part of the channels cannot lead to surface-tension-driven Marangoni flows because the walls are rigid.

As a note here we point out that for model surfaces, there are debates in the scientific community as to the range of applicability of the no-slip boundary condition, in particular when the surface is 'liquidophobic'. In some cases it may be appropriate to account for a non-zero slip, that will be modulated in the case of a chemically patterned surface, which potentially could induce recirculation effects and shifts of the global flow (see (Cottin-Bizonne 2004) and Lauga 2003).

The main way that chemical patterns can affect the flow concerns multiphase flows when the channel is not filled completely with a single fluid phase. For example, during the filling of the channel, the fluid pushes a gas phase (air). Similarly, two liquid phases can be coflowing in a channel, for example, so as to induce chemical exchange between the two phases (Kitamori). In such a context chemical patterns can act on the interface between the phases (triple line).

The best-known example is the so-called hydrophobic valve (Handique

1997), whereby a stripe of hydrophobic surface is patterned in an otherwise hydrophilic microchannel. Such a channel can be filled up spontaneously by capillarity until the front meniscus reaches the stripe, where it is arrested if the hydrophobicity is strong enough (allowing, for example, a precise metering of the liquid). An additional applied pressure (value dictated by simple capillarity considerations) is then required to force the fluid over the valve, a non-linearity which permits flow control. As previously stated, after it has been covered by the liquid, the hydrophobic stripe ceases to affect the flow. This scheme allows the fluid to invade in controlled sequences different stages of the microfluidic network corresponding to different operations. This is at the base of CD microfluidics where the microchannels are drawn on a CD and its rotation at increasing speeds provides the drive to overcome the hydrophobic valves.

A related version consists in having chemical patterns along the axis of the channel (the patterning can then sometimes be achieved microfluidically (Zhao 2001)). Suppose, for example, that the central third of the channel is hydrophilically coated, whereas the rest is hydrophobic. Then upon application of weak drivers, water only wets the hydrophilic centre, and thus flows only through the central third of the channel, as if limited on the sides by virtual (capillary) walls. If a stronger pressure is applied, the capillary effects are overcome and the whole channel can be accessed, as well as its lateral confluent. Again this allows dynamic control of the part of the network used at a given time. Further, patterns with features combining topography and surface chemistry can be of great use to guide and stabilize (by pinning on the wall of the triple line) the interface between two coflowing liquid phases for example in phase extraction processes.

Eventually the combination of hydrophobic surface properties with sharp nanometer scale topographic patterns (forest of pillars, or 'nanograss') seems to be a way to keep water away from the wall by a kind of 'fakir' effect. This can result in an effective physical slip of liquid on such a surface, with the corresponding reduction of hydrodynamic friction (Cottin-Bizonne 2003; Krupenkin 2004).

### 10.3.7 Miscellaneous remarks

We have focused here on ways whereby patterns on one or more of the walls of a microchannel can affect the geometry and characteristics of the flow in such a channel. The general message is that 2D patterns 'drawn' on the surface allow the design of three-dimensional flows with various functional consequences. Although we have focused mostly on very simple geometrical patterns, these ideas can be readily extended to any surface pattern, which permits in principle the generation of a whole variety of flow geometries. One example already quoted is the chaotic mixer of Stroock (2002a), but

many others may be of interest. It is actually possible with the analytical tools in the references given in this chapter to anticipate semi-quantitatively (possibly numerically) the flow pattern that will result from a given surface pattern, and thus to optimize the surface pattern for a given task before fabricating anything (see e.g. Ottino (2004) for chaotic mixing).

Given the focus in this book on small-scale patterns, we have left aside modifications of the shape of the channel itself which also can affect the flow geometry and properties; zigzag channels to induce mixing in two-phase flows with droplets (Song 2003), channels of varying cross-sections to induce recirculation patterns (Lauga 2004) and special shapes for turns in EOF flows (Molmo *et al.*, 2001). We have also left aside the possibility opened by depositing arrays of microelectrodes of various geometries which can be used to generate arrays of flows; in multiphase flows by electrically generated heating or dielectric effects (this last part in particular concerns many interesting devices allowing the motion of drops on surfaces, such as so called EWOD devices) and in monophasic electrolyte solutions by AC electro-osmotic effects taking advantage of the symmetry of the electrode pattern (Ajdari 2000; Brown 2001).

Eventually, by focusing on the effects of patterns on the flow geometry, we have deliberately left aside all the means by which patterns on the surface will be useful because of their functional interactions with elements dissolved or embedded in the fluid; separation in arrays of obstacles, detection on (specifically or not) adsorbing spots and biochips, controlled cell adhesion, chromatographic effects and dielectrophoretic trapping, etc.

## 10.4 Conclusion

The main message of this chapter is that by integrating actuators, and patterning surfaces, one may develop a substantial number of capabilities prone to form building blocks for lab-on-a-chip devices. In this context, PDMS is a remarkably appropriate material, and the chapter emphasizes its pertinence. PDMS has nonetheless a number of drawbacks. We mentioned that PDMS produces unwanted adsorption of proteins, an issue for which no universal solution exists at the moment. The difficulty seems to have been overcome for protein crystallisation. In the proteomic application discussed in this chapter, SDS micelles were used to transport the proteins in the separation channel; these ‘vehicles’ were further dropped to allow for trypsin digestion. Without SDS, proteins stick to the walls and are lost. Adsorption thus represents an issue for PDMS. One may hope that in the future, new soft materials will develop, offering alternatives to PDMS. The situation in this respect is open and it is difficult to foresee the time it will take to have novel successful materials available.

## 10.5 Acknowledgements

The authors acknowledge the support of ESPCI and CNRS for most of the work reported here. They have benefited from discussions with A. Dodge, E. Brunet, H. Willaime, M.C. Jullien, J. Goulpeau, G. Degré and L. Menetrier.

## 10.6 References

- Ajdari A., *Phys. Rev. Lett.* **75**, 755–758 (1995).  
 Ajdari A., *Phys. Rev. E.*, 61 R45-48 (2000).  
 Ajdari A., *Phys. Rev. E.*, 65, 016301 (2002).  
 Anderson J.L. and Idol W.K., *Chem. Eng. Common.* **38**, 93–106 (1985).  
 Anna S., Bontoux N. and Stone H., *Appl. Phys. Lett.* **82**, 364 (2003).  
 Barker S.L.R., Ross D., Tarlov M.J., Gaitan M. and Locascio L.E., *Anal. Chem.* **2000**; 72(24); 5925–5929.  
 Beebe D., Mensing G. and Walker G., *Ann. Rev. Biomed. Eng.* **4**, 261 (2002).  
 Brown A., Smith C. and Rennie A., *Phys. Rev. E.*, 63, 016305 (2001).  
 Brunet E., Dodge A., Chen S., Goulpeau J., Labas V., Royer N., Vinh J. and Tabeling P., *Proc. Micro. TAS 2004, Malmö, Sweden* (2004).  
 Chou H.P., Unger M.A. and Quake S.R., *Biomedical Microdevices* **3**: 323–330 (2001).  
 Cottin-Bizonne C., Barrat J.L., Bocquet L. and Charlaix E., *Nature Materials* **2**, 238 (2003).  
 Cottin-Bizonne C., Barkentin C., Charlaix E., Bocquet L. and Barrat J.L., *EPJE* **15**, 427–438, 2004.  
 Dodge M.C., Jullien Y.K., Lee X., Niu F., Okkels P. and Tabeling C., *R. Physique* **5** 557–563 (2004).  
 Dreyfus R., Willaime H. and Tabeling P., *Phys. Rev. Lett.*, **90**, 144505 (2003).  
 Erickson D. and Li. D., *Langmuir*. **18** 1883–1892 (2002).  
 Fu A., Spence C., Arnold G. and Quake S., *Nature Biotechnology*, **17**, 1109 (1999).  
 Giordano N. and Cheng J., *J. Phys: condens. Matter*, **13**, R271 (2001).  
 Gitlin I., Stroock A.D. and Whitesides G., *Appl. Phys. Lett.* **83**, 1986–1988 (2003).  
 Handique K., Gogoi B., Burke D., Mastrangelo C. and Burns M., *SPIE* **3224**, 185–195 (1997).  
 Johnson T.J., Ross D., Gaitan M. and Locascio L.E., *Anal. Chem.* **73**(15); 3656–3661 (2001).  
 Johnson T.J., Ross D. and Locascio L.E., *Anal. Chem.* **74**(1); 45–51 (2002).  
 Joseph P. and Tabeling P., *Phys. Rev.* **71** (6) 035303(R) (2005).  
 Kenis P.J.A., Ismagilov R. and Whitesides G., *Science*, **285**, 83–8(1999).  
 Kim E., Xia Y. and Whitesides G., *Nature*, **376**, 581 (1995).  
 Krupenkin T., Taylor J., Schnerder J. and Yang S., *Langmuir* **20**, 3824–3827 (2004).  
 Lauga E. and Stone H.A., *J. Fluid. Mech.*, vol 489, pp. 55–77 (2003).  
 Lauga E., Stroock A. and Stone H., *Phys. Fluids* **16**: 3051–3062 (2004).  
 Locascio L.E., *Anal. Chem.* **72**(24); 5925–5929 (2000).  
 Long D., Stone H. and Ajdari A., *A. Colloid Interf. Sci.* **212**, 338–349 (1999).  
 Maillefer D., Gamper S., Frehner B., Balmer P., van Lintel H. and Renaud P., *Prod. MEMS2001, Interlaken*, 414 (2001).  
 Molmo J.I., Herr A.E., Moisie B.P., Santiago J.A., Kenng T.W. and Brenner R.A., *Anal. Chem.* **73**, 1350–1360 (2001).

- Okkels F. and Tabeling P., *Phys. Rev. Lett.* **92** (3), 038301 (2004).
- Ottino M. and Wiggins S., *Science*; 305: 485–486 (2004).
- Pugmire D.L., Waddell E.A., Haasch R., Tarlov M.J. and Locascio L.E., *Anal. Chem.* (Article) 74(4): 871–878 (2002).
- Reyes D., Iossifidis D., Auroux P. and Manz A., *Anal. Chem.*, **74**, 2623 (2002).
- Scherrer A., Quake S., *Science*, **290**, 1536 (2000).
- Smith D., Babcock H. and Chu S., *Science*, **283**, 1724 (1999).
- Song M., Tice J.D., Ismagilov R. and Angew R., *Chem. Int. Ed.* 42; 768–772 (2003).
- Stone H.A., Stroock A. and Ajdari A., *Ann. Rev. Fluid Mechanics*, **36**, 381–411 (2004).
- Stroock A.D., Weck M., Chin D.T., Huck W., Kenis P., Ismagilov R. and Whitesides G., *Phys. Rev. Lett.*, 84, 3314–3317 (2000).
- Stroock A.D., Dertinger S., Whitesides G. and Ajdari A., *Science*, 295, 647–651 (2002a).
- Stroock A.D., Dertinger S., Ajdari A., Mezic I., Stone H.A. and Whitesides G., *Anal. Chem.* 74, 5306–5312 (2002b).
- Stroock A.D. and Whitesides G., *Acc Chem. Res.* **36**, 597–604 (2004).
- Tabeling P., *Une Introduction à la Microfluidique*, Collection Echelles, Paris (2003).
- Tabeling P., Chabert M., Dodge A., Jullien C. and Okkels F., *Phil. Trans. R. Soc. Lond A* 362, 987–1000 (2004).
- Thorsen T., Roberts R., Arnold F. and Quake S., *Phys. Rev. Lett.*, **86**, 18, 4163 (2001).
- Thorsen T., Maerkl S. and Quake S., *Science*, **298**, 582 (2002).
- Trethewey D. and Meinhard C., *Phys. Fluids*, **14**, 3 L9 (2002).
- Unger M., Chou H., Thorsen T., Scherer A. and Quake S., *Science*, **288**, 113 (2000).
- Whitesides G. and Stroock A.D., *Physics Today* 54, 42–48 (2001).
- Willaime H. and Tabeling P., submitted (2005).
- Zhao Bin, Moore J.S. and Beebe D.J., *Science*; 291: 1023–1026 (2001).

### 11.1 Introduction

Within the last decade, the use of microfluidic devices, ranging from single etched channel structures in glass substrates to complex multilayer fluidic networks, for the manipulation of biomolecules has grown exponentially. The popularity of this field can be attributed to its interdisciplinary nature. From a biological perspective, recent advances in genomics<sup>1,2</sup> and proteomics<sup>3</sup> have generated a need for cheaper high-throughput screening (HTS) platforms. However, the successful design of such platforms requires some knowledge in a variety of disciplines, ranging from engineering (design and manufacture of the microfluidic device) to material science (selecting the appropriate substrate for device fabrication) to fluid mechanics for the optimization of the flow and/or mixing conditions. With more microfluidic platforms being developed as collaborative projects between laboratories as well as through industrial partnerships, devices with highly advanced functionalities are being produced for applications such as protein crystallization<sup>4</sup> and vascularized tissue engineering<sup>5</sup>.

Microfluidic devices with biochemical applications have been fabricated from a wide range of substrates, including glass, silicon, hard polymers (polystyrene, polyvinylchloride, polymethylmethacrylate (PMMA)) and elastomeric materials (silicone rubber, polyurethane). Although some of the earliest microfluidic devices were manufactured from silicon and glass using standard MEMS technology<sup>6-8</sup>, there has been a growing trend in the use of less expensive polymeric materials for microfluidic devices<sup>9</sup>. While devices made from silicon and glass are typically chemically etched or micromachined, techniques such as embossing, casting and injection molding can be applied rapidly to prototype devices from hard and elastomeric polymers.

As the techniques for microfluidic device fabrication and flow control continue to be reported and refined, researchers have a virtual toolbox at their disposal from which they can create sophisticated devices for bioanalytical applications. In this section, we will examine how microfluidic devices have

been utilized to manipulate biomolecules. Major emphasis will be placed on research dedicated to the study of individual molecules (DNA, protein, and cells) in microchannels, presenting applications like molecular sizing and cell sorting. Transitioning from single molecule to multi-component systems, the chapter concludes with a treatment of a select group of microfluidic tools for molecular biology (polymerase chain reaction (PCR), electroporation, and protein crystallization).

## 11.2 Manipulation and sorting of biomolecules

### 11.2.1 DNA separation techniques

#### *Microfluidic capillary electrophoresis*

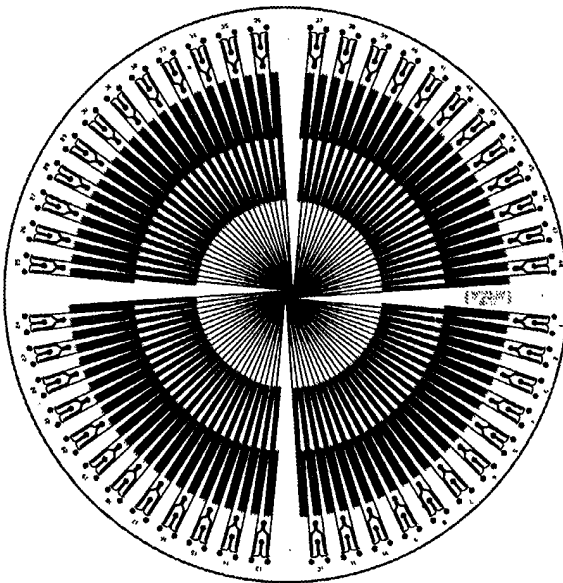
The development of some of the earliest bio-inspired microfluidic devices in the last decade originated as an extension of MEMS-based technology for analytical chemistry applications. The miniaturized ‘total chemical analysis system’ ( $\mu$ TAS) proposed by Manz and Widmer in 1990<sup>10</sup>, incorporating automated flow injection, chromatography, and electrophoresis on a micromachined substrate, provided the foundation for the chip-based analysis of biomolecules. Using photolithography and established chemical etching techniques, the first microfluidic devices, consisting of a network of micron-scale channels etched in planar glass substrates, created an enabling platform for the manipulation and characterization of small biomolecules at a fraction of the cost of conventional automated systems.

Some of the earliest microfluidic devices developed in the 1990s used free-flow capillary electrophoresis (CE) devices to separate small molecules like fluorescent dyes and amino acids<sup>11</sup>. Glass was routinely used as a substrate for these chips for several reasons. The excellent power dissipation characteristics of planar glass microfluidic devices allowed separations to be carried out using higher electrical fields while minimizing Joule heating, resulting in faster separation times than those achieved using air-cooled cylindrical capillaries. The surface chemistry at the glass/buffer surface in the microchannels is also optimal for CE. Silanol molecules (SiOH) present on the glass surface interact with free hydroxyl ions in the water to give the glass surface a net negative charge, creating an electric double layer with the surrounding hydrogen ions whose migration induces electroosmotic flow (EOF) in the presence of an applied field. The combination of EOF with electrokinetic separation of the samples in the microchannels gave researchers unprecedented control over the sample injection process, minimizing both loading times (ms) and volumes (pL) while virtually eliminating dead volume. In addition to glass, other materials have been used to fabricate free-flow microfluidic CE devices, including hard plastics and elastomers. While plastics and elastomers often require surface chemistry modifications for EOF, their

rapid prototyping characteristics, cost, and sealing characteristics have increased their popularity as substrates for microfluidic devices. Silicone rubber (polydimethylsiloxane (PDMS))-based microfluidic devices have been used to separate and sort of DNA restriction digests using free-flow CE<sup>12</sup>.

To improve the resolution of the early CE devices, separation media were added to the microchannels. Capillary gel electrophoresis (CGE)-based microfluidic devices were developed for DNA-based separations, filled with polyacrylamide<sup>13</sup>, cellulose-derivatives<sup>14,15</sup>, or other polymeric materials<sup>16,17</sup>, which act as a sizing matrix in the presence of an applied electric field. The resolution power of these devices is superior to bulk slab gels, requiring less than one minute to achieve single-base pair resolution for small oligonucleotides (10–25 base pairs)<sup>13</sup>. Microfluidic CGE devices have been used in several applications, including restriction fragment analysis<sup>18–20</sup>, genotyping<sup>21,22</sup>, and short tandem repeats<sup>23</sup>, while 96-channel arrays have been designed for four-color DNA sequencing with an average read length of 430 base pairs<sup>24</sup> (Fig. 11.1).

The major limitations of microfluidic CGE are detection sensitivity and band broadening. While small sample volumes can be injected into microfluidic CGE devices, the sample must sufficiently concentrated for detection of the individual analytes during the separation process. Simply loading excess amounts of sample in a large volume is insufficient, as it promotes diffusion-based band broadening. Consequently, several protocols have been developed



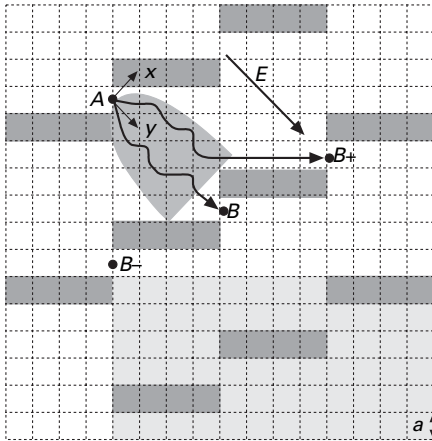
11.1 Overall layout of the 96-lane DNA sequencing microchannel plate (MCP). Reproduced with permission from ref 24. Copyright 2002 National Academy of Sciences, U.S.A.

in the past few years to concentrate the sample prior to injection into the separation matrix<sup>25</sup>. Recent examples include isotachopheretic (ITP) pre-concentration of DNA<sup>26</sup>, in which a discontinuous buffer system is combined with electrokinetic injection to stack and concentrate a DNA sample prior to separation, electrode-defined sample injection<sup>27</sup>, in which an array of electrodes is used to capture and concentrate DNA at an anode located outside of the separation matrix, and pulse-pressure injection using an integrated elastic membrane to concentrate the sample as a plug at the separation matrix boundary<sup>28</sup>.

### *Microfabricated separation elements*

Many microfluidic devices have been developed that incorporate nano- to microscale elements such as pillars, constrictions and asymmetric gratings into the microchannels to size and sort DNA molecules. The features in these devices often approximate the radius of gyration ( $R_g$ ) of single DNA fragments, exploiting properties like entropy and molecular diffusion coefficients to enhance the separation process.

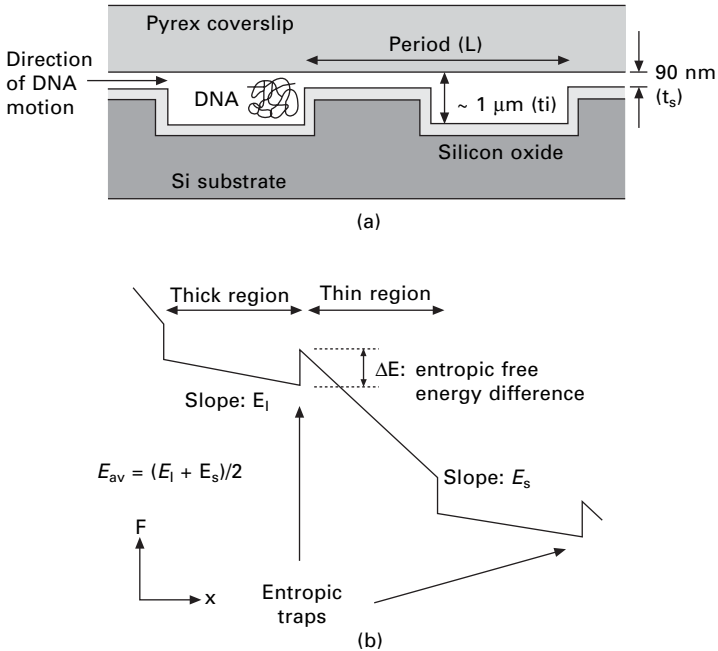
Several groups have fabricated microfluidic devices for sorting polydisperse DNA mixtures that use Brownian ratchets, combining passive diffusion with an applied electrical field to alter the migration path of individual molecules. One example uses periodic arrays of asymmetric micromachined barriers in which electrophoretic separation of DNA molecules is achieved in a direction normal to the applied field<sup>29,30</sup> (Fig. 11.2). Larger DNA fragments tend to migrate along the field lines between the barriers while the smaller fragments experience lateral diffusion and are deflected by the barriers, following a unique size-dependent path through the array. The separation efficiency of this device depends on the spacing between the barriers, as particles much smaller than the gap dimensions remain trapped in individual field lines and are poorly fractionated<sup>31</sup>. These devices have been principally used to separate large DNA molecular, resolving a mixture of  $\lambda$  and T2 DNA (48.5 kbp and 167 kbp respectively). Another variation that has been used to manipulate smaller DNA fragments (50 bp) utilizes a micromachined array of asymmetric, interdigitated platinum electrode pairs on a silicon wafer<sup>32</sup>. Net movement of charged DNA molecules added to the array surface is achieved by a cyclic charging of the electrode pairs. In the charged state, DNA molecule are attracted to the nearest positively charged electrode, while they undergo isotropic Brownian diffusion in the absence of a potential. The asymmetry of the electrode pairs creates a bias that, in association with the cycle duration, determines the net migration direction of the DNA fragments. Using a large number ( $10^4$ ) of short, sub-millisecond cycles, a theoretical separation time of 5.4 seconds has been proposed for the separation of 24 and 25 bp DNA fragments on a 1.25 cm long chip.



**11.2 Design of the sieve.** The unit cell of the periodic array, which contains three rectangular obstacles, is indicated by the shaded area at the lower right. Molecules are propelled by an electrophoretic force, which acts along the diagonal, and are channeled through the narrow gaps between obstacles. A molecule which passes through gap *A* subsequently executes a biased random walk and visits, with high probability, points located in the parabolic shaded region. It is most likely that the molecule arrives at *B*, but some paths pass around an obstacle and lead the molecule to *B+*. The probability of reaching *B+* is higher for smaller, more swiftly diffusing species. Reproduced with permission from ref. 29. Copyright 1998 American Physical Society.

Nanofluidic devices with a series of entropic traps have been developed for separating long DNA molecules (5–150 kbp), consisting of micron-scale channels separated into chambers by  $\sim 100$  nm constrictions<sup>33,34</sup> (Fig. 11.3). In the absence of a driving force, long DNA molecules remain confined to the chambers, whose depth approximates  $R_0$ . When an electric field is applied the DNA solution, the molecules stack up against the narrow constriction. To pass from chamber to chamber, a DNA molecule must overcome the entropic energy barrier created by the constriction. The activation barrier is independent of chain length, overcome only by the local deformation of DNA at the chamber/constriction interface. Larger DNA molecules statistically pass through the constrictions faster than shorter fragments because more monomers face the thin gap.

Entropic recoil devices, consisting of fabricated arrays of nanopillars (50–500 nm height), have also been used to separate DNA molecules based on configurational entropy<sup>35,36</sup>. Using a pulsed electric field, DNA molecules migrate into the entropically unfavorable nanopillar array. Upon removal of the field, longer DNA molecules that are only partially inserted in the array recoil, pulling themselves out of the array, while the smaller, fully inserted molecules remain trapped. Single-step separation of T2 and T7 phage DNA



11.3 (a) Schematic diagram of the device. (b) Free energy landscape for DNA in the channel.  $\Delta E$  is the entropic free energy difference between a DNA molecule in a thick region and a thin region.  $E_s$  and  $E_t$  are the electric field at thin and thick regions, respectively.  $E_{av}$  is the average electric field over the channel. Reproduced with permission from ref. 33. Copyright 1999 American Physical Society.

(167 and 39 kbp) has been achieved in the recoil devices using a single 2 s pulse (5V/s).

### 11.2.2 Protein separation techniques

#### *Coupled microfluidic-mass spectroscopy devices*

Unlike microfluidic devices designed to sort and manipulate DNA molecules, where techniques such as polymerase chain reaction (PCR) can be implemented to provide concentrated samples for analysis, no such amplification method exists for proteins<sup>37,38</sup>. The isolation and concentration of individual proteins from cell or tissues, which are often present in small relative concentrations, from the cocktail of proteins, salts and nucleic acids present in a typical sample digest is a major challenge faced by researchers who want to carry out proteomic analysis on microchips coupled to mass spectroscopy (MS) equipment. Consequently, several technologies used for macroscopic protein sample preparation for MS have been adapted to microfluidic systems.

### Microfluidic dialysis

One of the most effective techniques for rapid purification of crude protein preparations is dialysis, using a molecular weight cut-off membrane to remove salt and low molecular weight contaminants. Many microfluidic versions of these devices, developed for direct coupling with electrospray ionization mass spectroscopy (ESI-MS) equipment, consist of porous poly (vinylidene fluoride) dialysis membrane(s) sandwiched between two microchannel-patterned substrates<sup>39–41</sup>. The large surface-to-volume ratio of this configuration, where the dialysis membrane forms one common wall of the separated microchannels, enables very efficient low-volume clean-up reactions to be carried out. Xu *et al.* used a countercurrent flow configuration to rapidly desalt DNA and protein samples against an ammonium acetate buffer, using 1  $\mu\text{l}$  sample volumes and flow rates of 0.5  $\mu\text{l}/\text{min}$ <sup>39</sup>. More sophisticated dual membrane polycarbonate microfluidic devices have also been developed where a protein sample is sequentially dialyzed through a high molecular weight cutoff membrane to remove large impurities followed by desalting against a second membrane and direct coupling to ESI-MS<sup>40</sup>. A 20-fold signal/noise improvement in ESI-MS was observed in a parallel comparison of *E. coli* lysates (1 mg/ml total protein) cleaned up with dual membrane systems vs. unpurified samples.

### Solid-phase extraction

Solid-phase extraction (SPE), in which protein(s) are captured on stationary surfaces, such as a membranes or beads, and eluted at a later time, is another clean-up technique that has been implemented in microfluidic devices. Mimicking chromatography columns, many of these devices incorporate hydrophobic  $\mu\text{m}$ -scale beads into microchannels<sup>42–44</sup>, achieving surface/volume ratios of up to  $10^7 \text{ m}^{-1}$ . Bead packing is typically achieved through a combination of electroosmotic pumping and raised weir structures to trap the beads in a packed bed conformation, although examples of devices which use a combination of pressure and EOF to confine beads in a recirculating flow without any physical barriers have also been reported<sup>45</sup>. When used as a module coupled to a mass spectrophotometer, packed bed microfluidic devices have been used to concentrate and resolve a 1 nM peptide mixture<sup>44</sup>.

Potential problems with microfluidic bead-based SPE matrices include clogging and uneven packing due to back pressure effects<sup>38</sup>, motivating the development of alternative solid-support technologies such as monolithic porous matrices. Using porous polymer mixtures, UV-cure, acrylate-based polymers, in combination with porogenic solvents like cyclohexanol and methanol, have been directly photopolymerized in microchannels to create hydrophobic porous solid-phase protein extraction matrices. The micron-scale pore diameters (10–20  $\mu\text{m}$ ) provide a large surface-to-volume ratio for

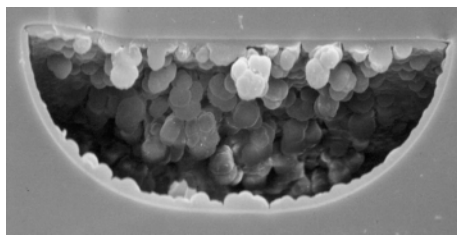
protein binding, while allowing small inorganic and organic polar molecules to pass through the matrix. Very high protein enrichment values have been reported using these porous constructs, up to  $10^3$  for green fluorescent protein and a small hydrophobic tetrapeptide<sup>46</sup> (Fig. 11.4).

### *On-chip protein isolation and identification*

The development of stand-alone microfluidic devices for protein analysis is still a challenging field. One of the major barriers that lab-on-a-chip proteomic devices face is sensitivity. With single cells containing as little as tens to hundreds of copies of single proteins, concentrated samples are clearly necessary to insure that even a single molecule of interest is present in a picoliter slug flowing through a microchannel. In this section, some recent advances in on-chip protein analysis and detection are discussed.

### Liquid-liquid separations

Flow in microfluidic systems is usually simple – viscous effects dominate and the low Reynolds number leads to laminar flow. Parallel flows between two or more liquid streams is established, where mixing only occurs at the interface through passive diffusion. As lateral diffusion rate for an individual analyte is size-dependent, protein sample clean-up can be achieved by co-flowing crude protein preparations against an extraction buffer solution. By modifying parameters such as microchannel dimensions and flow rate, liquid-liquid extraction techniques have been used for various applications, including simple desalting procedures, inorganic separations, and size-dependent purification of a protein samples<sup>47</sup>. A sophisticated liquid-liquid extraction device developed by Schilling and co-workers has been used to carry out cell lysis of intact *E. coli* cells and extraction of a large intracellular enzyme, beta-galactosidase<sup>48</sup>. Extraction was achieved by co-flowing two parallel streams containing an *E. coli* suspension and lysis buffer respectively through a plastic microchannel. As the cells at the interface were lysed,



11.4 SEM image of the monolithic ion-exchange concentrator. Reproduced with permission from ref. 46. Copyright 2001 American Chemical Society.

proteins and small biomolecules diffused into the lysis buffer while large membrane fragments and DNA remained confined to the cell suspension. A T-channel was subsequently used to separate the two streams, and the beta-galactosidase in the lysis buffer was detected and quantified using a fluorescence-based assay.

### Sodium dodecyl sulfate capillary gel electrophoresis

Sodium dodecyl sulfate (SDS) is an anionic denaturant that linearizes proteins and gives them a uniform negative charge, enabling size-dependent separation in a porous gel matrix under an applied electric field. Miniaturization of this technique was first reported in capillaries in the late 1980s<sup>49</sup> and more recently in microfluidic devices. Yao and co-workers used a glass microfluidic device filled with a SDS/polyacrylamide separation matrix to separate a fluorescently labeled mixture of six protein markers (9 kDa to 116 kDa) in 35 seconds using a 5 kV separation voltage and a laser-induced fluorescence (LIF) detector<sup>50</sup>. Conducting the experiments in parallel with a commercial capillary-based system (P/ACE 5000 capillary electrophoresis system (Beckman Coulter)), the protein separation time in the microchannels was 20-fold faster, with separation efficiencies typical of conventional capillary-based SDS/CGE.

### Isoelectric focusing

Isoelectric focusing (IEF) uses a pH gradient to separate amphoteric molecules like proteins and peptides based on their isoelectric point (pI). In a microfluidic device, sample is typically mixed with a carrier ampholyte mixture and an electric field is applied to set up the pH gradient<sup>51</sup>. Rapid separation of protein mixtures is achieved as the individual components migrate to and concentrate at the position where they are electrically neutral (pI). Early experiments were conducted in both glass and plastic microchips<sup>52-54</sup>, illustrating simple separations of fluorescently labeled protein and peptide mixtures. Hofmann *et al.* used glass microchips to separate nM concentrations of seven Cy5-labeled peptides in under 30 s<sup>52</sup>.

### Coupled separation technologies

For proteomic analysis, where the sample consists of a mixture of thousands of individual proteins, a combination of multiple separation techniques is clearly essential to separate proteins with very similar masses or pI values. Ramsey *et al.* used glass microfluidic chips with integrated electrodes to separate a fluorescently labeled tryptic digest using micellar electrochromatography (MEKC) in the first dimension and CZE in the second<sup>55</sup>. In

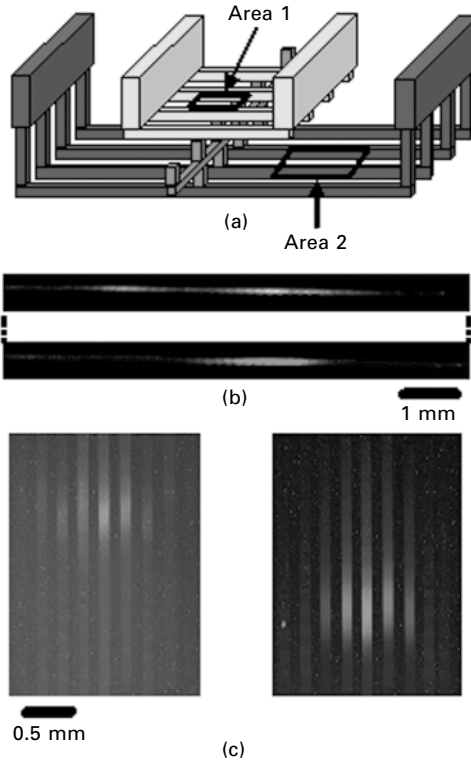
MEKC, the protein solution is separated according to the hydrophobicity/hydrophilicity of its individual components. The hydrophobic proteins interact with the non-polar micelles, migrating at a slower rate than polar proteins in an applied electric field. Using cross-channel architecture, samples separated by MEKC were actively monitored by LIF and electrokinetically injected into an orthogonal microchannel containing CZE buffer for subsequent size-dependent separation and analysis. With a 15 minute total analysis time, the total peak capacity of the device, defined as the product of the resolved sample peaks from each technique, was 4200. The system was able to generate detailed 2-D protein separation profiles that enabled the authors to resolve digests of human and bovine hemoglobin, which have 88% homology in their amino acid sequence.

Microfluidic separation techniques have also been developed that couple IEF with CE. Herr and co-workers used a PMMA microchip to separate and analyze nM concentrations of three fluorescein isothiocyanate (FITC)-labeled proteins<sup>56</sup>. Using IEF in the first dimension, the authors estimated that the individual protein components were concentrated by a factor of 73, resulting in a final focused concentration of 10  $\mu\text{M}$ . Simultaneous focusing and EOF-driven mobilization were used to transport concentrated bands of individual analytes to sorting junctions, where the applied field was removed to 'park' the samples and homogenize the local pH. Subsequent free solution-based CE-based separation was achieved by applying a potential orthogonal to the original separation using the same common buffer without the pH gradient at the terminal wells. The estimated peak capacity for the system was 1300 with a total separation time of around one hour, lower than the aforementioned value for MEKC/CZE. However, simple modifications suggested by the authors like reducing the sample volume in the second dimension or increasing the number of CE channels for parallel sampling may significantly improve the peak capacity of the device.

Another IEF-coupled device recently used to separate simple protein mixtures combines IEF with CGE in a PDMS microchip<sup>57</sup>. Wang *et al.* used PDMS microchips with two sets of integrated pressurized elastomeric valves to de-couple the two separation processes. The chip consists of a double-Y configuration with four reservoirs. Pneumatically closing off the valves connecting the chip to the CGE medium, a mixture of three fluorescently tagged proteins and native green fluorescent protein (GFP) were first separated by IEF. Subsequently analysis of the focused proteins was simply achieved by switching the open/closed state of the on-chip valves to initiate second-dimension separation by CGE. Using this chip, separation of two proteins with very similar pI values (ovalbumin and GFP) was achieved in ten minutes.

As a final example of coupled protein analysis devices, a modular microfluidic PDMS chip developed by Chen *et al.* has been used to combine IEF with SDS gel separation<sup>58</sup>. The fundamental design of the chip consists

of a set of 2-D stackable PDMS layers patterned with microchannels using soft lithography. Sealing between layers is passive, enabling reversible assembly of the device. IEF separation of three labeled proteins (fluorescein-conjugated bovine carbonic anhydrase II and bovine serum albumin, and Texas-Red conjugated ovalbumin) was accomplished in a four-layer device with buffer reservoirs on the top layer and a single square microchannel ( $100 \times 100 \mu\text{m}^2$  cross-section, 25 mm long) filled with commercial capillary IEF gel (Beckman) at its core. After IEF, the device was peeled apart and the IEF channel core was sandwiched between new PDMS layers containing discrete SDS buffer reservoirs and parallel microchannels containing SDS separation gel (Fig. 11.5). A potential applied between the reservoirs and the parallel microchannels was used to extract proteins from the IEF gel at regular intervals, forcing them into the SDS gel for separation in the second dimension. The spot sizes for the separated proteins in the SDS gel were comparable to those achieved by traditional 2-D electrophoresis.



11.5 (a) Schematic diagram of an on-chip 2D gel electrophoresis device. (b) Fluorescence image of area 1: first dimension, isoelectric focusing. (c) Fluorescence image of area 2: second dimension, SDS-gel electrophoresis. Figure courtesy of Dr. George Whitesides, Harvard University, USA.

### 11.2.3 Cell separation techniques

#### *Cell trapping*

The ability to manipulate individual cells in microfluidic devices is of general interest not only for high-throughput screening applications, but also to study the unique physical and biochemical properties of individual cells in nanoliter-scale environments. Keeping cells viable in a microfluidic environment can be challenging, placing geometric constraints on microchannel dimensions to minimize shear and requiring careful optimization of the chemical environment (pH, salinity) to prevent cell lysis. With these constraints in mind, several non-invasive techniques are presented that confine and separate cells in microfluidic devices while maintaining viability.

Dielectrophoresis (DEP) has been used to separate a wide variety of bacteria, yeast, and mammalian cells<sup>59-68</sup>. DEP uses non-uniform AC fields to polarize cells or particles in a suspension. Depending on the particle polarization factor, DEP can be used to drive the cells toward the strong field region (in close proximity to the electrodes) or the weak field region. Cells of different types having unique dielectric properties can be subjected to differential DEP forces, which can be exploited for cell separation<sup>60</sup>. Examples of DEP-based cell enrichments demonstrated in microfluidic flow cells include *E. coli* (20-fold), white blood cells (30-fold), and peripheral blood mononuclear cells (28-fold)<sup>67</sup>. Arai *et al.* used a combination of optical trapping and DEP to separate single microbes from a large background population in an etched glass microchannel<sup>59</sup>. Using an etched glass microchip with integrated electrodes, the authors confined individual yeast cells in optical traps and applied a 10 V p-p voltage across the electrodes. Cells not confined to the traps were drawn to the electrodes, enabling target cells to be dragged to the collection port without the risk of undesired cells falling in the optical trap during the recovery process. Another technique reported by Voldman *et al.* used a quadrupole DEP to spatially confine single cells in the presence of an opposing fluid flow<sup>68</sup>. While clearly not a high-throughput screening method, DEP is useful for bulk purifications of heterogeneous cell lines and single-cell analysis where target cells can be identified using colorimetric or fluorescent markers.

Mechanical traps represent another approach for size-dependent separations of different cell types<sup>69-72</sup>. Carlson *et al.* micromachined 2-D arrays of 5  $\mu\text{m}$  dia. channels in silicone coated with polyurethane to separate leukocytes from red blood cells (RBC) in whole blood<sup>69</sup>. The microchannel diameter approximates the human capillary dimensions (4–5  $\mu\text{m}$ ) and exploits the differential deformation properties and adhesion properties to silicon of individual cell types as they are forced through the lattice under an applied pressure gradient. While disc-shaped red blood cells (8  $\mu\text{m} \times 2 \mu\text{m}$ ) readily passed through the gradient, leukocytes (10  $\mu\text{m}$  dia.) remained trapped in the

channel entrances within the lattice under a 1.6 MPa pressure gradient. The depth of penetration into the channel array varied depending on the leukocyte sub-type, allowing additional fractionization of monocytes, granulocytes, and lymphocytes.

Dynamic cell compartmentalization has also been achieved in PDMS-based devices using integrated elastomeric valves<sup>73–75</sup>. The elastomeric valves in these devices are fabricated by a technique commonly referred to as multilayer soft lithography (MLS)<sup>76</sup>. MLS is a process used to create stacked 2-D microfluidic networks from elastomeric materials. Elastomeric valve structures are made by bonding a thick layer of microchannel-patterned PDMS, the ‘control’ layer, to a thin PDMS layer spin-coated on a second microchannel-patterned silicon wafer, the ‘flow’ layer. The spin coating process provides a method of precisely controlling the thickness of the silicone layer over the microchannels, which function as valve structures in the assembled devices at the interface where the control and flow layer channels overlap. Pneumatic actuation of the valves is accomplished by pneumatically pressurizing the control channels, causing the valves to expand and pinch off the flow channel. Chips fabricated using MLS have been used to demonstrate single-cell biochemical assays<sup>74,75</sup>, where each cell is compartmentalized in picoliter-scale compartments. The scalability of this process to make microfluidic chips with thousands of independently addressable compartments has been demonstrated by Thorsen *et al.* with a 2.5 cm<sup>2</sup> chip containing elastomeric 3574 valves, organized as an addressable 25 × 40 chamber microarray<sup>75</sup>.

### *Microfluidic fluorescence-activated cell sorters*

While conventional commercial fluorescent-activated cell sorters (FACS) are extremely efficient, with a very high throughput (up to  $3 \times 10^4$  cells/second – MoFlo Cytometer (Cytomation)), they are susceptible to frequent microbial contamination and prohibitively expensive for small laboratories. The need for sensitive yet inexpensive analytical technology for studying cell populations has consequently fueled the development of microfluidic cell-sorting devices.

The first microfluidic FACS developed by Fu *et al.* in the late 1990s used electrokinetic (EK) flow to sort bacteria expressing GFP from a background of non-fluorescing cells<sup>77</sup>. The PDMS-based device consisted of a single T-channel hermetically sealed to a glass slide with one input well and two collection wells punched through the chip to the top surface. Cell adhesion to the PDMS was minimized by boiling in the device in 3.6 mM HCl to render the exposed surfaces hydrophilic. Platinum electrodes in the input and output wells were used to drive the cells through the 3 μm-wide T-Junction, where fluorescence was measured by a LIF system. Based on the

PMT intensity, the electroosmotic potential was adjusted to direct individual cells to the positive and negative collection wells. Using electric fields of up to 100 V/cm, 30-fold GFP cell population enrichments were reported in the microfluidic FACS devices with a viability rate of ~20%. Unlike conventional FACS machines, the electrokinetic microfluidic device is capable of reversible sorting. By simply reversing the potentials, cells can be drawn back through the detector region for secondary validation, reducing the number of false positives collected during the run.

Using electrokinetic flow for cell sorting creates several problems including restrictive buffer formulations, voltage instabilities due to ionic depletion, pressure imbalances, and evaporation<sup>63</sup>. Moreover, the electric fields used to drive the flow detrimentally affect the viability of the cell culture. McClain *et al.* used a glass microchip (250  $\mu\text{m}$  wide  $\times$  20  $\mu\text{m}$  deep) with a restricted cross channel (50  $\mu\text{m}$  wide, same depth) to look dynamically at *E. coli* viability as a function of field strength<sup>78</sup>. Cells were flowed through the device in the presence of a membrane-impermeable fluorescent dye (propidium iodide (PI)). In the presence of a high electric field in the cross channel (183 V/cm), a large uptake in PI was observed, indicative of electroporation of the cell membranes. The authors believe that most *E. coli* were killed within milliseconds of exposure to the high electric field.

Many microfluidic FACS have been developed that use pressure-based flow, significantly improving the viability of the sorted cells. Fu *et al.* developed an integrated PDMS-based microfluidic cell sorter that combined pressurized flow with integrated elastomeric valves and pumps<sup>73</sup>. The device designed by Fu *et al.* contained integrated peristaltic pumps consisting of three elastomeric valves to control the bulk flow rate precisely and pairs of switching valves to route cells to the waste and collection reservoirs. Using a LIF-based detection system, the authors sorted up to  $4 \times 10^5$  cells in a three hour period, reporting an 83-fold enrichment of EGFP-expressing cells from a background of non-fluorescing bacteria.

Another cell-sorting technique demonstrated in pressure-based devices utilizes hydrodynamic switching. Kruger *et al.* fabricated prototype FACS devices in Su-8 spin-coated on a silicon wafer that combined hydrodynamic focusing to confine the sample to the center of the microchannel with syringe pump-based pressure switches to route the fluidic output to the collection and waste reservoirs<sup>79</sup>. The focused sample is deflected into the selected output reservoir by introducing nanoliter-scale slugs of fluid through the switch channels into the X-shaped sorting junction. The major problem encountered by the authors using this technique was controlling the overall pressure balance in the device, with back pressure adversely affecting the hydrodynamic focusing upstream of the sorting junction. A refined prototype recently reported by Wolff *et al.* employs hydrodynamic switches to sort cells at a rate of  $12,000 \text{ s}^{-1}$ , a throughput rate that is comparable to commercial

FACS sorters ( $10,000\text{--}20,000\text{ s}^{-1}$ )<sup>80</sup>. Their silicon-based device used external computer-controlled electrostatic valves (The Lee Company) connected to either the waste or collection reservoirs to create a bias in the hydrodynamically focused cell stream. Using a LIF-based detection scheme, cells are collected in the appropriate output reservoir by computer-controlled actuation of the electrostatic valves. While the intrinsic switching time of the electrostatic valves (2 ms) limits the device performance, impressive results for rare-event sorting have been achieved. A 100-fold enrichment of fluorescent beads in a background of chicken red blood cells was achieved (from an initial  $2.4 \times 10^{-5}$  bead/cell ratio), with  $2 \times 10^7$  cells sorted in 27 minutes.

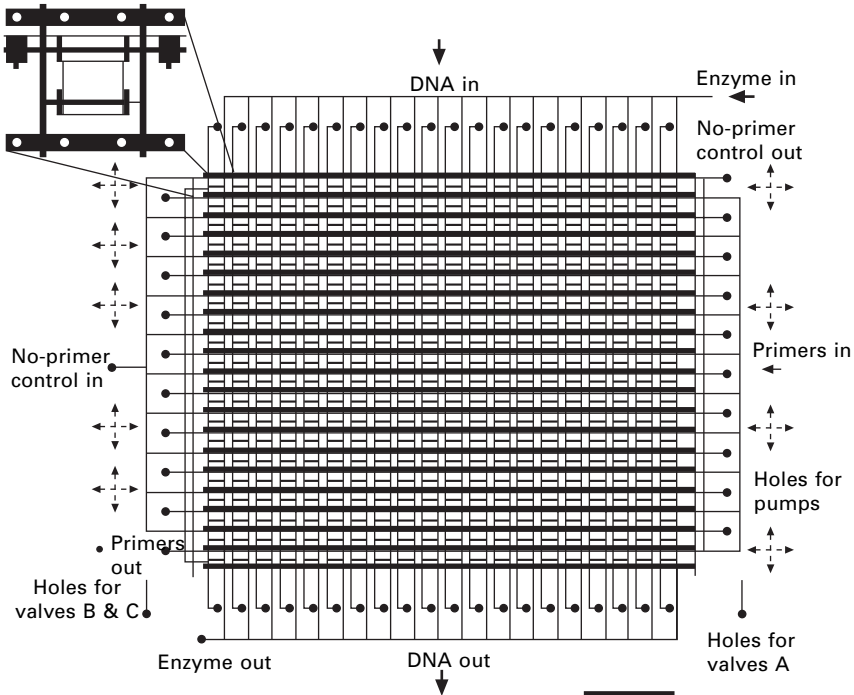
## 11.3 Microfluidic tools for molecular biology

### 11.3.1 Microfluidic PCR

One of the most fundamental widespread techniques used in molecular biology laboratories is PCR. The time-consuming nature of PCR, involving meticulous sample preparation, hours of thermocycling, and subsequent analysis, has motivated researchers in the last decade to build smaller, faster microfluidic devices to automate the process<sup>81–89</sup>.

PCR sample preparation, particularly for high throughput analysis of hundreds to thousands of samples, is a tedious manual procedure. When carried out manually using pipettors, potential problems include sample cross-contamination and leaving critical reagents out of the PCR mixture. Large-scale automation of this process in a microfluidic chip still remains a challenging task. Lu *et al.* recently used MLS to create a PDMS-based chip to simultaneously carry out 400 different PCR reactions<sup>89</sup> (Fig. 11.6). The device contained thousands of elastomeric valves and pumps, which were used to deliver, compartmentalize and mix nL volumes of the reagents for each reaction in parallel using two independent pressure supplies. Amplifications were carried out by placing the elastomeric chip hermetically sealed to a glass coverslip on a flatbed thermocycler (DNA Engine, MJ Research) and running a programmed amplification protocol for ~1 hour. After thermocycling, PCR products in the individual chambers were imaged using a modified DNA array scanner. The chip performance was very robust, as 98% of 3200 reactors tested produced the expected results. Forty-one ‘pipetting’ steps, loading the sample reagents through the punched hole interfaces, were necessary to carry out the experiment, much more efficient than the 1200 pipetting steps required if the same reactions were set up by hand.

Incorporating thermocycling elements for PCR on microfluidic chips is clearly desirable, particularly for rapid diagnostic applications<sup>84,85,90–95</sup>. The thermal mass of a typical PCR machine limits its intrinsic cycle times, with much of the process spent heating and cooling the sample block as transitions



11.6 Schematic diagram of the PCR chip layout, showing the various input, output, and control ports. Scale bar, 6.4 mm. Reproduced with permission from ref. 89. Copyright 2003 American Chemical Society.

between the annealing, elongation, and denaturation temperatures. A single-sample amplification chip was designed with a serpentine microchannel and three static temperature zones by Kopp *et al.*<sup>84</sup> The chip contains an etched glass microchannel bonded to three thermostated copper blocks corresponding to the PCR cycling temperatures. As the PCR-mixture is flowed through the serpentine channel, the solution passes repetitively through the temperature zones, resulting in efficient product amplification. Using this system, the authors amplified a 176-bp fragment from *N. gonorrhoeae* using total flow through times ranging from 90 seconds to 18.7 minutes. Product amplification improved with time, with runs at the high end (18.7 minutes) comparable to a 20 cycle run (50 minutes) using a commercial thermal cycler. A variation on this design developed by Liu *et al.* is a rotary PDMS device with integrated elastomeric pumps that cycles the PCR mixture through three temperature zones in a single circular channel<sup>95</sup>. Other integrated chips have been reported that combine thermocycling with subsequent product analysis<sup>92–94</sup>. Khandurina *et al.* fabricated a microfluidic chip that combined rapid sample amplification using an integrated Peltier cooler with electrophoretic separation<sup>92</sup>. The samples were rapidly cycled in a holding chamber on the etched glass microchips

followed by separation in an orthogonal channel containing 4% polydimethyl acrylamide and a fluorescent intercalating dye. Total analysis times of less than 20 minutes were achieved with as few as ten thermal cycles necessary for product detection by LIF.

### 11.3.2 Cell electroporation

With the wide variety of tools available to manipulate cells in microfluidic devices, there has been a growing interest in analyzing the mechanics and metabolic machinery of single cells. While several high-resolution techniques are available to detect, image, and analyze the contents of single cells, few methods exist for introducing foreign material into cells<sup>96</sup>. The plasma membrane is an efficient barrier to many compounds of interest, including fluorescent dyes, genetic material, and drugs. Rupturing this membrane, while preserving cell viability, is a delicate process. Several permeabilization methods have been developed, using mechanical (microinjection), chemical, and electrical techniques. Of these methods, electroporation is one of the most popular, in which the lipids in the plasma membrane re-orient to form hydrophilic pores in the presence of a strong electric field. The technique is very effective, but also results in high cell mortality. In bulk electroporation experiments, the mortality rate can be attributed to high electric fields commonly used in the process (kV/cm) combined with rough control over the exposure time. Recent advances in scaling down this process in microfluidic devices have significantly improved the electroporation process, enabling real-time monitoring of the membrane permeabilization state to maximize both cell loading with the material of interest and viability<sup>97–100</sup>.

Huang *et al.* developed a multilayer, silicon-based microfluidic electroporation device containing two electrodes in independent fluid-filled chambers separated by dielectric membrane (silicon nitride) containing a micromachined hole (2–10  $\mu\text{m}$  dia)<sup>99</sup>. By applying differential pressure between the two chambers, a single cell introduced into the top chamber is drawn into the hole, plugging it up. The low electrical conductance of the lipid membrane acts as an insulator in the system, isolating the two electrodes. When the voltage between two electrodes is increased, reversible electroporation of the cell occurs and aqueous pores form in cell membrane. Using a feedback circuit to limit the exposure time at the critical voltage threshold, the author demonstrated single-cell reversible electroporation of human prostate carcinoma (ND-1) cells. An improved version of this device was recently reported containing a microchannel for continuous sequential electroporation of single cells<sup>100</sup>. In addition to loading ND-1 cells with fluorescent dye, the authors also transfected the cells with the GFP gene to demonstrate the feasibility of single-cell genetic engineering.

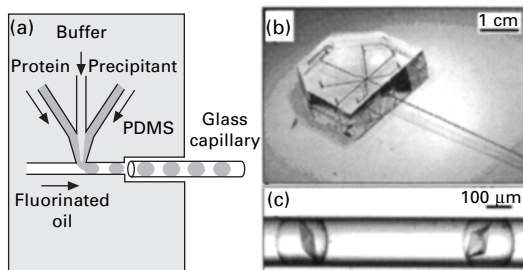
### 11.3.3 Protein crystallization

Protein crystallization is often regarded as a black art. Obtaining a high-resolution protein crystal in its native conformation is not a trivial process, and is often the result of years of work. Even in their crystallized state, proteins exist as a delicate, gel-like lattice of hydrogen bonds, salt bridges, hydrophobic and electrostatic interactions. Predicting the proper conditions for crystallization can be challenging, as slight changes in parameters like humidity, pH, salt concentration, or interfacial tension mean the difference between a perfect crystal or a disorganized mess. With the sequencing of the human genome, the demand for high-throughput protein crystallization has never been greater. Robotic systems have been developed to set up hundreds or thousands of crystallization experiments in parallel using standardized sets of solutions<sup>101</sup>. However, the relative costs of such systems, which work with nanoliters of solution, make them inaccessible for most laboratories.

Advantages of using microfluidic devices for protein crystallization include reduced reagent consumption, precise control over reagent mixing, inexpensive device prototyping, and the ability to create highly integrated addressable channel networks with multifunctional possibilities. Where a typical cell may only contain picograms of a protein of interest, minimization of the crystallization volume is clearly desirable for cost-effective high-throughput platforms.

To date, only a few microfluidic protein crystallization platforms have been developed. Juarez-Martinez *et al.* developed a silicone-based device with an array of etched microwells and integrated Peltier heating elements. Each well in the  $10 \times 10$  array was designed to hold  $5 \mu\text{l}$  of crystallization reagents, which required manual loading with a micropipette. Two Peltier elements were used to create a temperature gradient across the chip ( $12\text{--}40 \text{ }^\circ\text{C}$ ) and plastic sealing tape was used to cover the chambers to prevent evaporation. Using this chip, a model protein, hen egg white lysozyme, was crystallized to a resolution of  $1.78 \text{ \AA}$ <sup>102</sup>. Reducing the reagent volumes from microliters to nanoliters, protein crystallization has recently been carried out in a serial format using microdroplets<sup>103</sup> and in a parallel format within an addressable PDMS microarray<sup>4</sup>.

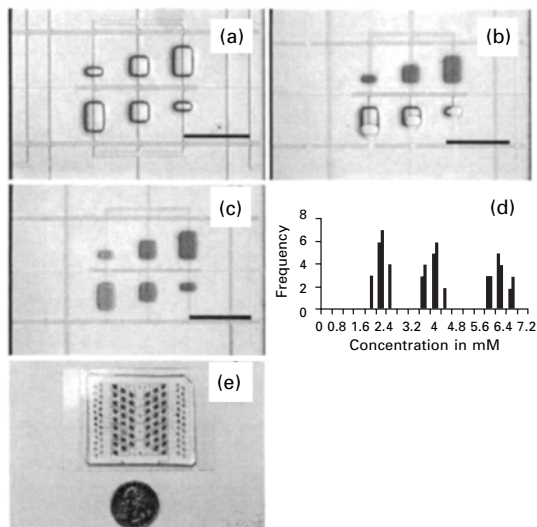
Zheng *et al.* used a multiphase microfluidic device to dynamically encapsulate multiple protein crystallization reagents (protein, precipitants, and additives) into nanoliter-size droplets broken off in a continuously flowing fluorinated oil stream (Fig. 11.7)<sup>103,130</sup>. Using a syringe pump to introduce the individual reagents into the chip, minimal mixing of the aqueous reagents is observed under the low Reynolds number flow conditions in the microchannels until the droplets break off in the oil stream. As the droplets flow down the channel in the continuous oil phase, active mixing (msec) is



11.7 (a) A schematic illustration of the method of forming droplets for protein crystallization trials in a PDMS/glass capillary composite microfluidic device. (b) A photograph of the composite device. All inlets and channels were filled with  $[\text{Fe}(\text{SCN})_x]^{(3-x)+}$  solution for clarity. (c) A microphotograph of thaumatin crystals grown inside droplets in a capillary. Droplets were generated by the method illustrated in (a). Reproduced with permission from ref. 130. Copyright 2004 WILEY-VCH Verlag GmbH & Co. KGaA.

achieved by introducing abrupt, serpentine-shaped bends in the microchannel, which promotes mixing by chaotic advection<sup>104</sup>. By actively controlling the relative volumetric flow rate of each of the aqueous components, droplets with different ratios of crystallization reagents can be generated. Subsequent crystallization is achieved by shutting off the pressure to spatially confine the droplets in the microchannel, followed by incubation at constant temperature in a vapor-saturated environment. Using this system, the authors were able to crystallize several proteins (lysozyme, thaumatin, bovine catalase and glucose isomerase).

A parallel approach for protein crystallization in microfluidic devices was developed by Hansen *et al.* Using MLS, Hansen and co-workers fabricated a multilayer PDMS device containing 480 elastomeric valves and performs 144 parallel reactions using only 10 nL of protein/ reaction (Fig. 11.8)<sup>4</sup>. The chip consists of a soda-lime glass microscope slide (Corning 2947) wet-etched to provide parallel chambers for crystallization reagents and protein interfaced with a multilayer PDMS device containing the microfluidic circuitry (flow channels and elastomeric valves). To set up the chip, crystallization reagents and protein sample are loaded in parallel into their respective chambers separated by an elastomeric valve to prevent premature mixing. The gas-permeable nature of PDMS allows the channels to be dead-end filled under pressure, with the gas escaping through the porous polymer. By releasing the barrier valve, the protein interacts with the crystallization reagents by free-interface diffusion. On-chip testing was carried out with 11 model proteins using two or more precipitant ratios, including three proteins with unpublished structures (bacterial primase catalytic core domain, type II topoisomerase ATPase domain, and a mycobacterial RNase), and a bacterial 70S ribosome. Crystal growth was observed for all tested proteins, including mycobacterial



**11.8** (a) Section of a device showing three pairs of compound reaction chambers. (b) Loading of reagents using pressurized outgas priming method. (c) A gradient of dye concentration. (d) Histogram showing the insensitivity of barrier interface metering (BIM) to fluid viscosity. (e) Prototype protein crystallization chip with 144 parallel reaction chambers (Scale bar = 1 mm). Reproduced with permission from ref. 4. Copyright 2002 National Academy of Sciences, U.S.A.

RNase, which had never been successfully crystallized by conventional methods. Recovery of proteins with large crystals ( $>30\ \mu\text{m}$ ) was also demonstrated by removing the PDMS top of the chip and flash freezing the crystals in cryoprotectant (25% ethylene glycol) for subsequent X-ray characterization.

## 11.4 Future trends

Tremendous progress has been made in the last decade on the design of bio-inspired microfluidic chips, providing the foundation for an exciting new platform having applications in a wide range of fields such as chemical engineering, public health, and pharmacology. While much of the research is still at the proof-of-concept stage, this technology has the potential to transform biochemical analysis in the same way that miniaturization transformed computing, making tools that are smaller, more integrated, less expensive, and a lot faster<sup>105</sup>.

One area in which microfluidics is positioned to have a great impact is proteomics. While the basic principles of miniaturized, parallel microarray-based protein assays were described more than a decade ago<sup>106,107</sup>, the recent explosive interest in protein-based HTS platforms has been fueled by progress

in genome-based sequencing projects<sup>1,2</sup>. Microfluidic devices provide an ideal, picoliter-scale environment for on-chip protein synthesis and subsequent analysis. *In vitro* transcription/translation kits, which are commercially available, can be used to synthesize proteins that are difficult to produce or toxic in whole-cell based systems, such as fusion proteins<sup>108</sup>. Cell-free systems can now be used to study the *in vitro* assembly of membrane proteins and viral particles, rapidly produce and analyze protein mutants, and enlarge the genetic code by incorporating unnatural amino acids<sup>109</sup>. As *in vitro* systems do not require recombinant hosts, problems related to cell culture conditions and heterogeneous protein expression at the single cell level are eliminated. Given the protein analysis tools already demonstrated in microfluidic devices, including on-chip separation techniques discussed earlier in the chapter, coupling these expression systems with a microfluidic platform is a logical fit to bridge the gap between genomics and proteomics.

The most recent trends in the pharmaceutical industry are directed towards living cell analysis, as cells represent the ultimate target for drugs and a new source of biological knowledge<sup>110</sup>. Bead-based microfluidic devices have been developed by Luminex (Austin, TX), which use internally color-coded microspheres coated with multiple probes for highly multiplexed single-cell assays<sup>111</sup>. Microfluidics-based cell-based enzyme assays with soluble substrates are being developed as well. Electrokinetic microfluidic chips are being developed by Caliper Technologies (Mountain View, CA) and Orchid Biosciences (Princeton, NJ) which use electrokinetic and hydrodynamic forces to mix cells and reagents<sup>112</sup>, permitting up to 12 samples to be analyzed in a parallel fashion in isolated channels. Continuous-flow microfluidic enzyme inhibition assays coupled directly to microtiter plates have also been developed using Ca<sup>2+</sup>-sensitive fluorescent indicators with 50–100 cells/data point<sup>113</sup>.

The mainstream acceptance of microfluidic hardware as replacements for common laboratory instrumentation, ending the tyranny of pipetting, will clearly depend on the development of robust, easy-to-use platforms. While many biological applications have been demonstrated in a microfluidic format, we are just beginning to see the integration of the pieces, combining microfabrication techniques with sensors and detectors to create truly stand-alone systems. As we develop a better understanding of the biology and physics at the microscale, the future looks bright for microfluidics.

## 11.5 Sources of further information and advice

There are several excellent review articles and books that have been published in the last few years that provide excellent background material for further reading. Recent general reviews and texts covering biological applications in microfluidic devices include 'Microfluidic devices fabricated in poly(dimethylsiloxane) for biological studies' by S.K. Sia and G.M.

Whitesides<sup>114</sup>, ‘Microfluidics meets MEMS’ by E. Verpoorte and N.F. De Rooij<sup>115</sup>, ‘Physics and applications of microfluidics in biology’ by D.J. Beebe, G.A. Mensing, and G.M. Walker<sup>116</sup>, and ‘Microfabricated devices in biotechnology and biochemical processing’ by T. Chovan and A. Guttman<sup>117</sup>. A few general textbooks are also recommended: *Microfluidics and Biomems Applications*<sup>118</sup>, *Microfluidic Technology and Applications*<sup>119</sup> and *Fundamentals and Applications of Microfluidics*<sup>120</sup>.

For DNA-based applications, the following recent review articles are recommended: ‘Microfluidic separation of DNA’ by R. Ashton, C. Padala, and R.S. Kane<sup>25</sup>, ‘Recent progress in microfluidic devices for nucleic acid and antibody assays’ by P.R. Selvaganapathy, E.T. Carlen, and C.H. Mastrangelo<sup>121</sup>, ‘Micro total analysis systems-Part II’ by P.A. Auroux *et al.*<sup>122</sup> and ‘Biochemical analysis with microfluidic systems’ by Bilitewski *et al.*<sup>123</sup>.

For protein-based applications, the following recent review articles are recommended: ‘Microfluidic systems in proteomics’ by N. Lion *et al.*<sup>37</sup>, ‘Microfluidics in structural biology: smaller, faster... better’ by C. Hansen and S.R. Quake<sup>124</sup>, ‘Lab-on-a-chip for drug development’ by B.H. Weigl, R.L. Bardell, and C.R. Cabrera<sup>125</sup>, ‘Adapting arrays and lab-on-a-chip technology for proteomics’ by D. Figeys<sup>126</sup>, and ‘Lab-on-a-chip: applications in proteomics’ by S. Mouradian<sup>127</sup>.

For cell-based applications, the following recent review articles are recommended: ‘Microfluidic devices for cellomics: a review’ by H. Andersson and A. van den Berg<sup>59</sup>, ‘Integration of cell culture and microfabrication technology’ by T.H. Park and M.L. Shuler<sup>128</sup>, and ‘A BioMEMS review: MEMS technology for physiologically integrated devices’ by A.C.R. Grayson *et al.*<sup>129</sup>.

## 11.6 References

1. Lander E.S., *et al.* Initial sequencing and analysis of the human genome. *Nature*, 2001, **409**, 860–921.
2. Venter J.C., *et al.* The sequence of the human genome. *Science*, 2001, **291**, 1304–1351.
3. Giot L. *et al.* A protein interaction map of *Drosophila melanogaster*. *Science*, 2003, **302**, 1727–1736.
4. Hansen C.L., Skordalakes E., Berger J.M. and Quake S.R., A robust and scalable microfluidic metering method that allows protein crystal growth by free interface diffusion. *Proc. Natl. Acad. Sci.*, 2002, **99** (26), 16531–16536.
5. Borenstein J.T., *et al.* Microfabricated technology for vascularized tissue engineering. *Biomed. Microdevices*, 2002, **4**, 167–175.
6. Harrison D.J., Manz A., Fan Z., Luedi H. and Widmer H.M. Capillary electrophoresis and sample injection systems integrated on a planar glass chip. *Anal. Chem.*, 1992, **64**, 1926–1932.

7. Harrison D.J., *et al.* Micromachining a miniaturized capillary-electrophoresis based chemical-analysis system on a chip. *Science*, 1993, **261**, 895–897.
8. Manz A., *et al.* Design of an open-tubular column liquid chromatograph using silicon chip technology. *Sens. Actuators B*, 1990, **1**, 249–255.
9. Ng J.M.K., Gitlin I., Stroock A.D. and Whitesides G.M., Components for integrated poly(dimethylsiloxane) devices. *Electrophoresis*, 2002, **23**, 3461–3473.
10. Manz A., Graber N. and Widmer H.M., Miniaturized total chemical analysis systems: A novel concept for chemical sensing. *Sensors. Actu. B.*, 1990, **1** (1-6), 244–248.
11. Harrison D.J., *et al.* Micromachining a miniaturized capillary electrophoresis-based chemical-analysis system on a chip. *Science*, 1993, **261**, 895–897.
12. Chou H.P., Spence C., Scherer A. and Quake S., A microfabricated device for sizing and sorting DNA molecules. *Proc. Natl. Acad. Sci. U.S.A.*, 1999, **96** (1), 11–13.
13. Effenhauser C.S., Paulus A., Manz A. and Widmer H.M., High-speed separation of antisense nucleotides on a micromachined capillary electrophoresis device. *Anal. Chem.*, 1994, **66** (18), 2949–2953.
14. Woolley A.T. and Mathies R.A., Ultra-high speed DNA sequencing using capillary electrophoresis chips. *Anal. Chem.*, 1995, **67** (20), 3676–3680.
15. Ramsey J.M., Jacobson S.C. and Knapp M.R., Microfabricated chemical measurement systems. *Nature Medicine*, 1995, **1**, 1093–1096.
16. Sunada W.M. and Blanch H.W. Polymeric separation media for capillary electrophoresis of nucleic acids. *Electrophoresis*, 1997, **18**, 2243–2254.
17. Barbier V. and Vivoy J., Advanced polymers for DNA separation. *Curr. Opin. Biotech.*, 2003, **14**, 51–57.
18. Selvaganapathy P.R., Carlin E.T., and Mastrangelo C.H., Recent progress in microfluidic devices for nucleic acid and antibody assays. *Proc. IEEE*, 2003, **91**(6), 954–975.
19. Woolley A.T. and Mathies R.A., Ultra-high speed DNA fragment separation using microfabricated capillary array. *Proc. Natl. Acad. Sci. U.S.A.*, 1994, **91**, 11348–11352.
20. McCormick R.M., Nelson R.J., AlonsoAmigo M.G., Benvegno J. and Hooper H.H., Microchannel electrophoretic separations of DNA in injection-molded plastic substrates. *Anal. Chem.*, 1997, **69** (14), 2626–2630.
21. Woolley A.T., Sensabaugh G.F. and Mathies R.A., High-speed DNA genotyping using microfabricated capillary array electrophoresis chips. *Anal. Chem.*, 1997, **69** (11), 2181–2186.
22. Cheng J., *et al.* Degenerate oligonucleotide primed polymerase chain reaction and capillary electrophoretic analysis of human DNA on microchip-based devices. *Anal. Biochem.*, 1998, **257** (2), 101–106.
23. Schmalzing D., *et al.* DNA typing in thirty seconds with a microfabricated device. *Proc. Natl. Acad. Sci U.S.A.*, 1997, **94** (19), 10273–10278.
24. Paegel B.M., Emrich C.M., Wedemayer G.J., Scherer J.R. and Mathies R.A., High throughput DNA sequencing with a microfabricated 96-lane capillary array electrophoresis bioprocessor. *Proc. Natl. Acad. Sci U.S.A.*, 2002, **99** (2), 574–579.
25. Ashton R., Padala C. and Kane R.S., Microfluidic separation of DNA. *Curr. Opin. Biotech.*, 2003, **14**, 497–504.
26. Xu Z.Q., Hirokawa T., Nishine T. and Arai A., High-sensitivity capillary gel electrophoretic analysis of DNA fragments on an electrophoresis microchip using electrokinetic injection with transient isotachophoretic preconcentration. *J. Chromatography A*, 2003, **990**, 53–61.

27. Brahmasandra S.N., Burke D.T., Mastrangelo C.H. and Burns M.A., Mobility, diffusion and dispersion of single-stranded DNA in sequencing gels. *Electrophoresis*, 2001, **22** (6), 1046–1062.
28. Solignac D. and Gijs M.A.M., Pressure pulse injection: a powerful alternative to electrokinetic sample loading in electrophoresis microchips. *Anal. Chem.*, 2003, **75** (7), 1652–1657.
29. Duke T.A.J. and Austin R.H., Microfabricated sieve for the continuous sorting of macromolecules. *Phys. Rev. Lett.*, 1998, **80** (7), 1552–1555.
30. Ertas D., Lateral separation of macromolecules and polyelectrolytes in microlithographic arrays. *Phys. Rev. Lett.*, 1998, **80** (7), 1548–1551.
31. Huang R.L., *et al.* Role of molecular size in ratchet fractionation. *Phys. Rev. Lett.*, 2002, **89** (17), Art. No. 178301.
32. Bader J.S., *et al.* DNA transport by a micromachined Brownian ratchet device. *Proc. Natl. Acad. Sci. U.S.A.*, 1999, 96 (23): 13165–13169.
33. Han J., Turner S.W. and Craighead H.G., Entropic trapping and escape of long DNA molecules at submicron size constriction. *Phys. Rev. Lett.*, 1999, **83** (8): 1688–1691.
34. Han J. and Craighead C.G., Separation of long DNA molecules in a microfabricated entropic trap array. *Science*, 2000, **288** (5468), 1026–1029.
35. Turner S.W.P., Cabodi M. and Craighead H.G., Confinement-induced entropic recoil of single DNA molecules in a nanofluidic structure. *Phys. Rev. Lett.*, 2002, **88** (12), Art. No. 128103.
36. Cabodi M., Turner S.W.P., Craighead H.G., Entropic recoil separation of long DNA molecules. *Anal. Chem.*, 2002, **74** (20), 5169–5174.
37. Lion N., *et al.* Microfluidic systems in proteomics. *Electrophoresis*, 2003, **24** (21), 3533–3562.
38. Lichtenberg J., de Rooij N.F., Verpoorte E., Sample pretreatment on microfabricated devices. *Talanta*, 2002, **56** (2), 233–266.
39. Xu N.Q., *et al.* A microfabricated dialysis device for sample cleanup in electrospray ionization mass spectrometry. *Anal. Chem.* 1998, **70** (17), 3553–3556.
40. Xiang F., Lin Y.H., Wen J., Matson D.W. and Smith R.D., An integrated microfabricated device for dual microdialysis and on-line ESI ion trap mass spectrometry for analysis of complex biological samples. *Anal. Chem.*, 1999, **71** (8), 1485–1490.
41. Lion N., Gellon J., Jensen H. and Girault H.H., On-chip protein sample desalting and preparation for direct coupling with electrospray ionization mass spectrophotometry. *J. Chrom. A.*, 2003, **1003** (1–2), 11–19.
42. Oleschuk R.D., Shultz-Lockyear L.L., Ning Y.B. and Harrison D.J., Trapping of bead-based reagents within microfluidic systems: On-chip solid-phase extraction and electrochromatography. *Anal. Chem.*, 2000, **72** (3), 585–590.
43. Li J. *et al.* Application of microfluidic devices to proteomics research – Identification of trace-level protein digests and affinity capture of target peptides. *Molec. Cell. Proteo.*, 2002, **1** (2): 157–168.
44. Bergkvist J. *et al.* Improved chip design for integrated solid-phase microextraction in on-line proteomic sample preparation. *Proteomics*, 2002, **2** (4), 422–429.
45. Lettieri G.L., Dodge A., Boer G., de Rooij N.F. and Verpoorte E., A novel microfluidic concept for bioanalysis using freely moving beads trapped in recirculating flows. *Lab Chip*, 2003, **3**, 34–39.

46. Yu C., Davey M.H., Svec F. and Frechet J.M.J., Monolithic porous polymer for on-chip solid-phase extraction and preconcentration prepared by photoinitiated *in situ* polymerization within a microfluidic device. *Anal. Chem.*, 2001, **73** (21), 5088–5096.
47. Weigl B.H. and Yager P., Microfluidics – Microfluidic diffusion-based separation and detection. *Science*, 1999, **283** (5400), 346–347.
48. Schilling E.A., Kamholz A.E. and Yager P., Cell lysis and protein extraction in a microfluidic device with detection by a fluorogenic enzyme assay. *Anal. Chem.*, 2002, **74** (8), 1798–1804.
49. Cohen A.S. and Karger B.L., High performance sodium dodecyl sulfate polyacrylamide gel electrophoresis of peptides and proteins. *J. Chrom.*, 1987, **397**, 409–417.
50. Yao S., *et al.* SDS capillary gel electrophoresis of proteins in microfabricated channels. *Proc. Natl. Acad. Sci. U.S.A.*, 1999, **96** (10), 5372–5377.
51. Figeys D. and Pinto D., Proteomics on a chip: Promising developments. *Electrophoresis*, 2001, **22** (2), 208–216.
52. Hofmann O., Che D.P., Cruickshank K.A. and Muller U.R., Adaptation of capillary isoelectric focusing to microchannels on a glass chip. *Anal. Chem.*, 1999, **71** (3), 678–686.
53. Mao Q.L. and Pawliszyn J., Demonstration of isoelectric focusing on an etched quartz chip with UV absorption imaging detection. *Analyst*, 1999, **124** (5), 637–641.
54. Xu J.D., Locascio L., Gaitan M. and Lee C.S., Room-temperature imprinting method for plastic microchannel fabrication. *Anal. Chem.*, 2000, **72** (8), 1930–1933.
55. Ramsey J.D., Jacobson S.C., Culbertson C.T., Ramsey J.M., High-efficiency, two-dimensional separations of protein digests on microfluidic devices. *Anal. Chem.*, 2003, **75** (15), 3758–3764.
56. Herr A.E., *et al.* On-chip coupling of isoelectric focusing and free-solution electrophoresis for multidimensional separations. *Anal. Chem.*, 2003, **75** (5), 1180–1187.
57. Wang Y.-C., Choi M.H. and Han J., On-chip IEF peak manipulation for 2D protein separation and MS coupling. *Proc. MicroTAS*, October 2003.
58. Chen X.X., Wu H.K., Mao C.D. and Whitesides G.M., A prototype two-dimensional capillary electrophoresis system fabricated in poly(dimethylsiloxane). *Anal. Chem.*, 2002, **74** (8), 1772–1778.
59. Andersson H. and van den Berg A., Microfluidic devices for cellomics: a review. *Sens. Actua. B*, 2003, **92**, 315–325.
60. Fiedler S., Shirley S., Schnelle T., Fuhr G., Dielectrophoretic sorting of particles and cells in a microsystem. *Anal. Chem.*, 1998, **70** (9), 1909–1915.
61. Markx G., Huang Y., Zhou X. and Pethig R., Dielectrophoretic characterization and separation of microorganisms. *Microbiology*, 1994, **140**, 585–591.
62. Cheng J., *et al.* Electric field controlled preparation and hybridization analysis of DNA/RNA from *E. coli* on microfabricated bioelectronic chips. *Nat. Biotechnol.*, 1998, **16**, 541–546.
63. Becker F., *et al.* Separation of human breast cancer cells from blood by differential dielectric affinity. *Proc. Natl. Acad. Sci. U.S.A.*, 1995, **92**, 860–864.
64. Wang X.-B. *et al.* Cell separation by dielectrophoretic field-flow fractionation. *Anal. Chem.*, 2000, **72** (4), 832–839.

65. Arai F., *et al.* High-speed separation system of randomly suspended single living cells by laser trap and dielectrophoresis. *Electrophoresis*, 2001, **22**, 283–288.
66. Xu J., *et al.* Dielectrophoretic separation and transportation of cells and bioparticles on microfabricated chips. *MicroTAS 2001*, 565–566.
67. Huang Y., *et al.* Electric manipulation of bioparticles and macromolecules on microfabricated electrodes. *Anal. Chem.*, 2001, **73** (7), 1549–1559.
68. Voldman J., Gray M.L., Toner M. and Schmidt M.A., A microfabrication-based dynamic array cytometer *Anal. Chem.*, 2002, **74** (16), 3984–3990.
69. Carlson R.H., *et al.* Self-sorting of white blood cells in a lattice. *Phys. Rev. Lett.*, 1997, **79** (11), 2149–2152.
70. Bakajin O., *et al.* Sizing, Fractionation and Mixing of Biological Objects via Microfabricated Devices. *MicroTAS 1998*, 193–198.
71. Wilding P., *et al.* Integrated cell isolation and polymerase chain reaction analysis using silicon microfilter chambers. *Anal. Biochem.*, 1998, **257**, 95–100.
72. Andersson H., van der Wijngaart W., Enoksson P., Stemme G. Micromachined flow-through filter-chamber for chemical reactions on beads, *Sens. Actua. B*, 2000, **67**, 203–208.
73. Fu A., Chou H.-P., Spence C., Arnold F.H. and Quake S.R., An integrated microfabricated cell sorter. *Anal. Chem.*, 2002, **74** (11), 2451–2457.
74. Wheeler A.R., *et al.* Microfluidic device for single-cell analysis. *Anal. Chem.*, 2003, **75** (14): 3581–3586.
75. Thorsen T., Maerkl S.J., Quake S.R., Microfluidic large-scale integration. *Science*, 2002, **298** (5593): 580–584.
76. Unger M.A., Chou H.P., Thorsen T. and Scherer A., Quake S. Monolithic Microfabricated Valves and Pumps by Multilayer Soft Lithography. *Science*, 2000, **288**, 113–116.
77. Fu A.Y., Spence C., Scherer A., Arnold F.H. and Quake S.R., A Microfabricated Fluorescence-Activated Cell Sorter. *Nature Biotech.*, 1999, **17**, 1109–1111.
78. McClain M.A., Culbertson C.T., Jacobson S.C. and Ramsey J.M., Flow cytometry of *Escherichia coli* on microfluidic devices. *Anal. Chem.*, 2001, **73** (21), 5334–5338.
79. Kruger J., *et al.* Development of a microfluidic device for fluorescence activated cell sorting. *J. Micromech. Microeng.*, 2002, **12** (4), 486–494.
80. Wolff A., *et al.* Integrating advanced functionality in a microfabricated high-throughput fluorescent-activated cell sorter. *Lab. Chip.*, 2003, **3** (1), 22–27.
81. Shoffner M., Cheng J., Hvichia G., Kricka L. and Wilding P., Chip PCR. I. Surface passivation of microfabricated silicon-glass chips for PCR. *Nucleic. Acids. Res.*, 1996, **24**, 375–79.
82. Cheng J., Shoffner M., Hvichia G., Kricka L. and Wilding P., Chip PCR. II. Investigation of different PCR amplification systems in microfabricated silicon-glass chips. *Nucleic. Acids. Res.*, 1996, **24**, 380–85.
83. Taylor T., Winn-Deen E., Picozza E., Woudenberg T. and Albin M., Optimization of the performance of the polymerase chain reaction in silicon-based micro-structures. *Nucleic Acids Res.*, 1997, **25**, 3164–68.
84. Kopp M., de Mello A., Manz A., Chemical amplification: continuous-flow PCR on a chip. *Science*, 1998, **280**:1046–48.
85. Giordano B., Ferrance J., Swedberg S., Huhmer A. and Landers J., Polymerase chain reaction in polymeric microchips: DNA amplification in less than 240 seconds. *Anal. Biochem.*, 2001, **291**, 124–32.

86. Wilding P., *et al.* Integrated cell isolation and polymerase chain reaction analysis using silicon microfilter chambers. *Anal. Biochem.*, 1998, **257**, 95–100.
87. Hong J., Fujii T., Seki M., Yamamoto T. and Endo I., PDMS (polydimethylsiloxane)-glass hybrid microchip for gene amplification. In *Annu. IEEE EMBS Conf. Microtechnology Med. Biol.*, 1st, Lyon, Fr., A. Dittmar and D. Beebe D, eds. 407–410, 2000.
88. Obeid P.J. and Christopoulos T.K., Continuous-flow DNA and RNA amplification chip combined with laser-induced fluorescence detection. *Anal. Chim. Acta.*, 2003, **494** (1–2), 1–9.
89. Liu J., Hansen C. and Quake S.R., Solving the ‘world-to-chip’ interface problem with a microfluidic matrix. *Anal. Chem.*, 2003, **75** (18), 4718–4723.
90. Lagally E., Simpson P. and Mathies R., Monolithic integrated microfluidic DNA amplification and capillary electrophoresis analysis system. *Sensor Actua. B*, 2000, **63**, 138–146.
91. Woolley A., *et al.* Functional integration of PCR amplification and capillary electrophoresis in a microfabricated DNA analysis device. *Anal. Chem.*, 1996, **68** (23), 4081–4086.
92. Khandurina J., *et al.* Integrated system for rapid PCR-based DNA analysis in microfluidic devices. *Anal. Chem.*, 2000, **72**(13), 2995–3000.
93. Rodriguez I., *et al.* Practical integration of polymerase chain reaction amplification and electrophoretic analysis in microfluidic devices for genetic analysis. *Electrophoresis*, 2003, **24** (1–2), 172–178.
94. Koh C.G., Tan W., Zhao M.Q., Ricco A.J. and Fan Z.H., Integrating polymerase chain reaction, valving, and electrophoresis in a plastic device for bacterial detection. *Anal. Chem.*, 2003, **75** (17), 4591–4598.
95. Liu J., Enzelberger M. and Quake S., A nanoliter rotary device for polymerase chain reaction. *Electrophoresis*, 2002, **23** (10), 1531–1536.
96. Olofsson J., *et al.* Single cell electroporation. *Curr. Opin. Biotech.*, 2003, **14**, 29–34.
97. Lin Y.-C. and Huang M.-Y., Electroporation chips for *in vitro* gene transfection. *J. Micromech. Microeng.*, 2001, **11**, 542–547.
98. Lin Y.-C., Jen C.-M., Huang M.-Y., Wu C.-Y., Lin X.-Z., Electroporation chips for continuous gene transfection. *Sensor Actuat. B*, 2001, **79**, 137–143.
99. Huang Y. and Rubinsky B., Microfabricated electroporation chip for single cell membrane electroporation. *Sensor Actuat. A*, 2001, **89**, 242–249.
100. Huang Y. and Rubinsky B., Flow-through micro-electroporation chip for high efficiency single-cell genetic manipulation. *Sensor Actuat. A*, 2003, **104**, 205–212.
101. van der Woerd M., Ferree D., Pusey M., The promise of macromolecular crystallization in microfluidic chips. *J. Struct. Biol.*, 2003, **142**, 180–187.
102. Juarez-Martinez G., Steinmann P., Roszak A.W., Isaacs N.W. and Cooper J.M., High-throughput screens for postgenomics: Studies of protein crystallization using microsystems technology. *Anal. Chem.*, 2002, **74** (14), 3505–3510.
103. Zheng B., Roach L.S. and Ismagilov R.F., Screening of protein crystallization conditions on a microfluidic chip using nanoliter-size droplets. *J. Am. Chem. Soc.*, 2003, **125**, 11170–11171.
104. Song H., Tice J.D. and Ismagilov R.F., A microfluidic system for controlling reaction networks in time. *Angew. Chem. Intl.*, 2003, **42** (7), 768–772.
105. Sassi A.P., Xue Q.F. and Hooper H.H., Making analysis in the life sciences faster through miniaturization. *Amer. Lab.*, 2000, **32** (20), 36.

106. Templin M.F., *et al.* Protein microarray technology. *Trends. Biotech.*, 2002, **20** (4), 160–166.
107. Ekins R.P., Chu F. and Bigarte E., Multispot, multianalyte immunoassay. *Ann. Biol. Clin.* (Paris), 1990, **48**, 655–666.
108. Martin G.A., Kawaguchi R., DeGiovanni A., Fukushima M. and Mutter W., High-yield, in vitro protein expression using a continuous-exchange, coupled transcription/translation system. *Biotechniques*, 2001, **31** (4), 948–950.
109. Jermutus L., Ryabova L.A. and Pluckthun A., Recent advances in producing and selecting functional proteins by using cell-free translation. *Curr. Opin. Biotech.*, 1998, **9** (5), 534–548.
110. Khandurina J. and Guttman A., Microchip-based high-throughput screening analysis of combinatorial libraries. *Curr. Opin. Chem. Biol.*, 2001, **6**, 359–366.
111. Yang L., Tran D.K. and Wang X., BADGE, BeadsArray for the detection of gene expression, a high-throughput diagnostic bioassay. *Genome Res.*, 2001, **11**, 1888–1898.
112. Khandurina J. and Guttman M., Bioanalysis in microfluidic devices. *J. Chromat. A.*, 2002, **943**, 159–183.
113. Sundberg S.A., High-throughput and ultra-high-throughput screening: solution- and cell-based approaches. *Curr. Opin. Biotech.*, 2000, **11**, 47–53.
114. Sia S.K. and Whitesides G.M., Microfluidic devices fabricated in poly(dimethylsiloxane) for biological studies. *Electrophoresis*, 2003, **24** (21), 3563–3576.
115. Verpoorte E. and De Rooij N.F., Microfluidics meets MEMS. *P. IEEE*, 2003, **91** (6), 930–953.
116. Beebe D.J., Mensing G.A. and Walker G.M., Physics and applications of microfluidics in biology. *Ann. Rev. Biomed. Eng.*, 2002, **4**, 261–286.
117. Chovan T. and Guttman A., Microfabricated devices in biotechnology and biochemical processing. *Trends Biotech.*, 2002, **20** (3), 116–122.
118. *Microfluidics and Biomems Applications*. Francis E.H., Tay, ed., Kluwer Academic Pub., 2002.
119. Koch M., Evans A. and Brunnschweiler A., *Microfluidic Technology and Applications*. Institute of Physics Pub., 2000.
120. Nguyen N.-T. and Wereley S.T., *Fundamentals and Applications of Microfluidics*. Boston: Artech House, 2002.
121. Selvaganapathy P.R., Carlen E.T. and Mastrangelo C.H., Recent progress in microfluidic devices for nucleic acid and antibody assays. *P. IEEE*, 2003, **91** (6), 954–975.
122. Auroux P.A., Iossifidis D., Reyes D.R., Manz A., Micro total analysis systems. 2. Analytical standard operations and applications. *Anal. Chem.*, 2002, **74** (12), 2637–2652.
123. Bilitewski U., Genrich M., Kadow S. and Mersal G., Biochemical analysis with microfluidic systems. *Anal. Bioanal. Chem.*, 2003, **377** (3), 556–569.
124. Hansen C. and Quake S.R., Microfluidics in structural biology: smaller, faster... better. *Curr. Opin. Struct. Biol.*, 2003, **13** (5), 538–544.
125. Weigl B.H., Bardell R.L. and Cabrera C.R., Lab-on-a-chip for drug development. *Adv. Drug Deliv. Rev.*, 2003, **55** (3): 349–377.
126. Figeys D., Adapting arrays and lab-on-a-chip technology for proteomics. *Proteomics*, 2002, **2** (4), 373–382.

127. Mouradian S., Lab-on-a-chip: applications in proteomics. *Curr. Opin. Chem. Biol.*, 2002, **6** (1), 51–56.
128. Park T.H. and Shuler M.L., Integration of cell culture and microfabrication technology. *Biotech. Prog.*, 2003, **19** (2), 243–253.
129. Grayson A.C.R., *et al.* A BioMEMS review: MEMS technology for physiologically integrated devices. *P. IEEE*, 2004, **92** (1): 6–21.
130. Zheng B., Dice J.T., Roach L.S. and Ismagilov R.F., A Droplet-Based, Composite PDMS/GlassCapillary Microfluidic System for Evaluating Protein Crystallization Conditions by Microbatch and Vapor-Diffusion Methods with On-Chip X-Ray Diffraction. *Angew. Chem. Intl.*, 2004, **43** (19), 2508–2511.

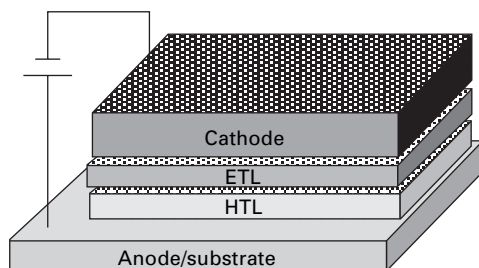
## Nonlithographic patterning: application of inkjet printing in organic-based devices

Y YOSHIOKA and G E JABBOUR,  
Arizona State University, USA

### 12.1 Introduction

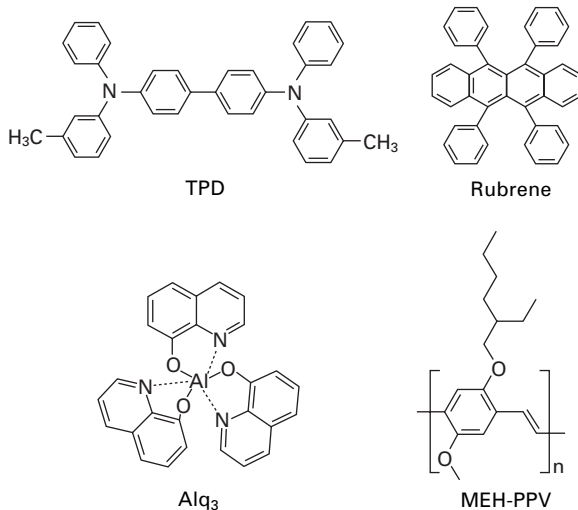
Organic light-emitting devices (OLEDs) are a subject of interest to many researchers and industries due to their promising attributes for applications in flat panel displays. The ease of fabrication, wide-viewing angle, wide range of colors, and mechanical flexibility are some of the attractive features of such devices. The flexible nature of OLEDs allows for new applications to emerge, such as wearable optoelectronics and roll-up displays.

A simple OLED structure consists of two thin organic layers sandwiched between two electrodes. One organic layer is the hole transport layer (HTL), which is designed to transport holes injected from the anode. The other layer is the electron transport layer (ETL), which is responsible for the transport of electrons injected from the cathode, as shown in Fig. 12.1. Either of the layers may be used as the light-emission source, but most often a dopant is used to take on this function. Some of the often used materials in university settings are: triphenyldiamine (TPD-used as HTL), rubrene (dopant), tris-(8-hydroxyquinoline) aluminum (Alq<sub>3</sub>-used as ETL and sometimes as light emitter). Although the above materials are small molecules, OLEDs can also be fabricated from polymers where in this case the construction of the device is a little simpler. In this regard, a single layer of polymer material can be



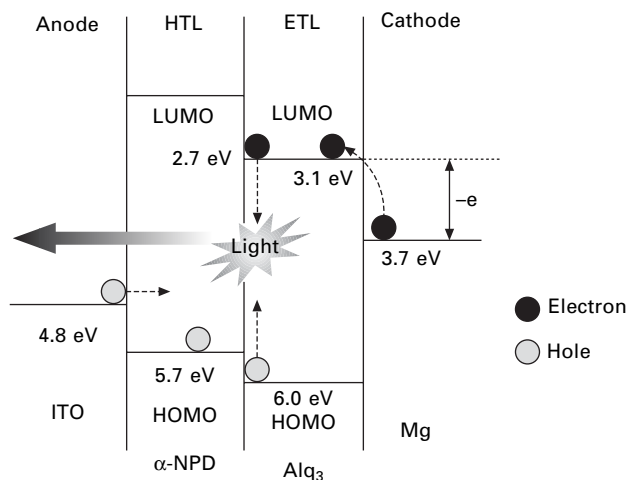
12.1 Schematic image of the two-layer OLED.

spin coated onto a given substrate and used as a charge transporter and light emitter, simultaneously. One of the more popular materials used in early research is polyphenylene vinylene (PPV) and its more soluble derivative poly[1-methoxy-4-(2-ethylhexyloxy-2,5-phenylene vinylene)] (MEH-PPV), Fig. 12.2.



12.2 The molecular structures of TPD, rubrene, Alq<sub>3</sub>, and MEH-PPV.

Upon application of an external voltage, holes are injected from the anode into the highest occupied molecular orbital (HOMO) of the HTL, and electrons are injected from the cathode into the lowest unoccupied molecular orbital (LUMO) of the ETL. The injected holes and electrons are driven towards the oppositely charged electrode, under the influence of the electric field. The capture of oppositely charged carriers on a molecular site of the light-emitting material (or on a part of the polymer chain in the case of polymer-based OLEDs) forms excited molecular states (excitons). Light output is generated via radiative decay of excitons. Figure 12.3 shows an example of an energy level diagram for a two-layer OLED, using common electrodes, such as ITO, magnesium, and the electron and hole transport materials, Alq<sub>3</sub> and *m*-NPB (N,N'-bis(naphthalene-1-yl)-N,N'-bis(phenyl)benzidine), respectively. Since there is no dopant used, Alq<sub>3</sub> will function as an ETL and light-emitting medium. The HOMO of the HTL lies only slightly above that of the ETL, which is not a significant barrier for hole injection into the HOMO level of the Alq<sub>3</sub>. The electron injection from the ETL to the HTL is hindered because of the larger offset between the LUMO of the ETL and that of the HTL. This potential barrier confines most electrons to the ETL. This electron barrier along with the low hole mobility in the ETL (and the low electron



12.3 Energy level diagram of the two-layer OLED.

mobility in the HTL) enhances the chance of electron-hole collision capture, and thus the formation of excitons.

OLEDs are traditionally patterned via either vacuum deposition masks or UV lithographs. Developments in few alternative techniques have been demonstrated for OLED patterning, including: screen printing,<sup>[1,2]</sup> cold welding,<sup>[3–5]</sup> soft lithography,<sup>[6]</sup> imprint lithography,<sup>[7–9]</sup> gravure printing,<sup>[10,11]</sup> dry lift-off,<sup>[12]</sup> and soft contact lamination.<sup>[13–16]</sup> Most of these alternative patterning methods have gained interest over the last ten years; only greater understanding and further work are needed to bring such areas to maturity. As with conventional printing methods, each has particular advantages and disadvantages and each might find its place in certain aspects of organic electronics fabrication. However, all of the techniques above require a physical entity through which a given pattern is transferred to the underlying substrate. This entity (e.g. stencil for screen printing) must be changed when a new pattern is needed. Moreover, these techniques require physical contact between the pattern-transfer entity (mask, stencil, etc.) or coating tool (screen). This might not be a desirable option for several applications. Fortunately, inkjet printing is a maskless, non-contact printing and patterning technique suitable for OLED fabrication on rigid and flexible substrates.<sup>[17–21]</sup> Inkjet technology has also the advantages of being simple and a relatively fast printing technique.

In recent years, inkjet printing has been used in a variety of fields including ceramics, metals, organic semiconductors, and biopolymers.<sup>[22]</sup> For applications in OLEDs, inkjet printing has been used to deposit a patterned polymer layer on top of a given anode,<sup>[17–19]</sup> or to deposit PEDOT-PSS (polyethylenedioxythiophene-polystyrenesulfonate) and/or electroluminescent polymers.<sup>[20,21]</sup> Many companies including Cambridge Display Technology (CDT), Seiko-

Epson,<sup>[23]</sup> and Toshiba have demonstrated display prototypes deposited using inkjet, ranging in size from several inches to 40 inches. In these examples, inkjet was used to dispose the polymers in a pre-defined subpixel pattern (a pixel consists of three subpixels: red, green and blue), which was fabricated via photo-lithographic techniques. However, recent developments in the use of inkjet printing as a tool to pattern a given electrode, promises a low cost, maskless, and non-contact approach that can potentially generate different patterns on a given delicate substrate. In this regard, this chapter highlights such an approach.

## 12.2 Inkjet printing technology

### 12.2.1 History of inkjet printing technologies

Basically, inkjet printing technology<sup>[24]</sup> is divided into two categories, continuous inkjet and drop-on-demand inkjet. In 1878, the concept of jetting liquids was originally proposed by Lord Rayleigh.<sup>[25]</sup> However, the realization of inkjet devices did not emerge until the 1960s–1970s. In the early 1960s, Sweet of Stanford University developed the principal mechanism of the continuous inkjet printing process.<sup>[26]</sup> In a continuous inkjet system, a stream of ink is ejected continuously from a nozzle, then breaks up into a series of droplets. In the late 1970s, IBM launched a project to apply continuous inkjet technology to computer printers.<sup>[27]</sup> Currently, continuous inkjet printing is mainly used for such applications as industrial labeling and marking on cans, packages and address labels.

Drop-on-demand inkjet methods emerged in the late 1970s. A drop-on-demand device ejects ink droplets individually, and only when required. Two main methods of drop formation, piezoelectric inkjet and thermal inkjet are used. Piezoelectric inkjet ejects a droplet due to a pressure wave created by the deformation of the piezoelectric crystal.<sup>[28]</sup> In 1979, Canon patented an evaporative bubble system, where ink drops are ejected due to a vapor bubble (bubble jet) formed upon rapid heating of a resistive element in contact with the ink.<sup>[29]</sup> Shortly thereafter, Hewlett-Packard independently invented a similar inkjet technology and named it thermal inkjet.<sup>[30]</sup>

Significant improvements in performance (e.g. reliability, resolution and speed) and lower printer prices have made inkjet printers very popular. For instance, the resolution of the first model of Hewlett Packard inkjet printer was only 96 dots per inch (dpi). However, in 2004, a resolution range from 1,200 dpi to 4,800 dpi was available in the market. Such an advance allows for an unprecedented jetting of minute ink volumes of the order of 2 pL. Faster printing can be achieved by increasing the frequency of droplet ejection (to obtain a laser-compatible throughput, it should be faster than 8 kHz)<sup>[31]</sup> and the number of nozzles in a printhead. Due to recent developments in

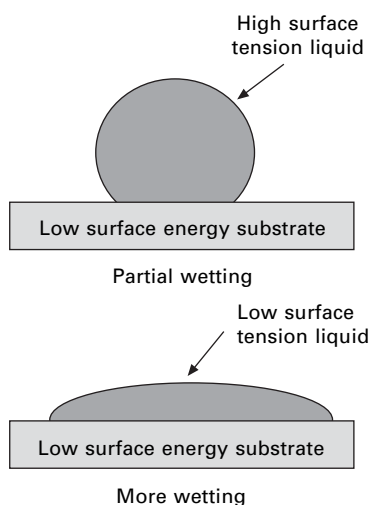
microelectromechanical systems, frequencies higher than 50 kHz, and high nozzle densities of nearly 200 nozzles per inch have been achieved. The price range of inkjet printers was around \$1,000–\$6,000 in the early 1980s. Currently, one can purchase an inkjet system for a price between \$25–\$1,000.<sup>[32]</sup>

## 12.3 Design aspects of inkjet printing

### 12.3.1 Ink formulation

To formulate inks suitable for the inkjet dispensing process, the physical and chemical properties of the fluid must be well regulated for consistent formation of drops at a given electric pulse. If using a commercial printhead (i.e., HP, Lexmark, Canon, or Epson), the viscosity of inks should be comparable to water.

The range of the ink viscosity should be 4–20 mPa s. The ink viscosity must be low enough to allow the ink channel to be refilled in about 100  $\mu$ s but must be high enough to avoid the formation of satellites (small droplet segments separated from the main stream of ink) during the printing process.<sup>[33]</sup> When a droplet impacts a hydrophilic surface, it spreads on the substrate to cover a larger area. On the other hand, a high surface energy gives a small footprint and a poor wetting on the substrate. If one wants to achieve full area coverage (a layer formation), it is necessary to add surfactants, which increase the wetting by lowering the surface tension of the ink (Fig. 12.4). If other solvents beside water are used, care must be taken to ensure that the



12.4 Schematic images of the droplets: (above) where high surface tension liquid is deposited and (below) where low surface tension liquid was deposited.

solvent does not chemically attack the cartridge, either through dissolution with the cartridge organic components or corrosion of its metal parts.

During the jetting process, the nozzles of the printhead often clog. This is due to the presence of particles (or aggregation) in the ink or possibly the fast evaporation of ink on the nozzle plate, which tends to dry up non-volatile ingredients of the ink and thus clog the printhead. Therefore, during the ink formulation, it is common to add a humectant (substance added to maintain moisture),<sup>[34]</sup> such as a water-soluble, high boiling point liquid, e.g., glycerol or ethylene glycol.

In order to use inkjet to print insoluble materials (e.g. metals, ceramics, or carbon nanotube), it is necessary to disperse the required materials as fine particles suspended in a suitable liquid. In fact, currently, inks of commercial inkjet printers generally contain color pigments having a size range of 100–400 nm, rather than colorants dissolved to form an ink solution. The dispersion of particles must be extremely good to avoid sedimentation and aggregation. To achieve stable pigment ink, polymeric or colloidal binders<sup>[35]</sup> or additives<sup>[36,37]</sup> are often added. The sonication of ink is a well-known method for reducing the sedimentation rate.<sup>[38,39]</sup>

### 12.3.2 Resolution

The resolution of inkjet printing is normally in the range of 30–100  $\mu\text{m}$ . The drop size of commercial inkjet printers is decreasing in order to attain higher resolution (droplet volumes are 2–40 picoliters). Printing on a hard substrate is quite different from printing onto absorbent paper, and there is a lack for detailed study of the wetting and drying process on various substrates. The shape, thickness, and surface morphology of droplets and layers are greatly influenced by energetics of the substrate surface and ink, as well as the process of solvent evaporation. The evaporation of the solvent can be controlled by changing the temperature, pressure, or relative humidity of the deposition and drying environment.

For display applications, uniformity of inkjet printed features is of a particular concern. Generally, a circular drop on the solid surface evaporates from the edges and flows outward. This capillary flow tends to carry most of the dispersed materials to the edge, a phenomenon known as the coffee ring effect.<sup>[40]</sup> This leads to a highly non-uniform thickness profile of a dried droplet with a thick ring around the edge of the drop. This process has been analyzed for larger drops and is attributed to a higher evaporation rate at the contact line of a pinned drop compared to its center.<sup>[40,41]</sup>

The capillary flow rate can be modified by controlling the solute concentration and molecular weight, surface tension and viscosity of the liquid. A higher solute concentration tends to push edges of droplets more outwards.<sup>[42,43]</sup> If the inter-particle interactions are not sufficiently larger

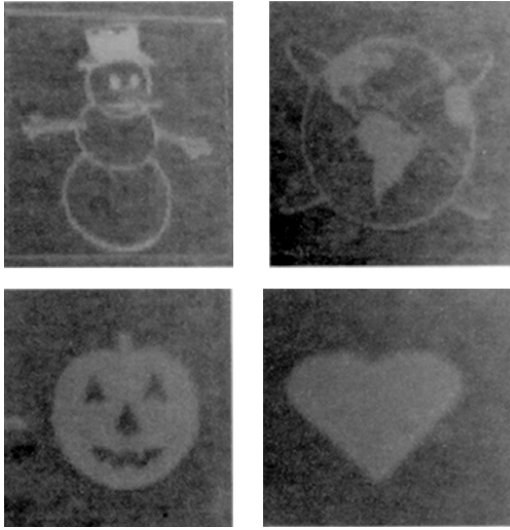
than particle-substrate interactions, particles cannot freely diffuse across the substrate and may segregate on the substrate surface, thus becoming immobilized.<sup>[44]</sup> The use of high-viscosity solvents may hinder the capillary flow of solutes within the drop during drying on the substrate surface. For non-circular droplets, including a line of liquid, deposition behavior can be more complicated. The line may break up into separate drops or into liquid bulges, depending on the boundary conditions of the moving contact line (edge of the droplet), printing speed, and frequency of the jetted droplet.<sup>[45]</sup> A discussion of these topics has recently been published.<sup>[46,47]</sup>

Heating the substrate on the hot plate during inkjet printing is the simplest way to obtain fast solvent evaporation. By heating the substrate near or over the boiling point of the printing solvent, the liquid in the droplet is flash-evaporated on contact and thus a finer resolution can be obtained. However, care must be taken when applying higher temperature to the substrate so as not to increase the risk of the orifice clogging at the printheads, since this approach might induce faster evaporation of ink on the nozzle plate.

Recently, in order to confine inkjet drops to precise locations, a surface energy pattern has been defined on the glass substrates before inkjet printing (surface-energy assisted inkjet).<sup>[48,49]</sup> Using photolithographic process, the hydrophilic glass substrate was patterned by polyimide (hydrophobic polymer). The hydrophobic bank efficiently prevents a drop from spreading out beyond the confined areas of hydrophilic surface. Fine feature sizes of several microns to submicron have been successfully demonstrated.

### 12.3.3 Recent inkjet printing of materials and devices

Many different materials have been successfully printed. The inkjet process has been studied in some detail in the context of printing ceramic powders<sup>[50]</sup> to make alumina,<sup>[35]</sup> zirconia,<sup>[33]</sup> titania,<sup>[51]</sup> barium strontium titanate,<sup>[51]</sup> functionally graded materials (e.g. zirconia/alumina),<sup>[52]</sup> sol-gel ceramics,<sup>[53]</sup> ferroelectric thin film,<sup>[54]</sup> magnetic nanoparticles,<sup>[55]</sup> diamond nanoparticles,<sup>[56]</sup> Y<sub>2</sub>O<sub>3</sub> nanoparticles,<sup>[57]</sup> (Fig. 12.5) and superconducting oxides<sup>[58]</sup> (followed by the high-temperature sintering process (300–800 °C)). A recent review has been published highlighting the use of inkjet to print various materials.<sup>[22]</sup> The main success of inkjetting ceramic powder has been in achieving low viscosity and well dispersed particle ink, while maintaining a high particle concentration in order to build high-density printed materials. Nowadays, arranging the mixture of solution with a wax and surfactant, suspensions comprising up to 45 vol% of ceramic particles can be deposited by inkjet printing.<sup>[59]</sup> By printing thousands of layers, an array of pillars with submillimeter height was formed by using piezoelectric ceramic powder (PZT) or lead zirconate titanate materials.<sup>[60]</sup>



12.5 Inkjet printed Y<sub>2</sub>O<sub>3</sub> nanoparticles. (University of Arizona).

Some approaches have been made to inkjet print metal lines. One approach is to print palladium salt followed by metallization through electroless plating methods.<sup>[61,62]</sup> A second approach is to print an organometallic liquid (e.g. silver,<sup>[63]</sup> copper,<sup>[64]</sup> and gold<sup>[65]</sup>), followed by the metallization by applying a high-temperature (200–300 °C). A third approach is to use metal colloids or metal nanoparticles, such as gold,<sup>[66]</sup> silver,<sup>[67,68]</sup> and cobalt,<sup>[67]</sup> followed by a sintering process (> 300 °C). However, the required temperature for the metal conversion process is still high for some materials (e.g. biological) and plastic-based substrates. Therefore, attaining high-conductivity metal electrodes for optics and electronics is challenging. Recently, the sintering temperature was reduced down to 150–200 °C by modifying the structure of the organometallic compound precursor.<sup>[69,70]</sup> More research is being done in this area.

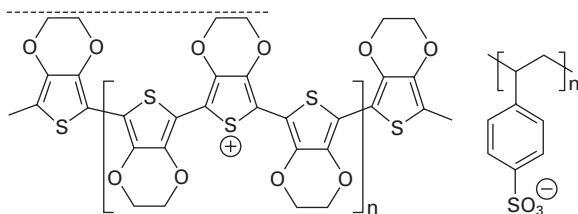
For biomedical applications, inkjet printing was first used for immobilizing active enzyme membranes to create biosensors.<sup>[71]</sup> It has been expanded to operate for the microdeposition of protein,<sup>[72]</sup> cell,<sup>[73]</sup> DNA,<sup>[74]</sup> and bacterial colonies<sup>[75]</sup> for the development of microarray-based bioanalytical arrays,<sup>[76,77]</sup> which are used in clinical diagnosis to evaluate drug candidates. Oligonucleotides have been synthesized by selectively depositing four types of nucleotides through different print heads.<sup>[78,79]</sup>

Dielectric layers and organic compounds, including photoresists,<sup>[80]</sup> self-assembled monolayers,<sup>[81]</sup> semiconducting polymer (MEH-PPV)<sup>[82]</sup> and organic nanoparticles<sup>[83]</sup> have been patterned by inkjet with a resolution range of 100 μm. Inkjet printing has been used to fabricate organic/polymeric LEDs,<sup>[17–21]</sup> microelectromechanical structures and devices with conducting

polymer-based electronic parts; organic thin film transistors,<sup>[48]</sup> organic RC (resistor-capacitor) filter circuits<sup>[84]</sup> and all-polymer capacitors.<sup>[85]</sup> It has also been used to fabricate arrays of refractive microlenses using sol-gel materials<sup>[86]</sup> or using UV-curable optical epoxies.<sup>[87]</sup>

## 12.4 Inkjet anode patterning of OLEDs

Here, we discuss our recent development in modifying the conductivity of polymeric anodes by inkjet printing of an oxidizing ink. This process results in a simplified and practical method for direct patterning of conductive polymers to create a variety of images including gray-scale. PEDOT-PSS coated polyethylene terephthalate (PET) films (Orgacon<sup>TM</sup> EL-350) and paper films were kindly donated by Agfa (Mortsel, Belgium). The molecular structure of PEDOT-PSS is shown in Fig. 12.6. The PEDOT-PSS layer is about 500 nm thick and has a sheet resistance of 350  $\Omega$ /sq. The physical dimensions of the PET or paper-based substrates are 11 inch  $\times$  8 inch, with a thickness of about 125  $\mu$ m. No ITO is present on these substrates and

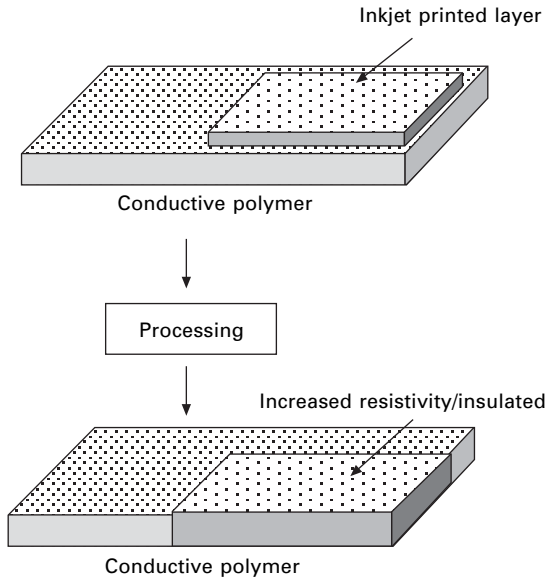


12.6 The molecular structure of PEDOT-PSS: poly(3,4-ethylenedioxy)-thiophene-poly(styrene sulfonate).

PEDOT-PSS was solely used as the anode for the OLEDs described below.

The oxidizing agent was loaded into the inkjet cartridge. A small amount of surfactant was also added to this aqueous solution to enhance the wetting of ink. In this study, a slightly modified desktop color jet printer was used. The viscosity and surface tension of the solution were optimized for better image intensity and resolution. The extent of the chemical reaction between the oxidizing agent and the PEDOT-PSS can be controlled through adjustment of the volume of oxidizing agent ink dispensed and of the post-printing processing conditions. Figure 12.7 shows a schematic of the patterning process.

Upon ink-jet printing of the oxidizing agent (e.g. sodium hypochlorite) on the PEDOT-PSS layer, the substrates were moderately heated to enhance the chemical reaction. To end this reaction, the printed ink was thoroughly washed away with de-ionized water. The substrates were then dried and the organic layers were deposited thereafter.



12.7 The schematic of the inkjet printing of the oxidizing agent (above) and the resulting feature of the patterned substrate (bottom).

Since the chemical reaction between the oxidizing agent and the PEDOT-PSS can be mainly controlled by the spatial density (at a fixed solution concentration) of the inkjet droplets (darkness) over the substrate area, it is possible to use the color functions of a given word-processing or graphics program to command the printing process, and thus control the overall sheet resistivity of the PEDOT-PSS layer. Printing can be controlled through the HSL (hue, saturation, and luminosity) color function. In this case, the 'saturation' (S), which controls the respective quantity of RGB (red, green, and blue) color, was held at 0. The 'hue' (H), which identifies the composition of the color, was also held constant. Only 'luminosity' (L), which dictates the darkness of the color itself, was changed over nine different values (these values are obtained through PowerPoint software) as shown in Table 12.1.

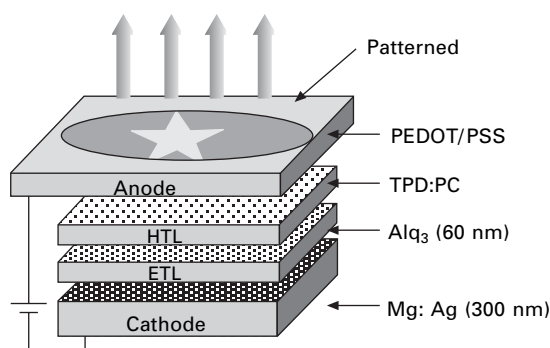
For the OLED fabrication, the hole transport layer (HTL) was deposited by spin casting (1,500 rpm, 1 minute) to a thickness of 55–60 nm. The HTL solution consisted of TPD and polycarbonate at 1 wt% concentration in chloroform. The relative percentage of TPD and PC was 70% and 30%, respectively. The electron transport layer (ETL), Alq<sub>3</sub> (tris-(8-hydroxyquinoline)-aluminum) was thermally sublimed at a rate of 1.0 Å/s for a thickness of 60 nm under high vacuum ( $10^{-6}$ – $10^{-7}$  torr). Both the HTL and the ETL cover the entire surface of the PEDOT-PSS electrode. A cathode of Mg and Ag was co-evaporated over the whole ETL in a ratio of 10 (Mg) to

*Table 12.1* HSL values and colors used in programming the ink -loads S=0 and H was not defined

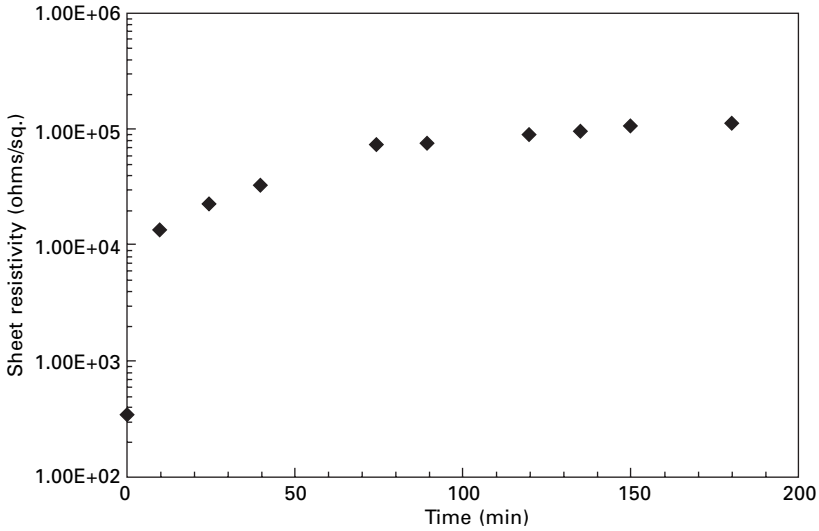
Color	No.	Luminosity (L)	Darkness (%)
	# 1	255	0
	# 2	230	10
	# 3	215	16
	# 4	200	22
	# 5	170	33
	# 6	140	45
	# 7	125	51
	# 8	110	57
	# 9	50	80
	# 10	0	100

1 (Ag). The thickness of the cathode was 300 nm. The devices were tested in a nitrogen glove box. The device structure of our OLEDs is shown in Fig. 12.8. Sheet resistivity measurements were made using four-point probe methods.

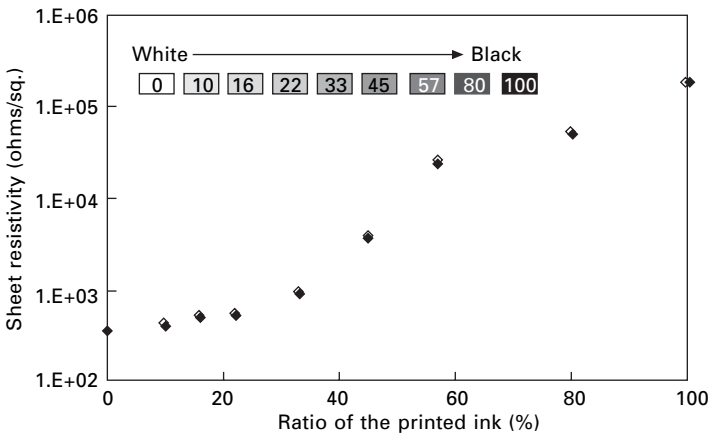
Figure 12.9 shows the time dependence of sheet resistivity at a given value of  $L = 0$  (darkness = 100%). The most significant change occurs within the first few minutes after the oxidizing agent is deposited on the surface. Further oxidation of PEDOT-PSS can be achieved for longer times. We suggest that the oxidizing agent and PEDOT-PSS layer first react quickly at their contact surface and the remaining oxidizing agent slowly diffuses into the inner regions of PEDOT-PSS and reacts thereafter. This diffusion can be enhanced by moderately heating the substrate. At a fixed processing time after printing the oxidizer (Fig. 12.10), a systematic increase of sheet resistivity



*12.8* The schematic image of the fabricated OLEDs where the PEDOT-PSS was patterned by inkjet printing. There was no patterning carried on the HTL, ETL, or cathode.



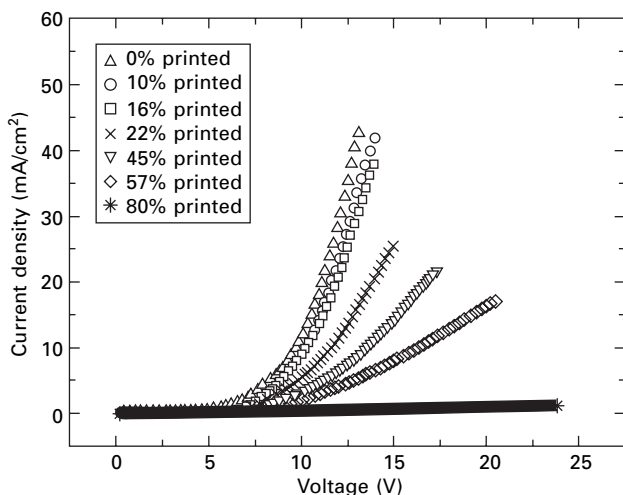
12.9 Measured PEDOT-PSS sheet resistivity with time for  $L = 0$  (darkness of 100%). The measurement was carried out in air, at room temperature, using a four-point probe.



12.10 Measured sheet resistivity for various darkness values. The measurement was carried out in air, at room temperature, using a four-point probe.

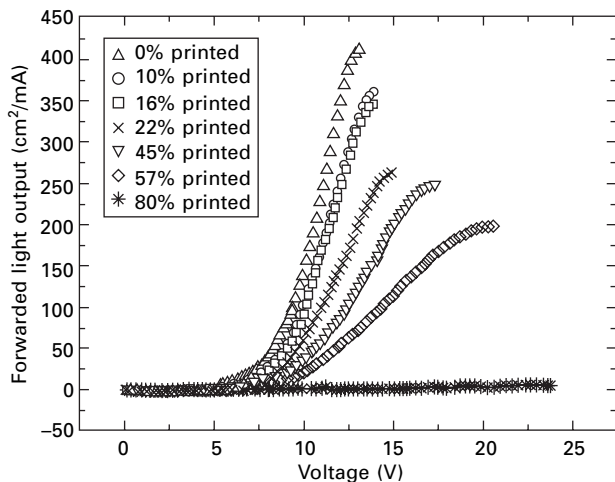
is observed with increasing ink load. In this case, a change in sheet resistivity of three orders of magnitude is observed as  $L$  varies from 255 (white, 0% darkness) to 0 (black, 100% darkness).

These passivated PEDOT-PSS layers with different sheet resistivities were used as the OLED anodes. The rest of the OLED layers were fabricated on top of PEDOT-PSS anode. Figure 12.11 shows the current density ( $\text{mA}/\text{cm}^2$ )



12.11 Current density vs. bias voltage of devices having various PEDOT-PSS sheet resistivity.

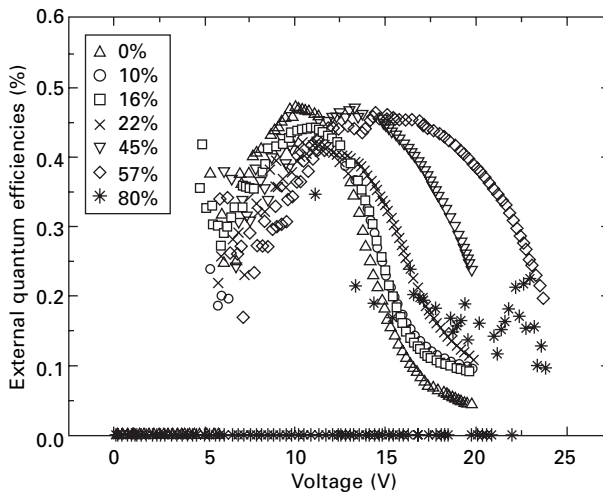
vs. bias voltage (V) for the various devices made with varying L values. As expected, a decrease in current density was observed with increasing sheet resistivity (decreasing L) of the PEDOT-PSS layer. The forward light output (Fig. 12.12) from the devices follows the current density behavior. Lower light output at a given voltage can be seen with increasing sheet resistivity. For example, at 10 V, the light output levels were measured to be 160 cd/m<sup>2</sup>, 107 d/m<sup>2</sup>, 61 cd/m<sup>2</sup>, 36 cd/m<sup>2</sup>, and 24 cd/m<sup>2</sup> for devices printed with the



12.12 Forward light output vs. bias voltage for OLEDs made with PEDOT-PSS having various sheet resistivities.

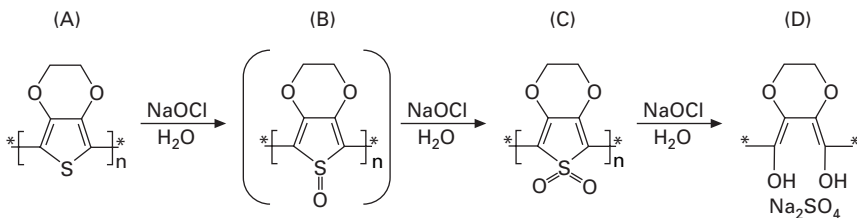
luminosity parameter  $L$  preset to 255 (0%), 230 (10%), 200 (22%), 140 (45%), and 110 (57%), respectively. Such a variation in brightness with increased sheet resistance at a given voltage introduces the potential for gray-scale electrical imaging, thus allowing us to print any graphical or photographic image into an active light-emitting device.

The peak external quantum efficiency (%) remains relatively constant at about 0.5% (Fig. 12.13), but shifts to higher voltage with increasing sheet resistivity. Although our materials are not purified and the fact that the processing was done in air and at room temperature without any optimization, the peak value above still compares well to the 0.7% found in similar devices recently published by Kim *et al.*<sup>[88]</sup>



12.13 External quantum efficiencies vs. bias voltage for OLEDs made with PEDOT-PSS having various sheet resistivities.

One of the proposed chemical mechanisms of this oxidation treatment is shown in Fig. 12.14. In this reaction, sodium hypochlorite is the oxidant and converts thiophene (A) in PEDOT<sup>[89]</sup> to its corresponding thiophene-1-oxide (B). Spontaneously, thiophene-1-oxide (B) is converted to its corresponding

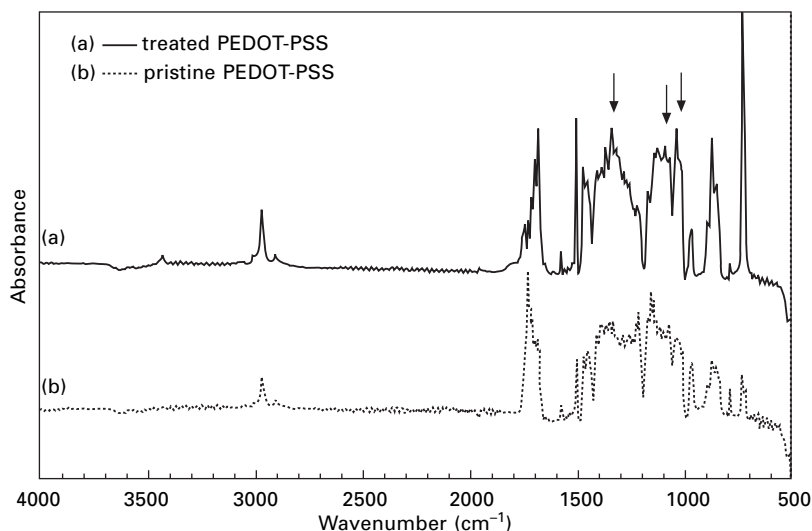


12.14 Chemical mechanism of the PEDOT oxidation with sodium hypochlorite.

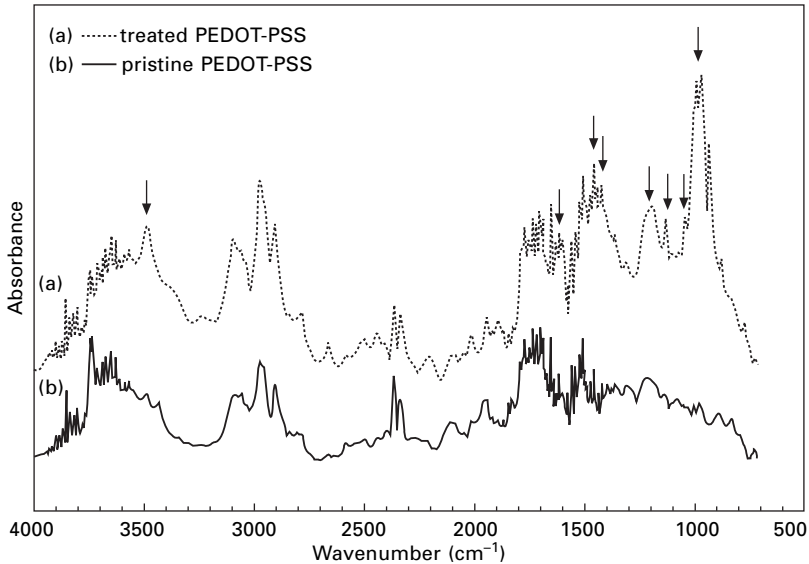
thiophene-1,1-dioxide (C). The thiophene-1-oxide (B) is presumed to be a reaction intermediate to thiophene-1,1-dioxide (C).<sup>[89,90]</sup> Finally, further oxidation of thiophene-1,1-dioxide causes the extrusion of  $\text{SO}_2$  from this compound and the attachment of hydroxyl groups due to the nucleophilic attack by water (D).

In Fig. 12.15, the FT-IR spectra of the treated (oxidized) PEDOT-PSS film and the pristine PEDOT-PSS film are compared over a range of wavenumbers from 500 to 4,000  $\text{cm}^{-1}$ . Minor differences in relative band intensities are observed. In the treated film, the absorbance at 1,343 and 1,132  $\text{cm}^{-1}$  results from the asymmetric and symmetric stretching vibration of the sulfonic ( $\text{S}=\text{O}$ ) group, respectively.<sup>[90-92]</sup> The absorbance at 1,044  $\text{cm}^{-1}$  is due to the symmetrical stretching vibration of the sodium sulphonate ( $\text{SO}_3$ ) group of PSS-Na.<sup>[91,92]</sup> For the PEDOT-PSS film used in this study, inkjet printing gives fewer units of oxidant relative to EDOT units in PEDOT-PSS, and we suspect that a complete oxidation (structure C) of PEDOT might not be possible.

To observe the completion of this oxidation reaction, structure (D) was synthesized by mixing the excess molar amount of  $\text{NaOCl}$  aqueous solution with the diluted PEDOT-PSS dispersion (Baytron P, Bayer). The solution was allowed to dry and the resulted powders were analyzed by the FT-IR along with pristine PEDOT-PSS powders. Figure 12.16 shows the FT-IR spectra of both powders. Distinct differences are observed in relative band intensities. The bands due to the hydroxyl group, O–H stretching, bending vibrations, and C–O stretching vibrations are found at 3,493, 1,410 and



12.15 FT-IR spectra of (a) inkjet treated (oxidized) PEDOT-PSS film and (b) pristine PEDOT-PSS film on the plastic substrates.



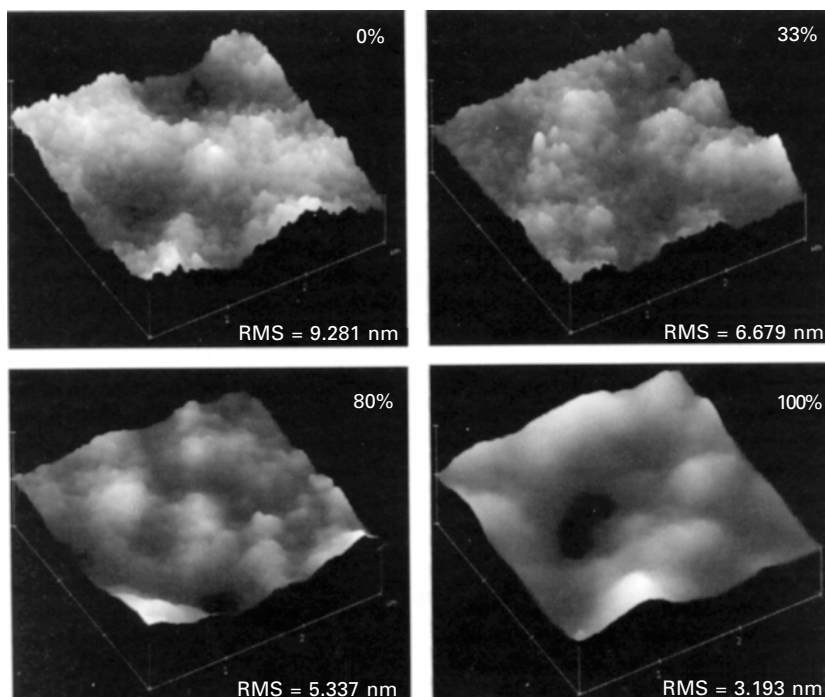
12.16 FT-IR spectra of (a) fully oxidized PEDOT-PSS structure and (b) pristine PEDOT-PSS structure with KBr pellets.

$1,201\text{ cm}^{-1}$ , respectively. The absorbance at  $1,616\text{ cm}^{-1}$  is due to the stretching vibrations ( $\text{C}=\text{C}$ ) of the conjugated olefine (unsaturated open-chain hydrocarbons). The band at  $1,134\text{ cm}^{-1}$  results from the stretching vibrations of  $\text{SO}_4$  in the sulphate ion ( $\text{SO}_4^{2-}$ ).<sup>[92]</sup> Finally an additional band at  $974\text{ cm}^{-1}$  is due to the vibrations of the  $\text{O}-\text{Cl}$  group in the remaining sodium hypochlorite.<sup>[93]</sup>

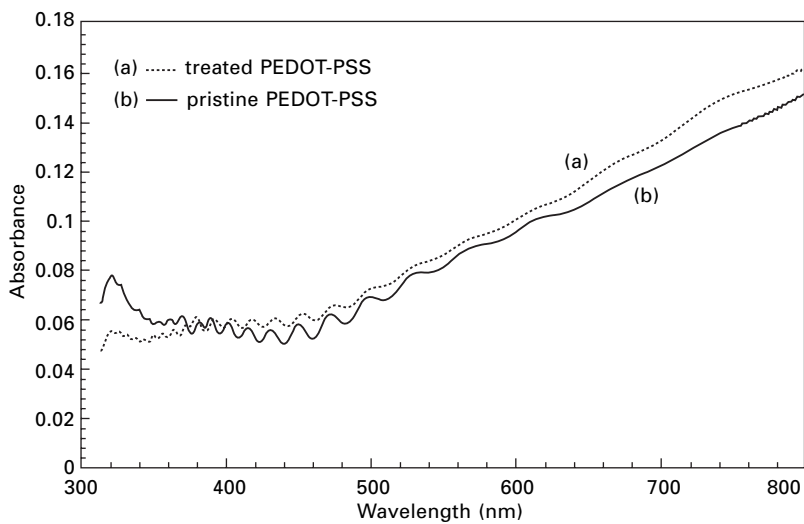
AFM in ‘contact mode’ was used to image the surface and highlight the morphological changes between the pristine PEDOT-PSS surface (0%) and the treated surfaces (33, 80, and 100%) as shown in Fig. 12.17. The root-mean-square (RMS) roughness of the surface decreased from 9.3 nm to 3.2 nm as the values of  $L$  decreased from 255 to 0. Although changes in PEDOT-PSS morphology were observed, no distinct film thickness difference between conductive and non-conducting (oxidized) surfaces at the inkjet printed edge was detected by the step profilometer.

The UV-vis spectra of treated PEDOT-PSS and pristine PEDOT-PSS shows only small differences in light absorption in the visible area (Fig. 12.18). Unlike the electron transfer reaction in electrochromic materials,<sup>[94,95]</sup> the oxidation reaction here slightly darkens the PEDOT-PSS layer. Since no new bands are observed, this indicates that the treated films still contain some PEDOT structures doped with PSS.<sup>[96]</sup>

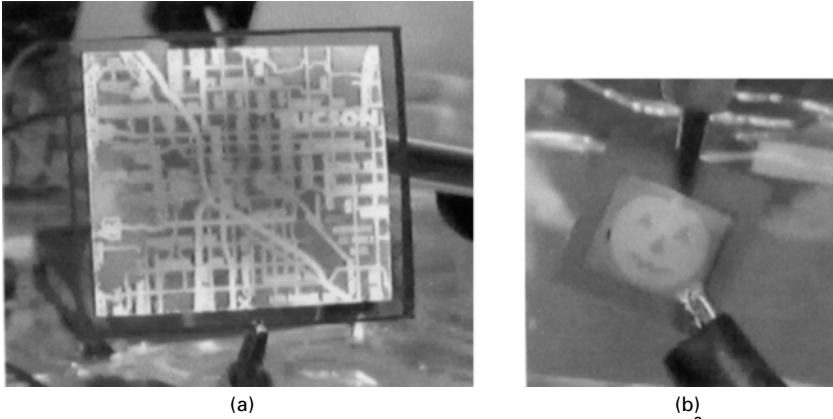
The technique discussed above can be easily extended to print any design including photographs. Figure 12.19 shows printed images on flexible plastic, and paper substrates; the electroluminescent images of a Tucson road map.



12.17 AFM images of PEDOT-PSS layers with different sets of HSL values ( $3 \times 3 \mu\text{m}^2$ ).



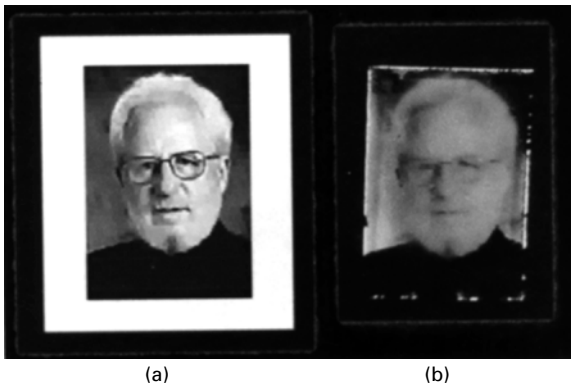
12.18 Optical absorption spectra of (a) treated PEDOT-PSS and (b) pristine PEDOT-PSS.



12.19 (a) Photograph of gray-scale OLED ( $5.7 \times 6.8 \text{ cm}^2$ ) that was patterned on PEDOT-PSS surface by inkjet printer on plastic substrates. Conductivities were modified to exhibit the contrasts, and (b) Photograph of OLED ( $2.57 \times 2.57 \text{ cm}^2$ ) that was made onto the paper substrates by the same procedure.

The image of a pumpkin was patterned onto the PEDOT-PSS coated paper surface, and a semi-transparent Mg:Ag (10:1) semi-transparent cathode was used. It is worth emphasizing the point that all layers were deposited over the entire surface of the substrate, without any patterning. Figure 12.20 shows a portrait of Nobel Laureate Prof. Alan Heeger and the equivalent OLED picture made with our method described above.

In conclusion, we demonstrated that a commercial inkjet printer can be implemented in patterning conductive polymers through the use of oxidizing agent. Such a technique can be useful in patterning applications related to certain types of displays, signage, solar cells, and labels, to mention but a few applications.



12.20 Photographs (a) of Nobel Prize laureate and (b) of gray-scale OLED ( $3.6 \times 2.7 \text{ cm}^2$ ) that was patterned on PEDOT-PSS surface by inkjet printer on plastic substrates.

## 12.5 Acknowledgements

We are grateful for the donation of the PEDOT-PSS substrates by Agfa, and the inkjet printheads by Hewlett-Packard. We thank our colleagues Prof. Paul Calvert and Prof. Nasser Peyghambarian for fruitful discussions.

## 12.6 References

1. Pardo D.A., Jabbour G.E. and Peyghambarian N., "Application of screen printing in the fabrication of organic light-emitting devices", *Adv. Mater.* 2000, **12**, 1249–1252.
2. Jabbour G.E., Radspinner R. and Peyghambarian N., "Screen printing for the fabrication of organic light-emitting devices", *IEEE J. Sel. Top. Quantum. Electron.* 2001, **7**, 769–773.
3. Kim C., Burrows P.E. and Forrest S.R., "Micropatterning of organic electronic devices by cold-welding", *Science* 2000, **288**, 831–833.
4. Kim C., Shtein M. and Forrest S.R., "Nanolithography based on patterned metal transfer and its application to organic electronic devices", *Appl. Phys. Lett.* 2002, **80**, 4051–4053.
5. Kim C. and Forrest S.R., "Fabrication of organic light emitting devices by low-pressure cold welding", *Adv. Mater.* 2003, **15**, 541–545.
6. Koide Y., Such M.W., Basu R., Evmenenko G., Cui J., Dutta P., Hersam M.C. and Marks T.J., "Hot microcontact printing for patterning ITO surfaces. Methodology, morphology, microstructure, and OLED charge injection barrier imaging", *Langmuir*, 2003, **19**, 86–93.
7. Wang X. Sun, Chen L. and Chou S.Y., "Direct nanoimprint of submicron organic light-emitting structures", *Appl. Phys. Lett.* 1999, **75**, 2767–2769.
8. Cheng X., Hong Y., Kanicki J. and Guo L.J., "High-resolution organic polymer light-emitting pixels fabricated by imprinting technique", *J. Vac. Sci. Technol. B* 2002, **20**, 2877–2880.
9. Chou S.Y., Krauss P.R., Zhang W., Guo L. and Zhaung L., "Sub-10 nm imprint lithography and applications", *J. Vac. Sci. Technol. B* 1997, **15**, 2897–2904.
10. Mäkelä T., Jussila S., Vilkmann M., Kosonen H. and Korhonen R. "Roll-to-roll method for producing polyaniline patterns on paper", *Synth. Met.* 2003, **135-136**, 41–42.
11. Jabbour G.E., Yoshioka Y., Tuomikoski M., Kololuoma T. and Kopola H., "Prospects of printing techniques in low cost organic electronics and optoelectronics", *Northern Optics* 2003, O6.1 (p35) Finnish Optical Society Conference, June 16–18, Espoo, Finland.
12. Duffy D.C., Jackman R.J., Vaeth K.M., Jensen K.F. and Whitesides G.M., "Patterning electroluminescent materials with feature sizes as small as 5  $\mu\text{m}$  using elastometric membranes as masks for dry lift-off", *Adv. Mater.* 1999, **11**, 546–552.
13. Loo Y.-L., Willett R.L., Baldwin K.W. and Rogers J.A., "Additive, nanoscale patterning of metal films with a stamp and a surface chemistry mediated transfer process: Applications in plastic electronics", *Appl. Phys. Lett.* 2002, **81**, 562–564.
14. Zaumseil J., Someya T., Bao Z., Loo Y.-L., Cirelli R. and Rogers J.A., "Nanoscale organic transistors that use source/drain electrodes supported by high resolution rubber stamp", *Appl. Phys. Lett.* 2003, **82**, 793–795.

15. Zaumseil J., Baldwin K.W. and Rogers J.A., "Contact resistance in organic transistors that use source and drain electrodes formed by soft contact lamination", *J. Appl. Phys.* 2003, **93**, 6117–6124.
16. Lee T.-W., Zaumseil J., Bao Z., Hsu J.W.P. and Rogers J.A., "Organic light-emitting diodes formed by soft contact lamination", *Proc. Nation. Acad. Sci. USA* 2004, **101**, 429–433.
17. Hebner T.R., Wu C.C., Marcy D., Lu M.H. and Sturm J.C., "Ink-jet printing of doped polymers for organic light emitting devices", *Appl. Phys. Lett.* 1998, **72**, 519–521.
18. Yang Y., Chang S., Bharathan J. and Liu J., "Organic/polymeric electroluminescent devices processed by hybrid ink-jet printing", *J. Mater. Sci.* 2000, **11**, 89–96.
19. Bharathan J. and Yang Y., "Polymer electroluminescent devices processed by inkjet printing: I. Polymer light-emitting logo", *Appl. Phys. Lett.* 1998, **72**, 2660–2662.
20. Kobayashi H., Kanabe S., Seki S., Kigchi H., Kimura M., Yudasaka I., Miyashita S., Shimoda T., Towns C.R., Burroughes J.H. and Friend R.H., "A novel RGB multicolor light-emitting polymer display", *Synth. Met.* 2000, **111**, 125–128.
21. Shibusawa M., Kobayashi M., Hanari J., Sunohara K. and Ibaraki N., "A 17-inch WXGA full-color OLED display using the polymer ink-jet technology", *IEICE Trans. Electron.* 2003, **E86**, 2269–2274.
22. Calvert P., "Inkjet printing for materials and devices", *Chem. Mater.* 2001, **13**, 3299–3305.
23. Shimoda K., Morii S., Seki and Kiguchi H., "Inkjet printing of light-emitting polymer displays", *MRS Bull.* 2003, **28**, 821–827.
24. Le H.P., "Progress and trends in ink-jet printing technology", *J. Imag. Sci. Tech.* 1998, **42**, 49–62.
25. Rayleigh Lord, "On the instability of jets", *Proc. London Math Soc* 1878, **10**, 4–13.
26. Sweet R.G., "Signal apparatus with fluid drop recorder", *US Patent* 1971, no. 3,596, 275.
27. Buehner W.L., Hill J.D., Williams T.H. and Woods J.W., "Application of ink-jet technology to a word processing output printer", *IBM J. Res. Dev.* 1977, **21**, 2–7.
28. Zoltan S.L., "Pulse droplet ejection system", *US Patent* 1974, no. 3,857,049, to Clevite Corporation.
29. Endo L., Sato Y., Saito S., Nakagiri T. and Ohno S., "Liquid jet recording process and apparatus thereof", *UK Patent* 1979, no. 2,007,162, to Canon.
30. Vaught J.L., Cloutier F.L., Donald D.K., Meyer J.D., Tacklind C.A. and Taub H.H., "Thermal inkjet printer", *US Patent* 1984, no. 4,490,728, to Hewlett-Packard.
31. Bohórquez J.H., Canfiel B.P., Courian K.J., Drogo F., Hall C.A.E., Holstun C.L., Scandalis A.R. and Shepard M.E., "Laser-comparable inkjet text printing", *Hewlett-Packard J.* 1994, **45**, 9–17.
32. Gaynor J., "Predicted and unpredicted changes in non-impact printing: 1981–2001", *J. Imag. Sci. Tech.* 2002, **46**, 292–299.
33. Blazdell P.F. and Evans J.R.G., "Application of a continuous ink jet printer to solid freeform of ceramics", *J. Mater. Proc. Tech.* 2000, **99**, 94–102.
34. Kang H.R., "Water-based ink-jet ink. I. Formulation", *J. Imag. Sci.* 1991, **35**, 179–188.
35. Sachs E., Cima M., Williams P., Brancazio D. and Cornie J., "Three dimensional printing: Rapid tooling and prototypes directly from a CAD model", *J. Eng. Ind.* 1992, **114**, 481–488.

36. Wong R., Hair M.L. and Croucher M.D., "Sterically stabilized polymer colloids and their use as ink-jet inks", *J. Imag. Tech.* 1988, **14**, 129–131.
37. Spinelli H.J., "Polymeric dispersants in ink jet technology", *Adv. Mater.* 1998, **10**, 1215–1218.
38. Rashid H., Tay B.Y. and Edirisinghe M.J., "Dispersion of ceramic ink using an ultrasonic disruptor", *J. Mater. Sci. Lett.* 2000, **19**, 799–801.
39. Tay B.Y., Rashid H. and Edirisinghe M.J., "On the preparation of ceramic ink for continuous jet printing", *J. Mater. Sci. Lett.* 2000, **19**, 1151–1154.
40. Deegan R.D., Bakajin O., Dupont T.F., Huber G., Nagel S.R. and Witten T.A., "Capillary flow as the cause of ring stains from dried liquid drops", *Nature* 1997, **389**, 827–829.
41. Fischer B.J., "Particle conversion in an evaporating colloidal droplet", *Langmuir* 2002, **18**, 60–67.
42. Deegan R.D., "Pattern formation in drying drops", *Phys. Rev. E* 2000, **61**, 475–485.
43. Deegan R.D., Bakajin O., Dupont T.F., Huber G., Nagel S.R. and Witten T.A., "Contact line deposits in an evaporating drop", *Phys. Rev. E* 2000, **62**, 756–765.
44. Maenosono S., Dushkin C.D., Saita S. and Yamaguchi Y., "Growth of a semiconductor nanoparticle ring during the drying of a suspension droplet", *Langmuir* 1999, **15**, 957–965.
45. Duineveld P.C., "The stability of ink-jet printed lines of liquid with zero receding contact angle on a homogeneous substrate", *J. Fluid. Mech.* 2003, **477**, 175–200.
46. Creagh L.T. and McDonald M., "Design and performance of inkjet printer heads for non-graphical arts applications", *MRS Bull.* 2003, **28**, 807–811.
47. Derby B. and Reis N., "Inkjet printing of highly loaded particulate suspensions", *MRS Bull.* 2003, **28**, 815–818.
48. Sirringhaus H., Kawase T., Friend R.H., Shimoda T., Inbasekaran M., Wu W. and Woo E.P., "High-resolution inkjet printing of all-polymer transistor circuits", *Science*, 2000, **290**, 2123–2126.
49. Burns S.E., Cain P., Mills J., Wang J. and Sirringhaus H., "Inkjet printing of polymer thin-film transistor circuits", *MRS Bull.* 2003, **28**, 829–834.
50. Evans J.R.G., "Direct ink jet printing of ceramics: experiment in technology", *British Ceram. Trans.* 2001, **100**, 124–128.
51. Kaydonova T., Miedaner A., Curtis C., Alleman J., Perkins J.D. and Ginley D.S., "Direct inkjet printing of composite thin barium strontium titanate films", *J. Mater. Res.* 2003, **18**, 2820–2825.
52. Mott M., Song J.-H. and Evans J.R.G., "Microengineering of ceramics by direct ink-jet printing", *J. Am. Ceram. Soc.* 1999, **82**, 1653–1658.
53. Atkinson A., Doorbar J., Hudd A., Segal D.L. and White P.J., "Continuous ink-jet printing using sol-gel 'ceramic' inks", *J. Sol-gel. Sci. Tech.* 1997, **8**, 1093–1097.
54. Okamura S., Takeuchi R. and Shiosaki T., "Fabrication of ferroelectric Pb(Zr,Ti)O<sub>3</sub> thin films with various Zr/Ti ratios by inkjet printing", *Jpn. J. Appl. Phys.* 2002, **41**, 6714–6717.
55. Voit W., Zapka W., Belova L. and Rao K.V., "Application of inkjet technology for the deposition of magnetic nanoparticles to form micron-scale structures", *IEE Proc. Sci. Meas. Technol.* 2003, **150**, 252–256.
56. Fox N.A., Youh M.J., Steeds J.W. and Wang W.N., "Patterned diamond particle films", *J. Appl. Phys.* 2000, **87**, 8187–8191.
57. Laine R. and Jabbour G., "Big things come in small packages", *oe magazine* 2002, July, 45–46.

58. Glowacki B.A., "Preparation of  $\text{Bi}_2\text{Sr}_2\text{CaCu}_2\text{O}_{8-x}$  tracks and thick film by jet printing", *Supercond. Sci. Technol.* 2000, **13**, 584–591.
59. Ainsley C., Reis N. and Derby B., "Rapid prototyping of ceramic casting cores for investment casting", *Key Eng. Mater.* 2002, **206-213**, 297–300.
60. Thornell G., Klintberg L., Laurell T., Nilsson J. and Johansson S., "Desktop microfabrication – initial experiments with a piezoceramic", *J. Micromech. Microeng.* 1999, **9**, 434–437.
61. Shah P., Kevrekidis Y. and Benziger J., "Ink-jet printing of catalyst patterns for electroless metal deposition", *Langmuir*, 1999, **15**, 1584–1587.
62. Guo T.-F., Chang S.-C., Pyo S. and Yang Y., "Vertically integrated electronic circuits via a combination of self-assembled polyelectrolytes, ink-jet printing, and electroless metal plating process", *Langmuir* 2002, **18**, 8142–8147.
63. Teng K.F., and Vest R.W., "Metallization of solar cells with ink jet printing and silver metallo-organic inks", *IEEE Trans. Comp. Hybr. Manuf. Tech.* 1988, **11**, 291–297.
64. Rozenberg G.G., Bresler E., Speakman S.P., Jeynes C. and Steinke J.H.G., "Patterned low temperature copper-rich deposits using inkjet printing", *Appl. Phys. Lett.* 2002, **81**, 5249–5251.
65. Nur H.M., Song J.H., Evans J.R.G. and Edirisinghe M.J., "Ink-jet printing of gold conductive tracks", *J. Mater. Sci. Mater. Electron.* 2002, **13**, 213–219.
66. Fuller S.B., Wilhelm E.J. and Jacobson J.M., "Ink-jet printed nanoparticles microelectromechanical systems", *J. Microelec. Sys.* 2002, **11**, 54–60.
67. Szczech J.B., Megaridis C.M. and Gamota D.R., "Fine-line conductor manufacturing using drop-on-demand PZT printing technology", *IEEE Trans. Electron. Packing Manuf.* 2002, **25**, 26–33.
68. Ago H., Murata K., Yumura M., Yotani J. and Uemura S., "Ink-jet printing of nanoparticle catalyst for site-selective carbon nanotubes growth", *Appl. Phys. Lett.* 2003, **82**, 811–813.
69. Huang D., Liao F., Molesa S., Radinger D. and Subramanian V., "Plastic-compatible low resistance printable gold nanoparticle conductors for flexible electronics", *J. Electrochem. Soc.* 2003, **150**, G412–G417.
70. Hong C.M., "Inkjet printed copper source/drain metallization for amorphous silicon thin-film transistors", *IEEE Electron Dev. Lett.* 2000, **21**, 384–386.
71. Hart A.L., Turner A.P.F. and Hopcroft D., "On the use of screen- and ink-jet printing to produce amperometric enzyme electrodes for lactate", *Biosensors & Bioelectronics* 1996, **11**, 263–270.
72. Roda A., Guardigli M., Russo C., Pasini P. and Baraldini M., "Protein microdeposition using a conventional inkjet printer", *BioTechniques*, 2000, **28**, 492–496.
73. Wilson W.C., Jr. and Boland T., "Cell and organ printing I: protein and cell printers", *Anal. Rec. A* 2003, **272A**, 491–4996.
74. Okamoto T., Suzuki T. and Yamamoto N., "Microarray fabrication with covalent attachment of DNA using bubble jet technology", *Nature Biotech.* 2000, **18**, 438–441.
75. Xu T., Petridou S., Lee E.H., Roth E.A., Vyavahare N.R., Hickman J.J. and Boland T., "Construction of high-density bacterial colony arrays and patterns by the ink-jet method", *Biotech. Bioengin.* 2004, **85**, 29–33.
76. de Gans B.-J. and Schuber U.S., "Inkjet printing of polymer micro-arrays and libraries: instrumentation, requirements, and perspective", *Macromol. Rapid Commun.* 2003, **24**, 659–666.

77. Zaugg F.G. and Wagner P., "Drop-on-demand printing of protein biochip arrays", *MRS Bull.* 2003, **28**, 837–842.
78. Houghes T.R., Mao M., Jones A.R., Burchard J., Marton M.J., Shanon K.W., Lefkowitz S.M., Ziman M., Schelter J.M., Meyer M.R., Kobayashi S., Davis C., Dai H., He Y.D., Stephanianitts S.B., Calvet G., Walker W.L., West A., Coffey E., Shoemaker D.D., Stoughton R., Blanchard A.P., Friend S.H. and Linsley P.S., "Expression profiling using microarrays fabricated by an ink-jet oligonucleotide synthesizer", *Nat. Biotech.* 2001, **19**, 342–347.
79. Butler J.H., Cronin M., Anderson K.M., Biddison G.M., Chatelain F., Cummer M., Davi D.J., Fisher L., Frauendorf A.W., Frueh F.W., Gjerstad C., Harper T.F., Kernahan S.D., Long D.Q., Pho M., Waler J.A., II and Brennan T.M., "In situ synthesis of oligonucleotide arrays by using surface tension", *J. Am. Chem. Soc.* **2001**, **123**, 8887–8894.
80. Perçin G., Lundgren T.S. and Yakub B.T.K., "Controlled ink-jet printing and deposition of organic polymers and solid particles", *Appl. Phys. Lett.* 1998, **73**, 2375–2377.
81. Fan H., Lu Y., Stump A., Reed S.T., Baer T., Schunk R., Perez-Luna V., López G.P. and Brinker C.J., "Rapid prototyping of patterned functional nanostructures", *Nature*, 2000, **405**, 56–60.
82. Kumar P., Metha A., Dadmun M.D., Zheng J., Peyser L., Bartko A.P., Dickson R.M., Thundat T., Sumpter B.G., Noid D.W. and Barnes M.D., "Narrow-bandwidth spontaneous luminescence from oriented semiconducting polymer nanostructures", *J. Phys. Chem.* 2003, **107**, 6252–6257.
83. Magdassi S. and Moshe M.B., "Patterning of organic nanoparticles by ink-jet printing of microemulsions", *Langmuir* 2003, **19**, 939–942.
84. Chen B., Cui T., Liu Y. and Varahramyan K., "All-polymer RC filter circuits fabricated with inkjet printing technology", *Solid-State Electron.* 2003, **47**, 841–847.
85. Liu Y., Cui T. and Varahramyan K., "All-polymer capacitor fabricated with inkjet printing technique", *Solid State Electron.* 2003, **47**, 1543–1548.
86. Danzebrink R. and Aegerter M.A., "Deposition of micropatterned coating using an ink-jet technique", *Thin Solid Films* 1999, **351**, 115–118.
87. Cox W.R., Guan C. and Hayes D.J., "Microjet printing of micro-optical interconnects and sensors", *SPIE Photo. West Proc.* 2000, **3852**, 400–407.
88. Kim W.H., Mäkinen A.J., Nikolov N., Shashindhar R., Kim H. and Kafafi Z.H., "Molecular organic light-emitting diodes using highly conducting polymers", *Appl. Phys. Lett.* 2002, **80**, 3844–3846.
89. Lin S. and Carlson R.M., "Susceptibility of environmentally important heterocycles to chemical disinfection: reaction with aqueous chlorine, chlorine dioxide, and chloramines", *Environ. Sci. Technol.* 1984, **18**, 743–748.
90. Jiang B. and Tilley T.D., "General, efficient route to thiophene-1-oxides and well-defined, mixed thiophene-thiophene-1-oxide oligomers", *J. Am. Chem. Soc.* 1999, **121**, 9744–9745.
91. Weiss R.A., Sen A., Willis C.L. and Pottick L.A., "Block copolymer ionomers: 1. synthesis and physical properties of sulphonated poly(styrene-ethylene/butylenes-styrene)", *Polymer* 1999, **32**, 1867–1874.
92. Socrates G., *Infrared characteristics group frequencies*, 1980, John Wiley & Son.
93. Servaty R., Schiller J., Binder H., Kohlstrunk B. and Arnold K., "IR and NMR studies on the action of hypochlorous acid on chondroitin sulfate and taurine", *Bioorg. Chem.* 1998, **26**, 33–43.

94. Heuer H.W., Wehrmann R. and Kirchmeyer S., "Electrochromic window based on conducting poly(3,4-ethylenedioxythiophene)-poly(styrene sulfonate)", *Adv. Func. Mater.* 2002, **12**, 89–94.
95. Argun A.A., Cirpan A. and Reynolds J.R., "The first truly all-polymer electrochromic devices", *Adv. Mater.* 2003, **15**, 1338–1341.
96. Zotti G., Zecchin S., Schiavon G., Louwet F., Groenendaal L., Crispin X., Osikowicz W., Salaneck W. and Fahlman M., "Electrochemical and XPS studies toward the role of monomeric and polymeric surface counterions in the synthesis, composition, and properties of Poly(3,4-ethylenedioxythiophene)", *Macromolecules* 2003, **36**, 3337–3344.

## High-resolution, printing techniques for plastic electronics

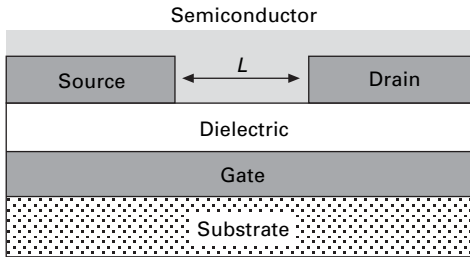
---

G BLANCHET, DuPont Central Research and J ROGERS,  
University of Illinois and Beckman Institute, USA

### 13.1 Introduction

The most widely used techniques for micro and nanofabrication – photolithography, electron beam lithography and related methods – are extremely well suited to the types of application in microelectronics and display systems for which they were principally designed. There are considerable challenges, however, in adapting these techniques to new applications in such fields as plastic and molecular electronics. In these cases, the complexity, the high capital and operating costs and the difficulty in patterning large areas represent significant disadvantages. In addition, the chemicals that are required for these methods – the resists, etchants, developers, solvents, etc., – are incompatible with many interesting organic electronic materials. As a result, some of the oldest and conceptually simplest forms of lithography – embossing, molding, stamping, writing, etc., – are now being examined as tools for forming micro or nanostructures<sup>1</sup> that can be implemented in these and other applications. Considerable progress has been made in the last few years, mainly by combining these approaches or variants of them with new materials, chemistries and processing techniques. This chapter highlights three high-resolution patterning methods that have demonstrated applications for building flexible, plastic circuits. This emerging type of electronics is of interest because it enables important classes of consumer devices – electronic paper, wearable computers or sensors, disposable wireless ID tags, etc., – that would be difficult to realize with conventional electronics. Low-cost, large-area patterning techniques are essential to the commercialization of such systems.

The thin film transistors (TFTs) are among the key building blocks of these circuits.<sup>2</sup> Figure 13.1 shows a cross-sectional view. A thin insulating film (i.e. the gate dielectric) isolates source and drain electrodes and a semiconductor layer from an underlying gate electrode. The region between the source/drain electrodes is known as the channel. The separation between these electrodes defines the channel length,  $L$ ; their lengths define the channel



**13.1** Schematic cross-sectional view of an organic thin film transistor. The semiconductor is deposited on top of source and drains electrodes that are electrically isolated from a gate electrode by a dielectric layer. The separation between the electrodes defines the channel length,  $L$ .

width,  $W$ . In an accumulation mode device, the channel has a high effective resistance when no voltage is applied to the gate: the transistor is in its 'off' state. When a voltage is applied to the gate, current flows between the source and drain electrodes if there is a potential difference between them: the transistor is in its 'on' state. For many systems, the transistor must produce enough 'on' current to activate or switch another part of a circuit or device (e.g. a pixel in a display) without producing 'off' currents that could induce unwanted switching. These characteristics are governed by the mobility of the semiconductor and its doping level, the efficiency with which it is coupled to the source/drain electrodes (i.e. the resistances associated with the contacts), the capacitance of the gate dielectric, and the ratio  $W/L$ . Reducing the channel length increases the 'on' currents.

The ability to print (at low cost, over large areas on plastic sheets) the source/drain electrodes at high resolution and with low contact resistances to the semiconductor is therefore crucial to achieving good performance. Several techniques have been demonstrated for this patterning task, including a type of photolithographic processes that relies on the photochemical conversion of polymers from non-conducting to conducting states,<sup>3,4</sup> specialized adaptations of inkjet<sup>5</sup> and screen printing,<sup>6,7</sup> and certain types of molding<sup>8</sup> and imprinting<sup>9</sup> techniques. The following describes three patterning approaches that have demonstrated applications in plastic electronics. Two of them represent forms of contact printing with a stamp;<sup>10-14</sup> the third uses scanning lasers in a type of thermal transfer patterning.<sup>15</sup>

## 13.2 Contact printing with high-resolution stamps

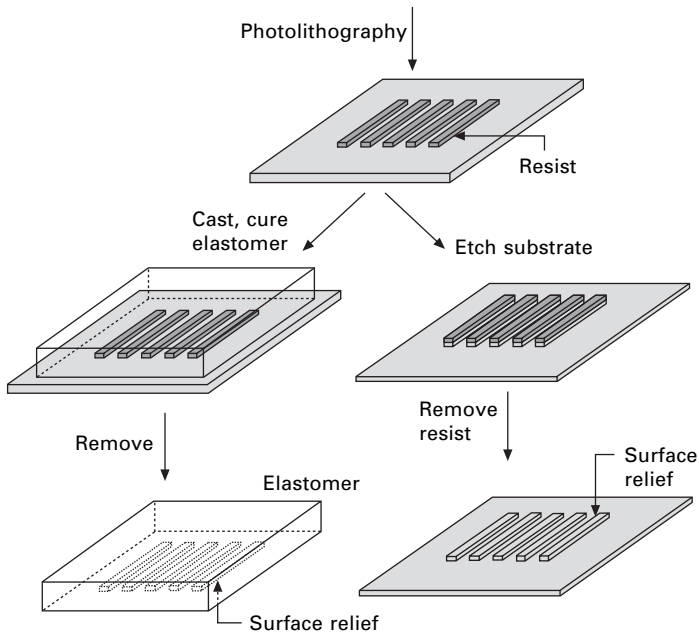
Contact printing involves the use of an element with surface relief (i.e. the 'stamp') for patterned transfer of material (i.e. the 'ink') to a substrate. Historically this approach has been used primarily to produce printed text or images with features that are one hundred microns or larger in their minimum

dimension. The use of this method for patterning functional materials in active systems which incorporate micron or nanometer sized features is much less well explored. The nature of the inks and their role in process steps after the printing define the classes of materials that can be patterned. The resolution is determined by the nature of the ink and its interaction with the stamp and/or substrate, the resolution of the stamp, and the conditions that convert the pattern of ink into a pattern of functional material. This section describes printing methods that have sub-micron resolution and which can define electrodes for high-performance plastic electronic devices.

### 13.2.1 High-resolution stamps

The printing process can be separated into two parts; fabrication of the stamp and use of this stamp to pattern features defined by the relief on its surface. These two processes are typically quite different, although it is possible in some cases to use patterns generated by a stamp to produce a replica of that stamp. The structure from which the stamp is derived, which is known as the 'master', can be fabricated with any technique that is capable of producing well defined patterns of surface relief. This master can then be used directly as the stamp, or it can be used to produce stamps via molding or printing procedures. It is important to note that the technique for producing the master does not need to be fast or low in cost. It is also not essential for it to have other characteristics that might be desirable for a given patterning task; it is used just once to produce a master which is directly or indirectly used to fabricate stamps. Each one of these stamps can then be used many times for printing. In a common approach for the high-resolution techniques that are the focus of this chapter, an established lithographic method, such as one of those developed for the microelectronics industry, defines the master.

Figure 13.2 schematically illustrates two possible routes to stamps. Both use photolithography to define a pattern of resist on a silicon wafer. Stamps are generated from this structure by casting against this master or by etching the substrate with the patterned resist as a mask. In the first approach, the master can be used many times to produce many stamps, typically using a light or heat-curable prepolymer. In the second, the etched substrate serves as the stamp; additional stamps can be generated either by repeating the lithography and etching or by using the original stamp to print replica stamps. For feature sizes larger than  $\sim 1$ – $2$  microns, contact or proximity mode photolithography with a photomask produced by direct-write photolithography represent convenient methods to fabricate the master. Other techniques must be used for features smaller than  $\sim 2$  microns. Established methods include projection mode photolithography,<sup>16</sup> direct write electron beam (or focused ion beam) lithography,<sup>17,18</sup> scanning probe lithography<sup>19–22</sup> and laser interference lithography.<sup>23</sup> The first two have features (i.e. flexibility in



**13.2** Schematic illustration of two methods for producing high-resolution stamps. The first step of both involves patterning a layer of resist on a flat substrate. A technique such as photolithography can be used for this purpose. This structure, known as the ‘master’, is converted to a stamp either by etching or by molding. In the first case (right frames), the resist acts as a mask for etching the underlying substrate. Removing the resist yields a stamp. This structure can be used directly as a stamp to print patterns or to produce additional stamps. In the molding approach (left frames), a prepolymer is cast against the relief structure formed by the patterned resist on the substrate. Curing (thermally or optically) and then peeling the resulting polymer away from the substrate yields a stamp. In this approach, many stamps can be made with a single ‘master’ and each stamp can be used many times.

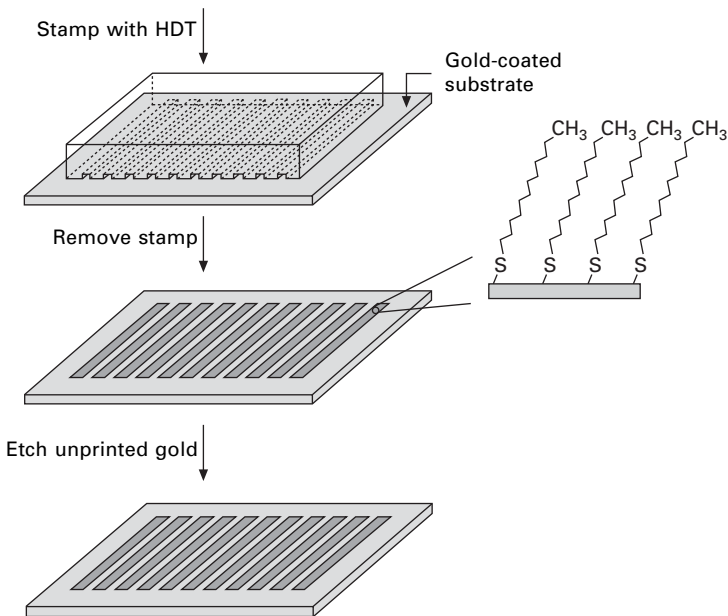
pattern design; well developed technology base, etc.) that make them useful for generating masters for plastic electronic systems. The circuit applications described in the following used masters formed by contact or projection mode photolithography. Some stamps that were designed to demonstrate patterning capabilities and resolution use masters formed by electron beam and laser interference lithography.

### 13.2.2 Microcontact printing

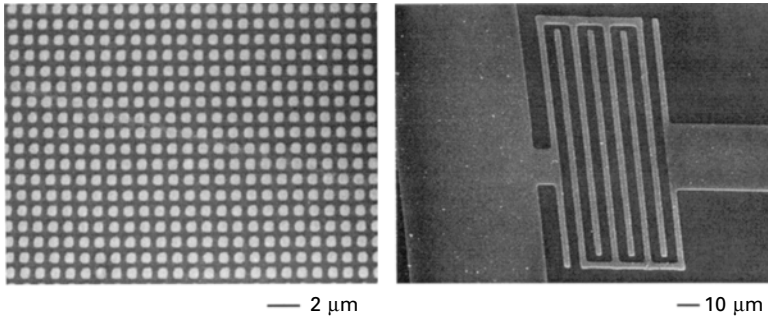
Microcontact printing ( $\mu$ CP) uses high-resolution rubber stamps with ‘inks’ (e.g. alkanethiols) that form self-assembled monolayers (SAMs) on the surface (e.g. thin gold film) that is printed.<sup>13</sup> In one  $\mu$ CP approach, these SAMs act

as resists for etching material in the unprinted areas, as illustrated in Fig. 13.3. Figure 13.4 shows patterns of thin films of gold and silver generated in this manner. The typical edge resolution is  $\sim 50\text{--}100\text{ nm}$ ; features with dimensions greater than  $\sim 200\text{ nm}$  can be generated easily, over large areas in a single patterning step. One of the advantages of this method is that it is applicable not only to ultraflat surfaces of silicon wafers but also to curved objects and even to plastic substrates. Figure 13.5 shows examples of high resolution patterns formed on small-scale cylindrical objects – optical fiber and microcapillary tubes.<sup>24</sup> These simple devices (integrated photomasks for optical fiber Bragg gratings and intravascular stents), require only one patterned layer.

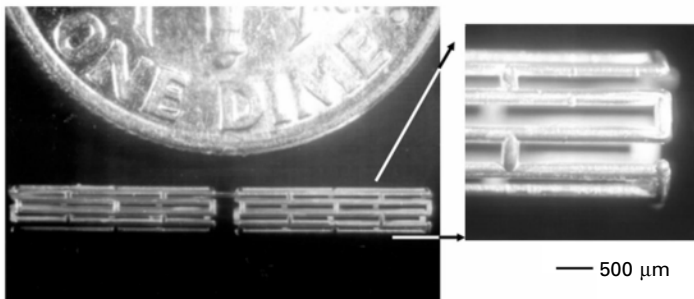
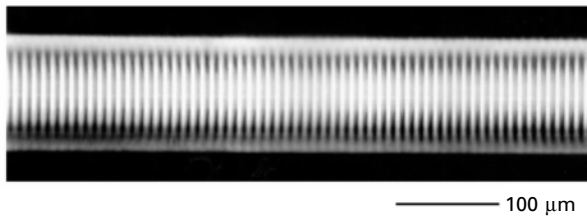
For plastic electronics and many other systems, multiple layers must be patterned on top of each other with good overlay registration. A challenge with  $\mu\text{CP}$  is that the elastomeric stamps tend to deform during the printing. This deformation can alter, in ways that are difficult to control, the precise



**13.3 Steps for microcontact printing.** The stamp is first inked with a solution of a material that is capable of forming a self-assembled monolayer (SAM) on the substrate that will be printed. In the case illustrated here, the ink is a millimolar concentration of hexadecanethiol (HDT) in ethanol. The substrate consists of a thin layer of Au on a flat support. Removing the stamp after a few seconds of contact leaves a patterned SAM of HDT on the surface of the Au film. The printed SAM can act as a resist for the aqueous based wet etching of the exposed regions of the Au. The pattern of Au that results after etching and removal of the ink can be used to build devices of various types, including those for plastic electronics.



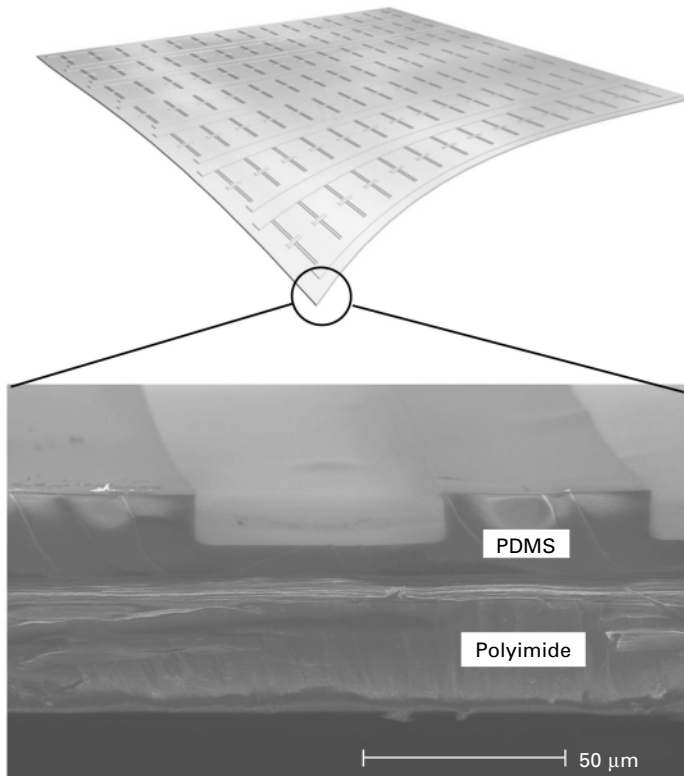
**13.4** Scanning electron micrographs of structures formed by microcontact printing a self-assembled monolayer ink of hexadecanethiol onto a thin metal film of Au (left) and Ag (right) followed by wet etching of the unprinted areas. The left frame shows an array of Au (20 nm thick) dots with ~500 nm diameters. The right frame shows a printed structure of Ag (100 nm thick) in the geometry of interdigitated source/drain electrodes for a transistor in a simple inverter circuit. An edge resolution of ~100 nm can be easily achieved with this technique.



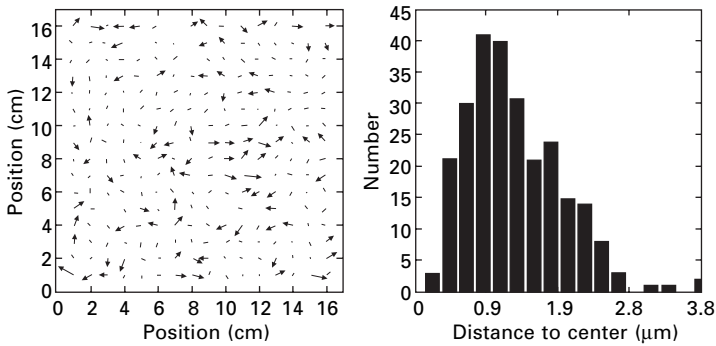
**13.5** Examples of structures microcontact printed onto the curved surfaces of cylinders. The top frame shows 3 mm lines and spaces of Au printed on the outer surface of an optical fiber. The bottom frames show a free-standing metallic structure in the form of an intravascular stent formed by printing, electroplating and then etching away the cylindrical support.

alignment of features. There are at least two simple strategies to reduce these problems: (i) eliminate significant mechanical manipulation of the stamp during printing,<sup>25</sup> and (ii) implement composite stamps that use PDMS layers

bonded to stiff supports.<sup>26</sup> The second approach has the advantage that it provides flexibility in the choice of means to perform the printing. Figure 13.6 shows a stamp with this construction, designed for plastic electronics applications.<sup>27</sup> It consists of a thin layer of PDMS on top of a sheet of polyimide. The relatively high in-plane modulus of the polyimide prevents distortions that can frustrate registration. The small thickness of this layer enables the stamp to be bent in a manner that facilitates printing. Figure 13.7 shows a vector diagram of distortions measured across a stamp designed for a relatively large area plastic active matrix backplane circuit. (These stamps show an overall isotropic shrinkage of  $\sim 0.025\%$ , which can be incorporated into the design of the master. Misalignments associated with this shrinkage are not shown in the figure.) The histogram of displacements on the right indicates maximum distortions of less than a few microns. This value, which is more than a factor of ten smaller than that previously reported by us for



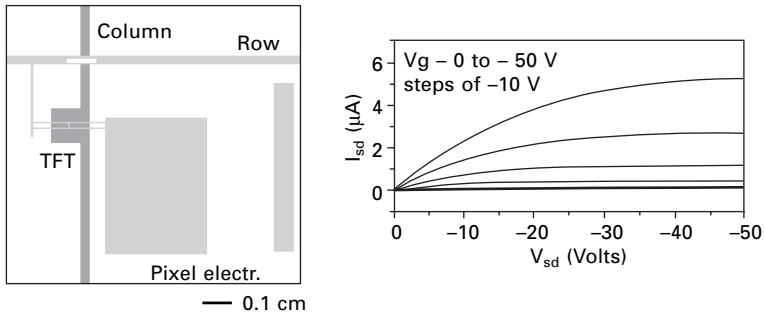
**13.6** Composite stamp that uses a thin layer of PDMS against a rigid, but flexible, thin sheet of polyimide. The high modulus of the polyimide reduces in-plane deformations to levels that can meet the requirements for multilayer registration in many plastic electronic systems.



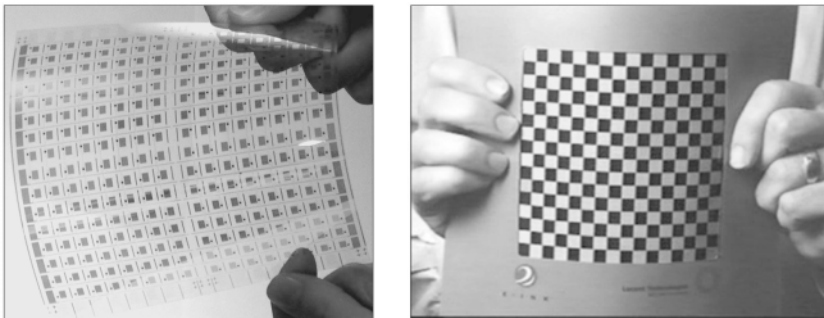
13.7 Vector diagram (left frame) of feature misalignment in a composite stamp designed for an active matrix circuit for a display. The histogram in the right frame shows the distribution of alignment errors observed in this system. These micron-level distortions are small enough to satisfy the requirements of many applications in plastic electronics. A small overall isotropic shrinkage ( $\sim 0.025\%$ ) in the stamp is not shown here; this dimensional change can be incorporated into the design of the master.

this application,<sup>25</sup> should satisfy many interesting applications in plastic electronics (e.g. flexible displays).

Microcontact printing can be used in plastic electronics to form high-resolution source/drain electrodes with short channel lengths.<sup>14</sup> Depositing an organic semiconductor on top of these electrodes yields a transistor with a layout like that shown in Fig. 13.1. This basic approach has been used to build large area plastic backplane circuits for active matrix electronic paperlike displays.<sup>25</sup> In that system,  $\mu$ CP with ‘inks’ of hexadecanethiol ( $\sim 1$  mM in ethanol) defined source/drain electrodes and interconnections in thin films (20 nm) of Au. Glass resin films spin cast to thicknesses of  $\sim 1$   $\mu$ m served as gate dielectrics.<sup>25,28</sup> The substrate consisted of a 250  $\mu$ m thick sheet of poly(ethylene terephthalate) (PET) with a thin (100 nm) coating of indium tin oxide (ITO) for the gate. Figure 13.8 shows the layout of a unit cell (i.e. a single pixel driver) in this display and typical current-voltage characteristics of the drive transistor. The channel length in this case is  $\sim 15$   $\mu$ m; the leads that connect the source/drain electrodes to the row and pixel electrodes are  $\sim 15$   $\mu$ m wide. Images of the entire circuit and a display, built by laminating this circuit against an unpatterned sheet of electronic ink, appear in Fig. 13.9. The high resolution of  $\mu$ CP is important to achieving the necessary performance (transistor current output and switching speed) for this application. Resolution limits of existing forms of  $\mu$ CP prevent patterning of transistors with  $L < \sim 0.5$   $\mu$ m. An alternative technique, described below, provides resolution for building devices with  $L$  deep into the nanometer regime.



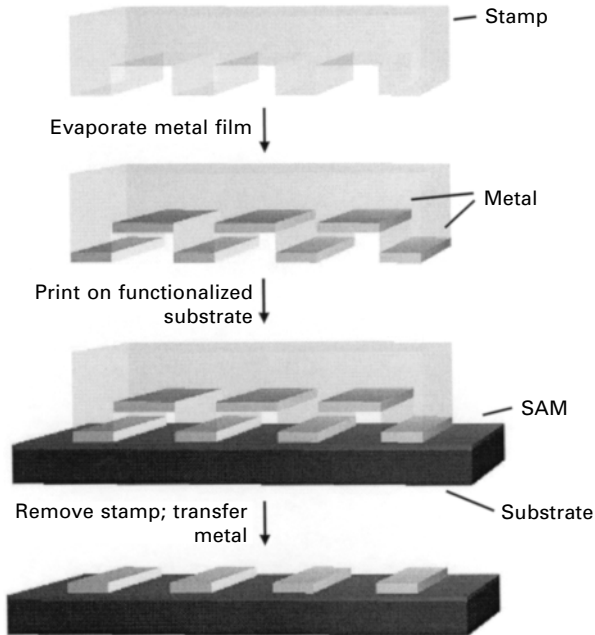
**13.8** Schematic illustration of the layout of a unit cell in an active matrix display circuit (left frame). It consists of a transistor connected to row and column electrodes and a pixel electrode pad. This circuit drives an overlying layer of electronic ink. The frame on the right shows the current-voltage characteristics of a typical transistor in a large active matrix circuit that contains several hundred unit cells like the one illustrated in the left frame. The structure consists of a substrate (PET), a gate electrode (ITO), a gate dielectric (GR), source and drain electrodes (20 nm Au and 1.5 nm Ti), and a layer of the organic semiconductor pentacene (25 nm).



**13.9** Mechanically flexible plastic active matrix circuit (left frame) for an electronic paperlike display (right frame). Microcontact printing defined the critical features in the circuit.

### 13.2.3 Nanotransfer printing

Nanotransfer printing (nTP) is a more recent high-resolution printing technique. This method uses surface chemistries as interfacial ‘glues’ and ‘release’ layers (rather than ‘inks’) to control the transfer of solid material layers from relief features on a stamp to a substrate.<sup>10–12,29</sup> This approach is purely additive (i.e. material is deposited only in locations where it is needed) and it can generate complex two- or three-dimensional structures in single or multiple layers with nanometer resolution. It has been explored so far by our group and, in independent efforts, by groups at Princeton<sup>30</sup> and IBM/Zürich.<sup>31</sup> Figure 13.10 schematically illustrates the process. The method uses elastomeric

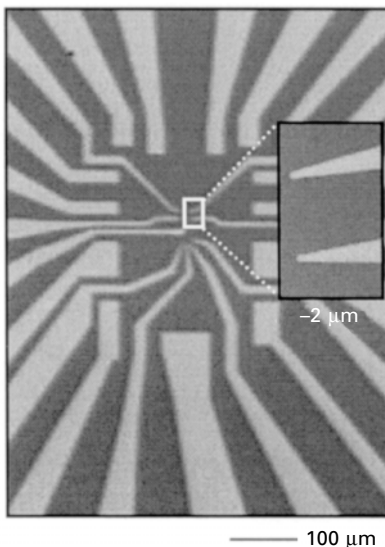


**13.10** Schematic illustration of steps for nanotransfer printing. Depositing a layer of metal using a collimated flux normal to the surface of the stamp yields a thin discontinuous coating on the raised and recessed regions of the stamp but not on its sidewalls. Contacting this coated stamp to a substrate that supports suitable surface chemical groups leads to covalent bonding between the metal and the substrate. In one example, self-assembled monolayers with exposed thiol groups allow printing of Au patterns on GaAs substrates. If the adhesion between the metal and the stamp is poor, then removing the stamp leaves a pattern in the geometry of the relief features.

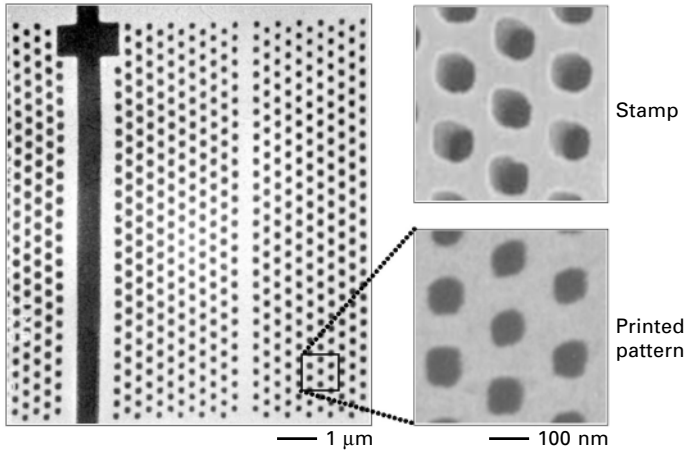
stamps similar to those of  $\mu$ CP, or hard stamps formed using the etching procedures outlined in Fig. 13.2. Depositing a thin layer of solid material onto the raised features of the stamp constitutes the ‘inking’ step. All of the examples described here use electron beam evaporation of a thin layer of Au (20–50 nm) or a bilayer of Au (20–50 nm)/Ti (2–5 nm). Other material systems are also possible. Contacting this coated stamp with a substrate that supports a suitable surface chemistry results in covalent bonding between the coating and the substrate. If the surface of the stamp is treated such that the coating does not adhere well to it, then removing the stamp leaves a pattern with the geometry of the relief features. nTP can be used with SAMs and other surface chemistries for printing onto flexible or rigid substrates with hard inorganic or soft polymer stamps. The stamps typically have depths of relief  $>0.2 \mu\text{m}$  for patterning metal films with thicknesses  $<50 \text{ nm}$ .

Figure 13.11 shows an example of patterning on micron length scales using nTP. Fabrication of this pattern involved transfer of a 20 nm Au coating from a PDMS stamp formed by casting against photoresist patterned by contact mode photolithography. A vertical, collimated flux of Au and slightly re-entrant sidewalls on the relief features of the stamp ensured that Au was deposited only on the raised and recessed regions and not the sidewalls. For the case of Fig. 13.11, a SAM formed by exposing a silicon wafer to a silane solution (3-mercaptopropyltrimethoxysilane) yields exposed thiol groups that enable transfer of Au from the stamp to the substrate.<sup>11</sup> Sulfur-gold bonds can form when this surface is brought into contact with an Au-coated (20 nm) PDMS stamp.

Figure 13.12 shows a printed pattern that has nanometer resolution.<sup>11</sup> In this case a hard stamp of GaAs, formed by electron beam lithography and etching, was used. The metal coating consisted of a bilayer of Au (20 nm) and Ti (5 nm). The gold adheres poorly to the surface of the GaAs. The Ti layer forms a ~3 nm oxide layer at ambient conditions. Exposing this oxide to an oxygen plasma breaks bridging oxygen bonds, thus creating defect



**13.11** Steps for nanotransfer printing a thin layer of Au onto a silicon wafer using a self-assembled monolayer (SAM) surface chemistry. Plasma oxidizing the surface of the wafer generates  $-OH$  groups. Solution or vapor phase exposure of the wafer to 3-mercaptopropyltrimethoxysilane yields a SAM with exposed thiol groups. Contacting an Au-coated PDMS stamp to this surface produces thiol linkages that bond the gold to the substrate. Removing the stamp completes the transfer printing process. The resolution demonstrated here is limited only by the contact photolithography used to generate the master for the stamp.



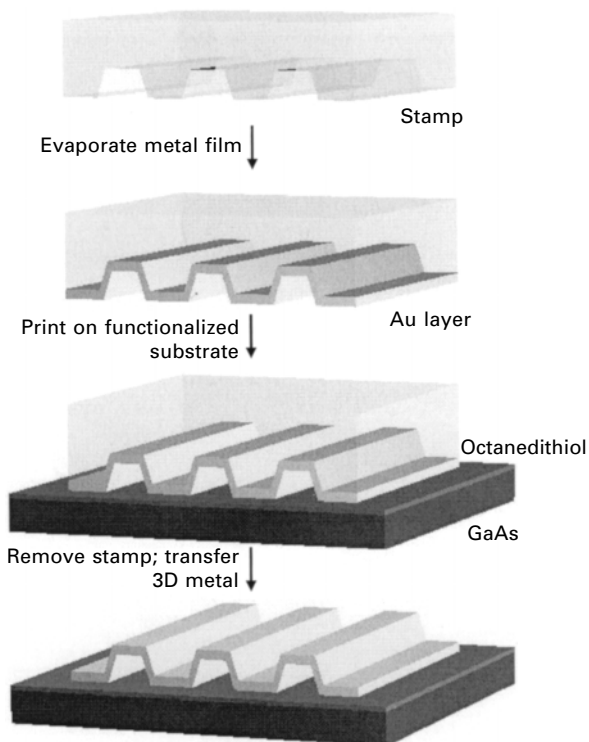
**13.12** Scanning electron micrograph (SEM) of a pattern produced by nanotransfer printing. The structure consists of a bilayer of Au(20 nm)/Ti (5 nm) (white) in the geometry of a photonic bandgap waveguide printed onto a thin layer of PDMS on a sheet of plastic (PET; black). Electron beam lithography and etching of a GaAs wafer produced the stamp that was used in this case. The transfer chemistry used condensation reactions between titanol groups on the surface of the Ti and silanol groups on the surface of the substrate. The frames on the right show SEMs of the Au/Ti coated stamp (top) before printing and on the substrate (bottom) after printing. The electron beam lithography and etching used to fabricate the stamp limit the minimum feature size ( $\sim 70$  nm) and the edge resolution ( $\sim 5$ – $10$  nm) of this pattern.

sites where water molecules can adsorb. The result is a titanium oxide surface with some fractional coverage of hydroxyl ( $-\text{OH}$ ) groups (titanol).<sup>32,33</sup> The substrate is a thin film of PDMS ( $10$ – $50$   $\mu\text{m}$  thick) cast onto a sheet of PET ( $175$   $\mu\text{m}$  thick). Exposing the PDMS to an oxygen plasma produces surface ( $-\text{OH}$ ) groups (silanol).<sup>34</sup> Placing the plasma oxidized, Au/Ti-coated stamp on top of this substrate leads to intimate, conformal contact between the raised regions of the stamp and the substrate, without applying any pressure to the stamp. The soft, conformable PDMS is important in this regard.

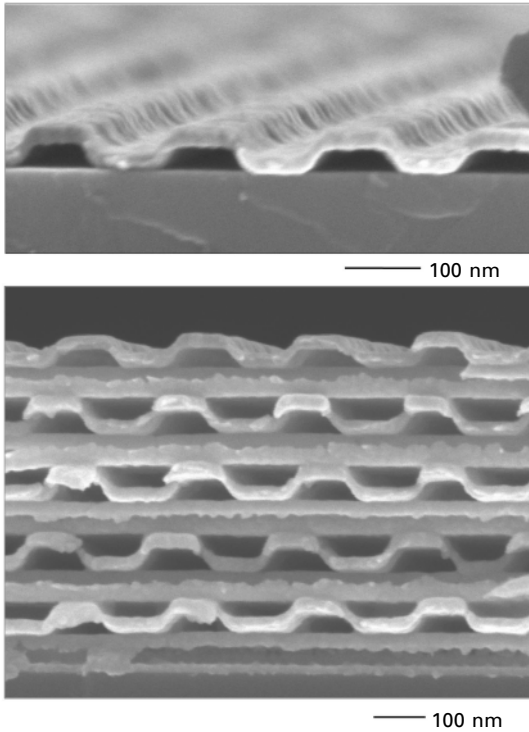
A dehydration reaction likely takes place at the ( $-\text{OH}$ )-bearing interfaces during contact; this reaction results in permanent Ti-O-Si bonds that produce strong adhesion between the two surfaces. Peeling the substrate and stamp apart transfers the Au/Ti bilayer from the raised regions of stamp (to which the metal has extremely poor adhesion) to the substrate. The frames on the right (Fig. 13.12) show images of the metal coated stamp before printing (top) and the transferred pattern (bottom). The resolution appears to be limited only by the resolution of the stamp itself, and perhaps by the grain size of the metal films. Although we have not yet quantified the accuracy in multilevel

registration that can be achieved with nTP, we expect it to be similar to that of embossing techniques that use rigid stamps or to that of  $\mu$ CP with composite stamps.

In addition to two-dimensional (2D) patterns like those in Figs 13.11 and 13.12, it is possible to build certain classes of three-dimensional (3D) structures with nTP.<sup>12</sup> Figure 13.13 schematically illustrates one example. Here a conformal coating of Au on the stamp yields, after printing, arrays of closed nanochannels. Figure 13.14 presents a scanning electron micrograph of a structure formed in this manner. In this case, a SAM formed from octanedithiol on a substrate of GaAs provides the surface chemistry for transferring the Au nanochannel structures (20 nm Au thickness).<sup>29</sup> The PDMS stamps were generated by casting and curing against a pattern of relief on an InP wafer formed by interference lithography and etching. Because the stamp is soft and nTP is purely additive, it is easy to build multilayer structures by printing multiple times on a single substrate. Figure 13.14 also



**13.13** Schematic illustration of steps for forming a type of three-dimensional structure by nTP. Printing with a stamp that has a conformal coating of metal produces sealed nanochannels on the substrate. This illustration depicts printing of a structure of Au onto a GaAs substrate by use of an octanedithiol monolayer.



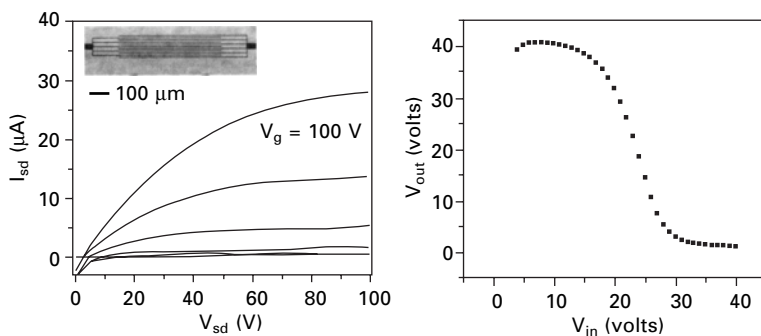
**13.14** Scanning electron micrograph of a printed nanochannel structure made of a thin layer (20 nm) of Au bonded to a GaAs wafer by an octanedithiol monolayer (top frame). The bottom frame shows a multilayer nanochannel structure formed by multiple printing steps. The nanochannels bond to one another by gold-gold cold welding. This structure consists of ten layers of crossed channels. Additional layers are possible.

shows a multilayer nanochannel lattice structure formed in this way. Cold welding bonds one Au nanochannel structure to the next. We observed no degradation in the structural integrity that would prevent more than the ten layers illustrated here.

Our experience indicates that the processing windows for the current versions of nTP are narrower than those of  $\mu$ CP. There are at least three processing aspects that are important to achieving high fidelity with nTP: (i) the deposition procedures must be carefully controlled to avoid cracking or buckling of the metal films when PDMS stamps are used, (ii) PDMS stamps must be handled carefully before and during the printing to avoid surface strains that can damage the metal coatings and (iii) the surface chemistry must provide a high density of bonding sites, and the surfaces of the stamps and substrates must come into uniform, intimate contact to allow efficient transfer. For the first issue, high deposition rates and surface treatments that

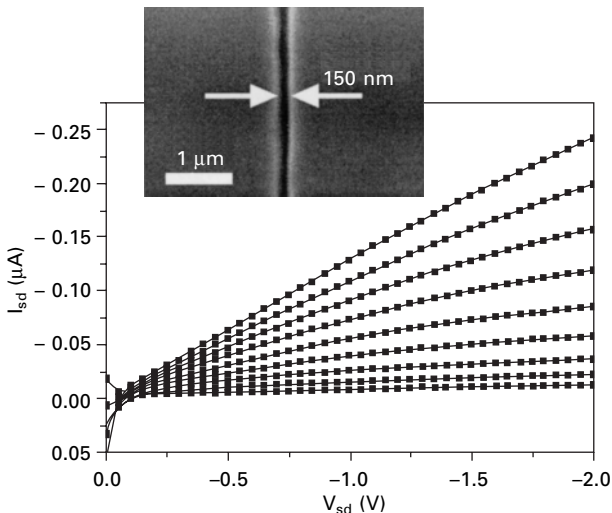
facilitate wetting of the metals on the surfaces of the stamps are important. For the second, composite stamp designs that use rigid backings and relatively thin PDMS layers are helpful. In the case of the third issue, suitable chemistries must be employed with substrates that present a low degree of roughness. With well controlled procedures, patterns over large areas (several  $\text{cm}^2$ ) that are free of defects or cracks (as observed by high-resolution scanning electron and atomic force microscopy) can be produced.<sup>27</sup> We note that in many cases, XPS analysis shows that a residual, ultra-thin layer of organic material can transfer from the stamp with the metal film to the substrate when PDMS based stamps are used. This layer is on the order of 1–4 nm thick, depending on the processing conditions. It can be removed using various dry or wet etching procedures.<sup>27</sup>

Like  $\mu\text{CP}$ , nTP can pattern electrodes for plastic electronic components. Figure 13.15 shows an optical micrograph (inset) and current-voltage characteristics (left frame) of a transistor that incorporates interdigitated source/drain electrodes of Au/Ti patterned by nTP on PDMS/PET using procedures described previously.<sup>10</sup> Laminating this structure against a substrate that supports an organic semiconductor, gate dielectric (GR) and gate electrode (ITO) forms a transistor with the source/drain electrodes on top of the semiconductor. The transistor shown here uses the n-type organic semiconductor copper hexadecafluorophthalocyanine (FCuPc). The right frame of Fig. 13.15 shows the transfer characteristics of a laminated complementary logic gate whose electrodes and connecting lines are defined by nTP. The p-channel transistor in this circuit uses pentacene for the semiconductor.<sup>10</sup>

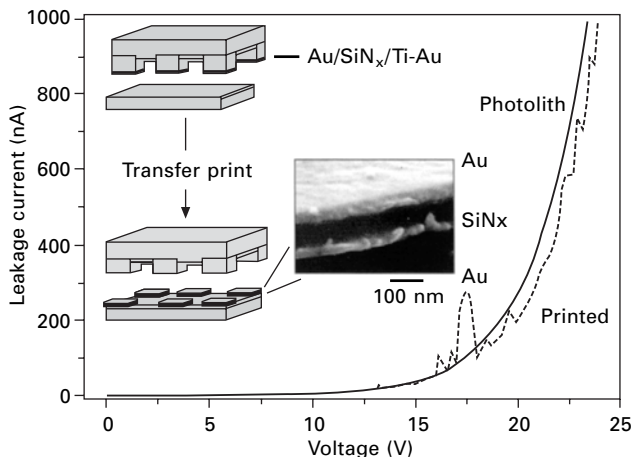


13.15 The frame on the left shows current-voltage characteristics of an n-channel transistor formed with electrodes patterned by nanotransfer printing. Laminating these electrodes against a substrate (PET) that supports an organic semiconductor (FCuPc), a gate dielectric (GR) and a gate electrode (ITO) completes the device. The inset shows an optical micrograph of the interdigitated electrodes. The frame on the right shows the transfer characteristics of a simple complementary logic gate that uses this device and a similar one for the p-channel (pentacene) transistor.

The high resolution of nTP and its multilayer capabilities are useful for plastic electronic systems. Figure 13.16 shows a scanning electron micrograph and current-voltage characteristics of a transistor with  $L = 150$  nm. In this device, an Au-coated stamp is simply placed into contact with the semiconductor (pentacene) to form a top contact device.<sup>35</sup> nTP can also form complex multilayer devices with electrical functionality on plastic substrates<sup>11</sup>. Figure 13.17 shows a metal/insulator/metal (MIM) structure of Au (50 nm), SiN<sub>x</sub> (100 nm; by plasma enhanced vapor deposition), Ti (5 nm) and Au (50 nm) formed by transfer printing with a silicon stamp that is sequentially coated with these layers. In this case, a short reactive ion etch (with CF<sub>4</sub>) after the second Au deposition removes the SiN<sub>x</sub> from the sidewalls of the stamp. nTP transfers these layers in a patterned geometry to a substrate of Au(15 nm)/Ti(1 nm) on PDMS(50 μm)/PET. Interfacial cold welding between the Au on the surfaces of the stamp and substrate bonds the multilayers to the substrate. These MIM capacitors have performance similar to devices fabricated on silicon wafers by photolithography and lift-off.<sup>11</sup> This example illustrates the ability of nTP to print patterns of materials whose growth conditions (high temperature SiN<sub>x</sub> by PECVD in this case) prevent their direct deposition or processing on the substrate of interest (PET in this case). The cold welding transfer approach has also been exploited in other ways for patterning components for plastic electronics.<sup>30,36</sup>



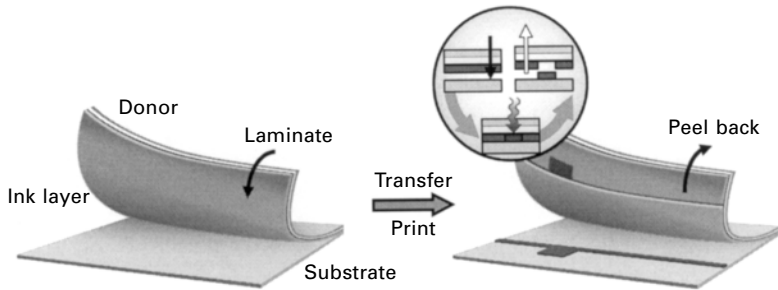
**13.16** Current-voltage characteristics from a nanoscale organic transistor formed by contact of a metal coated stamp against a thin film of the organic semiconductor pentacene. The gate voltage varies between +1.0 V and -2.2 V in steps of 0.4 V. The channel length is ~150 nm. The inset shows a scanning electron micrograph of the separation between the source and drain electrodes on the stamp.



**13.17** Multilayer thin film capacitor structure printed in a single step onto a plastic substrate using the nanotransfer printing technique. A multilayer of Au/SiN<sub>x</sub>/Ti/Au was first deposited onto a silicon stamp formed by photolithography and etching. Contacting this stamp to a substrate of Au/PDMS/PET forms a cold weld that bonds the exposed Au on the stamp to the Au-coating on the substrate. Removing the stamp produces arrays of square (250 μm × 250 μm) metal/insulator/metal capacitors on the plastic support. The dashed line shows the measured current-voltage characteristics of one of these printed capacitors. The solid line corresponds to a similar structure formed on a rigid glass substrate using conventional photolithographic procedures. The slightly higher level of noise in the printed devices results, at least partly, from the difficulty in making good electrical contacts to structures on the flexible plastic substrate.

### 13.3 Thermal transfer printing

Although the techniques described above have many attractive features, they do not yet exist in the form of commercial tools. Thermal transfer printing, which is the third technique presented in this chapter, is an established technique previously developed for digital printing applications. Because suitable output engines are commercially available, thermal transfer may well be a suitable route for early commercialization of organic electronic devices.<sup>15</sup> Figure 13.18 illustrates this approach, in which patterning proceeds via the purely additive, selective transfer of a solid film. This type of dry printing removes the strenuous solvent compatibility requirements and expands considerably the range of usable materials. In addition, thermal printing maintains features desirable in large-scale manufacturing such as high speed, resolution and the ability to perform multilayer registration. A donor film that is coated with a thin layer to be patterned is placed against a flexible substrate onto which the circuit is to be printed. A 40 W 780 nm infra-red

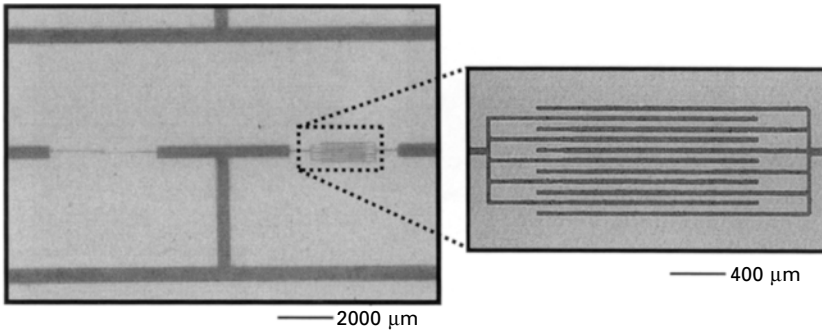


**13.18** Sequence for patterning structures using thermal transfer printing. A donor sheet that is coated with a layer of the material to be printed is placed against a substrate. The inset shows the process by which local heating with a laser causes the transfer of some part of the material from the donor to the substrate. Repeating these laminations, laser transfer printing, removing steps provides an additive, dry multilayer route to patterning for plastic electronics.

diode laser, split into 250  $2.7 \mu\text{m} \times 5 \mu\text{m}$  individually addressable spots, is focused through the donor base at a thin absorbing layer on to which the material to be imaged is coated. The efficient conversion of light to heat at this interface decomposes a thin layer of adjacent organics into gaseous products while somewhat softening the remaining film. The expansion of the gaseous decomposition products propels the thin conducting layer on to the receiver film. The desired conducting pattern is printed by rastering the laser beam thereby selectively transferring the individual  $5 \mu\text{m} \times 2.7 \mu\text{m}$  pixels comprising the image from the donor layer onto the substrate.

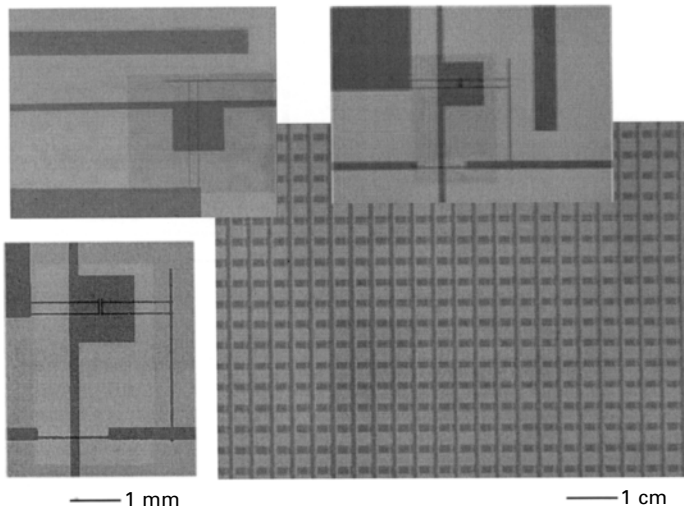
Since the beam is fully addressable, any pattern can be formed. In addition, after printing a first layer, the donor film can be removed and another donor sheet whose top layer has a different functionality (i.e. dielectric) can be positioned and exposed in registry on top of the conducting layer. Multilayer electronic circuitry can be readily built in this fashion.<sup>15</sup> Although a variety of conductors are compatible with this approach, we focus on a polymer system that consists of dinonylnaphthalene sulfonic acid doped polyaniline (DNNSA-PANI) mixed with several weight percent of single walled carbon nanotubes (SWNT). Figures 13.19–22 show some typical structures formed by thermal transfer printing.

Figure 13.19 presents optical micrographs of the source/drain layer of a complementary logic gate (i.e. inverter). The left-hand side of the pattern shows the inverter while the right-hand side shows a magnified view of the interdigitated source/drains. This layout is designed to balance the difference in mobilities between p- and n-type semiconductors (pentacene and FCuPc, respectively) that were evaporated through a shadow mask on top of the electrodes.



13.19 Optical micrographs of thermal transfer printed patterns of the doped conducting polymer DNNSA-PANI/SWNT. The image on the left shows printed source/drain electrodes and interconnections for an organic complementary logic gate. The image on the right shows a magnified view of interdigitated source/drain electrodes for the n-channel transistor of this simple circuit.

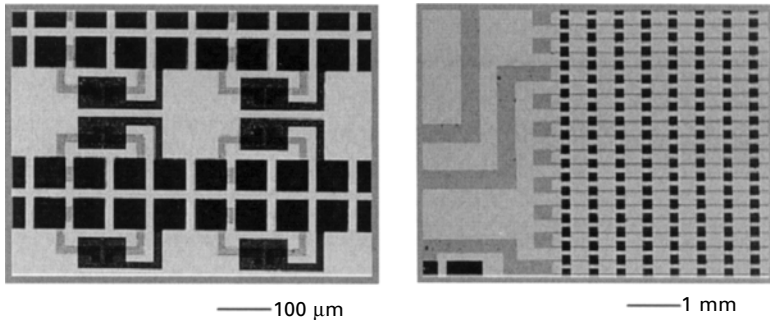
Figure 13.20 shows examples of patterns for active matrix backplane circuits. The one in the background corresponds to the source/drain level of an electrophoretic backplane that provides a display with 100 dots per inch resolution. The channel lengths of the transistors in this case are 20 microns. The other frames, each of which show a single transistor of large backplane circuit, illustrate the flexibility of thermal printing. In the upper right frame the source-drain and gate levels were printed using DNNSA-PANI, and pentacene was evaporated through a shadow mask. The upper left frame illustrates the ability to print the gate level with a thin layer of Ni. The



13.20 Optical micrographs of various circuit and transistor structures formed by thermal transfer printing.

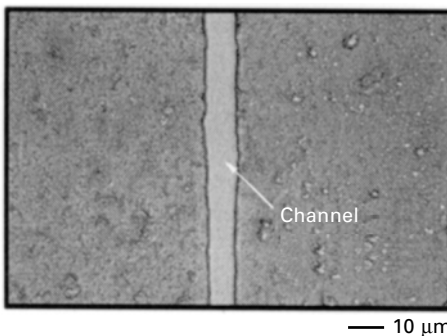
bottom left-hand side shows a TFT with all three layers patterned by thermal transfer; the source/drain, the gate and the dielectric.

Figure 13.21 illustrates the ability to print multiple layers of different conducting materials with good registration. The figure on the left shows a serpentine of 10 micron DNNSA-PANI lines and 50 micron squares printing using a high-conductivity composite. The overprint of 50 micron squares of the conducting composite onto DNNSA-PANI is also illustrated on the right image. As illustrated by these examples, the pattern geometries are flexible. The edge resolution, which is on the order of three microns, is comparable to the size of the laser spot used for printing.



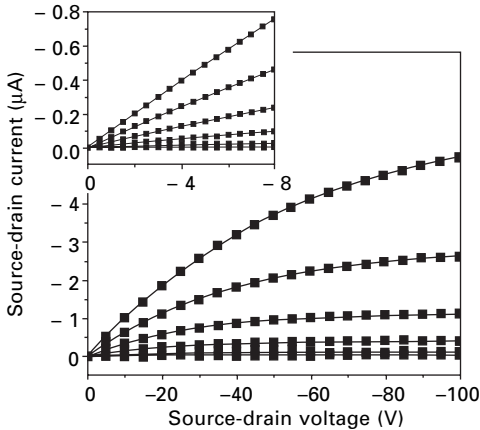
13.21 Optical micrographs of some patterns that consist of multiple thermal transfer printed layers of conducting films. The results illustrate multilayer printing with good registration.

The printed DNNSA-PANI/SWNT forms an excellent material for the source/drain electrodes of organic transistors. Figure 13.22 shows a  $\sim 10$ -micron channel fabricated in this manner. Depositing an organic semiconductor



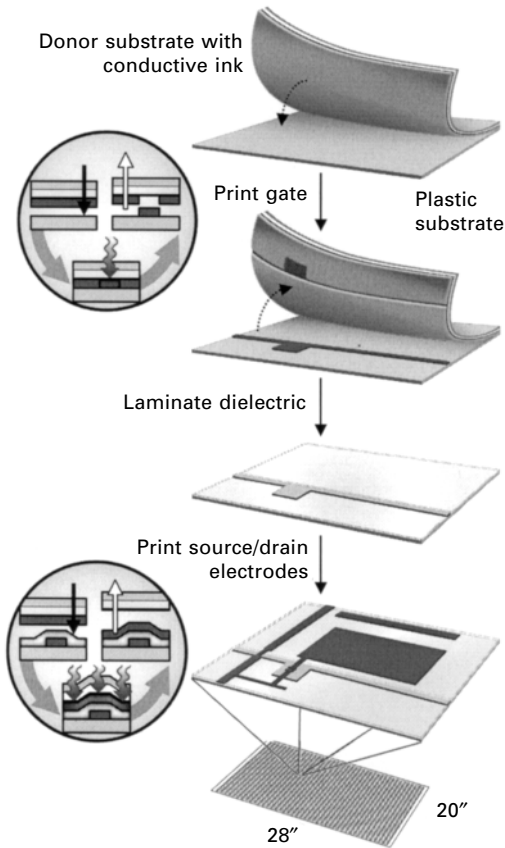
13.22 Optical micrograph of source and drain electrodes of a conducting polymer patterned by thermal transfer printing (left frame). This structure defines a transistor channel length of  $\sim 7$  microns. This result represents the lower limit for reliably patterning transistor channels with the current version of this technique.

on top of such printed electrodes yields high-performance transistors. Figure 13.23 shows the current-voltage characteristics of a p-channel transistor that uses a thin film of pentacene as the semiconductor. The good electrical performance of the thermal transfer printed devices derives, in part, from the low contact resistance between the source/drain electrodes and the organic semiconductors. Recent measurements quantify the ohmic behavior of these contacts and provide some morphological evidence for their low resistance.<sup>37</sup>



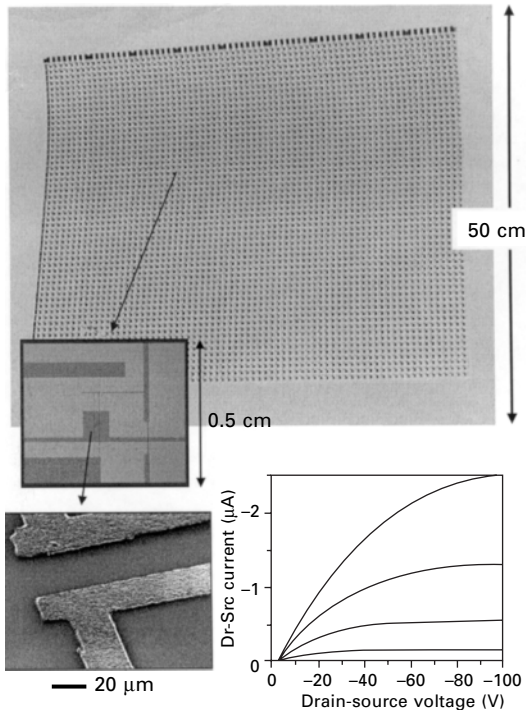
**13.23** Current-voltage characteristics of an organic transistor that uses thermal transfer printed polymer source/drain electrodes with an unpatterned ITO gate, GR gate dielectric, and PET substrate. A thin (25 nm) film of pentacene deposited onto the electrodes provides the semiconductor. The gate voltage varies from 0 to  $-100$  V in steps of  $-20$  V. The channel length and width are  $15\ \mu\text{m}$  and  $0.5\ \text{mm}$ , respectively. The inset shows the linear behavior of the device at small source-drain voltages.

Not only can these printing techniques form individual transistors with good characteristics, but they can also be used for large area circuits that have sufficient performance for such systems as electrophoretic displays with clear commercial value. Figure 13.24 show the processing sequence for a large area backplane illustrated in Fig. 13.25. In this case thermal transfer printing forms the source-drain and gate levels (according to the procedures illustrated in Fig. 13.18); the uniform dielectric layer is formed by lamination, and the semiconductor (pentacene) is deposited by thermal evaporation. In this approach, the PANI/SWNT donor sheet and a flexible plastic substrate are positioned and held in contact by vacuum. Gates are then printed by selectively transferring DNNSA-PANI/SWNT from a donor film to this substrate as previously described. The receiver is then removed for the lamination of a  $1\ \mu\text{m}$  methacrylate co-polymer layer over the whole area and



**13.24** Sequence for patterning arrays of interconnected transistors for active matrix display circuits by thermal transfer printing. The first step defines the gate level. The second involves the transfer of the gate dielectric. The final printing step defines the source/drain electrodes and interconnections. Depositing the organic semiconductor on top completes the circuit. Existing printing tools enable circuit formation over areas as large as  $\sim 6$  square feet.

re-positioned in registry for the printing of the source and drain layer. The backplane is completed by evaporation of unpurified pentacene through a shadow mask. Although the printing system maintains a  $2\text{--}5\ \mu\text{m}$  registration when imaging via the transfer of sequential layers onto a fixed substrate, it lacks built-in registration once the substrate is removed. Registration was achieved in the case of the system in Fig. 13.25 by aligning the substrate onto preset orthogonal edges on a carrier sheet that could, in turn, be precisely located onto the drum of the printer. Even with this rudimentary approach, it was possible to achieve registration errors of less than  $200\ \mu\text{m}$  over the  $4000\ \text{cm}^2$  area. The circuit contains 5000 transistors with  $20\ \mu\text{m}$  channels



**13.25** Active matrix backplane circuit formed by thermal transfer. A photograph of a 50 cm  $\times$  75 cm printed panel is shown on the top. The micrograph at the middle left illustrates a unit cell of the circuit. The scanning electron micrograph on the bottom left provides a high-resolution view of the source/drain electrodes and the channel region. The graph on the bottom right shows the electrical characteristic of one of the transistors in the large printed panel. The gate voltage varies from 0 to  $-100$  V in  $-20$  V steps.

printed onto a 50 cm  $\times$  80 cm flexible substrate. Micrographs of a typical transistor are shown in the lower left-hand corner. The current-voltage characteristics of a typical transistor are also shown in the lower right.<sup>15</sup>

## 13.4 Conclusion

This chapter summarizes some of our recent work in the area of high-resolution printing techniques that have potential applications in plastic electronics. Microcontact and nanotransfer printing are attractive because they provide simple and potentially low cost routes to structures with dimensions deep into the sub-micron regime. Nanotransfer printing offers true nanometer resolution in an additive fashion that allows complex 3D and multilayer fabrication. For plastic electronics, the ability of both of these techniques to pattern high-resolution source and drain electrodes out of materials that are

compatible with known organic semiconductors represent important features. This resolution enables channel lengths that are sufficiently small to produce transistors with large 'on' currents even with the moderate to low mobilities that are available from organic semiconductors. Microcontact printing has been demonstrated for patterning of large area ( $\sim 16 \text{ cm} \times 16 \text{ cm}$ ) functional circuits for flexible paperlike displays. Composite stamp designs that enable good multilayer registration make it possible to achieve micron-level distortions over these areas. Additional work will be required to invent methods for using these types of printing techniques to pattern the dielectric and semiconductor layers.

Thermal transfer printing has enormous flexibility in the materials that can be patterned. The method can process large areas with good registration at high speed with commercial engines and it benefits from its completely 'dry' and purely additive operation. Etchants and solution routes for depositing or patterning the key materials are not required. In addition, our vast experience in formulating materials for thermal imaging enables us easily to design formulations with widely different functionalities, readily balancing the adhesion between the layers that are sequentially transferred, such that interfaces have intimate physical and electrical contact. Although current systems have pixel sizes of  $5 \times 2.2 \mu\text{m}$ , which limit the resolution, systems with  $2 \times 2 \mu\text{m}$  pixels are in the process of being commercialized. For applications that demand sub- $5 \mu\text{m}$  resolution, it may be possible to combine microcontact or nanotransfer printing with thermal transfer printing: high resolution source/drain electrodes printed with  $\mu\text{CP}$  or  $\text{nTP}$  could be used with other components that are patterned by thermal transfer. These and other strategies that combine and match different patterning techniques may provide an attractive means for building plastic circuits.

## 13.5 Acknowledgements

We wish to thank our collaborators at DuPont and Bell Labs and University of Illinois at Urbana/Champaign, many of whom were instrumental in some of the work described here.

## 13.6 References

1. Mirkin C.A. and Rogers J.A., 'Emerging Methods for Micro- and Nanofabrication', *MRS Bull.*, 2001 **26** 506–07.
2. Sze S., *Semiconductor Devices: Physics and Technology*, New York, Wiley, 1985.
3. Drury C.J., Mutsaers C.M.J., Hart C.M., Matters M. and de Leeuw D. M., 'Low-cost all-polymer integrated circuits', *Appl. Phys. Lett.*, 1998 **73** 108–10.
4. Gelinck G.H., Geuns T.C.T. and de Leeuw D.M., 'High-performance all-polymer integrated circuits', *Appl. Phys. Lett.*, 2000 **77** 1487–89.
5. Sirringhaus H., Kawase T., Friend R.H., Shimoda T., Inbasekaran M., Wu M. and

- Woo E.P., 'High-resolution inkjet printing of all-polymer transistor circuits', *Science*, 2000 **290** 2123–26.
6. Garnier F., Hajlaoui R., Yassar A. and Srivastava P., 'All-polymer field-effect transistor realized by printing techniques', *Science*, 1994 **265** 1684–86.
  7. Bao Z., Feng Y., Dodabalapur A., Raju V.R. and Lovinger A.J., 'High-performance plastic transistors fabricated by printing techniques', *Chem. Mater.*, 1997 **9** 1299–1301.
  8. Rogers J.A., Bao Z. and Raju V.R., 'Non-photolithographic fabrication of organic transistors micron feature sizes', *Appl. Phys. Lett.*, 1998 **72** 2716–18.
  9. Behl M., Seekamp J., Zankovych S., Torres C.M.S., Zentel R. and Ahopelto J., 'Towards plastic electronics: Patterning semiconducting polymers by nanoimprint lithography', *Adv. Mater.*, 2002 **14** 588–91.
  10. Loo Y.-L., Willett R.W., Baldwin K. and Rogers J.A., 'Additive, nanoscale patterning of metal films with a stamp and a surface chemistry mediated transfer process: Applications in plastic electronics', *Appl. Phys. Lett.*, 2002 **81** 562–64.
  11. Loo Y.-L., Willett R.W., Baldwin K. and Rogers J.A., 'Interfacial chemistries for nanoscale transfer printing', *J. Am. Chem. Soc.*, 2002 **124** 7654–55.
  12. Zaumseil J., Meitl M.A., Hsu J.W.P., Acharya B., Baldwin K.W., Loo Y.-L. and Rogers J.A., 'Three-dimensional and Multilayer Nanostructures Formed by Nanotransfer Printing', *Nano Lett*, 2003 **3** 1223–27.
  13. Kumar A. and Whitesides G.M., 'Features of gold having micrometer to centimeter can be formed through a combination of stamping with an elastomeric stamp and an alkanethiol ink followed by chemical etching', *Appl. Phys. Lett.*, 1993 **63** 2002–04.
  14. Rogers J.A., Bao Z. and Makhija A., 'Non-photolithographic fabrication sequence suitable for reel-to-reel production of high performance organic transistors and circuits that incorporate them', *Adv. Mater.*, 1999 **11** 741–45.
  15. Blanchet G., Loo Y.-L., Rogers J.A., Gao F. and Fincher C., 'Large area dry printing of organic transistors and circuits', *Appl. Phys. Lett.*, 2003 **82** 463–65.
  16. Moreau W.M., in *Semiconductor Lithography: Principles and Materials*; Moreau, W.M., ed. Plenum: New York, 1988.
  17. Gibson J.M., 'Reading and Writing with Electron Beams', *Phys. Today.*, 1997 **50** 56–61.
  18. Matsui S. and Ochiai Y., 'Focused Ion Beam Applications to Solid State Devices', *Nanotechnology*, 1996 **7** 247–258.
  19. Sohn L.L. and Willett R.L., 'Fabrication of Nanostructures Using Atomic-Force Microscope-Based Lithography', *Appl. Phys. Lett.*, 1995 **67** 1552–54.
  20. Betzig E. and Trautman K., 'Near-Field Optics – Microscopy, Spectroscopy, and Surface Modification Beyond the Diffraction Limit', *Science*, 1992 **257** 189–95.
  21. Bard A.J., Denault G., Lee C., Mandler D. and Wipf D.O., 'Scanning Electrochemical Microscopy: A New Technique for the Characterization and Modification of Surfaces', *Acc. Chem. Res.*, 1992 **23** 357.
  22. Strosio J.A. and Eigler D.M., 'Atomic and Molecular Manipulation with the Scanning Tunneling Microscope', *Science*, 1991 **254** 1319–26.
  23. Nole J., 'Holographic Lithography Needs No Mask', *Laser Focus World*, 1997 **33** 209–12.
  24. Rogers J.A., 'Rubber Stamping for Plastic Electronics and Fiber Optics', *MRS Bull.* 2001 **26** 530–34.
  25. Rogers J.A., Bao Z., Baldwin K., Dodabalapur A., Crone B., Raju V.R., Kuck V., Katz H.E., Amundson K., Ewing J. and Drzaic P., 'Paper-like electronic displays:

- Large area, rubber stamped plastic sheets of electronics and electrophoretic inks', *Proc. Nat. Acad. Sci. USA.*, 2001 **98** 4835–40.
26. Rogers J.A., Paul K.E. and Whitesides G.M., 'Quantifying Distortions in Soft Lithography', *J. Vac. Sci. Techn. B.*, 1998 **16** 88–97.
  27. Menard E., Bilhaut L., Zaumseil J. and Rogers J.A., 'Improved Chemistries, Thin Film Deposition Techniques and Stamp Designs for Nanotransfer Printing', *Langmuir*, 2004 **20** 6871–78.
  28. Bao Z., Kuck V., Rogers J.A. and Paczkowski M.A., 'Silsequioxane resins as high performance solution processable dielectric materials for organic transistor applications', *Adv. Func. Mater.*, 2002 **12** 526–31.
  29. Loo Y.-L., Hsu J.W.P., Willett R.L., Baldwin K.W., West K.W. and Rogers J.A., 'High-resolution transfer printing on GaAs surfaces using alkane dithiol self-assembled monolayers', *J. Vac. Sci. Techn. B.*, 2002 **20** 2853–56.
  30. Kim C., Shtein M. and Forrest S.R., 'Nanolithography based on patterned metal transfer and its application to organic electronic devices', *Appl. Phys. Lett.*, 2002 **80** 4051–53.
  31. Schmid H., Wolf H., Allenspach R., Riel H., Karg S., Michel B. and Delamarche E., 'Preparation of metallic films on elastomeric stamps and their application for contact processing and contact printing', *Adv. Func. Mater.*, 2003 **13** 145–53.
  32. Nakamura M., Kato S., Aoki T., Sirghi L. and Hatanaka Y., 'Role of terminal OH groups on the electrical and hydrophilic properties of hydro-oxygenated amorphous TiOx : OH thin films', *J. Appl. Phys.*, 2001 **90** 3391–95.
  33. Nakamura M., Aoki T. and Hatanaka Y., 'Hydrophilic characteristics of rf-sputtered amorphous TiO<sub>2</sub> film', *Vacuum*, 2000 **59** 506–13.
  34. Schueller O.J.A., Duffy D.C., Rogers J.A., Brittain S.T. and Whitesides G.M., 'Reconfigurable diffraction gratings based on elastomeric microfluidic devices', *Sens. Act. A.*, 1999 **78** 149–59.
  35. Zaumseil J., Someya T., Baldwin K., Bao Z., Loo Y.-L. and Rogers J.A., 'Nanoscale Organic Transistors Formed by Soft Contact Lamination and Source/Drain Electrodes Supported by High Resolution Rubber Stamps', *Appl. Phys. Lett.*, 2003 **82** 793–95.
  36. Kim C., Burrows P.E. and Forrest S.R., 'Micropatterning of organic electronic devices by cold-welding', *Science*, 2000 **288** 831–33.
  37. Lefenfeld M., Blanchet G. and Rogers J.A., 'High performance contacts in plastic transistors and logic gates that use printed electrodes of DNNSA-PANI doped with single walled carbon nanotubes', *Adv. Mater.*, 2003 **15** 1188–91.

- AB diblock copolymers 2–3
- AB polymer blend thin films 57–8, 59
- ABA polymer blend thin films 48–57
- ABA triblock copolymers 2–3
- Abbott's TestPack 285, 286
- ABC triblock terpolymers 2–3
- accumulation mode TFT 374
- acid chlorides 145
- active matrix display electronics 107
  - inkjet printing 277–80, 295
  - microcontact printing 380–1
  - thermal transfer printing 391–2, 393–5
- actuators 299, 300–7
  - PDMS actuators 300–2
    - application of PDMS actuation technology 302–7
- additive processes 267–8
- adsorbate terminal groups 243, 246–7
- alcohols 126
- aldehydes 127
- alignment
  - approaches to long-range ordering 23–32
    - multi-layer patterning with 231
- alkanethiol SAMs 240–7
- alkenes 125–6
- alkyl chain length 123–4
- alkyl halides 124–5
- alkynes 125–6
- aluminium (Alq<sub>3</sub>) 349, 350
- anisotropic buckling 176–8, 179
- anisotropic dewetting 168–70
- annealing 5–6, 23–4
- anode patterning for OLEDs 357–66
- antennae 275, 276
- antibody assays 285–6
- aperture size 238
  - NSOM 256–8
- apertureless NSOM 257, 260–2
- Arnold tongues 305
- array compatibility 146–7
- aspect ratios 10
  - nanostencils 225
    - strategies for improving 20–2
- asymmetric waves 180, 181
- asymmetrically wetting blends 57–8, 59
- atomic force microscopy (AFM) 120–1
  - and chemomechanical nanopatterning of silicon 128–33
    - feature characterisation 131
    - scribing 130–1
  - future trends in chemomechanical surface modification 145
    - end-effector development 145–7
  - inkjet printing of OLEDs 364, 365
  - scanned AFM nanostencil 231–2
- axial stiffness 134–6
- azobenzene-containing films 260, 261
- backscattering 45, 190
- bending, of nanostencils 233
- beta-galactosidase 327–8
- bilayer structure 57–8, 59
- biomedical applications *see* medicine
- biomolecules (biological molecules) 320–48
  - future trends 339–40
  - manipulation and sorting 321–34
    - cell separation techniques 331–4
    - DNA separation techniques 321–5
    - protein separation techniques 325–30
  - microfluidic tools for molecular biology 334–9
  - near-field photolithography 239–40, 261–2
- block copolymer nanolithography 1–38
  - long-range ordering 23–32
    - electric field alignment 27–9
    - epitaxial patterning methods 25–6
    - flow-induced alignment 30–2
    - graphoepitaxy 26–7
    - solvent directional crystallisation 29–30
    - solvent-mediated methods 24
    - thermal methods 23–4
  - methods for pattern transfer 10–22
    - reactive ion etching 16–19

- strategies for improving aspect ratios 20–2
- wet techniques for selective domain removal 13–16
- block copolymer self-assembly 1, 2–12, 32
  - glass transition temperature 4
  - islands, holes and terraces 6–8
  - morphology in thin films 5–6
  - wetting layers and neutral substrates 8–10
- block copolymers 84–5, 87
- blood typing test 285, 286
- Boehringer Mannheim's MicroSpot system 285–6
- brush layers (wetting layers) 8–9
- buckling 175–81
  - anisotropic 176–8, 179
  - microshaping metal surfaces by self-organised buckling 178–81
  - spinodal wrinkling 175–6, 177
- buried microchannels 209, 212
  
- cantilever systems 250
- capillarity 165–8
- capillary electrophoresis (CE) 321–3, 329
- capillary flow inkjet printing 354–5
- capillary force lithography (CFL)
  - pressure-assisted 163–5
  - self-organised polymeric microstructures by 161–3
  - by thermally-induced capillarity 156–8
- capillary gel electrophoresis (CGE) 322–3, 328, 329
- capillary lithography 155–65
- capillary zone electrophoresis (CZE) 328–9
- carboxylic acid terminated adsorbates 241–2, 254–5
- CD microfluidics 316
- cell-based assays 107, 340
- cell electroporation 336
- cell separation techniques 331–4
- cell sorting 302, 332–4
- cell trapping 331–2
- cellular attachment 246
- ceramic powders 355–6
- chain length
  - adsorbates and scribed silicon 123–4
  - photo-oxidation of SAMs 242–3, 245
- chain scission 195–6
- chaotic mixers 303–4, 312, 316
- chemical confinement 62, 63
- chemical decomposition 192–3, 194, 213
- Chemical Inkjet Printer (ChIP) 289–90
- chemical printing 289–90
- chemical vapour deposition 228
- chemically-amplified soft lithography 95, 97
- chemically-assisted ion beam deposition (CAIBD) 197, 198, 211, 213
- chemomechanical surface modification 120–54
  - background 120–1
  - chemistry of scribed silicon 121–2, 123–8
  - chemomechanical patterning of silicon 122–3, 128–33
  - future trends 144–8
    - AFM patterning 145
    - chemistry 144–5
    - end-effector development 145–7
    - MALDI 147–8
    - microcontact printing 148
  - patterning silicon at the micron scale 133–6
  - preparation of masters for microcontact printing 144
  - preparation of surfaces for MALDI mass spectrometry 136–44
- chip-scale packaging 275–7
- chrome masks 77, 78, 79
- clogging 232–3
- coffee ring effect 354
- cohesive mechanical failure (CMF) 98, 99
- cold welding 388, 389
- collision cascades 186
- colour 354, 358, 359
- combinatorial libraries 232
- combinatorial study 64
- complementary logic gate 390, 391
- complete wetting 165–6
- complex lab-on-a-chip 306–7
- compliant mechanism end-effector 134–6
- composite stamps 378–80
- computer-aided design (CAD) 77
- computer numerical controlled (CNC) milling machine 144
- conductive inks 293
- conductive oxides, transparent 93
- conductive substrate materials 90–3, 94
- confined polymer thin films 155–83
  - influence of dispersion force on patterning 165–8
  - patterning by capillary lithography 155–65
  - patterning by polymer dewetting 168–75
  - patterning by stress for metal/polymer bilayer 175–81
  - polymer blends 42
    - chemical and topographical confinement 62–3
- confinement-controlled dewetting 170–3
- conformal contact 101–3, 104, 248
- conjugated polymer blends 60–1
- conjugated polymers 253
- contact angles 43, 124
- contact photolithography 78, 81
- contact printing *see* microcontact printing;
  - nanotransfer printing
- continuous inkjet printing 268–70, 352
- controlled drug release 291
- correlation length 53–5
- Coulomb forces 185–6
- coupled microfluidic-mass spectrometry devices 325–7

- coupled protein separation technologies 328–30
- cross-linking 195–6
- crossed wire arrays 105, 106
- crystallisation
  - proteins 305–6, 337–9
  - solvent directional 29–30
- crystals, lattice damage in 190, 214
- curing 293, 294
- current density 360–1
- cyanohydroxycinnamic acid (CHCA) 137
- cylindrical electrostatic lenses 202
- cylindrical microdomains 2–3, 5
  - perpendicular 9–10
  - smaller diameters and higher aspect ratios 22
- decal-transfer microlithography (DTM) 78, 98, 99
- deep reactive ion etching (DRIE) 192
- deep ultraviolet (DUV) lithography 226
- defects formed by etching 91–3
- deformation of stamps 377–80
- degree of polymerisation 3
- demand mode inkjet printing 270–1, 352
- dendrimer-based inks 88–9, 91
- deposition rate 221–2
- depth profiling 44–6, 50, 51
- dewetting
  - patterning of confined polymer thin films 168–75
    - anisotropic dewetting 168–70
    - drop patterning by confinement-controlled dewetting 170–3
    - selective dewetting 173–5
  - spinodal 44, 56
  - thin film polymer blends 39–40, 44, 58, 59
- diagnostics 285–90
- dialysis, microfluidic 326
- diamond-like carbon wine glass 207
- diblock copolymers 2–3
- dielectric layers 356–7
- dielectric polymers 276–7
- dielectrophoresis (DEP) 331
- diffraction limit 238, 247
  - photolithography beyond *see* near-field photolithography
- dihydroxybenzoic acid (DHB) 137, 139–43
- dinonylnaphthalene sulphonic acid doped polyaniline (DNNSA-PANI) 390–5
- direct-write processes 199–200, 375–6
  - see also* focused ion beam; ion beam lithography; proton beam writing
- directly deposited masks 199
- dispersion force 165–8
  - polymer blend systems 165–7
  - ultra-thin liquid films 167–8
- displays 107
  - high-resolution printing techniques 380–1, 391–2, 393–5
  - inkjet printing 277–80, 295
- DNA microarrays 239, 286–9, 295
- DNA separation techniques 321–5
  - microfabricated separation elements 323–5
  - microfluidic capillary electrophoresis 321–3
- domain removal 12, 13–19
  - dry techniques 16–19
  - wet techniques 13–16
- drop-on-demand inkjet printing 270–1, 352
- drop patterning 170–3
- drop size control 304–5
- droplet protein crystallisation device 337–8
- drug release, controlled 291
- dry etching *see* reactive ion etching
- dual-beam instrument 203
- dynamic scaling hypothesis 42
- dynamic secondary ion mass spectrometry (dynamic SIMS) 46
- dynamic stencil 231–2
- elastic recoil detection (ERD) 45
- elastomer membranes 224–5
- elastomeric membrane printing (EMP) 95–7, 99
- elastomeric phase masks 101–3, 248
- elastomeric (soft) stamps 76, 78, 144
  - materials used for 84–5
  - replication using 85–103
  - see also* soft lithography
- elastomeric valves 302–7, 332
- electric field 257–8
- electric field alignment 20–1, 27–9
- electric stimuli 64
- electrical interconnect 271–4
- electrical microcontact printing (E-mCP) 78, 101, 102
- electrical properties, modification of 196–7
- electrochemical etching 214
- electrode-defined sample injection 323
- electrokinetic microfluidic chips 340
- electrokinetic microfluidic FACS 332–3
- electroless plating 174, 175
- electron beam lithography 77, 78, 80–1, 238, 239, 375–6
- electron-ion interactions 186, 187–9
- electron microscope 203
  - see also* scanning electron microscope
- electron transport layer (ETL) 349, 350–1
- electro-osmotic flows (EOF) 307, 308–10
- electrophoresis 313–15
- electroplating moulds 209, 212
- electroporation, cell 336
- electrostatic accelerators 203, 204, 205
- electrostatic forces 185–6
- embedded passives 274–5, 276
- end-effector 122, 123, 133–4
  - compliant mechanism 133–6
  - development 145–7
  - energy levels 189, 350–1

- energy loss 188, 189  
 energy regimes 185–6  
   *see also* high-energy ion beams; low-energy ion beams  
 entropic recoil devices 324–5  
 entropic traps 324, 325  
 environmental controls 294  
 enzyme assays 340  
 epitaxial patterning methods 25–6  
 epoxides 126  
 etchants 91  
 etched SNOM probes 250  
 etching 10, 11, 12  
   soft lithography 87, 88  
     defects due to etching 91–3  
 evaporation-condensation mechanism (Lifshitz-Slyozov theory) 42  
 evaporation of metal using nanostencils 227–8, 229  
 evaporation rate of solvent 58–9, 60  
 evaporative bubble inkjet system 270, 352  
 excitation of electrons 189  
 excitons 350–1  
 external quantum efficiency 362  
 extraction, microfluidic systems and 303–4
- fabrication of masters 76  
   high-resolution stamps 375–6  
   nanoimprint lithography 210  
   soft lithography 77–84  
 fabrication requirements 146  
 fast-growth mode 57  
 fibroblasts 246  
 field effect device (FED) displays 279  
 film thickness 6–8  
   *see also* thin films  
 flexible manufacturing 267–8  
 Flory interaction parameter 3  
 flow-induced alignment 30–2  
 flow switching 302  
 fluid-phase nanolithography 258  
 fluorescence-activated cell sorters (FACS) 332–4  
 fluoropolymer mould 163–5  
 focused ion beam (FIB) 199–200, 210–11, 213  
   equipment 202–3  
   FIB milling and fabrication of nanostencils 225–6, 227  
   techniques 206–8, 375–6  
 focusing  
   cylindrical electrostatic lenses 202  
   MeV ion microbeams 203–6  
 force, tip 130, 131, 132  
 force-deflection equation 135–6  
 forward recoil spectrometry (FRoS) 45  
 Foturan 196  
 free energy minimisation 178, 181  
 FT-IR spectra 363–4  
 full-wafer nanostencil 226, 228  
 functional groups 127–8, 145  
 functionalised monolayers 127–8, 145
- gas assisted etching (GAE) 197, 198, 213  
 genomics 239, 339–40  
 germanium 145  
 glass slides 143  
 glass transition temperature 4  
 glasses, photosensitive 196  
 glufibrinopeptide B 141–3  
 gold  
   NSOM 257–8  
   scribing thiol on gold 120–1  
 grain size 257–8  
 graphoepitaxy 26–7, 28  
 grooves 312–13, 314, 315  
 growth exponent ( $\alpha$ ) 42, 53  
 growth mechanism, for thin film polymer blends 55–6, 57  
 gyroid phase 3
- h*-PDMS 84, 87  
 hard (rigid) stamps 76  
 helical flow 312, 313  
 hemi-elliptical microlenses 280–1  
 Hertz Knudsen equation 220  
 high-energy ion beams  
   ion-atom interactions 185, 186–90  
     electronic interactions 187–9  
     nuclear interactions 189–90  
   ion beam equipment 203–6  
   lithographic techniques using resist materials 208–10  
 high-resolution printing techniques 373–98  
   contract printing with high-resolution stamps 374–89  
     high-resolution stamps 375–6  
     microcontact printing 376–81, 395–6  
     nanotransfer printing 381–9, 395–6  
     thermal transfer printing 389–95, 396  
 high-throughput screening HTS platforms 320, 339–40  
 hole transport layer (HTL) 349, 350–1  
 holes 6–8  
   patterning by polymer dewetting 169, 173–4  
 hot electrons 243, 245  
 hot spots 137  
 HSL colour function 358, 359  
 Human Genome Project 295  
 humectant 354  
*hv*-PDMS 84, 87  
 hydrodynamic dispersion 308, 309  
 hydrodynamic switching 333–4  
 hydrogel stamps 85  
 hydrophilic PDMS stamps 87–8, 89  
 hydrophobic valve 315–16
- image setting 77, 78, 79–80  
*in vitro* transcription/translation kits 340  
 indium-tin-oxide (ITO) 93

- ink molecules 88–90, 91
- inkjet printing 267–98, 349–72
  - additive processes and flexible manufacturing 267–8
  - anode patterning of OLEDs 357–66
  - biomedical applications 285–91, 356
  - block diagram of inkjet printing system 294
  - design aspects 353–7
    - ink formulation 353–4
    - materials and devices 355–7
    - resolution 354–5
  - display manufacturing applications 278–80
  - electronics manufacturing applications 271–8
    - chip-scale packaging 275–7
    - electrical interconnect 271–4
    - embedded passives 274–5, 276
    - organic electronics 277–8
  - equipment 293–4
  - future trends 294–5
  - implementation considerations 291–3
    - fluid requirements 291–2
    - fluid/substrate interactions 292
    - post-processing 293
    - throughput 293
  - integrated electro-optic assemblies 282–5
    - photonics applications 280–2
    - technology 268–71, 352–3
- inorganic precursors 64
- integrated elastomeric valves 302–7, 332
- integrated electro-optic assemblies 282–5
- integrated peristaltic pumps 306–7, 333
- interblock repulsion 3
- interdisciplinary research 107–8
- inverter 390, 391
- ion beam deposition (IBD) 197, 198, 211, 213
- ion beam lithography (IBL) 77, 78, 200, 208–10, 211–14
- ion beam patterning 184–217
  - future trends 210–14
  - ion beam equipment 202–6
    - high-energy systems 203–6
    - low-energy systems 202–3
  - microfabrication applications 197–202
    - direct-write processes 199–200
    - ion track lithography 201–2
    - masked processes 197–9
  - techniques 206–10, 213
    - high-energy ion lithography using resist materials 208–10
    - low-energy techniques 206–8
- ion implantation 196–7
- ion-solid interactions 184–97
  - calculating the effect of ions in solids 190–1
  - direct removal of material 191–4
  - high-energy interactions 185, 186–90
  - ion beam deposition 197
  - lattice damage in crystals 190
    - low-energy collisions 185, 186, 187
    - modification of material properties 195–7
- ion species 185–6
- ion track lithography (ITL) 201–2, 213
- ion tracks 190
- ionisation 185
- islands 6–8
- isoelectric focusing (IEF) 328, 329–30
- isotachophoretic (ITP) preconcentration of DNA 323
- lab-on-a-chip devices 299
  - complex 306–7
  - protein isolation and identification 327–30
- lamellar microdomains 2–3, 5
  - perpendicularly-oriented 9–10
- Laplace pressure 52, 167–8
- large areas, patterning 106–7, 108
- large integrated microfluidic devices 305–6
- laser, overwriting with 293
- laser ablation 310
- laser beam lithography 78
- laser image setting 77, 78, 79–80
- laser interference lithography 375–6
- laser photoplotting 77, 78, 80–1
- laser scanning confocal microscopy (LSCM) 47
- lateral deflection 188
- lateral imaging techniques 46–7
- lateral stiffness 134–6
- lattice constant 3–4
- lattice damage 190, 214
- layer inversion 58
- Lifshitz-Slyozov theory (evaporation-condensation mechanism) 42
- lift-off 10, 11, 12, 95–7, 218, 222
- light-directed chemical synthesis 239
- light-emitting polymers (LEPs) 60–1, 278–9, 295
- light output 361–2
- line-of-sight deposition 222
- line width
  - chemomechanical surface modification 131, 132, 145, 147
  - NSOM 256–8
- linear-elastic beam theory 135
- linear energy transfer (LET) 189
- liquid crystal displays (LCDs) 279–80
- liquid-liquid separations 327–8
- living cell analysis 340
- localised heating 252–3
- logic gate 387
- London force 173
- long-range ordering 23–32
  - electric field alignment 27–9
  - epitaxial patterning methods 25–6
  - flow-induced alignment 30–2
  - graphoepitaxy 26–7
  - solvent directional crystallisation 29–30
  - solvent-mediated methods 24

- thermal methods 23–4
- low-energy ion beams
  - ion-atom collisions 185, 186, 187
  - ion beam equipment 202–3
  - patterning techniques 206–8
- low-stress silicon nitride 224
- luminosity 358, 359
  
- magnetic domains, nanometre scale 214
- magnetic quadrupole multiplet 203–6
- Marangoni instability 59
- masks
  - directly deposited 199
  - elastomeric phase masks 101–3, 248
  - masked ion bombardment processes 197–9
    - mask materials and fabrication 199
  - near-field optics 248
  - photomasks 77–84
  - repair 207
  - see also* stencils
- mass-mapping 136
- mass spectroscopy-microfluidic coupled devices 325–7
- matrix assisted laser desorption/ionisation (MALDI) mass spectrometry (MS)
  - future research directions 147–8
  - MALDI TOF mass spectrometry 136
  - preparation of surfaces for 136–44
- mechanical cell trapping 331–2
- mechanical self-alignment 231
- medicine 285–91, 356
  - controlled drug release 291
  - diagnostics and discovery 285–90
  - tissue engineering 290–1
- MEH-PPV 350
- melting-solidification front 24
- meniscus 156, 161
- mercury arc lamps 242, 243, 245
- metal/insulator/metal (MIM) capacitors 388, 389
- metal lines, inkjet printing 356
- metal/polymer bilayer 175–81
- metals
  - incorporation into microdomains 18
  - microshaping metal surfaces by self-organised buckling 178–81
  - see also under individual metals*
- metastable states 41
- MeV ion lithography *see* proton beam writing
- MeV ion microbeams 203–6
  - see also* high-energy ion beams
- micellar electrochromatography (MEKC) 328–9
- microchannels 307
  - methods of patterning surfaces 310–11
  - modifications of shape 317
  - see also* microfluidics
- microcontact printing (mCP or  $\mu$ CP) 62, 78, 85–101, 148, 219–20
  - conductive substrate materials 90–3
  - hydrophilic PDMS stamps 87–8, 89
  - molecular ‘inks’ 88–90, 91
  - new variations 93–101
    - chemically-amplified soft lithography 95, 97
    - decal-transfer microlithography 78, 98, 99
    - elastomeric membrane printing 95–7, 99
    - electrical microcontact printing 78, 101, 102
    - nanotransfer printing 78, 98–101, 381–9, 395–6
    - patterning of reactive SAMs 93–5
    - positive mCP 95, 96
    - plastic electronics 376–81, 395–6
    - preparation of masters by scribing 144
- microdomains 1, 2–4
  - orientation in thin films 5–6
  - removal techniques 12, 13–19
  - wetting layers and neutral substrates 8–10
  - see also* block copolymer nanolithography
- microelectrode arrays 317
- microelectromechanical systems (MEMS) 218–19, 299
  - fabrication of nanostencils 225–6
- microfabricated devices
  - DNA separation elements 323–5
  - flow of process of microfabrication 77, 78
  - NSOM probes 249
  - see also* soft lithography
- microfabricated troughs 27, 28
- microfiche masks 78, 79–80
- microfluidic dialysis 326
- microfluidic fluorescence-activated cell sorters (FACS) 332–4
- microfluidic PCR 334–6
- microfluidics 299–319
  - application of PBW 209, 212
  - manipulation of biomolecules *see* biomolecules
  - nanopatterning 307–17
    - patterning chemistry and wettability 315–16
    - patterning surface charges 313–15
    - patterning surfaces 310–11
    - patterning topography 311–13
    - small scale patterning within microchannels 307–8
    - standard flows 308–10
  - PDMS technology 300–2
    - application of PDMS actuation technology to microfluidics 302–7
    - soft lithography 107, 108–9
- microlens array reduction photolithography (MAP) 78, 82–4
- microlenses 248–9
  - integrated electro-optic assemblies 282–3, 284
  - microlens arrays 280–2, 283

- micromachining 77, 78
- micromixers 303–4, 312, 316
- micromoulding in capillaries (MIMIC) 78, 98
- microscope projection photolithography (MPP) 78, 81–2, 83
- microshape engineering 178–81
- MicroSpot system 285–6
- microstructures, self-organised 161–3
- microtransfer moulding 78
- Millipede 251
- miniaturisation of antibody assays 285–6
- miniaturised MALDI-MS sample supports 137–8, 139, 140, 143
- miniaturised total chemical analysis system 321
- mixed monolayers 127, 128
- mixing, in microfluidic systems 303–4, 312, 316
- modification of material properties 195–7, 214
- molecular beam epitaxy (MBE) 229
- molecular biology
  - inkjet printing 356
  - microfluidic tools for 334–9
  - near-field photolithography 239–40, 261–2
  - see also* biomolecules
- molecular electronics 240
- molecular 'inks' 88–90, 91
- monofunctional compounds 123–4
- monolithic ion-exchange concentrator 326–7
- morphology evolution, in polymer blend thin films 48–63
- moulding replication 300–1
- multicomponent blends 63–4
- multilayer nanostencil patterning 231
- multilayer soft lithography 332
- multilayer thermal transfer printing 392
- multilevel stamping 103–5
- multiphase flows 304–5, 315–16
- multi-photon processes 261
- mylar foils 45
  
- nanoinprint lithography (NIL) 156, 210, 219–20, 310
- nanomanipulators 207–8
- nanoparticles 63
- nanoshaving 120–1
- nanostencils *see* stencils
- nanotomography 47
- nanotransfer printing (nTP) 78, 98–101, 381–9, 395–6
- near-edge X-ray absorption fine structure (NEXAFS) 47
- near-field optics 247–9
- near-field photolithography 238–66
  - NSOM *see* near-field scanning optical microscopy
  - photochemistry of SAMs 240–7
- near-field scanning optical microscopy (NSOM) 47, 249–50
  - apertureless 260–2
  - lithography based upon 250–60
- negative resist materials 195–6, 209, 210, 211, 212
- nerve conduits 290–1
- nerve growth factor (NGF) 290–1
- neutral substrates 9–10, 20–1
- neutron reflectivity (NR) 46
- 96-channel DNA sequencing microchannel plate 322
- nitrene 246
- nitrobenzenesulphonic acid (NBSA) 92
- no-slip boundary condition 308, 309, 315
- nodal waves 179–80
- non-planar devices 108
- nuclear-ion interactions 186, 189–90
- nuclear reaction analysis (NRA) 45
  
- octanol 92
- octylcarboxypentamethyleneoxyazobenzene 252
- oligonucleotide arrays 239, 286–9
- oligoethylene glycol (OEG) terminated SAMs 259–60
- optical absorption spectra 364, 365
- optical cell trapping 331
- optical microscopy (OM) 46
- optical properties, modification of 196
- order-disorder transition (ODT) 3
- organic compounds, inkjet printing 356–7
- organic electronics 277–8, 373–4
  - see also* high-resolution printing techniques
- organic-inorganic hybrids 64
- organic light-emitting devices (OLEDs) 93, 228–9, 349–52
  - inkjet anode patterning of 357–66
- organometallic polymers 18, 19
- orientation 5–6
  - controlling long-range ordering 23–32
  - neutral substrates 9–10
- osmium 18
- oxidation 240–7, 253, 254
- oxidising ink 357–66
- oxygen 17
- ozone 244, 254
- ozonolysis 13–15, 245
  
- packaging, chip-scale 275–7
- palladium 93, 94
- parallel reaction chambers PDMS proton crystallisation device 338–9
- partial wetting 165–7
- particle accelerators 203, 204, 205
- passive control mechanisms 134–6, 146
- passives, embedded 274–5, 276
- pattern definition 222–3
- pattern replication 62
- pattern shape 139–43, 147
- patterned self-assembly 105, 106, 108
- PEDOT-PSS 357–66
- PEG-3 196

- peptide arrays 286–9
- peripheral nerve regeneration 290–1
- peristaltic pumps 306–7, 333
- perpendicularly-oriented microdomains 9–10, 20–1
- phase change inks 292
- phase separation 39–40, 41–2
  - see also* polymer blends
- phase-shifting lithography 78, 101–3, 104, 248
- phosphine-containing ligands 246–7
- phosphors 279
- photochemical reactions 239–40
  - photochemistry of SAMs 240–7
- photolithography 10, 11, 76, 218–19, 238
  - beyond the diffraction limit *see* near-field photolithography
  - production of high-resolution stamps 375–6
- photomasks 77–84
  - fabrication of photoresist-based masters using transparency masks 81–4
  - fabrication of transparency-based 79–81
- photonic crystal 253–4
- photonics 280–2
  - photonic circuits and waveguides 283–5
- photo-oxidation of SAMs 240–7, 253, 254
- photoplotting, laser 77, 78, 80–1
- photoresist layer 10, 11, 218, 251–4
- photosensitive glasses 196
- photovoltaics 60–1
- physical vapour deposition (PVD) 220–2
  - local PVD through stencil membranes 222–4
- piezoelectric inkjet 270, 352
- pigment ink 354
- plasma etching (sputter etching) 191–2, 213
- plasmas 185
- plastic electronics 277–8, 373–4
  - see also* high-resolution printing techniques
- plating 10, 11, 12
- Poiseuille profile 308, 309
- polybutadiene (PB) 13–15, 165–7
- polydimethylsiloxane (PDMS) 84, 87, 248
  - actuators 300–2
    - application to microfluidics 302–7
    - adsorption of proteins 307, 317
    - characteristics relevant to microfluidics 301
    - PDMS valves 302–7
    - hydrophilic PDMS stamps 87–8, 89
    - MAP 82–4
    - physical and chemical properties 300
    - preparation of masters for microcontact printing 144
- polyethylenimine (PEI) 92
- polyferrocenyl dimethylsilane (PFS) 18, 19
- polyisoprene (PI) 13–15
- polylactide (PLA) 15
- polymer blends 39–75
  - dewetting 39–40, 44, 58, 59
  - dispersion force and pattern formation in film systems 165–7
  - experimental techniques 44–8
  - phase separation 39–40, 41–2
  - research directions 63–4
  - surface-induced patterns 48–63
    - asymmetrically wetting blends 57–8
    - chemical and topographical confinement 62–3
    - solvent-induced patterns 58–61
    - symmetrically wetting blends 48–57
  - wetting 39–40, 43–4
- Polymer Jet technology 276–7
- polymer light-emitting diode (PLED) displays 278–9, 295
- polymerase chain reaction (PCR), microfluidic 334–6
- polymerisation, degree of 3
- polymethylmethacrylate (PMMA) 15–16, 17, 144, 195–6
- polyolefins 84–5
- poly(pentamethylidistyrene) (PPMDSS) 17–18
- polyphenylene vinylene (PPV) 253–4, 350
- polystyrene (PS) 13–16, 165–7
- polystyrene-*block*-butadiene-*block*-styrene (SBS) 84–5, 87
- polystyrene-*block*-ethylene-*co*-butylene-*block*-styrene (SEBS) 84–5, 87
- poly(*tert*-butyl acrylate (PtBA) 15
- polytetrafluoroethylene (PTFE) 193, 194
- positive microcontact printing 95, 96
- positive resist materials 195–6, 209, 210
- post-processing 293
- power spectra 176, 177
- precisely positioned single ions (PPSI) 201–2, 213
- precision 146
- precursor gases 197, 198
- pressure-assisted capillary force lithography (PACFL) 163–5
- pressure-based microfluidic FACS 333–4
- pressure-driven flows 307, 308, 309–10
- projection mask processes 199
- projection mode photolithography 375–6
- protease enzyme immobilisation 147
- protein separation techniques 325–30
  - coupled microfluidic-mass spectroscopy devices 325–7
  - on-chip protein isolation and identification 327–30
- proteins 256
  - complex lab-on-a-chip and preparation of proteic samples 306–7, 317
  - crystallisation 305–6, 337–9
  - inkjet printing 285–6
  - patterning by SNP 259–60
- proteomics 137, 239, 339–40
- proton 184–5

- proton beam-induced decomposition 193, 194, 213
- proton beam writing (PBW) 77, 78, 200, 208–10, 211–14
- pulled NSOM probes 249–50
- pulse-pressure injection 323
- pulsed electrostatic deflector 200
- pulsed laser deposition (PLD) 229
- quadrupole lenses 203–6
- rate constant 242, 243
- reactive blending 64
- reactive functional groups 127–8, 145
- reactive ion etching (RIE) 192, 193, 194, 208, 209, 210–11, 213
  - block copolymer lithography 16–19
  - CFL by thermally-induced capillarity 156–7, 158
  - etching equipment 202
- reactive SAMs 93–5
- read-write head assembly 272–3
- recessed surfaces 230–1
- refractive index modification 196
- refractive X-ray lenses 208, 209
- registration of masters 76
  - soft lithography 103–6
- replica moulding (REM) 78, 144
- replication of masters 76, 210
  - soft lithography 85–103
- resist layer 10, 11, 218, 251–4
- resist materials 195–6
  - high-energy ion lithography using 208–10, 211, 212
- resistless lithography 231–2
- resistors 274–5
- resolution
  - high-resolution printing techniques *see* high-resolution printing techniques
  - inkjet printing 354–5
- ridged PDMS masks 248
- roughness, surface 50–1, 53, 55
- rubrene 349, 350
- rupture, film 51, 55
- Rutherford backscattering (RBS) 45, 190
- sample supports
  - determination of work life 147–8
  - miniaturised 137–8, 139, 140, 143
- scanned AFM nanostencil 231–2
- scanning electron microscope (SEM) 120, 203
  - and chemomechanical nanopatterning of silicon 131, 132, 133
- scanning near-field optical microscopy (SNOM) *see* near-field scanning optical microscopy (NSOM)
- scanning near-field photolithography (SNP) 254–60
- scanning probe lithography 77, 78, 375–6
- scanning probe methods 219
  - metal patterns on tip of scanning probes 230–1
- scanning probe microscopy (SPM) 249
- scattering
  - Rutherford backscattering 45, 190
  - in shadow-mask patterning 222–3
- scribed silicon *see* silicon
- scribing
  - preparation of masters for microcontact printing 144
  - system 122–3, 133
    - compliant end-effector 133–6
    - end-effector development 145–7
  - see also* chemomechanical surface modification
- secondary amines 246
- selective dewetting 173–5
- selective domain removal 12, 13–19
- selective pattern release (SPaR) 98, 99
- self-alignment 231
- self-assembled monolayers (SAMs) 240
  - microcontact printing 87, 376–7
  - patterning of reactive SAMs 93–5
  - NSOM and patterning 254–60
  - photochemistry of 240–7
- self-assembly *see* block copolymer self-assembly
- self-organised buckling 176–8, 179
  - microshaping metal surfaces by 178–81
- self-organised polymeric microstructures 161–3
- semiconductor chip manufacturing 238–9
- separated block formation 169–70
- shadow masks *see* stencils
- shear alignment 30–2
- shear-force feedback systems 250, 251
- sheet resistivity 359–60
- sieve 323, 324
- silanisation 138
- silicon 121, 145
  - chemistry of scribed silicon 121–2, 123–8
    - general properties 123–4
    - preparation of functionalised monolayers 127–8
    - preparation of mixed monolayers 127
    - reaction with alcohols 126
    - reaction with aldehydes 127
    - reaction with alkenes and alkynes 125–6
    - reaction with alkyl halides 124–5
    - reaction with epoxides 126
  - chemomechanical nanopatterning 128–33
  - chemomechanical patterning 122–3
  - patterning at the micron scale 133–6
  - preparation of surfaces for MALDI MS 138–44
- silicon-based polymers 17–18
- silicon nitride 224
- silicon-on-insulator (SOI) wafers 224

- sinapinic acid (SA) 137
- single-ended accelerator 203, 204
- single ion lithography 201–2, 213
- slip 315–16
  - no-slip boundary condition 308, 309, 315
- sodium dodecyl sulphate (SDS)
  - capillary gel electrophoresis 328, 329–30
  - micelles 317
- sodium hypochlorite 362–4
- soft lithography 76–119, 156, 219–20, 239, 248
  - advantages 106
  - developments in techniques 77–106
    - elastomeric materials used for stamps 84–5
    - fabrication of masters 77–84
    - registration 103–6
    - replication using elastomeric stamps 85–103
  - disadvantages 107
  - interdisciplinary use 107–8
- soft moulding (SOMO) 158–60
- solder 271–4
  - columns 276–7
- Solder Jet technology 271–4, 276–7
- solid-phase extraction (SPE) 326–7
- solubility, modification of 195–6
- solvent-assisted micromoulding 78
- solvent directional crystallisation 29–30
- solvent-induced capillarity 158–60
- solvent-induced patterns 58–61
- solvent-mediated methods for long-range ordering 24
- spacer bumps 280
- spherical microdomains 2–3, 5
- spin-coating 59–60
- spinodal decomposition 39–40, 41–2, 51
- spinodal dewetting 44, 56
- spinodal wrinkling 175–6, 177
- spiral microchannels 314–15
- spread coefficient 43
- spreading
  - control in inkjet printing 292
  - deposition through stencils 222–3
- spring constant 130
- sputter etching 191–2, 213
- sputtering 186
- sputtering yields 191–2
- square microlenses 280–1
- SRIM (Stopping and Range of Ions in Matter) suite 190–1
- standard flows 308–10
- stencils 199, 218–37
  - limitations of stencil technology 232–3
  - nanofabrication using nanostencils 227–32
    - multilayer patterning with alignment 231
  - planar surfaces 227–9
  - recessed surfaces 230–1
  - scanned AFM nanostencil 231–2
  - surface patterning by deposition through 220–4
  - ultra-thin solid-state membranes 224–7
    - fabrication of nanostencils 225–6, 227
    - full-wafer nanostencil for high-throughput nanopatterning 226
    - materials 224–5
- Stokes equation 308, 309
- stopping power 188, 189
- straggling 188
- stress
  - bending of nanostencils 233
  - patterning by stress for metal/polymer bilayer 175–81
- stripes 313–14
- strong segregation limit 3
- SU-8 polymer 196, 225
- substrate
  - chemical confinement from 62
  - conductive substrate materials 90–3, 94
  - inkjet printing 293–4
  - new substrates and chemomechanical surface modification 145
- subtractive processes 267
- surface charge patterning 313–15
- surface chemistry patterning 315–16
- surface-directed spinodal decomposition (SDSD) 42
- surface energy-assisted inkjet 355
- surface force microscopy (SFM) 46–7, 50–1, 52
- surface roughness 50–1, 53, 55
- surfactants 353–4
- Sylgard 184 (184-PDMS) 84, 87
- symmetrically wetting polymer blends 48–57
- tandem accelerator 203, 205
- Taylor-Aris dispersion 303
- terminal group, and photo-oxidation of SAMs 243, 246–7
- ternary polymer blends 63–4
- terraces 6–8
- thermal desorption 252–3
- thermal inkjet printer 270, 352
- thermal methods for long-range ordering 23–4
- thermal transfer printing 389–95, 396
- thermally-induced capillarity 156–8
- thermocycling 334–6
- thin film transistors (TFTs) 277, 373–4
- thin films
  - block copolymers
    - long-range ordering 23–32
    - islands, holes and terraces 6–8
    - morphology in 5–6
    - wetting layers and neutral substrates 8–10
  - confined *see* confined polymer thin films
  - polymer blends *see* polymer blends
- thiol 120–1
- alkanethiol SAMs 240–7

- three-dimensional mapping techniques 47–8
  - three-dimensional shadow masks 230
  - three-dimensional structures, nTP and 385–6
  - throughput 293
  - tip force 130, 131, 132
  - tissue engineering 290–1
  - ToF-SIMS 131–3
  - topographic patterning 311–13, 314, 315, 316
  - topographical confinement 62
  - total chemical analysis system, miniaturised 321
  - transistors
    - microcontact printing 380–1
    - nanotransfer printing 387, 388
    - thermal transfer printing 392–3, 394–5
    - thin film 277, 373–4
  - transparency masks 78, 79–84
    - fabrication 79–81
    - fabrication of photoresist-based masters using 81–4
  - transparent conductive oxides 93
  - transverse electro-osmotic pump 312–13, 314
  - trenches, nanoscale 258–9
  - triblock copolymers 2–3
  - triblock terpolymers 2–3
  - trilayer structure 48–57
  - trilevel pattern transfer process 21–2
  - triphenyldiamine (TPD) 349, 350
  - tube etching 250
  - tuning fork systems 250
  - turning channels 314–15, 317
  - two-dimensional domains 50, 52, 53
  
  - ultra-dense memory devices 1
  - ultra-thin liquid films 167–8
  - ultra-thin solid-state membranes 224–7
  
  - unstable states 41
  - UV curing inks 293
  - UV interference lithography 25–6
  - UV radiation 15–16
  
  - valves, elastomeric 302–7, 332
  - variable focal length lens arrays 282, 283
  - vertical cavity surface lasers (VCSELs) 273–4
    - collimation of output 282–3, 284
  - vertically-oriented microdomains 9–10, 20–1
  - viscosity of inks 353
  - voltage multiplier stack 203
  
  - wafer-level packaging 275–7
  - wave number 176, 177, 180
  - waveguides 283–5
  - wavelength 176, 177–8
  - wells 292
  - wet techniques for selective domain removal 13–16
  - wettability 315–16
  - wetting 39–40, 43–4
    - partial 165–7
      - surface-induced patterns of binary polymer blends 48–58
        - asymmetrically wetting blends 57–8
        - symmetrically wetting blends 48–57
  - wetting layers (brush layers) 8–9
  - wrinkling, spinodal 175–6, 177
    - see also* buckling
- X-ray reflectivity (XR) 46
- 
- yttrium oxide ( $Y_2O_3$ ) nanoparticles 355, 356
- zigzag microchannels 314–15, 317